The Dissertation Committee for Kory Michael Mueller certifies that this is the approved version of the following dissertation:

New Approaches to Functional Organic Electronics: Development of Redox Active Materials for Energy Applications

Committee:

Simon M. Humphrey, Supervisor

Michael J. Rose

Richard A. Jones

Jonathan L. Sessler

Joshua R. Farrell

New Approaches to Functional Organic Electronics: Development of Redox Active Materials for Energy Applications

by

Kory Michael Mueller, B.S.

Dissertation

Presented to the Faculty of the Graduate School of

The University of Texas at Austin

in Partial Fulfillment

of the Requirements

for the Degree of

Doctor of Philosophy

The University of Texas at Austin

May 2016

Dedication

First and foremost to my wife, Deanna:

You give purpose to everything I do.

To my parents:

Thank you for all the love and support you have given me.

To Dr. Margaret Hill:

Thank you for igniting my love of science.

Acknowledgements

I would like to thank Dr. Bradley Holliday for his unwavering support and guidance, and for giving me the freedom to explore in my research. I would also like to thank Dr. Simon Humphrey for his gracious backing and guidance. To Dr. Raluca Gearba, thank you for your endless help and enlightening discussions.

I would like to thank Dr. Matt Raiford and Dr. Minh Nguyen for taking me under their wings and taking the time to teach me the fundamental skills to perform chemical research. You helped me through my early years and I owe much of my success to the strong foundation built on your guidance. I will always value your friendship.

To Matthew Moore, Owen Williams, Leander Cinninger, Dr. Daniel Evans, Dr. Sarah Moench and Dr. Kristen Suhr; I would like to say thank you for your generous help, suggestions, critiques and, most importantly, your friendship. You pushed me to compete at your level. Navigating graduate school with you has made the past five years a wonderful experience.

I am grateful to my parents, Randy and Cindy Mueller, for all of the sacrifices they made and time they dedicated to giving me every opportunity to succeed. I would also like to thank Richard and Carol Dippold for their steadfast support.

Finally, I would like to thank my wife, Deanna Mueller, whose love, support, sacrifices and patience go beyond repayment. I could not be where I am today without you by my side. I know how blessed I am.

To all of you who made this work possible – Thank you.

New Approaches to Functional Organic Electronics: Development of Redox Active Materials for Energy Applications

Kory Michael Mueller, Ph.D.

The University of Texas at Austin, 2016

Supervisor: Simon M. Humphrey

The electrochemical functionalization of graphene using diaryliodonium salts was explored as a new avenue for altering the physical, chemical and electronic properties of graphene. Control of the surface density of the grafted molecules was achievable up to 2.5 x 10^{14} molecules·cm^{-2}, and the grafting ratio of asymmetric diaryliodonium salts was shown to be unperturbed by the electronic nature of the aryl rings. Scanning Tunneling Microscopy coupled with Density Functional Theory calculations provided valuable insight into the mechanism by which the molecular grafting process is controlled.

Two bisphosphine ligands were synthesized to explore their ability to support light emission in copper(I) complexes. The ligand 3,4-bis(diphenylphosphino)thiophene was shown to efficiently promote thermally activated delayed fluorescence, while (5,5'-dimethyl-[2,2'-bithiophene]-3,3'-diyl)bis(diphenylphosphane)-supported complexes were found to exhibit dual emission and luminescent thermochromism.

A rare example of electronic communication between rhodium centers bridged by 9,10-diisocyanoanthracene was observed. Through the performed studies, it was shown that the electronic nature of the ligand *trans*- to the molecular bridge plays a critical role in facilitating communication. Switching from a neutral PNP pincer ligand to an anionic, cyclometallated PCP pincer ligand raised the energy of the lower lying occupied

molecular orbitals with respect to the singly occupied molecular orbital, and inverted the energetic ordering of the rhodium-based *d*-orbitals to better facilitate electronic communication though the system.

The triplet state in organic photovoltaic devices has become increasingly more important in improving device efficiencies. To better understand the triplet excited state in polythiophene based materials, a library of oligothiophenes has been synthesized. The photophyscial and electrochemical properties of these materials have been cataloged and studies into the structure and delocalization of the triplet exciton using transient resonance Raman spectroscopy have been performed.

Finally, a novel separation system for nuclear waste remediation consisting of ionophoric ligands chemically tethered to a conducting polymer core have been synthesized. These systems were shown to reversibly coordinate Th(IV) ions from solution based on the oxidation state of the polymer core. Furthermore, these systems were shown to undergo multiple extraction cycles and exhibit selective ion extraction.

Table of Contents

List of Tables

List of Figures

List of Schemes

Chapter 1: Functional Organic Electronics

1.1. Electronically Active Organic Materials

Organic electroactive materials have revolutionized the technological industry. The versatility in synthesis and processing, reduced production costs, control in design and inherent flexibility in the resulting devices makes the field of organic electronics highly lucrative.[1,2] However, despite the fact that the breadth of this field is of such great size that it precludes complete review, advancements are needed to push many of these technologies to a point where they will be commercially viable. We present herein new methodologies and studies of electronically modified materials for applications in the fields of graphene modification,[3–5] organic light emitting diodes (OLEDs),[6–10] mixed valence species,[11–13]organic photovoltaics (OPVs)[10,14–16] and conducting polymers.[10,17–19]

1.2. Covalent Functionalization of Graphene

For a material that was described by the Nobel Prize committee as "A thin flake of ordinary carbon, just one atom thick…" few, if any, materials ever synthesized can match the impressive list of physical properties that are displayed by graphene. True single layer graphene, which was first isolated in a manner which preserved its inherent electronic structure by Novoselov and Geim in 2004,[20] has shown impressive physical and chemical properties, including high electron mobility (2.5 x 10^5 cm^2 V^{-1} s^{-1}),[21] broadband optical transparency (98%),[22] excellent thermal conductivity (3000 W m^{-1} K^{-1}) and high elastic modulus (1 TPa).[23] Such qualities have made graphene an ideal material for use in microelectronic devices and one of the most promising replacements to silicon-based technologies, as well as indium tin oxide (ITO) supported devices. Examples of potential applications include, but are certainly not limited to, biomaterials, catalysis, supercapacitors, batteries, electrode materials, transistors, optoelectronic

devices, sensors and flexible electronics. The literature surrounding these graphene based materials is extensive and several recent reviews have been dedicated to these topics.[3,4,24–28]

In practice, the use of graphene in various applications requires chemical modification in order to tailor the chemical and electronic properties of the graphene sheet to the desired function. For example, graphene is a relatively insoluble material. Therefore, to use graphene in solution based applications and to ease processing requirements for many devices, attachment of solubilizing functionalities is often desired.[26] Another reason for which graphene is commonly modified is to increase its sensitivity as a sensor material by attaching chemioselective moieties to the surface. It is important to note that graphene itself is a zero band gap material as the valence and conductions bands actually touch at the Dirac points. Such an electronic structure limits the usefulness of pristine graphene as a field effect transistor.[24] Precise tuning of this band gap has been one of the key drivers for the development of well controlled modification techniques (Figure 1.1).

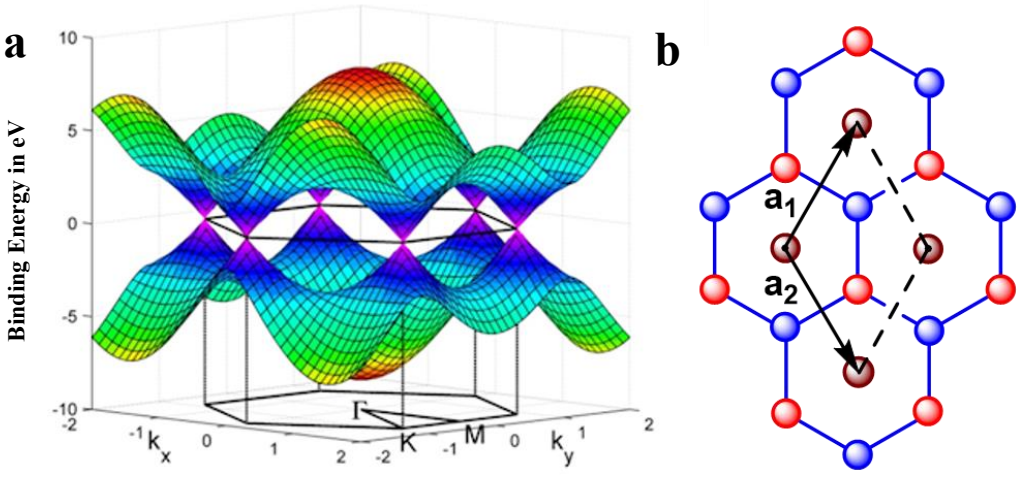

Figure 1.1. Electronic and physical structure of graphene. a) Visualization of the electronic band structure of graphene in the first Brillouin zone. b) Diagram of the Bravais lattice showing the A (red) and B (blue) sublattices.

A large number of functionalization strategies have been investigated to covalently modify graphene including cycloaddition reactions, condensation reactions with graphene oxide and covalent functionalization via free radical grafting. Recent reviews have been dedicated to compiling these varied techniques.[25,26,29–32] While a complete review of the methods of graphene modification are beyond the scope of this text, highlights of some of the more common methods for the modification of graphene are covered.

The use of dieneophiles to covalently modify graphene takes advantage of the extended π-network of graphene. Diels-Alder reactions can be used to modify the surface of graphene in which the graphene sheet can act either as the diene or the dienophile depending on the reaction conditions and substrates involved.[33] Azomethine ylides may undergo 1,3-dipolar cycloadditions with this π-system in a reaction isoelectronic to the analogous Diels-Alder reaction (Figure 1.2a). This technique has been extensively used for the modification of carbon based systems such as nanotubes, fullerenes and graphene.[26] Georgakilas *et al*.[34], for example, demonstrated that this technique may be used to covalently attach solubilizing groups to graphene. The thermally or photochemically induced decomposition of organic azides generates a nitrene intermediate that has been shown to be reactive with the graphene's π-network as well, forming a three-membered aziridine ring (Figure 1.2b).[35] Studies of the functionalization of epitaxial graphene (EG) with azidotrimethylsilane as the nitrene precursor demonstrated covalent attachments primarily on the basal planes and an increasing band gap that is associated with increasing modification surface densities.[36]

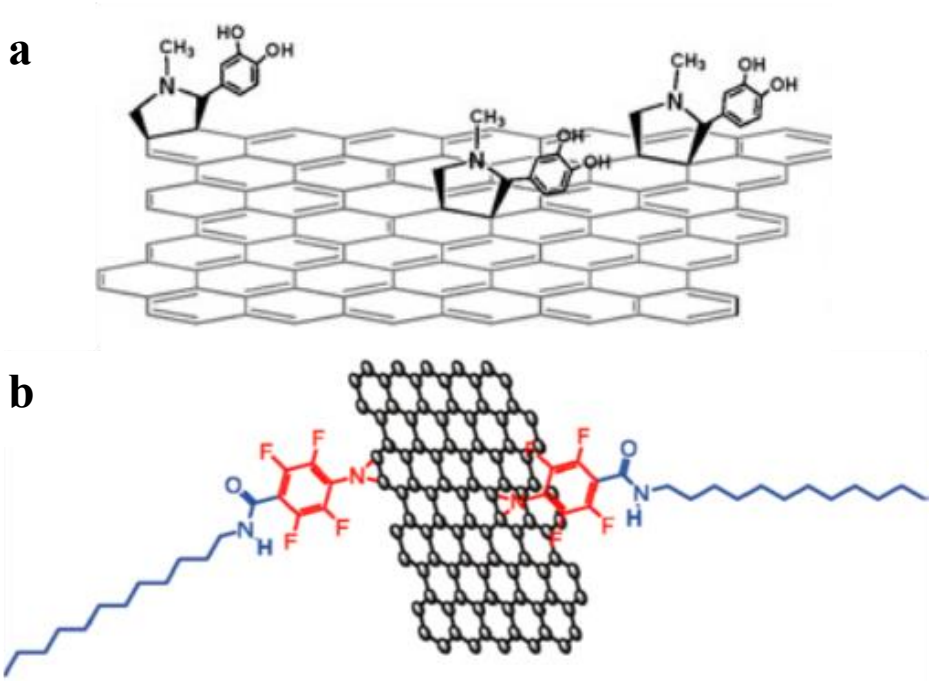

Figure 1.2. Cycloaddition reactions with graphene. a) Resulting graphene structure following the cycloaddition of azomethine ylide[34] and b) perfluorophenyl azide to the surface of graphene to improve solubility in common solvents.[35]

By far, the most common method of modifying graphene is through reactions of oxygenated functionalities that are present from the preparation of graphene oxide (GO). The popularity of this method is largely derived from the ease of synthesis and the low cost of production of GO from cheap and abundant precursors. First reported in 1958, Hummers and Offeman prepared GO using powdered flake graphite suspended in a highly oxidizing solution of potassium permanganate, sodium nitrate and sulfuric acid.[37] Since then, a large number of methods have been developed to synthesis GO using various solvents and oxidizing agents[38,39] and the subsequent functionalization through reactions with the oxygenated moieties have been well documented.[26,30,38,40,41] Generation of the GO leads to a large variety of oxygenated sites mainly comprised of hydroxyl,

epoxy, carboxy and carbonyl functional groups. These oxygenated sites may then undergo further reactions to link on a large variety of modifying groups (Figure 1.3). Frequently, following synthetic modifications, the remaining unfunctionalized oxygenated sites are reduced to restore as much of the π-system as possible to increase the conductivity of the final material. [39,42–44]

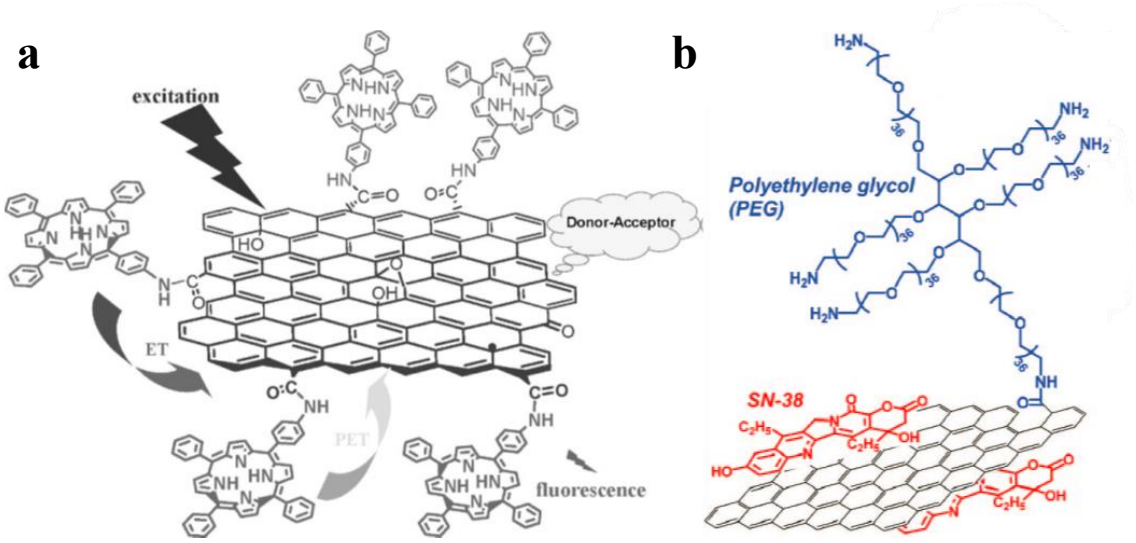

Figure 1.3. Functionalization of graphene via graphene oxide. a) A graphene hybrid material for optoelectronic applications synthesized by attaching 5-4 (aminophenyl)-10, 15, 20-triphenyl porphyrin to graphene oxide through a condensation reaction to form an amide linkage.[45] b) A drug delivery system using PEGylated graphene oxide attached via amide linkages to solubilize graphene π- stacked with the cancer fighting drug SN-38.[46]

The modification of graphene with free radical graftants represents the final major method of covalently modifying the chemical, physical and electronic properties of graphene. The thermally, photochemically or electrochemically generated organic radicals attack the delocalized π-network. Benzoyl peroxides have been shown to undergo photolytic decomposition in the presence of graphene, releasing CO_2 and

generating an organic radical which subsequently reacts with the graphene substrate (Figure 1.4a).[47] Much more common is the use of aryl diazonium salts as the free radical precursor (Figure 1.4b). For these precursors, electron transfer to the diazonium cation leads to the liberation of one equivalent of nitrogen gas and the generation of an aryl radical.[48]

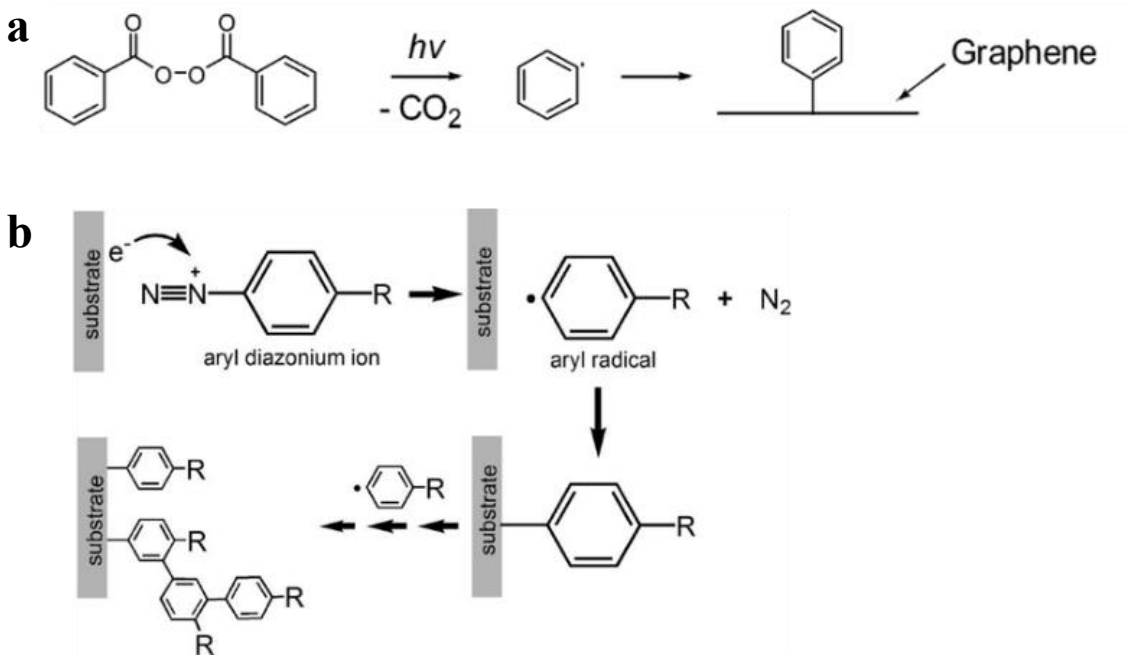

Figure 1.4. Free radical grafting to graphene. a) Simplified reaction diagram of the functionalization of graphene by free radicals generated by the photochemically-induced decomposition of benzoyl peroxide.[47] b) Free radical grafting of an aryl ring generated by electron transfer to an aryl diazonium salt followed by subsequent liberation of dinitrogen gas.[48]

Diazonium salts represent one of the most well studied methods for elucidating the effects of chemical modifications on the physical and electronic structure of graphene due to the ease of synthesis, the facile grafting procedures, the stability of the products and the relatively well defined mode of attachment.[29] Investigations into the grafting

mechanism of aryl diazonium salts with graphene, as well as the effects of the molecular modifications on band gap engineering, charge carrier transport, molecular doping and magnetic properties has made diazonium chemistry an intense area of research.[29,31,48–66] Despite the utility demonstrated by diazonium salts, there are some difficulties associated with these materials; the most important of these being the relatively low potential of reduction which can lead to issues in controlling the sites of modification, as well as the degree to which the substrate is modified.

As depicted in Figure 1.5, there is a large overlap of the occupied states of graphene (as well as most other electrode materials) with the unoccupied states of the diazonium salts. This results in spontaneous electron transfer and subsequent modification of the surface of graphene.[66] As such, radical grafting precursors displaying enhanced control of the modification process continues to be desired.

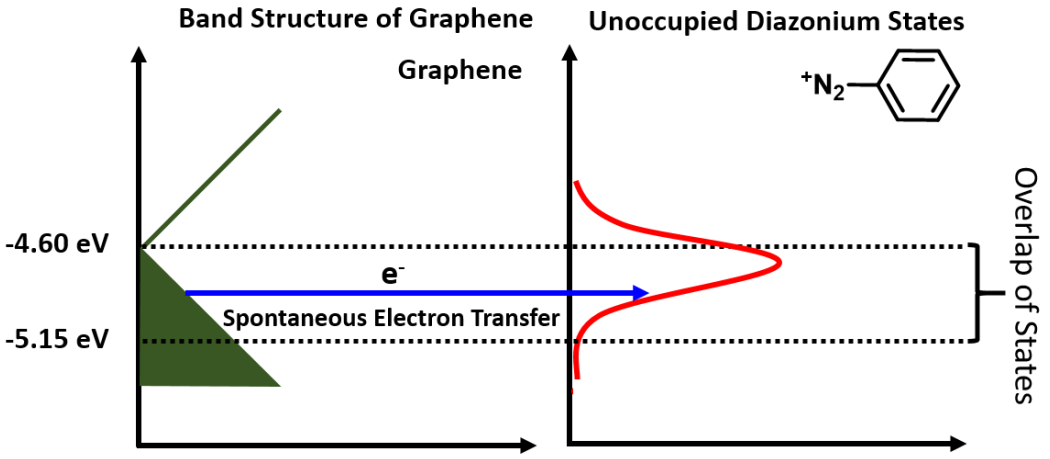

Figure 1.5. Spontaneous electron transfer to diazonium salts. Density of states (DOS) diagram depicting the overlap of the occupied states of graphene with the unoccupied states of an aryl diazonium salt. As a result of this overlap, spontaneous reduction of the diazonium salt can occur, making precise control over molecular grafting difficult.[66]

Diaryliodonium salts are a class of compounds containing a hypervalent iodine(III) atom coordinated by two aryl rings, resulting in a molecule with a single positive charge. These materials have been shown in the literature to be efficient precursors for the radical grafting of aryl rings onto a variety of substrates including glassy carbon[67], platinum[68], gold[69], conductive silicon[68] and indium tin oxide.[70] Furthermore, enhanced control of the grafting densities may be achieved using iodonium precursors, as a potential must be applied to the desired substrate to induce molecular grafting. A preliminary study has shown diaryliodonium salts to be capable of grafting to the surface of graphene[71] but much work remains in the development of this technique and the subsequent studies of the graftants effects on the electronic properties of graphene.

1.3. Organic Light Emitting Diodes (OLEDs)

Similar to graphene, the field of OLEDs has been one of rapid expansion. The wealth of literature surrounding OLED technology is astounding considering it was only in 1987 that Tang and van Slyke[72] first reported an electroluminescent device with an external quantum efficiency of 1%, demonstrating the potential utility of the technology. This device was designed using purely fluorescent materials. Within 12 years, movement to phosphorescent materials utilizing heavy transition metals with high spin-orbit coupling constants has drastically improved OLED performance and continues to dominate the literature today.[73,74] To facilitate the rapid progress of OLED technologies, a significant amount of integration from different scientific fields such as electrical engineering, synthetic chemistry, polymer chemistry, electrochemistry and materials science has been crucial to this success.[75] Detailed reviews of the literature surrounding

OLED materials, device fabrication and device architectures can be found in the following references.[6–10,75]

A representative OLED device structure is shown in Figure 1.6. OLEDs are typically fabricated in a stacked structure comprised of several layers of transport materials leading to a light emitting layer, all of which is sealed between a metal cathode and a transparent conductive oxide anode.

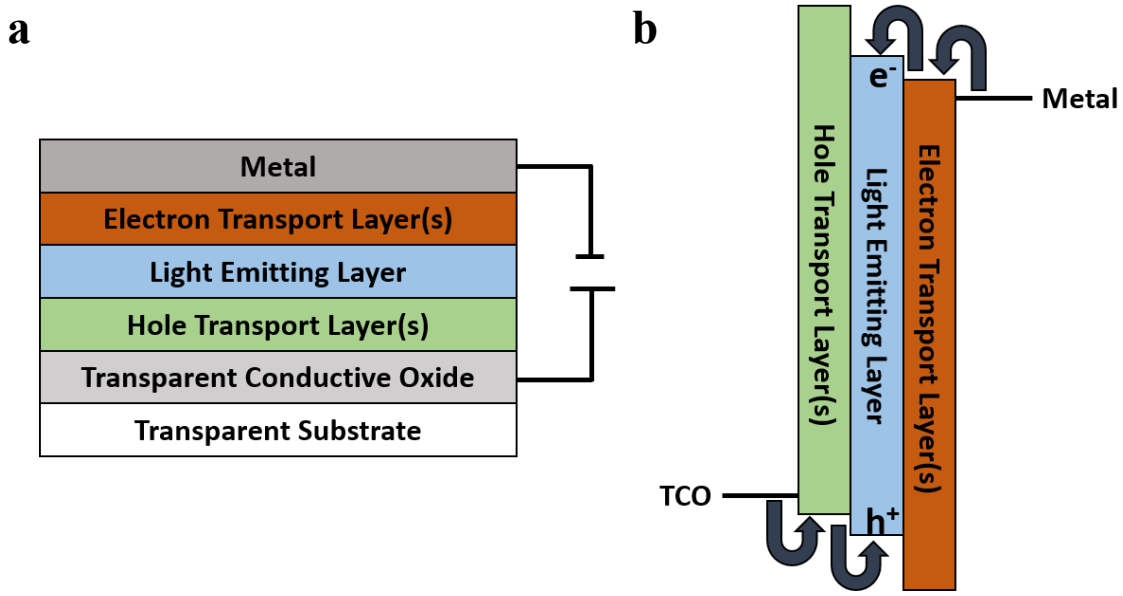

Figure 1.6. OLED architecture and operation. a) Typical stack structure of an organic light emitting diode (OLED). b) Simplified diagram of charge transport through an OLED device resulting in electron-hole recombination in the light-emitting layer which electrochemically generates an excited state.

Application of a potential to the respective electrodes injects charges into the device. Moving in towards the center of the device, hole and electron transfer layers facilitate charge migration to the light emitting layer where electron-hole recombination occurs on the light emitting material to form an electrochemically generated excited state which may be harvested as a photon.[76] Since electrochemical generation of excitons is

not governed by quantum mechanical selection rules, a stochastic distribution of singlet to triplet excitons is generated resulting in 25% singlet excitons and 75% triplet excitons.[77,78] While harvesting of singlet excitons is a spin-allowed process, triplet harvesting is spin forbidden, and special design strategies must be employed to collect these states. [8,75,76]

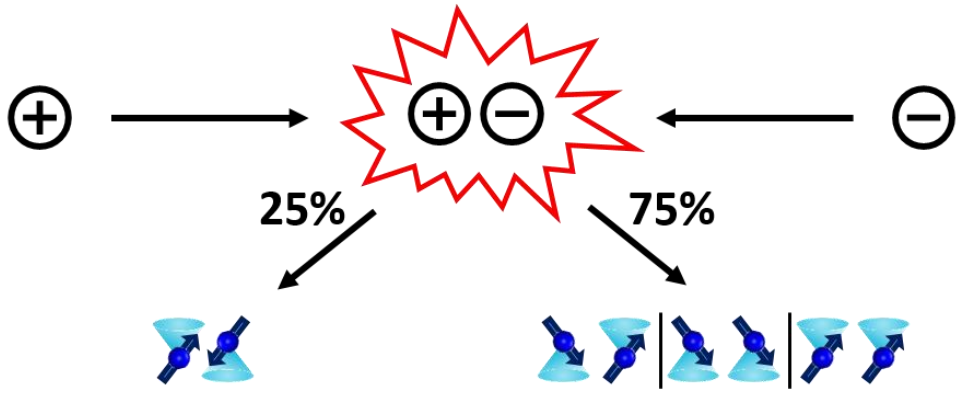

Figure 1.7. Spin distribution of electrochemically generated excited states. Electrochemical generation of an excited states is not governed by quantum mechanical selection rules, resulting in a statistical distribution of the excited states. Three of the possible four spin distributions in a closed-shell system result in a triplet state generating a 3:1 distribution of triplet excitons to singlet excitons.

As mentioned previously, incorporation of heavy atoms into the light emitting layer is currently the most widely researched and utilized strategy for improving quantum efficiencies as it addresses the issue created by the triplet excited states. Atoms with high spin-orbit coupling constants can drastically increase the rates of intersystem crossing, leading to much faster radiative rates from the triplet states. Metal complexes based on iridium and platinum are the most commonly employed for such systems as their large spin-orbit coupling constants and exceptional stability in both the ground and excited states make them ideal for light emitting applications. Numerous recent reviews have

been published explicitly on these systems.[79–85] Theoretically, internal quantum efficiencies near 100%, and external quantum efficiencies near 25%, should be achievable using these complexes and indeed have been approached.[86]

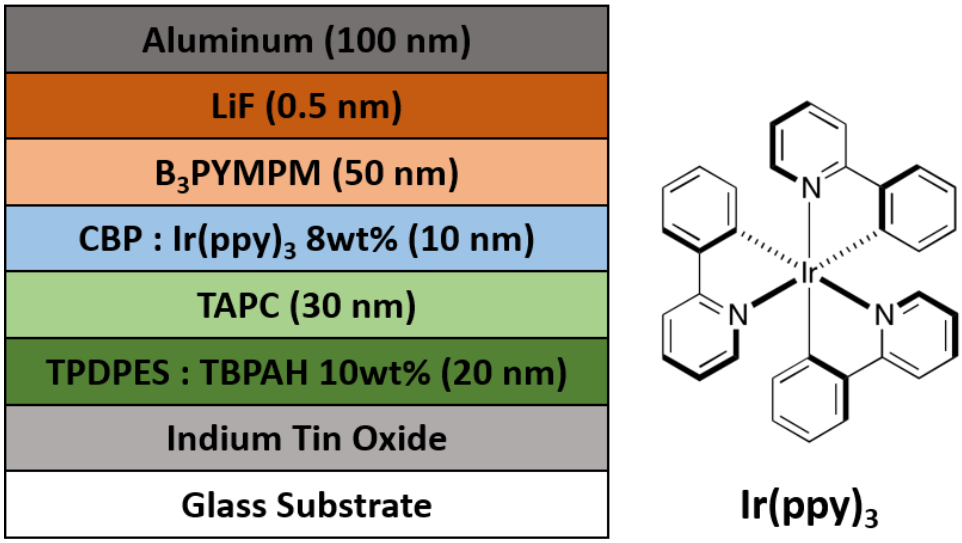

Figure 1.8. Device structure of a highly efficient OLED based on an iridium emitter. This device reported by Tanaka *et al.* [86] reached external quantum efficiencies up to 29%. Bis-4,6-(3,5-di-3-pyridylphenyl)-2-methylpyrimidine (B_3PYMPM); poly(arylene ether sulfone)-containing tetraphenylbenzidine (TPDPES); tris(4-bromophenyl)aminium hexachloroantimonate (TBPAH); 1,1-bis[4-[*N*,*N*-di(*p*-tolyl)amino]phenyl]cyclohexane (TAPC); 4,4'-*N*,*N'*-dicarbazolylbiphenyl (CBP).

To date, only phosphorescent emitters based on iridium have been able to match commercial demands. Despite their success, the expense of these precious metals and their low earth abundance make the use of cheaper, more earth abundant metals, such as copper, an attractive alternative.[87] However, since copper has a much lower spin-orbit coupling constant, alternative mechanisms for collecting the energy placed in the triplet excited states must be employed. Fortunately, design strategies based on thermally

activated delayed fluorescence, which can efficiently convert triplet excitons to singlet excitons using only ambient thermal energy, and copper-cluster based chemistries have been shown to be efficient strategies.[88,89] Several reviews have been written on copper based emitters.[88–94] While the field has not yet reached maturity compared to iridium and platinum based systems, highly efficient systems have been realized[95] and the explored materials hold promise as potential replacements for currently utilized emissive materials.[93]

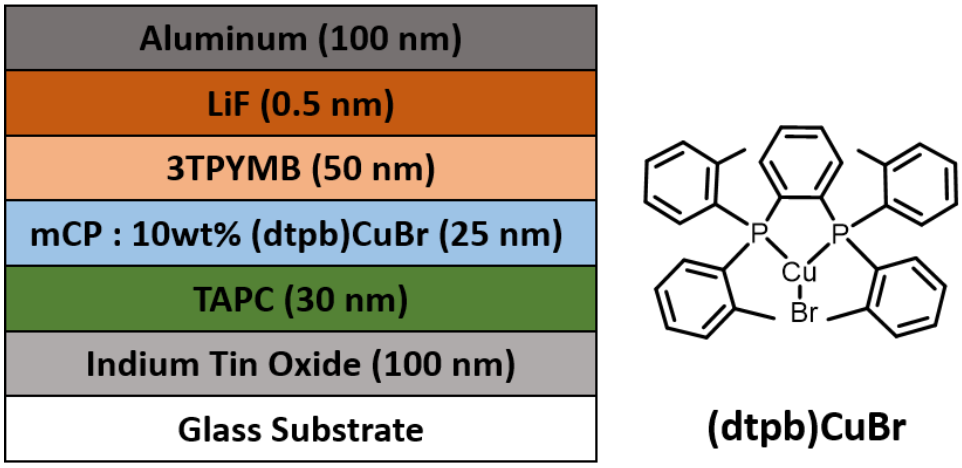

Figure 1.9. Device structure of a highly efficient OLED based a copper emitter. This device reported by Hashimoto *et al.* [95] reached external quantum efficiencies up to 21.3%. 1,1-bis[4-[*N*,*N*-di(*p*-tolyl)amino]phenyl]-cyclohexane (TAPC); 1,3-bis(carbazol-9-yl)benzene (mCP); tris[2,4,6-trimethyl-3-(pyridine-3-yl)phenyl]borane (3TPYMB).

The relative novelty of copper(I) complexes in the field of light emitting diodes leaves much to be explored. While the effects of supporting diimine ligands have been well documented, relatively few bis(phosphine) ligands have been utilized in these studies.[88,89,94] The development of new bis(phosphine) ligands and investigations into

their structure-property relationships in emissive copper complexes has the potential to open the door to new classes of efficient low-cost emissive materials.

1.4. Mixed Valence Compounds and Electronic Communication

Electron movement, distribution and delocalization stands directly at the heart of chemistry. Mixed valence compounds and materials displaying electronic communication constitute a unique class of materials in which the valence electrons and oxidation states of the atoms in the materials are not well defined as integer values, but rather as averaged states. Such systems provide an opportunity to study fundamental electron transfer processes in controlled, well defined systems.[96–99]

As the number of mixed valence compounds began to grow, they were classified by Robin and Day[100] into three classes of compounds based on the degree of communication between the redox centers in the system. In a class I systems, no electronic communication is observed between the redox centers and the electrons are trapped resulting in each redox site behaving independently of one another. At the other end of the spectrum, if there is a high degree of electronic communication between redox centers and the electron is completely delocalized over the centers of interest, it is labeled a class III system. Everything in between these two extremes fall into the class II category which is comprised of a large range of degrees of electronic communication and delocalization. In practice, true class III systems are rare. The distinguishing trait between a class II and a class III system is that a class III system will have delocalization on the vibrational time scale while class II will be localized.[101] Investigations into the electronic and photophysical properties of materials that border the class II/class III transition has been an area of considerable research.[102,103] To properly describe such systems, a complete theoretical treatment of mixed valence compounds within the formalisms

outlined by Marcus[104] and Hush[105] can be found in later publications by Hush[106,107]. A qualitative diagram and description of the different classes of mixed valence compounds following Marcus-Hush theory may be found in Figure 1.10 and the following text.

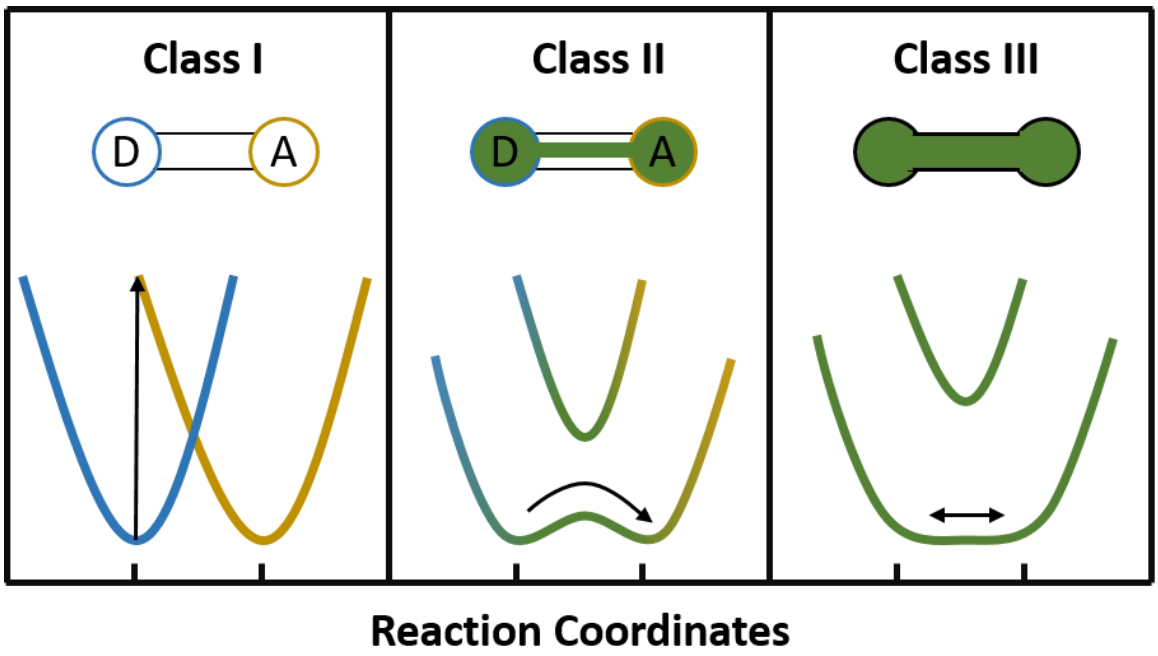

Figure 1.10. Electronic communication in mixed valence complexes. Qualitative diagram illustrating the potential energy planes and barriers for electron transfer for a two component system demonstrating the three classes of mixed valence compounds under the classification system set forth by Robin and Day.[100]

In a class I system (left), the electronic communication between the redox centers is insignificant, leading to localized donor and acceptor moieties. No mixing of the wavefunctions will be observed and electron transfer to the acceptor is achieved by absorption of light as the barrier to thermally-induced transfer is too high. In class II systems (center), electronic communication between the formal donor and acceptor moieties is present leading to a mixing of the wavefunctions. However, a barrier to electron transfer still exists, requiring either a photon or sufficient thermal energy to

stimulate electron transfer. In a class III system (right), full electronic communication and overlap of the wavefunctions is achieved. The distinction of donor and acceptor redox centers in the molecule is no longer relevant and the electron is fully delocalized across the two redox centers.

A large number of mixed valance transition metal complexes with bridging ligands are associated with d^5-d^6 metal centers as they tend to have similar coordination numbers and geometries.[103] Bridged metal centers with alternative electron counts, however, are much rarer. Rhodium metal centers are most commonly found in the +1 (d^8) and the +3 (d^6) oxidation state, but are capable of reaching the –1 (d^{10}) to +6 (d^3) states, all of which tend to have significantly different coordination numbers and geometric demands when similar ligand sets are applied.[108] This makes the design of mixed valence rhodium coordination compounds difficult. In the literature only a handful rhodium mixed valence systems have been realized (excluding systems containing metal-metal bonds). These systems are realized over several mixed oxidation states including Rh(I)-Rh(-I)[109], Rh(I)-Rh(II)[110–113], and Rh(II)-Rh(III)[114–116] (Figure 1.11).

The sparsity of the field leaves room for both fundamental and practical advances. Further development of mixed valence complexes of rhodium with unique ligand sets would not only provide structural and electronic insight into the preparation of these materials, but could potentially exhibit new and interesting reactivities for molecular and catalytic transformations, given the propensity of rhodium for facilitating such reactions.[109,117]

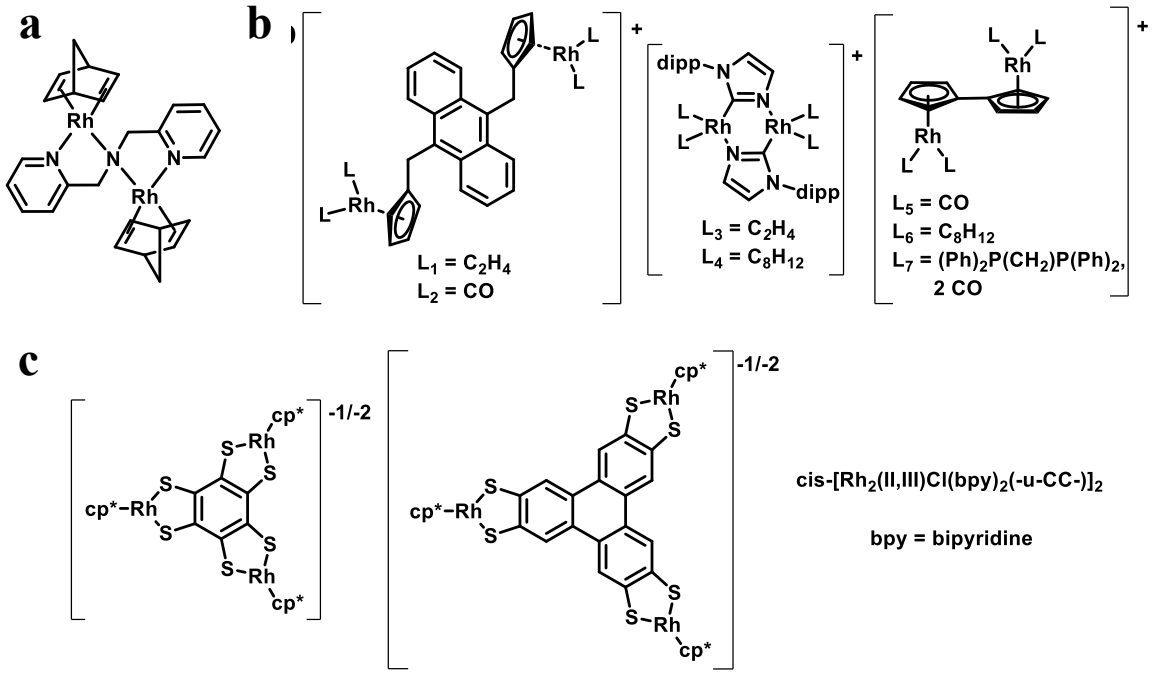

Figure 1.11. Molecular structures of rhodium mixed valence complexes. Averaged states between the a) Rh(I) and Rh(–I) states, b) the Rh(I) and Rh(II) states and c) Rh(II) and Rh(III) states are shown.

1.5. CONDUCTING POLYMERS IN SEPARATION APPLICATIONS

The ability to conduct and transport charges through an organic polymer systems was a significant advancement in the field of organic electronics and eventually led to a Nobel Prize in Chemistry for the discovery and development of conducting polymers which was awarded to Alan Heeger, Alan MacDiarmid and Hideki Shirakawa (2000).[118] These semiconducting materials have been developed extensively throughout the years and have found use in a wide range of applications.[17–19] The conductive behavior of these films is the result of the conjugated structure in the materials allowing for facile movement of the charge. This movement can be either charge transfer through the conjugated system of double bonds or by hopping between polymeric charges. Furthermore, conductivity in these systems may be greatly increased by doping of the

polymer either chemically or electrochemically, as the charge carrier concentrations are drastically increased with respect to the neutral systems.[119,120]

Separation methods using conductive polymers take advantage of the ability to attenuate the extraction capabilities of the polymeric system by electrochemically altering the charge carrier concentrations of the polymer backbone. For example, the efficient extraction of ions from solution may be greatly increased by doping the polymers with the opposite charge of the ion of interest. Furthermore, stimulated release may be achieved by altering the electronics of the polymer to coulombically repel the ions and release the ions back into solution to collect the analyte and regenerate an active separation material. In an alternate mechanism, doping the polymer with more or less electron density has been shown to modulate the coordinative ability of ligands which are covalently bound to the polymer core. Several reviews may be found covering systems which use electroactive polymers for separation applications.[121–127] Polypyrrole has been used quite frequently in these applications. Polypyrrole modified electrodes have been used to extract and detect nitrite ions by applying positive potentials to the polymer film to increase nitrite uptake as a necessity of charge balance.[128] Similar studies using potentiometric control were performed using polypyrrole coated electrodes which were sensitive to the presence of bromide ions.[129] Polyaniline films have been used extensively in the removal of hexavalent chromium, allowing for increased Cr(VI) removal rates and capacities.[130]

Polythiophene based systems have demonstrated utility in the field of separations as well.[131–133] Yates *et al*.[133] used poly(3-dodecylthiophene) to preconcentrate and release arsenobetaine in aqueous solution. Interactions with the hydrophobic dodecyl chains of the alkylated polythiophene system resulted in the extraction of arsenobetaine

from aqueous solution. This extraction was readily reversed by application of an external potential to the polymer, doping the system and inducing the release of the analyte.

More interesting systems are obtained when ionophoric ligands are incorporated onto the polymer backbone, which can lead to both increased selectivity and uptake in the conductive polymer films.[125] An interesting example by Lyskawa *et al.*[134] incorporated a tetrathiafulvalene-based redox responsive ligand onto poly(3,4-ethylenedixoythiophene). This system was able to demonstrate the uptake of Pb^{2+} ions when the concentration of positive charge carriers in the system is low and subsequently show ion expulsion when an oxidative potential is applied to the system. As such, this was the first polymeric system to demonstrate redox mediated ligand-based uptake and release of ions in solution, operating primarily on electrostatic control of the binding.

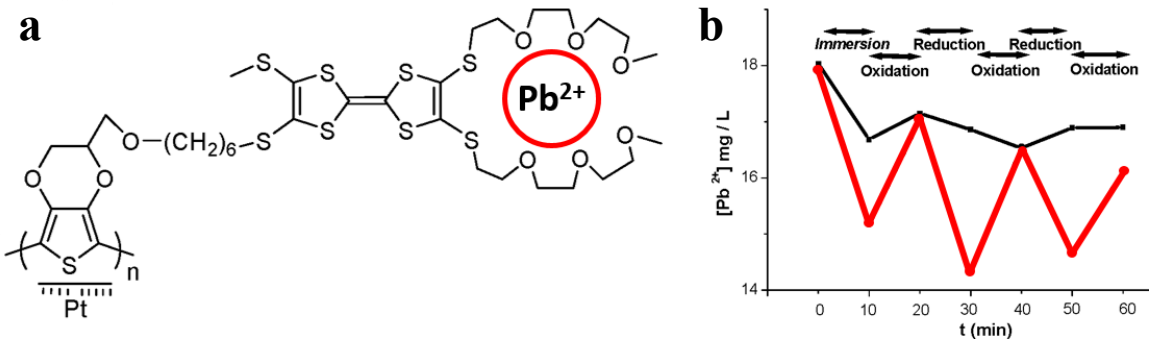

Figure 1.12. Polymer extraction with ionophoric ligands. a) Conductive polymer system designed by Lyskawa *et al.*[134] to reversibly bind lead(II) under redox mediated control. b) The polymer system demonstrates Pb^{2+} uptake from solution upon immersion. Electrochemical oxidation of the polymer induces release of the lead ions which may be reversed at lower potentials. This system is capable of performing efficiently over multiple cycles (red trace).

An interesting example of an electrochemically controlled polymeric system containing a hemilabile ligand was reported by the Mirkin lab.[135] In this study, a terthienyl ruthenium(II) complex was synthesized in which direct coordination of a

thienyl unit was observed. Electrochemical oxidation of this core was shown to induce dissociation of the thienyl-ruthenium(II) bond, removing electron density from the metal center. In the model system, the removal of electron density from the metal center drastically increased the reactivity of the Ru(II) center with small coordinating ligands such as acetonitrile.

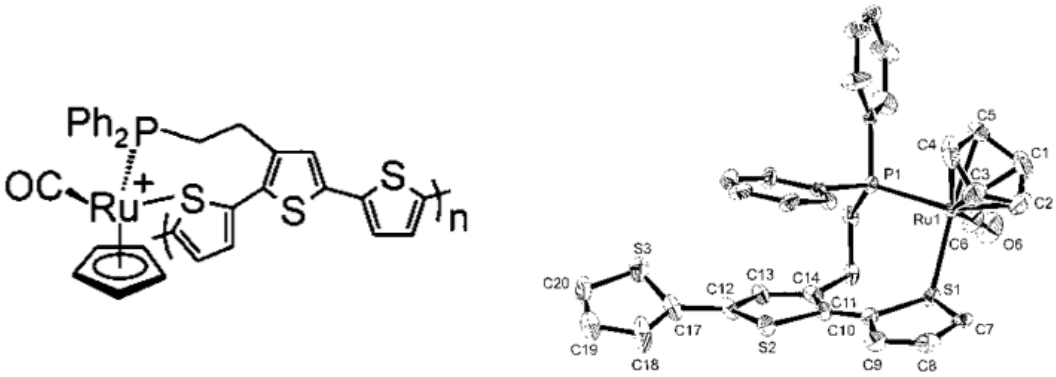

Figure 1.13. Hemilabile polymeric coordination systems. Polymeric hemilabile metal complex (left) synthesized by Weinberger *et al.*[135] capable of modulating the electron density at the metal center. Crystal structure (right) of the monomeric complex illustrating coordination of a thiophene ring to the Ru(II) center.

Application of these redox mediated separation systems would be of great utility to the field of nuclear waste separation as it provides a simple method of selective extraction without generating large volumes of additional waste. Current technologies for complexing, extracting and separating specific components of nuclear waste are focused on using platform based systems such as calixarenes[136], cavitands[137,138] and triopodal[139,140] bases to preorganize selective and efficient extractants such as carbamoylmethylphosphine oxides and diglycolamides in order to achieve cooperative effects.[141–143] To date, no such systems exist in the literature which preorganize these ligand systems onto a conductive polymer backbone.

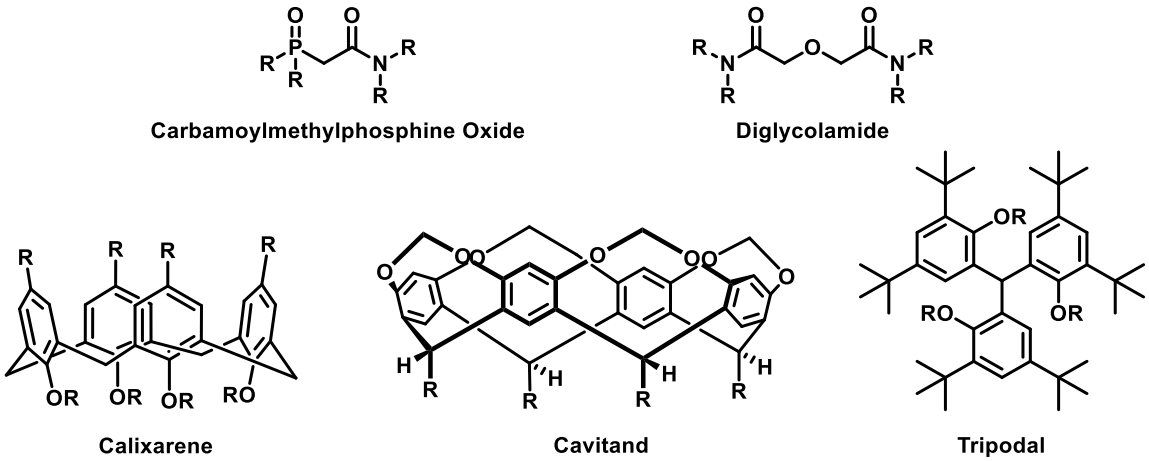

Figure 1.14. General structures of carbamoylmethylphosphine oxide and diglycolamide ligands commonly used in the separation of lanthanides from actinides in nuclear waste (top row). Common platform systems used to preorganize various ligands to improve extraction efficiency and selectivity (bottom row).

1.6. Organic Photovoltaic Devices: Harvesting Triplet Excitons

Improving the efficiency of organic photovoltaic (OPV) devices remains an intense area of research as the ease of synthetic modification and versatility in processing makes OPVs suitable in applications where the rigidity of silicon based inorganic solar cells proves impractical. Several reviews on recent advances have been published.[10,14–16] One of the major challenges within the industry is how to facility the efficient diffusion, separation and collection of the photochemically-generated excited states to the interfaces between the donor and acceptor materials.

To maximize the performance of OPV devices, a delicate balance of the thickness of the active absorbing layer must be struck. If the absorbing layer is too thin, the optical density of the absorbing layer will be low leading to poor photon harvesting. However, if the active layer is too thick, the diffusion path length for the exciton will be too great, leading to electron-hole recombination prior to encountering an interfacial boundary. One

of the most commonly explored options is the use of bulk heterojunction materials in which the donor and acceptor materials are inter-dispersed with one another to minimize the diffusion path length required while still allowing for deposition of thicker active layers.[14,144–147]

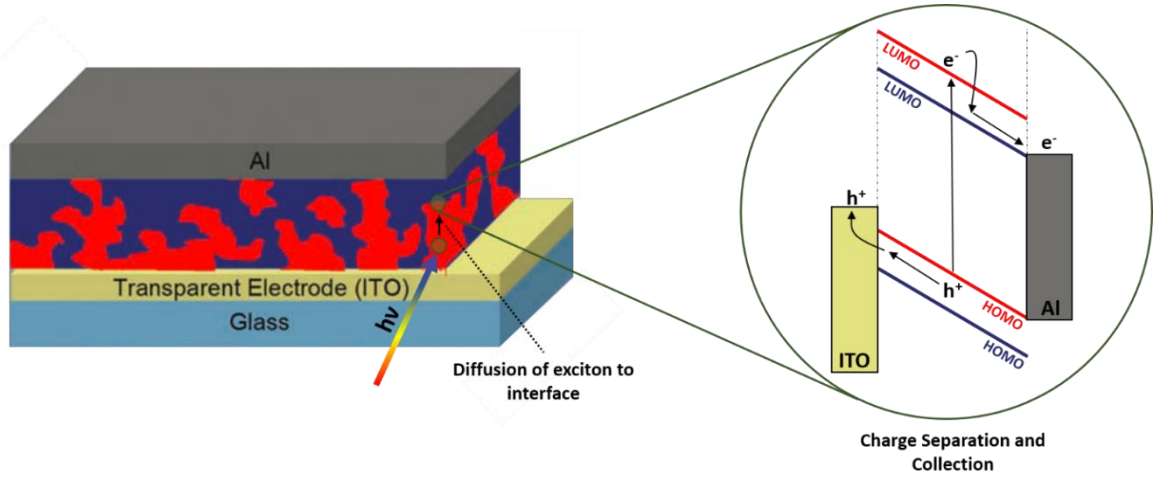

Figure 1.15. Bulk heterojunction OPVs allow for thicker active layers by distributing the donor and acceptor materials into randomly dispersed domains to decrease the average diffusion length required to reach an interfacial surface. Once the exciton has reached the interface, charge separation and collection may occur. Advanced strategies using ordered materials, such as rod-coil diblock co-polymers, are often employed to improved charge collection following charge separation by providing a direct path to the electrode materials.

More recently, strategies focused on harvesting triplet excitons in OPVs have been explored which take advantage of the intrinsic properties of the triplet excited state.[148–155] Singlet excitons are transferred primarily through dipole-dipole coupling which leads to Forester energy transfer mechanisms, limiting the diffusion path length to approximately 230 nm in an ideal system.[156] However, in practice, the diffusion lengths on the order of tens of nanometers are observed. This limits the thickness of the absorbing layers to approximately 100 nm. In contrast, the primary mechanism by which

triplet excitons diffuse in an OPV device is based on Dexter energy transfer through exchange coupling. As such, there is not a theoretical limit on the length of diffusion and, in practice, diffusion lengths up to tens of micrometers have been observed.[156] In addition to increased diffusion lengths, singlet fission may be used to increase the efficiency of triplet-harvesting solar cells. In the process of singlet fission, a molecule which is in the singlet excited state shares its energy with an adjacent chromophore leading to the generation of two triplet excited states.[151,152,155,157–159] This process is spin allowed as the net spin is conserved by generating triplet excited states whose spin states sum to form a singlet state. This process doubles the theoretical number of charge carriers generated during an absorption event, allowing for quantum efficiencies greater than 100% based on photon input to current output, albeit at a lower open circuit potential.[152]

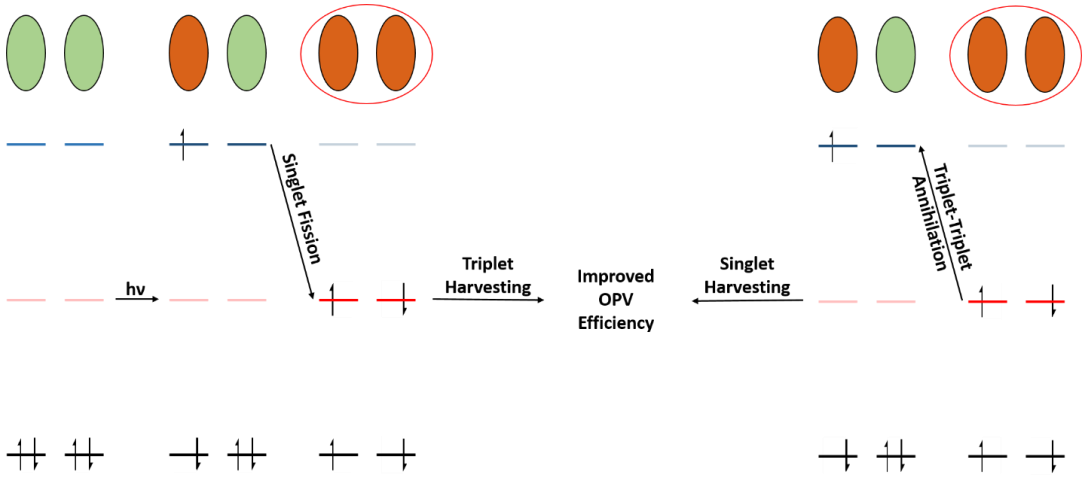

Figure 1.16. Singlet fission (left) results in the distribution of the energy of a singlet state over two molecules whose triplet excited states are approximately half that of the singlet excited state, resulting in two triplet excited states which may be collected as current in triplet harvesting OPV devices. In triplet-triplet annihilation (right), two triplet states combine to generate a singlet excited state on one molecule while the remaining chromophore is left in the ground state. This singlet exciton may be collected as current resulting in an increase in efficiency in singlet harvesting OPV devices.

While the increased diffusional path length of triplet excitons and the increased quantum yields from singlet fission hold many benefits for synthesis of efficient solar cells, the long lifetimes of the triplet excited state also increase the chances of triplet-triplet annihilation events, which are equated to the opposite of singlet fission.[160] In the triplet-triplet annihilation process, two triplet excitons on adjacent molecules combine on a single molecule and form a singlet exciton with approximately twice the energy of the triplet state, leaving the complimentary molecule in the ground state. While this deleterious event may lower the efficiency of OPV by removing charge carriers in triplet harvesting systems, careful optimization can take advantage of this effect to increase the number of singlet excitons formed and improve the efficiency of singlet harvesting solar cells.[161–163] Therefore, a fundamental understanding of the structure-property relationships of the triplet excited state must be realized to reach the full potential of OPV devices.

Polythiophene-based materials represent one of the most commonly used materials in OPV research.[164–168] A fundamental understanding of the structure and delocalization of the triplet excited state in thiophene-based systems presents the unique opportunity to optimize the utility of the triplet excited states in a material whose processing in OPVs is well developed.

1.7. REFERENCES

(1) *Nat. Mater.* **2013**, *12*, 591–591.

(2) So, F. *Organic electronics: materials, processing, devices and applications*; CRC Press: Boca Raton, FL, 2010.

(3) Zhang, X.; Rajaraman, B. R. S.; Liu, H.; Ramakrishna, S. *RSC Adv.* **2014**, *4*, 28987–29011.

(4) Novoselov, K. S.; Fal′ko, V. I.; Colombo, L.; Gellert, P. R.; Schwab, M. G.; Kim, K. *Nature* **2012**, *490*, 192–200.

(5) Yusoff, A. R. bin M. *Graphene-based Energy Devices*; John Wiley & Sons, 2015.

(6) Costa, R. D.; Ortí, E.; Bolink, H. J.; Monti, F.; Accorsi, G.; Armaroli, N. *Angew. Chem. Int. Ed.* **2012**, *51*, 8178–8211.

(7) Kitai, A. *Luminescent Materials and Applications*; John Wiley & Sons, 2008.

(8) Buckley, A. *Organic Light-Emitting Diodes (OLEDs): Materials, Devices and Applications*; Elsevier, 2013.

(9) Jou, J.-H.; Kumar, S.; Agrawal, A.; Li, T.-H.; Sahoo, S. *J. Mater. Chem. C* **2015**, *3*, 2974–3002.

(10) Li, Y. *Organic Optoelectronic Materials*; Springer, 2015.

(11) Gilbert, M.; Albinsson, B. *Chem. Soc. Rev.* **2015**, *44*, 845–862.

(12) Heckmann, A.; Lambert, C. *Angew. Chem. Int. Ed.* **2012**, *51*, 326–392.

(13) Brown, D. B. *Mixed-Valence Compounds: Theory and Applications in Chemistry, Physics, Geology, and Biology*; Springer Science & Business Media, 2012.

(14) Lu, L.; Zheng, T.; Wu, Q.; Schneider, A. M.; Zhao, D.; Yu, L. *Chem. Rev.* **2015**, *115*, 12666–12731.

(15) Brabec, C.; Scherf, U.; Dyakonov, V. *Organic Photovoltaics: Materials, Device Physics, and Manufacturing Technologies*; John Wiley & Sons, 2014.

(16) Brabec, C. J.; Dyakonov, V.; Parisi, J.; Sariciftci, N. S. *Organic Photovoltaics: Concepts and Realization*; Springer Science & Business Media, 2013.

(17) Kaur, G.; Adhikari, R.; Cass, P.; Bown, M.; Gunatillake, P. *RSC Adv.* **2015**, *5*, 37553–37567.

(18) Inzelt, G. *Conducting Polymers: A New Era in Electrochemistry*; Springer Science & Business Media, 2008.

(19) Chandrasekhar, P. *Conducting Polymers, Fundamentals and Applications: A Practical Approach*; Springer Science & Business Media, 2013.

(20) Novoselov, K. S.; Geim, A. K.; Morozov, S. V.; Jiang, D.; Zhang, Y.; Dubonos, S. V.; Grigorieva, I. V.; Firsov, A. A. *Science* **2004**, *306*, 666–669.

(21) Mayorov, A. S.; Gorbachev, R. V.; Morozov, S. V.; Britnell, L.; Jalil, R.; Ponomarenko, L. A.; Blake, P.; Novoselov, K. S.; Watanabe, K.; Taniguchi, T.; Geim, A. K. *Nano Lett.* **2011**, *11*, 2396–2399.

(22) Nair, R. R.; Blake, P.; Grigorenko, A. N.; Novoselov, K. S.; Booth, T. J.; Stauber, T.; Peres, N. M. R.; Geim, A. K. *Science* **2008**, *320*, 1308–1308.

(23) Lee, C.; Wei, X.; Kysar, J. W.; Hone, J. *Science* **2008**, *321*, 385–388.

(24) Akbar, F.; Kolahdouz, M.; Larimian, S.; Radfar, B.; Radamson, H. H. *J. Mater. Sci. Mater. Electron.* **2015**, *26*, 4347–4379.

(25) Liu, Z.; Lau, S. P.; Yan, F. *Chem. Soc. Rev.* **2015**, *44*, 5638–5679.

(26) Georgakilas, V.; Otyepka, M.; Bourlinos, A. B.; Chandra, V.; Kim, N.; Kemp, K. C.; Hobza, P.; Zboril, R.; Kim, K. S. *Chem. Rev.* **2012**, *112*, 6156–6214.

(27) Fan, X.; Zhang, G.; Zhang, F. *Chem. Soc. Rev.* **2015**, *44*, 3023–3035.

(28) Ge, S.; Lan, F.; Yu, F.; Yu, J. *New J. Chem.* **2015**, *39*, 2380–2395.

(29) Bekyarova, E.; Sarkar, S.; Niyogi, S.; Itkis, M. E.; Haddon, R. C. *J. Phys. Appl. Phys.* **2012**, *45*, 154009–154026.

(30) Kuila, T.; Bose, S.; Mishra, A. K.; Khanra, P.; Kim, N. H.; Lee, J. H. *Prog. Mater. Sci.* **2012**, *57*, 1061–1105.

(31) Sarkar, S.; Bekyarova, E.; Haddon, R. C. *Mater. Today* **2012**, *15*, 276–285.

(32) Criado, A.; Melchionna, M.; Marchesan, S.; Prato, M. *Angew. Chem. Int. Ed.* **2015**, *54*, 10734–10750.

(33) Sarkar, S.; Bekyarova, E.; Niyogi, S.; Haddon, R. C. *J. Am. Chem. Soc.* **2011**, *133*, 3324–3327.

(34) Georgakilas, V.; Bourlinos, A. B.; Zboril, R.; Steriotis, T. A.; Dallas, P.; Stubos, A. K.; Trapalis, C. *Chem. Commun.* **2010**, *46*, 1766–1768.

(35) Liu, L.-H.; Lerner, M. M.; Yan, M. *Nano Lett.* **2010**, *10*, 3754–3756.

(36) Choi, J.; Kim, K.; Kim, B.; Lee, H.; Kim, S. *J. Phys. Chem. C* **2009**, *113*, 9433–9435.

(37) Hummers, W. S.; Offeman, R. E. *J. Am. Chem. Soc.* **1958**, *80*, 1339–1339.

(38) Hansora, D. P.; Shimpi, N. G.; Mishra, S. *JOM* **2015**, 1–14.

(39) Jiang, K.; Ma, L.; Wang, J.; Chen, W. *Rev. Nanosci. Nanotechnol.* **2013**, *2*, 171–183.

(40) Nanda, S. S.; Papaefthymiou, G. C.; Yi, D. K. *Crit. Rev. Solid State Mater. Sci.* **2015**, *40*, 291–315.

(41) Yang, K.; Feng, L.; Hong, H.; Cai, W.; Liu, Z. *Nat. Protoc.* **2013**, *8*, 2392–2403.

(42) Pei, S.; Cheng, H.-M. *Carbon* **2012**, *50*, 3210–3228.

(43) Chua, C. K.; Pumera, M. *Chem. Soc. Rev.* **2013**, *43*, 291–312.

(44) Thakur, S.; Karak, N. *Carbon* **2015**, *94*, 224–242.

(45) Xu, Y.; Liu, Z.; Zhang, X.; Wang, Y.; Tian, J.; Huang, Y.; Ma, Y.; Zhang, X.; Chen, Y. *Adv. Mater.* **2009**, *21*, 1275–1279.

(46) Liu, Z.; Robinson, J. T.; Sun, X.; Dai, H. *J. Am. Chem. Soc.* **2008**, *130*, 10876–10877.

(47) Liu, H.; Ryu, S.; Chen, Z.; Steigerwald, M. L.; Nuckolls, C.; Brus, L. E. *J. Am. Chem. Soc.* **2009**, *131*, 17099–17101.

(48) Hossain, M. Z.; Walsh, M. A.; Hersam, M. C. *J. Am. Chem. Soc.* **2010**, *132*, 15399–15403.

(49) Lomeda, J. R.; Doyle, C. D.; Kosynkin, D. V.; Hwang, W.-F.; Tour, J. M. *J. Am. Chem. Soc.* **2008**, *130*, 16201–16206.

(50) Bekyarova, E.; Itkis, M. E.; Ramesh, P.; Berger, C.; Sprinkle, M.; de Heer, W. A.; Haddon, R. C. *J. Am. Chem. Soc.* **2009**, *131*, 1336–1337.

(51) Farmer, D. B.; Lin, Y.-M.; Afzali-Ardakani, A.; Avouris, P. *Appl. Phys. Lett.* **2009**, *94*, 213106.

(52) Farmer, D. B.; Golizadeh-Mojarad, R.; Perebeinos, V.; Lin, Y.-M.; Tulevski, G. S.; Tsang, J. C.; Avouris, P. *Nano Lett.* **2009**, *9*, 388–392.

(53) Fan, X.-Y.; Nouchi, R.; Yin, L.-C.; Tanigaki, K. *Nanotechnology* **2010**, *21*, 475208.

(54) Jacobsen, A.; Koehler, F. M.; Stark, W. J.; Ensslin, K. *New J. Phys.* **2010**, *12*, 125007.

(55) Koehler, F. M.; Jacobsen, A.; Ensslin, K.; Stampfer, C.; Stark, W. J. *Small* **2010**, *6*, 1125–1130.

(56) Lim, H.; Lee, J. S.; Shin, H.-J.; Shin, H. S.; Choi, H. C. *Langmuir* **2010**, *26*, 12278–12284.

(57) Niyogi, S.; Bekyarova, E.; Itkis, M. E.; Zhang, H.; Shepperd, K.; Hicks, J.; Sprinkle, M.; Berger, C.; Lau, C. N.; deHeer, W. A.; Conrad, E. H.; Haddon, R. C. *Nano Lett.* **2010**, *10*, 4061–4066.

(58) Sharma, R.; Baik, J. H.; Perera, C. J.; Strano, M. S. *Nano Lett.* **2010**, *10*, 398–405.

(59) Sinitskii, A.; Dimiev, A.; Corley, D. A.; Fursina, A. A.; Kosynkin, D. V.; Tour, J. M. *ACS Nano* **2010**, *4*, 1949–1954.

(60) Hong, J.; Niyogi, S.; Bekyarova, E.; Itkis, M. E.; Ramesh, P.; Amos, N.; Litvinov, D.; Berger, C.; de Heer, W. A.; Khizroev, S.; Haddon, R. C. *Small* **2011**, *7*, 1175–1180.

(61) Niyogi, S.; Bekyarova, E.; Hong, J.; Khizroev, S.; Berger, C.; de Heer, W.; Haddon, R. C. *J. Phys. Chem. Lett.* **2011**, *2*, 2487–2498.

(62) Gan, L.; Zhang, D.; Guo, X. *Small* **2012**, *8*, 1326–1330.

(63) Liu, J.; Wang, R.; Cui, L.; Tang, J.; Liu, Z.; Kong, Q.; Yang, W.; Gooding, J. *J. Phys. Chem. C* **2012**, *116*, 17939–17946.

(64) Liu, J.; Tang, J.; Gooding, J. J. *J. Mater. Chem.* **2012**, *22*, 12435–12452.

(65) Zhu, H.; Huang, P.; Jing, L.; Zuo, T.; Zhao, Y.; Gao, X. *J. Mater. Chem.* **2012**, *22*, 2063–2068.

(66) Paulus, G. L. C.; Wang, Q. H.; Strano, M. S. *Acc. Chem. Res.* **2013**, *46*, 160–170.

(67) Vase, K. H.; Holm, A. H.; Norrman, K.; Pedersen, S. U.; Daasbjerg, K. *Langmuir* **2007**, *23*, 3786–3793.

(68) Dirk, S. M.; Pylypenko, S.; Howell, S. W.; Fulghum, J. E.; Wheeler, D. R. *Langmuir* **2005**, *21*, 10899–10901.

(69) Matrab, T.; Combellas, C.; Kanoufi, F. *Electrochem. Commun.* **2008**, *10*, 1230–1234.

(70) Charlton, M. R.; Suhr, K. J.; Holliday, B. J.; Stevenson, K. J. *Langmuir* **2015**, *31*, 695–702.

(71) Chan, C. K.; Beechem, T. E.; Ohta, T.; Brumbach, M. T.; Wheeler, D. R.; Stevenson, K. J. *J. Phys. Chem. C* **2013**, *117*, 12038–12044.

(72) Tang, C. W.; VanSlyke, S. A. *Appl. Phys. Lett.* **1987**, *51*, 913–915.

(73) Baldo, M. A.; O'Brien, D. F.; You, Y.; Shoustikov, A.; Sibley, S.; Thompson, M. E.; Forrest, S. R. *Nature* **1998**, *395*, 151–154.

(74) O'Brien, D. F.; Baldo, M. A.; Thompson, M. E.; Forrest, S. R. *Appl. Phys. Lett.* **1999**, *74*, 442–444.

(75) *OLED Fundamentals: Materials, Devices, and Processing of Organic Light-Emitting Diodes*; Gaspar, D., Polikarpov, E., Eds.; CRC Press, 2015.

(76) Yersin, H. *Highly Efficient OLEDs with Phosphorescent Materials*; John Wiley & Sons, 2008.

(77) Baldo, M. A.; O'Brien, D. F.; Thompson, M. E.; Forrest, S. R. *Phys. Rev. B* **1999**, *60*, 14422–14428.

(78) Segal, M.; Baldo, M. A.; Holmes, R. J.; Forrest, S. R.; Soos, Z. G. *Phys. Rev. B* **2003**, *68*, 075211.

(79) Zanoni, K. P. S.; Coppo, R. L.; Amaral, R. C.; Iha, N. Y. M. *Dalton Trans.* **2015**, *44*, 14559–14573.

(80) Suzuri, Y.; Oshiyama, T.; Ito, H.; Hiyama, K.; Kita, H. *Sci. Technol. Adv. Mater.* **2014**, *15*, 054202.

(81) Liang, A.; Ying, L.; Huang, F. *J. Inorg. Organomet. Polym. Mater.* **2014**, *24*, 905–926.

(82) Choy, W. C. H.; Chan, W. K.; Yuan, Y. *Adv. Mater.* **2014**, *26*, 5368–5399.

(83) Yang, X.; Yao, C.; Zhou, G. *Platin. Met. Rev.* **2013**, *57*, 2–16.

(84) Baranoff, E.; Yum, J.-H.; Graetzel, M.; Nazeeruddin, M. K. *J. Organomet. Chem.* **2009**, *694*, 2661–2670.

(85) Flamigni, L.; Barbieri, A.; Sabatini, C.; Ventura, B.; Barigelletti, F. In *Photochemistry and Photophysics of Coordination Compounds II*; Balzani, V., Campagna, S., Eds.; Springer Berlin Heidelberg, 2007; pp 143–203.

(86) Tanaka, D.; Sasabe, H.; Li, Y.-J.; Su, S.-J.; Takeda, T.; Kido, J. *Jpn. J. Appl. Phys.* **2007**, *46*, L10-L12.

(87) Costa, R. D.; Tordera, D.; Ortí, E.; Bolink, H. J.; Schönle, J.; Graber, S.; Housecroft, C. E.; Constable, E. C.; Zampese, J. A. *J. Mater. Chem.* **2011**, *21*, 16108–16118.

(88) Tao, Y.; Yuan, K.; Chen, T.; Xu, P.; Li, H.; Chen, R.; Zheng, C.; Zhang, L.; Huang, W. *Adv. Mater.* **2014**, *26*, 7931–7958.

(89) Armaroli, N.; Accorsi, G.; Cardinali, F.; Listorti, A. In *Photochemistry and Photophysics of Coordination Compounds I*; Balzani, V., Campagna, S., Eds.; Springer Berlin Heidelberg, 2007; pp 69–115.

(90) Tsuge, K.; Chishina, Y.; Hashiguchi, H.; Sasaki, Y.; Kato, M.; Ishizaka, S.; Kitamura, N. *Coord. Chem. Rev.* **2016**, *306*, 636–651.

(91) Lavie-Cambot, A.; Cantuel, M.; Leydet, Y.; Jonusauskas, G.; Bassani, D. M.; McClenaghan, N. D. *Coord. Chem. Rev.* **2008**, *252*, 2572–2584.

(92) Ford, P. C.; Cariati, E.; Bourassa, J. *Chem. Rev.* **1999**, *99*, 3625–3648.

(93) Dumur, F. *Org. Electron.* **2015**, *21*, 27–39.

(94) Volz, D.; Wallesch, M.; Fléchon, C.; Danz, M.; Verma, A.; Navarro, J. M.; Zink, D. M.; Bräse, S.; Baumann, T. *Green Chem.* **2015**, *17*, 1988–2011.

(95) Hashimoto, M.; Igawa, S.; Yashima, M.; Kawata, I.; Hoshino, M.; Osawa, M. *J. Am. Chem. Soc.* **2011**, *133*, 10348–10351.

(96) Barbara, P. F.; Meyer, T. J.; Ratner, M. A. *J. Phys. Chem.* **1996**, *100*, 13148–13168.

(97) Brunschwig, B. S.; Sutin, N. *Coord. Chem. Rev.* **1999**, *187*, 233–254.

(98) Meyer, T. J. *Acc. Chem. Res.* **1978**, *11*, 94–100.

(99) Nelsen, S. F.; Ismagilov, R. F.; Trieber, D. A. *Science* **1997**, *278*, 846–849.

(100) Robin, M. B.; Day, P. In *Advances in Inorganic Chemistry and Radiochemistry*; Sharpe, H. J. E. and A. G., Ed.; Academic Press, 1967; Vol. 10, pp 247–422.

(101) Day, P.; Hush, N. S.; Clark, R. J. H. *Philos. Trans. R. Soc. Lond. Math. Phys. Eng. Sci.* **2008**, *366*, 5–14.

(102) Demadis, K. D.; Hartshorn, C. M.; Meyer, T. J. *Chem. Rev.* **2001**, *101*, 2655–2686.

(103) Brunschwig, B. S.; Creutz, C.; Sutin, N. *Chem. Soc. Rev.* **2002**, *31*, 168–184.

(104) Marcus, R. A. *J. Chem. Phys.* **1956**, *24*, 966–978.

(105) Hush, N. S. *Trans. Faraday Soc.* **1961**, *57*, 557–580.

(106) Hush, N. S. In *Progress in Inorganic Chemistry*; Cotton, F. A., Ed.; John Wiley & Sons, Inc., 1967; pp 391–444.

(107) Hush, N. S. *Electrochimica Acta* **1968**, *13*, 1005–1023.

(108) Cotton, F. A.; Wilkinson, G.; Murillo, C. A.; Bochmann, M. *Advanced Inorganic Chemistry*, 6th ed.; John Wiley & Sons, 1999.

(109) Tejel, C.; Ciriano, M. A.; del Río, M. P.; van den Bruele, F. J.; Hetterscheid, D. G. H.; Tsichlis i Spithas, N.; de Bruin, B. *J. Am. Chem. Soc.* **2008**, *130*, 5844–5845.

(110) Tommasino, J. B.; De Montauzon, D.; He, X.; Maisonnat, A.; Poilblanc, R.; Verpeaux, J. N.; Amatore, C. *Organometallics* **1992**, *11*, 4150–4156.

(111) Carano, M.; Careri, M.; Cicogna, F.; D'Ambra, I.; Houben, J. L.; Ingrosso, G.; Marcaccio, M.; Paolucci, F.; Pinzino, C.; Roffia, S. *Organometallics* **2001**, *20*, 3478–3490.

(112) Nafady, A.; Chin, T. T.; Geiger, W. E. *Organometallics* **2006**, *25*, 1654–1663.

(113) He, F.; Ruhlmann, L.; Gisselbrecht, J.-P.; Choua, S.; Orio, M.; Wesolek, M.; Danopoulos, A. A.; Braunstein, P. *Dalton Trans.* **2015**, *44*, 17030–17044.

(114) Shibata, Y.; Zhu, B.; Kume, S.; Nishihara, H. *Dalton Trans.* **2009**, 1939–1943.

(115) Sakamoto, R.; Kambe, T.; Tsukada, S.; Takada, K.; Hoshiko, K.; Kitagawa, Y.; Okumura, M.; Nishihara, H. *Inorg. Chem.* **2013**, *52*, 7411–7416.

(116) Festus Agbo, S. F. *Int. J. Chem.* **2011**, *3*, 9698–1916.

(117) Evans, P. A. *Modern Rhodium-Catalyzed Organic Reactions*; John Wiley & Sons, 2005.

(118) Press Release: The 2000 Nobel Prize in Chemistry http://www.nobelprize.org/nobel_prizes/chemistry/laureates/2000/press.html (accessed Feb 18, 2016).

(119) Balint, R.; Cassidy, N. J.; Cartmell, S. H. *Acta Biomater.* **2014**, *10*, 2341–2353.

(120) Bredas, J. L.; Street, G. B. *Acc. Chem. Res.* **1985**, *18*, 309–315.

(121) Li, X.; Wang, Y.; Yang, X.; Chen, J.; Fu, H.; Cheng, T.; Wang, Y. *TrAC Trends Anal. Chem.* **2012**, *39*, 163–179.

(122) Sairam, M.; Nataraj, S. K.; Aminabhavi, T. M.; Roy, S.; Madhusoodana, C. D. *Sep. Purif. Rev.* **2006**, *35*, 249–283.

(123) Pellegrino, J. *Ann. N. Y. Acad. Sci.* **2003**, *984*, 289–305.

(124) Sarrazin, J.; Persin, M.; Cretin, M. *Macromol. Symp.* **2002**, *188*, 1–12.

(125) Fabre, B.; Simonet, J. *Coord. Chem. Rev.* **1998**, *178–180,*1211–1250.

(126) Simonet, J. *Pure Appl. Chem.* **1998**, *70*, 1253–1257.

(127) Bagheri, H.; Ayazi, Z.; Naderi, M. *Anal. Chim. Acta* **2013**, *767*, 1–13.

(128) Tian, Y.; Wang, J.; Wang, Z.; Wang, S. *Sens. Actuators B Chem.* **2005**, *104*, 23–28.

(129) Liljegren, G.; Forsgard, N.; Zettersten, C.; Pettersson, J.; Svedberg, M.; Herranen, M.; Nyholm, L. *Analyst* **2005**, *130*, 1358–1368.

(130) Qiu, B.; Xu, C.; Sun, D.; Wang, Q.; Gu, H.; Zhang, X.; Weeks, B. L.; Hopper, J.; Ho, T. C.; Guo, Z.; Wei, S. *Appl. Surf. Sci.* **2015**, *334*, 7–14.

(131) Li, X.; Li, C.; Chen, J.; Li, C.; Sun, C. *J. Chromatogr. A* **2008**, *1198–1199*, 7–13.

(132) Caris, J. A.; Chaves, A. R.; Queiroz, M. E. C. *J. Braz. Chem. Soc.* **2012**, *23*, 57–64.

(133) Yates, B. J.; Temsamani, K. R.; Ceylan, Ö.; Öztemiz, S.; Gbatu, T. P.; LaRue, R. A.; Tamer, U.; Mark Jr, H. B. *Talanta* **2002**, *58*, 739–745.

(134) Lyskawa, J.; Le Derf, F.; Levillain, E.; Mazari, M.; Sallé, M.; Dubois, L.; Viel, P.; Bureau, C.; Palacin, S. *J. Am. Chem. Soc.* **2004**, *126*, 12194–12195.

(135) Weinberger, D. A.; Higgins, T. B.; Mirkin, C. A.; Stern, C. L.; Liable-Sands, L. M.; Rheingold, A. L. *J. Am. Chem. Soc.* **2001**, *123*, 2503–2516.

(136) Mokhtari, B.; Pourabdollah, K.; Dallali, N. *J. Radioanal. Nucl. Chem.* **2010**, *287*, 921–934.

(137) Boerrigter, H.; Verboom, W.; Reinhoudt, D. N. *J. Org. Chem.* **1997**, *62*, 7148–7155.

(138) Boerrigter, H.; Tomasberger, T.; Verboom, W.; Reinhoudt, D. N. *Eur. J. Org. Chem.* **1999**, *1999*, 665–674.

(139) Peters, M. W.; Werner, E. J.; Scott, M. J. *Inorg. Chem.* **2002**, *41*, 1707–1716.

(140) Matloka, K.; Gelis, A.; Regalbuto, M.; Vandegrift, G.; Scott, M. J. *Dalton Trans.* **2005**, 3719–3721.

(141) Dam, H. H.; Reinhoudt, D. N.; Verboom, W. *New J. Chem.* **2007**, *31*, 1620–1632.

(142) Dam, H. H.; Reinhoudt, D. N.; Verboom, W. *Chem. Soc. Rev.* **2007**, *36*, 367–377.

(143) Lewis, F.; Hudson, M.; Harwood, L. *Synlett* **2011**, 2609–2632.

(144) Halls, J. J. M.; Walsh, C. A.; Greenham, N. C.; Marseglia, E. A.; Friend, R. H.; Moratti, S. C.; Holmes, A. B. *Nature* **1995**, *376*, 498–500.

(145) Van De Wetering, K.; Brochon, C.; Ngov, C.; Hadziioannou, G. *Macromolecules* **2006**, *39*, 4289–4297.

(146) Yu, G.; Heeger, A. J. *J. Appl. Phys.* **1995**, *78*, 4510–4515.

(147) Thompson, B. C.; Fréchet, J. M. J. *Angew. Chem. Int. Ed.* **2008**, *47*, 58–77.

(148) Shao, Y.; Yang, Y. *Adv. Mater.* **2005**, *17*, 2841–2844.

(149) Castrucci, J. S.; Josey, D. S.; Thibau, E.; Lu, Z.-H.; Bender, T. P. *J. Phys. Chem. Lett.* **2015**, *6*, 3121–3125.

(150) Zhen, H.; Hou, Q.; Li, K.; Ma, Z.; Fabiano, S.; Gao, F.; Zhang, F. *J. Mater. Chem. A* **2014**, *2*, 12390–12396.

(151) Tritsch, J. R.; Chan, W.-L.; Wu, X.; Monahan, N. R.; Zhu, X.-Y. *Nat. Commun.* **2013**, *4*, 2679.

(152) Lee, J.; Jadhav, P.; Reusswig, P. D.; Yost, S. R.; Thompson, N. J.; Congreve, D. N.; Hontz, E.; Van Voorhis, T.; Baldo, M. A. *Acc. Chem. Res.* **2013**, *46*, 1300–1311.

(153) Winroth, G.; Podobinski, D.; Cacialli, F. *J. Appl. Phys.* **2011**, *110*, 124504.

(154) Arif, M.; Yang, K.; Li, L.; Yu, P.; Guha, S.; Gangopadhyay, S.; Förster, M.; Scherf, U. *Appl. Phys. Lett.* **2009**, *94*, 063307.

(155) Bardeen, C. J. *Nat. Mater.* **2014**, *13*, 1001–1003.

(156) Yost, S. R.; Hontz, E.; Yeganeh, S.; Van Voorhis, T. *J. Phys. Chem. C* **2012**, *116*, 17369–17377.

(157) Musser, A. J.; Al-Hashimi, M.; Maiuri, M.; Brida, D.; Heeney, M.; Cerullo, G.; Friend, R. H.; Clark, J. *J. Am. Chem. Soc.* **2013**, *135*, 12747–12754.

(158) Monahan, N.; Zhu, X.-Y. *Annu. Rev. Phys. Chem.* **2015**, *66*, 601–618.

(159) Smith, M. B.; Michl, J. *Chem. Rev.* **2010**, *110*, 6891–6936.

(160) Singh-Rachford, T. N.; Castellano, F. N. *Coord. Chem. Rev.* **2010**, *254*, 2560–2573.

(161) Ceroni, P. *Chem. – Eur. J.* **2011**, *17*, 9560–9564.

(162) Tayebjee, M. J. Y.; McCamey, D. R.; Schmidt, T. W. *J. Phys. Chem. Lett.* **2015**, *6*, 2367–2378.

(163) Shang, Y.; Hao, S.; Yang, C.; Chen, G. *Nanomaterials* **2015**, *5*, 1782–1809.

(164) Ewbank, P. C.; Laird, D.; McCullough, R. D. In *Organic Photovoltaics*; Brabec, C., Dyakonov, V., Scherf, U., Eds.; Wiley-VCH Verlag GmbH & Co. KGaA, 2008; pp 1–55.

(165) Hsing-Ju Wang; Chih-Ping Chen; Ru-Jong Jeng. *Mater. 1996-1944* **2014**, *7*, 2411–2439.

(166) McCullough, R. D.; Lowe, R. D.; Jayaraman, M.; Anderson, D. L. *J. Org. Chem.* **1993**, *58*, 904–912.

(167) Reid, O. G.; Pensack, R. D.; Song, Y.; Scholes, G. D.; Rumbles, G. *Chem. Mater.* **2014**, *26*, 561–575.

(168) Elschner, A.; Kirchmeyer, S. In *Organic Photovoltaics*; Brabec, C., Dyakonov, V., Scherf, U., Eds.; Wiley-VCH Verlag GmbH & Co. KGaA, 2008; pp 211–242.

Chapter 2: Electrochemically Induced Covalent Modification of Epitaxial Graphene with Diaryliodonium Salts: Investigations into the Control and Mechanism of Grafting[1]

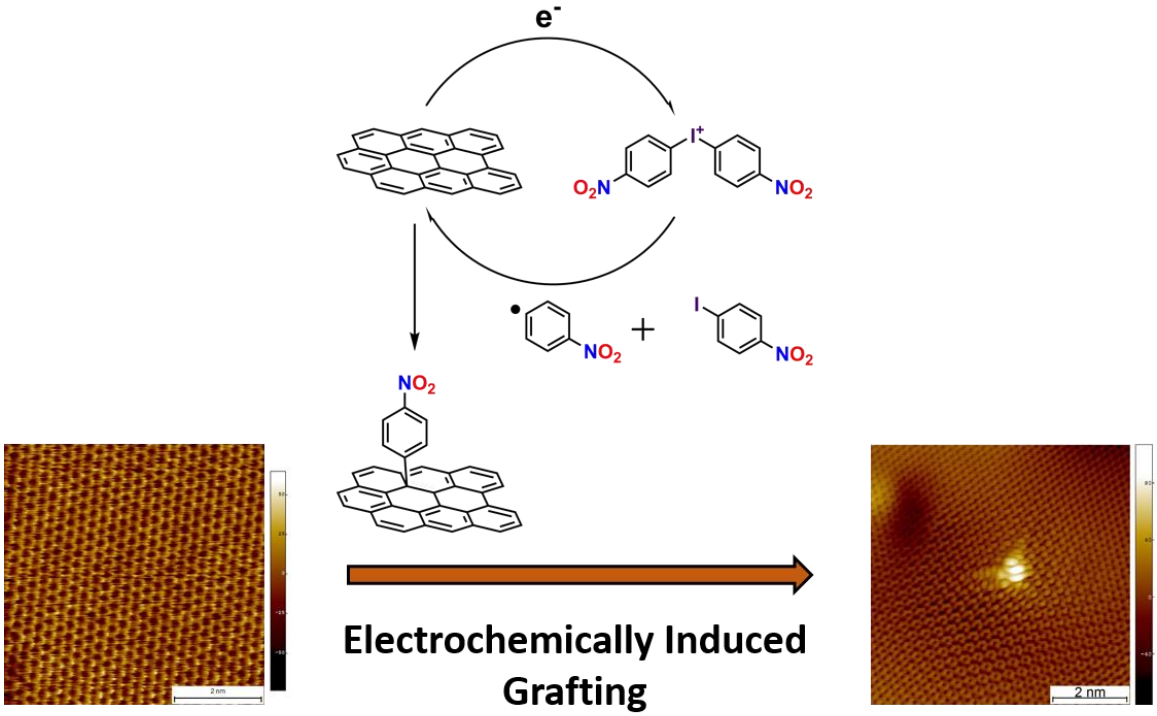

1 Portions of this chapter were published in:
K. J. Stevenson, P. A. Veneman, R. I. Gearba, K. M. Mueller, B. J. Holliday, T. Ohta and C. K. Chan, *Faraday Discuss.*, **2014**, *172*, 273–291.
R. I. Gearba, K. M. Mueller, P. A. Veneman, B. J. Holliday, C. K. Chan and K. J. Stevenson, *J. Electroanal. Chem.*, **2015**, 753, 9–15.
R. I. Gearba performed STM/STS studies and data analysis; P. A. Veneman performed Raman studies under the supervision of K. J. Stevenson; T. Ohta and C. K. Chan prepared the epitaxial graphene samples. Additional work: Minjung Kim performed DFT calculations under the supervision of J. R. Chelikowsky.

2.1. INTRODUCTION

The ability to modify the structural, physical and electrical properties of graphene in a precise and reproducible manner is highly sought after. To achieve this goal, much research has focused on using radical graftants to tailor the structure of graphene.[29,66] Though relatively new in the field of graphene modification, diaryliodonium salts (DAISs) are a quickly emerging class of compounds for the free radical covalent functionalization of the surface of graphene.[71] The mechanism by which DAISs graft is thought to be similar to the diazonium salts (Figure 2.1).[67,169–171] Electron transfer from graphene to the diaryliodonium cation leads to the homolytic fission of one C – I bond, resulting in an iodoarene and a neutral aryl radical. The unpaired electron in this aryl radical resides in a sp^2-hybridized orbital in the plane of the arene ring resulting a highly localized and reactive species. DAISs have been previously studied for their capacity to graft onto several carbon substrates (highly ordered pyrolytic graphite (HOPG), glassy carbon (GC) and carbon powder.[67,169,172] Electrochemically driven functionalization using DAISs has been reported on non-carbacious substrates as well, including hydride terminated silicon {100},[68] platinum,[68] gold[69] and indium tin oxide.[70] Unlike the more commonly employed diazonium salts, spontaneous grafting of aryl species using DIASs is avoided by virtue of a more negative reduction potential associated with formation of the aryl radical. Furthermore, undesirable azoic linkages are excluded through the use of DAISs.[173]

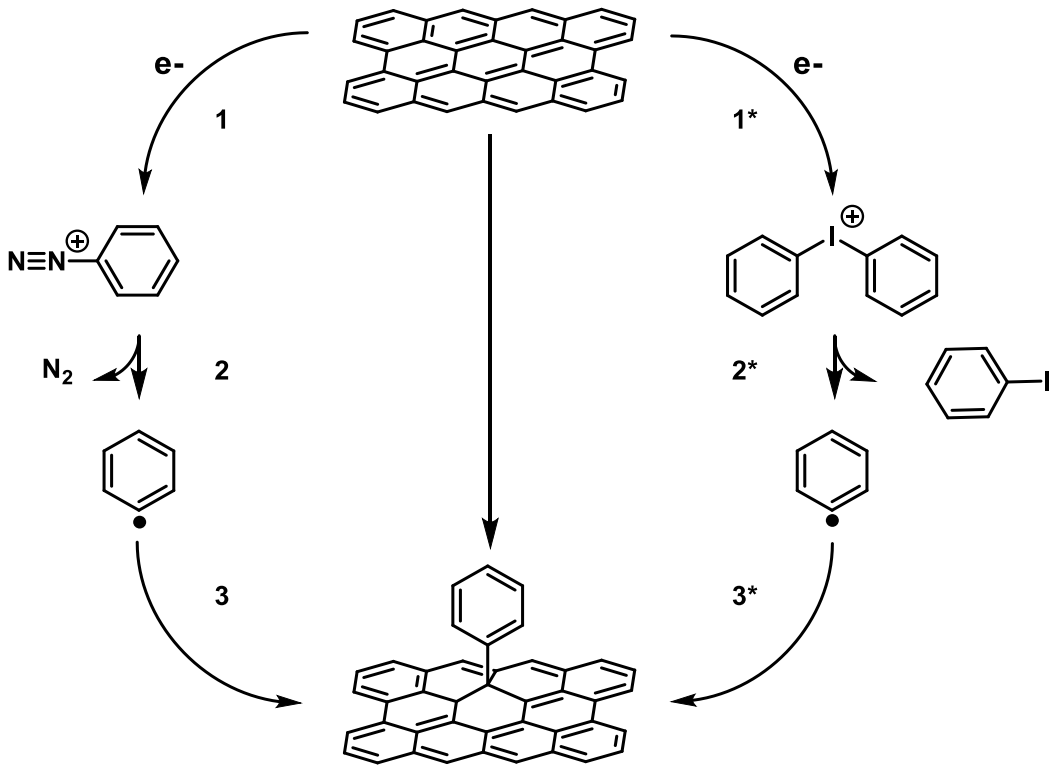

Figure 2.1. The grafting mechanism of aryl diazonium salts and DAISs to graphene proceeds through three major steps: (1) Electron transfer from the graphene to the diazonium salt initiates the process. This process may occur spontaneously with diazonium salts or by actively applying a reductive potential, whereas (1*) DAISs requires an applied potential. (2) Fission of the C – N bond or (2*) C – I liberates a leaving group and generates an aryl radical. (3/3*) Formation of a C – C bond through a radical reaction with the sp^2-network generates a sp^3-hybridized carbon at the point of attachment.

Prior to this work, only one study by Chan *et al.*[71] reported the use of DAISs for the covalent functionalization of graphene. These studies were carried out utilizing epitaxially-grown graphene (EG) by the sublimation of silicon from N-type 6H-SiC(0001) in an argon atmosphere. Covalent modification was achieved by the electrolysis of bis(4-trifluoromethylphenyl)iodonium tetrafluoroborate, $[(CF_3Ph)_2I][BF_4]$, at the surface of an EG working electrode.

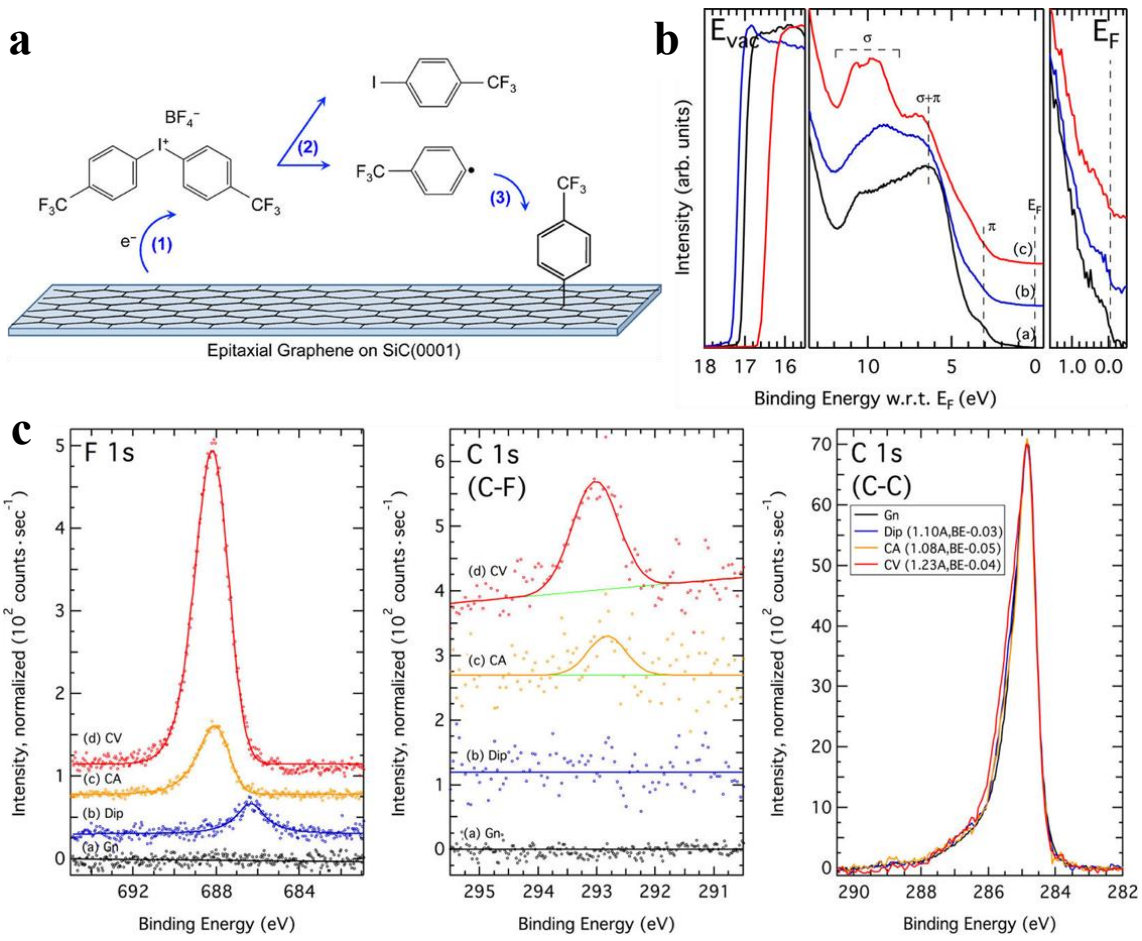

Figure 2.2. a) Schematic illustrating the electrochemically induced grafting of $[(CF_3Ph)_2I][BF_4]$ to the surface of epitaxial graphene by Chan *et al.*[71] b) Ultraviolet photoelectron spectroscopy and c) X-ray photoelectron spectroscopy studies on the resulting material confirm the existence of molecular attachments and increase in the work function of the resulting material.

Reduction of $[(CF_3Ph)_2I][BF_4]$ occurred at –1.05 eV (vs. Ag/Ag^+) illustrating the increased reduction potential compared to that of the diazonium salts. Analysis of the resulting material via X-ray photoelectron spectroscopy (XPS) confirmed the presence of 4-trifluoromethylphenylene covalently bound to the surface of graphene.

Functionalization of the surface of graphene was further supported by Raman spectroscopy and the increased hydrophobicity of the graphene sample as determined by water contact angle measurements. Ultraviolet photoelectron spectroscopy further indicated covalent attachment of 4-trifluorophenylene to the surface of graphene as evidenced by both an increase in the work function of the covalently modified sample with respect to the pristine EG sample and a modulation of the density of states.

These initial studies by Chan *et al*.[71] showed promise for utilizing DAISs to tailor the properties of graphene, however, many questions still remain about the grafting mechanism and the effects of the modification on electronic properties. To this end, investigations into the control of the covalent modification of graphene with DAISs were undertaken. Control over the extent of surface functionalization was investigated using a symmetric DAIS sporting electroactive functionalities. To better understand the electronic effects of the aryl ring substituents on the grafting ratios of DAISs, studies were performed employing both symmetric and asymmetric salts. These initial studies were carried out on glassy carbon. The results of the control studies on glassy carbon were then translated to EG to determine if control might still be achieved. The resulting modified surfaces were then characterized via electrochemical studies, Raman spectroscopy and scanning tunneling microscopy (STM). Using these techniques, along with Density Functional Theory (DFT) calculations, insights into the mechanism of molecular grafting were obtained. Furthermore, the relative reactivity of atomic vacancies to the pristine basal plane was explored.

2.2. Results and Discussion

2.2.1. Synthesis of Diaryliodonium Salts and Electrochemical Characterization on Glassy Carbon

Prior to functionalizing the graphene samples, grafting studies were performed on glassy carbon (GC) as a more accessible control system. Both the symmetric bis(4-nitrophenyl)iodonium tetrafluoroborate (DNP) and the asymmetric (4-nitrophenyl)phenyliodonium tetrafluoroborate (NPP) salts are used in this study as an intimate probe into the chemistry and mechanisms of the radical grafting. The synthesis of these molecules (Scheme 2.1) was achieved using modified literature procedures following the method described by Bielawski *et al*.[174]

Scheme 2.1. Synthesis of the diaryliodonium salts.

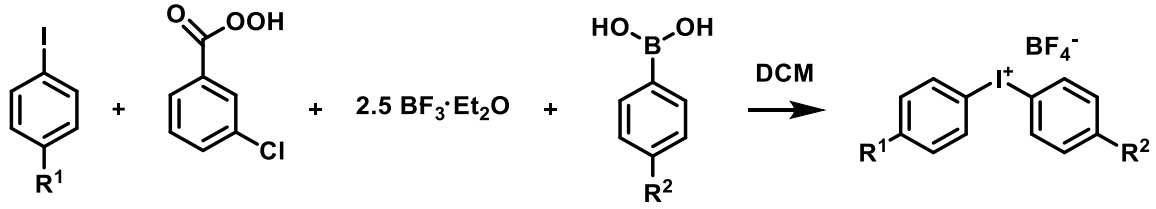

NPP: R^1 = H, R^2 = NO_2
DNP: R^1 = NO_2, R^2 = NO_2

Initial studies on the control and grafting of DAISs were performed using the symmetric DNP salt. Figure 2.3 shows a representative sequential voltammetric response for the reduction of a 1.0 mM solution of DNP in CH_3CN at a GC working electrode.

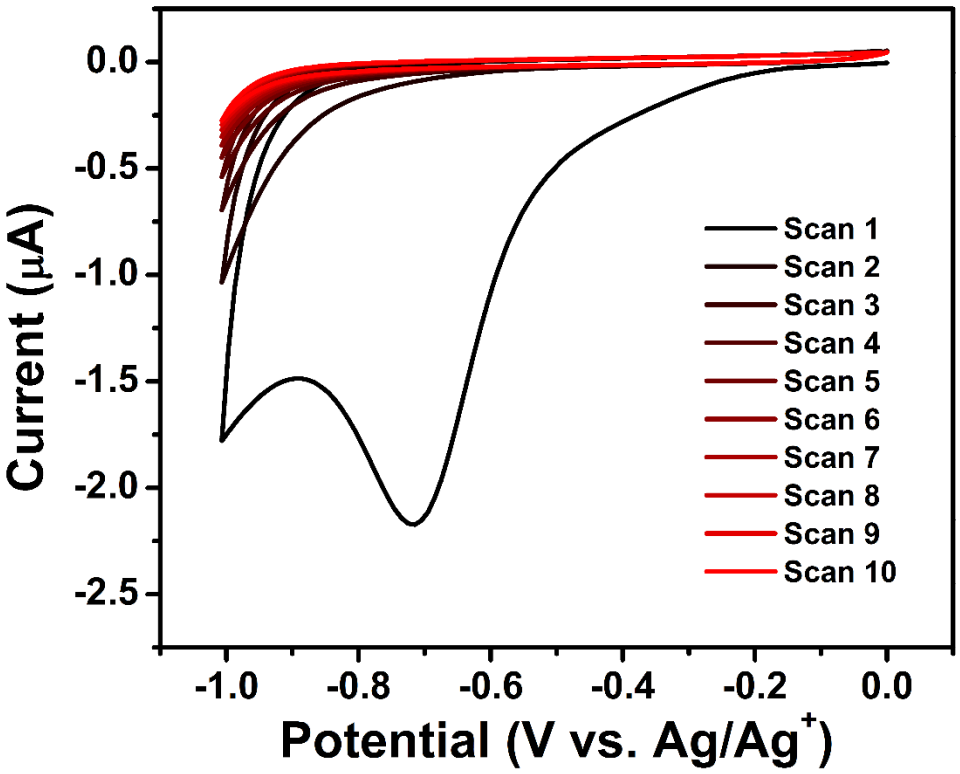

Figure 2.3. Cyclic voltammograms of 1.0 mM DNP in CH_3CN containing 0.1 M $TBAPF_6$ taken with a glassy carbon working electrode at a scan rate of 50 $mV \cdot s^{-1}$. A drastic decrease in the Faradaic current is observed following the first reductive scan. This indicates grafting of the nitrophenylene to the glassy carbon surface.

The first scan shows an irreversible wave at with a potential of peak current ($E_{p,c}$) at – 0.72 V vs. Ag/Ag^+ corresponding to the reduction and concomitant decomposition of the DNP salt into 1-iodo-4-nitrobenzene and a nitrophenyl radical. Subsequent attenuation of the faradaic signal in the following cycles is attributed to the passivation of the GC electrode surface by the covalently grafted nitrophenyl-molecules.[67,169,172] Further confirmation of this passivation layer on the surface of the GC electrode can be seen in Figure 2.4 where a marked decrease in the intensity of the ferrocene redox couple shows the presence of an insulating layer on the electrode surface.[169,173]

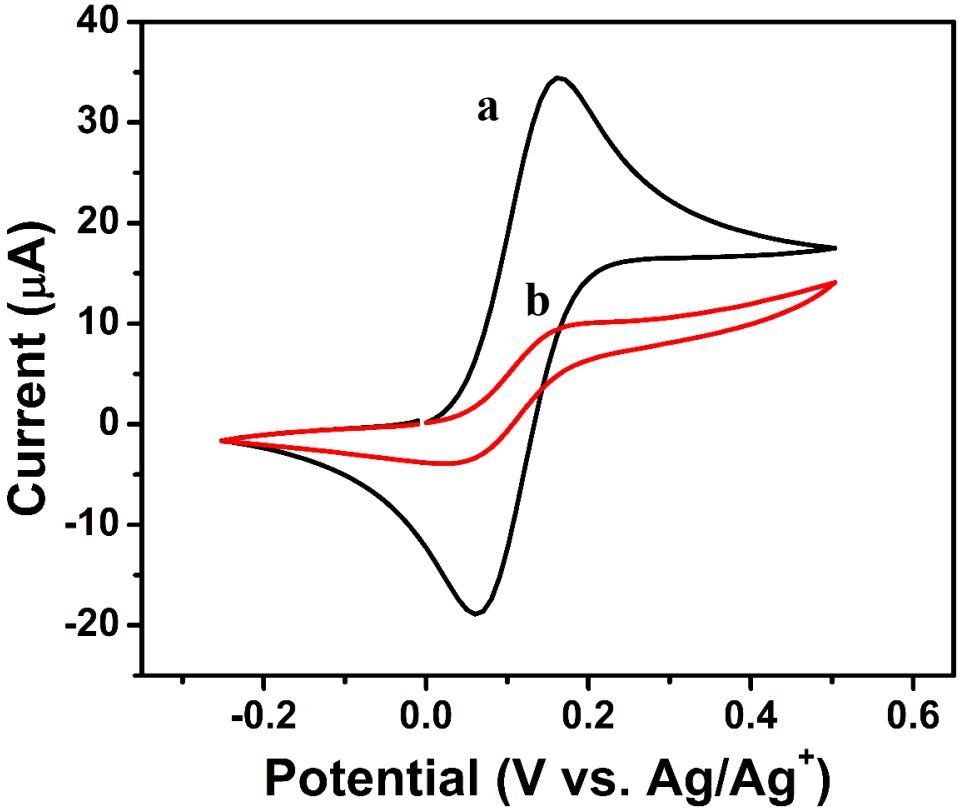

Figure 2.4. a) Ferrocene scan taken on a pristine glassy carbon electrode. b) Ferrocene scan taken after molecular grafting of nitrophenylene to the surface of the glassy carbon electrode (1.0 mM DNP; 10 scans; 50 $mV \cdot s^{-1}$). A reduction of the peak current from 34.5 μA to 9.7 μA was observed, resulting in a 72% reduction of the peak anodic current.

2.2.2. Quantification and Control of Surface Coverages

Quantitative determination of the surface concentration of nitrophenylene molecules was determined electrochemically through the integration of the peak associated with the one electron reduction of the nitrophenyl-moieties (Figure 2.5).[67,70,173,175–177] This highly reversible process is evidenced by a peak-to-peak separation of ΔE_p = 59 mV. The anodic peak at E_p = –1.50 V may be integrated which allows for the determination of charge transfered (Q) during the reduction event. The charge can be directly related to the surface density (Γ) using equation 2.1.

$$\Gamma = \frac{QN_A}{n\,F\,A} \qquad \text{(eq. 2.1)}$$

where N_A is Avogadro's number, n is the number of electrons transferred during the redox event (n = 1 in for the observed reduction), F is Faraday's constant, and A is the electroactive surface area of the electrode expressed in cm^2. The electroactive area of the electrode was determined using ferrocene as an electrochemical probe by employing the Randles-Sevcik equation.[178]

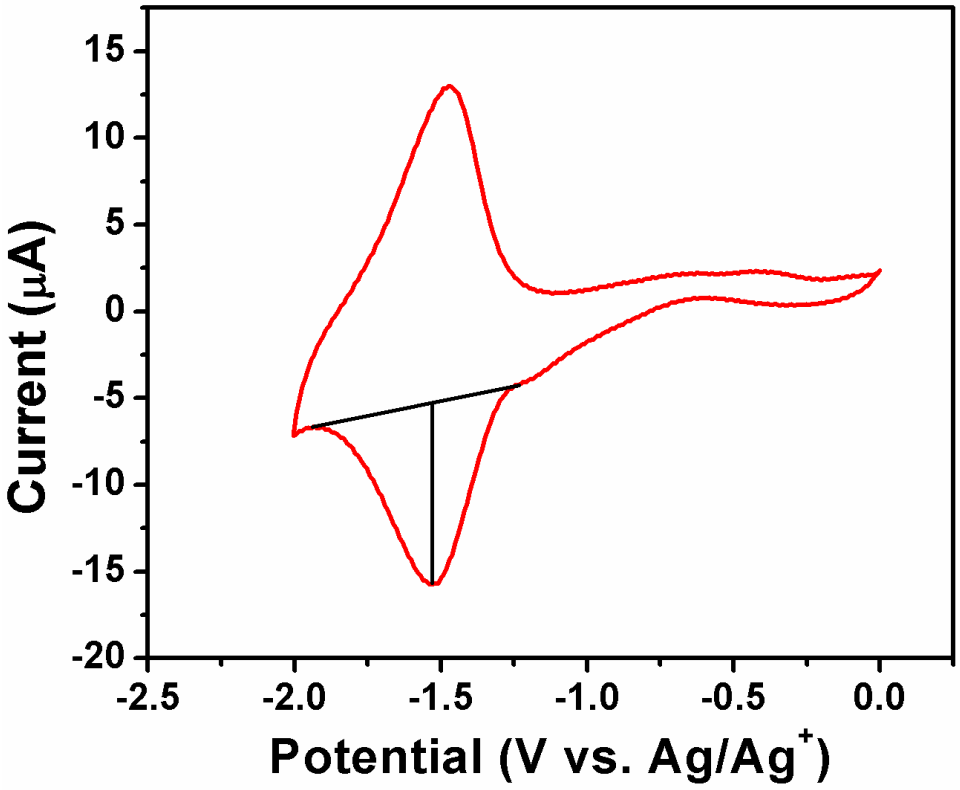

Figure 2.5. Representative cyclic voltammogram of the reduction of the surface-confined nitrophenyl-molecular grafts on glassy carbon (scan rate = 1.00 $V{\cdot}s^{-1}$). Integration of the cathodic peak allowed for quantification of the charge (Q) passed and was used to determine the resulting surface coverages.

Under conditions which give extremely high surface coverages (i.e. 1.0 mM DNP, 10 Scans), electrochemical grafting results in the formation of multilayers. Such grafting conditions correlate to "saturated" coverages where coulometric integration revealed a surface concentration of (3.0 ±0.6) x 10^{14} molecules·cm^{-2} on the electrodes surface. This value correlates well with previous studies performed on glassy carbon using DAISs. For example, Vase *et al*.[67] demonstrated a saturation surface coverage of (2.4 ±0.6) x 10^{14} molecules·cm^{-2} with 3,3'-dinitrodiphenyliodonium hydrogensulfate. However, this number is lower than that observed from the grafting 4-nitrophenyldiazonium tetrafluoroborate, which showed a saturation coverage of 2.5 x 10^{15} molecules·cm^2,[177] highlighting the increased reactivity of the diazonium precursor. Furthermore, it is speculated that the increased size of the diaryliodonium precursor compared to DAISs likely contributes to the reduced surface concentrations.

While high concentrations of surface modifications can be used to deduce the relative reactivity of the radical precursor, much lower surface coverages are often desired to facilitate fundamental studies and to fine tune physical properties. In principle, reproducible control over the degree of functionalization can be achieved by varying the time under which the electrode is placed at potential low enough to reduce the diaryliodonium salt; this is most commonly accomplished using chronoamperometry.[71] However, reproducible results through chronoamperometry proved difficult to obtain, which was likely the result of instrument limitations. Control over the surface coverages using cyclic voltammetry with a constant grafting procedure while varying the salt concentration, however, yielded excellent control (Figure 2.6) of the surface grafting density. Using the previously described grafting procedure (*supra vida*) for quantifying the surface functionalization density by the electrochemical reduction of nitrophenyl-functionalities, calibration curves of the surface functionalization were obtained. A linear

dependence was also obtained by monitoring the peak current from the reduction of the DNP salt. Both calibration curves scale linearly with solution concentration up to approximately 0.8 mM DNP. In a similar study by Vase *et al*. [67], bis(3-nitrophenyl)iodonium bisulfate showed the cathodic peak current $i_{p,c}$ that also varied in a linear fashion with concentration between 0.2 and 1.0 mM. Exceeding 0.8 mM concentrations (i.e. $\Gamma > 2.2 \times 10^{14}$ molecules·cm^{-2}) leads to a second region where the surface coverage increases much more slowly with increasing DNP concentrations. This discontinuity is explained by a switch from the formation of sub-monolayer coverages, in which the nitrophenyl-radicals graft to the surface of the electrode, to the generation of multi-layers where grafting begins to occur onto previously chemisorbed species.

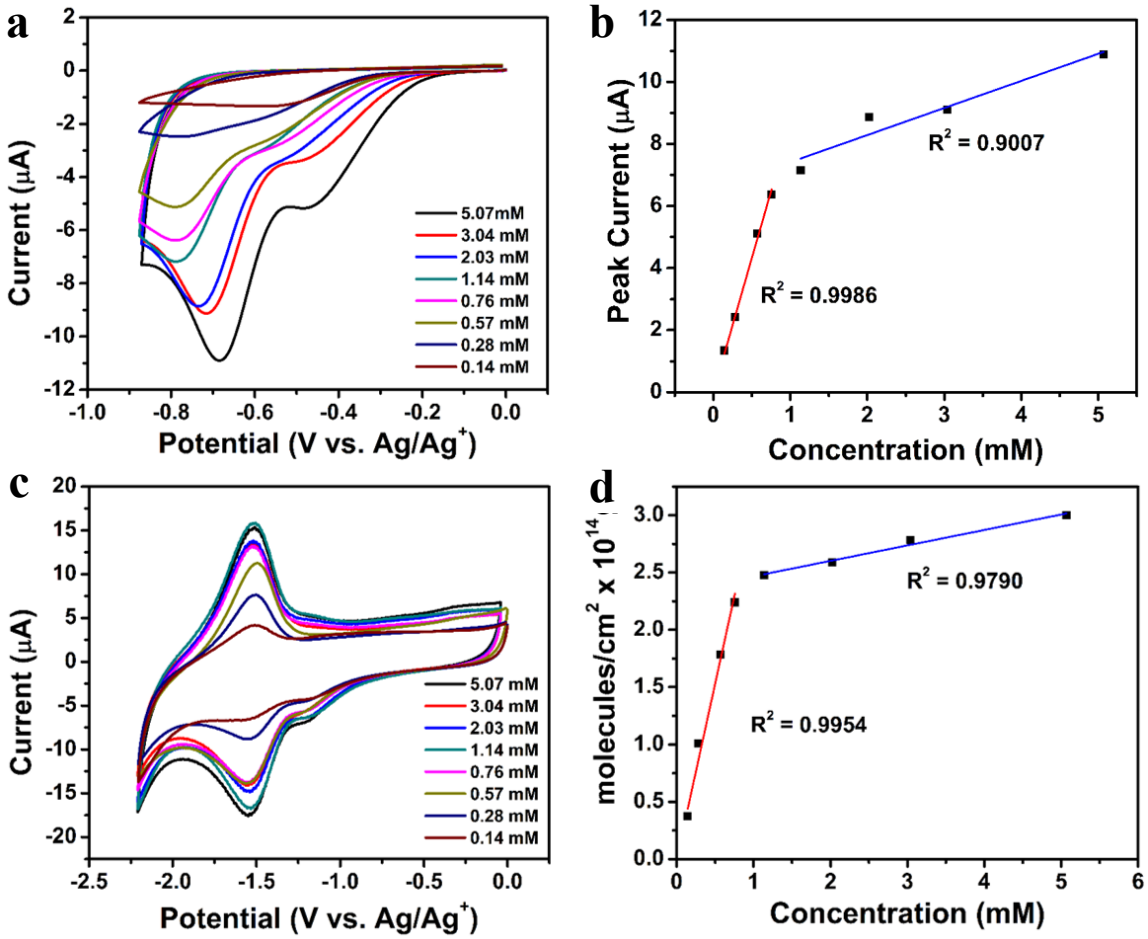

Figure 2.6. a) Potential sweeps showing the reduction of DNP at various concentrations (50 $mV \cdot s^{-1}$). b) A plot of the peak current versus the concentration of the DNP salt yielded a linear trend up to approximately 0.8 mM concentrations. c) Nitrophenyl-reductions from the covalently grafted films generated from the various concentrations of DNP salt. d) Linear control of the surface coverages versus the concentration of the DNP grafting solutions yielded a linear trend up to approximately 0.8 mM concentrations of DNP.

While the two calibration curves shown in Figure 2.6b and Figure 2.6d are in excellent agreement with each other, inspection of the grafting scans used to generate the calibration curve revealed an interesting trend: the shift in $E_{p,c}$ to more positive potentials (–795 to –680 mV) when DNP concentrations exceed approximately 1.0 mM is accompanied with a concurrent increase in the prominence of a pre-wave that occurs

approximately 200 mV positive of the $E_{p,c}$. The origin of the pre-wave during the reduction of iodonium salts has been unclear. In the closely related family of diazonium salts, it has been speculated that the origin of a pre-wave is due to differences in the potential of zero charge of the electrode surface.[67] However, the concentration dependence of the pre-wave, as well as the observed anodic shift in $E_{p,c}$ indicates the possibility of the formation of a pre-adsorbed layer of unreduced DNP. To test this hypothesis, solutions of DNP were prepared with varied concentrations within the range of linear control, and were subjected to two reductive scans from 0 to –0.450 V versus Ag/Ag^+ (approximate $E_{p,c}$ for the pre-wave event). The resulting surface coverage was monitored. Results showed an extremely low degree of surface functionalization with weak, distorted signals and no observable linear trend. These results are in agreement with the hypothesis of a physisorbed layer of DNP that is electronically affected by the interaction with the electrode. This interaction is expected to cause the anodic shift that is observed in the cyclic voltammograms at high concentrations.

2.2.3. Electrochemically Induced Grafting with Asymmetric Diaryliodonium Salts: Studies into the Relative Reactivity of Substituted Phenyl Rings

Asymmetric DAISs provide a unique opportunity to graft two different aryl species to the surface of an electrode starting from a single precursor. However, the ratio of the two aromatic moieties that are grafted to the electrode surface is an important detail that needs to be controlled in order to appropriately tune the properties of the functionalized surface. Previous studies have examined how the electronic nature of the substituent's on the benzene ring influences the dissociation of the iodonium salts.[67] Computational and experimental studies by Fontanesi et al.[170] have shown that the dissociation of alkynyl(aryl)iodonium salts is largely influenced by the electronic nature of the aryl group substituents. Electron withdrawing functionalities favor the grafting of

the aryl ring versus the alkynyl group by destabilizing the aryl C – I bond, leading to the formation of the aryl radical bearing the withdrawing moiety.[171] A similar conclusion was reached for DAISs by Vase *et al*.[67] who showed that approximately 80% of the grafted species contain the nitro functionality when using the asymmetric (3-nitrophenyl)phenyl iodonium hydrogensulfate salt (compared to symmetrical bis(3-nitrophenyl) iodonium hydrogensulfate salt). Such arguments follow intuition, as the electron withdrawing group would be expected to promote the reduction of the withdrawn aryl ring while simultaneously weakening C – I bond and, therefore, promote fission.

To compare our observed functionalization ratios to those observed in the literature, both DNP and NPP were grafted onto GC electrodes under highly functionalizing conditions (Figure 2.7). Electrochemical grafting of DNP and NPP was accomplished as the result of 10 potential sweeps at 50 $mV \cdot s^{-1}$ from 0 to –0.85 V and 0 to –0.95 V, respectively. In both cases, the concentration of the salt solution was 0.5 mM. The reduction of DNP occurs at a more positive potential ([DNP] = 0.5 mM, $E_{p,c}$ = –0.680 V) compared to NPP ([NPP] = 0.5 mM, $E_{p,c}$ = –0.820 V). This is easily rationalized by considering the more electron deficient nature of the DNP due to the second nitro-functionality which facilitates electron transfer to generate the radical species. In both cases, a drastic reduction in the faradaic current is observed following the first sweep, indicating molecular grafting and passivation of the glassy carbon surface.

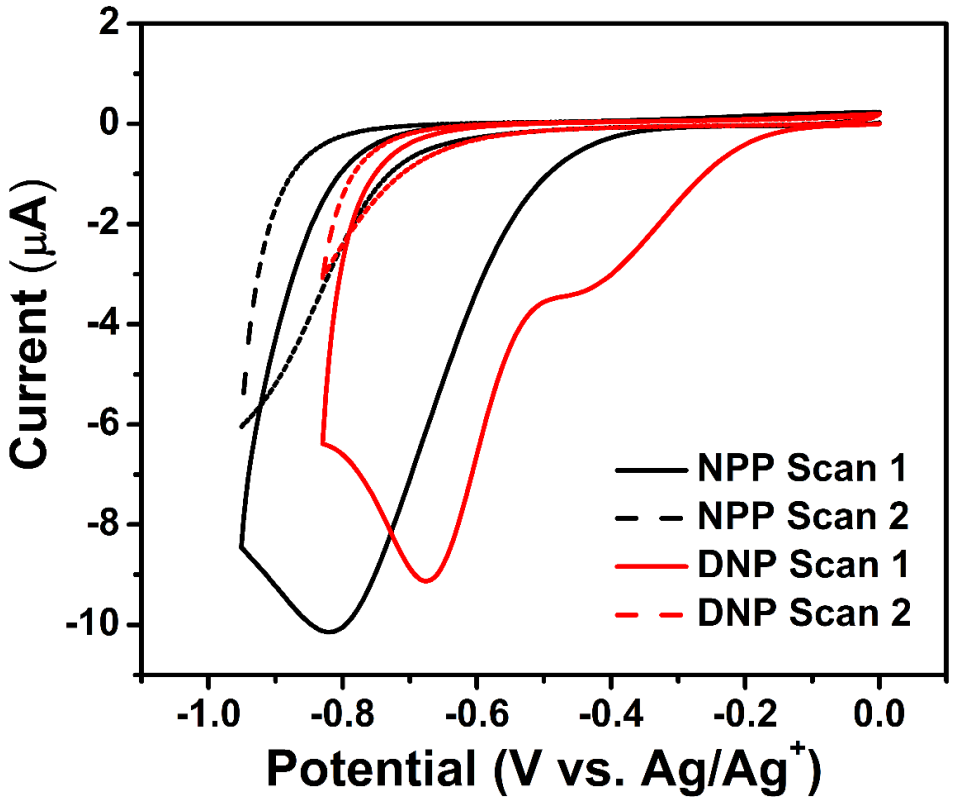

Figure 2.7. Comparison of the first two potential sweeps observed from the reduction and grafting of DNP (red) and NPP (black) to a glassy carbon surface (0.5 mM at 50 $mV \cdot s^{-1}$). Ten reductive sweeps were performed using each diaryliodonium salt.

Electrochemical quantification of the grafting densities, as determined by an average for five different glassy carbon electrodes for each salt, showed a coverage of (3.0 ±0.6) x 10^{14} $molecules \cdot cm^{-2}$ for DNP while a coverage of (2.7 ±0.4) x 10^{14} $molecules \cdot cm^{-2}$ was found for NPP (Figure 2.8). This equates to a grafting ratio of approximately 90% of the nitrophenylene molecules when using the asymmetric NPP salt. However, while exploring lower coverages, a reduced ratio of grafted nitrophenyl- to phenyl-moieties was observed, indicating effects other than the electronic nature of the DAISs may be influencing the final composition of the grafted film at high surface concentrations. To investigate these effects further, the composition of films generated

from the electrolysis of diaryliodonium stock solutions within the linear control range were examined via electrochemical methods.

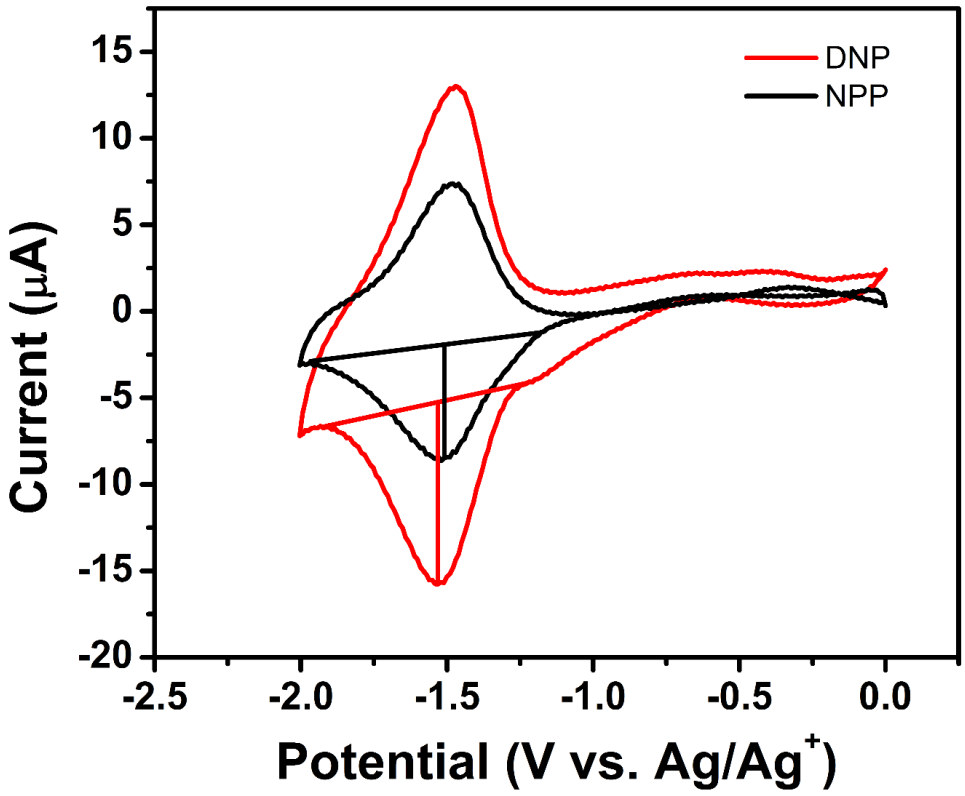

Figure 2.8. Comparison of the electrochemical response of the surface confined nitrophenyl-functionalities from DNP (red) and NPP (black) modified electrodes as a result of the grafting conditions described in Figure 2.7.

Control of the molecular grafting was once again obtained using cyclic voltammetry by varying the salt concentration and sweeping twice from 0 V to –0.85 V and from 0 to –0.95 V for DNP and NPP, respectively (Figure 2.9). Similar to the DNP calibration curve, the deposition of nitrophenylenes from NPP gave a linear increase in surface coverages with increasing concentrations of NPP up to 0.8 mM concentrations.

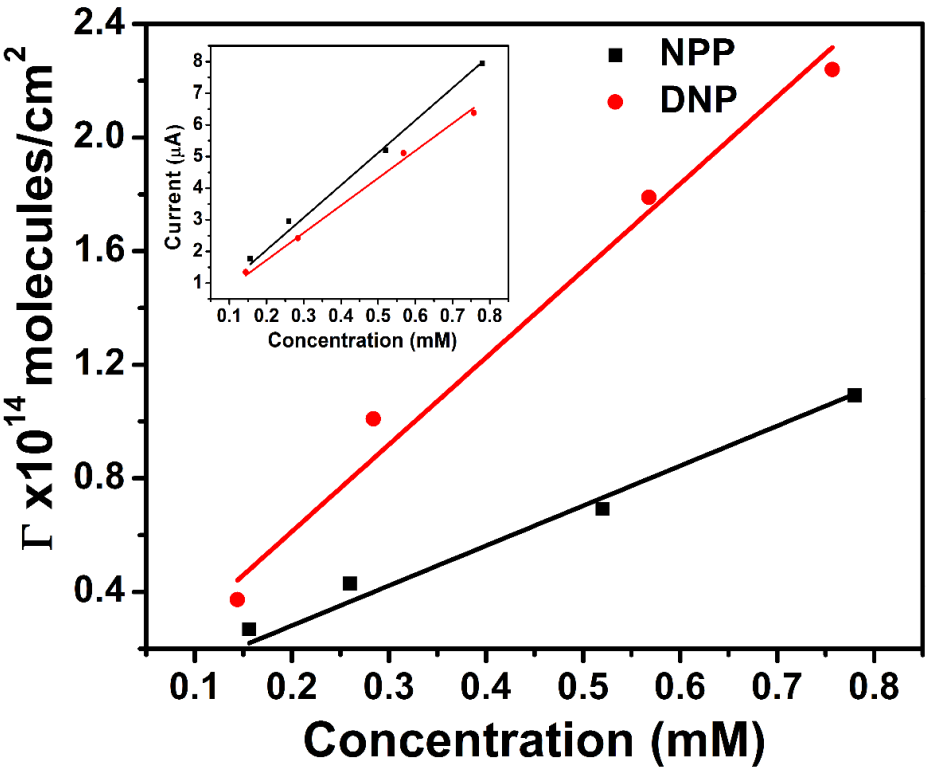

Figure 2.9. Comparison of the electrochemically observed surface concentrations (Γ) of nitrophenyl-groups from the modification of glassy carbon with grafting solutions with various concentrations of DNP and NPP. A slope of 3.06 x 10^{14} molecules·mM^{-1} was observed for concentration dependence of DNP while the slope for NPP was found to be 1.41 x 10^{14} molecules·mM^{-1}. The peak currents from the grafting scans for DNP and NPP showed similar values (inset) suggesting an equivalent number of aryl-radicals generated for each species at a given concentration.

A decreased slope in the NPP calibration curve is expected given the competing pathway for phenyl grafting, however, the slope of the curve is much less than the decrease of 10% expected from the ratios observed at high functionalization conditions. In fact, the slope of the NPP calibration was observed to be half of that seen for DNP, despite similar magnitudes in peak currents during electrolysis of the salt. This implies an approximate 1 : 1 grafting ratio of nitrophenyl- to phenyl-groups, indicating very little

electronic influence on the grafting ratio as a result of the electron withdrawing nitro-substituent. These results seem to contradict the approximate 90% grafting ratio observed under high grafting conditions as well as the electronic control arguments for the favoured dissociation and generation of the aryl radical on the electronically withdrawn ring. However, we have found this result is reasonable when considering a mechanism which accounts for the electronics and sterics involved in the layer-by-layer deposition of the aryl functionalities.

As depicted in Figure 2.10, deposition of a monolayer of nitrophenyl-groups from DNP leaves the surface covered in aryl moieties that contain only electronically deactivated positions (denoted D) sterically accessible for further deposition of aryl groups; this would hinder the formation of multilayers and decrease the total concentration of nitrophenyl-groups detected electrochemically. However, for the asymmetric NPP salt, the deposition of phenyl groups alongside the nitrophenylenes increases the number of positions on the grafted layer that are available towards further grafting, allowing for the efficient multilayer growth which would lead to the appearance of a higher grafting ratio of nitrophenyl- to phenyl-rings. Furthermore, it is suspected that the effect of the substituent on the cleavage of the iodonium salt is more pronounced for the cleavage of the alkynyl(aryl)iodonium salts than for the class of DAISs studied here.[170,171]

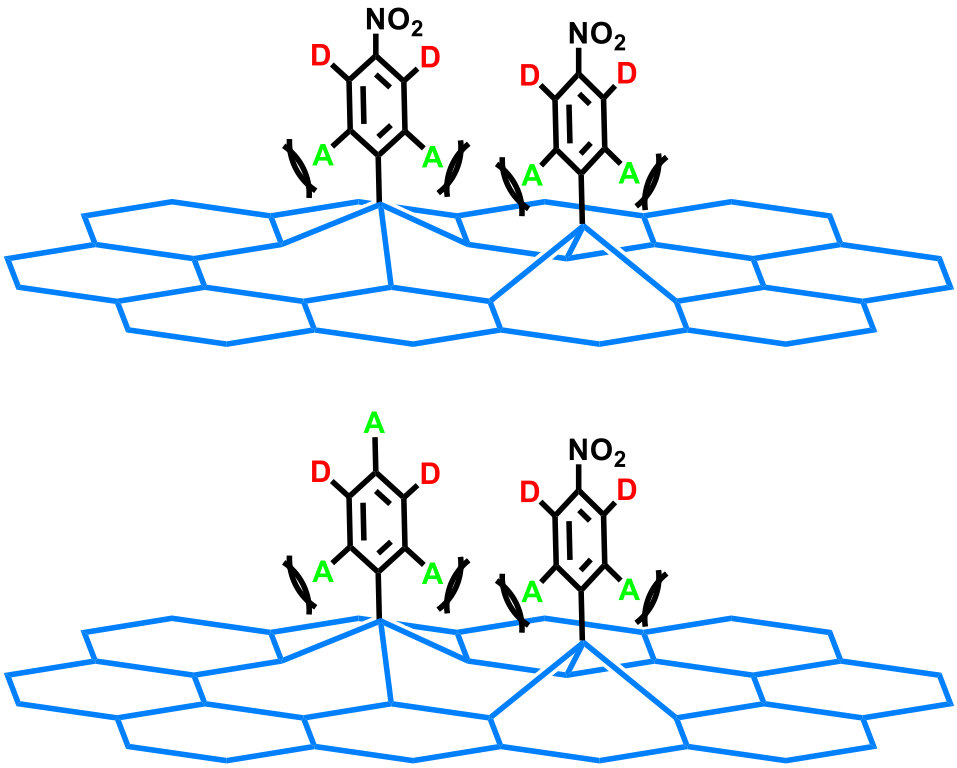

Figure 2.10. Diagram showing electronic and steric environments imposed on the first aryl layer when the glassy carbon electrode is modified with pure nitro functionalities from DNP grafting (top) versus the mixed coverage obtained via grafting of the asymmetric NPP (bottom). (A) Denotes activated positions while (D) denotes deactivated positions.

It should be noted that the observed grafting ratio of approximately 50% nitrophenyl- to phenyl- from the asymmetric NPP salt could be a consequence of the more negative potential required for the reduction of the NPP salt ($E_{p,c}$ = –820 mV) as compared to DNP salt ($E_{p,c}$ = –680 mV). The more negative reduction potential of NPP increases the likelihood of further reducing the aryl radicals to their anionic form, rendering them inactive towards grafting. This conversion should be more efficient for the electron deficient system containing the nitro functionality, thus lowering the observed grafting ratio of the nitrophenyl-groups.[172]

Further support that the electronic effects have less influence than previously thought can be found by inspection of the reported crystal structures of DAISs. As previously mentioned, it is suspected that the electronic effects play a significant role in strength of the C – I bond, thus altering its reactivity towards cleavage upon reduction. Support for this hypothesis should manifest itself in the crystal structures of DAISs as a lengthened bond between the iodine and the carbon from the aryl ring containing the electron withdrawing groups compared to the electron rich aryl ring. Figure 2.11 shows the distribution of the C – I bonds reported in the literature for DAISs.[179]

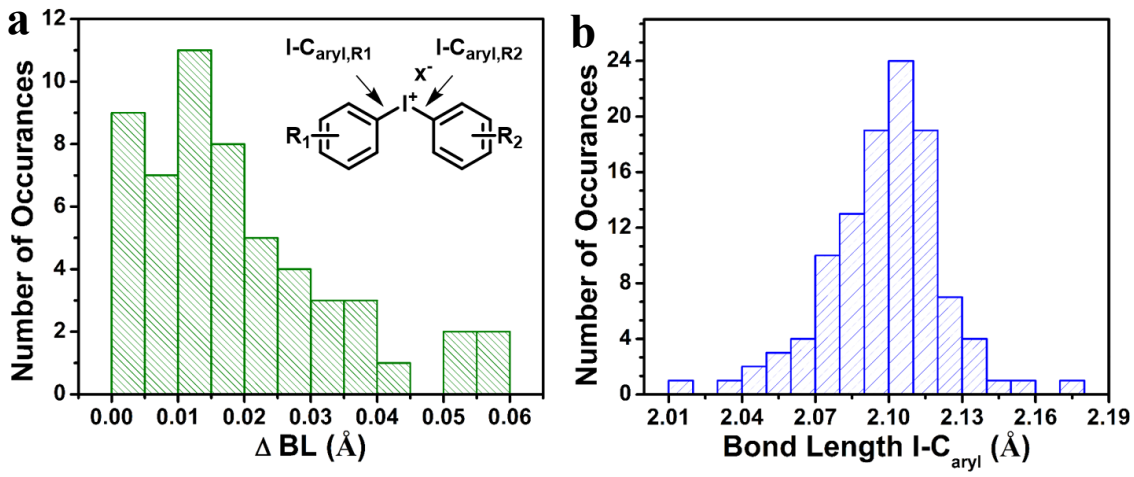

Figure 2.11. a) The distribution of the differences of the I–$C_{aryl,R1}$ and I–$C_{aryl,R2}$ bond lengths of the diaryliodonium salts found in the literature as determined by equation 2.2. b) Histogram of bond lengths from reported crystal structures.

The bonds fall within relatively narrow range between 2.018 Å and 2.174 Å and have an average bond length centered at 2.09 ±0.02 Å. However, the distribution of bond lengths is much less meaningful than comparing the differences in I–C_{aryl} bond lengths within individual DAISs. Figure 2.11a shows a histogram displaying the variations of the

differences in bond lengths (ΔBL) between two inequivalent I-C_{aryl} bonds within specific molecules calculated using the following equation:

$$\Delta BL = \left|(I - C_{aryl,R_1}) - (I - C_{aryl,R_2})\right| \quad \text{(eq. 2.2)}$$

We find that 80% of the reported structures display a ΔBL of 0.03 Å or less which indicates very little discrepancy between the different aryl groups. One would expect a much greater variation for significantly differing electronic functionalities with the rings containing electron withdrawing groups displaying longer bond lengths, however, examination of the crystal structures reveals the opposite trend. Crystal structures containing a significantly stronger electron withdrawing groups on one aryl ring are observed to have equivalent or even shorter bond lengths then the opposing aryl ring indicating a stronger I–C_{aryl} bond for the electron deficient moiety.[180–183] These bond lengths still fall within a very narrow range, however, which supports the idea that a synergistic effect is observed around the iodine(III) center where the total electronic nature of the salt is dispersed across both of the I–C_{aryl} bonds rather than a localized weakening of a specific C–I bond.

In order to determine if these trends in the literature hold true for the asymmetric system presented within this study, X-ray quality crystals of NPP were grown from a saturated solution in a CH_2Cl_2:MeOH:Et_2O (1:10:100, v/v/v) mixture (Figure 2.12). The bent geometry of NPP is consistent with that observed in the literature with a C1–I1–C7 bond angle of 94.15° (Figure 2.12). Furthermore, the aryl ring containing the strongly electron withdrawing nitro functionality shows a bond length of I1–C7 of 2.111(5) Å which is slightly contracted compared to the bond length of I1–C1 = 2.117(4) Å measured for the unsubstituted phenyl ring; this is consistent with the trends presented

above. However, the overlap in the standard deviation of the two bond lengths makes them statistically equivalent which is in agreement with the likelihood of equal grafting ratio.

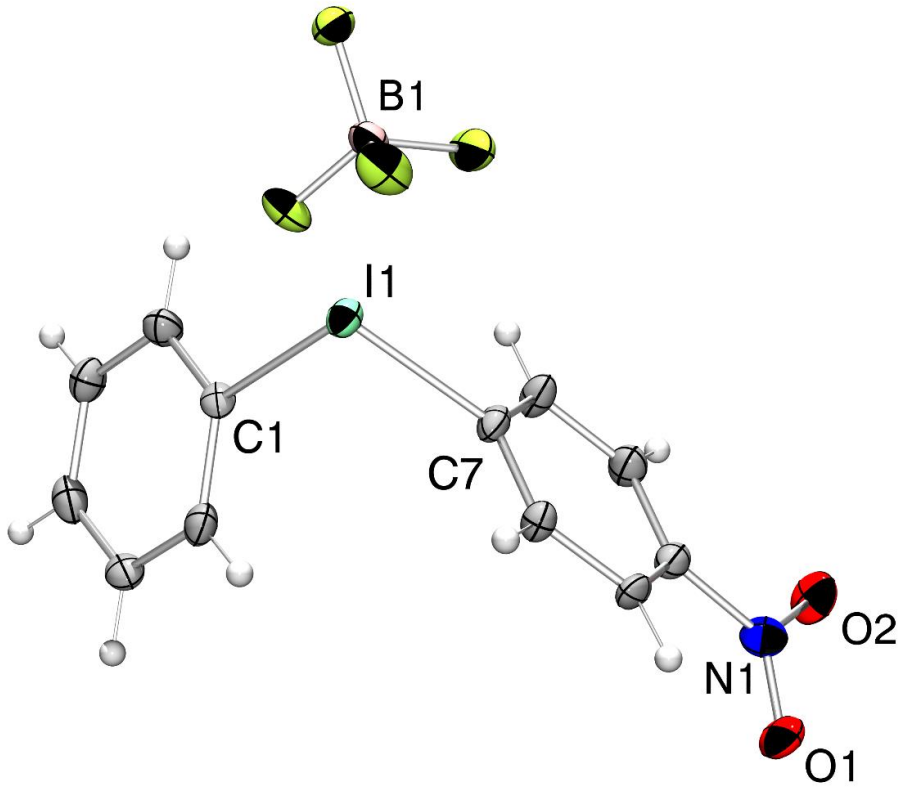

Figure 2.12. Molecular structure of NPP with thermal ellipsoids drawn at 30% probability.

2.2.4. Molecular Grafting to Epitaxial Graphene: Substrate Considerations

Fundamental studies into the nature of the electronic effects of molecular free radical graftants on graphene and the precise determination of the relative positions of molecular grafts requires high quality sheets of single layer graphene to unambiguously identify the effects of molecular modification when using Scanning Tunneling Microscopy (STM). A wealth of literature has been dedicated to the quest of synthesizing

ever-larger and more pristine sheets of graphene. These processes mainly focus on top-down approaches, such as chemical or mechanical exfoliations of graphene sheets from graphite, or from bottom-up approaches like chemical vapor deposition or epitaxial growth.[24,38,39,184–186]

As reported previously, graphene growth on SiC is mediated by the formation of a buffer layer (BL) or zero layer-graphene (Figure 2.13a).[187] This layer consists of carbon atoms arranged in a graphene-like lattice with 30% of the C-atoms covalently bound to the underlying SiC substrate. These dangling bonds in the SiC substrate negatively charge the BL and renders the graphene layer n-type doped. Although the graphene layer that grows on top of this BL is structurally nearly perfect, it is electronically coupled to the BL, which induces local variation in the density of states (Figure 2.13c).[188] Figure 2.13b shows a high resolution STM image of graphene on BL conductive 6H-SiC(0001). Coupling to the BL gives rise to an interference pattern characterized by the appearance of bright spots which possess six-fold symmetry. It has been shown that decoupling of the graphene from the SiC substrate and formation of the graphene sheet can be achieved by eliminating the Si–C bonds via hydrogen-intercalation.[187] In the literature, it has been shown using Angle Resolved Photoelectron Spectroscopy (ARPES) measurements that n-layer graphene transforms into (n+1) graphene layers after H-intercalation. As predicted by theory[189] and measured experimentally[187] the electronic structure of single layer graphene on the hydrogen-passivated SiC surface is minimally perturbed near the Dirac point. Figure 2.13e shows an STM image of a quasi-free graphene layer on insulating SiC obtained by H-passivation.

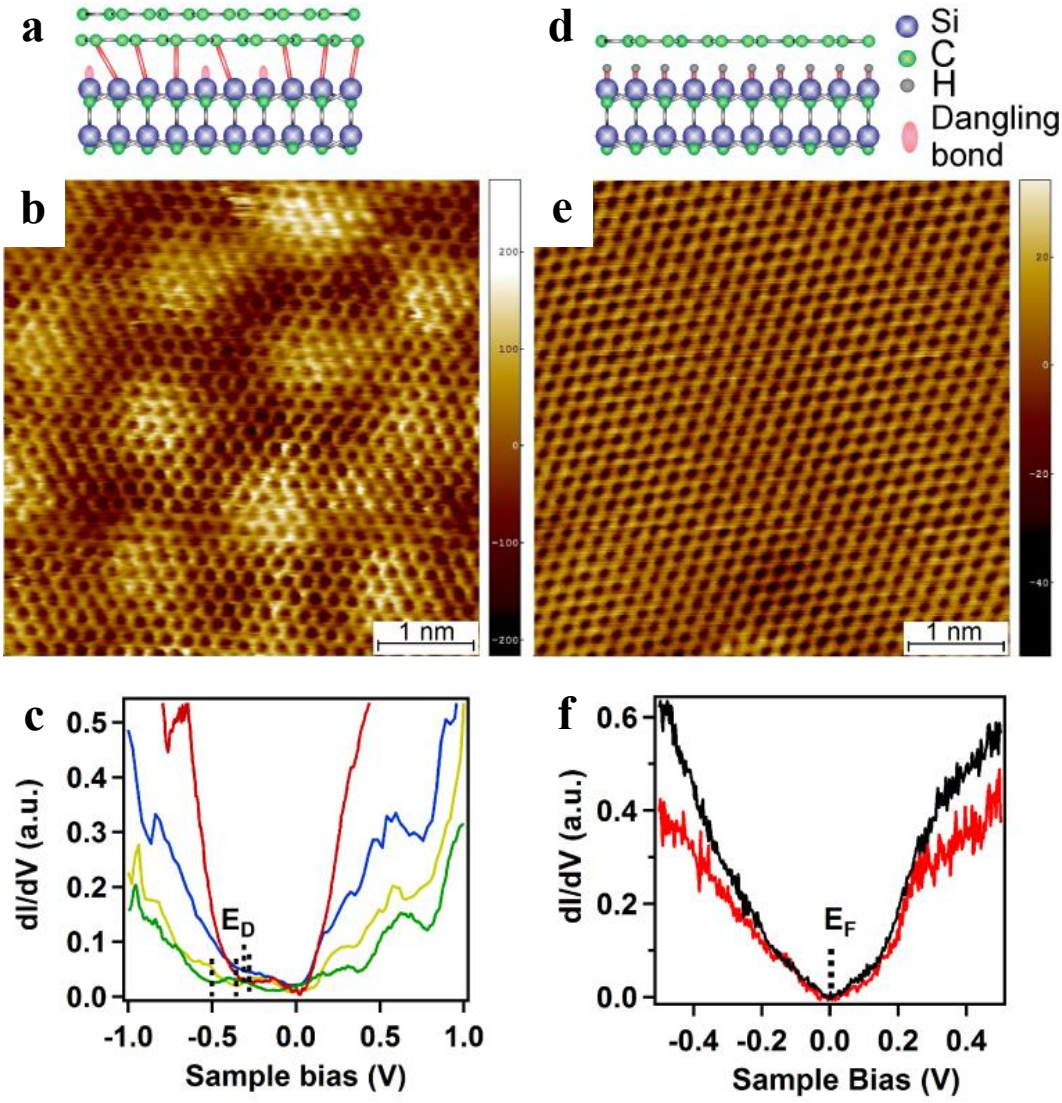

Figure 2.13. a) Graphical representation of epitaxial graphene on top of the buffer layer. b) STM image of BL epitaxial graphene (V_{bias} = 25 mV) on conductive SiC. Bright spots indicate areas of increased electron interference due to interactions with the underlying carbon buffer layer. c) Scanning tunneling spectroscopy (STS) of the BL graphene. The dI/dV curve shows significant variations in the local density of states (LDOS) and energy of the Dirac point (E_D). d) Representation of epitaxial graphene formed after hydrogen-intercalation to give semi-free standing graphene with minimal electronic interference from the underlying substrate. e) STM image of the BL-free graphene (V_{bias} = 25 mV) illustrating the absence of charge transfer regions. f) STS curves show consistent LDOS profiles across the buffer layer free graphene near the Fermi level (E_F).

The graphene film is extremely flat (80 pm). In contrast to the graphene on BL SiC, the local dI/dV measurements (Figure 2.13f) show no variation in the density of states and confirm the intrinsic doping in the BL-free graphene, making these samples ideal for studying the electronic changes induced in graphene by molecular grafting.

Contrary to what is reported in the literature,[190] atomic vacancy defects exist in graphene on H-intercalated SiC. Figure 2.14 shows high resolution STM images of such vacancies. By imaging the sample over a 7 X 7 nm grid, the average defect density (measured over approximately 30 images) was found to be (2 ±0.5) x 10^{12} vacancies·cm^{-2}. This defect density is four orders of magnitude larger than the natural point defect density in graphite.[191] Interestingly, it is noted that such defects were not observed on single layer graphene formed on BL conductive SiC. The relatively low growth temperature of graphene on SiC of 1550 °C (compared to the sublimation temperature of graphite at 3675 °C) facilitates the appearance of non-equilibrium defects such as vacancies.[192] Therefore these defects are expected to be present to some extent in the BL graphene samples as well. It is unclear what causes the high defect density on the BL-free compared to BL graphene; one can speculate that these defects may have been introduced during the H-intercalation process.

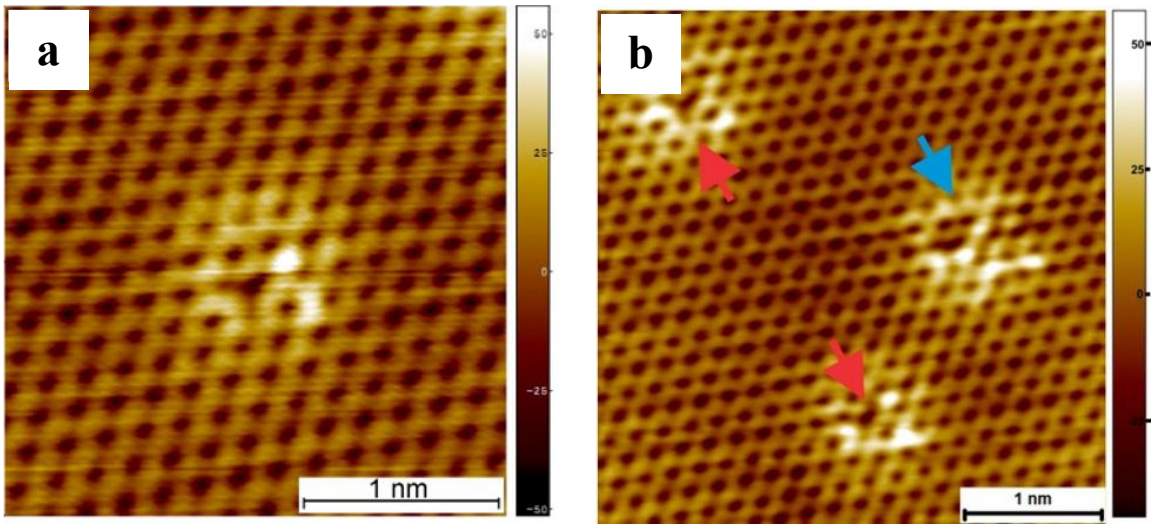

Figure 2.14. a) High resolution STM image (V_{bias} = 30 mV, $I_{setpoint}$ = 40 pA) of an atomic vacancy in graphene of hydrogen-passivated conducting SiC. An increase in the density of states is seen around the atomic point defect but no extended electronic perturbations are observed. b) Larger scale view of single (red arrows) and double (blue arrow) atomic vacancies.

Furthermore, Raman spectroscopy was used to quantify the relative defect densities corresponding to BL- and BL-free graphene samples (Figure 2.15). Cancado *et al.*[193] showed that Raman spectroscopy can be used in principle to quantify the amount of point defects in graphene.

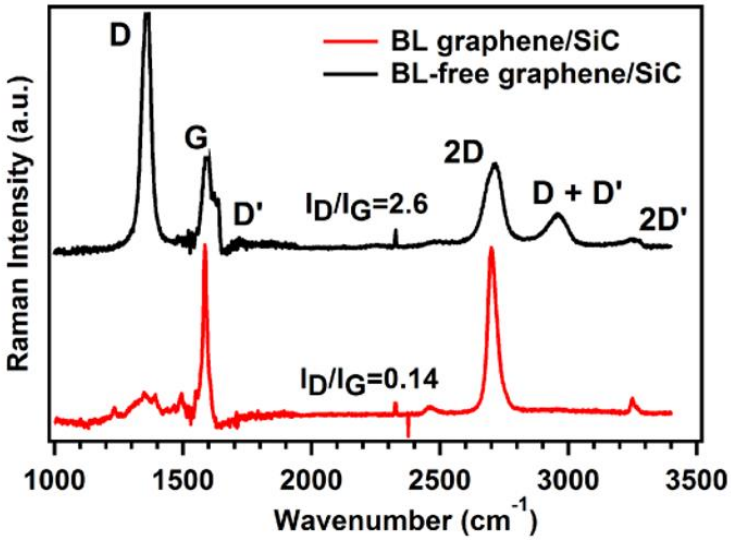

Figure 2.15. Raman spectra for buffer layer graphene on SiC (red) and buffer layer free graphene on SiC (black) measured at 514.5 nm. Raman spectra were background subtracted using a SiC blank. The black curve was shifted vertically for clarity.

The presence of sp^3 hybridized C-atoms on the covalent graphene lattice (peak at approximately 1350 cm^{-1} routinely called the D-peak) is indicative of defects located both at the step edges and the basal plane.[194,195] The area of the D peak for the BL-free graphene is larger than that of the D-peak for BL-graphene. The samples used in this study are monolayer graphene over approximately 80% of the surface area.[192] The remainder is covered by multilayer (2-3 ML) graphene mostly at the SiC step edges. Since this is true for both BL and BL-free graphene, it can be concluded that the increased area of the D-peak for the BL-free graphene is a clear indication of a significantly larger vacancy defect density. Single vacancies lead to the appearance of resonances at the Fermi level accompanied by scattering of the electron waves.[196,197] One dangling bond always remains due to bond order considerations; therefore it is commonly argued that one can expect higher reactivity at these point defects.

2.2.5. Electrochemically Induced Covalent Modification of Graphene with DNP

The graphene sample was covalently modified by attaching molecules using electrochemical methods developed using the glassy carbon electrodes. In brief, epitaxial single layer graphene grown on (0001) 6H-SiC was used as the working electrode in an electrochemical cell containing a solution of 0.15 mM DNP operated under nitrogen atmosphere in a glove-box.[71,198,199] The graphene substrates were electrochemically modified using two potential scans from 0 to –0.85 V (versus a Ag/Ag^+ reference electrode). The first scan (Figure 2.16) is characterized by the appearance of a Faradaic peak at approximately –0.6 V due to electrochemical reduction and dissociation of the DNP salt. As mentioned previously, the negative value of the reduction potential limits the spontaneous functionalization process which is characteristic of diazonium salts[68] and enables control over the degree of functionalization by varying the concentration of the diaryliodonium salt.[199] In order to study the mechanism and geometry of nitrophenylene attachments to the graphene lattice using STM and STS, a moderately low grafting density is necessary. The electrochemical redox response of the surface-confined nitro group was used to determine a grafting density of $(3.0 \pm 0.6) \times 10^{13}$ molecules·cm^{-2} when a 0.15 mM DNP grafting solution was utilized.[198,199] Since it has been observed in the literature that the nitro reduction is not completely reversible due to partial conversion to amino functionalities,[70] the nitro reduction scan was not performed on the covalently modified graphene substrates analyzed in STM.

The electrochemical reduction of DNP induces the homolytic cleavage of the carbon-iodine bond in the salt. The resulting radical resides in the sp^2-hybridized orbital of the carbon atom from which the iodine bond is cleaved on the nitrophenylene ring. Subsequently, the nitrophenyl radical covalently attaches to graphene, while the iodobenzene remains in solution. The fact that the radical resides in the sigma orbital and

is not delocalized into the π-orbital system is the key to achieving predictable control over the positioning of nitrophenyl functionalities, which, in this study, places the nitro-group at the para-position with respect to the carbon atom grafted at the surface of the graphene. This particular configuration is adopted in all the theoretical calculations presented below. The overall honeycomb framework of the graphene is expected to be preserved and, depending on the molecular coverage, one should be able to distinguish both partially saturated and/or conjugated structures.[61,200]

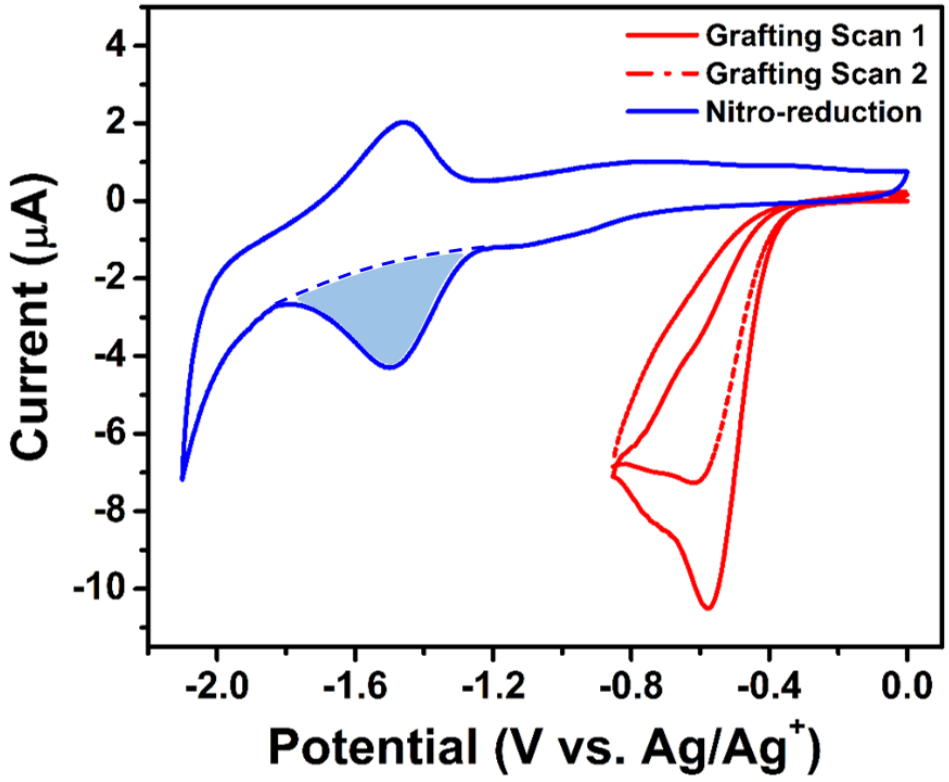

Figure 2.16. Reduction scans of the DNP salt (0.15 mM) onto buffer layer free graphene on conducting SiC, which induces covalent grafting, is shown in red. Electrochemical analysis of the surface confined nitrophenylenes is shown in blue. Integration of the cathodic peak yields a surface density of (3.0 ±0.6) x 10^{13} molecules·cm^{-2} was found.

Prior to the STM/STS studies, the molecularly functionalized graphene substrate was analyzed by Raman spectroscopy (Figure 2.17). Before modification, the Raman spectrum shows the signature spectra of single layer graphene with a G (E_{2g}) band at 1583 cm^{-1} and a 2D band (historically called G' which is associated with two in-plane transversal optical phonons near the K-point) at 2681 cm^{-1}.[194,201] The full width at half maximum (FWHM) of the 2D-peak is approximately 25 cm^{-1} which confirms the presence of a high content of monolayer graphene.

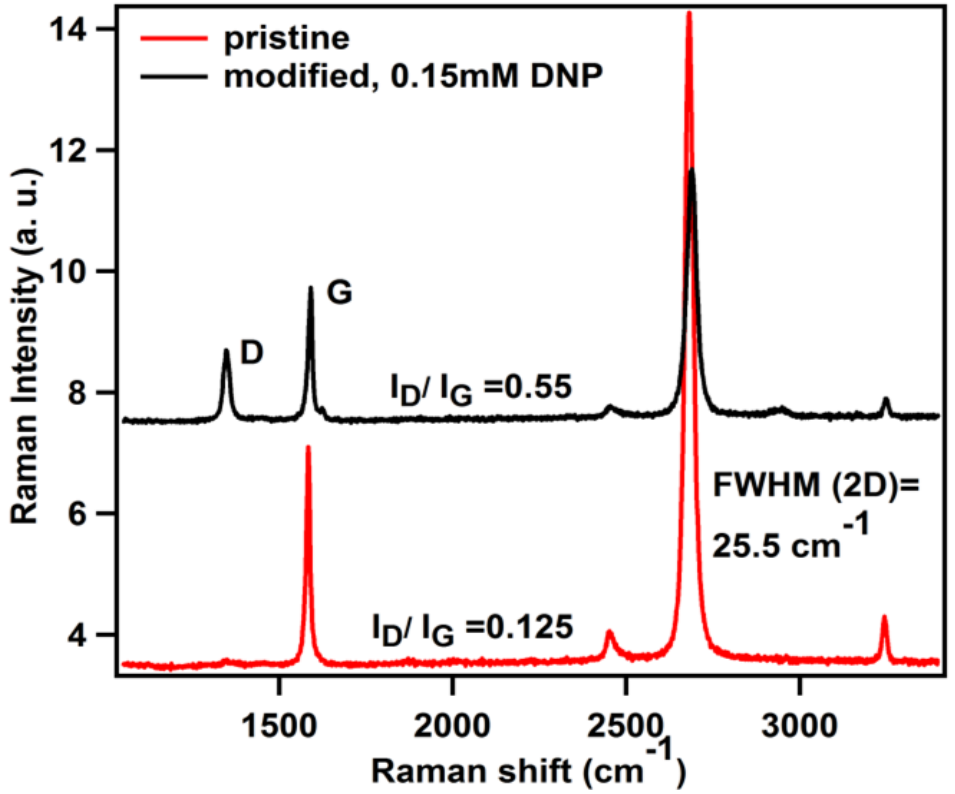

Figure 2.17. Raman spectra of buffer layer free graphene on SiC pre-modification (red) and post modification (black). Images are taken at 514.5 nm. The SiC background signal was subtracted from the spectra.

After nitrophenyl-functionalization, the intensity of the D peak increased, while the intensity of the 2D peak decreased with respect to the G peak. The intensity decrease of the 2D peak is associated with decreasing the number of the sp^2-bonds as the result of the nitrophenyl-addition which results in the activation of the A_{1g} vibration. In addition the ID/IG ratio increases from 0.125 to 0.55 after functionalization indicating an increase in the number of sp^3-hybridized carbons. An upshift in the position of both the G and 2D peaks is also observed by 6 and 8 cm^{-1}, respectively. The FWHM of the 2D peak remains constant.

The covalent nature of the attachment is further evident in the stability of the modifications as assessed by STM measurements which showed that the molecularly-modified graphene samples are stable in air well beyond one year.

2.2.6. Attachment of Spatially Isolated Nitrophenylenes

Figure 2.18 shows a STM image of monolayer buffer layer free epitaxial graphene on SiC surface with covalently attached nitrophenyl-moieties (grafted from a 0.15 mM DNP solution). Molecular grafts appear as triangular-shaped objects with increased electronic density of states. The covalent attachment of the nitrophenyl-molecules induces a strong electronic perturbation in the graphene lattice, altering the charge density of the graphene and giving rise to periodic oscillations similar to the previously observed Friedel oscillations.[202] The symmetry of these oscillations are strongly correlated with the trigonal symmetry of the graphene lattice. This three-fold electronic scattering pattern has been previously observed in covalently attached fluorine atoms onto graphite[203] as well as, around defect sites in graphite.[204] However, single atomic defects (vacancies) in epitaxial graphene on SiC (indicated by red arrow in Figure 2b and Figure 2d) are clearly distinct from other defect sites in graphitic structures.

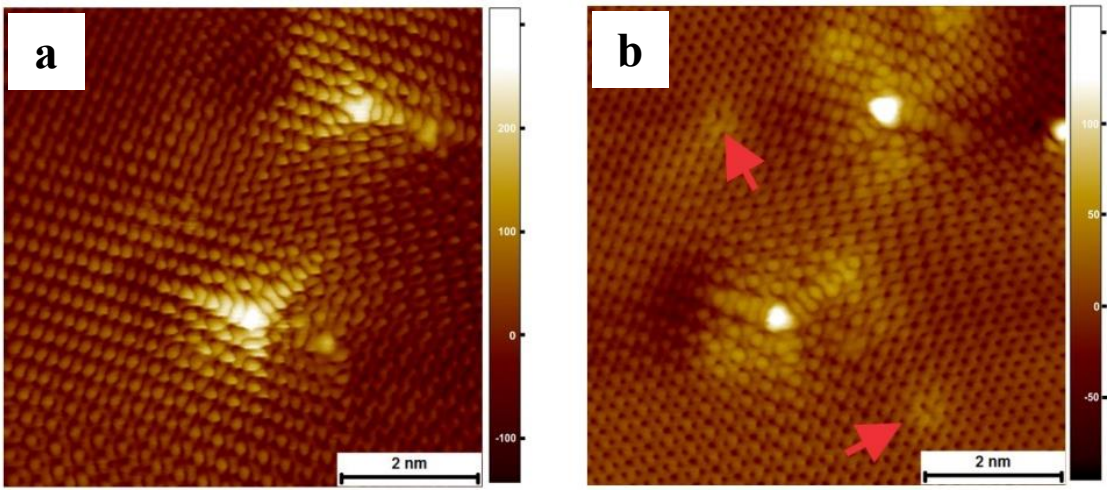

Figure 2.18. a) STM images image (V_{bias} = 70 mV, $I_{setpoint}$ = 40 pA) of single molecular modifications on the surface of buffer layer free epitaxial graphene on conductive SiC. b) STM images (V_{bias} = –500 mV, $I_{setpoint}$ = 40 pA) of single nitrophenyl-moieties covalently attached to graphene interspersed with atomic vacancies (red arrows). Nitrophenyl-modifications appear as bright objects with a three-fold dispersion of states while the atomic vacancies exhibit an increased density of states near the defect site with no extended perturbations to the electronic structure of the surrounding graphene.

In graphite, both measured and calculated STM images of vacancies show increased electronic density at the defect site accompanied by radial threefold symmetry electronic scattering waves. By contrast, vacancies in single layer graphene on SiC close to the Fermi level appear as hollow triangles with increased electronic density located on six adjacent C atoms and no Friedel oscillations are observed.[198]

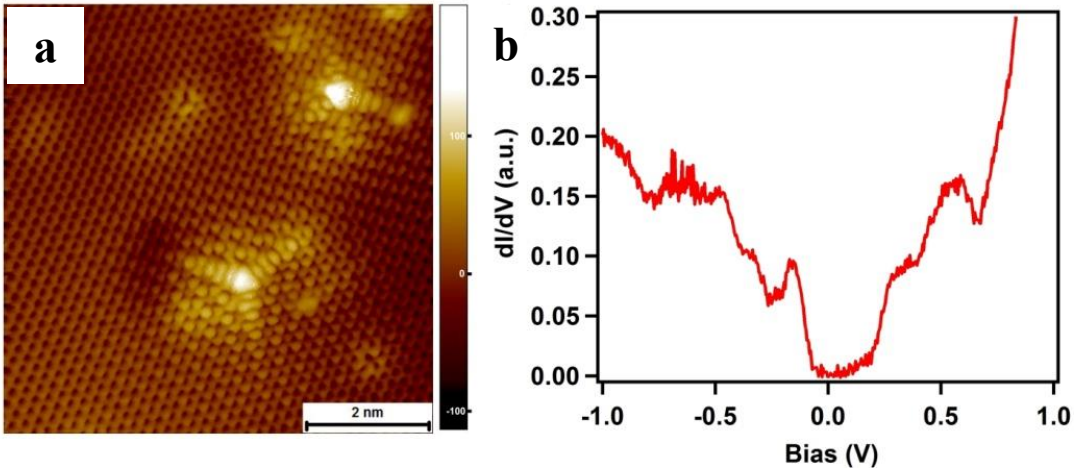

Figure 2.19. a) STM images (V_{bias} = 500 mV, $I_{setpoint}$ = 40 pA) of single nitrophenyl-moieties covalently attached to graphene interspersed with atomic vacancies. b) STS measurements taken at a grafting site. A bandgap of 0.2 eV is observed.

No significant difference is observed between the unoccupied and the filled states (unoccupied image was taken at V_{bias} = –500 mV in Figure 2.18b versus V_{bias} = 550 mV in Figure 2.19a for the occupied image). dI/dV measurements made at the location of the molecular graft (Figure 2.19b) shows the appearance of strong energy states at ±0.5 eV, –0.16eV and 0.3eV.

Structural relaxation calculations were performed in order to find the most favorable adsorption orientation of the nitrophenyl-molecule, and the lowest adsorption energy geometry was considered for all subsequent simulations (Figure 2.20). This orientation is similar to the previously performed simulations of benzene adsorption on a graphene sheet.[205]

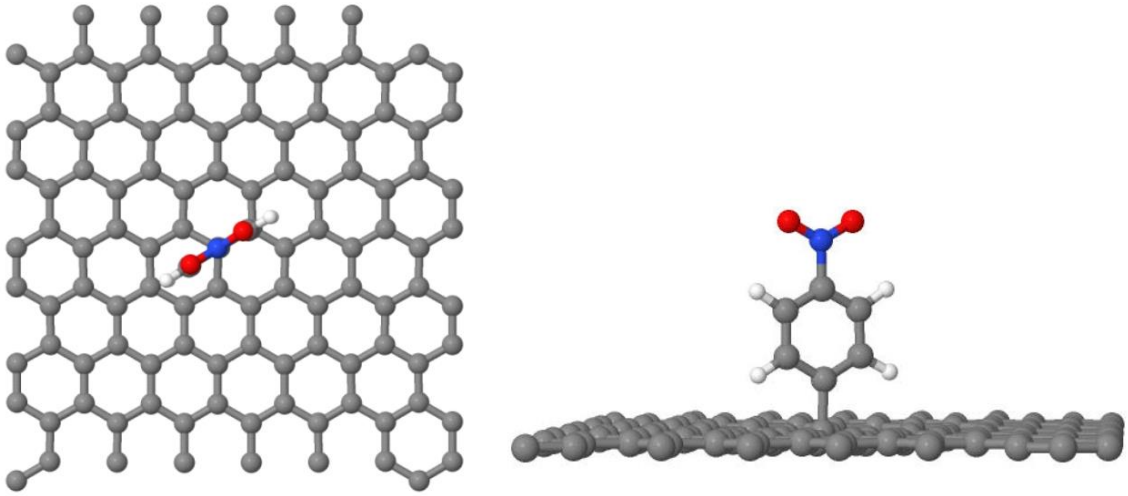

Figure 2.20. Density Functional Theory (DFT) optimized structure of a nitrophenyl-molecule chemisorbed to the surface of graphene.

Figure 2.21a shows density of states (DOS) plots within an energy window of ±3 eV of the Fermi level for both spin-up and spin-down channels. The Fermi level is set to zero for all DOS plots presented in this paper. A slight spin splitting between the highest occupied and the lowest unoccupied band is observed. As discussed in previous theoretical studies, attachment of the nitrophenyl-molecule creates a π-radical which is delocalized over the carbon atoms surrounding the adsorption site.[61,206] To investigate the origin of the triangular-shaped objects observed in the STM images, we visualize the iso-surface of the integrated local density of states (LDOS) within a 0.5 eV energy window from the Fermi level (displayed in gray in Figure 2.21b). Comparison with experimental data (STM image in Figure 2.21c) clearly indicates that the triangular shaped electron distributions arise from the presence of a nitrophenylene attached to the graphene lattice at the para position with respect to the nitro group.

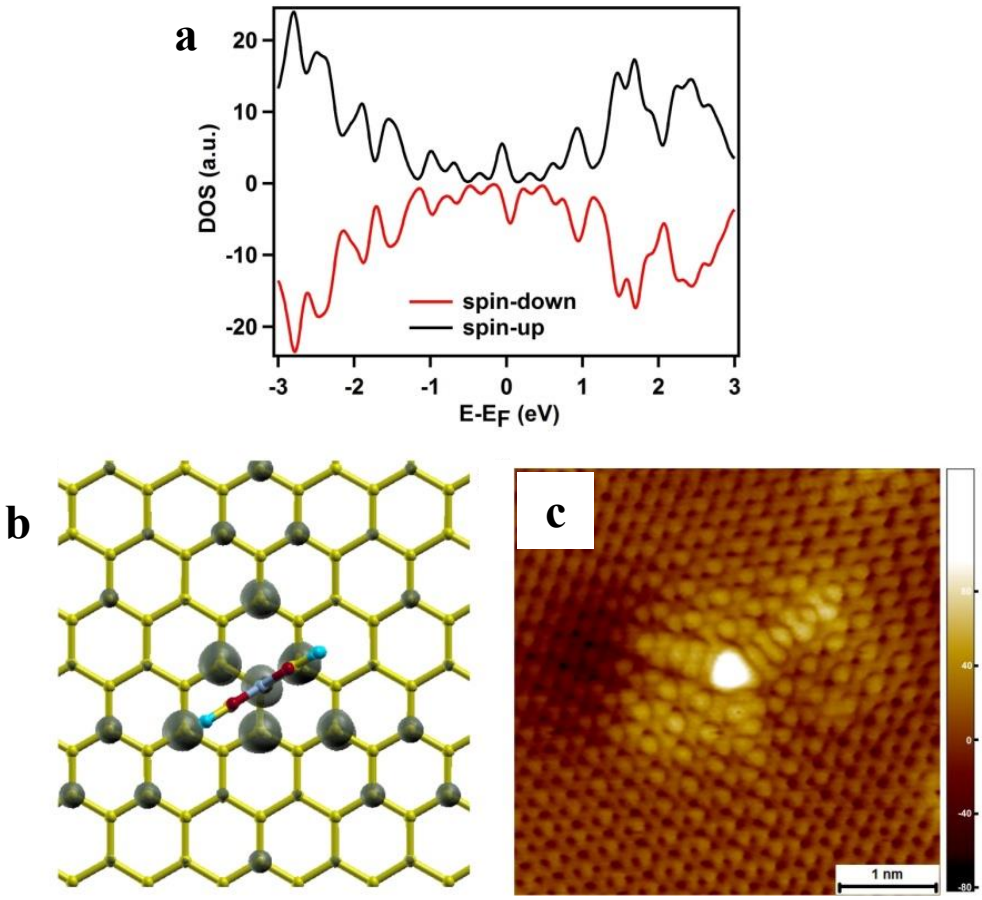

Figure 2.21. a) DFT calculated density of states for the spin up (majority, black) and spin down (minority, red) electrons resulting from the radical grafting of a single nitrophenyl-molecule. b) Integrated Density of States plot illustrating the spatial distribution of the LDOS integrated within an energy window of 0.5 eV from the Fermi level. C) STM image (V_{bias} = 500 mV, $I_{setpoint}$ = 40 pA) displays excellent agreement with the DFT predicted images.

2.2.7. Investigations into Pair-Wise Molecular Grafts

After careful analysis for this particular grafting density, a surprising result shows that the majority of grafts observed in the STM images are double triangles (Figure 2.22), suggesting that the pair-wise attachment of two nitrophenylenes occurs predominantly.

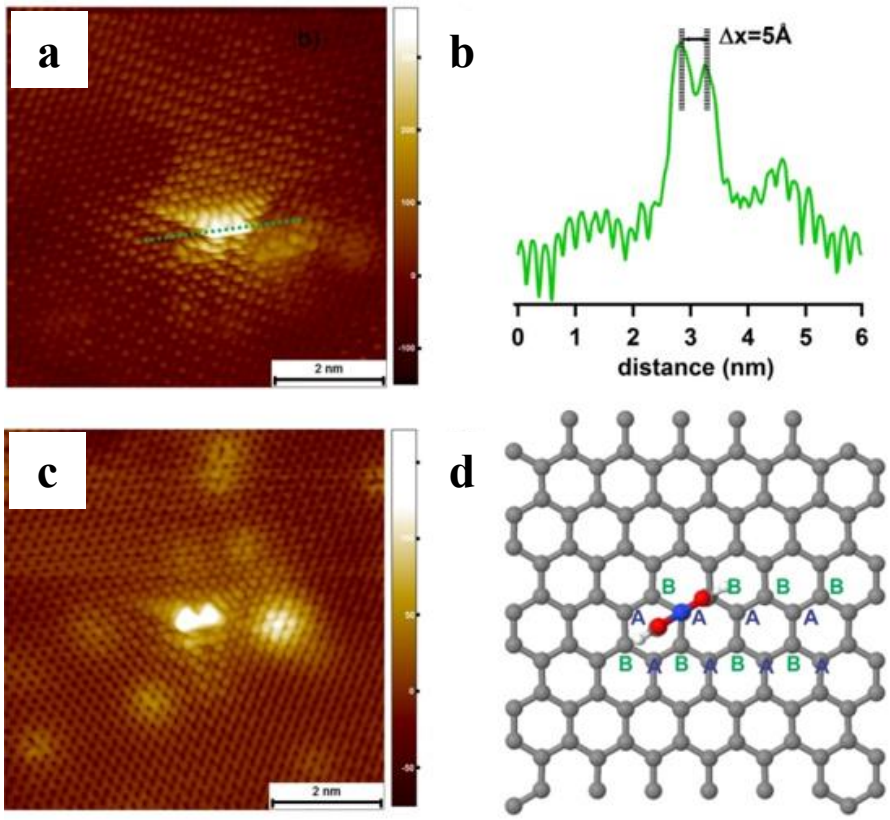

Figure 2.22. a) STM image (V_{bias} = 70 mV, $I_{setpoint}$ = 40 pA) of a pair-wise molecular graft. b) STM cross section of the paired grafts observed in a. c) STM image (V_{bias} = –500 mV, $I_{setpoint}$ = 40 pA) of a pair-wise molecular graft. d) Representation of a single nitrophenyl-graft and the corresponding A and B sub-lattices.

Since graphene has two inequivalent sub-lattices (denoted A and B in Figure 2.22d) the subsequent molecular attachment offers few scenarios. The attachment of the first nitrophenyl-molecule results in the appearance of a π-radical delocalized in the graphene lattice. As shown in Figure 2.21b, after the initial grafting of one nitrophenyl-molecule, an increased spin density is observed over the sites of the sub-lattice complementary to the one where the first molecule attached and follows previous findings on single atom vacancies and atom absorption (hydrogen) in graphene.[206] The attachment position of the second molecule is important as it results in distinct electronic

and magnetic properties. For instance, small paired substituents such as hydrogen in the A and B sub-lattices results in non-magnetic structures,[207] while addition in the same sub-lattice gives rise to unpaired spins on the other sub-lattice, resulting in ferromagnetism.[206] Inspection of the magnitude of the relative adsorption energy ($E_{abs,\ rel}$) for attachment at the different sites within the same graphene ring indicates that the second molecule should preferentially attach on the second graphene sub-lattice (positions denoted B, Figure 2.22d) in the *para*- ($E_{abs,\ rel} = -35.16$ kcal·mol^{-1}) and then the *ortho*-position ($E_{abs,\ rel} = -19.66$ kcal·mol^{-1}) in order to quench the spin.[208] As expected, spin-paired structures (paired additions in A and B sub-lattices) are thermodynamically favored. However, the DOS and LDOS iso-surface plots for the *ortho*-, *meta*- and *para*-position shown in Figure 2.23 are in contrast with the STM images.

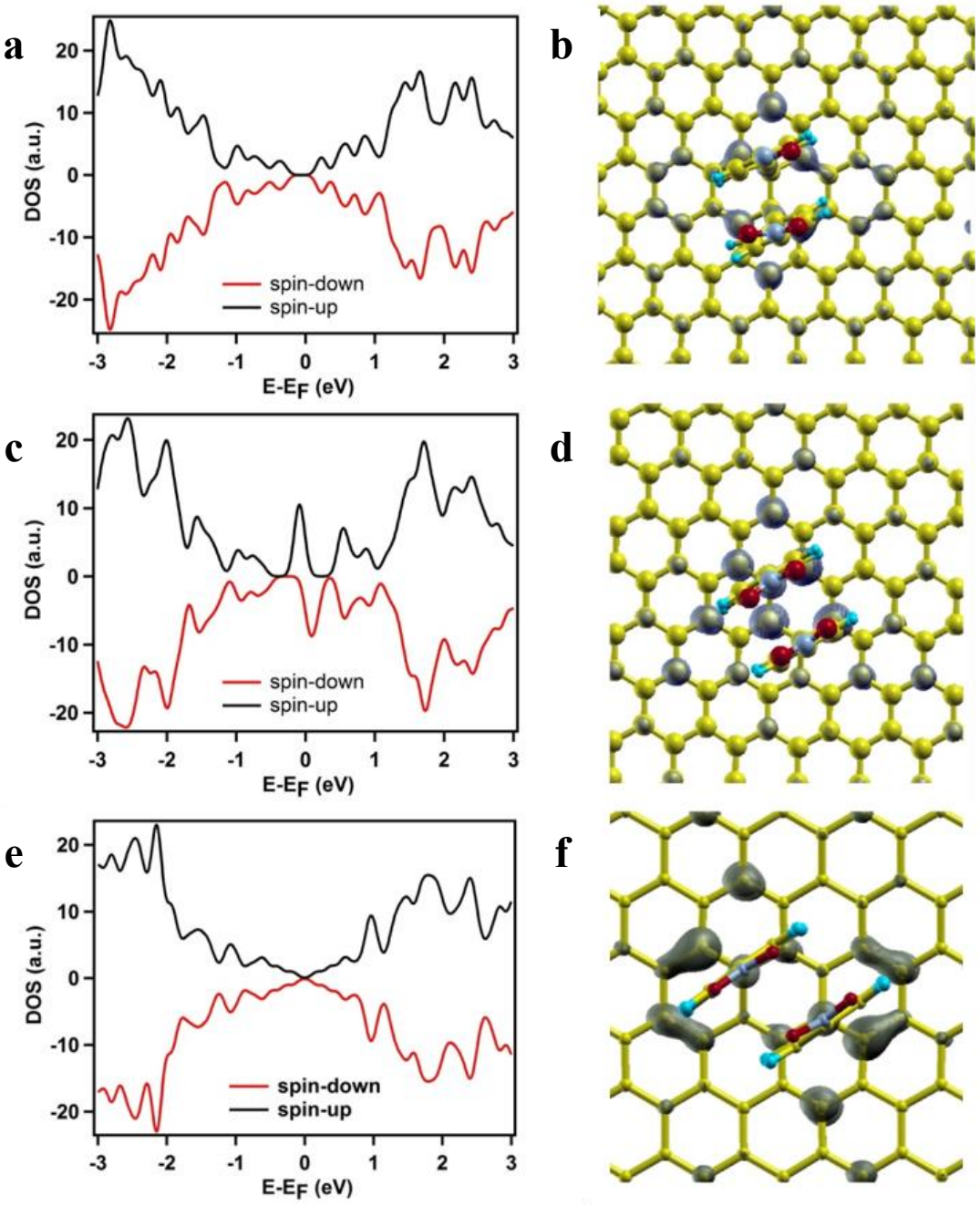

Figure 2.23. DFT-calculated density of states for the spin up (majority, black) and spin down (minority, red) electrons resulting from pair-wise grafting of two nitrophenyl-molecules in the a) *ortho*-, c) *meta*- and e) *para*-positions. Spatial distribution of the DOS integrated between within an energy window of 0.5 eV from the Fermi level for b) *ortho*-, d) *meta*- and f) *para*-positions.

Since radical delocalization is expected to extend beyond one graphene ring, additional attachment sites on adjacent graphene rings have also been explored. Previous calculations of hydrogen chemisorbed on graphene showed that the pattern of defect-induced states is delocalized over the sites of the complementary sub-lattice in which the defect lies and quickly decays with respect to distance. This implies that far from the defect, the driving force to graft on the sub-lattice with the unpaired electron is greatly diminished. The magnitude of the $E_{abs,\,rel}$ for absorption on the same sub-lattice (site A_1 in Figure 2.24a) or the opposite sub-lattice (site B which is color coded in orange in Figure 2.24a) was found to be –6.73 and –18.80 kcal·mol^{-1}, respectively. Both the A1 and B sites exhibit triangular features in the LDOS iso-surface plot. However, the two triangles exhibit the same orientation similarly with what is observed in the STM images only when the attachment of the second molecule proceeds in position A_1 on the same sub-lattice. As a consequence, no quenching of the excess spin is observed and the spin splitting close to the Fermi level is conserved. By contrast, when the second molecule attaches at the B_1 site (color coded orange atom) on the second sub-lattice, the spin splitting disappears since the two π-radicals created by two nitrophenylene molecules are now paired, but the integrated LDOS iso-surface shows the two triangular-like features having orientations dissimilar to the dispersion of states observed in the STM images.

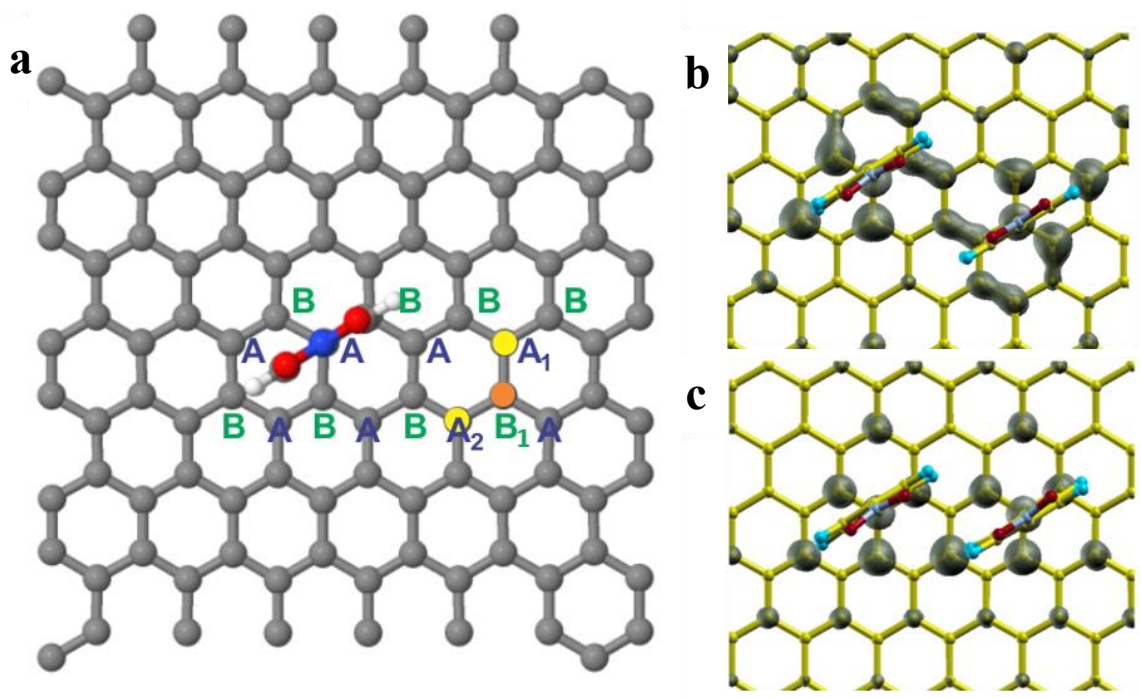

Figure 2.24. a) Graphical representation of the two sub-lattices of graphene and the positions of interest A_1 relative to the molecular graft. The resulting LDOS plots for the second molecule grafting at b) the B_1 and c) A_1 position.

The distance between the two molecules grafted on the same sub-lattice (position A_1) is 5 Å which is in good agreement with the STM observations (Figure 2.22b). This attachment geometry allows for the possibility of ferromagnetically coupled spins in nitrophenyl-functionalized graphene.

2.2.8. Extended Grafting Regions and Bulk Property Measurements

Isolated regions on the graphene substrate were also found to have extended modified regions (Figure 2.25). dI/dV data recorded at different positions within the extended modified region show a band gap opening at the Fermi level of approximately 0.4 eV. Ordered functionalized regions have been inferred to exist in modified graphene samples,[65] however, since STM measures the LDOS and strong electronic interaction are

expected to exist between nitrophenylenes within extended modified regions, one cannot assess based on STM images alone whether the observed regions are ordered or not. As discussed earlier in the case of defects in graphene, ferromagnetism is only possible when defects preferentially attach within the same sub-lattice.[206,209] The band gap opening in the modified graphene samples is further confirmed by the Angle Resolved Photoemission Spectroscopy (ARPES) measurements of the graphene Dirac point at the K-point of the Brillouin zone in Figure 2.25c-f. The removal of the buffer layer restores the slightly p-type character of graphene. Upon increasing functionalization with nitrophenylenes, the Dirac point shifts further below the Fermi level and indications of band gap opening appear. At high coverages, a broadening of the band dispersion is also observed, most likely associated with increased disorder in the graphene lattice.

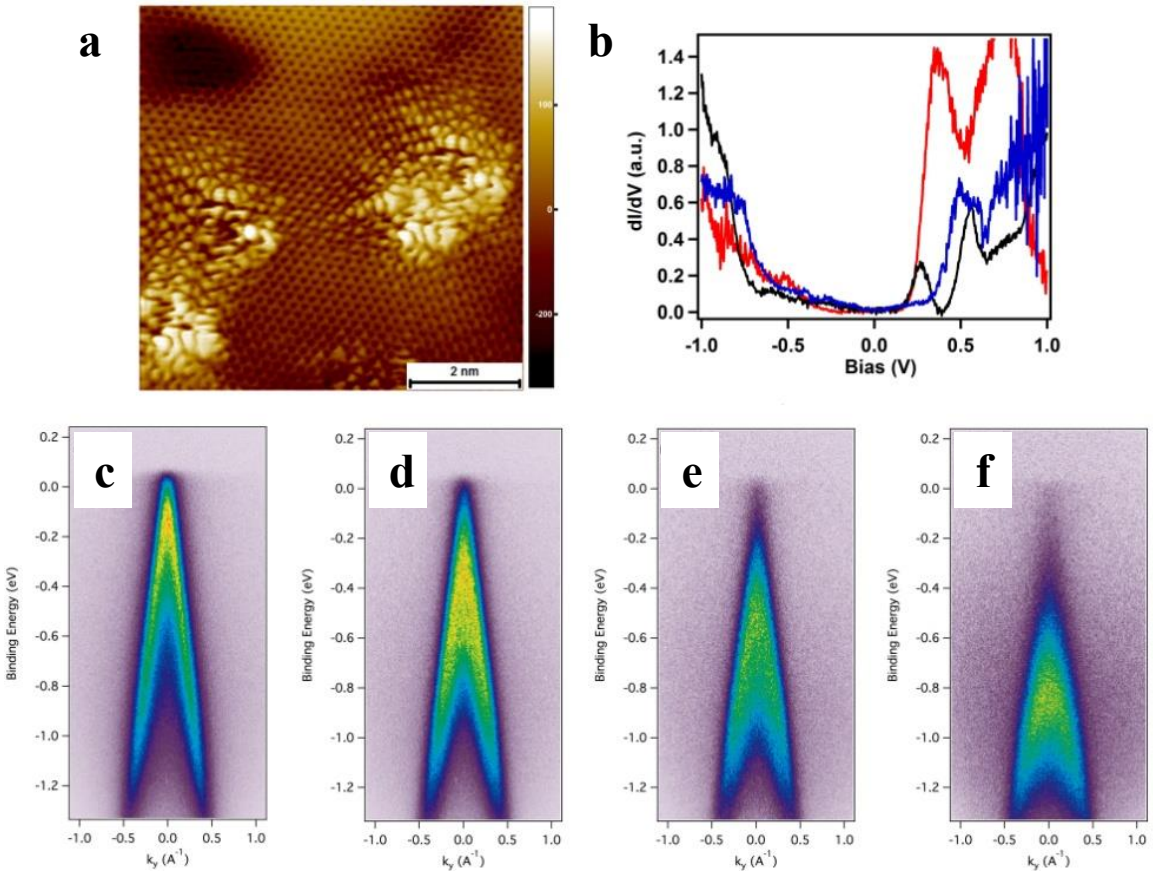

Figure 2.25. a) STM image (V_{bias} = 60 mV, $I_{setpoint}$ = 30 pA) showing regions of high molecular functionalization. b) dI/dV data recorded at different location within an extended modification showing the presence of a bandgap opening. Dispersion of the π-band at the $\overline{K}$-point perpendicular to the $\overline{K}$- $\overline{\Gamma}$ line ($k_y = k_\perp$) for c) pristine single layer graphene on H-intercalated (0001)SiC, graphene and with grafting densities of d) 4.3 x 10^{13}, e) 1 x 10^{14} and f) 2 x 10^{14} molecules·cm^{-2}.

Electrical measurements (Figure 2.26) on field effect transistors (FETs) fabricated using exfoliated graphene show that upon functionalization with nitrophenyl-substituents, at a grafting density of 4.0 x 10^{13} molecules·cm^{-2}, the graphene becomes p-doped and the doping density nearly doubles. The Dirac point shifts away from the Fermi level by approximately 50 meV.[210] An increased resistance upon functionalization is also

observed, which is indicative of a band gap opening and disruption of the sp^2-network; this is fully consistent with the photoemission and STS data.

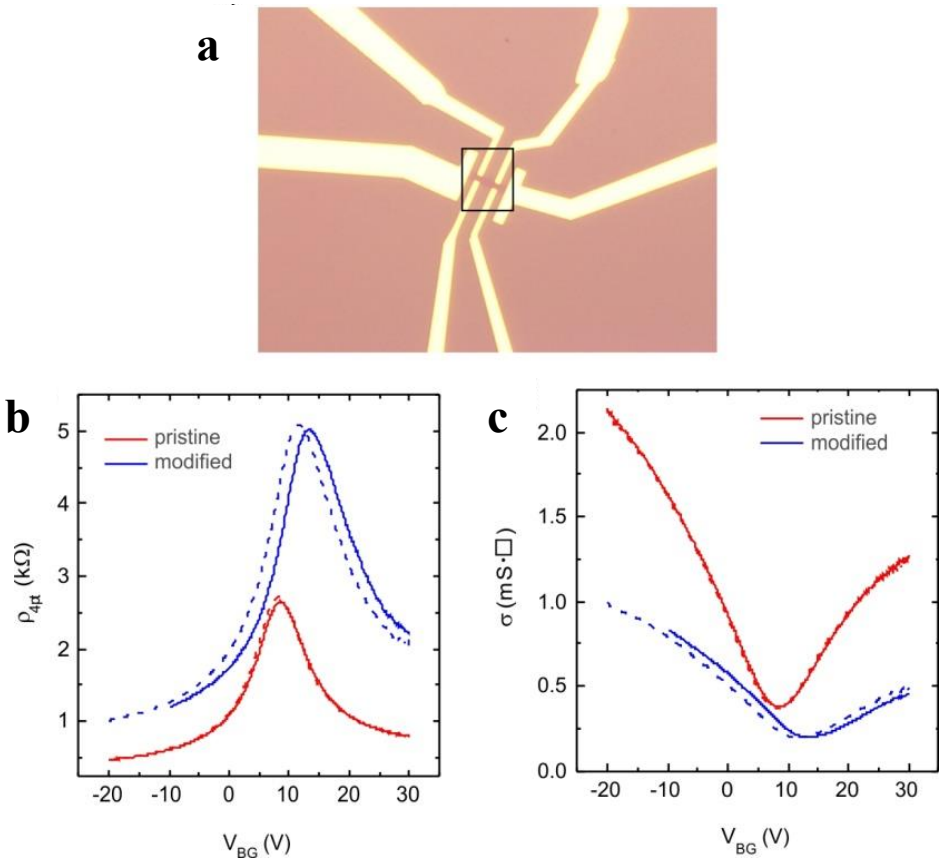

Figure 2.26. a) Optical picture of the graphene field effect transistors (GFET). Four point resistance b) and conductivity c) as a function of the applied back-gate voltage (V_{BG}). Slight contamination from the exfoliation process is present in the pristine devices (red curves in b and c). Solid and dashed lines are measured using different contact pairs on the same sample. The electron and hole mobility as well as doping levels before and after functionalization were calculated to be as follows pristine and modified graphene: Pristine graphene - electron mobility (7 x 10^3 $cm^2 \cdot V^{-1} \cdot s^{-1}$); hole mobility (5 x 10^3 $cm^2 \cdot V^{-1} \cdot s^{-1}$); carrier concentrations (5 x 10^{11} cm^{-2}). Modified graphene - electron mobility (2.9 x 10^3 $cm^2 \cdot V^{-1} \cdot s^{-1}$); hole mobility (1.7 x 10^3 $cm^2 \cdot V^{-1} \cdot s^{-1}$); carrier concentrations (10 x 10^{11} cm^{-2}).[210,211]

2.2.9. Investigations into the Relative Reactivity of Atomic Vacancies versus Pristine Basal Planes

The issue of whether the basal plane of graphene is more electrochemically active versus the plane edge and defect sites has been a pervasive question in the field of graphene modification. Where do redox-active molecules react and preferentially attach? Is it to the pristine graphene basal plane, or do they preferentially decorate the defect points, step edges and various other structural flaws that may be present on the sample?

The single vacancy density of buffer layer free graphene substrates before functionalization was estimated using STM to be (2 ±0.5) x 10^{12} vacancies·cm^{-2} (Figure 2.27).[198]

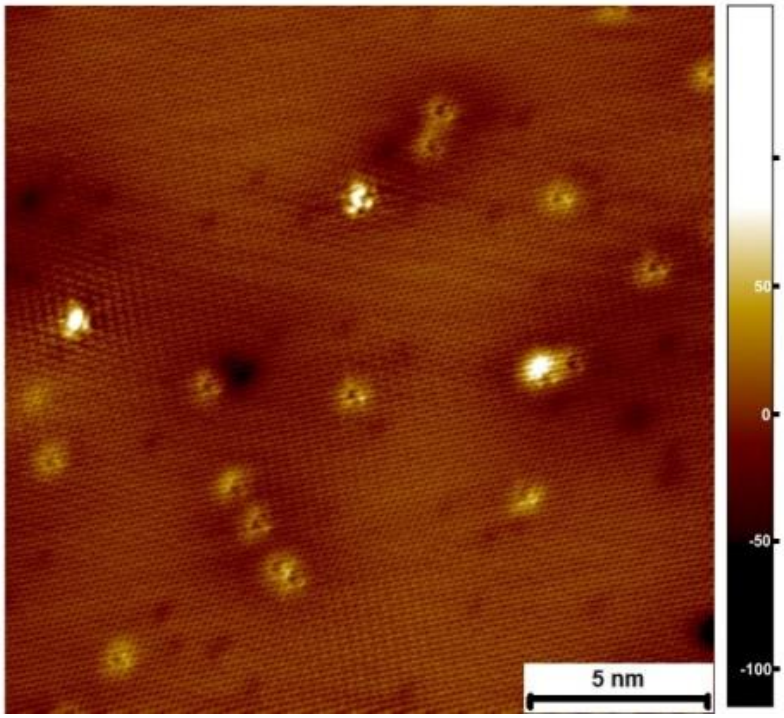

Figure 2.27. STM images (V_{bias} = 30 mV, $I_{setpoint}$ = 40 pA) of the pristine graphene substrates showing native single vacancies.

As these defect sites leave carbon atoms with dangling bonds, it is often speculated that single vacancies would exhibit higher reactivity with respect to the basal plane of graphene.[29,66,208] Since the grafting density ($\Gamma = (3.0 \pm 0.6) \times 10^{13}$ molecules·cm^{-2} for 0.15 mM DNP) is an order of magnitude larger than the single vacancy density, one could assume that all the defects would be functionalized. This observation is clearly not the case, as single vacancies are still present as shown in Figure 2.18. STM studies on BL-free graphene clearly show regions with modifications surrounded by defects densities of the order of 10^{12} defects·cm^{-2}, which is consistent with the defect densities prior to functionalization. This observation implies that the graphene basal plane exhibits high reactivity. It should be noted that defect passivation via hydrogenation during the H–intercalation process is another possibility which would lead to the defects sites becoming deactivated toward functionalization.

To contribute further to answering this question, we analyzed the grafting behavior for three samples: graphene on BL-free SiC, graphene on BL SiC and GC. These specific samples were chosen because of the varying defect densities. As discussed previously, the graphene samples have a very low number of step edges but the BL-free sample has a higher content of point defects (vacancies) as confirmed by Raman spectroscopy and STM. The GC electrode which consists of a combination of basal and edge planes should contain more defect sites than either graphene samples. The experiments were performed by sweeping the applied potential twice between the chosen potentials (referred to as stopping potentials). The resulting coverage was determined as shown previously by integration of the cathodic peak for nitrophenyl-reduction. Grafting was performed using a 0.15 mM DNP solution.

The stopping potentials for both GC and graphene samples are shown in Figure 11a, b. An additional point was taken outside of the grafting window at –1.02V. Figure

11c-e show the reduction scans for the nitrophenyl-moieties grafted on BL graphene, GC and BL-free graphene and for the different stopping potentials (respectively). A strong agreement was found between the BL and BL-free graphene samples (Figure 11f). Although more defective than any of the graphene samples the GC electrode shows similar coverages as well. These results demonstrate that although grafting at the defects site is thermodynamically favored the reaction is expected to be governed by kinetics.

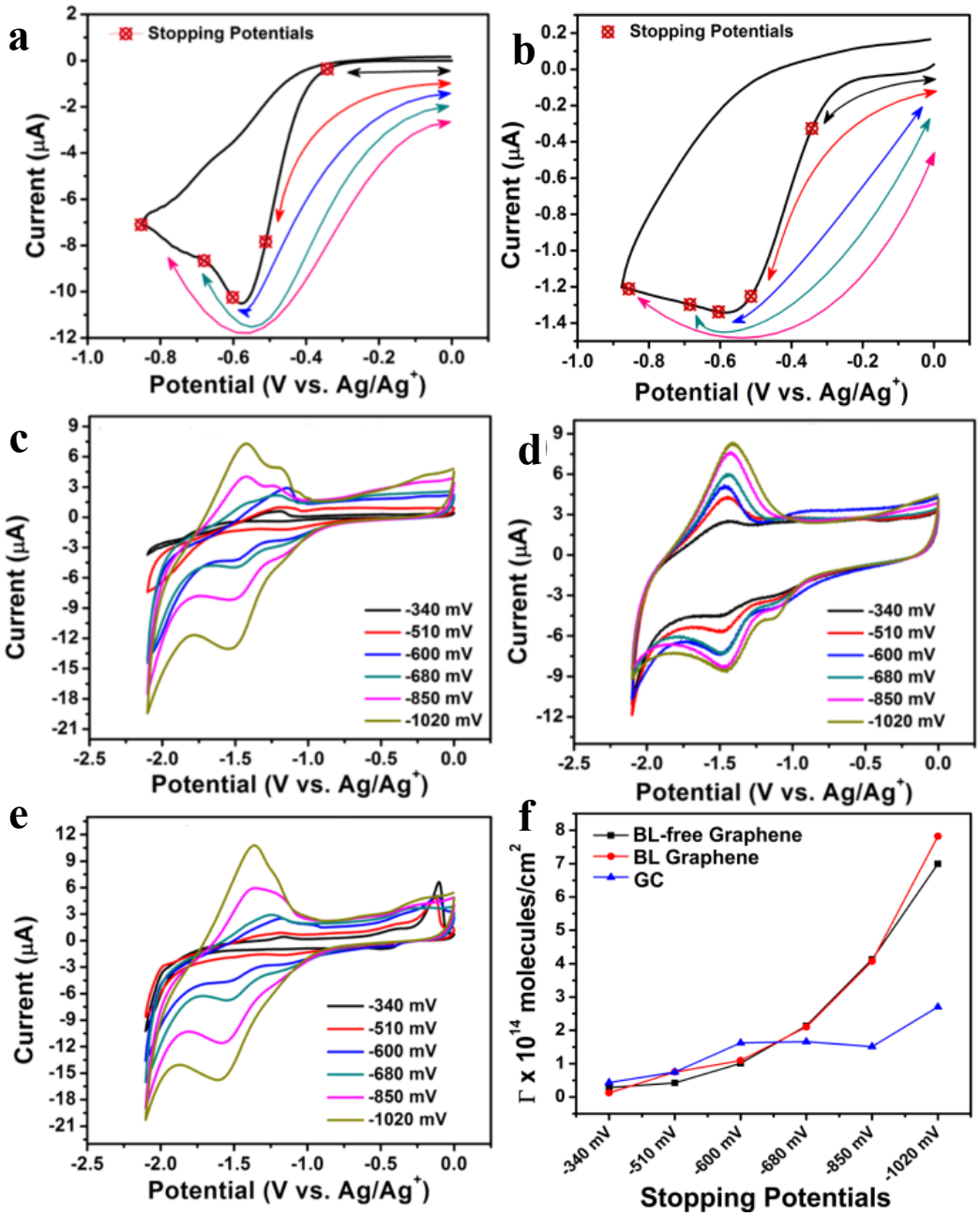

Figure 2.28. Stopping potentials overlaid on the voltammogram for covalent functionalization with BNPI on BL-free graphene on insulating a) SiC and b) glassy carbon. A final stopping potential at –1.02 V was also performed for each carbon substrate (point not shown in graphs (a) and (b)). The reduction of the nitrophenyl-moiety after grafting to BL graphene on insulating c) SiC, d) GC and e) BL-free graphene on insulating SiC. f) The grafting coverage estimated for each of the stopping potentials.

2.3. CONCLUSION

We demonstrated controlled modification of glassy carbon electrodes via cyclic voltammetry using the DNP diaryliodonium salt. The grafting density, calculated from the electrochemical measurements, can be reproducibly tuned from 4 x 10^{13} molecules·cm^{-2} to 3 x 10^{14} molecules·cm^{-2} before multilayer coverages begin to form. Furthermore, utilizing the asymmetric NPP salt, it was shown that the electronic influence from the electron withdrawing nitrophenyl-group has very little influence on the monolayer grafting ratios; this finding was supported by crystallographic data.

Controlled covalent grafting of the graphene surface was achieved using electrochemical tools employing diaryliodonium chemistry. Moderate grafting densities of (3.0 ±0.6) x 10^{13} molecules·cm^{-2} were reproducibly achieved from 0.15 mM DNP grafting solutions. Using buffer layer-free graphene substrates, we obtained atomically-resolved STM images of single site functionalization on graphene. Single modifications results triangular center with radial Friedel oscillations extending from the triangular center presenting three-fold symmetry. Simulated images of the density of states maps were accurately achieved using DFT calculations. Pair-wise additions were observed to be the most common molecularly grafted motif. Comparison of the DFT calculations with STM images reveal the second attachment preferentially occurs at a position on the same sub-lattice as the initial graft. This points towards a grafting mechanism in which after the first nitrophenyl-radical attaches to the graphene lattice the remaining unpaired electron get transferred and induces the splitting of a new diaryliodonium salt. This scenario results in the generation of a partial positive charge on the complementary graphene sub-lattice and renders the graphene p-type doped. As a consequence the subsequent grafting occurs on the same graphene sub-lattice as the initial graft. This can result in ferromagnetic properties in the resulting modified graphene sheet if long range

ordering of the molecular grafts is achieved. We speculate that by increasing the driving force for the electron transfer (biasing the graphene further from –0.85V) one can control the ratio of single to pair-wise grafts as well as the density of the p-type doping. Extended modified regions of approximately 2-6 nm are also observed, but are much rarer than the pair-wise additions. STS measurements in these regions indicate the opening of a band gap.

Investigations into the relative reactivity of atomic vacancy defect sites to pristine basal planes found that nitrophenyl-grafting from DAISs was found to occur preferentially in the defect free areas of graphene films suggesting that the basal plane of the graphene displays increased reactivity. This result indicates that the process is kinetically controlled and likely results from a fast eletron transfer rate from the basal plane versus defect sites.

Conversion of a sp^2-hybridized C-atom from the graphene lattice into an sp^3-carbon upon molecular addition offers a straightforward route for bandgap opening. Reproducible controlled modifications of graphene are expected to have a major impact in tuning the doping level and work function in graphene. Provided the formation of ordered functionalized regions, transistor applications might become a reality for graphene. In addition, tailoring the electronic nature of the attached molecule can open up routes for specifically p- or n-type doping in graphene, enabling its deployment in photovoltaic and battery applications.

2.4. EXPERIMENTAL

2.4.1. Synthesis and Characterization

All solvents were dried using an Innovative Technology Pure Solv solvent purifier with double purifying column and stored over 3 Å molecular sieves. 3-Chloroperbenzoic acid (*m*-CPBA) >77% (Sigma Aldrich), 4-nitrobenzeneboronic acid (Alfa Aesar), phenylboronic acid (Matrix) and 1-iodo-4-nitrobenzene (Alfa Aesar) were purchased and used as received. Deuterated solvents were purchased from Cambridge Isotope Laboratories and used without further purification. NMR spectra were recorded with a Varian DirectDrive 400 MHz spectrometer (^{1}H 400 MHz, ^{13}C{^{1}H} 100 MHz, ^{19}F 376 MHz). ^{1}H and ^{13}C{^{1}H} NMR were referenced to the residual solvent peaks while ^{19}F NMR was externally referenced to $CFCl_3$. Electrospray ionization (ESI+) data was collected on an Agilent 6530 quadrupole time of flight mass spectrometer.

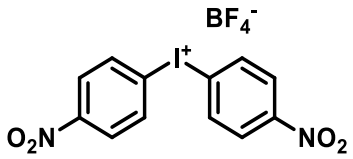

bis(4-nitrophenyl)iodonium tetrafluoroborate (DNP): Synthesis was achieved using modified literature procedures outlined by Olofsson *et al*.[174] In a 5 mL round bottom flask, 1-iodo-4-nitrobenzene (0.068 g, 0.273 mmol) was dissolved in 1 mL of CH_2Cl_2 followed by the addition of *m*-CPBA (>77%, 0.065 g, 0.290 mmol). $BF_3{\cdot}Et_2O$ (81 μL, 0.656 mmol) was added to the reaction mixture via syringe. The solution was stirred vigorously for 1 h and then cooled to 0 °C in an ice bath. 4-nitrophenylboronic acid (0.050 g, 0.300 mmol) was added to the reaction mixture and the resulting mixture was allowed to warm to room temperature over the course of 0.5 h. The reaction mixture was then subjected directly to a silica column. Impurities were eluted using CH_2Cl_2 and the product is collected using a CH_2Cl_2:CH_3OH (20:1, v/v) solution. The solution containing product is concentrated under a nitrogen stream and the product is precipitated using Et_2O. The residue was washed with Et_2O three times and dried in vacuum to yield product as off white solid (0.062 g, 50%). The product was stored under nitrogen at 0 °C. ^{1}H NMR (400 MHz, DMSO-d6): δ 8.49 (d, *J* = 9.0 Hz, 4H), 8.28 (d, *J* = 9.0 Hz, 4H). ^{19}F NMR (376 MHz, DMSO-d6): δ -148.28 (s). ^{13}C{^{1}H} NMR (100 MHz, DMSO-d6): δ 149.6, 136.8, 126.5, 123.0. HRMS (ESI): m/z calc'd for $C_{12}H_8IN_2O_4$ [M–BF_4^-]+ 370.95230; found 370.95180.

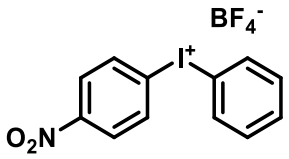

(4-nitrophenyl)phenyliodonium tetrafluoroborate (NPP): Synthesis was achieved using modified literature procedures outlined by Olofsson *et al*.[174] In a 25 mL round bottom flask, 1-iodo-4-nitrobenzene (0.650 g, 2.60 mmol) was dissolved in 10 mL of CH_2Cl_2 followed by the addition of *m*-CPBA (>77%, 0.640 g, 2.90 mmol). $BF_3{\cdot}Et_2O$ (850 μL, 6.80 mmol) was added to the reaction mixture via syringe. The solution was stirred vigorously for 30 minutes and then cooled to 0 °C in an ice bath. 4-phenylboronic acid (0.370 g, 3.00 mmol) was added to the reaction mixture and the resulting mixture was allowed to warm to room temperature over the course of 15 minutes. The reaction mixture was then subjected directly to a silica column. Impurities were eluted using CH_2Cl_2 and the product was collected using a CH_2Cl_2:CH_3OH (20:1, v/v) solution. The solution containing product was concentrated under a nitrogen stream and the product was precipitated using Et_2O. The residue was washed with Et_2O three times and dried under active vacuum to yield the product as an off white solid (0.685 g, 64%). The product was stored under nitrogen at 0 °C. ^{1}H NMR (400 MHz, DMSO-d6): δ 8.47 (d, J = 9.0 Hz, 2H), 8.31 (m, 4H), 7.69 (tt, J = 7.6, 1.1 Hz, 1H), 7.55 (t, J = 7.6, 2H).

2.4.2. Crystallography

Crystal structure determination for NPP X-ray experimental for NPP: crystals of NPP were grown by cooling a saturated solution of NPP in a CH_2Cl_2 : CH_3OH : Et_2O (1 : 10 : 100) to 0 °C. The data was collected on a Rigaku AFC12 diffractometer with a Saturn 724 + CCD using a graphite monochromator with MoKa radiation (λ = 0.71073 Å). The data was collected at 153 K using an Oxford Cryostream low temperature device. Data reduction was performed using the Rigaku Americas Corporation's Crystal Clear version 1.40.[212] The structure was solved by direct methods using SIR97[213] and refined by full-matrix least-squares on F^2 with anisotropic displacement parameters for the non-H atoms using SHELXL-97.[214] Structure analysis was aided by use of the programs PLATON98[215] and WinGX.[216,217] The hydrogen atoms on carbon were calculated in ideal positions with isotropic displacement parameters set to 1.2 x U_{eq} of the attached atom (1.5 x U_{eq} for methyl hydrogen atoms). The hydrogen atoms bound to nitrogen were located in a ΔF map and refined with isotropic displacement parameters. The data was checked for secondary extinction effects but no correction was necessary. Neutral atom scattering factors and values used to calculate the linear absorption coefficient are from the International Tables for X-ray Crystallography (1992).[218]

2.4.3. Electrochemistry

Electrochemical studies were performed under a nitrogen atmosphere in a dry-box with previously dried solvents using a GPES system from Eco. Chemie. B.V. The supporting electrolyte, [(*n*-Bu)$_4$N][PF_6] (TBAPF) was purchased from Oakwood and was recrystallized three times from hot ethanol, then dried for 3 days at 100 °C under active vacuum. All electrochemical experiments were carried out in a three electrode cell with a $Ag/AgNO_3$ reference electrode (silver wire dipped in a 0.01 M silver nitrate solution in a 0.1 M TBAPF solution in CH_3CN), a glassy carbon button working electrode (3.0 mm

diameter) or graphene on conductive SiC and a Pt wire coil counter electrode unless otherwise noted. The glassy carbon buttons were polished successively using 0.3 μm and 0.05 μm Al_2O_3 and rinsed with distilled water and acetone. Blank scans were performed to confirm a clean surface prior to grafting.

Electrochemically-induced free radical grafting to glassy carbon using DAISs was accomplished according to the following procedure. Stock solutions of the desired diaryliodonium salt were prepared in dry CH_3CN containing 0.1 M TBAPF. All grafts were performed via cyclic voltammetry using two cathodic sweeps at 50 $mV \cdot s^{-1}$. The potential sweeps used to accomplish the grafting were from 0 to –0.85 V for DNP and 0 to –0.95 V for NPP. Following grafting, the electrode was removed from the grafting solutions, washed with copious amounts of CH_3CN and transferred to a blank solution containing only 0.1 M TBAPF. The surface confined nitrophenyl-redox events are observed by two successive sweeps from 0 to –2.1 V at 1.00 $V \cdot s^{-1}$. The second scan is integrated to determine the charge transferred during the redox event.

Electrochemically-induced free radical grafting to graphene on conductive SiC using DNP was accomplished according to the following procedure. The electrical contact to the graphene was achieved using a thin gold foil wrapped around an alligator clip. Care was taken to avoid dipping the gold foil into the electrochemical solution. The solutions containing 0.15 mM DNP was prepared in acetonitrile containing 0.1 M TBAPF supporting electrolyte. The grafting was achieved using cyclic voltammetry by performing two cathodic sweeps from 0 to –0.85 V at 50 $mV \cdot s^{-1}$. After grafting the graphene working electrode was thoroughly washed with acetonitrile and transferred to a blank solution containing only 0.1 M TBAPF. The surface confined nitrophenyl-redox events were observed by two successive sweeps from 0 to –2.1 V at 100 $mV \cdot s^{-1}$. The second scan was integrated to determine the charge transferred during the redox event.

2.4.4. Preparation and Characterization of Epitaxial Graphene

Prior to graphitization, (0001) 6H-SiC (Si-face, semi-insulating, Vanadium doped, ii-vi Incorporated) substrates were etched in 1 atm of 45% H_2:Ar to reduce polishing defects and to produce well-ordered SiC atomic terraces. Graphitization was performed at high temperature (e.g. 1550°C) in Ar atmosphere at atmospheric pressure and resulted in the formation of a zero layer or buffer layer graphene (BL), covalently bound to the substrate.[192] Graphene decoupling was achieved by H-intercalation using 45% H_2:Ar mixture at 800 °C.

2.4.5. Raman Spectroscopy

Raman measurements were performed using a Renishaw inVia Raman microscope. The excitation laser wavelength of 514.5 nm from an Ar laser with a 50X objective were used. The laser was operated at low power (approximately 1 mW) to avoid damaging the graphene.

2.4.6. Scanning Tunneling Microscopy (STM) and Spectroscopy (STS)

The STM images and STS data were acquired using an Omicron system operated at 77 K using etched tungsten tips. Prior to imaging, the graphene substrates were washed with acetonitrile and degassed in vacuum at 425 K for several hours. The dI/dV data were recorded using an Ametek lock-in amplifier (7280 DSP) with a 20 mV wiggle voltage at 712 Hz.

2.4.7. Angle Resolved Photoemission Spectroscopy (ARPES)

Angle-Resolved Photoemission Spectroscopy (ARPES) measurements were performed using the 4.0.3 MERLIN beamline at the Advanced Light Source (Berkeley). A 20 x 60 μm p-polarized beam with a photon energy of 80 eV was used. The detector

pass energy was set to 20 meV. Prior to measurements, the graphene samples were degassed under vacuum for 30 min at 150 °C.

2.4.8. Density Functional Theory (DFT) Calculation Methods

The density functional theory (DFT) calculations were carried out employing a real-space pseudopotential method implemented in PARSEC package.[219,220] Within the real-space formalism, the Kohn-Sham equation was solved on a uniform grid and the grid spacing determines the convergence of calculations. For a grid spacing of 0.16 Å the total energy converged within 0.01 eV·atom^{-1}. The minimum energy structures were obtained by performing structural relaxation. All atoms were allowed to change positions until the force exerted on each atom was less than 0.004 Ry·a.u.$^{-1}$ (1 a.u. = 0.5292 Å) Norm-conserving pseudopotentials were generated within the local density approximation (LDA) employing Ceperley-Alder parametrization for the exchange-correlation functional.[205] The valence configurations and cutoff radii used are: C $2s^2 2p^2$ 1.49 a.u. and 1.52 a.u., N $2s^2 2p^3$ 1.50 a.u. for both , O $2s^2 2p^4$ 1.45 a.u. for both, and H $1s^1$ 1.49 a.u. Using these pseudopotentials, the graphene lattice parameter was calculated to be 2.44 Å, which is within 1% of experimental value. The simulation cell size of 17.05×16.88×15.88 Å^3 was used and includes 112 carbon atoms for the pure graphene sheet. One nitrophenylene molecule attached per cell corresponds to a density of 3.5 x 10^{13} molecules·cm^{-2}. For the K-point generation a Monkhorst-Pack scheme was used and 4 × 4 × 1 mesh was applied. In order to avoid the interaction between periodic images a slightly bigger simulation cell was used (19.49×16.88×15.88 Å^3) for the results presented in Figure 2.24.

2.5. REFERENCES

(24) Akbar, F.; Kolahdouz, M.; Larimian, S.; Radfar, B.; Radamson, H. H. *J. Mater. Sci. Mater. Electron.* **2015**, *26*, 4347–4379.

(29) Bekyarova, E.; Sarkar, S.; Niyogi, S.; Itkis, M. E.; Haddon, R. C. *J. Phys. Appl. Phys.* **2012**, *45*, 154009–154026.

(38) Hansora, D. P.; Shimpi, N. G.; Mishra, S. *JOM* **2015**, 1–14.

(39) Jiang, K.; Ma, L.; Wang, J.; Chen, W. *Rev. Nanosci. Nanotechnol.* **2013**, *2*, 171–183.

(61) Niyogi, S.; Bekyarova, E.; Hong, J.; Khizroev, S.; Berger, C.; de Heer, W.; Haddon, R. C. *J. Phys. Chem. Lett.* **2011**, *2*, 2487–2498.

(65) Zhu, H.; Huang, P.; Jing, L.; Zuo, T.; Zhao, Y.; Gao, X. *J. Mater. Chem.* **2012**, *22*, 2063–2068.

(66) Paulus, G. L. C.; Wang, Q. H.; Strano, M. S. *Acc. Chem. Res.* **2013**, *46*, 160–170.

(67) Vase, K. H.; Holm, A. H.; Norrman, K.; Pedersen, S. U.; Daasbjerg, K. *Langmuir* **2007**, *23*, 3786–3793.

(68) Dirk, S. M.; Pylypenko, S.; Howell, S. W.; Fulghum, J. E.; Wheeler, D. R. *Langmuir* **2005**, *21*, 10899–10901.

(69) Matrab, T.; Combellas, C.; Kanoufi, F. *Electrochem. Commun.* **2008**, *10*, 1230–1234.

(70) Charlton, M. R.; Suhr, K. J.; Holliday, B. J.; Stevenson, K. J. *Langmuir* **2015**, *31*, 695–702.

(71) Chan, C. K.; Beechem, T. E.; Ohta, T.; Brumbach, M. T.; Wheeler, D. R.; Stevenson, K. J. *J. Phys. Chem. C* **2013**, *117*, 12038–12044.

(169) Weissmann, M.; Baranton, S.; Coutanceau, C. *Langmuir* **2010**, *26*, 15002–15009.

(170) Fontanesi, C.; Bortolotti, C. A.; Vanossi, D.; Marcaccio, M. *J. Phys. Chem. A* **2011**, *115*, 11715–11722.

(171) Florini, N.; Michelazzi, M.; Parenti, F.; Mucci, A.; Sola, M.; Baratti, C.; Renzi, V. D.; Daasbjerg, K.; Pedersen, S. U.; Fontanesi, C. *J. Electroanal. Chem.* **2013**, *710*, 41–47.

(172) Vase, K. H.; Holm, A. H.; Pedersen, S. U.; Daasbjerg, K. *Langmuir* **2005**, *21*, 8085–8089.

(173) Saby, C.; Ortiz, B.; Champagne, G. Y.; Bélanger, D. *Langmuir* **1997**, *13*, 6805–6813.

(174) Bielawski, M.; Aili, D.; Olofsson, B. *J. Org. Chem.* **2008**, *73*, 4602–4607.

(175) Gui, A. L.; Liu, G.; Chockalingam, M.; Le Saux, G.; Luais, E.; Harper, J. B.; Gooding, J. J. *Electroanalysis* **2010**, *22*, 1824–1830.

(176) Maldonado, S.; Smith, T. J.; Williams, R. D.; Morin, S.; Barton, E.; Stevenson, K. J. *Langmuir* **2006**, *22*, 2884–2891.

(177) Allongue, P.; Delamar, M.; Desbat, B.; Fagebaume, O.; Hitmi, R.; Pinson, J.; Savéant, J.-M. *J. Am. Chem. Soc.* **1997**, *119*, 201–207.

(178) Tsierkezos, N. G. *J. Solut. Chem.* **2007**, *36*, 289–302.

(179) Bruno, I. J.; Cole, J. C.; Edgington, P. R.; Kessler, M.; Macrae, C. F.; McCabe, P.; Pearson, J.; Taylor, R. *Acta Crystallogr. B* **2002**, *58*, 389–397.

(180) Bailly, F.; Barthen, P.; Frohn, H.-J.; Köckerling, M. *Z. Für Anorg. Allg. Chem.* **2000**, *626*, 2419–2427.

(181) Frohn, H.-J.; Hirschberg, M. E.; Boese, R.; Bläser, D.; Flörke, U. *Z. Für Anorg. Allg. Chem.* **2008**, *634*, 2539–2550.

(182) Hubbard, C. R.; Himes, V. L.; Mighell, A. D.; Page, S. W. *Acta Crystallogr. B* **1980**, *36*, 2819–2821.

(183) Schäfer, S.; Wirth, T. *Angew. Chem. Int. Ed.* **2010**, *49*, 2786–2789.

(184) Li, Y.; Chopra, N. *JOM* **2014**, *67*, 34–43.

(185) Li, Y.; Chopra, N. *JOM* **2014**, *67*, 44–52.

(186) Whitener Jr., K. E.; Sheehan, P. E. *Diam. Relat. Mater.* **2014**, *46*, 25–34.

(187) Riedl, C.; Coletti, C.; Iwasaki, T.; Zakharov, A. A.; Starke, U. *Phys. Rev. Lett.* **2009**, *103*, 246804.

(188) Brar, V. W.; Zhang, Y.; Yayon, Y.; Ohta, T.; McChesney, J. L.; Bostwick, A.; Rotenberg, E.; Horn, K.; Crommie, M. F. *Appl. Phys. Lett.* **2007**, *91*, 122102.

(189) Deretzis, I.; La Magna, A. *Phys. Rev. B* **2011**, *84*, 235426.

(190) Goler, S.; Coletti, C.; Piazza, V.; Pingue, P.; Colangelo, F.; Pellegrini, V.; Emtsev, K. V.; Forti, S.; Starke, U.; Beltram, F.; Heun, S. *Carbon* **2013**, *51*, 249–254.

(191) Hiura, H. *J. Mater. Res.* **2001**, *16*, 1287–1292.

(192) Ohta, T.; Bartelt, N. C.; Nie, S.; Thürmer, K.; Kellogg, G. L. *Phys. Rev. B* **2010**, *81*, 121411.

(193) Cançado, L. G.; Jorio, A.; Ferreira, E. H. M.; Stavale, F.; Achete, C. A.; Capaz, R. B.; Moutinho, M. V. O.; Lombardo, A.; Kulmala, T. S.; Ferrari, A. C. *Nano Lett.* **2011**, *11*, 3190–3196.

(194) Ferrari, A. C.; Meyer, J. C.; Scardaci, V.; Casiraghi, C.; Lazzeri, M.; Mauri, F.; Piscanec, S.; Jiang, D.; Novoselov, K. S.; Roth, S.; Geim, A. K. *Phys. Rev. Lett.* **2006**, *97*, 187401.

(195) Malard, L. M.; Pimenta, M. A.; Dresselhaus, G.; Dresselhaus, M. S. *Phys. Rep.* **2009**, *473*, 51–87.

(196) Ugeda, M. M.; Brihuega, I.; Guinea, F.; Gómez-Rodríguez, J. M. *Phys. Rev. Lett.* **2010**, *104*, 096804.

(197) Chen, J.-H.; Cullen, W. G.; Jang, C.; Fuhrer, M. S.; Williams, E. D. *Phys. Rev. Lett.* **2009**, *102*, 236805.

(198) Stevenson, K. J.; Veneman, P. A.; Gearba, R. I.; Mueller, K. M.; Holliday, B. J.; Ohta, T.; Chan, C. K. *Faraday Discuss.* **2014**, *172*, 273–291.

(199) Gearba, R. I.; Mueller, K. M.; Veneman, P. A.; Holliday, B. J.; Chan, C. K.; Stevenson, K. J. *J. Electroanal. Chem.* **2015**, *753*, 9–15.

(200) Bekyarova, E.; Itkis, M. E.; Ramesh, P.; Haddon, R. C. *Phys. Status Solidi RRL - Rapid Res. Lett.* **2009**, *3*, 184–186.

(201) Ferrari, A. C.; Basko, D. M. *Nat. Nanotechnol.* **2013**, *8*, 235–246.

(202) Mizes, H. A.; Foster, J. S. *Science* **1989**, *244*, 559–562.

(203) Kelly, K. F.; Mickelson, E. T.; Hauge, R. H.; Margrave, J. L.; Halas, N. J. *Proc. Natl. Acad. Sci.* **2000**, *97*, 10318–10321.

(204) Kelly, K. F.; Halas, N. J. *Surf. Sci.* **1998**, *416*, L1085–L1089.

(205) Ceperley, D. M.; Alder, B. J. *Phys. Rev. Lett.* **1980**, *45*, 566–569.

(206) Yazyev, O. V.; Helm, L. *Phys. Rev. B* **2007**, *75*, 125408.

(207) Boukhvalov, D. W.; Katsnelson, M. I.; Lichtenstein, A. I. *Phys. Rev. B* **2008**, *77*, 035427.

(208) Jiang, D.; Sumpter, B. G.; Dai, S. *J. Phys. Chem. B* **2006**, *110*, 23628–23632.

(209) Yazyev, O. V. *Rep. Prog. Phys.* **2010**, *73*, 056501.

(210) Kim, S.; Jo, I.; Dillen, D. C.; Ferrer, D. A.; Fallahazad, B.; Yao, Z.; Banerjee, S. K.; Tutuc, E. *Phys. Rev. Lett.* **2012**, *108*, 116404.

(211) Kim, S.; Nah, J.; Jo, I.; Shahrjerdi, D.; Colombo, L.; Yao, Z.; Tutuc, E.; Banerjee, S. K. *Appl. Phys. Lett.* **2009**, *94*, 062107.

(212) *Crystal Clear, 1.40*; Rigaku Americas Corporation: The Woodlands, Texas, 2008.

(213) Altomare, A.; Burla, M. C.; Camalli, M.; Cascarano, G. L.; Giacovazzo, C.; Guagliardi, A.; Moliterni, A. G. G.; Polidori, G.; Spagna, R. *J. Appl. Crystallogr.* **1999**, *32*, 115–119.

(214) Sheldrick, G. M. *Acta Cryst.* **2008**, *A64*, 112–122.

(215) Spek, A. L. *PLATON, A Multipurpose Crystallographic Tool.*; Utrecht University: Utrecht University, The Netherlands, 1998.

(216) Farrugia, L. J. *J. Appl. Crystallogr.* **1999**, *32*, 837–838.

(217) Farrugia, L. J. *WinGX an Integrated System of Windows Programs for the Solution, Refinement and Analysis of Single Crystal X-Ray Diffraction Data*; University of Glasgow: Glasgow, U.K., 1999.

(218) In *International Tables for X-Ray Crystallography*; Wilson, A. J. C., Ed.; Kluwer Academic Press: Boston, 1992; Vol. C, p Tables 4.2.6.8 and 6.1.1.4.

(219) Chelikowsky, J. R.; Troullier, N.; Saad, Y. *Phys. Rev. Lett.* **1994**, *72*, 1240–1243.

(220) Kronik, L.; Makmal, A.; Tiago, M. L.; Alemany, M. M. G.; Jain, M.; Huang, X.; Saad, Y.; Chelikowsky, J. R. *Phys. Status Solidi B* **2006**, *243*, 1063–1079.

Chapter 3: Interesting Photophysical Properties from Luminescent Copper(I) Complexes

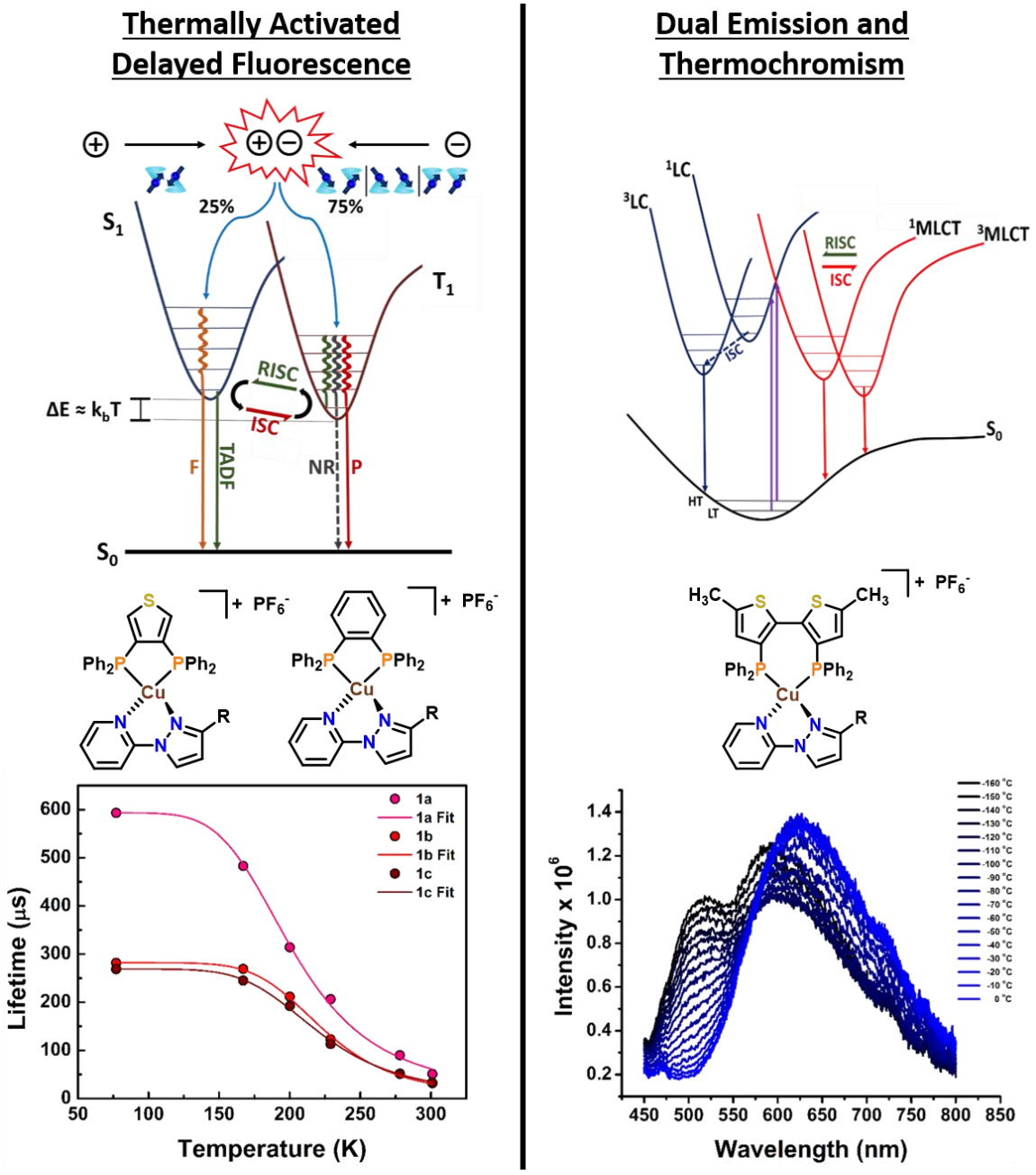

3.1. Highly luminescent copper(I) complexes based on 3,4-bis(diphenylphosphino)thiophene: A structural, computational, and photophysical comparative study with 1,2-bis(diphenylphosphino)benzene.

3.1.1. Introduction

Designing materials to overcome the "singlet-triplet bottleneck" in organic light emitting diodes (OLEDs) and light emitting electrochemical cells (LEECs) has been the focus of much research in recent years. This bottleneck is the result of the statistical distribution of electrochemically generated excited states that yield 75% triplet excitons, which cannot be harvested by simple organic molecules.[221] To circumvent this issue, emissive transition metal complexes are often employed. Complexes based on heavy metals have attracted the most attention, as the high spin-orbit coupling relaxes the rules for the disallowed emissive transition from the triplet excited state (T_1) to singlet ground state (S_0), however, the metals used tend to be costly and rare.[82,222] An alternative method for utilizing triplet excitons is thermally activated delayed fluorescence (TADF), which does not require high spin-orbit coupling to function efficiently, and thus allows for the use of cheaper, earth-abundant metals.[88]

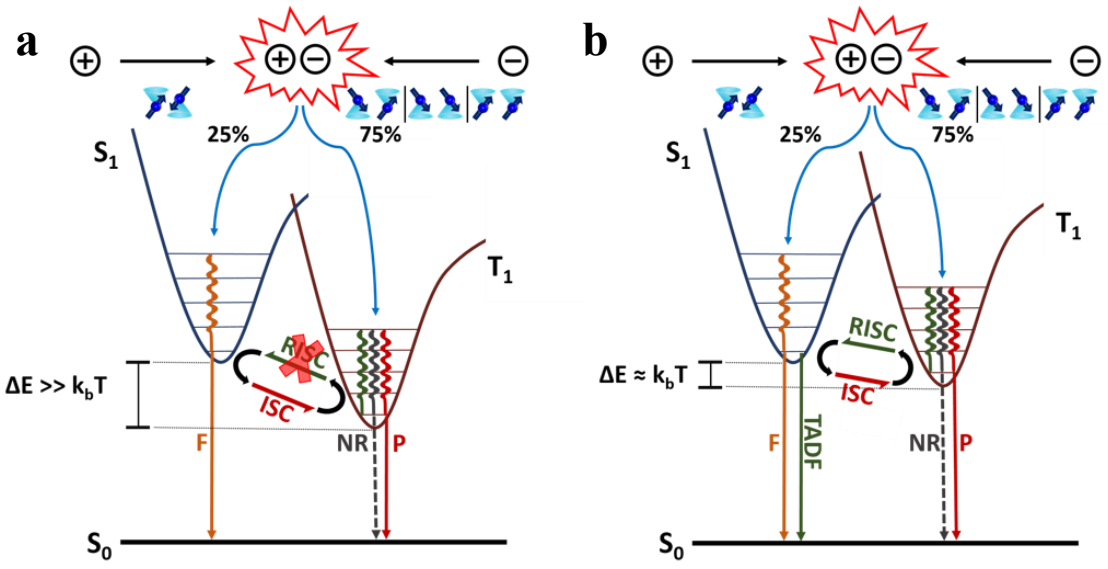

Figure 3.1. Depiction of the potential energy surfaces for active emitters in OLED and LEC devices showing the electrochemical generation of the excited state and the relevant photophysical processes. Electron-hole recombination on the emissive materials generates a distribution of triplet (75%) and singlet (25%) excited states which quickly decay into the lowest vibrational state of their respective potential energy surfaces. a) In materials which are not capable of TADF, a portion of the singlet excitons may be harvested as light while the rest undergo ISC to the triplet well. The triplet excitons in purely organic materials are inefficiently harvested resulting largely in non-radiative decay. Strategies involving heavy metals with high spin-orbit couplings are used in these systems to harvest the triplet-excitons. b) Materials capable of TADF are designed in such a way that the energy gap between the singlet and triplet excited state is accessible via thermal excitation, repopulating the singlet excited state and allowing for improved electrochemical quantum yields.

For materials to be capable of TADF, the T_1 state is required to be close in energy to the first singlet excited state (S_1). When the energy gap between S_1 and T_1 (ΔE_{ST}) is sufficiently small, reverse intersystem crossing (RISC) competes efficiently with intersystem crossing (ISC), allowing for thermal repopulation (Boltzmann population) of the emissive S_1 state. The quantum mechanically allowed $S_1 \rightarrow S_0$ transition is then capable of efficiently harvesting the singlet excitons, leading to improved quantum yields

and efficient utilization of all of the excited states. The efficiency of RISC, which is crucial to the TADF process, may be maximized through the careful design of the emitting material. A small ΔE_{ST} can be realized by increasing the spatial separation (decreasing the wavefunction overlap) of the highest occupied molecular orbital (HOMO) with respect to the lowest unoccupied molecular orbital (LUMO). The wavefunctions of the HOMO and LUMO approximate those of the hole-electron pair in TADF systems. Minimizing the overlap of the wavefunctions of the electron and hole effectively decreases the exchange energy of the excited state leading to a small value for ΔE_{ST}.[88,223]

A strategy for decreasing the overlap between the HOMO and LUMO units is to align the wavefunctions perpendicular to one another.[88] This makes mononuclear four-coordinate Cu(I) complexes an attractive option for TADF emitters as the d^{10} metal centers favor distorted tetrahedral geometries, which enforces a perpendicular alignment of bidentate ligands.[224] Commonly, emissive Cu(I) based materials include a diimine ligand and a bis(phosphine) ligand in the form of $[Cu(P\hat{}P)(N\hat{}N)]^{+/0}$.[225–230,87,231–249] In these complexes, the P-Cu(I)-P unit functions as the HOMO with the LUMO residing on either the π*-orbitals of either the (N^N) or (P^P) ligands, depending on identity of diimine ligand. Most of these complexes utilize a relatively small range of bis(phosphines), with bis[(2-diphenylphosphino)phenyl] ether[225–230,87,231–238] and 1,2-bis(diphenylphosphino) benzene (dppbz) (and its derivatives)[87,95,238–240,250–252] being the most common Cu(I) TADF emitters.

Derivatives of dppbz, often bearing steric modifications on flanking phenyl rings, have been explored in order to improve the performance and stability of the emitter.[95,239,252,253] Modifying the bridging aryl ring, however, has been largely unexplored. Replacing the six-membered bridging benzene ring with the five-membered, electron-rich thiophene ring provides an interesting and simple approach to modifying

both the electronics and coordination geometry of the ligand. Furthermore, placing a thiophene ring within the complex provides a platform for introducing electropolymerizable units, increasing the attractiveness of these materials as it potentially opens pathways for making single layer OLED devices. Herein, we report the synthesis of a series of Cu(I) complexes based on 3,4-bis(diphenylphosphino)thiophene (dppt) supported with 1-(2-pyridyl)pyrazole (pypz), 3-methyl-1-(2-pyridyl)pyrazole (pympz) and 3-trifluoromethyl-1-(2-pyridyl)pyrazole (pycf3pz) diimine ancillary ligands (Scheme 3.1). The selected pyrazole-pyridine ligands have been shown to support highly efficient TADF emitters.[234,247] To discern the effects of substituting thiophene for benzene in the dppbz based structures, the analogous dppbz based structures were synthesized and studied for direct comparison.

Scheme 3.1. General structures of the Cu(I) complexes **1a-c** and **2a-c**.

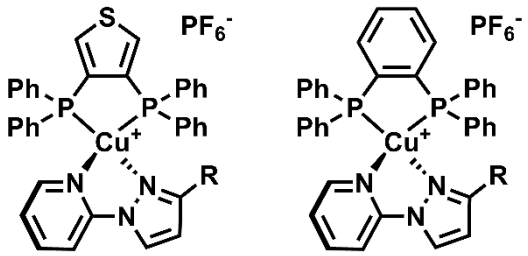

3.1.2. Results and Discussion

3.1.2.1. Synthesis 3,4-bis(diphenylphosphino)thiophene (dppt)

Briefly, the synthesis of dppt was accomplished via the one-pot dilithiation of 3,4-dibromothiophene with 2.15 equivalents of *n*-butyllithium in diethyl ether followed by quenching with chlorodiphenylphosphine to afford the air stable ligand as a clear gel (Scheme 3.2). Attempts to synthesize dppt in THF yielded a large mixture of products, whereas utilization of diethyl ether, which promotes the kinetic product, afforded the desired product with high selectivity.

Scheme 3.2. Synthesis of 3,4-bis(diphenylphosphino)thiophene (dppt).

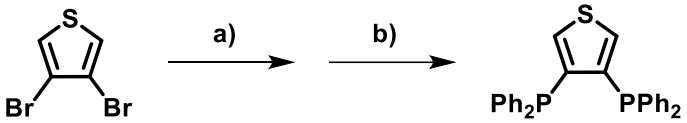

a) 2.15 *n*-butyllithium, Et_2O, –78 °C, 45 min. b) 2.15 chlorodiphenylphosphine, Et_2O, –78 °C - rt, overnight.

3.1.2.2. Synthesis and Crystal Structures of Complexes 1a-c and 2a-c

Complexes **1a-c** and **2a-c** were synthesized by stirring $[Cu(CH_3CN)_4][PF_6]$ with the desired bis(phosphine) for 45 minutes followed by addition of the corresponding pyrazole-pyridine ligand which led to the formation of a yellow solution in all cases. Purification and isolation of **1a-c** and **2b-c** was achieved by vapor diffusion of diethyl ether into a concentrated solution of [Cu(P^P)(N^N)][PF_6] in methylene chloride. The resulting crystals (Figure 3.2) were suitable for single crystal X-ray diffraction. The crystal structures for **1a-c** are shown in Figure 3.2 and the structures of **2b** and **2c** are shown in Figure 3.3. Complex **2a** could not be recrystallized therefore no crystal structure was obtained. Purification of **2a** was achieved by removing the solvent from the reaction mixture and washing the resulting solid with copious amounts of diethyl ether.

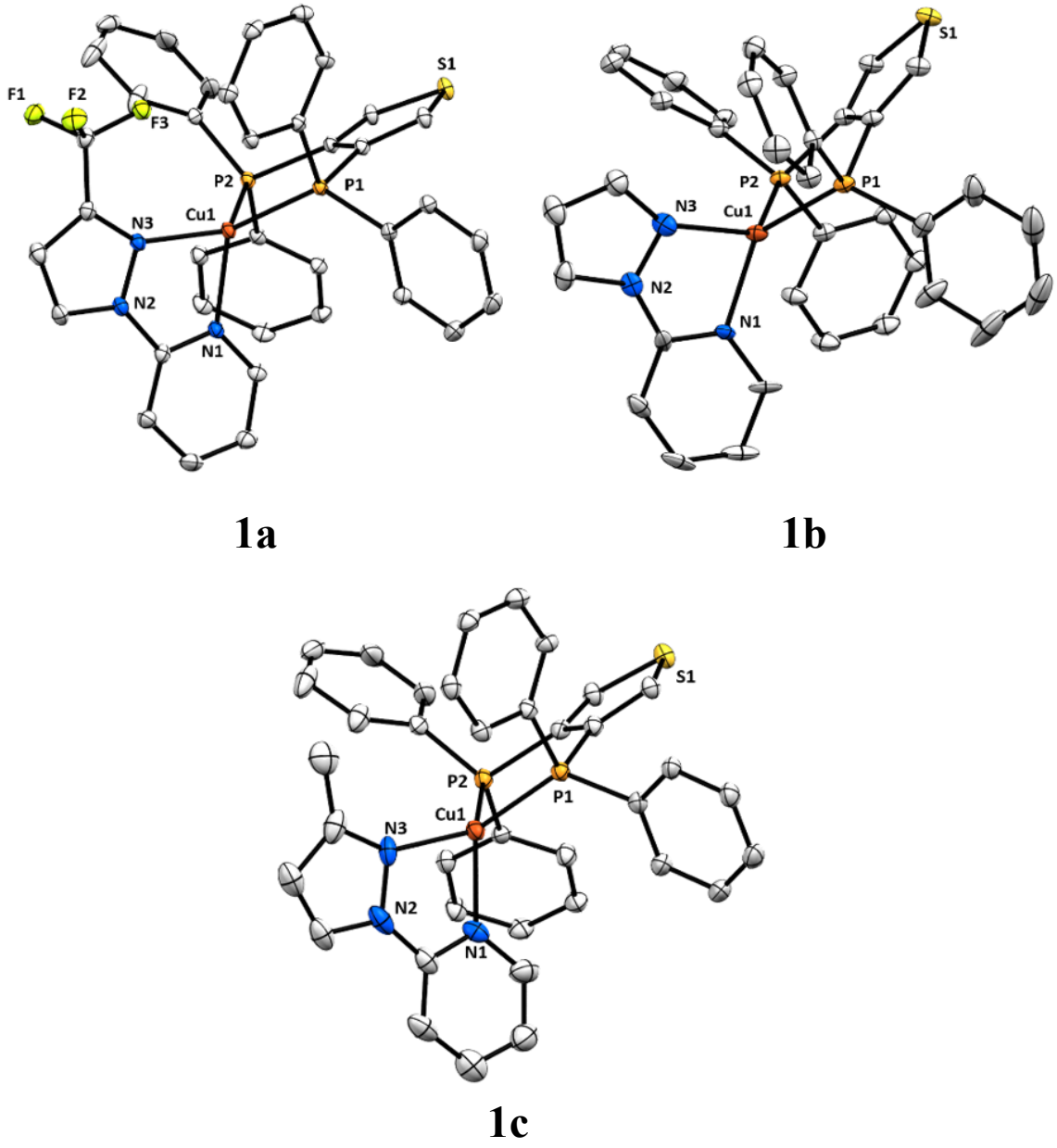

Figure 3.2. Molecular structures of complexes **1a-c**. Structures **1a** and **1b** displayed disorder of the diimine ligand. Structures shown are of the highest contributing conformations. Hydrogen atoms and the PF_6^- counter-anions are omitted for clarity. Ellipsoid plots are drawn at 30% probability.

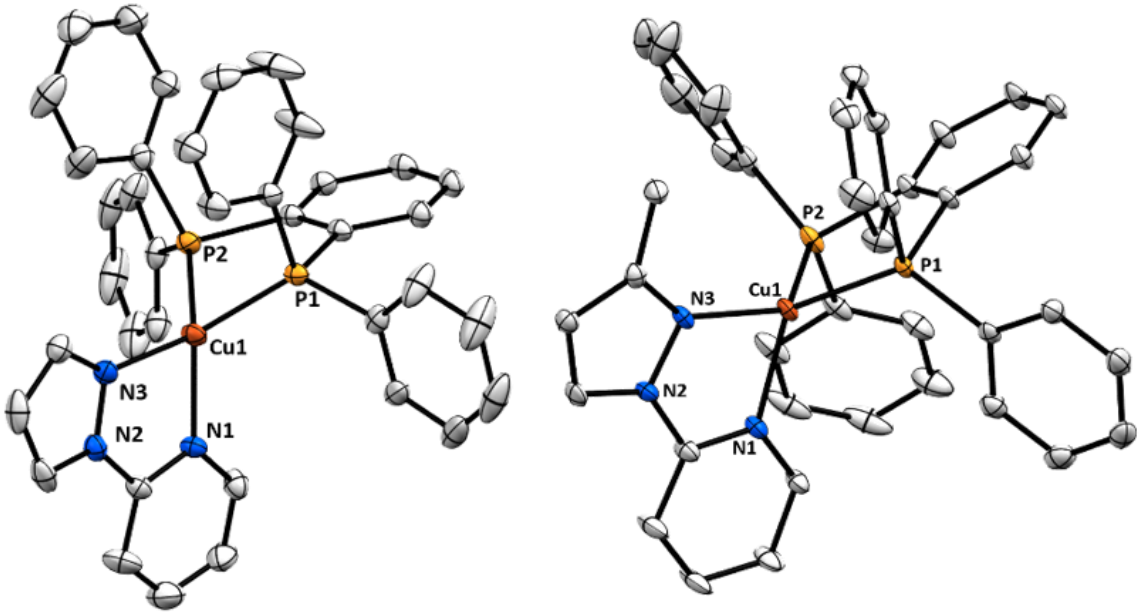

2b **2c**

Figure 3.3. Molecular structures of complexes **2b** and **2c**. Crystal structure of complex **2a** could not be obtained. Complex **2c** displayed disorder of the diimine ligand. The shown structure is of the highest contributing conformation. Hydrogen atoms and the PF_6^- counter-anions are omitted for clarity. Ellipsoid plots are drawn at 30% probability.

Table 3.1. Bond Lengths (Å), Angles (Degrees) and Dihedral Angles (degrees) of complexes **1a-c** and **2b-c**.

	Cu1-P1	***Cu1-P2***	***Cu1-N1***	***Cu1-N3***	***P-Cu-P***	***N-Cu-N***	***(N^N)(P^P)***
1a[a]	2.2592(7)	2.2473(7)	2.056(5)	2.068(3)	93.80(3)	80.0(2)	84.32
1b[a]	2.249(9)	2.2452(5)	2.05(1)	2.05(3)	93.6(2)	80.3(8)	79.6
1c	2.284(1)	2.270(1)	2.082(5)	2.091(4)	93.28(5)	80.2(2)	83.77
2a[b]	-	-	-	-	-	-	-
2b	2.246(1)	2.247(1)	2.044(4)	2.041(4)	87.93(4)	80.0(1)	87.47
2c[a]	2.224(1)	2.234(1)	2.065(7)	2.022(7)	91.74(4)	80.2(3)	79.9

[a] Crystal structures displayed disorder of the diimine ligand. Recorded values are of the major contributing conformation.
[b] Crystal structure could not be obtained.

A comparison of the key structural factors for complexes **1a-c** and **2b-c** can be found in Table 3.1. All synthesized complexes exhibit a distorted tetrahedral geometry which is characteristic of four-coordinate Cu(I).[224] Throughout both series, the Cu-P and Cu-N bond lengths fall within a narrow range of 2.22-2.28 Å and 2.05-2.09 Å, respectively. All complexes in **series 1** show intermolecular π-stacking interactions between the phenyl rings of adjacent dppt molecules. No remarkable π-interactions were observed with the diimine ligands. Within **series 1**, elongation of the pyrazole-copper (N3-Cu1) bond is observed in complexes **1a** and **1c** with respect to **1b**. This elongation likely results from steric interactions between dppt and the substituents on the pyrazole ring. **Series 2** does not exhibit any intermolecular π-stacking in the crystal structures. However, the structure of complex **2b** shows intramolecular π-stacking of the phenyl rings in the bis(phosphine) ligand leading to distortion of coordination geometry. As a result, the Cu(I) center of **2b** lies 34.82° below the PCCP plane. A comparison of coordination geometry of **2b** and **2c** is shown in Figure 3.4.

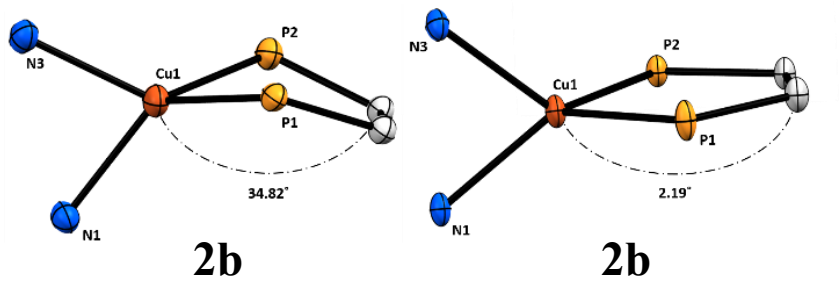

Figure 3.4. Coordination geometry around the Cu(I) center of **2b** and **2c** displaying the distortion of the 5-membered ring generated from the chelation of the phosphine ligand. **2b** shows considerable distortion as the intramolecular π-stacking forces the Cu(I) atom to deviate from planarity.

The N-Cu-N bond angles remain constant throughout the complexes at approximately 80°. Analysis of the P-Cu-P bite angles reveal a slightly wider bite angle for the dppt ligand compared with dppbz. This is expected, as moving to the five-membered thiophene based backbone should expand the external angles of the ring system.

3.1.2.3. Density Functional Theory (DFT) Studies

Investigations into the electronic structure of the prepared complexes using DFT calculations were performed. In these studies, the crystal structure coordinates were taken as the starting point for structural optimizations when possible (optimization of $\mathbf{2a}^+$ was initiated from a modified structure of $\mathbf{2c}^+$). Optimizations and energy calculations were carried out at the B3LYP functional level of theory using the LANL2DZ basis set and the LANL2 electron core potentials for copper. The 6-31G(d,p) basis set was employed for all other elements. The optimized structures all displayed distorted tetrahedral geometries and are in good agreement with X-ray diffraction data. However, the DFT optimized structures display a slight elongation of the coordinative bonds to the Cu(I) center. DFT results showed that the phosphine-copper bonds (P-Cu1) exhibited very little variation based on the identity of the bis(phosphine) ligands with an average bond length of 2.367 ±0.005 Å across the series; an average elongation of 0.12 ±0.01 Å when compared to the crystal structures. Similarly, the pyridine-copper (N1-Cu1) and pyrazole-copper (N3-C1) bonds showed a general elongation and little structural variation based on the identity of the diimine ligands. The wider bite angle of the dppt with respect to dppbz was corroborated by DFT.

HOMO-LUMO diagrams for the Cu(I) complexes are shown in Figure 3.5. The HOMO consists primarily of Cu(I) based *d*-orbitals mixing with the atomic orbitals from

the chelating phosphorous atoms. A slight stabilization of the HOMOs of complexes **1a-c**$^+$ with respect to **2a-c**$^+$ is observed in the calculations. The LUMO is predominantly composed of the diimine π*-orbitals. As expected, increasing the electron density of the diimine ligand by substitution of the 3-position on the pyrazole ring raises the energy level of the LUMO. Qualitatively, very little difference is observed in the spatial distribution of the frontier molecular orbitals between the complexes based on dppt and dppbz, suggesting the properties of the two series should be quite similar with subtle changes observed from electronic modulation.

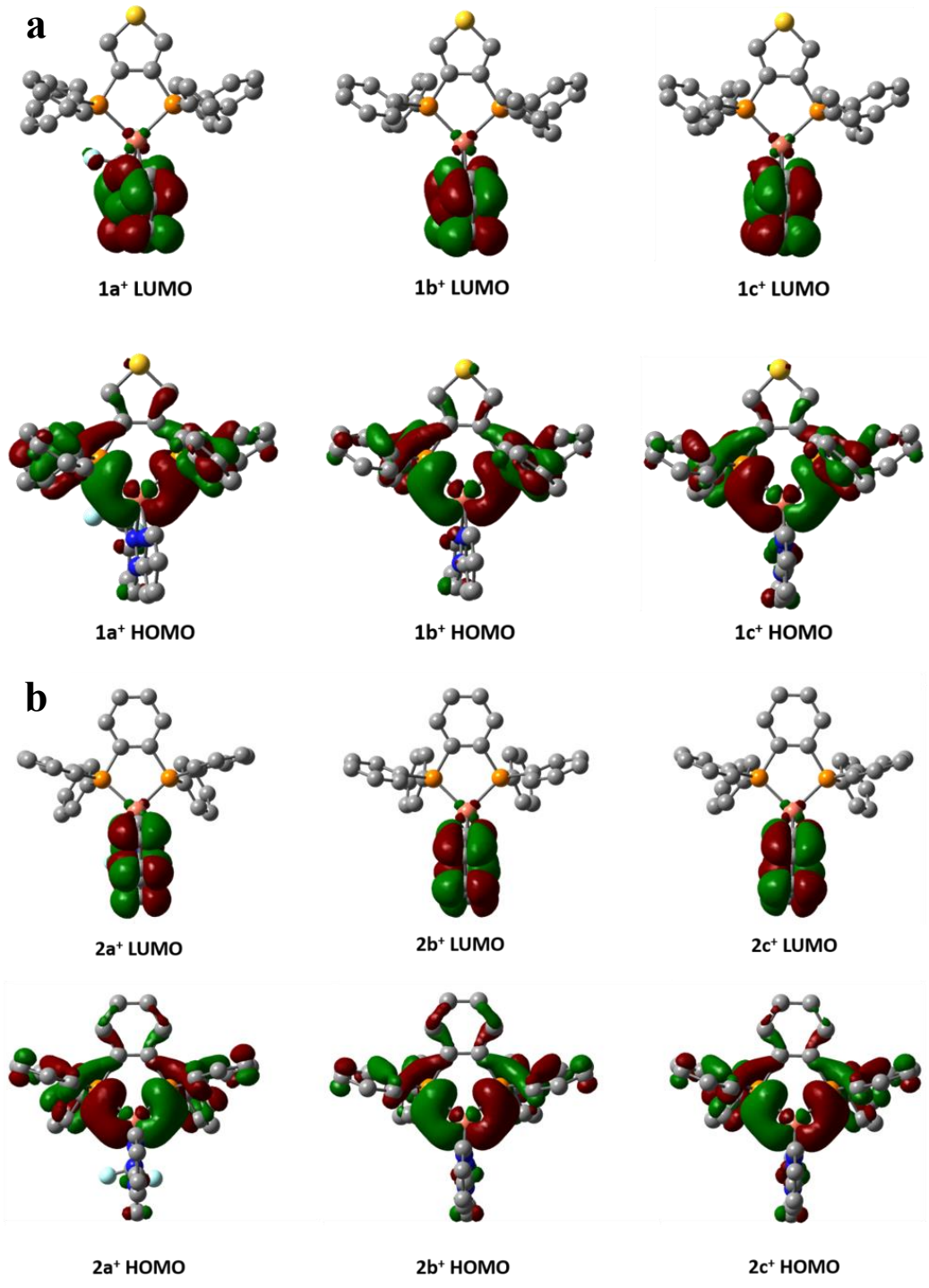

Figure 3.5. Kohn-Sham diagrams of the frontier molecular orbitals for a) **1a-c** and b) **2a-c** demonstrating perpendicular alignment of the HOMO and LUMO.

3.1.2.4. Ground State Photophysical and Electrochemical Properties

The electronic absorption spectra for complexes **1a-c** and **2a-c** exhibit similar characteristics (Figure 3.6). Simulated absorption spectra and representative natural transition orbitals (NTOs) are shown in Figure 3.7 and Figure 3.8, respectively. The spectra show a distinct absorption between 350 and 380 nm, which was not observed in the free ligands. This band was assigned as a singlet metal-to-ligand charge transfer (^{1}MLCT) involving electron transfer from the Cu(I) 3*d* orbitals to the π*-orbitals of the pyridyl-pyrazole based ligands.

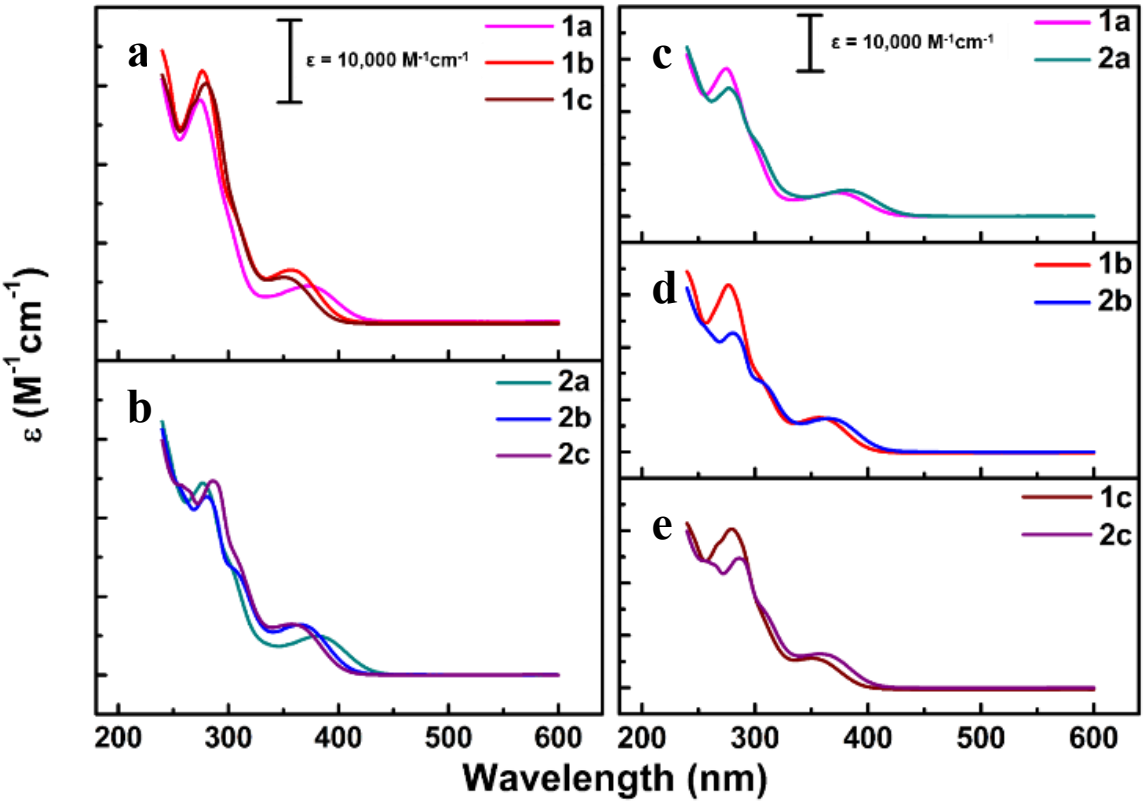

Figure 3.6. Electronic absorption spectra of a) **series 1** and b) **series 2**. Comparison of the absorption spectra of dppt and dppbz based complexes bearing the same diimine ligands [c) **1a** and **2a**, d) **1b** and **2b** and e) **1c** and **2c**].

This analysis is consistent with Time Dependent - DFT calculations which indicated that 99.6% of the first absorption results from the HOMO→LUMO transition. A second absorption at approximately 305 nm results from a second ^{1}MLCT between the Cu(I) *d*-orbitals and the π^*-orbitals of the bis(phosphine) ligand. At higher excitation energies, a mix of ligand-based π-to-π^* and inter-ligand charge transfers (ILCT) dominates the spectra. No low energy shoulders were observed in the absorption profiles indicating little to no formation of $[Cu(N\text{^}N)_2]^+$ or $[Cu(P\text{^}P)_2]^+$ species in solution from complex disproportionation.[243]

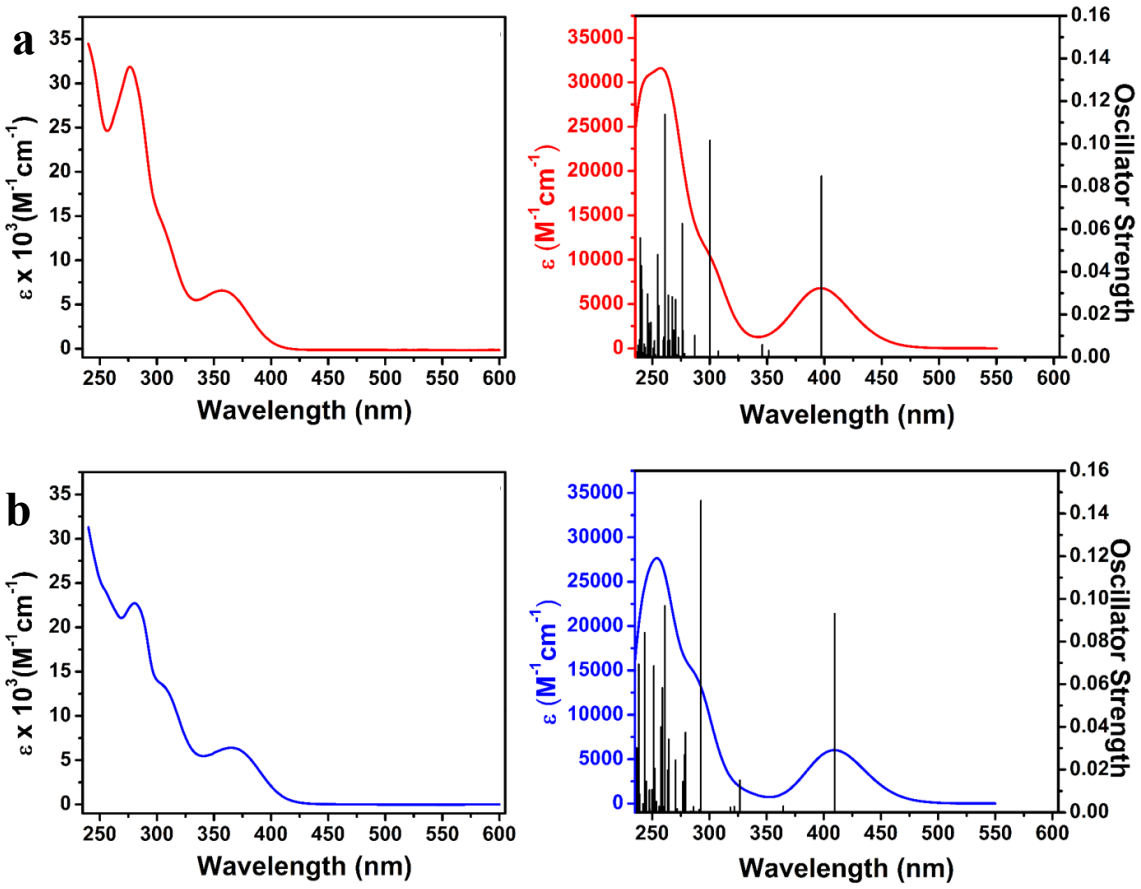

Figure 3.7. Experimental (left) and TD-DFT simulated (right) absorption spectra of a) **1b** and b) **2b**. The first 60 singlet excitations are shown in the simulations.

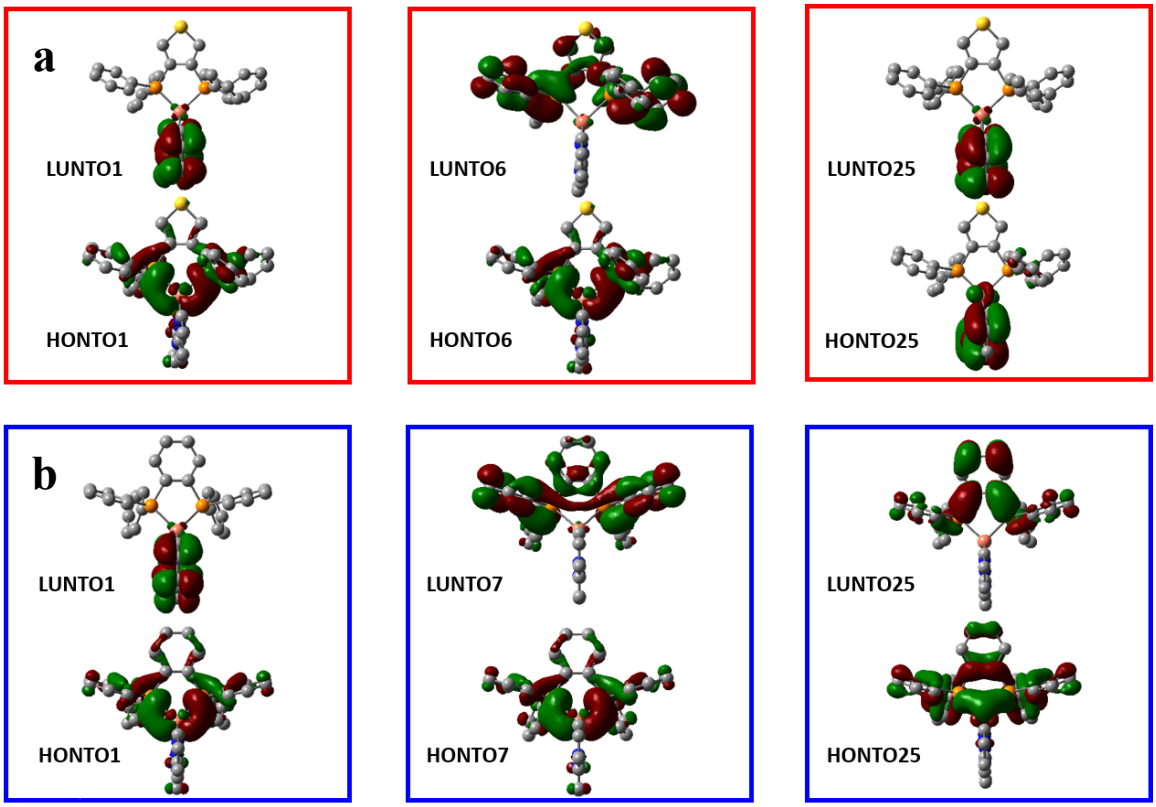

Figure 3.8. Representative NTOs for a) **series 1** and b) **series 2** exhibiting the first three excitations with an oscillator strength greater than 0.08. The modeled complexes for **series 1** and **2** were **1b** and **2b**, respectively.

The highest occupied NTO (HONTO) and the lowest unoccupied NTO (LUNTO) approximate the electron-hole pair in the excited state. The HONTO1/LUNTO1 pair represents the lowest energy absorption, which is assigned as a ^{1}MLCT, and is responsible for the stimulation of TADF processes.

Trends found within the UV-Vis are consistent with electronic control of the ground state properties. Within each bis(phosphine) series, a redshift in the peak absorption of the lowest energy ^{1}MLCT was observed as the electron density of the diimine ligand decreased (pympz > pypz > pycf3pz). This trend is seen in Figure 3.6 a,b and is attributed to the stabilization of the LUMO moving from electron donating to

electron withdrawing substituents on the pyrazole ring.[234] Comparison of the bis(phosphine) ligands revealed a consistent blue shift in the low energy ^{1}MLCT absorption of dppt with respect to dppbz (Figure 3.6c-e). This blue shift can be explained by examination of the bite angles of the bis(phosphine) ligands. Both dppt and dppbz have bite angles that are less than the ideal 109.5° angle for a tetrahedral complex. However, dppt has a wider bite angle that more closely approximates the ideal geometry, stabilizing the HOMO and blue shifting the absorption. This is consistent with the literature which has shown that wider bite angles lead to hypsochromic shifts in the spectra of tetrahedral Cu(I) complexes.[243]

Stabilization of the HOMO by dppt was confirmed by electrochemical analysis. Cyclic voltammetry (Figure 3.9) showed reversible oxidations for **1b** ($E_{1/2}$ = 0.54 V) and **1c** ($E_{1/2}$ = 0.67 V), which are anodically shifted from the values of **2b** ($E_{1/2}$ = 0.49 V) and **2c** ($E_{1/2}$ = 0.65 V), respectively. The peak oxidation of complex **1a** (E_a = 0.73 V) displays an anodic shift from **2a** (E_a = 0.68 V) as well, however, this event could not be separated from a second oxidation event which is believed to induce the irreversibility seen in these samples. Correspondingly, all the complexes display additional electrochemical events as the potential is pushed farther positive, leading to a loss of reversibility in the electrochemistry. No polymerization was observed in the electrochemical studies.

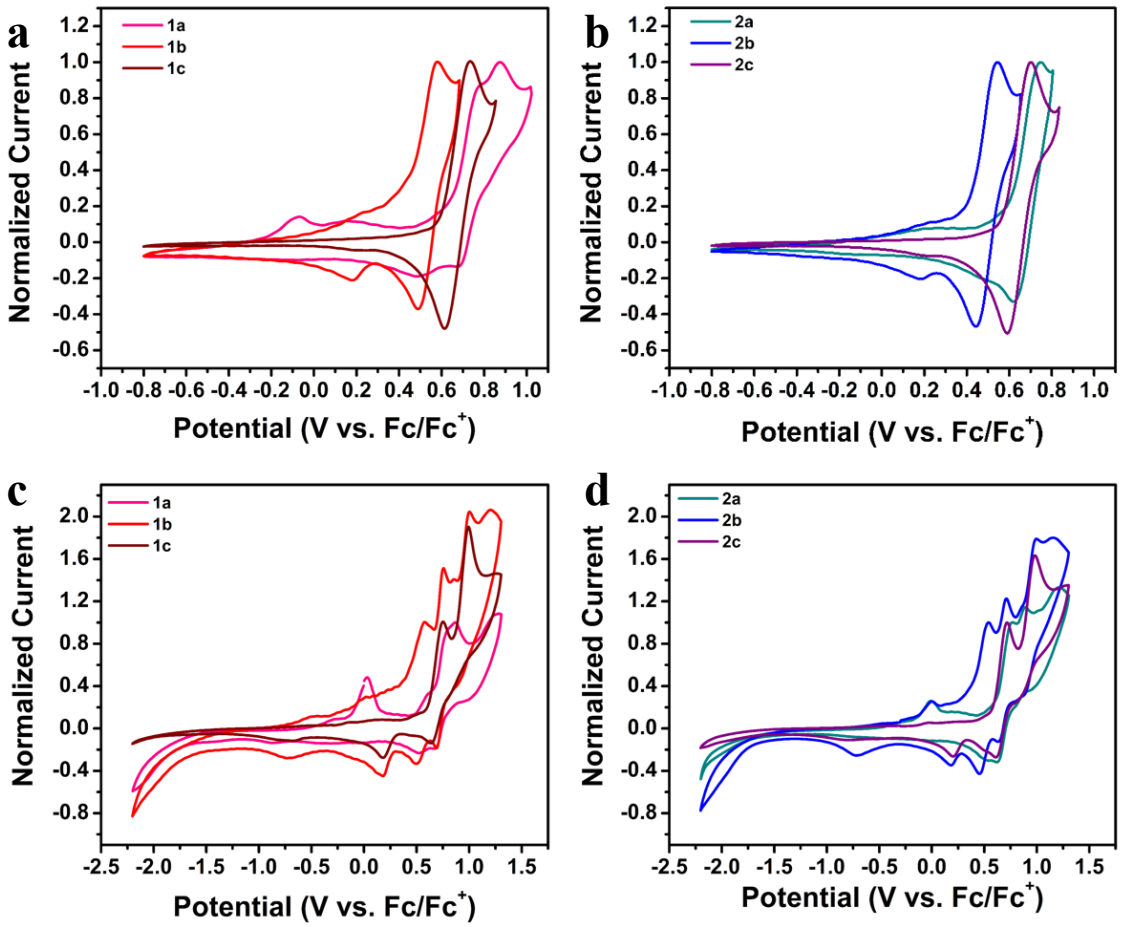

Figure 3.9. Electrochemical studies of [Cu(P^P)(N^N)][PF_6] complexes in dichloromethane with 0.1 M tetra-*n*-butylammonium hexafluorophosphate as supporting electrolyte. Stopping after the first oxidation event in both a) **1a-c** and b) **2a-c** reveals a reversible 1 electron transfer. The first oxidation event of complexes **1b** and **2b** could not be fully isolated leading to irreversible peaks for these complexes. Sweeps of the full electrochemical window of c) **series 1** and d) **series 2** are shown.

Interestingly, complexes **1b** and **2b** were oxidized much easier than would be expected from electronic arguments alone, requiring further investigation. It is well known in the literature that the formal oxidation of the Cu(I) center to Cu(II) leads to a rearrangement of the coordination geometry from tetrahedral to square planar. Therefore, the optimal geometry for electron transfer should be the intermediate structure between

the initial and final states. Structures that allow for increased flexibility in solution and better accommodation of the transition state from Cu(I) to Cu(II) should require a lower oxidation potential. Therefore, it is believed that the decrease in steric interactions between the pypz ligand and the bis(phosphine) ligands, compared to pympz and pycf3pz, allows complexes **1b** and **2b** to reach the preferred geometry for electron transfer at lower potentials than their congeners. Cuttell *et al*. noticed a similar phenomenon when moving from 1,10-phenanthroline to 2,9-dimethyl-1,10-phenanthroline.[225]

To test this hypothesis, DFT calculations were performed on $\mathbf{1b}^{2+}$ and $\mathbf{1c}^{2+}$ to investigate the magnitude of structural rearrangement allowed in the oxidized state (Figure 3.10). Oxidation to $\mathbf{1b}^{2+}$ induces a 24.4° rotation of the pypz ligand towards planarization with the P-Cu-P plane, moving from 74.9° to 50.5°. In comparison, the rearrangement of pympz in $\mathbf{1c}^{2+}$ is limited to only 12.9° (77.7° to 64.8°) of rotation before the methyl group clashes with the phenyl rings of dppt. These results are consistent with the lower oxidation potentials for **1b** and **2b**.

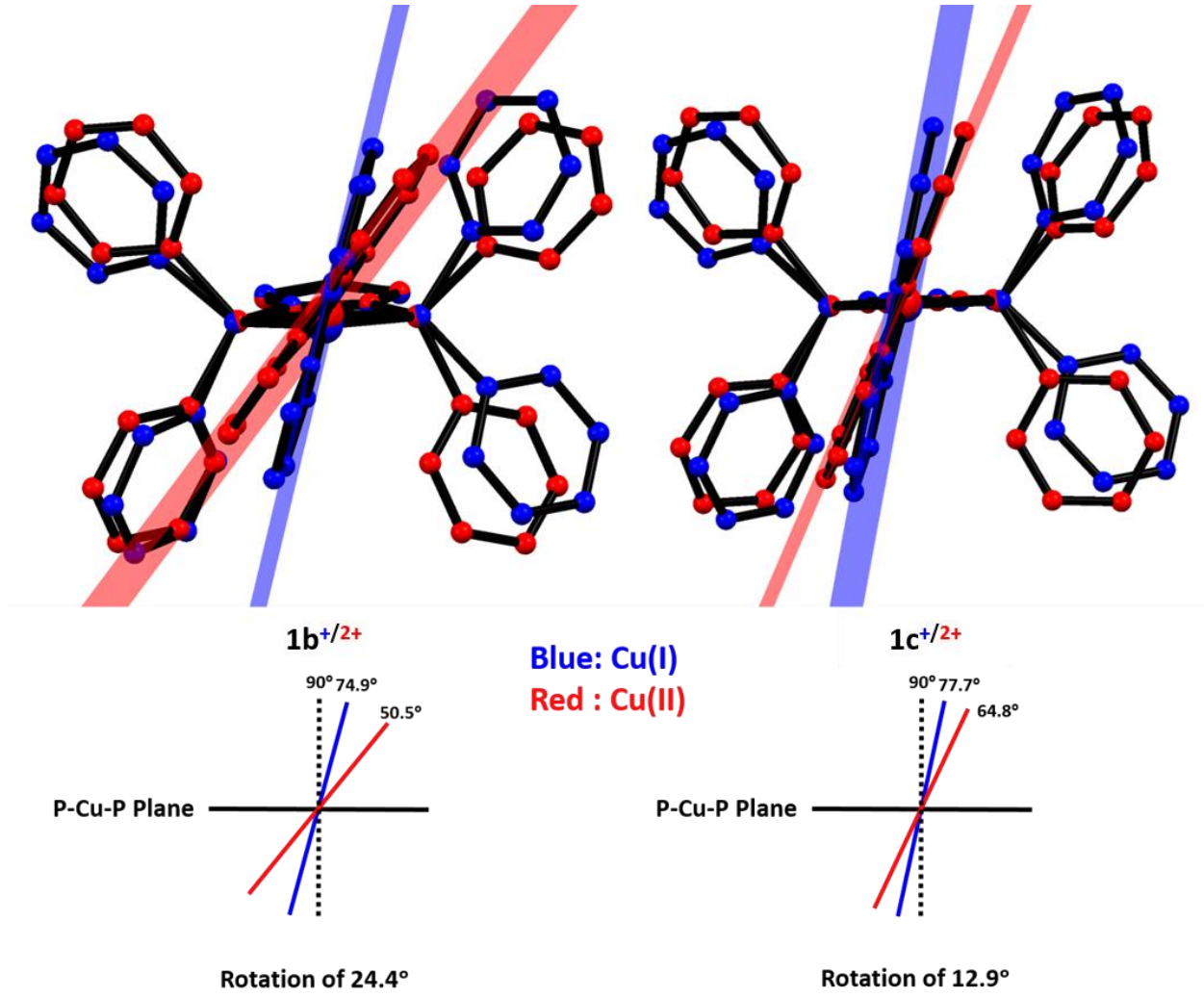

Figure 3.10. DFT structural comparison of native Cu(I) states of $\mathbf{1b}^{+}$ and $\mathbf{1c}^{+}$ to the oxidized forms, $\mathbf{1b}^{2+}$ and $\mathbf{1c}^{2+}$, respectively. Calculations suggest a planarization of the diimine ligand with respect to the P-Cu-P plane. Steric restrictions limit the rotation of $\mathbf{1c}^{2+}$ compared to $\mathbf{1b}^{2+}$. The increased flexibility lowers the barrier for oxidation of the complexes based on the less bulky pypz ligand.

The HOMO levels were determined experimentally using the onset of oxidation from the cyclic voltammograms for the reported series and then corrected to ferrocene (4.8 eV) to obtain the absolute HOMO level with respect to vacuum.[254] The optical band gaps were determined using the onset of absorption of the lowest energy ^{1}MLCT from the

UV-Vis spectra. LUMO values were then back calculated using the HOMO levels and the optical band gap. A summary of the energy levels and band gaps may be found in Figure 3.11.

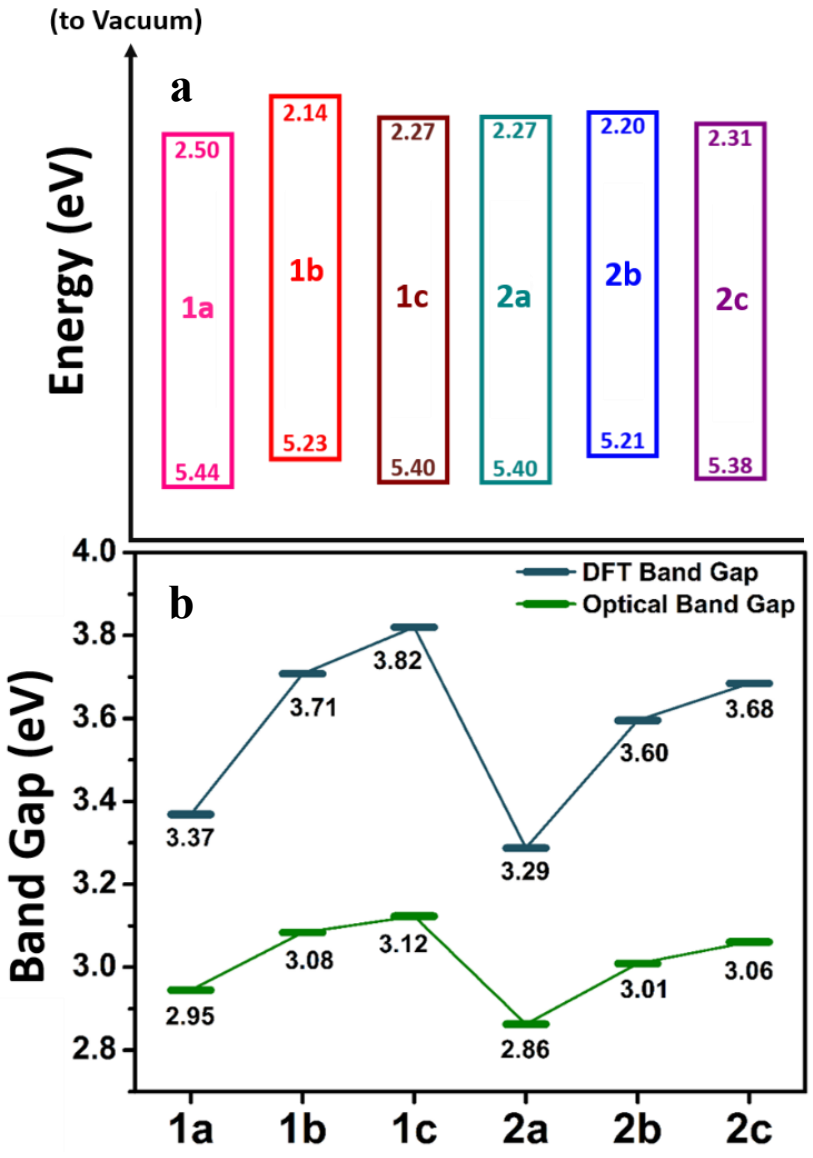

Figure 3.11. a) Experimentally determined HOMO and LUMO levels. b) Comparison of the experimentally determined and DFT predicted band gaps.

The HOMO levels of **1a**, **1b**, and **1c** are recurrently lower than **2a**, **2b**, and **2c** by 0.02 eV, 0.02 eV, and 0.05 eV, respectively. These values correlate well with the DFT results which predict the HOMO levels of **1a-c**$^{+}$ to be lower by 0.04 eV, 0.07 eV, and 0.10 eV, respectively. The band gaps of the complexes fall within a narrow range. Complexes **1a-c** fall between 2.95 eV and 3.12 eV whereas complexes **2a-c** range from 2.86 eV to 3.06 eV. Although DFT consistently overestimated the band gap (approximately 18 ±3 % over on average), the relative bandgap trend proved to be an excellent match with the experimental results (Figure 3.11b). Overall, the variation in the energy levels with respect to the identity of the chelating phosphine ligand is minimal, which should allow for dppt to replace dppbz in devices without changes in the device architecture. Potential OLED devices are shown in Figure 3.12.

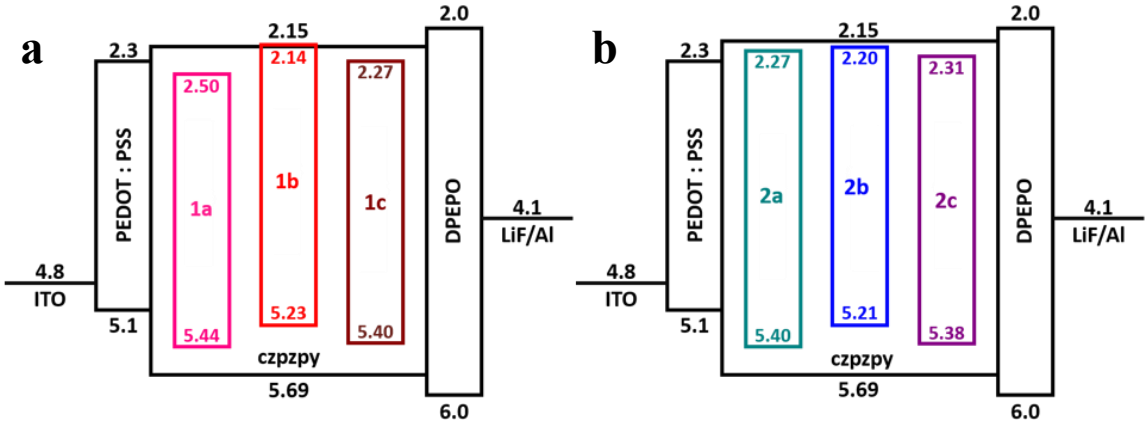

Figure 3.12. Potential device architectures for a) dppt and b) dppbz based series. ITO = indium tin oxide; PEDOT:PSS = poly(3,4-ethylenedioxythiophene) polystyrene sulfonate; czpzpy = 2-(9*H*-carbazolyl)-6-(1*H*-pyrazolyl)pyridine; DPEPO = bis[2-(diphenylphosphino)phenyl] ether oxide.

3.1.2.5. Excited State Photophysical Properties

Solution emission spectra of the complexes at room temperature yielded only ligand based fluorescence in deoxygenated 2-methyltetrahydrofuran (2-MeTHF) that matched the spectra of the unbound ligands. Conversely, when the complexes are trapped in a glassy 2-MeTHF solution at 77 K, no ligand based florescence is observed. This indicates the fluorescent profiles observed in solution were the result of the excitation of the Cu(I) complexes followed by ligand dissociation and subsequent emission. The emission spectra of **1a-c** and **2a-c** in frozen 2-MeTHF exhibited featureless emission profiles, which are characteristic of charge transfer based emissions (Figure 3.13). At 77 K, the rate of RISC is low from the lack of thermal energy, leading to phosphorescent emission from the T_1 state which is principally a triplet metal-to-ligand charge transfer (^{3}MLCT) state. The emission profiles displayed electronic control of the emission spectra based on the diimine ligands with the peak emission wavelength blue-shifting as the substituents on the pyrazole-pyridine ligands move from electron withdrawing to donating. A blue shift in the dppt series with respect to the dppbz series is also observed, consistent with the increased stabilization of the HOMO by dppt. A marked decrease in the lifetimes of dppt complexes at 77 K is observed as well. The reduction in the lifetime of the T_1 state can be rationalized by the incorporation of the sulfur atom into the chelating phosphine ligand. Modifying phosphorescent materials by replacing lighter elements with sulfur has been shown in the literature to increase ISC rates and to improve phosphorescent quantum yields as a result of the increased spin-orbit coupling.[255–257]

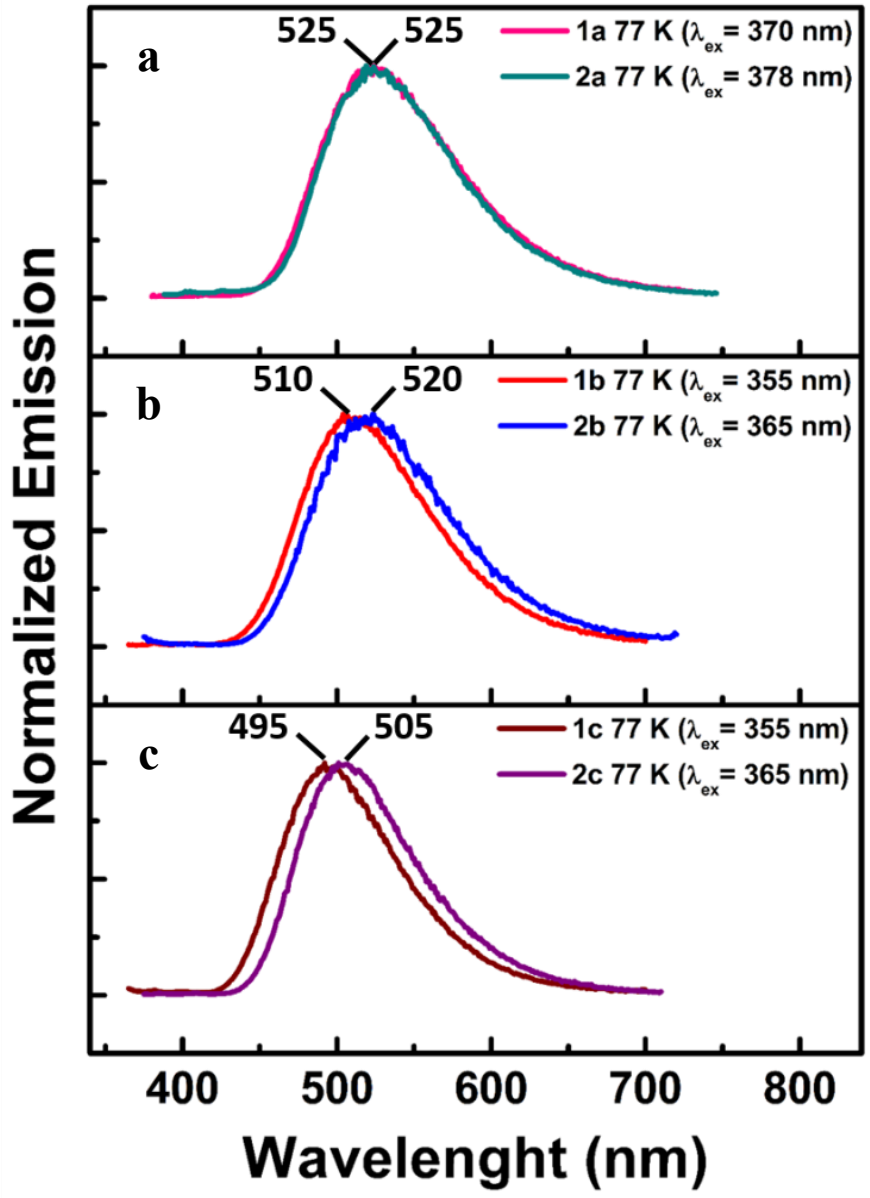

Figure 3.13. Emission spectra of a) **1a** and **2a**, b) **1b** and **2b** and c) **1c** and **2c** in a frozen solution of 2-MeTHF at 77 K.

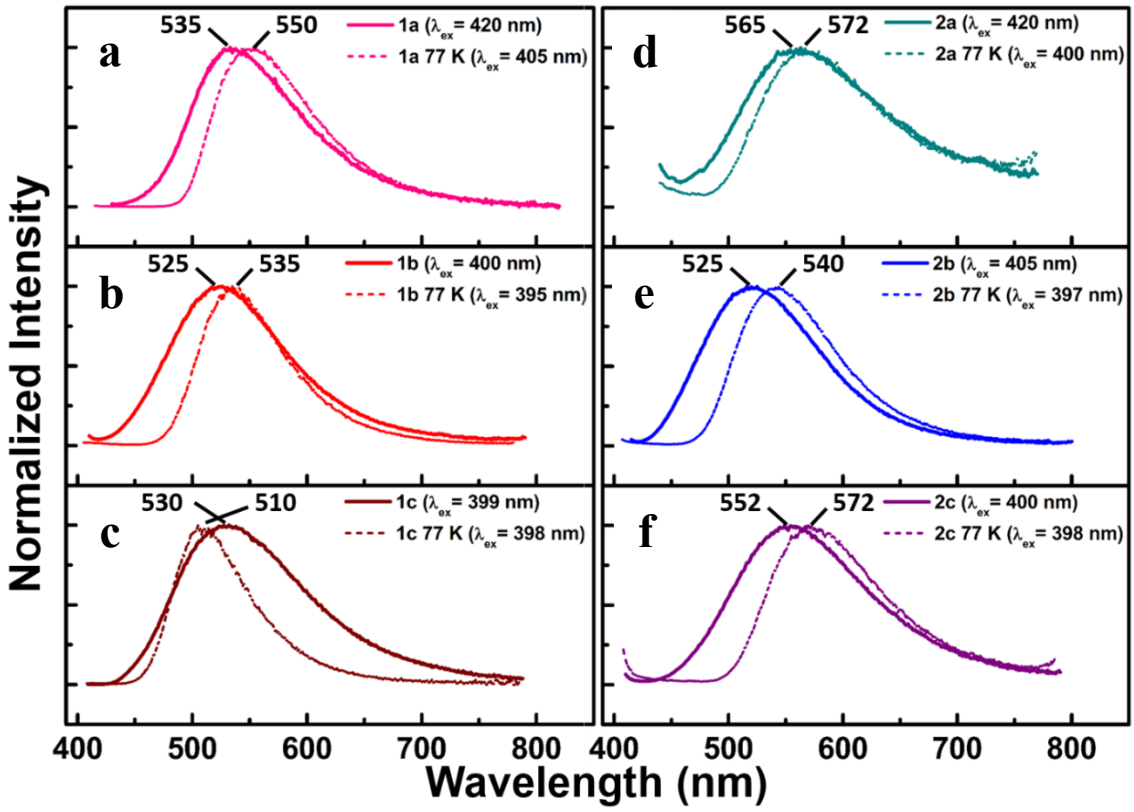

Figure 3.14. Solid state emission spectra of a) **1a**, b) **1b**, c) **1c**, d) **2a**, e) **2b**, and f) **2c** at both room temperature (301 K) and at 77 K. All spectra were taken from ground crystalline powders except for **2a** which could only be isolated as an amorphous solid.

Table 3.2. Photophysical Data for Complexes **1a-c** and **2a-c**.

	1a	**1b**	**1c**	**2a**	**2b**	**2c**
			Powder[a]			
λ_{max} (301 K) [nm]	535	525	530	565	525	552
ϕ_{PL} (301 K) [%]	60 (2)	58.6 (9)	58.7 (6)	8.58 (8)	60 (1)	56 (2)
τ (301 K) [μs]	51.2 (1)	32.0 (2)	33.0 (1)	19.0(4)	39.9 (2)	42.5 (1)
k_r (301 K) [s^{-1}]	$1.17x10^4$	$1.83x10^4$	$1.78x10^4$	$4.51x10^3$	$1.50x10^4$	$1.32x10^4$
k_{nr} (301 K) [s^{-1}]	$7.81x10^3$	$1.29x10^4$	$1.25x10^4$	$4.80x10^4$	$1.00x10^4$	$1.04x10^4$
λ_{max} (77 K) [nm]	550	535	510	572	540	572
τ (77 K) [μs]	593.3 (3)	282 (1)	269 (1)	603 (9)	600 (10)	458 (8)
			2-MeTHF			
λ_{max} (77 K) [nm]	525	510	495	525	520	505
τ (77 K) [μs]	643 (2)	440 (3)	415 (3)	866 (1)	609 (8)	644 (2)
			PMMA Films			
λ_{max} (301 K) [nm]	525	542	515	525	530	515
τ (301 K) [μs][b]	21.5 (7) 55 (1)	17.0 (8) 42.4 (1.0)	31 (1) 69 (1)	25.4 (5) 64.7 (1.0)	17.4 (5) 47 (1)	15.8 (7) 48.2 (7)

[a]All data was taken using crystalline powders except **2a** which could only be isolated as an amorphous solid.
[b] Lifetimes required a bi-exponential fit to model the data. Major contributing lifetime is given first.

The emission profiles of the complexes in the crystalline state at room temperature all yield broad, featureless spectra as well (Figure 3.14). However, a drastic decrease in the emission lifetimes from the frozen solutions at 77 K is observed. This room temperature emission is attributed to TADF based processes. At room temperature, thermal energy is sufficient to promote RISC, repopulating the ^{1}MLCT excited state from which luminescence is observed. This now represents a quantum mechanically allowed transition, drastically increasing the observed radiative rates. Interestingly, the emission profiles of all the complexes are red shifted from that of the frozen solution, despite emitting from the ^{1}MLCT. It is well documented that upon excitation, the Cu(I) center is formally oxidized to Cu(II) and a geometric rearrangement to a square planar geometry is initiated. This rearrangement in the excited state red shifts the emission profiles and

leaves the complexes susceptible to non-radiative deactivation pathways. However, rigid matrices restrict rearrangement, promoting higher quantum yields and blue shifting the emission profiles. Therefore, it is likely that the red-shift in emission at room temperature is the result of increased flexibility in the crystal lattice compared to the frozen matrix, allowing for increased stabilization of the excited state via planarization of the tetrahedral coordination sphere.

All the compounds, with the exception of **2a**, exhibit high luminescent quantum yields (φ) of approximately 60 % in the powdered crystalline state at room temperature (Table 3.2). The considerably lower quantum yield of **2a** (φ = 8.58%) is likely the result of matrix effects from isolation of the material in a non-crystalline state. Correspondingly, complex **2a** has the largest rate of non-radiative decay (k_{nr}) and the shortest lifetime. The pronounced impact of packing effects on the emissive properties of Cu(I) TADF emitters have been previously reported in the literature.[237]

From a tuning perspective, complexes **1a** and **1c** show electronic control of the emission profile from the substituted diimine ligands with complex **1c** at slightly higher energies than complex **1a**. The same holds true when comparing **2a** and **2c**. However, in both series the pypz-based complexes emit at higher energies than would be expected. As was observed in the frozen solutions, all the complexes based on dppt still display peak emissions that are equal to or higher in energy when compared to the dppbz analogues in the solid state. Examination of the radiative rates (k_r) showed faster emission rates for the dppt-based series. Although, the dppbz-based series displayed slower non-radiative decay rates, making the overall quantum yields comparable to the dppt series.

Cooling of the powdered samples to 77 K universally shifted the onset of emission to lower energies. Alongside the red shift in emission, a drastic increase in the observed radiative lifetimes was observed indicating an emission profile that results

primarily form the T_1 state with negligible contributions from TADF processes. Such behavior is consistent with TADF-based emitters.[88]

3.1.2.6. Variable Temperature Lifetime Studies

Further insight into the dependence of the TADF lifetime on temperature was investigated via variable temperature fluorimetry using powdered samples. The temperature dependence of TADF emitters is well documented and, as such, ΔE_{ST} can be calculated by modeling the profile of the emission lifetimes (τ_K) as a function of temperature (T) using equation 3.1.[234]

$$\tau_K = \frac{1+\frac{1}{3}exp\left(-\frac{\Delta E_{ST}}{k_b T}\right)}{\frac{1}{\tau_{(T_1)}}+\frac{1}{3\tau_{(S_1)}}exp\left(-\frac{\Delta E_{ST}}{k_b T}\right)} \qquad \text{(eq. 3.1)}$$

In this equation, k_b represents the Boltzmann constant. The lifetime of the triplet excited state ($\tau_{(T1)}$) is assumed to be the lifetime of emission at T = 77 K, leaving the singlet lifetime ($\tau_{(S1)}$) and ΔE_{ST} as free variables in the fitting process. The experimental data and fitted curves may be found in Figure 3.15.

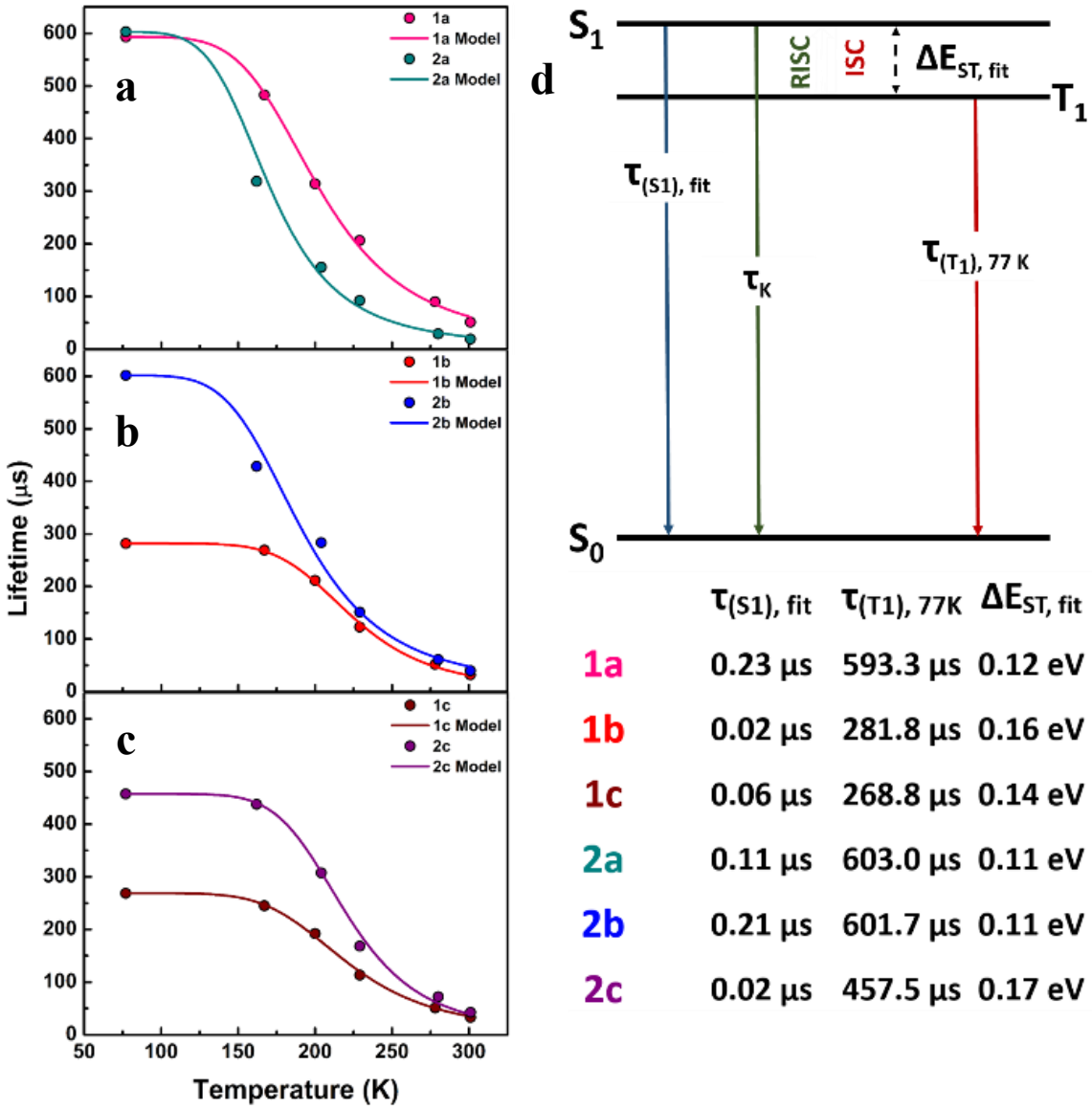

Figure 3.15. Variable temperature lifetimes of the solid state materials comparing a) **1a** and **2a**, b) **1b** and **2b** and c) **1c** and **2c**. d) Simplified Jablonski diagram depicting the variables used in equation (3.1) and the corresponding values used to generate the model fitting for each complex.

The fitted values for ΔE_{ST} show no discernible trends based on the identity of the diimine or bis(phosphine) ligands indicating only minor electronic influence on this energy gap. However, a strong correlation between the (N^N)(P^P) dihedral angle and

ΔE_{ST} was observed. As discussed above, perpendicular alignment of the HOMO and LUMO wavefunctions (which approximate the electron-hole pair in the excited state) generally leads to smaller values for ΔE_{ST} in tetrahedral complexes. In the data, it is observed that as the angle (N^N)(P^P) approaches perpendicular (**1b** ≈ **2c** < **1c** <**1a** < **2b** < 90°), the energy gap ΔE_{ST} (**2c** > **1b** > **1c** > **1a** > **2b**) is minimized. This demonstrates the efficacy of optimizing the orientation of the HOMO with respect to the LUMO and it is this orientation that is the dominant factor in tuning ΔE_{ST} in the reported complexes. It should also be noted that, when designing TADF emitters with short delayed fluorescent lifetimes, simple tuning of ΔE_{ST} is not the only determining factor in emitter efficiency. The involved radiative lifetimes and the rate of RISC must also be considered. An example of this can be seen when comparing complexes **1b** and **2b**. Complex **1b** has a much larger ΔE_{ST} (0.16 eV) than complex **2b** (0.11 eV). However, the radiative lifetime at room temperature for complex **1b** (32.0 μs) is faster than that of **2b** (39.9 μs) with an equivalent quantum yield. The increase in the radiative rate of **1b** is a result of the shorter lifetime of the S_1 state. This shows that to design an efficient TADF emitter, a balance of all the emission parameters is required.

To emulate the emission spectra of complexes in a device, 4% weight solutions of the emitter complexes to PMMA were dissolved in methylene chloride and drop cast onto quartz tubes resulting in uniform, colorless films (Figure 3.16). The emission profiles of the films at room temperature are blue shifted with respect to the powdered form for the complexes containing pympz and pycf3pz, while the emission from complexes **1b** and **2b** are slightly shifted to lower energy. In general, little variation across the series of complexes is observed. Lifetimes of the emissive films could only be fitted using bi-exponential models suggesting two different environments exist within the PMMA films.

The lack of extra emission peaks likely precludes the presence of possible disproportionation products.

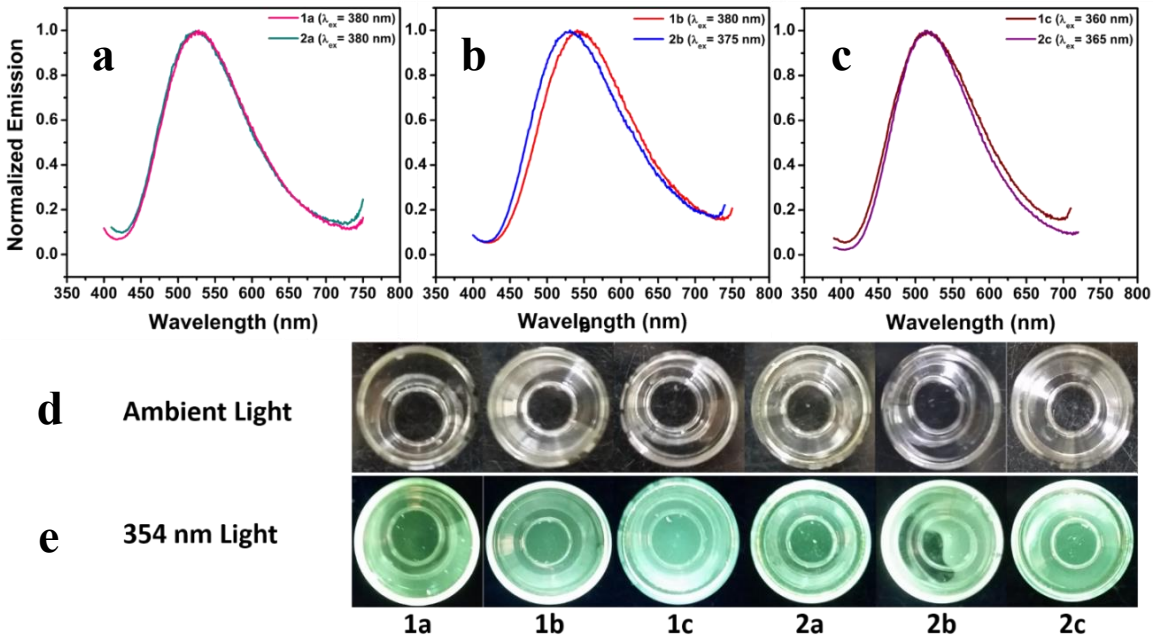

Figure 3.16. Emission data for a) **1a** and **2a**, b) **1b** and **2b** and c) **1c** and **2c** in a 4% (wt/wt) PMMA film at room temperature. Pictures of the films under d) ambient light and e) 354 nm light are shown.

3.1.3. Conclusion

In this report, a series of Cu(I) complexes based on 3,4-bis(diphenylphosphino)thiophene (dppt) was synthesized, and these complexes were shown to be active TADF emitters. To test the viability of these materials, a corresponding series of emitters based on 1,2-bis(diphenylphosphino)benzene (dppbz) was synthesized and studied for comparison. Structural comparisons of the complexes revealed a wider bite angle for the dppt ligand which offered greater stabilization of the HOMO with respect to dppbz as indicated by electronic absorption spectroscopy and cyclic voltammetry. These results were supported by DFT calculations. Furthermore,

DFT calculations revealed a remarkably similar distribution of the frontier molecular orbitals of the dppt and dppbz complexes. As a result, similar photophysical properties were observed throughout the complexes with slight emission tuning observed from the chelating phosphine and diimine ligands. One noticeable influence of the dppt ligand was the decreased lifetime of the phosphorescent states at 77 K due to the increased spin-orbit coupling from incorporation of the sulfur atom. The efficiency of both series of emitters at room temperature was very similar with quantum yields of approximately 60%.

Variable temperature lifetime studies were performed to estimate the energy separation of the singlet and triplet excited states, ΔE_{ST}, of the Cu(I) complexes. No correlation between the supporting ligands and the magnitude of ΔE_{ST} was observed. However, a strong structural trend was discerned, as the value of ΔE_{ST} decreased with increasing orthogonality of the dihedral angle formed from the N-Cu-N and P-Cu-P plane in the crystal structures.

From these results, it is clear that replacement of the bridging benzene ring in dppbz with thiophene results in equally efficient TADF emitters. In fact, the slight stabilization of the HOMO leading to a hypsochromic shift in the emission profiles of dppt-based complexes coupled with an increase in the rate of triplet based emission represent an improvement over dppbz complexes. Moreover, the reduced cost and increased synthetic flexibility of the thiophene-bridged bis(phosphine) backbone opens up a greater range of control not afforded by a bridging benzene scaffold, making dppt an appealing ligand for future TADF emitters.

3.1.4. Experimental

3.1.4.1. Synthesis and Characterization

Dry solvents were collected in solvent bulbs from an Innovative Technology PureSolv 400 solvent purification system and stored over 3Å molecular sieves. 1,2-Bis(diphenylphosphino)benzene (dppbz) (Sigma Aldrich), *n*-butyllithium (1.6 M in hexanes) (Sigma Aldrich), chlorodiphenylphoshine (Sigma Aldrich), and 3,4-dibromothiophene (Matrix) were purchased and used as received. Tetrakis(acetonitrile)copper(I) hexafluorophosphate ($[Cu(CH_3CN)_4][PF_6]$), 1-(2-pyridyl)pyrazole (pypz), 3-methyl-1-(2-pyridyl)pyrazole (pympz), and 3-trifluoromethyl-1-(2-pyridyl)pyrazole (pycf3pz) were prepared according to literature procedures.[234,258]

NMR spectra were recorded with a Varian DirectDrive 400 MHz spectrometer (^1H 400 MHz, $^{13}C\{^1H\}$ 100 MHz, $^{31}P\{^1H\}$ 161 MHz, ^{19}F 376 MHz). ^1H and $^{13}C\{^1H\}$ NMR spectra were referenced to residual solvent peaks. The $^{31}P\{^1H\}$ spectra was externally referenced to a 75% phosphoric acid sample and the ^{19}F spectra was externally referenced to $CFCl_3$. Chemical ionization (CI+) mass spectra were collected on a Micromass Autospec Ultima mass spectrometer. Electrospray ionization (ESI+) and atmospheric pressure chemical ionization (APCI) were collected on an Agilent 6530 quadrupole time of flight mass spectrometer. Elemental analysis services were provided by Midwest Microlabs, LLC.

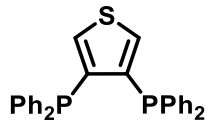

3,4-bis(diphenylphosphino)thiophene (dppt): A 200 mL Schlenk flask was charged with 3,4-dibromothiophene (3.00 g, 12.40 mmol) followed by the cannula addition of 100 mL of dry Et_2O. The resulting mixture was stirred vigorously and cooled to –78 °C for 30 minutes before *n*-butyllithium (1.6 M in hexanes, 16.66 mL, 26.66 mmol) was added to the reaction dropwise via syringe. The reaction was allowed to proceed for 45 minutes at –78 °C after which a solution of chlorodiphenylphosphine (5.88 g, 26.66 mmol) in 10 mL of dry Et_2O was transferred to the reaction flask via syringe. Following complete addition, the cooling bath was removed and the reaction was allowed to warm to room temperature overnight. The reaction was then quenched with water (5 mL) and allowed to stir for 10 minutes. The resulting mixture was then transferred to a separatory funnel along with water (100 mL). The aqueous phase was extracted with CH_2Cl_2 (3 x 200 mL) and the organic phases were combined, dried over Na_2SO_4, filtered, and evaporated to dryness to yield a pale yellow oil. The product was purified through a silica gel column using 30% CH_2Cl_2 in hexanes as the eluent. The final product was collected as a clear gel which solidified slowly upon standing (5.579 g, 12.33 mmol) in 99% yield. ^{1}H NMR (CD_2Cl_2, 400 MHz): δ 7.33-7.21 (m, 20H), 6.97 (t, J = 2.3, 2H). $^{13}C\{^1H\}$ NMR (CD_2Cl_2, 100 MHz): δ 141.8 (t, J_p = 8.7), 137.5 (t, J_p = 3.8), 133.9 (t, J_p = 10.1), 132.9, 129.0, 128.7 (t, J_p = 3.4). $^{31}P\{^1H\}$ NMR (CD_2Cl_2, 161 MHz): δ –23.0. HRMS (CI+) *m/z* Calcd. for $C_{28}H_{22}P_2S^+$ $(M)^+$ 453.0996. Found: 453.0984.

General Synthesis of [Cu(N^N)(P^P)][PF_6]: In a glovebox, [$Cu(CH_3CN)_4$][PF_6] was dissolved in methylene chloride (1 eq., 0.15 M) with rapid stirring. To this solution, the desired bis(phosphine) dissolved in methylene chloride (1 eq., 0.15 M) was added dropwise. The resulting solution was allowed to stir for 45 minutes before a solution of the desired pyrazole-pyridine ligand in methylene chloride (1 eq., 0.15 M) was added dropwise. The resulting yellow solutions were allowed to stir for 2 hours before being transferred to a Schlenk line and dried under a nitrogen stream. The resulting pale yellow solids were transferred to a glovebox, dissolved in a minimal volume of methylene chloride, and recrystallized via vapor diffusion of diethyl ether into the saturated solution of [Cu(N^N)(P^P)][PF_6]. The resulting crystals were collected and washed with diethyl ether to yield the pure complexes.

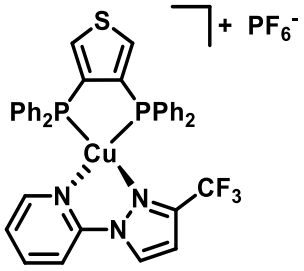

[Cu(pycf3pz)(dppt)][PF_6] (**1a**): Yellow crystalline solid; Yield 72%. ^{1}H NMR (CD_2Cl_2, 400 MHz): δ 8.73 (s, 1H), 8.15 (t, J = 7.5, 1H), 8.04 (d, J = 8.2, 1H), 7.65 (t, J = 3.2, 2H), 7.56-6.82 (m, 23H). ^{13}C{^{1}H} NMR (CD_2Cl_2, 100 MHz): δ 148.7, 147.2, 142.0, 140.6, 134.8, 133.4, 132.9, 131.1, 130.8, 130.6, 129.4 (t, J_p = 4.6), 124.7, 121.6, 118.2, 113.1, 109.9. ^{31}P{^{1}H} NMR (CD_2Cl_2, 161 MHz): δ –20.8. ^{19}F NMR (CD_2Cl_2, 376 MHz): δ –62.1. HRMS (ESI+) *m/z* Calcd. for $C_{37}H_{28}CuF_3N_3P_2S^+$ $(M–PF_6)^+$ 728.0722. Found: 728.0727. Anal. Calcd. for $C_{37}H_{28}CuF_9N_3P_3S$: C, 50.84; H, 3.23; N, 4.81. Found: C, 50.11; H, 3.20; N, 4.84.

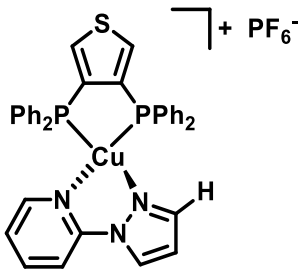

[Cu(pypz)(dppt)][PF$_6$] (**1b**): Colorless crystalline solid; Yield 90%. ^{1}H NMR (CD_2Cl_2, 400 MHz): δ 8.52 (d, J = 2.7, 1H), 8.11 (td, J = 8, 1.6, 1H), 7.89 (d, J = 8.6, 1H), 7.70 (d, J = 1.2, 1H), 7.66 (pt, J = 3.1, 3H), 7.48-7.22 (m, 21H), 6.83 (t, J = 1.6, 1H). ^{13}C{^{1}H} NMR (CD_2Cl_2, 100 MHz): δ 148.8, 148.2, 142.9, 141.7, 134.5 (bs), 132.9 (t, J_p = 8.4), 132.5 (t, J_p = 17.9), 130.8, 129.4 (t, J_p = 5.0), 128.7, 123.7, 112.4, 111.7. ^{31}P{^{1}H} NMR (CD_2Cl_2, 161 MHz): δ –20.5. HRMS (ESI+) *m/z* Calcd. for $C_{36}H_{29}CuN_3P_2S^+$ $(M–PF_6)^+$ 660.0848. Found: 660.0842. Anal. Calcd. for $C_{36}H_{29}CuF_6N_3P_3S$: C, 53.64; H, 3.63; N, 5.21. Found: C, 52.83; H, 3.61; N, 5.48.

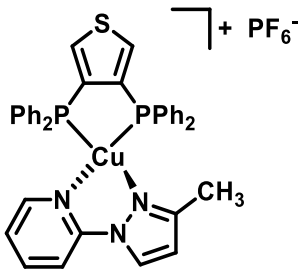

[Cu(pympz)(dppt)][PF$_6$] (**1c**): Pale yellow crystalline solid; Yield 69%. ^{1}H NMR (CD_2Cl_2, 400 MHz): δ 8.38 (d, *J* = 2.7, 1H), 8.07 (td, *J* = 8, 1.6, 1H), 7.80 (d, *J* = 8.6, 1H), 7.71 (t, *J* = 3.2, 2H), 7.63 (d, *J* = 4.7, 1H), 7.49-7.29 (m, 21H), 6.57 (d, *J* = 2.7, 1H), 1.88 (s, 3H). ^{13}C{^{1}H} NMR (CD_2Cl_2, 100 MHz): δ 152.9, 148.7, 148.5, 141.4 (t, J_p = 18), 134.6, 132.8 (t, J_p = 8), 130.7, 129.4 (t, J_p = 5.0), 129.2, 122.9, 111.7, 111.5, 14.2. ^{31}P{^{1}H} NMR (CD_2Cl_2, 161 MHz): δ –20.6. HRMS (ESI+) *m/z* Calcd. for $C_{37}H_{31}CuN_3P_2S^+$ $(M–PF_6)^+$ 674.1004. Found: 674.1002. Anal. Calcd. for $C_{37}H_{31}CuF_6N_3P_3S$: C, 54.18; H, 3.81; N, 5.12. Found: C, 53.99; H, 3.75; N, 5.17.

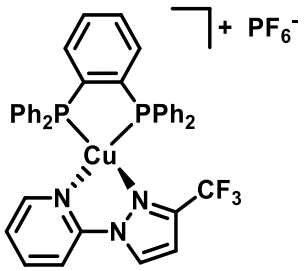

[Cu(pycf3pz)(dppbz)][PF_6] (**2a**): Yellow solid; Yield 96%. ^{1}H NMR (CD_2Cl_2, 400 MHz): δ 8.73 (s, 1H), 8.13 (t, *J* = 7.6, 1H), 8.03 (d, *J* = 8.3, 1H), 7.70-7.61 (m, 2H), 7.60-7.49 (m, 2H), 7.48-7.18 (m, 14H), 7.47-6.88 (m, 8H), 6.82 (d, *J* = 4.7, 1H). ^{13}C{^{1}H} NMR (CD_2Cl_2, 100 MHz): δ 148.7, 147.3, 141.9, 141.0 (t, J_p = 34.4), 135.5, 133.1 (bs), 131.9, 131.2, 130.7, 130.5, 129.4, 124.5, 113.0, 110.0. ^{31}P{^{1}H} NMR (CD_2Cl_2, 161 MHz): δ –5.34. ^{19}F NMR (CD_2Cl_2, 376 MHz): δ –61.9. HRMS (ESI+) *m/z* Calcd. for $C_{39}H_{30}CuF_3N_3P_2^+$ $(M–PF_6)^+$ 722.1158. Found: 722.1160. Anal. Calcd. for $C_{39}H_{33}CuF_6N_3P_3$: C, 53.96; H, 3.48; N, 4.84. Found: C, 53.89; H, 3.39; N, 4.80.

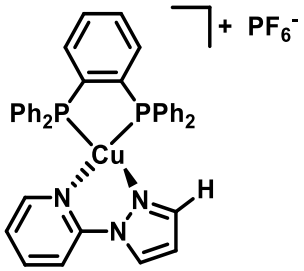

[Cu(pypz)(dppbz)][PF$_6$] (**2b**): Colorless crystalline solid; Yield 80%. ^{1}H NMR (CD_2Cl_2, 400 MHz): δ 8.48 (d, *J* = 2.8, 1H), 8.09 (dt, *J* = 7.9, 1.6, 1H), 7.84 (d, *J* = 8.2, 1H), 7.65-7.52 (m, 6H), 7.42 (t, *J* = 7.3, 4H), 7.34 (t, *J* = 7.2, 8H), 7.31-7.14 (m, 9H), 6.81 (dd, *J* = 2.7, 1.9, 1H). ^{13}C{^{1}H} NMR (CD_2Cl_2, 100 MHz): δ 148.8, 148.2, 142.8, 141.5, 141.4 (t, J_p = 34.7), 135.1(t, J_p = 4.6), 133.1 (t, J_p = 8.0), 131.7, 130.7, 129.4 (t, J_p = 5.0), 128.5, 123.6, 112.3, 111.7. ^{31}P{^{1}H} NMR (CD_2Cl_2, 161 MHz): δ –5.25. HRMS (ESI+) *m/z* Calcd. for $C_{38}H_{31}CuN_3P_2^+$ $(M–PF_6)^+$ 654.1284. Found: 654.1286. Anal. Calcd. for $C_{38}H_{31}CuF_6N_3P_3$: C, 57.04; H, 3.91; N, 5.25. Found: C, 56.97; H, 3.94; N, 5.28.

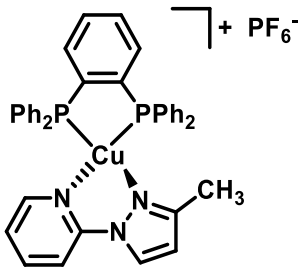

[Cu(pympz)(dppbz)][PF$_6$] (**2c**): Yellow crystalline solid; Yield 87%. ^{1}H NMR (CD_2Cl_2, 400 MHz): δ 8.32 (d, *J* = 2.7, 1H), 8.04 (dt, *J* = 8.0, 1.6, 1H), 7.74 (d, *J* = 8.2, 1H), 7.66-7.56 (m, 4H), 7.52 (d, *J* = 4.3, 1H), 7.48-7.08 (m, 21H), 6.54 (d, *J* = 2.7, 1H), 1.85 (s, 3H). ^{13}C{^{1}H} NMR (CD_2Cl_2, 100 MHz): δ 152.9, 148.6, 141.4 (t, J_p = 34.7), 141.3, 135.4 (t, J_p = 4.2), 133.0, 131.9, 130.6, 129.5 (t, J_p = 5.0), 129.1, 122.8, 111.5, 111.4, 14.2. ^{31}P{^{1}H} NMR (CD_2Cl_2, 161 MHz): δ –4.49. HRMS (ESI+) *m/z* Calcd. for $C_{39}H_{33}CuN_3P_2^+$ $(M–PF_6)^+$ 668.1440. Found: 668.1441. Anal. Calcd. for $C_{39}H_{33}CuF_6N_3P_3$: C, 57.53; H, 4.16; N, 5.16. Found: C, 57.46; H, 4.16; N, 5.22.

3.1.4.2. Crystallography

The X-ray diffraction data for **1a**, **1b**, **1c**, **2b**, and **2c** were collected on an Agilent Technologies SuperNova Dual Source diffractometer using a μ-focus Cu Kα radiation source (λ = 1.5418 Å) equipped with collimating mirror monochromators that operated at 100 K. Data collection, unit cell refinement and data reduction were performed using Agilent Technologies CrysAlisPro V 1.171.37.31.[259] The structures were solved by direct methods using SuperFlip.[260]

Structures were refined by full-matrix least-squares on F^2 with anisotropic displacement parameters for the non-H atoms using SHELXL-2014.[261] Structure analysis was aided by use of the programs PLATON98[215] and WinGX.[216,217] The hydrogen atoms were calculated in ideal positions with isotropic displacement parameters set to 1.2 x U_{eq} of the attached atom (1.5 x U_{eq} for methyl hydrogen atoms).

The function, $\Sigma w(|F_o|^2 - |F_c|^2)^2$, was minimized, where $w = 1/[(\sigma(F_o))^2 + (0.013*P)^2 + (87.56*P)]$ and $P = (|F_o|^2 + 2|F_c|^2)/3$. $R_w(F^2)$ refined to 0.222, with $R(F)$ equal to 0.0857 and a goodness of fit, S, = 1.03. Definitions used for calculating $R(F)$, $R_w(F^2)$ and the goodness of fit, S, are given as follows: $R_w(F^2) = \{\Sigma w(|F_o|^2 - |F_c|^2)^2/\Sigma w(|F_o|)^4\}^{1/2}$ where w is the weight given each reflection. $R(F) = \Sigma(|F_o| - |F_c|)/\Sigma|F_o|\}$ for reflections with $F_o > 4(\sigma(F_o))$. $S = [\Sigma w(|F_o|^2 - |F_c|^2)^2/(n - p)]^{1/2}$, where n is the number of reflections and p is the number of refined parameters.

The data were checked for secondary extinction effects but no correction was necessary. Neutral atom scattering factors and values used to calculate the linear absorption coefficient are from the International Tables for X-ray Crystallography (1992).[218] All Figures were generated using SHELXTL/PC.[262] Tables of positional and thermal parameters, bond lengths and angles, torsion angles and figures are found elsewhere.

3.1.4.3. Photophysical Measurements

Absorption spectra were recorded on a Varian Cary 6000i UV-Vis-NIR spectrophotometer with Starna Quartz cells. Luminescent measurements were recorded on a Photon Technology International QM 4 spectrophotometer equipped with a 6-in. diameter K Sphere-B integrating sphere. Quantum yield measurements were collected using the integrating sphere. Quantum yields were calculated by dividing the area under the emission peak by the difference between the area under the excitation peak of the sample and the $BaSO_4$ reference material ($A_{em,\ sample}$ / ($A_{ex,\ blank} - A_{ex,\ sample}$)) and the reported quantum yields are the average of three trials. Low temperature lifetime measurements were taken using a variety of cooling baths. Temperatures were monitored using a low temperature thermocouple corrected to a calibration curve.

3.1.4.4. Electrochemistry

Electrochemical measurements were recorded in a dry-box under a nitrogen atmosphere using a GPES system from Eco. Chemie B. V. All experiments were carried out in a CH_2Cl_2 solution containing 0.1 M [(*n*-Bu)$_4$N][PF_6] ($TBAPF_6$) as supporting electrolyte. The $TBAPF_6$ was purified via recrystallization three times from boiling ethanol before being dried for 3 days under active vacuum at 80 °C. A three-electrode cell consisting of a $Ag/AgNO_3$ reference electrode (Ag wire incubated in a 0.01 M $AgNO_3$ solution with 0.1M $TBAPF_6$ in CH_3CN), a glassy carbon working electrode (3.0 mm), and a Pt wire coil counter electrode was utilized. All measured potentials were corrected to the ferrocene/ferrocenium redox couple measured as an external reference.

3.1.4.5. Computational Methods

All calculations were carried out using the Gaussian 09 package program.[263] Crystal structure coordinates were used as the starting point for Density Functional Theory (DFT) geometric optimizations of the ground state molecules.[237] Optimization of $\mathbf{1b}^{2+}$ and $\mathbf{1c}^{2+}$ used the optimized geometry of $\mathbf{1b}^{+}$ and $\mathbf{1c}^{+}$, respectively, as the initial guess. Time dependent DFT (TD-DFT) calculations were performed on the optimized ground state geometry to determine the first 60 singlet transitions.[264–266] All calculations were performed at the gradient corrected functional level using Becke's three parameter B3LYP functional.[267–270] The LANL2DZ basis set and electron core potential[271–274] was used for the Cu atom while the 6-31G(d,p)[275–282] basis set was used for the remaining elements. When pertinent, natural transition orbitals were visualized.[283]

3.2. Dual Emission from Discrete Copper(I) Complexes Displaying Excitation Dependent Emission and Luminescent Thermochromism

3.2.1. Introduction

Interest in the field of new materials for optoelectronic applications has grown in recent years, as the development of more efficient devices becomes ever more important for decreasing energy demands and moving towards environmentally friendly technologies. To this end, organic light emitting diodes (OLEDs) and light emitting electrochemical cells (LEECs) look to play a key role in reducing the energy demands of the lighting sector.[284,285] While the precise mechanism of light emission from OLED/LEEC devices depends on the architecture of the device, a key step in the process is electron-hole combination on an emissive material.[285,286] Often, these emissive materials are based on transition metal complexes which offer increased stability and electrochemical quantum efficiencies compared to purely organic fluorescent emitters.[6,82,93,222]

Understanding the relationship between the structure and the optoelectronic properties of these emissive compounds is vital for the design of increasingly efficient materials. Active emitters based on copper(I) complexes are of particular interest, as they allow for the design of highly emissive materials based on a cheap and earth abundant metal.[93,232,245] Common design strategies for these emissive complexes center around tetranuclear copper clusters,[92,287–289] binuclear copper(I) complexes,[92,290–292] three-coordinate trigonal planar geometries[95,252,253,293] and four-coordinate tetrahedral complexes of which complexes with the structure $[Cu(P\text{^}P)(N\text{^}N)]^{0/+}$ (where (P^P) represents a chelating bisphosphine ligand and (N^N) indicates an aromatic bidentate nitrogen donor) dominate the literature.[87,225–227,229–231,233–240,243,244,247,248] In these studies, a wide range of (N^N) ligands have been investigated, while the number of (P^P) ligands

remains relatively underexplored. The development of new (P^P) ligand architectures is important to further understand these emissive materials and what role the bisphosphine ligand plays in these systems. Additionally, new ligand scaffolds may provide an entryway into more complex and interesting materials. In particular, incorporation of thiophene-based scaffolds has the potential to lead to electropolymerizable materials.[294]

Herein, we report our studies of a series of three copper(I) complexes based on (5,5'-dimethyl-[2,2'-bithiophene]-3,3'-diyl)bis(diphenylphosphane) (**4**) of the general structure [Cu(**4**)(N^N)][PF_6] ((N^N) = 3-trifluoromethyl-1-(2-pyridyl)pyrazole (pycf3pz), **5**; 1-(2-pyridyl)pyrazole (pypz), **6**; 3-methyl-1-(2-pyridyl)pyrazole (pympz), **7**). The pyrazole-pyridine ligands were chosen as their complexes have been shown in the literature to promote efficient emission from materials in addition to being generally air stable.[234] The electrochemical and photophysical properties of the materials reported herein have been correlated to structural and electronic properties to extract information about copper(I) complex design.

3.2.2. Results and Discussion

3.2.2.1. Synthesis of Ligand 4

Ligand **4** was synthesized as shown in Scheme 3.3. To synthesize 3,3',5,5'-tetrabromo-2,2'-bithiophene (**1**), bromination of 2,2'-bithiophene was performed using 4.1 equivalents of Br_2. Next, methylation of the 3 and 3' positions was achieved by lithium-halogen exchange using *n*-butyllithium, followed by quenching with iodomethane to generate **2.** Methylation of the 3 and 3'positions was desired to increase material stability and prevent electropolymerization of the ligand during the electrochemical and photophysical studies of the discrete complexes.

Scheme 3.3. Synthesis of ligand **4**.

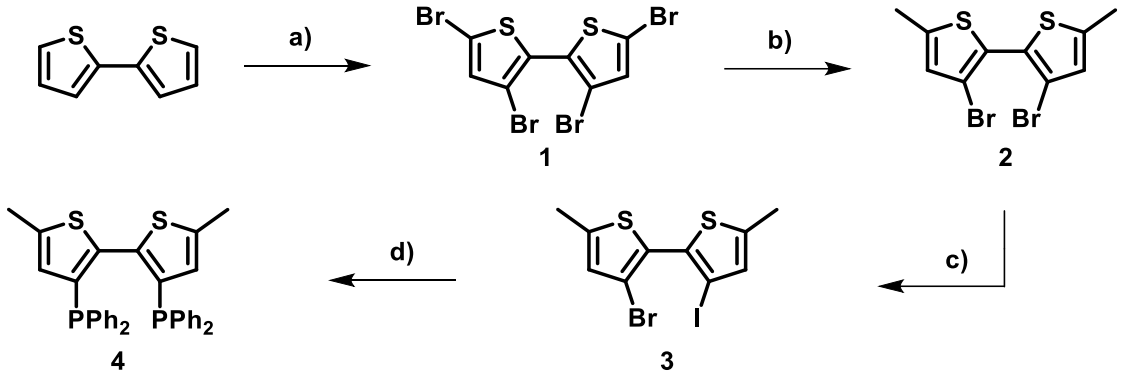

a) (i) 4.1 Br_2, $CHCl_3$/AcOH, 0 °C - rt, 1 h; (ii) $CHCl_3$/CH_3COOH, rt - reflux, overnight, 88%. b) (i) 2.15 *n*-butyllithium, THF, –78 °, 45 min; (ii) 2.15 CH_3I, THF, –78 °C - rt, overnight, 80%. c) (i) 1.07 *n*-butyllithium, THF, –78 °C, 30 min; (ii) 1.07 I_2, THF, –78 °C, 1 h; (iii) THF, –78 °C - rt, overnight, 80%. d) 2.2 $HP(Ph)_2$, 2.2 KOAc, 0.02 $Pd(OAc)_2$, *N,N*-dimethylacetamide, 130 °C, 3 h, 74%.

Attempts to directly synthesize **4** from **2** via lithium-halogen exchange followed by quenching with chlorodiphenylphosphine failed to yield the material in an appreciable yield as did reactions with potassium diphenylphosphide as these conditions led to the formation of cyclophospane/cyclophosphonium byproducts. Attempts at palladium-mediated coupling reactions to convert **2** to **4** failed to generate the desired product as well. Synthesis of **4** was ultimately achieved by following a procedure developed by Bonnafoux *et al.*[295] for the catalytic palladium phosphination of biaryl-based diphosphines. Performing a halogen exchange reaction to generate 3-bromo-3'-iodo-5,5'-dimethyl-2,2'-bithiophene (**3**) followed by coupling using the adapted palladium catalyzed procedure generated **4** as an air stable, colorless crystalline solid. The overall yield for the synthesis of ligand **4** was 42%. Evaporation of a saturated hexanes/CH_2Cl_2 solution of **4** gave crystals suitable for single crystal X-ray diffraction (Figure 3.17). A torsion of 132.2(2)°, as defined by the S–C–C–S structural unit, is observed. The source of this torsion is attributed primarily to the steric and electronic repulsion of the diphenylphosphane entities.

3.2.2.2. Synthesis of Complexes 5-7

Synthesis of complexes **5-7** was realized in a straightforward manner (see Scheme 3.4). Under nitrogen atmosphere, tetrakis(acetonitrile) copper(I) hexafluorophosphate ($[Cu(CH_3CN)_4][PF_6]$) was dissolved in CH_2Cl_2, which was subsequently followed by the addition of **4** and then the desired pyrazole-pyridine ligand. Vapor diffusion of diethyl ether into the reaction solution led to the precipitation of the products as highly crystalline materials suitable for single crystal X-ray diffraction.

Scheme 3.4. Synthesis of complexes **5-7**.

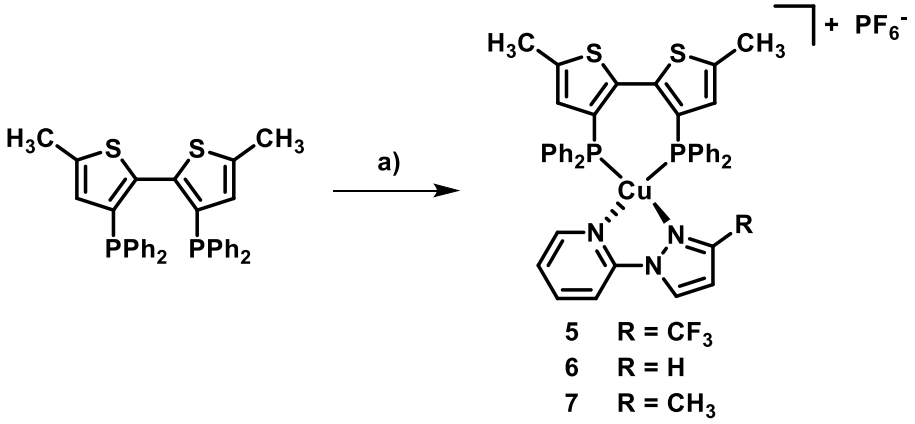

a) (i) 1 $[Cu(CH_3CN)_4][PF_6]$, CH_2Cl_2, rt, 45 min; (ii) 1 pyrazole-pyridine, CH_2Cl_2, rt, 2 h.

The complexes bearing larger substituents, **5** and **7**, crystallize in the $P\,2_1/c$ space group and display two crystallographically-unique molecules in the asymmetric unit; this is in contrast to complex **6** which crystallized in the $P\bar{1}$ space group and contained only a single structure in the asymmetric unit. All three structures display a distorted tetrahedral geometry about the copper(I) center. Chelation of ligand **4** displays a bite angle that ranges from 104.51(6) - 108.42(4)° and phosphorous – copper bond lengths which fall in a narrow range (2.200(2) – 2.249(1) Å). The decrease in sterics of complex **6** is quite evident in the copper-nitrogen bond lengths. Coordination of the pyridine and pyrazole rings displayed nitrogen – copper bond lengths of 1.97(2) Å and 2.06(1) Å, respectively,

which are considerably shorter than the bond lengths observed in the remaining congeners.

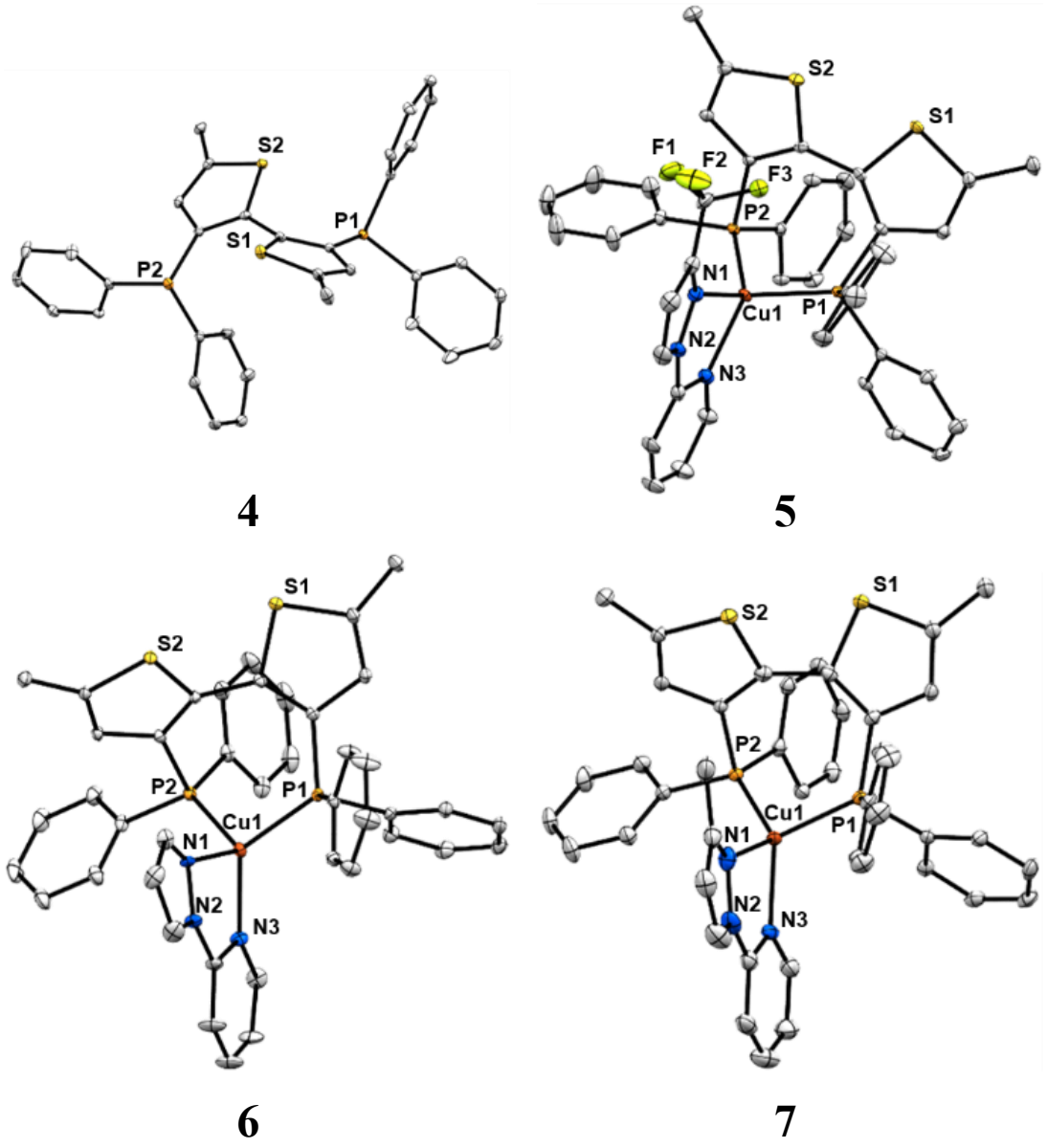

Figure 3.17. Crystal structures of **4-7.** For clarity, hydrogen atoms and the PF_6^- counter-anion in **5-7** are omitted. Thermal ellipsoid plots are drawn at 30% probability. Disorder was present in complexes **5** and **6**. Only the major contributing positions are shown.

Table 3.3. Bond Lengths (Å), Angles (Degrees) and Dihedral Angles (degrees) of **5**, **6** and **7**.

	Cu1-P1	Cu1-P2	Cu1-N1	Cu1-N3	P1-Cu1-P2	N1-Cu1-N3	∠(N^N)(P^P)
5	2.212(1)	2.225(1)	2.061(3)	2.135(3)	108.42(4)	78.1(1)	83.07
	2.223(1)	2.249(1)	2.074(5)	2.111(5)	106.20(5)	78.9(2)	85.97
6	2.2284(6)	2.2188(6)	1.97(2)	2.06(1)	107.07(2)	81.3(6)	87.04
7	2.200(2)	2.216(2)	2.069(5)	2.121(6)	106.68(6)	80.3(2)	83.36
	2.209(2)	2.216(2)	2.081(5)	2.103(6)	104.51(6)	79.3(2)	85.8

3.2.2.3. Electronic Absorption and Electrochemistry of 4-7

Studies into the electronic properties of complexes **5-7** were performed via cyclic voltammetry (Figure 3.18a). Electrochemical measurements for ligand **4** are also shown for comparison. In the free ligand, an irreversible oxidation is observed at an onset potential (E_{on}) of 0.49 V with a peak potential ($E_{p,a}$) of 0.70 V, followed by a second distinct event seen at $E_{p,a}$ = 1.04 V. These are assigned as oxidations of the phosphine unit and bithiophene unit, respectively. Cyclic voltammograms of the complexes demonstrate that coordination to the copper(I) center leads to a drastic decrease in the intensity of the first oxidation event relative to the second oxidation with a concomitant shift in the onset of oxidation to higher potentials. Additionally, a small reductive-backwave associated with the first redox event is observed in complexes **5** and **6.** This suggests that the first oxidation event of these complexes is associated with oxidation of the copper(I) center with a large contribution from the phosphorous atoms. The identity of the pyrazole-pyridine unit also influences the potential at which the copper(I) center is oxidized. Interestingly, the potential for oxidation increases in the order of **6** > **7** > **5** indicating that steric effects may also influence the electronic nature of the complex. The

second oxidation event in the complexes at approximately $E_{p,a}$ = 1.05 V shows only minor shifts from that of the free ligand.

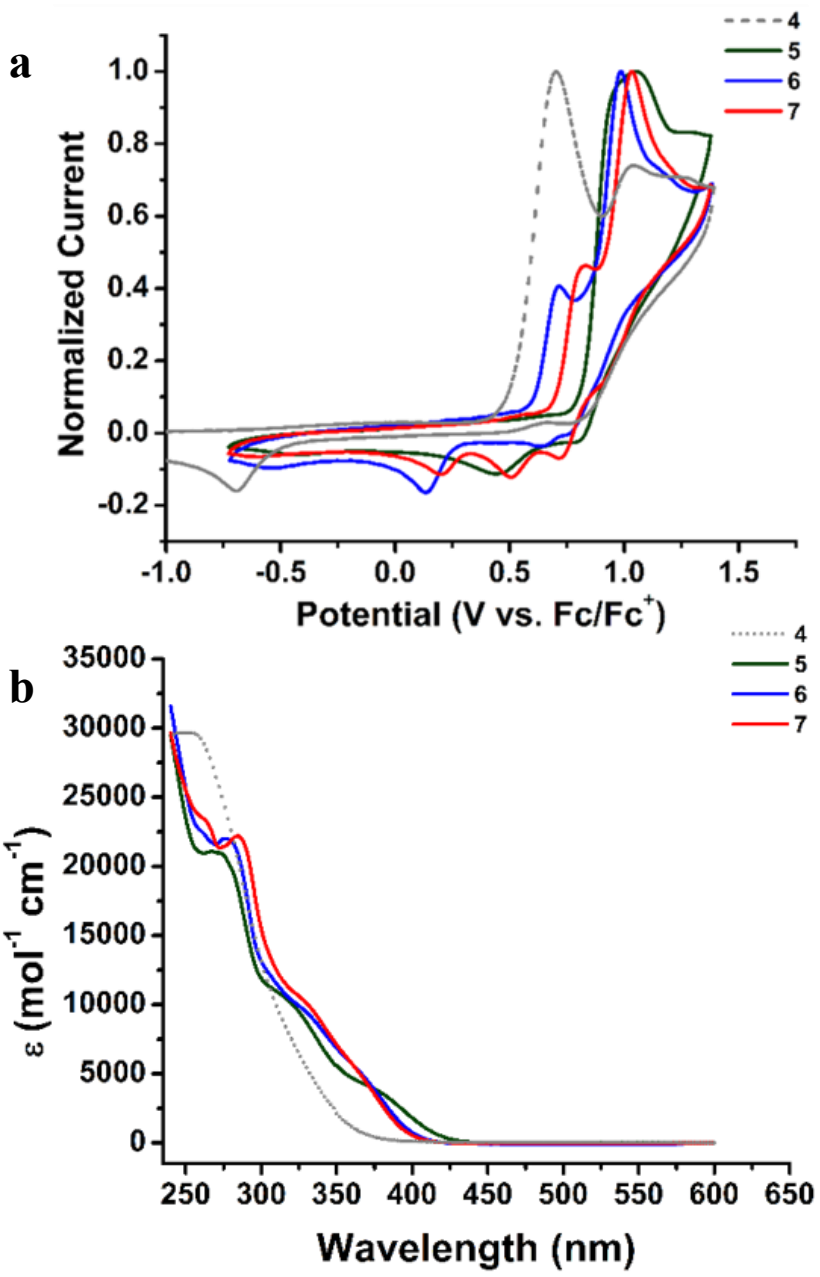

Figure 3.18. (a) Cyclic voltammograms of **4-7** (0.5 mM) taken in CH_2Cl_2 containing 0.1 M $TBAPF_6$. (b) Electronic absorption spectra of **4-7** taken in CH_2Cl_2.

Investigations into the electronic absorption spectra of ligand **4** and complexes **5-7** are shown in Figure 3.18b. For each of the complexes, a new, low energy absorption event is seen prior to the onset of absorption for ligand **4**. This is characteristic of $[Cu(P\hat{}P)(N\hat{}N)]^+$ complexes and is attributed to a singlet metal-to-ligand charge-transfer (^{1}MLCT) resulting in electron transfer from an occupied copper-based orbital with significant contributions from the coordinating phosphorous atoms ($d_{Cu/P}$) to the chelating (N^N) ligand π*-orbital (π_{NN}*).[87,234,247,248] Electronic control of this transition by the pyrazole-pyridine ligands is evident as the absorption energy decreases with decreasing electron density on the pyrazole-pyridine ligand (**5** (398 nm) > **6** (402 nm) > **7** (420 nm)). A second absorption band is seen at slightly higher energies, whose onset correlates more closely to that of the free ligand. However, the increased prominence of the shoulder suggests mixed orbital character in the transition. This is tentatively assigned as a transition primarily involving a π-to-π* transition centered on ligand **4** (π_{PP}-to-π_{PP}*), with small contributions of charge transfer character from the metal center. This is consistent with electronic control from the pyrazole-pyridine ligand as the order of transition energy now decreases with increasing electron density transferred to the metal center from the supporting (N^N) ligand (**5** < **6** < **7**).

3.2.2.4. Density Functional Theory (DFT) Studies

To corroborate these assignments, Density Functional Theory (DFT) (Figure 3.19) and Time Dependent - Density Functional Theory (TD-DFT) calculations were performed on each of the complexes. The lowest unoccupied molecular orbital (LUMO) exhibits similar spatial distributions in each of the complexes, as seen in the Kohn-Sham diagram, primarily residing on the π_{NN}*-orbital. The π_{PP}*-orbital was found to be the third highest unoccupied molecular orbital (LUMO+2) for all three complexes.

Investigation of the highest occupied molecular orbitals (HOMO) reveals a much more complicated picture. DFT suggests that the HOMO and the next highest occupied energy level (HOMO–1) are quite close in energy. These HOMO and HOMO–1 orbitals in each complex consist of two fundamentally different orbitals: a largely bithiophene-based π-orbital with small contributions from the metal center (π_{PP}) and an orbital in which the main contributions arise from mixing of the *d*-orbitals of the copper with the atomic orbitals of the chelating phosphorus atoms ($d_{Cu/P}$). The latter orbital is consistent with the assignment of the first oxidation event in each complex while the former is consistent with the second oxidation event (see above). Inspection of the HOMO and HOMO–1 diagrams as the complexes move towards more electron rich copper(I) centers reveals a slight stabilization of the π_{PP}-orbital with a simultaneous increase in the energy of the $d_{Cu/P}$-orbital, leading to a switching of the orbitals from a π_{PP}-based HOMO in complexes **5** and **6** to a HOMO centered on the $d_{Cu/P}$-orbital in **7**. Destabilization of the $d_{Cu/P}$-orbital across the series is attributed to an increase in the electron density on the Cu(I) center from the more strongly coordinating pyrazole-pyridine ligands.

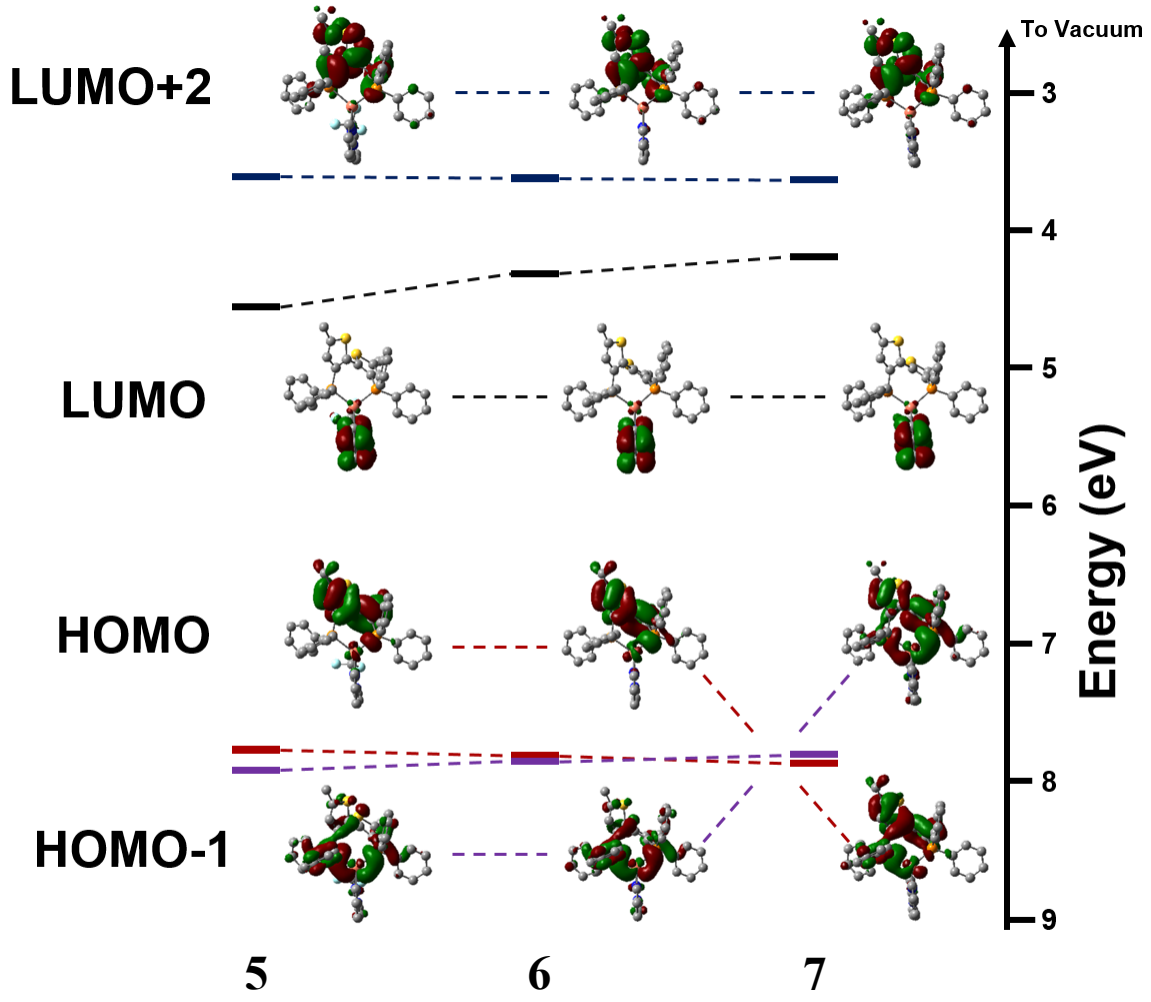

Figure 3.19. DFT calculated Kohn-Sham orbitals and energy levels of complexes **5-7** illustrating the evolutions of the LUMO+2, LUMO, HOMO and HOMO–1. Orbitals assigned as π_{PP}* and π_{NN}* are shown in blue and black traces, respectively whereas the $\pi_{PP/Cu}$ orbitals and $d_{Cu/P}$-orbitals are shown in red and purple, respectively. An inversion of the orbitals comprising the HOMO and HOMO–1 in complexes **5** and **6** is seen in complex **7**.

The results of the TD-DFT calculations support the transition assignments in the electronic absorption spectra (Figure 3.20). Universally, the first transition for the reported copper(I) complexes was shown to be a ^{1}MLCT to the π_{NN}*-orbital. Contributions from both the $d_{Cu/P}$-orbital and $\pi_{PP/Cu}$-orbital are seen in the highest

occupied natural transition orbital, with a drastic increase in the $d_{Cu/P}$ character moving from **5** to **6** and **7.**

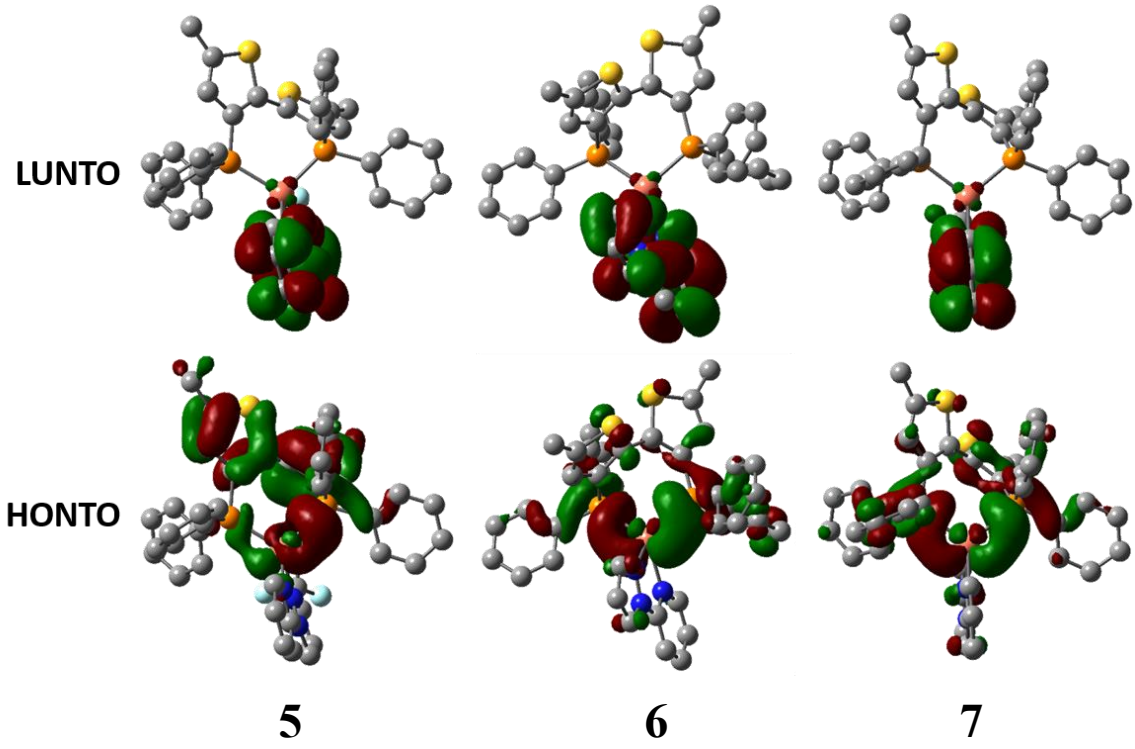

Figure 3.20. Kohn-Sham orbitals representing the highest occupied natural transition orbital (HONTO) and the lowest unoccupied natural transition orbital (LUNTO) for complexes **5**, **6** and **7**.

3.2.2.5. Emissive Properties: Excitation and Temperature Dependence

In the solid state, the emission profiles of the materials display interesting photophysical properties. A strong dependence of the emission on the excitation wavelength was observed both at room temperature and at 77 K (Figure 3.21). Interestingly, longer wavelength excitations lead to increased emission intensity from a higher energy (HE) emission band, which is assigned as phosphorescent emission from the ligand centered (^{3}LC) π_{PP}-to-π_{PP}* transition. The lifetimes of these bands were

observed to be on the order of tens of microseconds, suggesting triplet-based emission. Conversely, the low energy (LE) emission, which was stimulated from the higher energy excitations, was attributed to a ^{3}MLCT involving the $d_{Cu/P}$ and π_{NN}* molecular orbitals. The assignment of triplet-based emission is supported by the long lifetimes at both room temperature and at 77 K. A tabulation of the measured lifetimes and quantum yields (φ) may be found in Table 3.4. The large Stokes shift of the LE emission suggests an excited state which undergoes a much larger geometric rearrangement than the HE emission. This can be explained by considering the nature of the transition in these materials. In the events leading up to the LE emission, absorption of light leads to a formal oxidation of the copper(I) center as the electron is transferred to the pyrazole-pyridine ligand, formally leaving the copper center in the +2 oxidation state. This induces a change in the coordination geometry, as the complex changes from a metal center that favors a tetrahedral coordination geometry to one that now favors square planar geometries. While a steric clash between the diphenylphsophine ligands and the pyrazole-pyridine should disrupt and limit this change, a large amount of the excited state energy is lost during the rearrangement process leading to a large Stokes shift. Such a phenomena is commonly observed in similar materials.[225,236,237,246] For the HE emission, the π_{PP}-to-π_{PP}* transition has a much shorter radiative lifetime and is expected to have a much smaller rearrangement in the excited state, limiting the Stokes shift in the excited state.

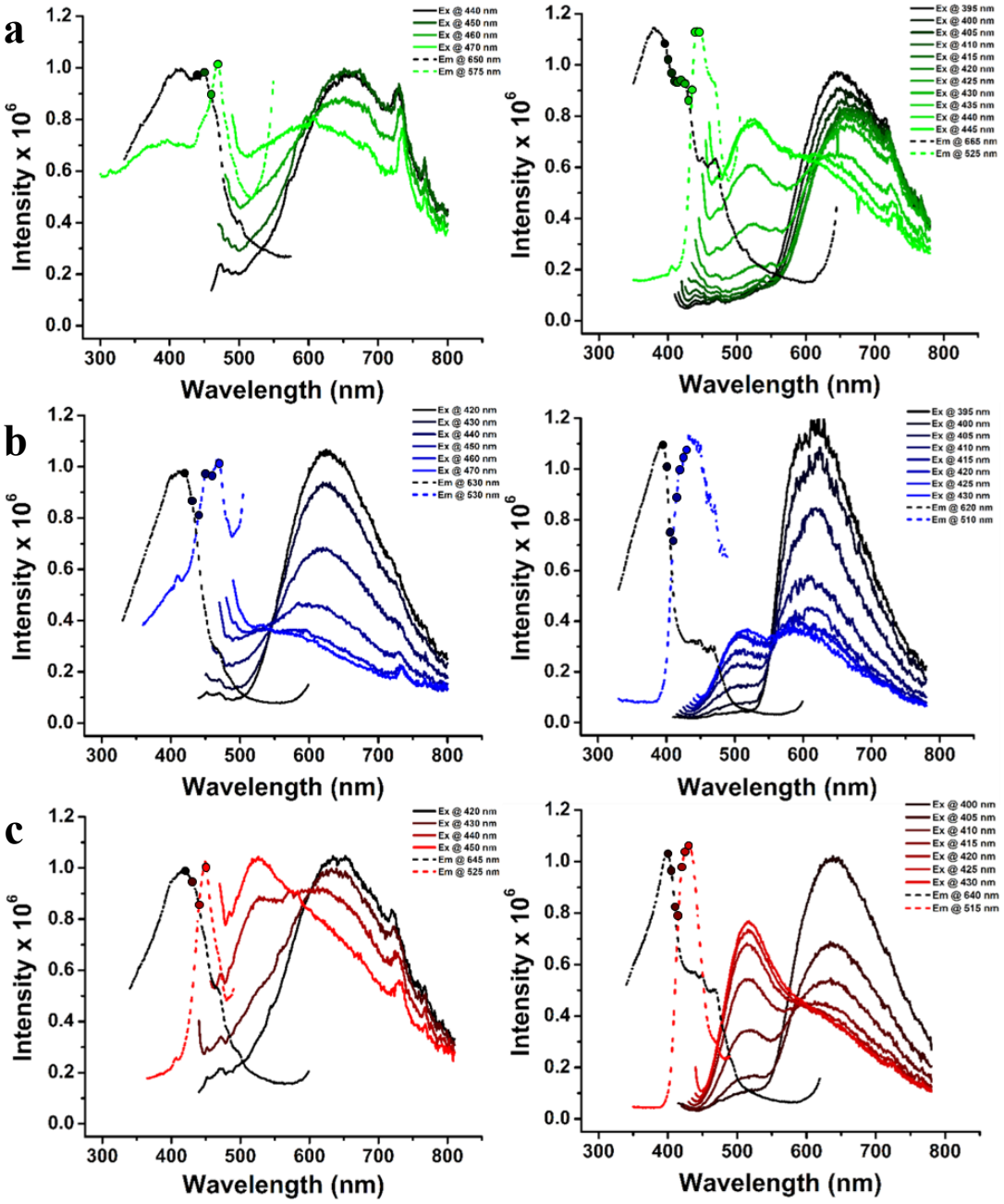

Figure 3.21. Excitation dependence studies illustrating the evolution of the emission profile with varying excitation wavelengths at room temperature (left column) and at 77 K (right column) for a) **5**, b) **6** and c) **7**.

Table 3.4. Photophysical measurements

Solid State						
Room Temperature						
	HE Emission Lifetimes*			**LE Emission Lifetimes***		**Quantum Yield (φ)**
	Ex 470 nm/Em 575 nm			**Ex 440 nm/Em 650 nm**		**Ex 440 nm**
5	τ_1	321 (10)	0.66	τ_1 321 (1.5)	17.30	0.096(7)
	τ_2	4.5 (2)	99.34	τ_2 7.7 (0.3)	82.70	
	Ex 470 nm/Em 530 nm			**Ex 420 nm/Em 630 nm**		**Ex 420 nm**
6	τ_1	343 (40)	6.20	τ_1 538 (12)	82.10	0.078(2)
	τ_2	21 (2)	93.80	τ_2 12 (3)	17.90	
	Ex 450 nm/Em 525 nm			**Ex 420 nm/Em 630 nm**		**Ex 420 nm**
7	τ_1	-	0.00	τ_1 349 (3)	100.00	0.077(2)
	τ_2	65 (12)	100.00	τ_2 -	0.00	
77 K: Solid State						
	HE Emission Lifetimes*			**LE Emission Lifetimes***		**Quantum Yield (φ)**
5	**Ex 445 nm/Em 525 nm**			**Ex 395 nm/Em 655 nm**		-
	τ_2	8.0 (6)	100.00	τ_1 544 (20)	100.00	
6	**Ex 430 nm/Em 510 nm**			**Ex 395 nm/Em 620 nm**		-
	τ_2	69 (29)	100.00	τ_1 1049 (17)	100.00	
7	**Ex 430 nm/Em 515 nm**			**Ex 400 nm/Em 640 nm**		-
	τ_2	7 (1)	100.00	τ_1 538 (22)	100.00	
Solution (CH_2Cl_2)						
Room Temperature						
	HE Emission Lifetimes*			**LE Emission Lifetimes***		**Quantum Yield (φ)**
5	**Ex 410 nm/Em 520 nm**			**Ex 330 nm/Em 680 nm**		-
	τ_2	12.1 (1)	100.00	τ_1 114.9 (6)	100.00	
6	**Ex 410 nm/Em 520 nm**			**Ex 330 nm/Em 720 nm**		-
	τ_2	7 (2)	100.00	τ_1 50.0 (9)	100.00	
7	**Ex 410 nm/Em 520 nm**			**Ex 330 nm/Em 690 nm**		-
	τ_2	7.8 (6)	100.00	τ_1 196 (2)	100.00	
77 K: Frozen Solution State						
	HE Emission Lifetimes*			**LE Emission Lifetimes***		**Quantum Yield (φ)**
5	**N/A**			**Ex 390 nm/Em 615 nm**		-
	τ_2	-	-	τ_1 930 (40)	100.00	
6	**Ex 410 nm/Em 500 nm**			**Ex 390 nm/Em 615 nm**		-
	τ_2	9.0 (6)	100.00	τ_1 1043 (9)	100.00	
7	**Ex 410 nm/Em 500 nm**			**Ex 380 nm/Em 640 nm**		-
	τ_2	8 (1)	100.00	τ_1 591 (6)	100.00	

*For lifetimes in which the HE and LE bands could not be isolated, the lifetimes were fit with a bi-exponential decay where τ_1 represents the contribution from the LE band and τ_2 represents the contribution from the HE band. The percent contributions of each lifetime to the observed luminescent decay profile are shown. Ex = Excitation wavelength; Em = Wavelength of monitored emission.

Excitation dependent emission was also observed from complexes **5-7** in drop cast PMMA films (5% by weight) showing the phenomena is not exclusively caused by crystal packing effects (Figure 3.22). The HE emission band in these films was greatly reduced, however, resulting in primarily LE emission. This indicates that matrix and dielectric effects may play key role in the distribution of the generated excited states. Interestingly, the PMMA films show warm white light emission when excited at wavelengths shorter than 300 nm (Figure 3.23).

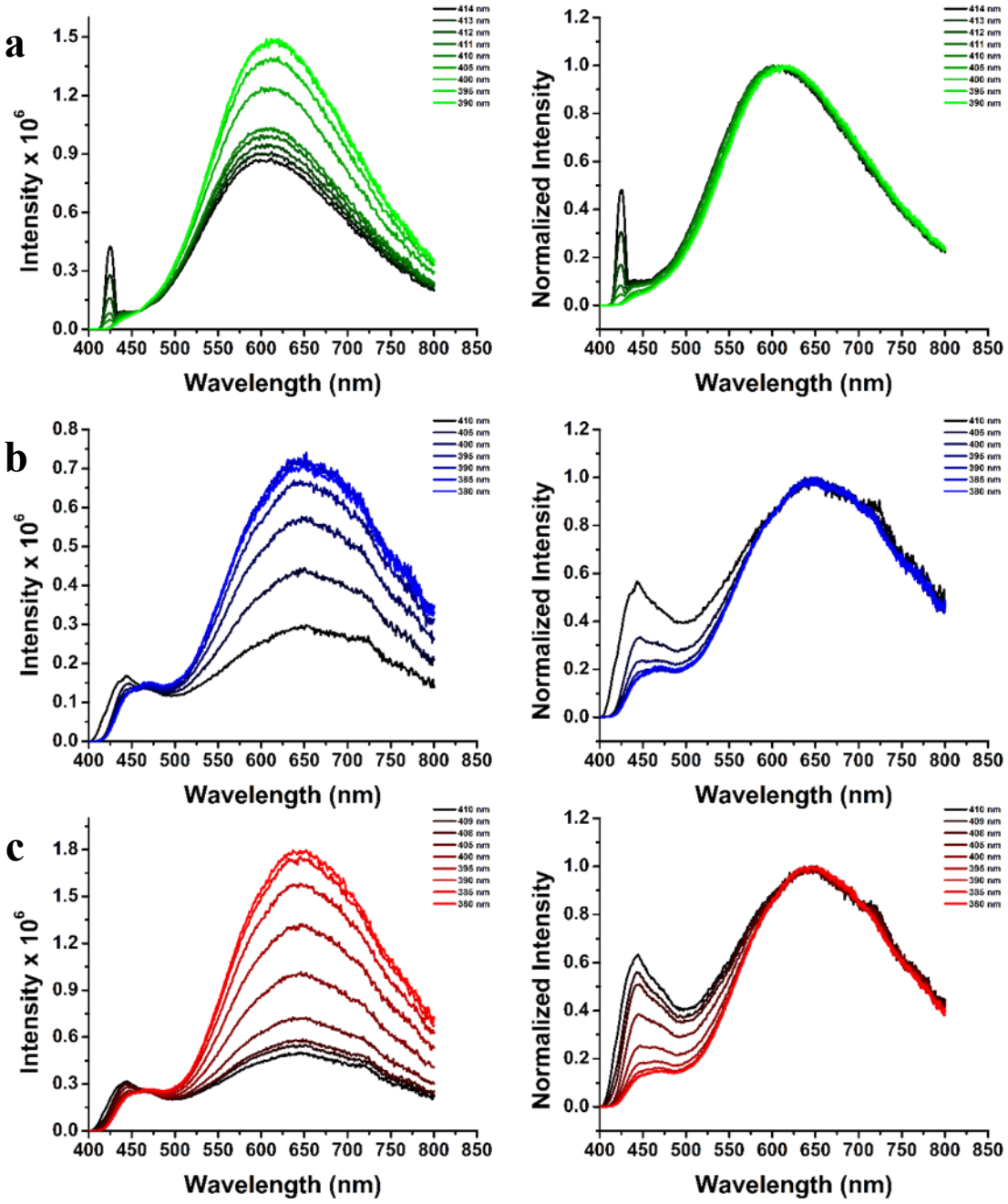

Figure 3.22. Excitation dependence studies illustrating the evolution of the emission profile with varying excitation wavelengths at room temperature (left column) and 77 K (right column) for a) **5**, b) **6** and c) **7** in dropcast PMMA films (5 wt%).

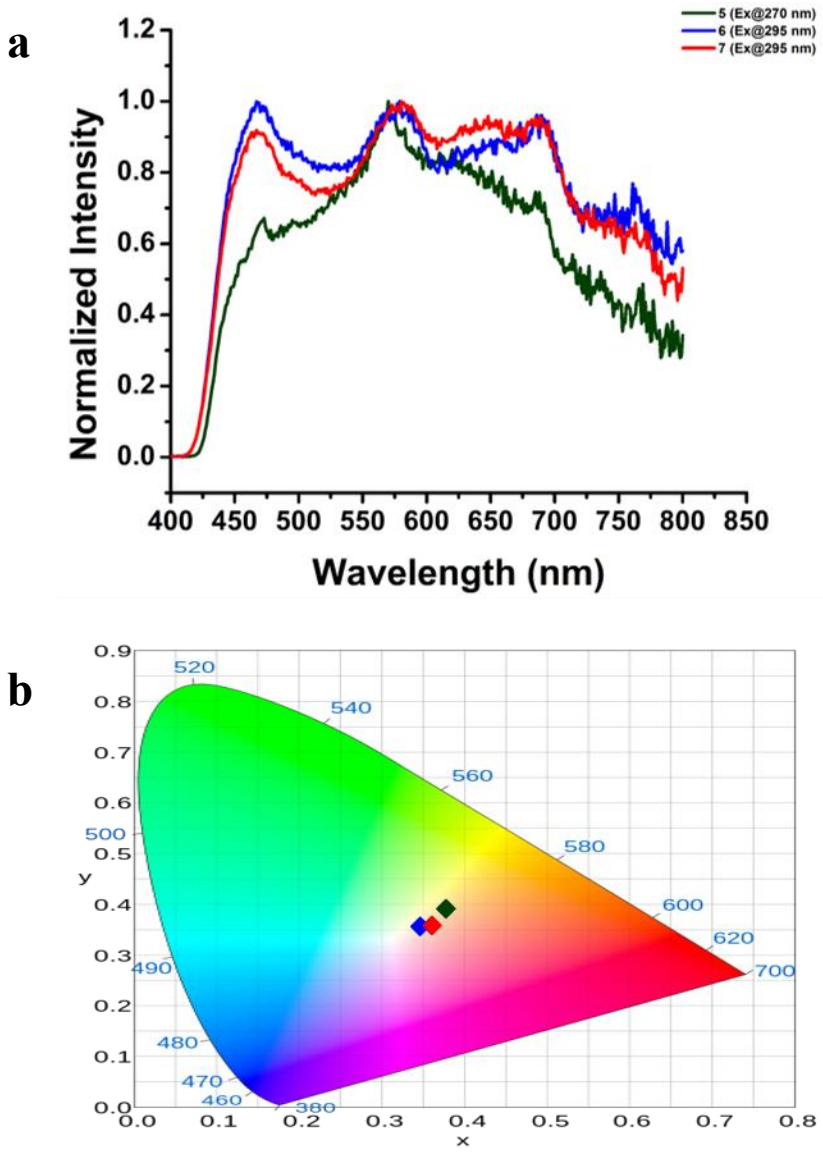

Figure 3.23. a) Warm white light emission from the Cu(I) complexes as a result of sub-300 nm excitation wavelengths. b) Resulting CIE coordinates of **5** (0.384, 0.404), **6** (0.353, 0.369) and **7** (0.367, 0.371).

Photophysical measurements taken in solution (CH_2Cl_2, deoxygenated) exhibited dual emission as well (Figure 3.24). Measurements taken in both dilute solution, as well as concentrated solutions, exhibited both LE and HE emission bands which suggests that the LE emission is not a consequence of aggregation-induced emission or excimer formation. As the excitation wavelength is swept from 330 nm to 410 nm, an increase in the intensity of both the HE and LE emission is observed with the HE band increasing at a greater rate. Plotting the CIE indices versus the excitation wavelengths exhibits a linear dependence on the excitation wavelength (Figure 3.25). In contrast with the photophysical measurements taken in the solid state and in PMMA film, the HE emission has a much greater prominence across the investigated excitation wavelengths. It is likely that non-radiative pathways are much more prominent in solutions for the LE emission due to distortion in the excited from the formal oxidation of Cu(I) to Cu(II), thus lowering the intensity of the LE emission relative to the HE. Measurements taken on the frozen CH_2Cl_2 solutions at 77 K display primarily LE emission, supporting this hypothesis. In fact, the HE emission is not observed at all in complex **5** and only at excitation energies below 400 nm does the HE emission band have appreciable intensity in **6** and **7**.

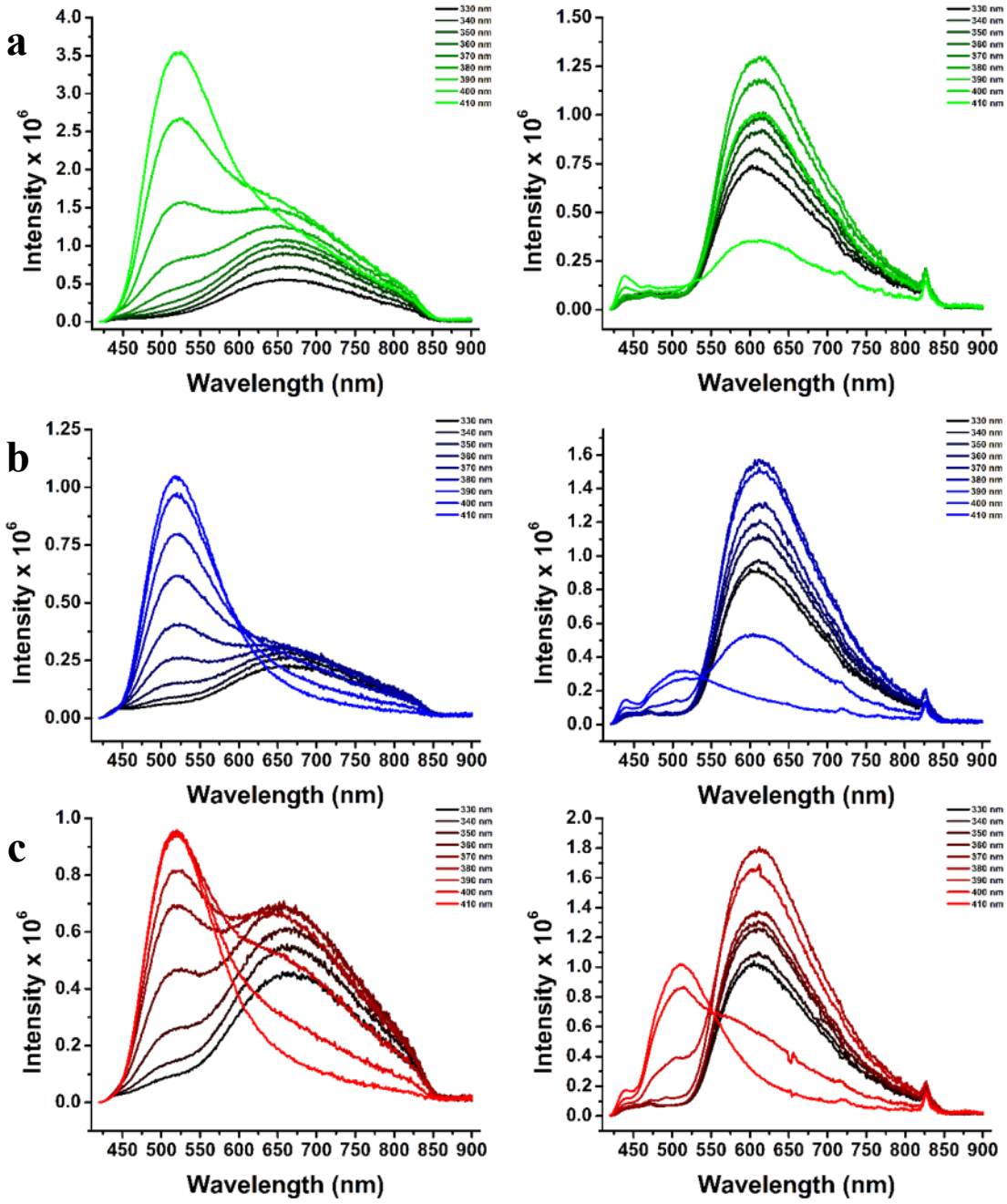

Figure 3.24. Wavelength dependence emission spectra of a) **5**, b) **6** and c) **7** taken in solution (0.1 mM) at room temperature (left) and in frozen CH_2Cl_2 solution at 77 K (right).

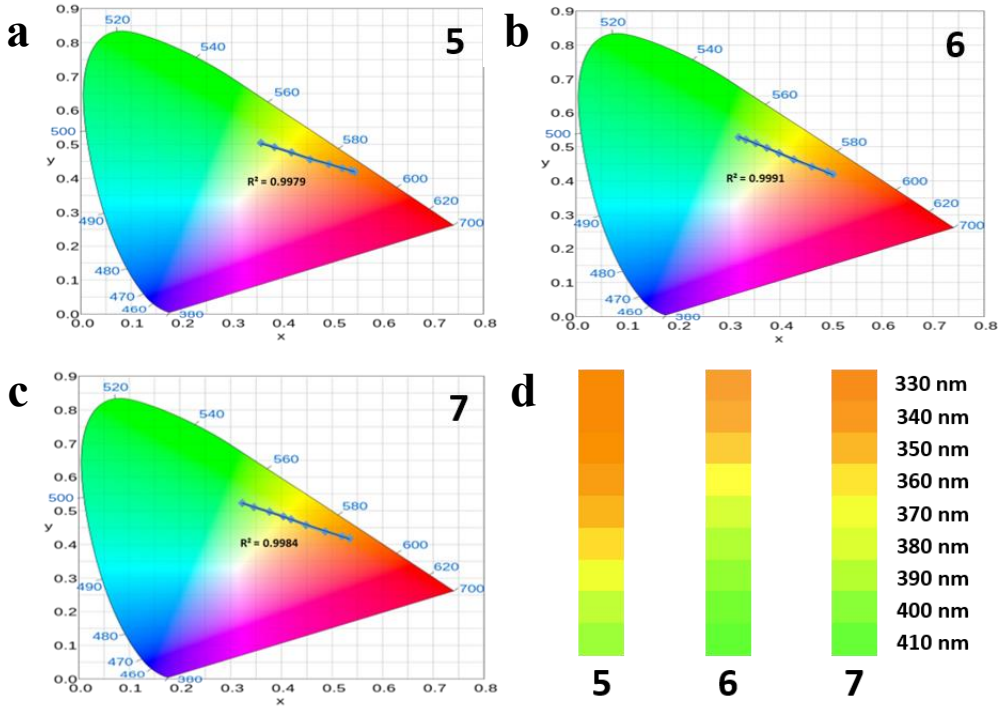

Figure 3.25. Linear dependence of the CIE coordinates of a) **5**, b) **6** and c) **7** on the excitation wavelength in CH_2Cl_2. d) Comparison of the emission color profiles of **5-7**.

The phenomena of dual emission is not unknown in copper-based materials; dual emission from luminescent copper(I) halide clusters has been extensively studied in the literature.[92,287,296,297] In the case of these reported copper(I) clusters, this emission is rationalized by invoking a system of two poorly coupled excited states assigned as a cluster-centered state (^{3}CC) and a halogen-to-ligand charge transfer (^{3}XLCT). The probability of populating each of these separate emissive states was shown to depend on the excitation wavelength at a given temperature. Furthermore, a dependence of the emission profile on temperature was observed as well. It was concluded that structural contraction at low temperatures lowered the energy and increased the distortion of the ^{3}CC excited state, effectively altering the branching ratio at a given excitation

wavelength. These studies prompted investigations into the temperature dependence of the emission profiles of **5-7**.

The temperature dependent emission profiles of complexes **5** and **7**, which are shown in Figure 3.26, do indeed show an evolving emission profile as a function of temperature.

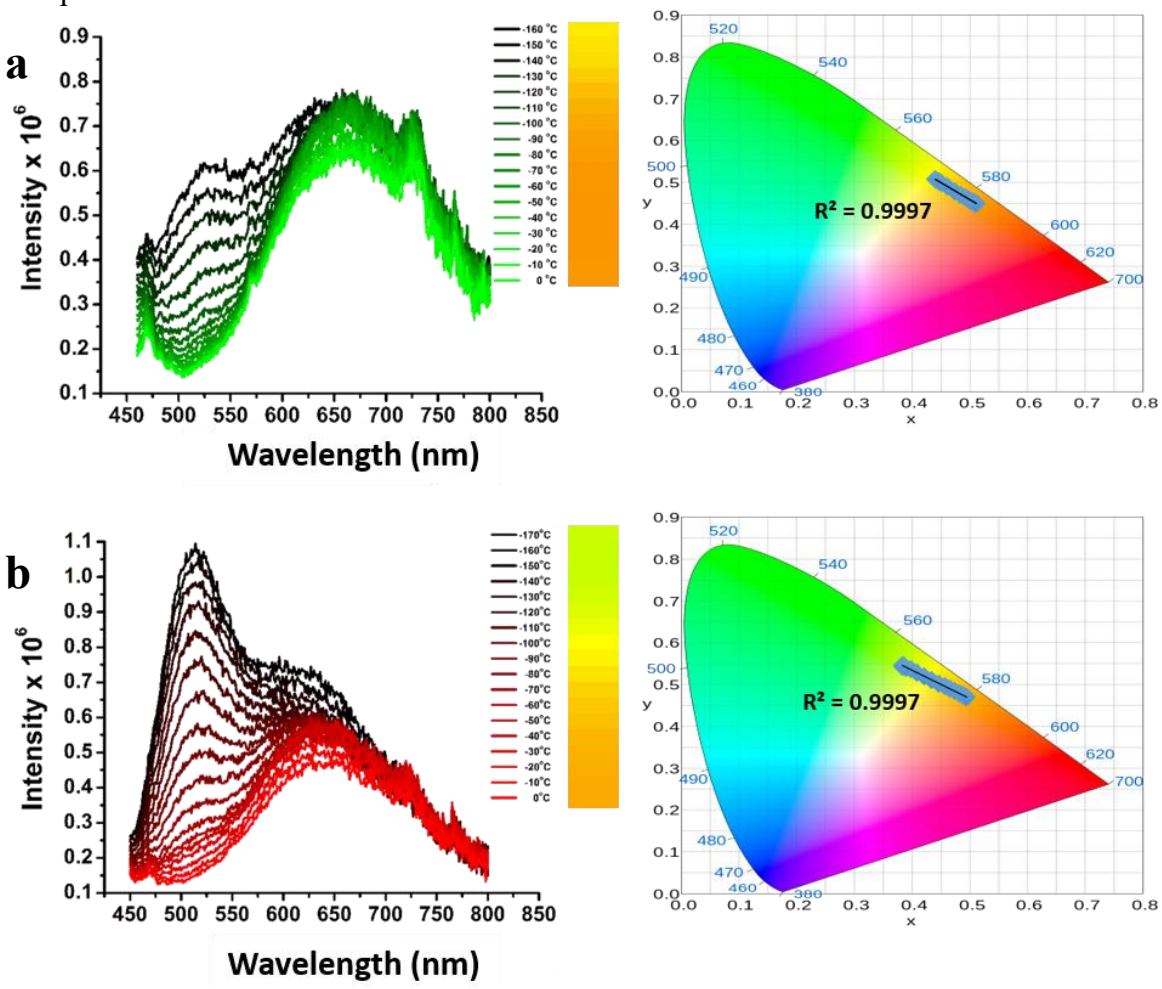

Figure 3.26. Temperature dependence of the emission profiles (left) and CIE coordinates (right) for a) **5** (Excitation at 440 nm) and b) **7** (Excitation at 425 nm).

At the lowest temperatures, two distinct emission profiles are observed; a high energy (HE) band and low energy (LE) band are observed (**5** - λ_{HE} = 530 nm, λ_{LE} = 660

nm; **7** - λ_{HE} = 515 nm, λ_{LE} = 640 nm). As the temperature is increased, the intensity of both bands begins to decrease with the HE band intensity lowering at a higher rate than the LE band. As the complexes reach 0 °C, the HE band is nearly indiscernible and the LE band dominates the spectra (**5** - λ_{LE} = 665 nm; **7** - λ_{LE} = 645 nm). No discernable shifting in the position of the HE emission was detected while a 5 nm redshift was observed in both **5** and **7**.

The evolution of the emission profile in the temperature dependence study of **6** began in a similar fashion to that of **5** and **7** with a HE band (λ_{HE} = 520 nm) and LE band (λ_{LE} = 595 nm) at low temperatures that decreased as temperature increased from –160 °C to –90 °C, with minimal shifting in the positions of the peak emissions (Figure 3.27). From –90 °C to 0 °C, the HE band continues to diminish whereas the LE band begins to increase in intensity and a noticeable redshift from 595 nm to 630 nm is observed. It is important to note that at all temperatures, independent lifetimes for the HE and LE bands were measured, indicating minimal coupling of these two excited states. Such an observation is consistent with two excited states that are expected to undergo structural relaxation along different geometric coordinates.[296]

All three studied complexes exhibit a linear dependence of the CIE coordinates on the temperature at which emission is monitored. Such systems have application in temperature sensing applications.[287]

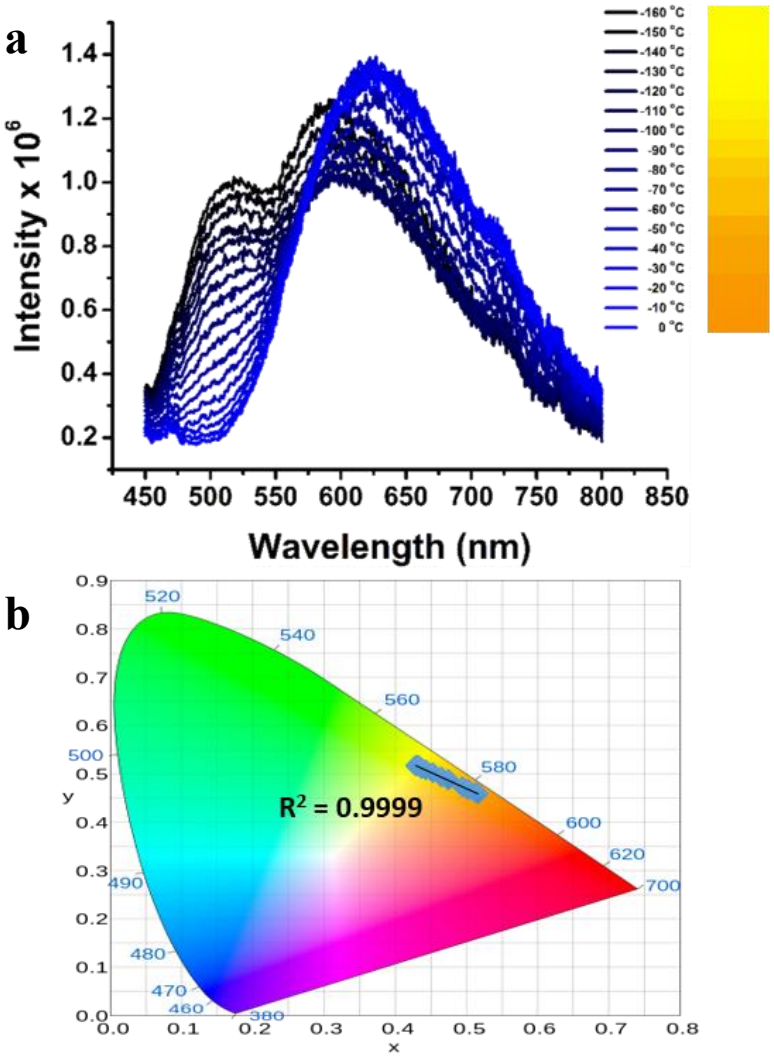

Figure 3.27. Temperature dependence of the emission profiles for **6**. a) Emission spectra were taken at an excitation wavelength of 425 nm. b) The resulting CIE coordinates are shown.

Adapting the arguments suggested by Kyle et al.[296] and Ford et al.[92] to the presented case, a proposed model for the wavelength-dependence and luminescent thermochromism exhibited by **5-7** is shown in Figure 3.28.

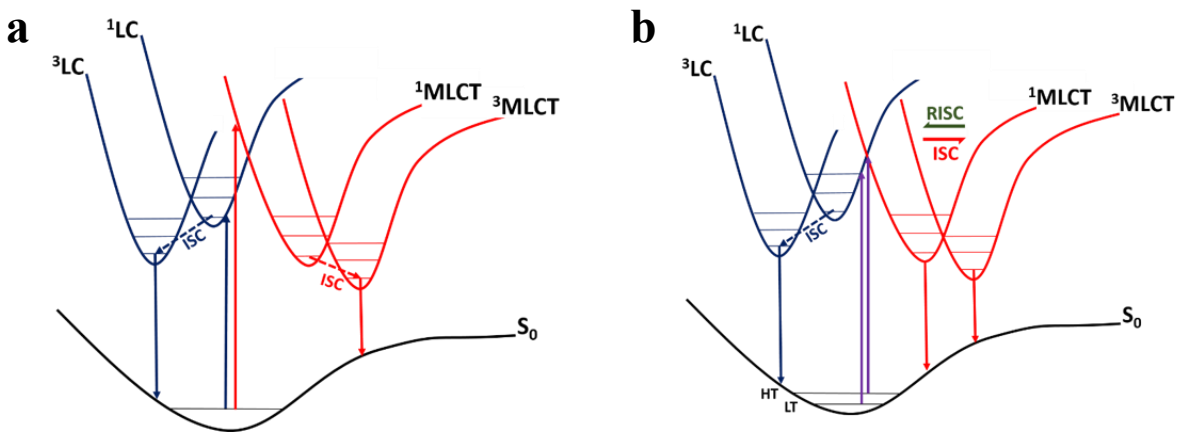

Figure 3.28. Proposed qualitative energy diagrams showing both the singlet and triplet MLCT and LC potential energy planes for (a) Simple model of the energy planes of **5-7** showing excitation dependent population of the excited states at a constant temperature. (b) Altered model for describing the temperature dependent emission profiles of **5-7**. At low temperatures (LT), population of higher vibrational energy levels is attenuated and excitation of the complexes at a given excitation wavelength favors transfer to the ^{1}LC and only ISC processes proceed efficiently. At higher temperatures (HT), excitation to the ^{1}MLCT is now accessible. Furthermore, thermal repopulation of and emission from the ^{1}MLCT energy well becomes significant at elevated temperatures.

The wavelength dependence at a given temperature can be understood by inspection of Figure 3.28a. At low energy excitations, only significant population of the ^{1}LC state is observed, as the geometry of the excited state overlaps more efficiently with that of the excited state geometry. Moving to higher energy excitations increasingly allows for population of the previously described ^{1}MLCT state which exhibits a much larger distortion, requiring additional energy input to efficiently trigger the transition. In both of the aforementioned cases, intersystem crossing (ISC) to the respective triplet manifolds occurs followed by emission.

To explain the temperature-dependence profiles of **5-7**, the addition of a new process to the working model is required. It is well known in the literature that

luminescent tetrahedral copper(I) complexes bearing (P^P) and (N^N) ligands frequently are capable of utilizing a process known as thermally activated delayed fluorescence (TADF) to promote efficient emission.[88] TADF may occur when the energy gap between the singlet and triplet state (ΔE_{ST}) is sufficiently small to allow for thermal back-population of the singlet excited state (i.e. reverse intersystem crossing (RISC)).[88]

With this in mind, rationalization of the temperature dependence profiles is reasonable when considering the requirements for structural rearrangement in the excited state and TADF-based processes. Following the MLCT transition, formal oxidation of the copper(I) center to copper(II) induces a large distortion of coordination geometry from tetrahedral to square planar.[225,236,237,246] The distortion of the LC state, however, is minimal as much of the character of the transition is moved away from the copper(I) center. In low temperature environments, the accessibility of higher vibrational states is restricted, as thermal energy is much less prevalent. As such, the excitation ratio favors population of the LC potential energy planes and an increase in the emission intensity of the HE band relative to the LE band is observed in **5-7**. When the complexes are warmed, the range of accessible vibrational modes increases, and the excitation ratio begins to favor the MLCT transition. This assessment is supported by the observation that the LE emission bands display a slight redshift at warmer temperatures whereas the HE emission bands emit at a consistent wavelength. Furthermore, the increase in thermal energy available at higher temperatures requires that the contributions from TADF processes be considered. For **5** and **7**, an increase in temperature leads to a shortened lifetime, though no increase in the emission intensity is observed within the experimental temperature range, indicating only a small contribution from the TADF process as ISC occurs at a much greater rate than RISC. Complex **6**, however, shows both a drastic decrease in the emission lifetime and an increase in the emission intensity of the MLCT band, indicating

that at temperatures above –90 °C, the ΔE_{ST} of **6** is sufficiently small to allow for efficient RISC and TADF-based emission.

3.2.3. Conclusions

In this study, a new series of copper(I) complexes based on (5,5'-dimethyl-[2,2'-bithiophene]-3,3'-diyl)bis(diphenylphosphane) (**4**) was synthesized and characterized. The crystal structures of complexes **5**-**7** all exhibit distorted tetrahedral coordination geometries around the copper(I) center. The large amount of steric bulk around the metal center effectively protected the copper(I) from oxidation yielding air stable complexes in both the solid and solution states.

Complexes **5-7** exhibit interesting emission profiles that indicate not only an interplay between two decoupled excited states, but also the involvement of TADF related processes. This was shown in both the excitation and temperature dependence of the emission profiles in the solid state as well as in solution and PMMA films. DFT and experimental studies suggest that an interplay between the $d_{Cu/P}$-to-π_{NN}* and the π_{PP}-to-π_{PP}* electronic transitions play a critical role in governing the electronic and photophysical properties of the reported complexes. Low energy excitations and low temperatures favor emission from HE emissive state which primarily involves the π_{PP} and π_{PP}* orbitals of ligand **4**. However, as the temperature and excitation energies are increased, LE emission becomes more favored. This suggests that the increased distortion of the MLCT state resulting from the $d_{Cu/P}$-to-π_{NN}* transition plays a significant role in governing this emissive pathway.

The structure property relationships elucidated here may be used to maximize dual emission which could then be utilized in applications such as white light emission, solvent sensing, temperature sensing and non-linear optics.[287]

3.2.4. Experimental

3.2.4.1. Synthesis and Characterization

Dry solvents were collected in solvent bulbs from an Innovative Technology PureSolv 400 solvent purification system and stored over 3Å molecular sieves. 2,2'-Bithiophene (Matrix), bromine (Alfa Aesar), *n*-butyllithium (1.6 M in hexanes) (Sigma Aldrich), iodomethane (Sigma Aldrich), iodine (Sigma Aldrich), palladium(II) acetate (Strem) and diphenylphosphine (Strem) were purchased and used as received. Tetrakis(acetonitrile)copper(I) hexafluorophosphate ($[Cu(CH_3CN)_4][PF_6]$), 1-(2-pyridyl)pyrazole, 3-methyl-1-(2-pyridyl)pyrazole (pympz), 3-trifluoromethyl-1-(2-pyridyl)pyrazole and 3,3',5,5'-tetrabromo-2,2'-bithiophene (**1**) were prepared according to literature procedures.[234,298,299]

NMR spectra were recorded with a Varian DirectDrive 400 MHz spectrometer (^{1}H 400 MHz, $^{13}C\{^1H\}$ 100 MHz, $^{31}P\{^1H\}$ 161 MHz, ^{19}F 376 MHz). ^{1}H and $^{13}C\{^1H\}$ NMR spectra were referenced to residual solvent peaks. The $^{31}P\{^1H\}$ spectra was externally referenced to a 75% phosphoric acid sample and the ^{19}F spectra was externally referenced to $CFCl_3$. Chemical ionization (CI+) mass spectra were collected on a Micromass Autospec Ultima mass spectrometer. Electrospray ionization (ESI+) and atmospheric pressure chemical ionization (APCI) were collected on an Agilent 6530 quadrupole time of flight mass spectrometer. Elemental analysis services were provided by Midwest Microlabs, LLC.

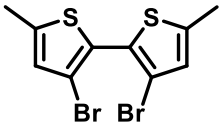

3,3'-dibromo-5,5'-dimethyl-2,2'-bithiophene (**2**): A 500 mL Schlenk flask actively pressurized with N_2 was charged with **1** (4.97 g, 10.32 mmol) followed by the addition of 200 mL of dry THF via cannula. The reaction was then placed in a dry ice/acetone bath and allowed to cool over the course of an hour. At –78 °C, *n*-butyllithium (1.6 M in hexanes, 13.86 mL, 22.18 mmol) was added dropwise to the reaction via syringe. The resulting mixture was allowed to stir for 45 minutes at –78 °C before adding iodomethane (3.15 g, 22.18 mmol) dropwise via syringe. After complete addition, the cooling bath was removed and the mixture was allowed to warm to room temperature and stirred overnight. The reaction was then quenched with excess water. The resulting mixture was poured into water (200 mL), extracted with CH_2Cl_2 (3 x 150 mL), dried over Na_2SO_4. The solvent was then removed via rotary evaporation. The crude material was purified with a silica column chromatography using hexanes as the eluent. Removal of the solvent yielded **2** as a colorless solid in 80 % yield (2.896 g, 8.22 mmol). ^{1}H NMR (CD_2Cl_2, 400 MHz): δ 6.76 (q, J = 1.2 Hz, 2H), 2.48 (t, J = 1.2 Hz, 6H). $^{13}C\{^1H\}$ NMR (CD_2Cl_2, 100 MHz): δ 142.5, 128.0, 127.0, 111.6, 15.6. HRMS (CI+) *m/z* Calcd. for $C_{10}H_8Br_2S_2^+$ $(M)^+$ 351.8416. Found: 351.8414.

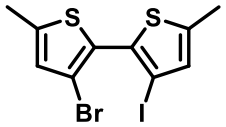

3-bromo-3'-iodo-5,5'-dimethyl-2,2'-bithiophene (**3**): A 200 mL Schlenk flask actively pressurized with N_2 was charged with **2** (3.70 g, 10.51 mmol) followed by the addition of 100 mL of dry THF via cannula. The reaction was then placed in a dry ice/acetone bath and allowed to cool over the course of an hour. At –78 °C, *n*-butyllithium (1.6 M in hexanes, 7.03 mL, 11.24 mmol) was added dropwise to the reaction via syringe. The resulting mixture was allowed to stir for 30 minutes at –78 °C before solution of iodine (2.85 g, 11.24 mmol) dissolved in minimal dry THF was added dropwise via syringe. After complete addition, the reaction was allowed to proceed at –78 °C for one hour before the cooling bath was removed, and the mixture was allowed to warm to room temperature over the course of an hour. The reaction was then quenched with excess water (0.5 mL) and the solvent was removed under a nitrogen stream. The resulting residue was then extracted with CH_2Cl_2 (100 mL) and water (100 mL). The organic and aqueous layers were combined and the aqueous layer was extracted with CH_2Cl_2 (3 x 100 mL), dried over Na_2SO_4 and the solvent removed via rotary evaporation. The crude material was then purified by recrystallization from boiling hexanes to yield **3** as a tan crystalline solid in 80% yield (3.362 g, 8.42 mmol). ^{1}H NMR (CD_2Cl_2, 400 MHz): δ 6.83 (q, J = 1.1 Hz, 1H), 6.76 (q, J = 1.1 Hz, 1H), 2.49 (m, 6H). $^{13}C\{^1H\}$ NMR (CD_2Cl_2, 100 MHz): δ 144.3, 142.7, 133.9, 133.8, 131.5, 128.9, 128.6, 112.0, 15.6, 15.4. HRMS (CI+) *m/z* Calcd. for $C_{10}H_8BrIS_2^+$ $(M)^+$ 397.8293. Found: 397.8296.

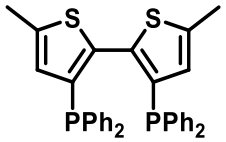

(5,5'-dimethyl-[2,2'-bithiophene]-3,3'-diyl)bis(diphenylphosphane) (**4**): In a glovebox, **3** (2.88 g, 7.18 mmol), potassium acetate (1.55 g, 15.80 mmol) and diphenylphosphine (2.94 g, 15.80 mmol) was dissolved in 70 mL of dimethylacetamide (DMA) in a Schlenk flask and sealed with a septa. Palladium(II) acetate (0.032 g, 0.14 mmol) dissolved in 10 mL of DMA was quickly syringed into the reaction mixture and the flask was quickly transferred to a Schlenk line, placed under positive nitrogen pressure and lowered into a preheated oil bath at 130 °C. The reaction was allowed to proceed for 3 hours at which time the mixture was removed from the oil bath and allowed to cool to room temperature. The solution was dried under a nitrogen stream and the residue was extracted with CH_2Cl_2 until no residue remained in the reaction flask. The organic layer was then washed with water (3 x 100 mL), dried over Na_2SO_4 and dried under a nitrogen stream. The crude product was purified through silica gel chromatography using 30% by volume solution of CH_2Cl_2 in hexanes to yield the product as pale yellow crystalline solid in 74% yield (2.978 g, 5.29 mmol). ^{1}H NMR (CD_2Cl_2, 400 MHz): δ 7.30 (m, 20H), 6.39 (d, J = 1.2 Hz, 2H), 2.37 (d, J = 1.2 Hz, 6H). ^{13}C{^{1}H} NMR (CD_2Cl_2, 100 MHz): δ 141.9 (t, J = 1.5 Hz), 140.0 (d, J = 43.5 Hz), 138.8 (dd, J = 6.9, 3.8 Hz), 137.1 (dd, J = 10.7, 5.4 Hz), 133.4 (m), 130.4, 128.7 (t, J = 3.5 Hz), 128.6, 15.4. ^{31}P{^{1}H} NMR (CD_2Cl_2, 161 MHz): δ –26.9. HRMS (CI+) *m/z* Calcd. for $C_{34}H_{29}P_2S_2^+$ $(M+H)^+$ 563.1186. Found: 563.1199.

General Synthesis of **5-7**: In a glovebox, $[Cu(CH_3CN)_4][PF_6]$ was dissolved in dry CH_2Cl_2 (1 eq., 0.15 M) with rapid stirring. To this solution, ligand **4** dissolved in methylene chloride (1 eq., 0.15 M) was added dropwise. The resulting solution was allowed to stir for 1 hour before a solution of the desired pyrazole-pyridine ligand in methylene chloride (1 eq., 0.15 M) was added dropwise. The resulting yellow solutions were allowed to stir for 2 hours before being transferred to a Schleck line and dried under a nitrogen stream. The resulting pale yellow solids were transferred to a glovebox, dissolved in a minimal volume of CH_2Cl_2, and recrystallized via vapor diffusion of diethyl ether into the saturated solution. The resulting crystals were collected and washed with diethyl ether to yield the pure complexes.

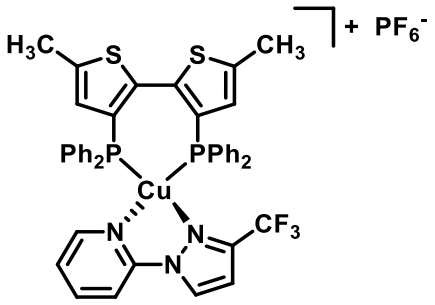

[Cu($C_{34}H_{28}P_2S_2$)(pycf3pz)][PF_6] (**5**): 81%, Yellow crystalline solid. ^{1}H NMR (CD_2Cl_2, 400 MHz): δ 8.82 (d, *J* = 2.9 Hz, 1H), 8.11 - 7.99 (m, 2H), 7.41 (t, *J* = 7.1 Hz, 4H), 7.33 (q, *J* = 4.7 Hz, 8H), 7.22 (t, *J* = 7.6 Hz, 4H), 7.15 (d, *J* = 2.9 Hz, 1H), 6.99 (ddd, *J* = 6.3, 5.3, 2.2 Hz, 1H), 6.92 (q, *J* = 6.7 Hz, 4H), 6.68 (dd, *J* = 5.5, 0.8 Hz, 1H), 5.92 (s, 2H), 2.31 (s, 6H). ^{13}C{^{1}H} NMR (CD_2Cl_2, 100 MHz): δ 147.7, 146.6, 142.9 (t, *J* = 4.2 Hz), 141.2, 133.4 (t, *J* = 8.4 Hz), 132.8 (t, *J* = 9.2 Hz) 131.2, 130.9, 130.8 (t, *J* = 3.8 Hz), 129.3 (t, *J* = 14.4 Hz), 129.2 (q, *J* = 5.7 Hz), 124.2, 120.3 (q, *J* = 270.1 Hz), 112.8, 109.6, 14.7. ^{31}P{^{1}H} NMR (CD_2Cl_2, 161 MHz): δ –11.2. ^{19}F NMR (CD_2Cl_2, 376 MHz): δ –62.5 (d, *J* = 3.3 Hz). HRMS (ESI+) *m/z* Calcd. for $C_{43}H_{37}N_3P_2S_2^+$ $(M–PF_6)^+$ 838.0912. Found: 838.0913. Elemental Anal. Calcd. for $C_{43}H_{34}N_3P_3F_9S_2Cu$: C, 52.47; H, 3.48; N, 4.27. Found: C, 52.25; H, 3.77; N, 3.99.

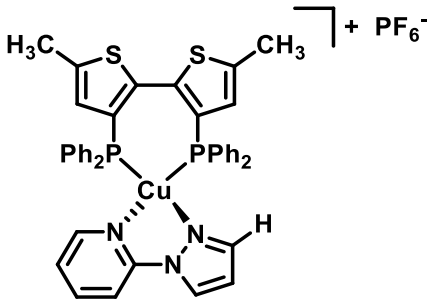

[Cu($C_{34}H_{28}P_2S_2$)(pypz)][PF_6] (**6**): 94%, Pale yellow crystalline solid. ^{1}H NMR (CD_2Cl_2, 400 MHz): δ 8.56 (d, *J* = 2.8 Hz, 1H), 8.10 (td, *J* = 8.0, 1.7 Hz, 1H), 7.93 (d, *J* = 8.4 Hz, 1H), 7.64 (s, 1H), 7.53 (dd, *J* = 5.3, 1.7 Hz, 1H), 7.39 (t, *J* = 7.3 Hz, 4H), 7.30 (s, 8H), 7.22 (ddd, *J* = 7.4, 5.2, 1.0 Hz, 1H), 7.13 (s, 8H), 6.79 (dd, *J* = 2.9, 1.9 Hz, 1H), 6.00 (d, *J* = 1.3 Hz, 2H), 2.33 (d, *J* = 0.8 Hz, 6H). ^{13}C{^{1}H} NMR (CD_2Cl_2, 100 MHz): δ 148.6, 148.0, 143.2 (t, *J* = 4.2 Hz), 142.6 (d, *J* = 1.6 Hz), 141.5, 137.6, 133.2, 130.7, 130.5, 130.4 - 130.0 (m), 129.2 (t, *J* = 5.0 Hz), 128.7, 123.7, 112.1 (d, *J* = 87.7 Hz), 15.11. ^{31}P{^{1}H} NMR (CD_2Cl_2, 161 MHz): δ –11.5. HRMS (ESI+) *m/z* Calcd. for $C_{42}H_{35}N_3P_2S_2^+$ $(M–PF_6)^+$ 770.1038. Found: 770.1029. Elemental Anal. Calcd. for $C_{42}H_{35}N_3P_3F_6S_2Cu$: C, 55.05; H, 3.85; N, 4.59. Found: C, 53.40; H, 3.81; N, 4.38.

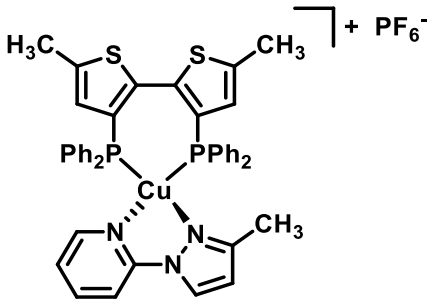

[Cu($C_{34}H_{28}P_2S_2$)(pympz)][PF_6] (**7**): 92%, Pale yellow crystalline solid. ^{1}H NMR (CD_2Cl_2, 400 MHz): δ 8.44 (d, *J* = 2.8 Hz, 1H), 8.03 (ddd, *J* = 8.5, 7.4, 1.7 Hz, 1H), 7.82 (d, *J* = 8.5 Hz, 1H), 7.69 (dd, *J* = 5.3, 1.7 Hz, 1H), 7.39 (t, *J* = 7.5 Hz, 4H), 7.30 (q, *J* = 7.5 Hz, 8H),7.24 - 7.04 (m, 8H), 7.17 (ddd, *J* = 7.5, 5.5, 0.8 Hz, 1H), 6.57 (d, *J* = 2.8 Hz, 1H), 5.98 (q, *J* = 1.2 Hz, 2H), 2.31 (d, *J* = 1.2 Hz, 6H), 1.70 (s, 3H). ^{13}C{^{1}H} NMR (CD_2Cl_2, 100 MHz): δ 152.7 (t, *J* = 1.5 Hz), 148.0, 147.8, 142.8 (t, *J* = 4.0 Hz), 140.8, 133.3 (m), 132.9 (m), 130.7 (m), 129.4, 129.3 (t, *J* = 4.3 Hz), 122.63, 111.28 (d, *J* = 17.1 Hz), 14.66, 12.97. ^{31}P{^{1}H} NMR (CD_2Cl_2, 161 MHz): δ –12.1. HRMS (ESI+) *m/z* Calcd. for $C_{43}H_{37}N_3P_2S_2^+$ $(M–PF_6)^+$ 784.1195. Found: 784.1185. Elemental Anal. Calcd. for $C_{43}H_{37}N_3P_3F_6S_2Cu$: C, 55.51; H, 4.01; N, 4.52. Found: C, 54.89; H, 4.24; N, 4.31.

3.2.4.2. Crystallography

The X-ray diffraction data for **5** and **7** were collected on an Agilent Technologies SuperNova Dual Source diffractometer using a μ-focus Cu Kα radiation source (λ = 1.5418 Å) equipped with collimating mirror monochromators that operated at 100 K. Data collection, unit cell refinement and data reduction were performed using Agilent Technologies CrysAlisPro V 1.171.37.31.[259] The structures were solved by direct methods using SuperFlip.[260]

The X-ray diffraction data for ligand **4** was collected was collected at 153 K on a Rigaku SCX-Mini diffractometer with a Mercury 2 CCD using a Rigaku Tec 50 low-temperature device. Data reduction was performed using the Rigaku Americas Corporation's Crystal Clear version 1.40.[212] The X-ray diffraction data for **6** was collected on a Nonius Kappa CCD diffractometer using a graphite monochromator with MoKα radiation (λ = 0.71073 Å). Data reduction was performed using DENZO-SMN.[300]

Structures were refined by full-matrix least-squares on F^2 with anisotropic displacement parameters for the non-H atoms using SHELXL-2014.[261] Structure analysis was aided by use of the programs PLATON98[215] and WinGX.[216,217] The hydrogen atoms were calculated in ideal positions with isotropic displacement parameters set to 1.2 x U_{eq} of the attached atom (1.5 x U_{eq} for methyl hydrogen atoms).

The function, $\Sigma w(|F_o|^2 - |F_c|^2)^2$, was minimized, where $w = 1/[(\sigma(F_o))^2 + (0.013*P)^2 + (87.56*P)]$ and $P = (|F_o|^2 + 2|F_c|^2)/3$. $R_w(F^2)$ refined to 0.222, with $R(F)$ equal to 0.0857 and a goodness of fit, S, = 1.03. Definitions used for calculating $R(F)$, $R_w(F^2)$ and the goodness of fit, S, are given as follows: $R_w(F^2) = \{\Sigma w(|F_o|^2 - |F_c|^2)^2/\Sigma w(|F_o|)^4\}^{1/2}$ where w is the weight given each reflection. $R(F) = \Sigma(|F_o| - |F_c|)/\Sigma|F_o|\}$ for reflections with $F_o > 4(\sigma(F_o))$. $S = [\Sigma w(|F_o|^2 - |F_c|^2)^2/(n - p)]^{1/2}$, where n is the number of reflections and p is the number of refined parameters.

The data were checked for secondary extinction effects but no correction was necessary. Neutral atom scattering factors and values used to calculate the linear absorption coefficient are from the International Tables for X-ray Crystallography (1992).[218] All Figures were generated using SHELXTL/PC.[262] Tables of positional and thermal parameters, bond lengths and angles, torsion angles and Figures are found elsewhere.

3.2.4.3. Photophysical Measurements

Absorption spectra were recorded on a Varian Cary 6000i UV-Vis-NIR spectrophotometer with Starna Quartz cells. Luminescent measurements were recorded on a Photon Technology International QM 4 spectrophotometer equipped with a 6-in. diameter K Sphere-B integrating sphere. Quantum yield measurements were collected using the integrating sphere. Quantum yields were calculated by dividing the area under the emission peak by the difference between the area under the excitation peak of the sample and the $BaSO_4$ reference material ($A_{em,\ sample}$ / ($A_{ex,\ blank} - A_{ex,\ sample}$)) and the reported quantum yields are the average of three trials. Low temperature lifetime measurements were taken using a variety of cooling baths. Temperatures were monitored using a low temperature thermocouple corrected to a calibration curve.

3.2.4.4. Electrochemistry

Electrochemical measurements were recorded in a dry-box under a nitrogen atmosphere using a GPES system from Eco. Chemie B. V. All experiments were carried out in a CH_2Cl_2 solution containing 0.1 M [(*n*-Bu)$_4$N][PF_6] ($TBAPF_6$) as supporting electrolyte. The $TBAPF_6$ was purified via recrystallization three times from boiling ethanol before being dried for 3 days under active vacuum at 80 °C. A three-electrode cell consisting of a $Ag/AgNO_3$ reference electrode (Ag wire incubated in a 0.01 M

$AgNO_3$ solution with 0.1M $TBAPF_6$ in CH_3CN), a glassy carbon working electrode (3.0 mm), and a Pt wire coil counter electrode was utilized. All measured potentials were corrected to the ferrocene/ferrocenium redox couple measured as an external reference.

3.2.4.5. Computational Methods

All calculations were carried out using the Gaussian 09 package program.[263] Crystal structure coordinates were used as the starting point for Density Functional Theory (DFT) geometric optimizations of the ground state molecules.[237] Time dependent DFT (TD-DFT) calculations were performed on the optimized ground state geometry to determine the first 60 singlet transitions.[264–266] All calculations were performed at the gradient corrected functional level using Becke's three parameter B3LYP functional.[267–270] The LANL2DZ basis set and electron core potential[271–274] was used for the Cu atom while the 6-31G(d,p)[275–282] basis set was used for the remaining elements. When pertinent, natural transition orbitals were visualized.[283]

3.3. REFERENCES

(6) Costa, R. D.; Ortí, E.; Bolink, H. J.; Monti, F.; Accorsi, G.; Armaroli, N. *Angew. Chem. Int. Ed.* **2012**, *51*, 8178–8211.

(82) Choy, W. C. H.; Chan, W. K.; Yuan, Y. *Adv. Mater.* **2014**, *26*, 5368–5399.

(87) Costa, R. D.; Tordera, D.; Ortí, E.; Bolink, H. J.; Schönle, J.; Graber, S.; Housecroft, C. E.; Constable, E. C.; Zampese, J. A. *J. Mater. Chem.* **2011**, *21*, 16108–16118.

(88) Tao, Y.; Yuan, K.; Chen, T.; Xu, P.; Li, H.; Chen, R.; Zheng, C.; Zhang, L.; Huang, W. *Adv. Mater.* **2014**, *26*, 7931–7958.

(92) Ford, P. C.; Cariati, E.; Bourassa, J. *Chem. Rev.* **1999**, *99*, 3625–3648.

(93) Dumur, F. *Org. Electron.* **2015**, *21*, 27–39.

(95) Hashimoto, M.; Igawa, S.; Yashima, M.; Kawata, I.; Hoshino, M.; Osawa, M. *J. Am. Chem. Soc.* **2011**, *133*, 10348–10351.

(212) *Crystal Clear, 1.40*; Rigaku Americas Corporation: The Woodlands, Texas, 2008.

(215) Spek, A. L. *PLATON, A Multipurpose Crystallographic Tool.*; Utrecht University: Utrecht University, The Netherlands, 1998.

(216) Farrugia, L. J. *J. Appl. Crystallogr.* **1999**, *32*, 837–838.

(217) Farrugia, L. J. *WinGX an Integrated System of Windows Programs for the Solution, Refinement and Analysis of Single Crystal X-Ray Diffraction Data*; University of Glasgow: Glasgow, U.K., 1999.

(218) In *International Tables for X-Ray Crystallography*; Wilson, A. J. C., Ed.; Kluwer Academic Press: Boston, 1992; Vol. C, p Tables 4.2.6.8 and 6.1.1.4.

(221) Yersin, H. In *Transition Metal and Rare Earth Compounds*; Topics in Current Chemistry; Springer Berlin Heidelberg, 2004; pp 1–26.

(222) Yersin, H.; Rausch, A. F.; Czerwieniec, R.; Hofbeck, T.; Fischer, T. *Coord. Chem. Rev.* **2011**, *255*, 2622–2652.

(223) Turro, N. J. *Modern Molecular Photochemistry*; Benjamin/Cummings Pub. Co.: Menlo Park, Calif., 1978.

(224) Raithby, P. R.; Shields, G. P.; Allen, F. H.; Motherwell, W. D. S. *Acta Crystallogr. Sect. B* **2000**, *56*, 444–454.

(225) Cuttell, D. G.; Kuang, S.-M.; Fanwick, P. E.; McMillin, D. R.; Walton, R. A. *J. Am. Chem. Soc.* **2002**, *124*, 6–7.

(226) Kuang, S.-M.; Cuttell, D. G.; McMillin, D. R.; Fanwick, P. E.; Walton, R. A. *Inorg. Chem.* **2002**, *41*, 3313–3322.

(227) Zhang, Q.; Zhou, Q.; Cheng, Y.; Wang, L.; Ma, D.; Jing, X.; Wang, F. *Adv. Mater.* **2004**, *16*, 432–436.

(228) Armaroli, N.; Accorsi, G.; Holler, M.; Moudam, O.; Nierengarten, J.-F.; Zhou, Z.; Wegh, R. T.; Welter, R. *Adv. Mater.* **2006**, *18*, 1313–1316.

(229) McCormick, T.; Jia, W.-L.; Wang, S. *Inorg. Chem.* **2006**, *45*, 147–155.

(230) Zhang, Q.; Zhou, Q.; Cheng, Y.; Wang, L.; Ma, D.; Jing, X.; Wang, F. *Adv. Funct. Mater.* **2006**, *16*, 1203–1208.

(231) Czerwieniec, R.; Yu, J.; Yersin, H. *Inorg. Chem.* **2011**, *50*, 8293–8301.

(232) Hsu, C.-W.; Lin, C.-C.; Chung, M.-W.; Chi, Y.; Lee, G.-H.; Chou, P.-T.; Chang, C.-H.; Chen, P.-Y. *J. Am. Chem. Soc.* **2011**, *133*, 12085–12099.

(233) Bergmann, L.; Friedrichs, J.; Mydlak, M.; Baumann, T.; Nieger, M.; Bräse, S. *Chem. Commun.* **2013**, *49*, 6501–6503.

(234) Chen, X.-L.; Yu, R.; Zhang, Q.-K.; Zhou, L.-J.; Wu, X.-Y.; Zhang, Q.; Lu, C.-Z. *Chem. Mater.* **2013**, *25*, 3910–3920.

(235) Chen, X.-L.; Lin, C.-S.; Wu, X.-Y.; Yu, R.; Teng, T.; Zhang, Q.-K.; Zhang, Q.; Yang, W.-B.; Lu, C.-Z. *J. Mater. Chem. C* **2015**, *3*, 1187–1195.

(236) Keller, S.; Constable, E. C.; Housecroft, C. E.; Neuburger, M.; Prescimone, A.; Longo, G.; Pertegás, A.; Sessolo, M.; Bolink, H. J. *Dalton Trans.* **2014**, *43*, 16593–16596.

(237) Linfoot, C. L.; Leitl, M. J.; Richardson, P.; Rausch, A. F.; Chepelin, O.; White, F. J.; Yersin, H.; Robertson, N. *Inorg. Chem.* **2014**, *53*, 10854–10861.

(238) Czerwieniec, R.; Yersin, H. *Inorg. Chem.* **2015**, *54*, 4322–4327.

(239) Igawa, S.; Hashimoto, M.; Kawata, I.; Yashima, M.; Hoshino, M.; Osawa, M. *J. Mater. Chem. C* **2013**, *1*, 542–551.

(240) Li, X.-L.; Ai, Y.-B.; Yang, B.; Chen, J.; Tan, M.; Xin, X.-L.; Shi, Y.-H. *Polyhedron* **2012**, *35*, 47–54.

(241) Blasse, G.; McMillin, D. R. *Chem. Phys. Lett.* **1980**, *70*, 1–3.

(242) Breddels, P. A.; Berdowski, P. A. M.; Blasse, G.; McMillin, D. R. *J. Chem. Soc. Faraday Trans. 2 Mol. Chem. Phys.* **1982**, *78*, 595–601.

(243) Saito, K.; Arai, T.; Takahashi, N.; Tsukuda, T.; Tsubomura, T. *Dalton Trans.* **2006**, 4444–4448.

(244) Saito, K.; Tsukuda, T.; Tsubomura, T. *Bull. Chem. Soc. Jpn.* **2006**, *79*, 437–441.

(245) Barbieri, A.; Accorsi, G.; Armaroli, N. *Chem. Commun.* **2008**, 2185–2193.

(246) Czerwieniec, R.; Kowalski, K.; Yersin, H. *Dalton Trans.* **2013**, *42*, 9826–9830.

(247) Li, Q.; Xu, S.-X.; Wang, J.-L.; Xia, H.-Y.; Zhao, F.; Wang, Y.-B. *Int. J. Quantum Chem.* **2014**, *114*, 1685–1691.

(248) Nishikawa, M.; Sawamura, S.; Haraguchi, A.; Morikubo, J.; Takao, K.; Tsubomura, T. *Dalton Trans.* **2015**, *44*, 411–418.

(249) Ohara, H.; Kobayashi, A.; Kato, M. *Dalton Trans.* **2014**, *43*, 17317–17323.

(250) Moudam, O.; Kaeser, A.; Delavaux-Nicot, B.; Duhayon, C.; Holler, M.; Accorsi, G.; Armaroli, N.; Séguy, I.; Navarro, J.; Destruel, P.; Nierengarten, J.-F. *Chem. Commun.* **2007**, 3077–3079.

(251) Tsuboyama, A.; Kuge, K.; Furugori, M.; Okada, S.; Hoshino, M.; Ueno, K. *Inorg. Chem.* **2007**, *46*, 1992–2001.

(252) Osawa, M. *Chem. Commun.* **2014**, *50*, 1801–1803.

(253) Osawa, M.; Hoshino, M.; Hashimoto, M.; Kawata, I.; Igawa, S.; Yashima, M. *Dalton Trans.* **2015**, *44*, 8369–8378.

(254) Al-Ibrahim, M.; Roth, H.-K.; Schroedner, M.; Konkin, A.; Zhokhavets, U.; Gobsch, G.; Scharff, P.; Sensfuss, S. *Org. Electron.* **2005**, *6*, 65–77.

(255) Pownall, H. J.; Schaffer, A. M.; Becker, R. S.; Mantulin, W. W. *Photochem. Photobiol.* **1978**, *27*, 625–628.

(256) Lancelot, G. *Mol. Phys.* **1976**, *31*, 241–254.

(257) Saadeh, H.; Goodson, T.; Yu, L. *Macromolecules* **1997**, *30*, 4608–4612.

(258) Kubas, G. J. *Inorg. Synth.* **1979**, 90–92.

(259) *CrysAlisPro, 1.171.37.31*; Agilent Technologies UK Ltd.: Oxford, UK, 2013.

(260) Palatinus, L.; Chapuis, G. *J. Appl. Crystallogr.* **2007**, *40*, 786–790.

(261) Sheldrick, G. M. *Acta Crystallogr. Sect. C Struct. Chem.* **2015**, *71*, 3–8.

(262) Sheldrick, G. M. *SHELXTL/PC*; Siemens Analytical X-ray Instruments, Inc.: Madison, Wisconsin, USA, 1994.

(263) Frisch, M. J.; Trucks, G. W.; Schlegel, H. B.; Scuseria, G. E.; Robb, M. A.; Cheeseman, J. R.; Scalmani, G.; Barone, V.; Mennucci, B.; Petersson, G. A.; Nakatsuji, H.; Caricato, M.; Li, X.; Hratchian, H. P.; Izmaylov, A. F.; Bloino, J.; Zheng, G.; Sonnenberg, J. L.; Hada, M.; Ehara, M.; Toyota, K.; Fukuda, R.; Hasegawa, J.; Ishida, M.; Nakajima, T.; Honda, Y.; Kitao, O.; Nakai, H.; Vreven, T.; Montgomery, J. A., Jr.; Peralta, J. E.; Ogliaro, F.; Bearpark, M.; Heyd, J. J.; Brothers, E.; Kudin, K. N.; Staroverov, V. N.; Kobayashi, R.; Normand, J.; Raghavachari, K.; Rendell, A.; Burant, J. C.; Iyengar, S. S.; Tomasi, J.; Cossi, M.; Rega, N.; Millam, N. J.; Klene, M.; Knox, J. E.; Cross, J. B.; Bakken, V.; Adamo, C.; Jaramillo, J.; Gomperts, R.; Stratmann, R. E.; Yazyev, O.; Austin, A. J.; Cammi, R.; Pomelli, C.; Ochterski, J. W.; Martin, R. L.; Morokuma, K.;

Zakrzewski, V. G.; Voth, G. A.; Salvador, P.; Dannenberg, J. J.; Dapprich, S.; Daniels, A. D.; Farkas, O.; Foresman, J. B.; Ortiz, J. V.; Cioslowski, J.; Fox, D. J. *Gaussian 09, Revision B.01*; Gaussian, Inc.: Wallingford, CT, 2009.

(264) Bauernschmitt, R.; Ahlrichs, R. *Chem. Phys. Lett.* **1996**, *256*, 454–464.

(265) Casida, M. E.; Jamorski, C.; Casida, K. C.; Salahub, D. R. *J. Chem. Phys.* **1998**, *108*, 4439–4449.

(266) Stratmann, R. E.; Scuseria, G. E.; Frisch, M. J. *J. Chem. Phys.* **1998**, *109*, 8218–8224.

(267) Becke, A. D. *J. Chem. Phys.* **1993**, *98*, 5648–5652.

(268) Lee, C.; Yang, W.; Parr, R. G. *Phys. Rev. B* **1988**, *37*, 785–789.

(269) Miehlich, B.; Savin, A.; Stoll, H.; Preuss, H. *Chem. Phys. Lett.* **1989**, *157*, 200–206.

(270) Stephens, P. J.; Devlin, F. J.; Chabalowski, C. F.; Frisch, M. J. *J. Phys. Chem.* **1994**, *98*, 11623–11627.

(271) Dunning Jr., T. H.; Hay, P. J. In *Modern Theoretical Chemistry*; Schaefer, H. F., Ed.; Plenum: New York, 1977; Vol. 3, pp 1–28.

(272) Hay, P. J.; Wadt, W. R. *J. Chem. Phys.* **1985**, *82*, 270–283.

(273) Wadt, W. R.; Hay, P. J. *J. Chem. Phys.* **1985**, *82*, 284–298.

(274) Hay, P. J.; Wadt, W. R. *J. Chem. Phys.* **1985**, *82*, 299–310.

(275) Ditchfield, R.; Hehre, W. J.; Pople, J. A. *J. Chem. Phys.* **1971**, *54*, 724–728.

(276) Hehre, W. J.; Ditchfield, R.; Pople, J. A. *J. Chem. Phys.* **1972**, *56*, 2257–2261.

(277) Hariharan, P. C.; Pople, J. A. *Theor. Chim. Acta* **1973**, *28*, 213–222.

(278) Hariharan, P. C.; Pople, J. A. *Mol. Phys.* **1974**, *27*, 209–214.

(279) Gordon, M. S. *Chem. Phys. Lett.* **1980**, *76*, 163–168.

(280) Francl, M. M.; Pietro, W. J.; Hehre, W. J.; Binkley, J. S.; Gordon, M. S.; DeFrees, D. J.; Pople, J. A. *J. Chem. Phys.* **1982**, *77*, 3654–3665.

(281) Rassolov, V. A.; Pople, J. A.; Ratner, M. A.; Windus, T. L. *J. Chem. Phys.* **1998**, *109*, 1223–1229.

(282) Rassolov, V. A.; Ratner, M. A.; Pople, J. A.; Redfern, P. C.; Curtiss, L. A. *J. Comput. Chem.* **2001**, *22*, 976–984.

(283) Martin, R. L. *J. Chem. Phys.* **2003**, *118*, 4775–4777.

(284) Forrest, S. R. *Org. Electron.* **2003**, *4*, 45–48.

(285) Meier, S. B.; Tordera, D.; Pertegás, A.; Roldán-Carmona, C.; Ortí, E.; Bolink, H. J. *Mater. Today* **2014**, *17*, 217–223.

(286) Minaev, B.; Baryshnikov, G.; Agren, H. *Phys. Chem. Chem. Phys.* **2014**, *16*, 1719–1758.

(287) Cariati, E.; Lucenti, E.; Botta, C.; Giovanella, U.; Marinotto, D.; Righetto, S. *Coord. Chem. Rev.* **2016**, *306,* 566–614.

(288) Harvey, P. D.; Knorr, M. *Macromol. Rapid Commun.* **2010**, *31*, 808–826.

(289) Liu, Z.; Djurovich, P. I.; Whited, M. T.; Thompson, M. E. *Inorg. Chem.* **2012**, *51*, 230–236.

(290) Deaton, J. C.; Switalski, S. C.; Kondakov, D. Y.; Young, R. H.; Pawlik, T. D.; Giesen, D. J.; Harkins, S. B.; Miller, A. J. M.; Mickenberg, S. F.; Peters, J. C. *J. Am. Chem. Soc.* **2010**, *132*, 9499–9508.

(291) Zink, D. M.; Bächle, M.; Baumann, T.; Nieger, M.; Kühn, M.; Wang, C.; Klopper, W.; Monkowius, U.; Hofbeck, T.; Yersin, H.; Bräse, S. *Inorg. Chem.* **2013**, *52*, 2292–2305.

(292) Leitl, M. J.; Küchle, F.-R.; Mayer, H. A.; Wesemann, L.; Yersin, H. *J. Phys. Chem. A* **2013**, *117*, 11823–11836.

(293) Lotito, K. J.; Peters, J. C. *Chem. Commun.* **2010**, *46*, 3690–3692.

(294) Holliday, B. J.; Swager, T. M. *Chem. Commun.* **2005**, 23–36.

(295) Bonnafoux, L.; Gramage-Doria, R.; Colobert, F.; Leroux, F. R. *Chem. – Eur. J.* **2011**, *17*, 11008–11016.

(296) Kyle, K. R.; Ryu, C. K.; Ford, P. C.; DiBenedetto, J. A. *J. Am. Chem. Soc.* **1991**, *113*, 2954–2965.

(297) Maini, L.; Braga, D.; Mazzeo, P. P.; Ventura, B. *Dalton Trans.* **2011**, *41*, 531–539.

(298) Kubas, G. J.; Monzyk, B.; Crumblis, A. L. In *Inorganic Syntheses*; Angelici, R. J., Ed.; John Wiley & Sons, Inc.: Hoboken, NJ, USA, 1990; Vol. 28, pp 68–70.

(299) Imin, P.; Imit, M.; Adronov, A. *Macromolecules* **2011**, *44*, 9138–9145.

(300) Otwinowski, Z.; Minor, W. In *Methods in Enzymology, Macrocolecular Cyrstallography, Part A*; Carter Jr., C. W., Sweet, R. M., Eds.; 1997; Vol. 276, pp 307–326.

Chapter 4: Electronic Communication across 9,10-Diisocyanoanthracene-bridged Rhodium Centers: The Influence of Pincer Ligands.

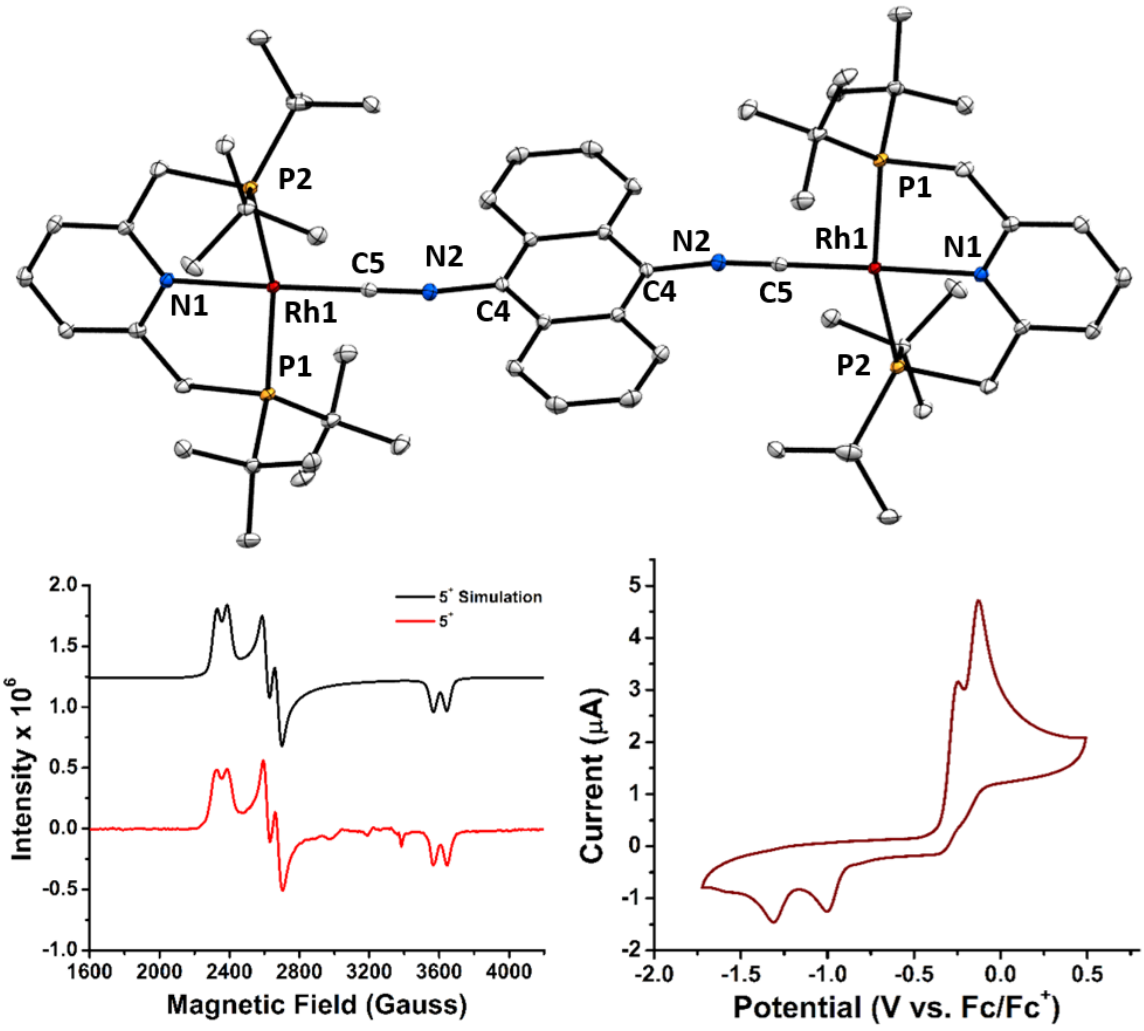

4.1. INTRODUCTION

The development of systems capable of electronic communication across two redox centers has blossomed since Creutz and Taube were the first to design such a system.[301,302] Classically, the utility of these materials has played a key role as model systems for investigations targeted at developing a better understanding of the effects of solvent and geometry on the electron transfer process[96,101] and have been significantly developed within the envelope of Marcus Theory.[97,104,303–305] The knowledge gained from these studies has played a key role in the fields of biochemistry and materials science.[11,12,306–311] Furthermore, it has been observed that metal centers in electronic communication with one another can lead to cooperative effects that have showed markedly different properties and reactivity than the isolated units.[310,312–316] Such characteristics are of interest in the field of transition metal catalysis as control over the electron density and oxidation state is critical to the performance of the catalyst.

Rhodium has long played an important role in the field of catalysis. The vast majority of rhodium chemistry is built around the Rh(I)/Rh(III) oxidations states which are relatively stable yet easily interconverted. The ability to readily facilitate changes in the oxidation state, coordination number and geometry make rhodium an ideal metal for a wide range of chemical transformations.[108,117] Mononuclear metal centers in the Rh(II) oxidation state, however, are much more difficult to isolate due to the increased reactivity of the d^7-electron configuration, which places the unpaired electron in a highly destabilized orbital. While the increased reactivity of these complexes makes them difficult to isolate and study, they are of key interest in catalytic processes as the Rh(II) state may play a key role in catalytic cycles, as well as facilitate transformations previously inaccessible.[317,318] A recent push to synthesize and isolate Rh(II) complexes

has shown that pincer ligands bearing bulky substituents are quite capable of stabilizing the 2+ oxidation state and the resulting complexes exhibit interesting reactivity.[319–323]

With this in mind, the ability to synthesize ligand-bridged Rh(I)-centers stabilized by pincer ligands which are capable of displaying electronic communication with partial Rh(I/II) character would be of significant interest to the field of catalysis. To accomplish such a goal, proper matching of the metal redox centers to the bridging ligand is crucial for electronic communication.[12,102,103,310,324] It has been shown that aryl isocyanides are capable of supporting electronic communication in Rh(I) coordination polymers.[325,326] Furthermore, a rare example of a discrete Rh(I/II) mixed valence state was supported by anthracene-based core.[111] Using this precedence as a guide, 9,10-diisocyanoanthracene was chosen to act as the bridging ligand in this study. Herein, we report the synthesis, characterization and study of two complexes based on the [(μ^2-9,10-diisocyanoanthracene)Rh_2]$^{2+}$ core stabilized by either 2,6-bis-(di-*tert*-butylphosphinomethyl)pyridine (PNP) or 1,3-bis-(di-*tert*-butylphosphinomethyl)benzene (PCP) to determine the efficacy of the pincer ligands in promoting electronic communication between the rhodium centers.

4.2. Results and Discussion

4.2.1. Synthesis, Characterization and Crystal Structures of PNP-Based Complexes

[(PNP)Rh(μ^2-9,10-diisocyanoanthracene)Rh(PNP][BF_4]$_2$ (**1**) was prepared via a two-step reaction shown in Scheme 4.1.

Scheme 4.1. Synthesis of complex **1**.

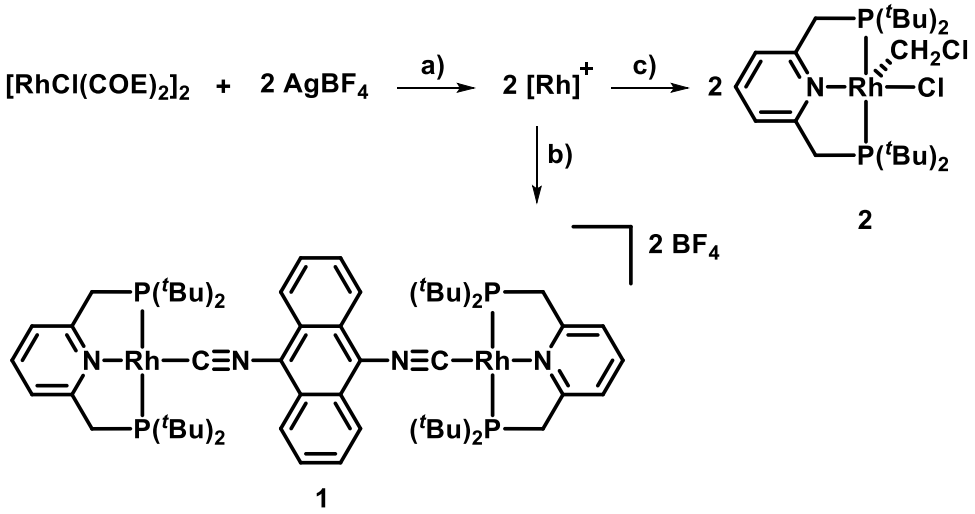

a) CH_2Cl_2, rt, 45 min. b) (i) 2 PNP, CH_2Cl_2/CH_3CN (2:1), rt, 10 min. (ii) 1 eq. 9,10-diisocyanoanthracene, CH_2Cl_2/CH_3CN (2:1), rt, 10 min. c) 2 PNP, CH_2Cl_2, rt, overnight. (Note: Stoichiometry is based on $[RhCl(COE)_2]_2$)

$[RhCl(COE)]_2$ (COE = cyclooctene) was dissolved in CH_2Cl_2 and stirred with 2 equivalents of $AgBF_4$ to precipitate the AgCl salt as a gray precipitate. The deep red solution containing the activated Rh(I) precursor was then filtered directly into a CH_2Cl_2/CH_3CN (2:1) solution containing 2 equivalents of the PNP ligand resulting in an orange solution. Dropwise addition of a solution containing 1 equivalent of 9,10-diisocyanoanthracene induced a darkening of the solution to a deeper orange and led to the appearance of a doublet in the $^{31}P\{^1H\}$ NMR at 76.9 ppm. Concentration of the reaction mixture *in vacuo* followed by the addition of a large amount of Et_2O resulted in a yellow powder which, following dissolution in CH_2Cl_2, filtration and recrystallization by vapor diffusion of Et_2O into a concentrated solution of **1** in CH_2Cl_2 led to the formation of large orange crystals suitable for single X-ray crystallography (Figure 1.1).

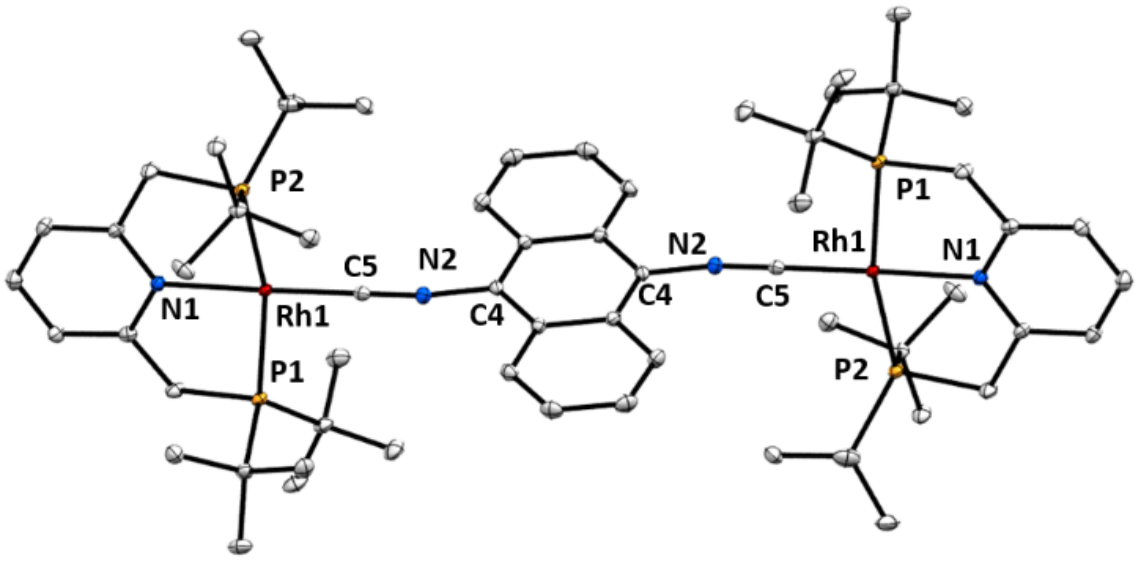

Figure 4.1. Molecular structure of complex **1**. Thermal ellipsoids are drawn at 30% probability. The BF_4^- counter anions and solvent molecules are omitted for clarity. Select bond lengths (Å) and angles (degrees): (Rh1–Rh1) 11.5193(3), (Rh1–N1) 2.103(3), (Rh1–C5) 1.859(3), (Rh1–P1) 2.2919(7), (Rh1–P2) 2.2912(7), (N2–C5) 1.178(4), (C5–N2–C4) 165.2(3).

The Rh(I) metal-centers display a square planar coordination geometry and are quite similar to $[(PNP)RhL]^+$ (L = neutral donor) complexes in the literature.[327–329] An inversion center is present in the structure relating the two metal centers by symmetry. For structural comparisons, the molecular structure of the bridging 9,10-diisocyanoanthracene ligand was obtained via single crystal X-ray diffraction (Figure 4.2). The structure of the ligand also contains an inversion center. Upon coordination to Rh(I), an elongation of the isocyanide bond C(5)–N(1) is observed as well as an increased distortion in the C(5)–N2–C(4) bond angle by nearly 14.4° indicating significant back-bonding into the π*-orbitals of the isocyanide ligand.

Figure 4.2. a) Molecular structure of complex 9,10-diisocyanoanthracene. Thermal ellipsoids are drawn at 30% probability. A crystallographic inversion center resides at the center of the anthracene ring generating half of the molecule through symmetry. Select bond lengths (Å) and angles (degrees): (N1–C7) 1.165(2), (C7–N1–C1) 179.6(1). b) Packing diagram highlighting the herring bone stacking pattern in the crystal lattice. The alternating stacks sit at a 24.7° angle with respect to each other. Significant π-stacking interactions are present with as indicated by the short inter-planar distances between the anthracene ring systems (3.801(2) Å) and perfectly coplanar arrangement of the stacks (dihedral angle = 0°).

Interestingly, initial attempts to synthesize complex **1** in the absence of CH_3CN quickly led to the formation of a brown solution prior to the addition of 9,10-diisocyanoanthracene. Concentration of this solution *in vacuo* followed by slow vapor diffusion led to the formation of dark brown needles suitable for single crystal X-ray diffraction. The crystal structure of the isolated compound, which can be found in Figure 4.3, revealed the oxidative addition of a solvent CH_2Cl_2 molecule resulting in complex $[(PNP)RhCl(CH_2Cl)][BF_4]$ (**2**). The $[BAr^F{}_4]^-$ analog of **2** has been recently reported in the literature as a co-crystal with $[(PNP)Rh(H)Cl]$ $[BAr^F{}_4]$.[330]

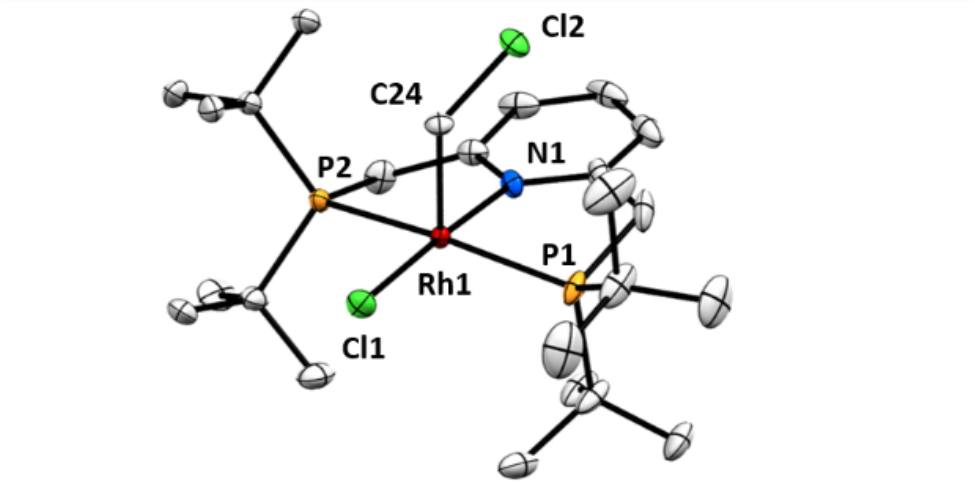

Figure 4.3. Molecular structure of complex **2**. Thermal ellipsoids are drawn at 30% probability. The BF_4^- counter anion is omitted for clarity. Disorder of the *tert*-butyl groups is present in the structure. The major contributing conformation is shown. Select bond lengths (Å): (Rh1–N1) 2.061(5), (Rh1–P1) 2.329(1), (Rh1–P2) 2.365(1), (Rh1–Cl1) 2.333(2), (Rh1–C24) 2.080(5).

4.2.2. Synthesis, Characterization and Crystal Structures of the PCP-Base Complexes

Preparation of [(PCP)Rh(μ^2-9,10-diisocyanoanthracene)Rh(PCP] (**5**) required a separate procedure which may be found in Scheme 4.2.

Scheme 4.2. Synthesis of complex **5.**

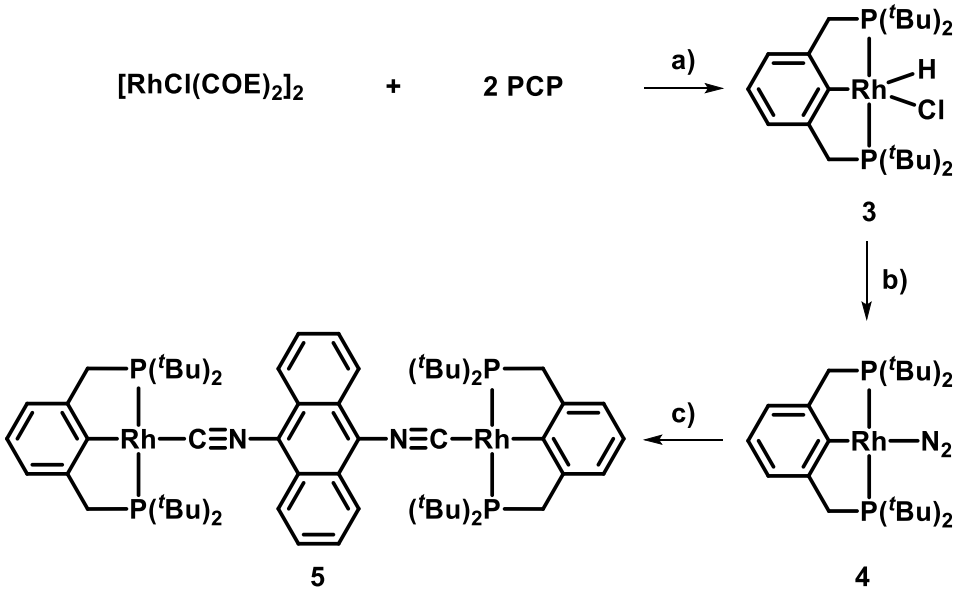

a) toluene, 150 °C, 5 hr. b) 2.4 eq. potassium *tert*-butoxide, THF, rt, 45 min. c) 9,10-diisocyanoanthracene, toluene/CH_2Cl_2/CH_3CN (1:1:1), rt, 30 min.

Adapting literature procedures,[320] $[RhCl(COE)_2]_2$ and 2 equivalents of PCP ligand were dissolved in toluene and reacted in a bomb flask for 5 hours at 150 °C resulting in cyclometallation and C-H activation at the *ortho*-postion with respect to the two methylene arms, generating [(PCP)Rh(H)Cl] (**3**). Quantitative conversion to [(PCP)Rh(N_2)] (**4**) was achieved via deprotonation of the metal center with potassium *tert*-butoxide in tetrahydrofuran (THF). This was confirmed by ^{1}H- and ^{31}P{^{1}H} NMR as deprotonation led to the disappearance of the hydride resonance found at –27.8 ppm and a shift in the phosphorous signal from 74.4 ppm to 96.8 ppm Following isolation, dissolution of **4** in a 1:1:1 mixture of toluene/CH_2Cl_2/CH_3CN followed by dropwise

addition of 1 equivalent of 9,10-diisocyanoanthracene resulted in a deep red solution and a shift in the $^{31}P\{^{1}H\}$ NMR from 96.8 ppm to 90.6 ppm was observed. Pumping the mixture to dryness yielded a dark purple powder which was subsequently dissolved in a minimal amount of CH_2Cl_2, filtered and purified by vapor diffusion of Et_2O into a concentrated solution of the crude product yielded pure **5** as deep orange crystals suitable for single crystal X-ray diffraction (see Figure 4.4).

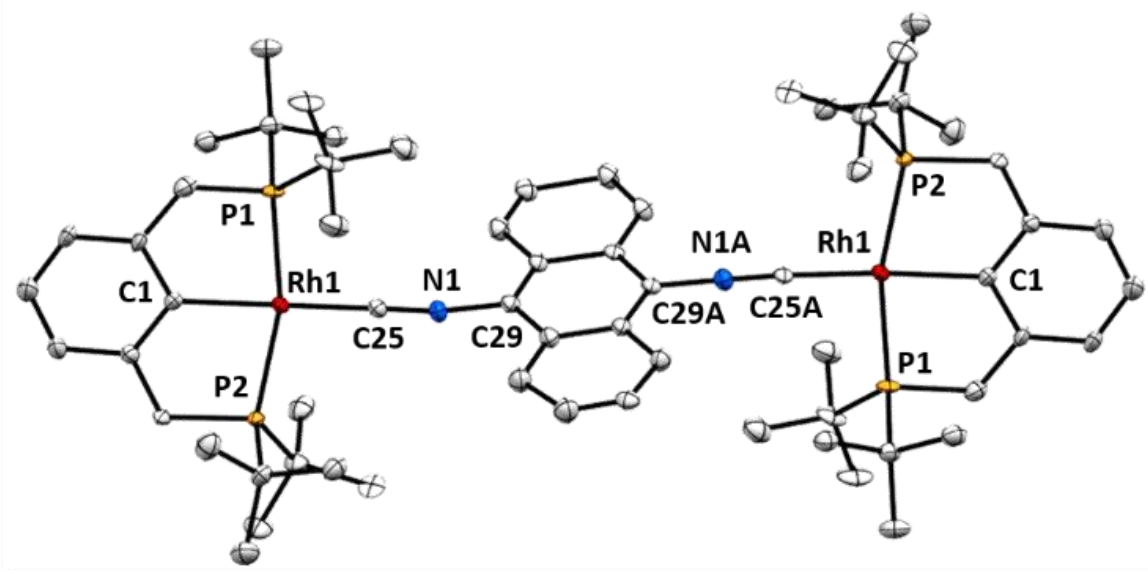

Figure 4.4. Molecular structure of complex **5**. Thermal ellipsoids are drawn at 30% probability. Disorder of the 9,10-diisocyanoanthracene ligand is present in the structure. A representative conformation is shown. Select bond lengths (Å) and angles (degrees): (Rh1–Rh1) 11.63 (2)*, (Rh–C1) 2.08(1), (Rh1–{P1/P2}) 2.275(6)*, (Rh1–{C25/C25A}) 1.90(3)*, ({N1/N1A}–{C25/C25A}) 1.19(1)*, ({C25/C25A}–{N1/N1A}–{C29/C29A}) 169(3)*. Average bond lengths and angles are denoted by (*) and are associated with the presence of disorder in the structure as well as a second crystallographically unique asymmetric unit.

As expected, the geometry around the Rh(I) centers is square planar.[331] An inversion center is once again present in the molecule. Similar to complex **1**, the crystal structure of **5** shows and an elongation of the isocyanide C(25)-N(1) bond lengths and a large distortion of the C(25)-N(1)-C(29) bond angles compared to the free ligand. Comparison of complexes **1** and **5** reveal an increased isocyanide C-N bond length in **5**. The increased bond length of the isocyanide unit, despite residing in a coordination position *trans*- to the strongly donating cyclometallated carbon in the PCP ligand, suggests significant back-bonding to the bridging ligand.

Infrared spectroscopy (IR) revealed a significant shift in the isocyanide stretch upon coordination to the metal centers (Figure 4.5). In the free ligand, the isocyanide resonance occurs at 2112 cm^{-1}, which shifts to 2022 cm^{-1} and 1953 cm^{-1} for **1** and **5**, respectively. The decrease in the frequency of the C-N stretch upon coordination and the lower frequency observed in complex **5** is consistent with the trends observed in the crystal structure, and indicates an increase in the amount of back-bonding in **5** compared to **1**.

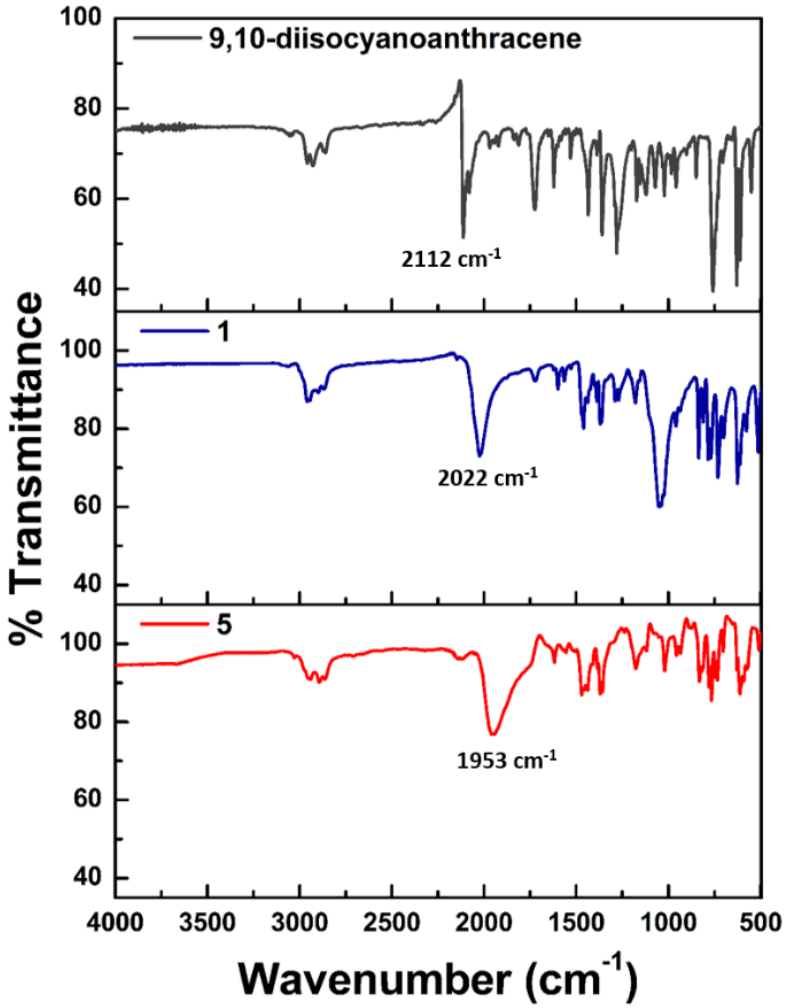

Figure 4.5. Infrared spectra of the 9,10-diisocyanoanthracene (top), **1** (middle) and **5** (bottom).

4.2.3. Electrochemical Studies of 1 and 5

The cyclic voltammograms of complexes **1** and **5** in CH_2Cl_2 are shown in Figure 4.6. Complex **1** displays a quasi-reversible redox event at 0.592 V. This event is diffusion controlled, as evidenced by the linear dependence of the peak current on the square root of the scan rate (i_p vs. $\nu^{-1/2}$), and is attributed to the Rh(I/II) redox couple (Figure 4.7).[321] Pushing the oxidation potential more positive leads to a second irreversible oxidation

event at approximately 1.22 V that results in the loss of reversibility of the Rh(I/II) redox-couple. No indication of significant electronic communication was observed in the electrochemistry. As such, the oxidative event corresponds to a 2-electron oxidation with one electron being supplied from each of the rhodium centers.

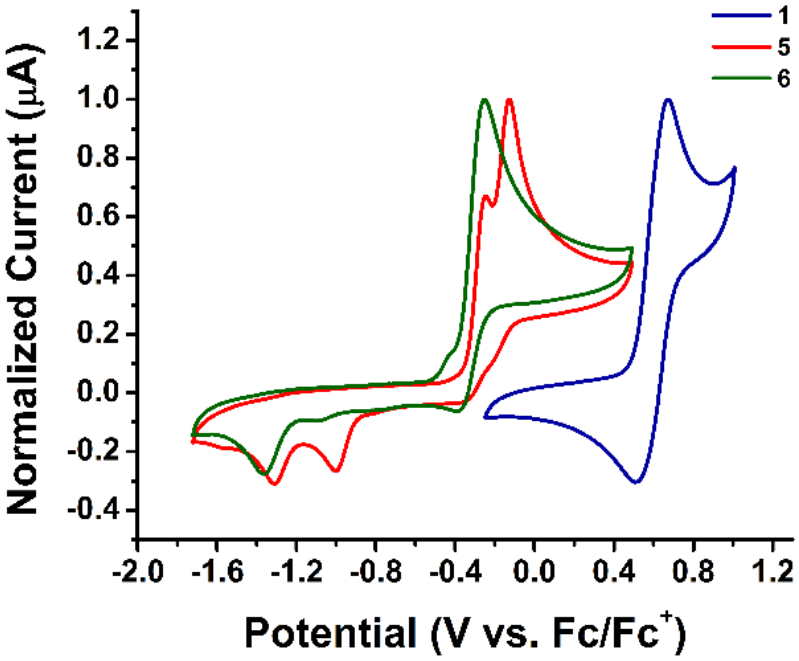

Figure 4.6. Cyclic voltammograms of complexes **1**, **5** and **6** taken in a CH_2Cl_2 (0.1 M $TBAPF_6$ as supporting electrolyte, working electrode = glassy carbon button (3.0 mm), counter electrode = platinum wire, reference electrode = $Ag/AgNO_3$). All potentials are externally referenced to the redox potential of ferrocene.

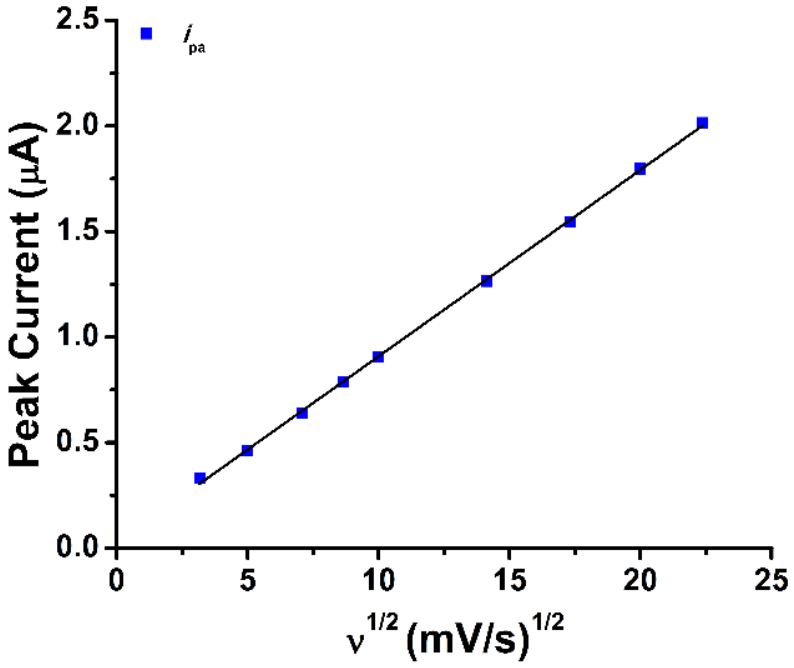

Figure 4.7. Scan rate dependence for **1** in CH_2Cl_2 (0.1 M $TBAPF_6$) ranging from 25 mV s^{-1} to 500 mV s^{-1}.

The electrochemistry of complex **5** showed marked differences from that of complex **1**. A large cathodic shift in the first oxidation potential is observed with the onset of oxidation (E_{on}) and the peak current potential (E_{pa}) coming at –0.342 V and –0.248 V, respectively compared to an E_{on} = 0.475 V and an E_{pa} = 0.674 for **1**. This difference of nearly 820 mV highlights the increased electron density on the rhodium center as the result of coordination of the PCP-ligand. However, all reversibility of this oxidation event is lost. Interestingly, a second irreversible oxidation event is observed at a potential 121 mV higher (E_{pa} = –0.127 V). Integration of the differential pulse voltammetry (DPV) showed these peaks to be present in a 1:1 ratio. Both peaks are shown to be diffusion controlled as determine by the scan rate dependence studies. The cyclic voltammogram of complex **5** also exhibited two back-waves at E_{pc} = –1.001 V and

–1.311 V that were shown to be dependent on the oxidation of **5** (Figure 4.8). Integration of the cyclic voltammogram shows these reductions occur in a 1:1 ratio at an intensity that is 28% that of the oxidative waves.

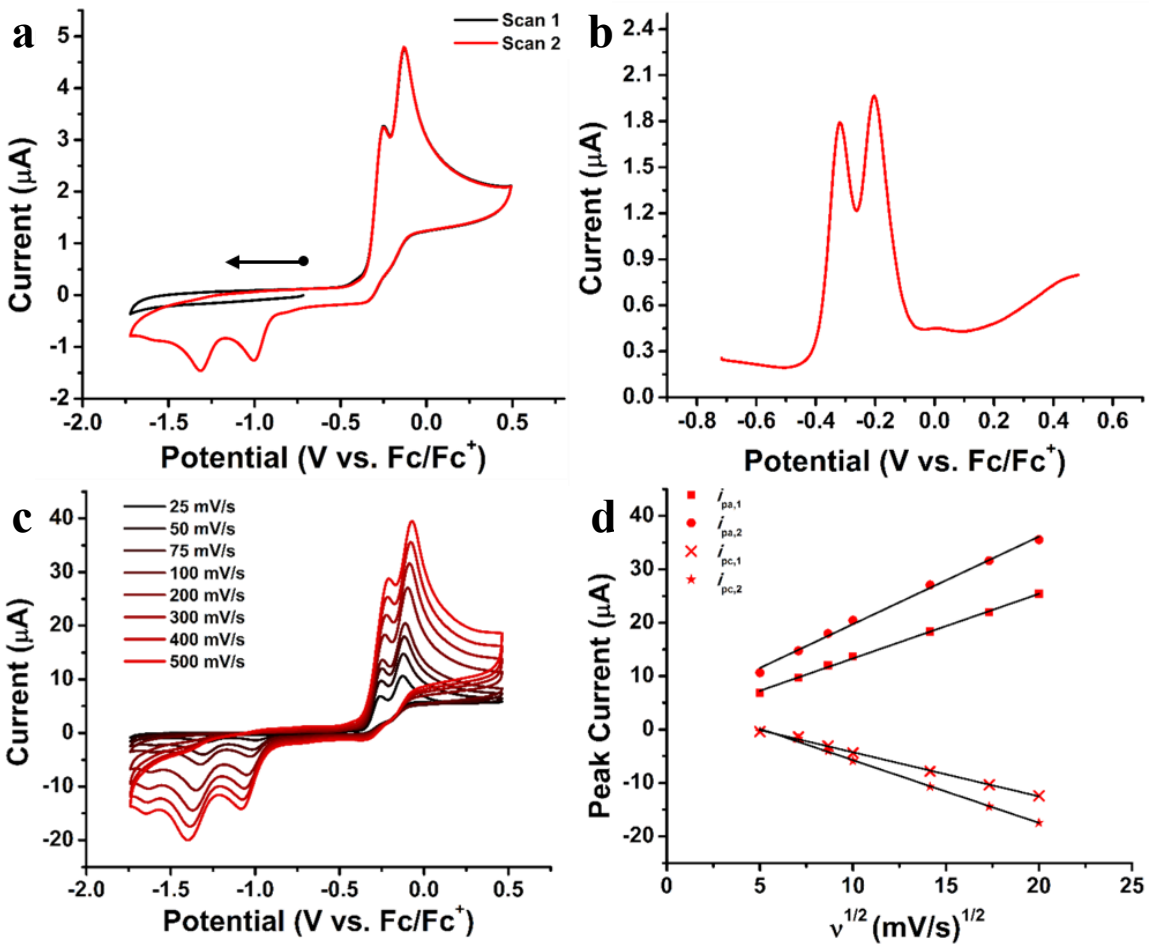

Figure 4.8. a) Cyclic voltammogram starting with a negative sweep illustrating the dependence of the reductive peaks on the oxidation of **5**. b) Differential pulse voltammogram (DPV) of **5**. Integration of the signal reveals an approximate 1:1 ratio of the oxidative events; $E_{pa,1}$ = –0.318 V, $E_{pa,1}$ = –0.203 V. c) Scan rate dependance cyclic voltammograms of **5** and d) the corresponding peak currents plotted against the square root of the scan rate (ν) ranging from 25 mV s^{-1} to 500 mV s^{-1}.

The appearance of two oxidation events in close proximity indicate the possibility of electronic communication in the complex. However, due to the irreversibility of the electron transfers, direct evaluation of the electronic communication is hard to ascertain. Furthermore, comparison of the electrochemistry of **5** to literature reports of that of the [(PCP)RhL] core show different profiles. As reported by Doherty *et al.*,[332] [(PCP)Rh($NCCH_3$)] displays a reversible one-electron oxidation which is observed at –0.71 V vs. Fc/Fc^+ and no back-waves are observed when the potential is stopped below –0.25 V. Only when the potential is swept to 0.75 V resulting in an irreversible oxidation at 0.12 V is a back-wave at –1.35 V is generated.

The results of Doherty *et al*. are inconsistent with the profile observed from complex **5**, which leaves open the possibility of three scenarios (Scheme 4.3).

Scheme 4.3. Scenarios for the electrochemical oxidations of complex **5**.*

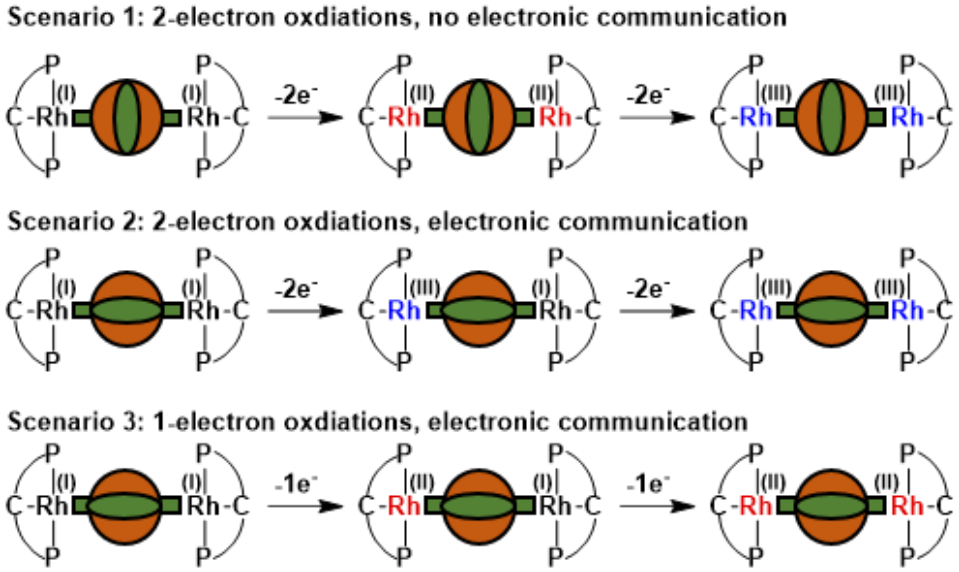

* In the scenarios where electronic communication is depicted, formal separated oxidation states of the metal centers are used for clarity of discussion. In actuality, some degree of averaged valence states for the metal centers would be observed following the first oxidation.

In the first scenario, each oxidation event corresponds to a two-electron oxidation and no electronic communication is observed, resulting in the generation of a Rh(II)-Rh(II) species followed by further oxidation to the Rh(III)-Rh(III) complex. In scenario two, each oxidation event is once again a two-electron oxidation, but electronic communication is observed, resulting in the formal generation of a Rh(III)-Rh(I) state followed by oxidation to the Rh(III)-Rh(III) state. Scenario three is similar to scenario two, only now just one-electron oxidations are observed, resulting in the generation of a Rh(II)-Rh(I) state followed by further oxidation to the Rh(II)-Rh(II) state.

4.2.4. Synthesis of [(PCP)Rh(2-isocyano-1,3-dimethylbenzene)] (6) and Electrochemical Comparisons with 5

To elucidate the proper oxidation scheme for complex **5**, the use of model complex **6** is employed. The synthesis of **6** is shown in Scheme 4.4.

Scheme 4.4. Synthesis of complex **6**.

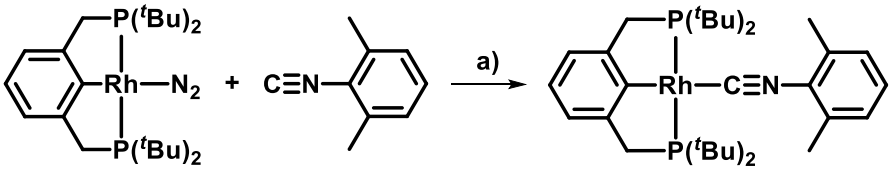

4 **6**

a) toluene, rt, 60 min.

The electrochemistry of complex **6** shows a single irreversible oxidation event with an E_{on} = –0.402 V with an E_{pa} = –0.252 V that induces an oxidation-dependent reduction event at E_{pa} = –1.365 V. Scan rate dependence studies show the oxidation is diffusion controlled and integration of the voltammogram shows the current of the oxidation dependent reduction is 18% that of the oxidation. DPV shows only a single peak with a full width half max equal to that of the dimeric complex **5** (Figure 4.9). Overall, the spectra of **6** displays half the number of electrochemical events of **5**. If

scenario one were to be followed, the lack of communication would require each rhodium center to oxidize independent of one another, leading the molecule to behave in a way that would resemble the model complex **6**. Therefore, for scenario one to be viable, two successive oxidations of complex **6** to Rh(II) and then to Rh(III) should be observed. However, since **6** displays only a single oxidative and reductive event, scenario one may be disregarded.

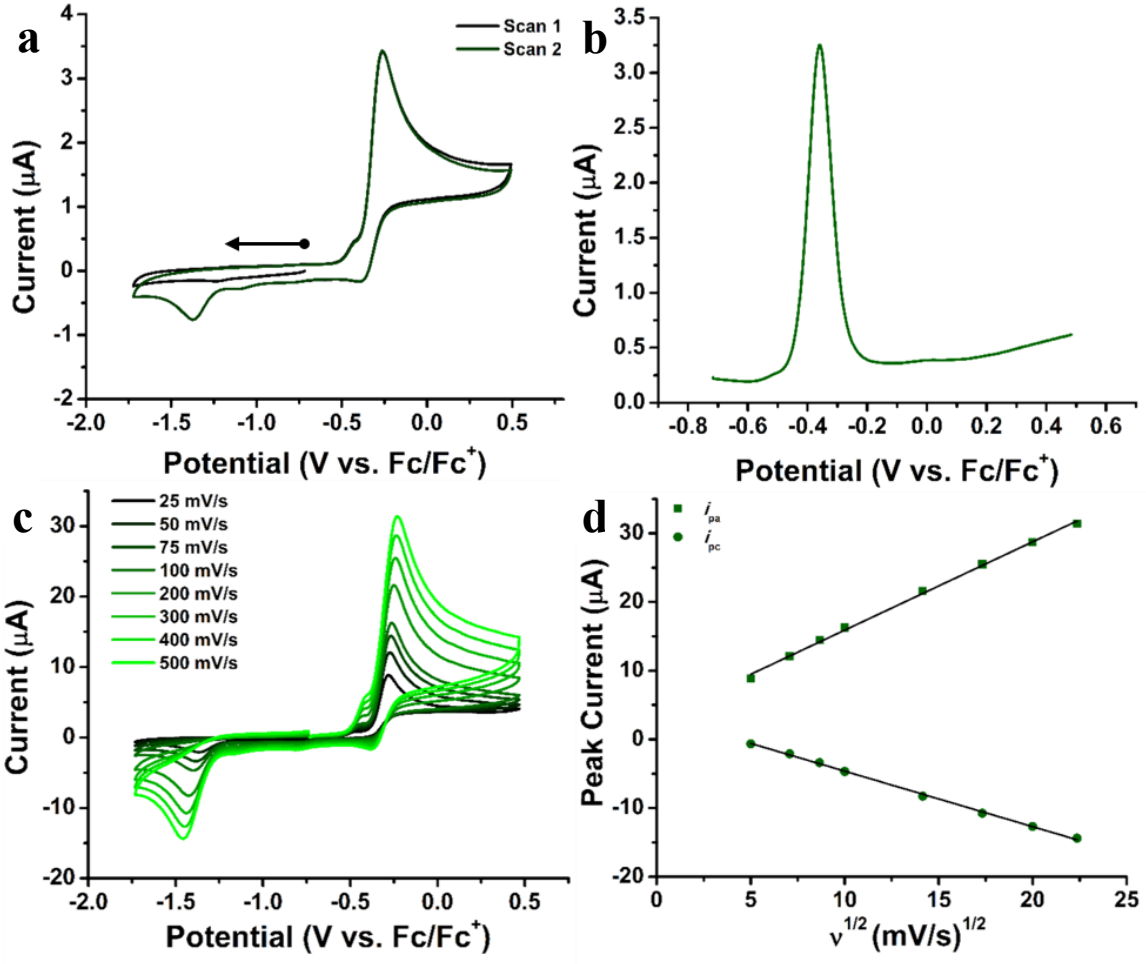

Figure 4.9. a) Cyclic voltammogram starting with a negative sweep illustrating the dependence of the reductive peaks on the oxidation of **6**. b) Differential pulse voltammogram (DPV) of **6**. Integration of the signal reveals an approximate 1:1 ratio of the oxidative events; $E_{pa,1} = –0.318$ V, $E_{pa,1} = –0.203$ V. c) Scan rate dependance cyclic voltammograms of **6** and d) the corresponding peak currents plotted against the square root of the scan rate (ν) ranging from 25 mV s^{-1} to 500 mV s^{-1}.

To differentiate between scenarios two and three, quantifications of the number of electrons transferred in each oxidation event is required. The irreversibility of the electrochemistry limits the methods available for quantification, however, due to the fast electron transfer as indicated by the scan rate dependence studies for complexes **5** and **6**,

the diffusion coefficient and number of electrons transferred can determined via chronoamperometry at a microdisk electrode using methods outlined by Denuault *et al.*[333] Analysis shows a diffusion coefficient of 1.49 x 10^{-5} $cm^2 \cdot s^{-1}$ for **6** corresponding to a one-electron (n_{exp} = 1.13) oxidation which supports scenario three. Performing the same analysis on complex **5** using a potential step that jumped both oxidative events gave a diffusion coefficient of 1.10 x 10^{-5} $cm^2 \cdot s^{-1}$ resulting in a two-electron (n_{exp} = 2.37) oxidation, further substantiating scenario three. To corroborate these findings, bulk electrolysis (Figure 4.10) was performed on solutions of **5** and **6** to verify the number of electrons transferred which was found to be 1 (n_{exp} = 1.10) for **6** and 2 (n_{exp} = 2.33) total for **5** which is in good in agreement with the microdisk chronoamperometry.

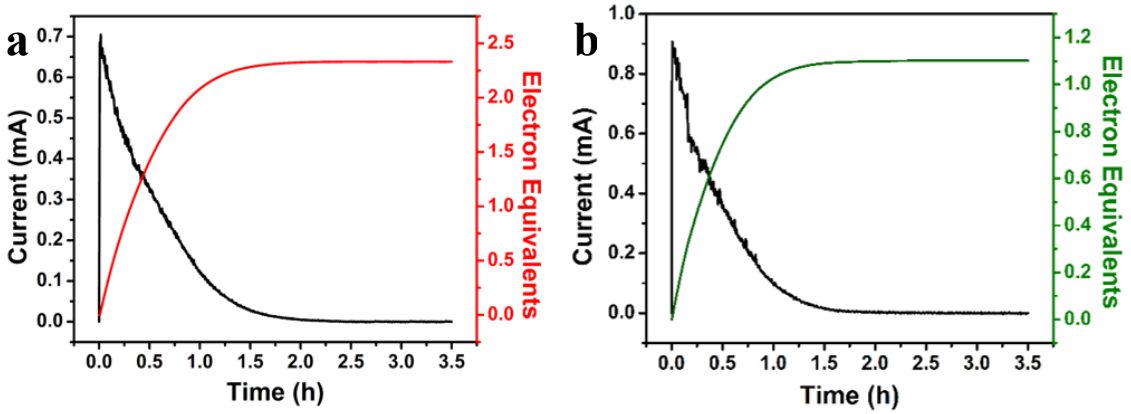

Figure 4.10. Bulk electrolysis of a) **5** and b) **6** in a CH_2Cl_2 solution of 0.1 M $TBAPF_6$ allowing for the quantification of the number of equivalents of electrons transferred per mole of complex.

Using the measured diffusion coefficients and number of electrons transferred, the predicted peak currents from the Randles-Sevcik equation and the Levich currents derived from the Levich equation were found to compare favorably with the experimental

results from the scan rate dependence (Figure 4.11) and rotating disc electrode experiments (Figure 4.12), respectively.[334]

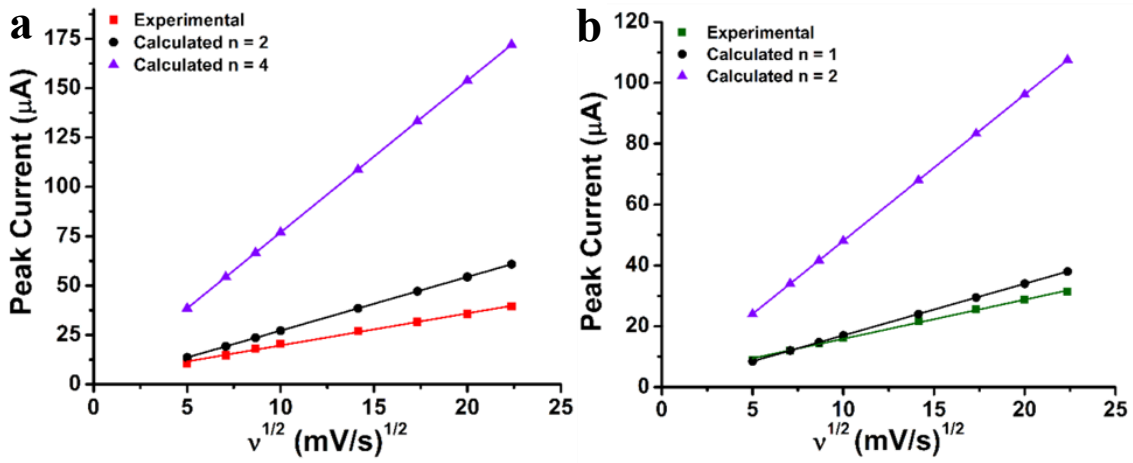

Figure 4.11. Scan rate dependance plots showing the peak current versus the square root of the scan rate for a) **5** and b) **6**. The experimental peak currents are compared to the calculated values using the Randles-Sevcik equation.[334] The experimentally measured diffusion coefficients for each complex are used with the relevent numbers of electrons transferred.

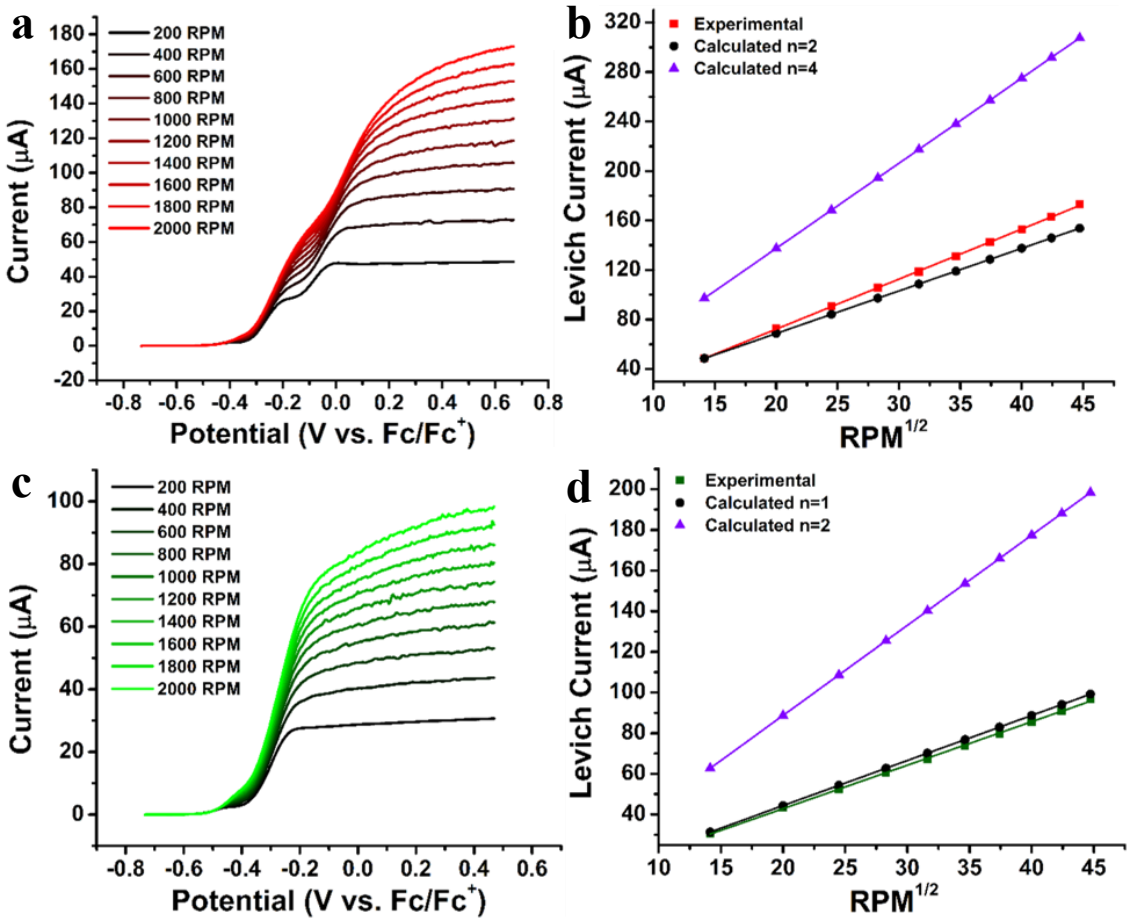

Figure 4.12. Voltammograms taken at a rotating disk eletrode for a) **5** and c) **6** in CH_2Cl_2. The steady state currents for b) **5** and d) **6** are plotted versus the square root of the rotation rate in revolutions per minute (RPM). The experimental peak currents are compared to the calculated values using the Levich equation. The experimentally measured diffusion coefficients for each complex are used with the relevent numbers of electrons transferred.

4.2.5. Electron Paramagnetic Resonance (EPR) Studies of 5 and 6

To study the extent of electron delocalization across the molecule, electron paramagnetic resonance (EPR) was used to investigate the paramagnetic species generated following oxidation of the Rh(I) complexes. Attempts to chemically generate $\mathbf{1}^+$ were unsuccessful. However, the addition of one equivalent of ferrocenium

tetrafluoroborate to complex **5** at room temperature for 20 seconds followed by flash-freezing in liquid N_2 yielded the spectra of $\mathbf{5}^+$ shown in Figure 4.13a.

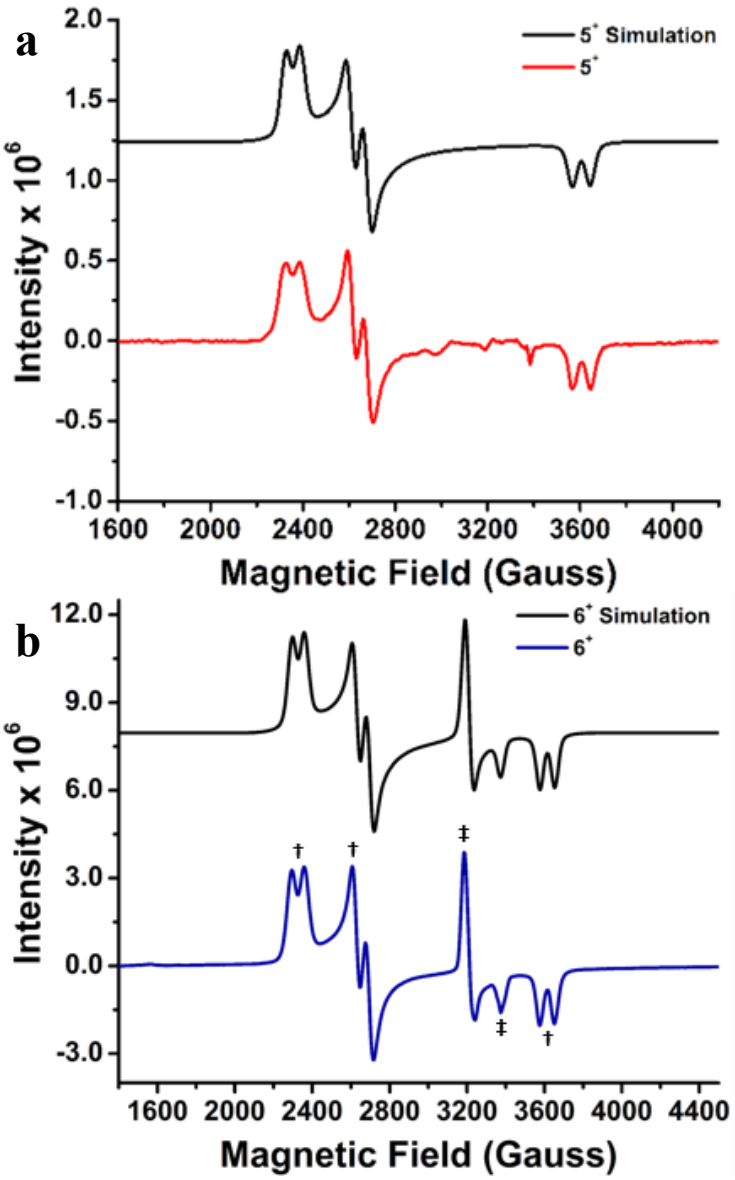

Figure 4.13. X-band EPR spectra of complexes $\mathbf{5}^+$ (a) and $\mathbf{6}^+$(†) / $\mathbf{6a}^+$(‡) (b) in frozen CH_2Cl_2 at 86 K. Simulated spectra are shown in black. Experimental conditions: concentration of Rh(I) - 4 mM, microwave frequency - 9.43 GHz, microwave power - 39.91 mW, modulation amplitude - 6 Gauss, conversion time - 40.00 ms, time constant - 40.96 ms.

The spectrum of $\mathbf{5}^+$ in frozen CH_2Cl_2 at 86 K display a rhombic signal showing hyperfine splitting from the rhodium center. The spectrum is consistent with previous literature reports of a Rh(II) pincer complex in frozen solution.[320] The rhombic pattern likely indicates a four-coordinate square-planar coordination environment around the rhodium center following oxidation to the Rh(II) state. Furthermore, the magnitude of the coupling constants and g-factors indicate a largely rhodium based radical. No coupling to phosphorous was observed. Treatment of **6** with ferrocenium tetrafluoroborate in a similar manner as **5** led to the generation of an EPR signal. Interestingly, two separate species are observed in the frozen solution. The peaks of $\mathbf{6}^+$, indicated by (†) in Figure 4.13b, correspond to a Rh(II)-environment similar to that the dimeric complex suggesting very little delocalization of the spin density in $\mathbf{5}^+$. The second species ($\mathbf{6a}^+$), labeled with (‡), exhibits an axial signal suggesting a complex of higher symmetry. Rh(II) species with axial symmetry in the literature have been shown to be in five-coordinate geometries indicating ligand association following oxidation.[335,336] The lack of a second signal in the EPR spectra of $\mathbf{5}^+$ hints at an increased stability of the oxidized state compared to the model complex.

Table 4.1. EPR parameters of complexes $\mathbf{5}^+$, $\mathbf{6}^+$ and $\mathbf{6a}^+$

Complex	g_x	g_y	g_z	a_x(G)	a_y(G)	a_z(G)
$\mathbf{5}^+$	2.861	2.552	1.869	60.6	68.0	76.7
$\mathbf{6}^+$	2.895	2.53	1.864	63.0	68.6	72.7
$\mathbf{6a}^+$	2.105	2.105	1.997	15.0	15.0	15.0

Attempts to investigate the spectra of the singly oxidized state of **5** and **6** following chemical oxidation were unsuccessful due to the instability of the products. Investigations into the resulting products of the chemical oxidation of **5** yielded unidentified byproducts and starting material. Similar attempts with complex **6** also

yielded starting material, however, the reaction of **6** with one equivalent silver tetrafluoroborate (Scheme 4.5) yielded [(PCP)Rh(H)(2-isocyano-1,3-dimethylbenzene)] (**7**). Similar complexes to **7** (Figure 4.14) have been reported in the literature.[337,338] The agostic hydrogen interaction is stronger in **7** than in previously reported structures as evidenced by a shortening of the rhodium-hydrogen contact distance and an increase in the C-H bond length. The appearance of the C-H agostic Rh(I) complex is likely the result of radical abstraction of a hydrogen atom by the Rh(II) species generating a Rh(III) hydrido species followed by reductive elimination of the C-H unit.[337,339]

Scheme 4.5. Preparation of **7**.

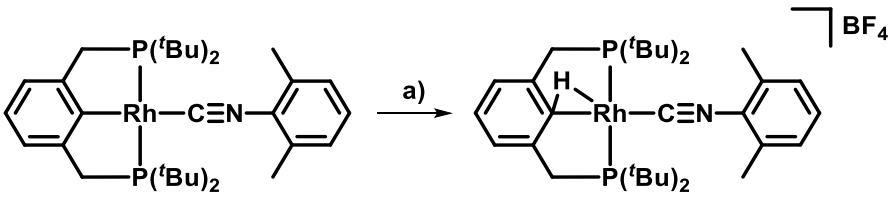

6 **7**

a) 1 $AgBF_4$, acetone, rt, 10 min.

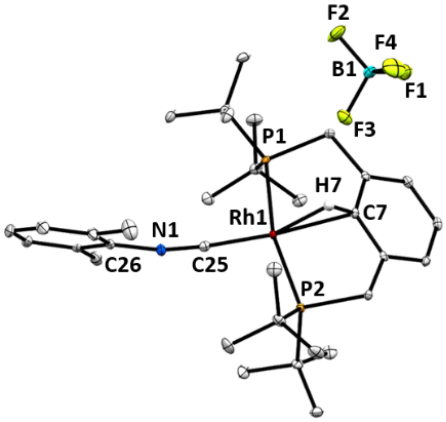

Figure 4.14. Molecular structure of complex **7**. Select bond lengths (Å) and angles (degrees): (Rh – C7) 2.273(2), (Rh1 – P1) 2.3256(7), (Rh1 – P2) 2.3429(7), (Rh1 – C25) 1.868(2), (Rh1 – H7) 1.89(2), (C7 – H7) 1.06(3), (N1 – C25) 1.178(3), (Rh1 – H7 – C7) 97(2), (C25 – N1 – C26) 167.3(2).

4.2.6. UV-Vis and Spectroelectrochemistry

UV-Vis spectroscopy of the complexes provided additional insight into the electronic structure of the materials (Figure 4.15).

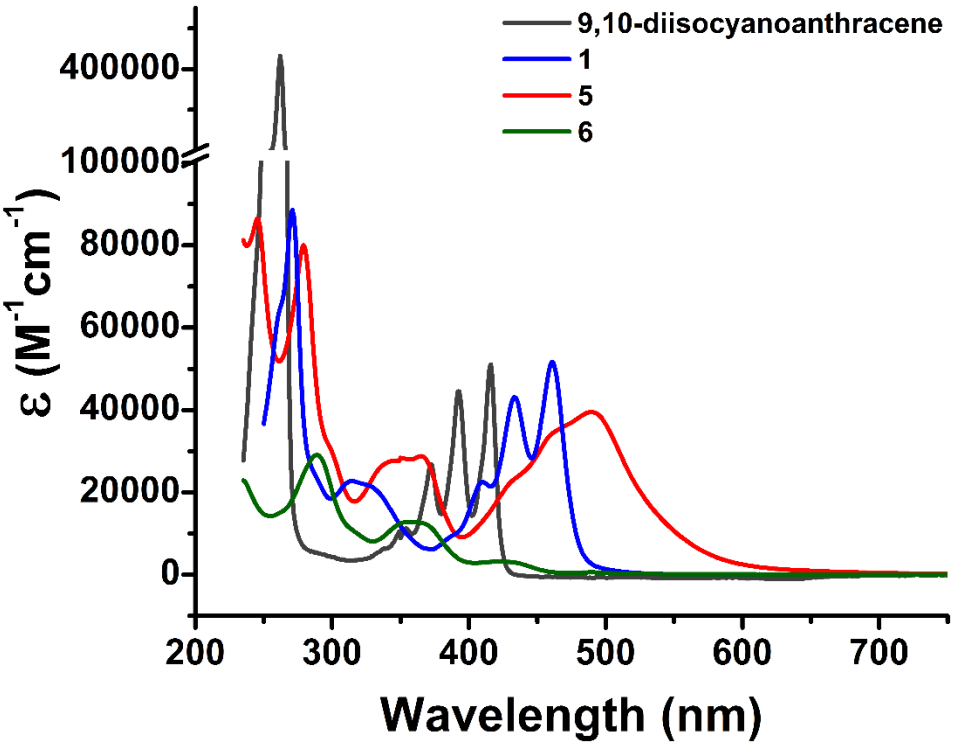

Figure 4.15. Electronic absorption spectra of complexes **1**, **5** and **6** in CH_2Cl_2. The bridging ligand, 9,10-diisocyanoanthracene, is shown for comparison.

Coordination of 9,10-diisocyanoanthracene to the Rh(I)-centers results in a drastic decrease in the n-to-π^* (260 nm < λ_{max} < 280 nm) transition and a large red-shift of the structured anthracene-based π-to-π^* absorption (400 nm < λ_{max} < 500 nm), suggesting extended conjugation to the Rh(I) metal centers. Furthermore, a noticeable broadening of the vibronic bands in the π-to-π^* absorption is observed upon coordination. Such broadening of the vibronic structure would be expected upon coordination to rhodium as an infinite number of dihedral angles of the Rh(I)-pincer units with respect to the

anthracene ring are theoretically possible. However, the broadening is greatly exaggerated in moving from complex **1** to **5,** suggesting effects other than conformational accessibility are in play. It has been reported in the literature that increasing the charge transfer (CT) character of an absorption in a conjugated organic molecule can lead to a broadening of the vibronic structure.[340,341] Therefore, it is likely that there is increased metal contribution to the CT event in these systems as the electron density on the rhodium increases from **1** to **5,** resulting in the observed broadening. This increased mixing would be beneficial for promoting electronic communication.

Spectroelectrochemistry was obtained for complex **5** (Figure 4.16). Application of a –0.24 V potential, corresponding to the peak of the first electrochemical oxidation event, leads to the growth of a broad absorption near the onset of the anthracene π-to-π^*/CT event (≈ 610 nm) with a concomitant asymmetric narrowing of the full width-half max. The emergence of an absorption event at 650 nm has been recently observed in literature from a Rh(I)/Rh(II) mixed valence state, however, no lower energy absorption events were observed.[113] Stepping the potential further positive to 0.00 V reversed the growth of the broad, low energy absorption. Furthermore, a drastic change in the π-to-π^*/CT absorption is observed as the peak blue shifts ≈ 30 nm and the vibrational states are increasingly resolved. The removal of electron density from the metal center at potentials past the second oxidative event results in a decrease in the amount CT character present in the transition leading to an absorption much more similar in character to the free ligand.

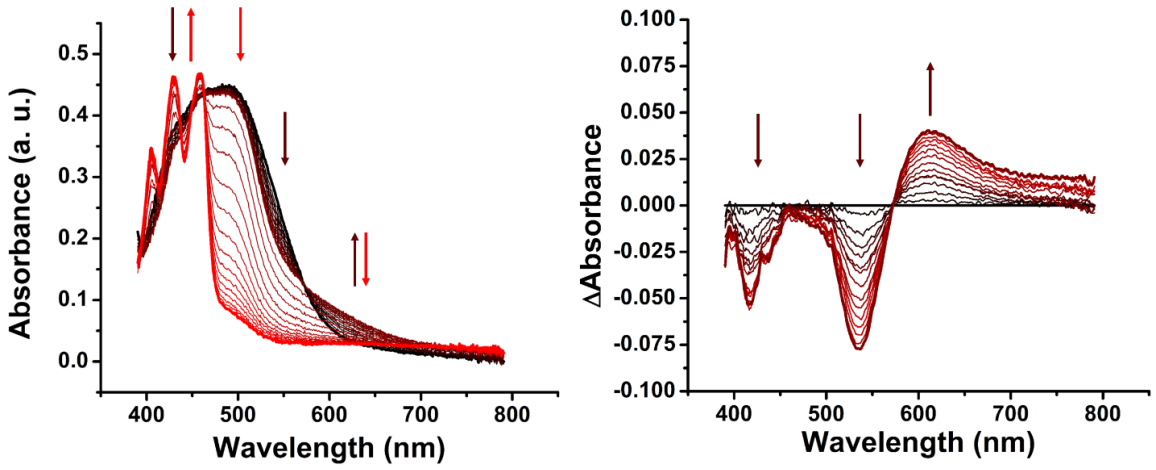

Figure 4.16. Spectroelectrochemistry (left) of complex **5** performed in CH_2Cl_2. Holding the potential at –0.24 V leads to the evolution of the black trace to the maroon trace. A narrowing of the anthracene absorption centered at 480 nm and the emergence of a new absorption event at 610 nm is observed. These changes are more readily visualized in the differential absorbance spectra of the spectroelectrochemistry (right). Stepping the potential to 0 V leads to the evolution of the maroon trace to the red trace. The changes in the spectra are highlighted by maroon and red arrows for the –0.24 V and 0 V potential steps, respectively.

4.2.7. Density Functional Theory (DFT) Comparison of 1^+ and 5^+

To gain insight into electronic effects of the supporting pincer ligands, DFT calculations were performed using the crystal structures of **1** and **5** as the initial guess for the geometry optimizations of $\mathbf{1}^+$ and $\mathbf{5}^+$. A comparison of the ten highest molecular orbitals relative to the singly occupied molecular orbital (SOMO) is shown in Figure 4.17. An increase in the delocalization of the SOMO of $\mathbf{5}^+$ relative to $\mathbf{1}^+$ is observed which is consistent with the increased electronic communication within the system. Furthermore, an inversion in the ordering of the lower molecular orbitals occurs. These effects are related to the increased sigma donation of the PCP ligand. In complex $\mathbf{1}^+$, the strongest donating ligands are the *tert*-butylphosphine arms of the PNP ligand. Therefore, the frontier molecular orbitals interacting with the phosphine ligand reside at higher

energies than the orbitals based on pyridine-rhodium interactions. In complex $\mathbf{5}^{+}$, the strongest field ligand is now the cyclometallated aryl ring which results in the inversion of the molecular orbitals. Furthermore, a much closer energy spacing of the molecular oribtals is observed in $\mathbf{5}^{+}$ with the two orbitals closest in energy to the SOMO residing within 0.25 eV. For complex $\mathbf{1}^{+}$, DFT predicts an energy gap of 1.27 eV before the next highest lying molecular orbital is found. It is speculated that at ambient conditions, a mixing of the two highest molecular orbitals with the SOMO further helps facilitate electronic communication within the system.

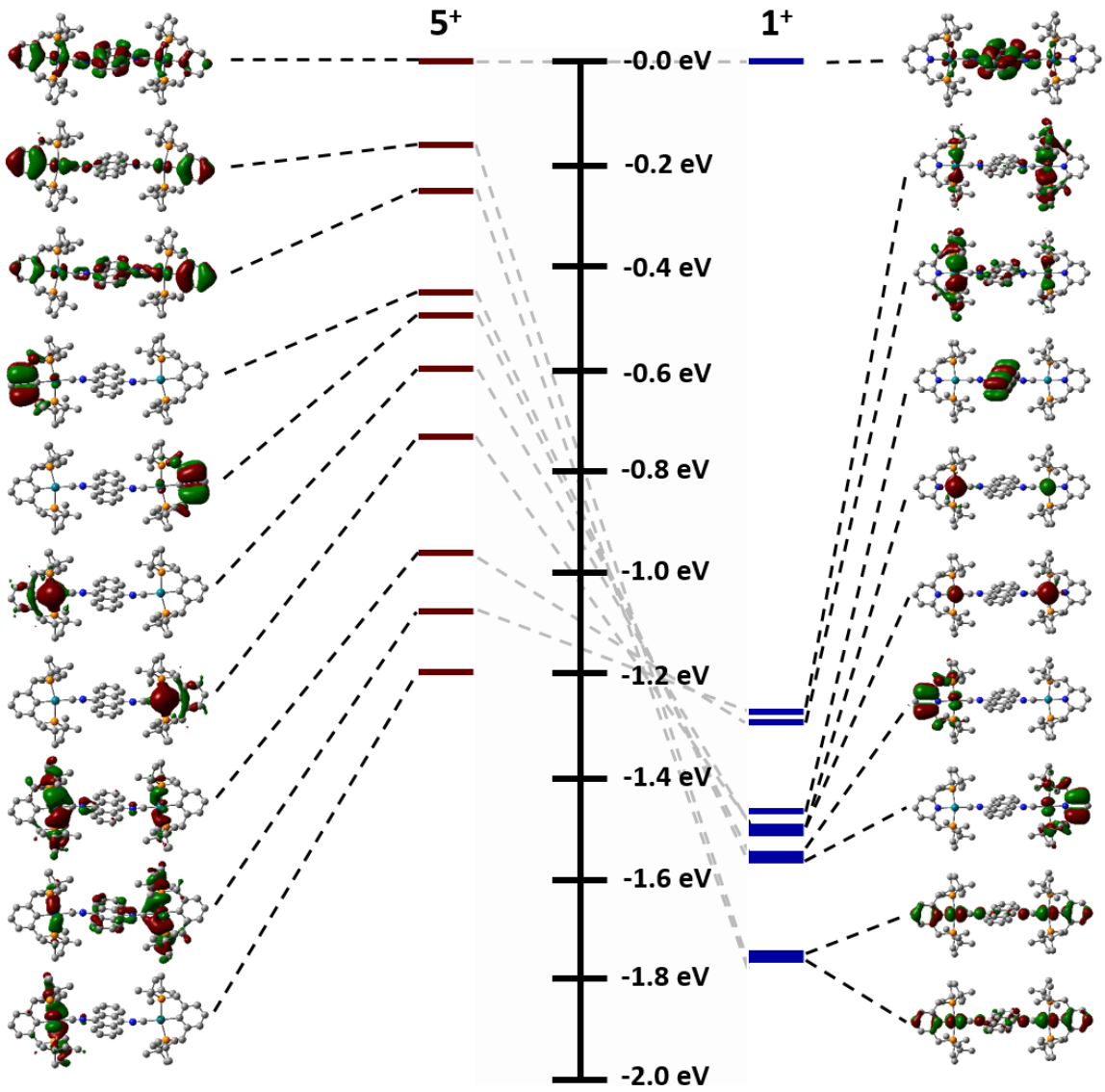

Figure 4.17. Kohn-Sham diagrams of the first ten occupied molecular orbitals of $\mathbf{5}^{+}$ and $\mathbf{1}^{+}$. The relative energies with respect to the SOMO, which is defined as 0.0 eV, are plotted.

4.3. CONCLUSIONS

The synthesis and characterization of two bridged rhodium(I) complexes, [(PNP)Rh(μ^2-9,10-diisocyanoanthracene)Rh(PNP][BF_4]$_2$ (**1**) and [(PCP)Rh(μ^2-9,10-diisocyanoanthracene)Rh(PCP] (**5**) was achieved. The resulting structures of both complexes exhibit a square planar environment around the d^8-metal centers which are bridged by 9,10-diisocyanoanthracene.

Electrochemical investigations into the electronic communication of **1** and **5** reveal no communication **1** while complex **5** exhibits electronic communication. The extent of the communication of complex **5** in the oxidized state is quite weak and would be best classified as a class II system on the border of a class I type system. This is evidenced by the lack of a low energy intervalence charge transfer in the near IR of the spectroelectrochemistry as well as the localization of the electron on a single rhodium center as determined by EPR spectroscopy The irreversibility of the system limits the utility of the investigated material in practical applications. However, important design principals may be drawn from this study to improve the communication in bridged rhodium centers involving the d^7 and d^8 states. Incorporation of the strong field PCP ligand facilitates electronic communication in complex **5** upon electrochemical oxidation. The increased sigma donation into the rhodium center coupled with a decrease in the π-acidity of the PCP and overall lower charge of **5** compared to **1** results in a better overlap of the rhodium based *d*-orbitals with that of the bridging ligand increasing the extent of electronic communication between the rhodium centers.

4.4. EXPERIMENTAL

4.4.1. Synthesis and Characterization

All reactions and manipulations were carried out either in a dry box under an inert N_2 atmosphere or by using standard Schlenk techniques. Dry solvents were collected in solvent bulbs from an Innovative Technology PureSolv 400 solvent purification system, sparged with nitrogen, and stored over 3Å molecular sieves. $AgBF_4$ (Strem), 2,6-bis(di-*tert*-butylphosphinomethyl)pyridine (PNP) (Sigma Aldrich), 1,3-bis(di-*tert*-butylphosphinomethyl)benzene (PCP) (Sigma Aldrich), 2-isocyano-1,3-dimethylbenzene (Sigma Aldrich), potassium *tert*-butoxide (Alfa Aesar) and ferrocenium tetrafluoroborate (Sigma Aldrich) were purchased from commercially available sources and used without further purification. Preparations of $[RhCl(COE)_2]_2$ and 9,10-diisocyanoanthracene[342] were accomplished according to literature procedures.

NMR spectra were recorded with a Varian DirectDrive 400 MHz spectrometer (^1H 400 MHz, $^{13}C\{^1H\}$ 100 MHz, $^{31}P\{^1H\}$ 161 MHz. ^1H- and $^{13}C\{^1H\}$ NMR spectra were referenced to residual solvent peaks. The $^{31}P\{^1H\}$ spectra was externally referenced to a 75% phosphoric acid sample. Chemical ionization (CI+) mass spectra were collected on a Micromass Autospec Ultima mass spectrometer. Electrospray ionization (ESI+) and atmospheric pressure chemical ionization (APCI) were collected on an Agilent 6530 quadrupole time of flight mass spectrometer. Elemental analysis services were provided by Midwest Microlabs, LLC.

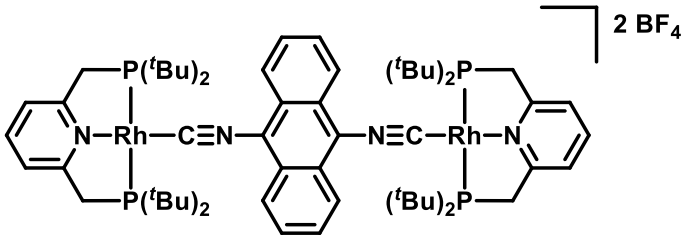

[(PNP)Rh(μ²-9,10-diisocyanoanthracene)Rh(PNP][BF₄]₂ (**1**): In a dry box, $[RhCl(COE)_2]_2$ (0.0800 g, 0.111 mmol) and $AgBF_4$ (0.0434 g, 0.223 mmol) was weighed out in a 10 mL flask and dissolved in 6 mL of CH_2Cl_2. The mixture was allowed to stir for 45 minutes resulting in the formation of a blood red solutions and a light gray precipitate. The reaction mixture was then filtered through Celite® directly into a Schlenk flask containing a CH_2Cl_2/CH_3CN (2:1) solution of PNP (0.0882 g, 0.223 mmol) resulting in an orange solution. A solution of 9,10-diisocyanoanthracene (0.0254 mmol, 0.111 mmol) dissolved in 15 mL of CH_2Cl_2 was added dropwise to the reaction mixture resulting in a deep orange solution. The Schlenk flask was then sealed with a rubber septa, transferred to a Schlenk line and was concentrated under reduced pressure to a volume of approximately 2 mL. The Schlenk flask was then transferred to a glove box where excess Et_2O was added to the flask, causing precipitation of a yellow powder. The supernatant was decanted off and the residue was redissoved in minimal CH_2Cl_2 and subsequently precipitated with Et_2O. This process was repeated 3 times. Following the third precipitation, the solid was dissolved in minimal CH_2Cl_2, filtered through Celite® and recrystallized by slow diffusion of Et_2O into the saturated CH_2Cl_2 solution resulting in pure product in the form of large, orange, plate-like crystals suitable for single crystal X-ray diffraction (0.128 g, 83%). ^1H NMR (CD_2Cl_2, 400 MHz): δ 8.40 (m, 4H), 7.87 (t, J = 7.8 Hz, 2H), 7.78 (m, 4H), 7.56 (d, J = 7.8 Hz, 4H), 3.76 (t, J = 3.9, 8H), 1.40 (t, J = 7.3, 72H). $^{13}C\{^1H\}$ NMR (CD_2Cl_2, 100 MHz): δ 165.0, 140.0, 128.8, 126.6, 123.8, 121.9, 121.6, 36.6 (t, J = 7.7 Hz), 36.0 (t, J = 6.9 Hz), 29.6 (t, J = 3.1). $^{31}P\{^1H\}$ NMR (CD_2Cl_2,

161 MHz): δ 76.9 (d, J = 126.7 Hz). HRMS (ESI+) *m/z* Calcd. for $C_{62}H_{94}N_4P_4Rh_2^{2+}$ (M–$2BF_4)^{2+}$ 612.2264 Found: 612.2280. Elemental Anal. Calcd. for $C_{62}H_{94}N_4P_4Rh_2B_2F_8 \cdot 2CH_2Cl_2$: C, 49.00; H, 6.30; N, 3.57. Found: C, 49.02; H, 6.34; N, 3.59.

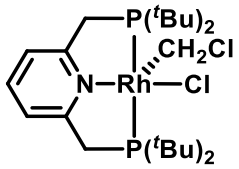

[(PNP)RhCl(CH₂Cl)][BF₄] (**2**): In a dry box, $[RhCl(COE)_2]_2$ (0.0800 g, 0.111 mmol) and $AgBF_4$ (0.0434 g, 0.223 mmol) were weighed out in a 10 mL flask and dissolved in 6 mL of CH_2Cl_2. The mixture was allowed to stir for 45 minutes resulting in the formation of a deep red solution and a light gray precipitate. The reaction mixture was then filtered through Celite® directly into a Schlenk flask containing a solution of PNP (0.0882 g, 0.223 mmol) in CH_2Cl_2 resulting in an orange solution that began to slowly turn brown over the course of 5 minutes. The Schlenk flask was then sealed with a rubber septa, transferred to a Schlenk line and reaction was allowed to stir overnight before concentrating to approximately 1 mL under reduced pressure. The reaction flask was then sealed and transferred to a glovebox where excess Et_2O was added to the flask causing precipitation of a brown powder. The supernatant was decanted off and the residue was redissoved in minimal CH_2Cl_2 and subsequently precipitated with Et_2O. This process was repeated 3 times. Following the third precipitation, the solid was dissolved in minimal CH_2Cl_2, filtered through Celite® and recrystallized by slow diffusion of Et_2O into the saturated CH_2Cl_2 solution over the course of 4 days resulting in pure product as deep orange crystals (0.049 g, 67%). ^{1}H NMR (CD_2Cl_2, 400 MHz): δ 7.93 (t, J = 7.8 Hz, 2H), 7.68 (d, J = 7.8 Hz, 1H), 5.76 (td, J = 6.2, 3.3 Hz, 2H), 4.01 (m, 4H), 1.49 (dt, J = 29.1,

7.1 Hz, 36H). $^{13}C\{^{1}H\}$ NMR (CD_2Cl_2, 100 MHz): δ 165.5, 140.9, 124.0 (t, J = 5.3 Hz), 44.2 (d, J = 36.6 Hz), 38.7 (t, J = 8.0 Hz), 37.8 (t, J = 8.4 Hz), 35.6 (t, J = 8.4 Hz), 30.1 (t, J = 1.9 Hz), 29.4 (t, J = 1.5 Hz). $^{31}P\{^{1}H\}$ NMR (CD_2Cl_2, 161 MHz): δ 47.5 (d, J = 99.7 Hz). HRMS (ESI+) *m/z* Calcd. for $C_{24}H_{45}Cl_2NP_2Rh^+$ $(M–PF_6)^+$ 582.1454. Found: 582.1454. Elemental Anal. Calcd. for $C_{24}H_{45}NP_2Cl_2BF_4Rh$: C, 43.01; H, 6.77; N, 2.09. Found: C, 43.15; H, 6.73; N, 2.04.

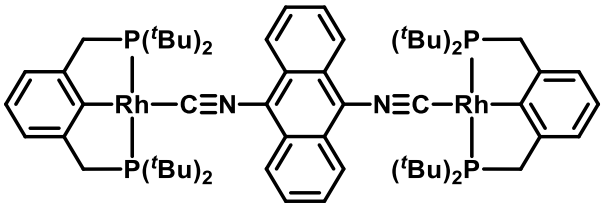

[(PCP)Rh(μ²-9,10-diisocyanoanthracene)Rh(PCP][BF₄]₂ (**5**): In a dry box, $[RhCl(COE)_2]_2$ (0.1048 g, 0.146 mmol) and PCP (0.1153 g, 0.292 mmol) were weighed out in a 15 mL bomb flask and dissolved in 4 mL of toluene. The flask was sealed and dropped into an oil bath preheated to 150 °C and allowed to react for 5 hours with vigorous stirring. The reaction was then cooled to room temperature and transferred to a dry box where the solution was filtered through Celite® into a 50 mL Schlenk flask. The Schlenk flask was then sealed with a rubber septa and transferred to a Schlenk line where the solvent was removed under reduced pressure at 30 °C to yield **3** as a yellow solid consistent with literature reports.[343,344] The ^{1}H- and $^{31}P\{^{1}H\}$ NMR confirm pure product and the material was carried on without further purification assuming quantitative yield. ^{1}H NMR (CD_2Cl_2, 400 MHz): δ 6.96 (d, J = 7.4 Hz, 2H), 6.82 (t, J = 7.4 Hz, 1H), 3.26 (m, 4H), 1.38 (q, J = 6.7 Hz, 36H), –27.8 (dt, J = 26.1, 12 Hz, 1H). $^{31}P\{^{1}H\}$ NMR (CD_2Cl_2, 161 MHz): δ 74.4 (d, J = 115.7 Hz). In a dry box, complex **3** was dissolved in 30 mL of THF and potassium *tert*-butoxide (0.0393 g, 0.351 mmol) was slowly added to

the reaction mixture resulting in a brown solution. The reaction was transferred to a Schlenk line and the solvent was removed under reduced pressure at room temperature. In a dry box, the residue was extracted with toluene and filtered through Celite® to give complex **4** as a dark yellow powder consistent with literature reports.[345] Purity was confirmed by ^{1}H- and ^{31}P{^{1}H} NMR and the material was carried on without further purification assuming quantitative yield. ^{1}H NMR (CD_2Cl_2, 400 MHz): δ 7.07 (m, 3H), 3.32 (t, J = 3.9 Hz, 4H), 1.23 (t, J = 6.4 Hz, 36H). ^{31}P{^{1}H} NMR (CD_2Cl_2, 161 MHz): δ 96.8 (d, J = 146.5 Hz). In a 100 mL Schlenk flask, **4** was dissolved in 45 mL of a 1:1:1 toluene/CH_2Cl_2/CH_3CN mix. A solution of 9,10-diisocyanoantrhacene (0.0333 g, 0.146 mmol) dissolved in minimal volume CH_2Cl_2 is added dropwise to the reaction mixture to give a dark blood red solution. The reaction flask was transferred to a Schlenk line and the solvent was removed under reduced pressure at room temperature to give a purple solid. In a dry box, the solid is dissolved in minimal CH_2Cl_2 and filtered through Celite® and recrystallized by slow diffusion of Et_2O into the saturated solution over the course of 3 weeks yielded pure **5** as large orange plate-like crystals (0.085 g, 48%). ^{1}H NMR (CD_2Cl_2, 400 MHz): δ 8.51 (m, 4H), 7.60 (m, 4H), 7.02 (d, J = 7.4 Hz, 4H), 6.80 (t, J = 7.4 Hz, 2H), 3.47 (t, J = 4.0 Hz, 8H), 1.35 (t, J = 46.5 Hz, 72H). ^{13}C{^{1}H} NMR (CD_2Cl_2, 100 MHz): δ 190.7, 179.5, 154.2 (td, J = 12.2, 3.0 Hz), 127.1, 126.5, 124.8, 123.9, 122.0, 119.9 (t, J = 9.2 Hz), 39.1 (td, J = 12.9, 3.0 Hz), 35.4 (td, J = 6.9, 1.5 Hz), 30.2 (t, J = 3.4 Hz). ^{31}P{^{1}H} NMR (CD_2Cl_2, 161 MHz): δ 90.6 (d, J = 150.0 Hz). HRMS (MALDI+) *m/z* Calcd. for $C_{64}H_{95}N_2P_4Rh_2^+$ $(M+H)^+$ 1221.45558 Found: 1221.45675. Elemental Anal. Calcd. for $C_{64}H_{94}N_2P_4Rh_2$: C, 62.95; H, 7.76; N, 2.29. Found: C, 62.75; H, 7.77; N, 2.24.

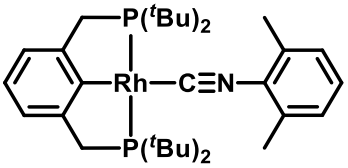

[(PCP)Rh(2-isocyano-1,3-dimethylbenzene)] (**6**): Synthesis of **6** was similar to that of **5**, leading to the quantitative generation of complex **4** from $[RhCl(COE)_2]_2$ (0.1095 g, 0.153 mmol). In a dry box, **4** was dissolved in 30 mL of toluene in a Schlenk flask and 2-isocyano-1,3-dimethylbenzene (0.0400 g, 0.305 mmol) dissolved in 5 mL of toluene was added to the reaction mixture and allowed to stir for 1 hour. The flask was then sealed and transferred to a Schlenk line where the solvent was removed under reduced pressure at room temperature leaving an orange residue. This residue was then washed with Et_2O yielding **6** as a pure orange powder (0.118 g, 62%). ^{1}H NMR (CD_2Cl_2, 400 MHz): δ 7.07 (m, 3H), 7.00 (d, *J* = 7.4 Hz, 2H), 6.78 (t, *J* = 7.4 Hz, 1H), 3.41 (t, *J* = 3.7 Hz, 4H), 2.42 (s, 6H), 1.36 (t, *J* = 6.2 Hz, 36H). ^{13}C{^{1}H} NMR (CD_2Cl_2, 100 MHz): δ 181.9 (dt, *J* = 30.5, 7.5 Hz), 174.9 (dt, *J* = 51.9, 13.4 Hz), 154.0 (td, *J* = 12.9, 3.0 Hz), 133.4, 131.0, 128.0, 125.6, 123.3, 119.8 (t, *J* = 8.7 Hz), 39.1 (td, *J* = 10.2, 2.5 Hz), 35.4 (td, *J* = 6.9, 2.3 Hz), 30.1 (t, *J* = 3.5 Hz), 19.2. ^{31}P{^{1}H} NMR (CD_2Cl_2, 161 MHz): δ 89.0 (d, *J* = 151.4 Hz). HRMS (CI+) *m/z* Calcd. for $C_{33}H_{52}NP_2Rh^+$ $(M)^+$ 627.2630. Found: 627.2632. Elemental Anal. Calcd. for $C_{33}H_{52}NP_2Rh$: C, 63.15; H, 8.35; N, 2.23. Found: C, 62.71; H, 8.33; N, 2.14.

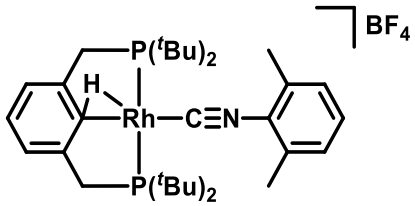

[(PCP)Rh(H)(2-isocyano-1,3-dimethylbenzene)][BF_4] (**7**): In a dry box, **6** (0.0100 g, 0.016 mmol) and $AgBF_4$ (0.0031 g, 0.016 mmol) were weighed out in a 5 mL flask and dissolved in 2 mL of acetone. The mixture was allowed to stir for 10 minutes, resulting in the formation of a green solution and a light gray precipitate. The solution was filtered through Celite® and the resulting product was precipitated by the slow diffusion of Et_2O in the acetone solution. Red-yellow crystals suitable for single X-ray diffraction were collected.

4.4.2. Electrochemistry

Electrochemical measurements were recorded in a dry-box under a nitrogen atmosphere using a GPES system from Eco. Chemie B. V. All experiments were carried out in a CH_2Cl_2 solution containing 0.1 M [(*n*-Bu)$_4$N][PF_6] ($TBAPF_6$) as supporting electrolyte. The $TBAPF_6$ was purified via recrystallization three times from boiling ethanol before being dried for 3 days under active vacuum at 80 °C. A $Ag/AgNO_3$ reference electrode (Ag wire incubated in a 0.01 M $AgNO_3$ solution with 0.1M $TBAPF_6$ in CH_3CN) was utilized and all measured potentials were corrected to ferrocene as an external reference. Cyclic voltammetry, differential pulse voltammetry, and scan rate dependence studies were performed using a glassy carbon button (3.0 mm) working electrode with a platinum wire counter electrode. Electrochemistry performed at a platinum button (1.6 mm) working electrode yielded identical results. Rotating disk experiments were performed using a glassy carbon button (3.0 mm) at rotation rates ranging from 200 to 2000 revolutions per minute (RPM) with a platinum wire counter

electrode. Measurements of the diffusion coefficient and number of electrons transferred via chronoamperometry were performed using a 25 μm platinum button microelectrode utilizing a platinum wire counter electrode.[333] Bulk electrolysis was performed using glassy carbon rods as the working and counter electrode. The experiment was performed in an H-cell with glass frits separating the compartments containing the working and counter electrodes. The first data point was discarded due to charging currents and the steady state current was subtracted from all the data points to account for background currents.

4.4.3. Infrared and UV-Vis Spectroscopy

Infrared spectra were taken on a Nicolet iS50 FT-IR spectrometer. Absorption spectra were recorded on a Varian Cary 6000i UV-Vis-NIR spectrophotometer using air free quartz cells. Spectroelectrochemistry was recorded at a platinum mesh in a thin cell (0.1 cm path length).

4.4.4. Electron Paramagnetic Resonance (EPR)

EPR experiments were recorded on a Bruker EMX-Plus X-band spectrometer. Simulated spectra were obtained using SimFonia software from Bruker.

4.4.5. Crystallography

The X-ray diffraction data for 9,10-diisocyanoanthracene, **1** and **2** was collected on a Rigaku AFC12 diffractometer with a Saturn 724 + CCD using a graphite monochromator with MoKa radiation (λ = 0.71073 Å). The data was collected at 153 K using an Oxford Cryostream low temperature device. Data reduction was performed using the Rigaku Americas Corporation's Crystal Clear version 1.40.[212] The X-ray diffraction data for **5** was collected on an Agilent Technologies SuperNova Dual Source diffractometer using a μ-focus Cu Kα radiation source (λ = 1.5418 Å) equipped with

collimating mirror monochromators that operated at 100 K. Data collection, unit cell refinement and data reduction were performed using Agilent Technologies CrysAlisPro V 1.171.37.31.[259] The structures were solved by direct methods using SuperFlip.[260] The X-ray diffraction data for **7** was collected on a Nonius Kappa CCD diffractometer using a graphite monochromator with MoKα radiation (λ = 0.71073 Å). Data reduction was performed using DENZO-SMN.[300]

Structures were refined by full-matrix least-squares on F^2 with anisotropic displacement parameters for the non-H atoms using SHELXL-2014.[261] Structure analysis was aided by use of the programs PLATON98[215] and WinGX.[216,217] The hydrogen atoms were calculated in ideal positions with isotropic displacement parameters set to 1.2 x U_{eq} of the attached atom (1.5 x U_{eq} for methyl hydrogen atoms). The function, $\Sigma w(|F_o|^2 - |F_c|^2)^2$, was minimized, where $w = 1/[(\sigma(F_o))^2 + (0.013*P)^2 + (87.56*P)]$ and $P = (|F_o|^2 + 2|F_c|^2)/3$. $R_w(F^2)$ refined to 0.222, with $R(F)$ equal to 0.0857 and a goodness of fit, S, = 1.03. Definitions used for calculating $R(F)$, $R_w(F^2)$ and the goodness of fit, S, are given as follows: $R_w(F^2) = \{\Sigma w(|F_o|^2 - |F_c|^2)^2/\Sigma w(|F_o|)^4\}^{1/2}$ where w is the weight given each reflection. $R(F) = \Sigma(|F_o| - |F_c|)/\Sigma|F_o|\}$ for reflections with $F_o > 4(\sigma(F_o))$. $S = [\Sigma w(|F_o|^2 - |F_c|^2)^2/(n - p)]^{1/2}$, where n is the number of reflections and p is the number of refined parameters.

The data was checked for secondary extinction effects but no correction was necessary. Neutral atom scattering factors and values used to calculate the linear absorption coefficient are from the International Tables for X-ray Crystallography (1992).[218] All Figures were generated using SHELXTL/PC.[262] Tables of positional and thermal parameters, bond lengths and angles, torsion angles and Figures are found elsewhere.

4.4.6. Computational Methods

DFT optimizations were performed using the Vienna ab initio simulation package (VASP).[346–349] Core electrons were treated using the projector-augmented wave method.[350,351] Valence electrons were described with a plane wave basis set with default kinetic energy cutoffs (228.993 eV for Rh, 250.0 eV for H, 400.0 eV for C, 255.083 eV for P, 400.0 eV for N). No significant difference was found using potentials with a higher cutoff. All calculations considered spin-polarization. The generalized gradient approximation (GGA) using the Perdew-Wang 91 (PW91) functional was chosen to evaluate the exchange-correlation energy.[352,353] A single Γ point sampling of the Brillouin zone was used. Optimized structures were obtained by minimizing the forces on each atom until they fell below 0.01 eV $Å^{-1}$. Structures were place in a vacuum with at least 9 Å of inter-molecular distance.

Following optimization, single point energies were carried out at a higher level of theory using B3PW91.[267,352–356] These calculations were performed using Gaussian.[263] The LANL2DZ basis set and electron core potential[271–274] was used for the rhodium atom while the 6-31G(d,p)[275–282] basis set was used for the remaining elements.

4.5. REFERENCES

(11) Gilbert, M.; Albinsson, B. *Chem. Soc. Rev.* **2015**, *44*, 845–862.

(12) Heckmann, A.; Lambert, C. *Angew. Chem. Int. Ed.* **2012**, *51*, 326–392.

(96) Barbara, P. F.; Meyer, T. J.; Ratner, M. A. *J. Phys. Chem.* **1996**, *100*, 13148–13168.

(97) Brunschwig, B. S.; Sutin, N. *Coord. Chem. Rev.* **1999**, *187*, 233–254.

(101) Day, P.; Hush, N. S.; Clark, R. J. H. *Philos. Trans. R. Soc. Lond. Math. Phys. Eng. Sci.* **2008**, *366*, 5–14.

(102) Demadis, K. D.; Hartshorn, C. M.; Meyer, T. J. *Chem. Rev.* **2001**, *101*, 2655–2686.

(103) Brunschwig, B. S.; Creutz, C.; Sutin, N. *Chem. Soc. Rev.* **2002**, *31*, 168–184.

(104) Marcus, R. A. *J. Chem. Phys.* **1956**, *24*, 966–978.

(108) Cotton, F. A.; Wilkinson, G.; Murillo, C. A.; Bochmann, M. *Advanced Inorganic Chemistry*, 6th ed.; John Wiley & Sons, 1999.

(111) Carano, M.; Careri, M.; Cicogna, F.; D'Ambra, I.; Houben, J. L.; Ingrosso, G.; Marcaccio, M.; Paolucci, F.; Pinzino, C.; Roffia, S. *Organometallics* **2001**, *20*, 3478–3490.

(113) He, F.; Ruhlmann, L.; Gisselbrecht, J.-P.; Choua, S.; Orio, M.; Wesolek, M.; Danopoulos, A. A.; Braunstein, P. *Dalton Trans.* **2015**, *44*, 17030–17044.

(117) Evans, P. A. *Modern Rhodium-Catalyzed Organic Reactions*; John Wiley & Sons, 2005.

(212) *Crystal Clear, 1.40*; Rigaku Americas Corporation: The Woodlands, Texas, 2008.

(215) Spek, A. L. *PLATON, A Multipurpose Crystallographic Tool.*; Utrecht University: Utrecht University, The Netherlands, 1998.

(216) Farrugia, L. J. *J. Appl. Crystallogr.* **1999**, *32*, 837–838.

(217) Farrugia, L. J. *WinGX an Integrated System of Windows Programs for the Solution, Refinement and Analysis of Single Crystal X-Ray Diffraction Data*; University of Glasgow: Glasgow, U.K., 1999.

(218) In *International Tables for X-Ray Crystallography*; Wilson, A. J. C., Ed.; Kluwer Academic Press: Boston, 1992; Vol. C, p Tables 4.2.6.8 and 6.1.1.4.

(259) *CrysAlisPro, 1.171.37.31*; Agilent Technologies UK Ltd.: Oxford, UK, 2013.

(260) Palatinus, L.; Chapuis, G. *J. Appl. Crystallogr.* **2007**, *40*, 786–790.

(261) Sheldrick, G. M. *Acta Crystallogr. Sect. C Struct. Chem.* **2015**, *71*, 3–8.

(262) Sheldrick, G. M. *SHELXTL/PC*; Siemens Analytical X-ray Instruments, Inc.: Madison, Wisconsin, USA, 1994.

(263) Frisch, M. J.; Trucks, G. W.; Schlegel, H. B.; Scuseria, G. E.; Robb, M. A.; Cheeseman, J. R.; Scalmani, G.; Barone, V.; Mennucci, B.; Petersson, G. A.; Nakatsuji, H.; Caricato, M.; Li, X.; Hratchian, H. P.; Izmaylov, A. F.; Bloino, J.; Zheng, G.; Sonnenberg, J. L.; Hada, M.; Ehara, M.; Toyota, K.; Fukuda, R.; Hasegawa, J.; Ishida, M.; Nakajima, T.; Honda, Y.; Kitao, O.; Nakai, H.; Vreven, T.; Montgomery, J. A., Jr.; Peralta, J. E.; Ogliaro, F.; Bearpark, M.; Heyd, J. J.; Brothers, E.; Kudin, K. N.; Staroverov, V. N.; Kobayashi, R.; Normand, J.; Raghavachari, K.; Rendell, A.; Burant, J. C.; Iyengar, S. S.; Tomasi, J.; Cossi, M.; Rega, N.; Millam, N. J.; Klene, M.; Knox, J. E.; Cross, J. B.; Bakken, V.; Adamo, C.; Jaramillo, J.; Gomperts, R.; Stratmann, R. E.; Yazyev, O.; Austin, A. J.; Cammi, R.; Pomelli, C.; Ochterski, J. W.; Martin, R. L.; Morokuma, K.; Zakrzewski, V. G.; Voth, G. A.; Salvador, P.; Dannenberg, J. J.; Dapprich, S.; Daniels, A. D.; Farkas, O.; Foresman, J. B.; Ortiz, J. V.; Cioslowski, J.; Fox, D. J. *Gaussian 09, Revision B.01*; Gaussian, Inc.: Wallingford, CT, 2009.

(267) Becke, A. D. *J. Chem. Phys.* **1993**, *98*, 5648–5652.

(271) Dunning Jr., T. H.; Hay, P. J. In *Modern Theoretical Chemistry*; Schaefer, H. F., Ed.; Plenum: New York, 1977; Vol. 3, pp 1–28.

(272) Hay, P. J.; Wadt, W. R. *J. Chem. Phys.* **1985**, *82*, 270–283.

(273) Wadt, W. R.; Hay, P. J. *J. Chem. Phys.* **1985**, *82*, 284–298.

(274) Hay, P. J.; Wadt, W. R. *J. Chem. Phys.* **1985**, *82*, 299–310.

(275) Ditchfield, R.; Hehre, W. J.; Pople, J. A. *J. Chem. Phys.* **1971**, *54*, 724–728.

(276) Hehre, W. J.; Ditchfield, R.; Pople, J. A. *J. Chem. Phys.* **1972**, *56*, 2257–2261.

(277) Hariharan, P. C.; Pople, J. A. *Theor. Chim. Acta* **1973**, *28*, 213–222.

(278) Hariharan, P. C.; Pople, J. A. *Mol. Phys.* **1974**, *27*, 209–214.

(279) Gordon, M. S. *Chem. Phys. Lett.* **1980**, *76*, 163–168.

(280) Francl, M. M.; Pietro, W. J.; Hehre, W. J.; Binkley, J. S.; Gordon, M. S.; DeFrees, D. J.; Pople, J. A. *J. Chem. Phys.* **1982**, *77*, 3654–3665.

(281) Rassolov, V. A.; Pople, J. A.; Ratner, M. A.; Windus, T. L. *J. Chem. Phys.* **1998**, *109*, 1223–1229.

(282) Rassolov, V. A.; Ratner, M. A.; Pople, J. A.; Redfern, P. C.; Curtiss, L. A. *J. Comput. Chem.* **2001**, *22*, 976–984.

(300) Otwinowski, Z.; Minor, W. In *Methods in Enzymology, Macrocolecular Cyrstallography, Part A*; Carter Jr., C. W., Sweet, R. M., Eds.; 1997; Vol. 276, pp 307–326.

(301) Creutz, C.; Taube, H. *J. Am. Chem. Soc.* **1969**, *91*, 3988–3989.

(302) Creutz, C.; Taube, H. *J. Am. Chem. Soc.* **1973**, *95*, 1086–1094.

(303) Marcus, R. A. *Discuss. Faraday Soc.* **1960**, *29*, 21–31.

(304) Marcus, R. A. *J. Chem. Phys.* **1965**, *43*, 679–701.

(305) Marcus, R. A. *Rev. Mod. Phys.* **1993**, *65*, 599–610.

(306) Wenger, O. S. *Chem. Soc. Rev.* **2012**, *41*, 3772–3779.

(307) Kaim, W. *Coord. Chem. Rev.* **2011**, *255*, 2503–2513.

(308) Kaim, W.; Bruns, W.; Poppe, J.; Kasack, V. *J. Mol. Struct.* **1993**, *292*, 221–228.

(309) Garner, C. D. *J. Chem. Soc. Dalton Trans.* **1997**, No. 21, 3903–3908.

(310) Ward, M. D. *Chem. Soc. Rev.* **1995**, *24*, 121–134.

(311) *Mixed Valency Systems: Applications in Chemistry, Physics and Biology*; Prassides, K., Ed.; Springer Netherlands: Dordrecht, 1991.

(312) Lorkovic, I. M.; Duff, R. R.; Wrighton, M. S. *J. Am. Chem. Soc.* **1995**, *117*, 3617–3618.

(313) Slone, C. S.; Mirkin, C. A.; Yap, G. P. A.; Guzei, I. A.; Rheingold, A. L. *J. Am. Chem. Soc.* **1997**, *119*, 10743–10753.

(314) Gregson, C. K. A.; Gibson, V. C.; Long, N. J.; Marshall, E. L.; Oxford, P. J.; White, A. J. P. *J. Am. Chem. Soc.* **2006**, *128*, 7410–7411.

(315) Broderick, E. M.; Guo, N.; Vogel, C. S.; Xu, C.; Sutter, J.; Miller, J. T.; Meyer, K.; Mehrkhodavandi, P.; Diaconescu, P. L. *J. Am. Chem. Soc.* **2011**, *133*, 9278–9281.

(316) Arumugam, K.; Varnado, C. D.; Sproules, S.; Lynch, V. M.; Bielawski, C. W. *Chem. – Eur. J.* **2013**, *19*, 10866–10875.

(317) Pandey, K. K. *Coord. Chem. Rev.* **1992**, *121*, 1–42.

(318) DeWit, D. G. *Coord. Chem. Rev.* **1996**, *147*, 209–246.

(319) Smith, D. A.; Herbert, D. E.; Walensky, J. R.; Ozerov, O. V. *Organometallics* **2013**, *32*, 2050–2058.

(320) Salem, H.; Shimon, L. J. W.; Leitus, G.; Weiner, L.; Milstein, D. *Organometallics* **2008**, *27*, 2293–2299.

(321) Feller, M.; Ben-Ari, E.; Gupta, T.; Shimon, L. J. W.; Leitus, G.; Diskin-Posner, Y.; Weiner, L.; Milstein, D. *Inorg. Chem.* **2007**, *46*, 10479–10490.

(322) Doux, M.; Mézailles, N.; Ricard, L.; Le Floch, P.; Adkine, P.; Berclaz, T.; Geoffroy, M. *Inorg. Chem.* **2005**, *44*, 1147–1152.

(323) Gerisch, M.; Krumper, J. R.; Bergman, R. G.; Tilley, T. D. *Organometallics* **2003**, *22*, 47–58.

(324) Balzani, V.; Juris, A.; Venturi, M.; Campagna, S.; Serroni, S. *Chem. Rev.* **1996**, *96*, 759–834.

(325) Jaffe, I. *Rev. Inorg. Chem.* **1993**, *13*, 1.

(326) Carson, C. G.; Gerhardt, R. A.; Tannenbaum, R. *J. Phys. Chem. B* **2007**, *111*, 14114–14120.

(327) Chaplin, A. B.; Weller, A. S. *Organometallics* **2011**, *30*, 4466–4469.

(328) Hanson, S. K.; Heinekey, D. M.; Goldberg, K. I. *Organometallics* **2008**, *27*, 1454–1463.

(329) Feller, M.; Iron, M. A.; Shimon, L. J. W.; Diskin-Posner, Y.; Leitus, G.; Milstein, D. *J. Am. Chem. Soc.* **2008**, *130*, 14374–14375.

(330) Adams, G. M.; Chadwick, F. M.; Pike, S. D.; Weller, A. S. *Dalton Trans.* **2015**, *44*, 6340–6342.

(331) Huang, K.-W.; Grills, D. C.; Han, J. H.; Szalda, D. J.; Fujita, E. *Inorganica Chim. Acta* **2008**, *361*, 3327–3331.

(332) Mark D. Doherty, S. J. K. *J. Organomet. Chem.* **2014**, *762*, 94–97.

(333) Denuault, G.; Mirkin, M. V.; Bard, A. J. *J. Electroanal. Chem. Interfacial Electrochem.* **1991**, *308*, 27–38.

(334) Bard, A. J.; Faulkner, L. R. *Electrochemical Methods: Fundamentals and Applications*; Wiley, 2000.

(335) Dixon, F. M.; Masar, M. S.; Doan, P. E.; Farrell, J. R.; Arnold, F. P.; Mirkin, C. A.; Incarvito, C. D.; Zakharov, L. N.; Rheingold, A. L. *Inorg. Chem.* **2003**, *42*, 3245–3255.

(336) Hetterscheid, D. G. H.; de Bruin, B.; Smits, J. M. M.; Gal, A. W. *Organometallics* **2003**, *22*, 3022–3024.

(337) Montag, M.; Schwartsburd, L.; Cohen, R.; Leitus, G.; Ben-David, Y.; Martin, J. M. L.; Milstein, D. *Angew. Chem. Int. Ed.* **2007**, *46*, 1901–1904.

(338) Vigalok, A.; Uzan, O.; Shimon, L. J. W.; Ben-David, Y.; Martin, J. M. L.; Milstein, D. *J. Am. Chem. Soc.* **1998**, *120*, 12539–12544.

(339) Montag, M.; Efremenko, I.; Cohen, R.; Shimon, L. J. W.; Leitus, G.; Diskin-Posner, Y.; Ben-David, Y.; Salem, H.; Martin, J. M. L.; Milstein, D. *Chem. – Eur. J.* **2010**, *16*, 328–353.

(340) Frank, H. A.; Bautista, J. A.; Josue, J.; Pendon, Z.; Hiller, R. G.; Sharples, F. P.; Gosztola, D.; Wasielewski, M. R. *J. Phys. Chem. B* **2000**, *104*, 4569–4577.

(341) Laguitton-Pasquier, H.; Pansu, R.; Chauvet, J.-P.; Collet, A.; Faure, J.; Lapouyade, R. *Chem. Phys.* **1996**, *212*, 437–455.

(342) Holliday, B. J.; Farrell, J. R.; Mirkin, C. A.; Lam, K.-C.; Rheingold, A. L. *J. Am. Chem. Soc.* **1999**, *121*, 6316–6317.

(343) Kaska, W. C.; Nemeh, S.; Shirazi, A.; Potuznik, S. *Organometallics* **1988**, *7*, 13–15.

(344) Moulton, C. J.; Shaw, B. L. *J. Chem. Soc. Dalton Trans.* **1976**, No. 11, 1020–1024.

(345) Doherty, M. D.; Grills, D. C.; Huang, K.-W.; Muckerman, J. T.; Polyansky, D. E.; van Eldik, R.; Fujita, E. *Inorg. Chem.* **2013**, *52*, 4160–4172.

(346) Kresse, G.; Hafner, J. *Phys. Rev. B* **1993**, *47*, 558–561.

(347) Kresse, G.; Hafner, J. *Phys. Rev. B* **1994**, *49*, 14251–14269.

(348) Kresse, G.; Furthmüller, J. *Comput. Mater. Sci.* **1996**, *6*, 15–50.

(349) Kresse, G.; Furthmüller, J. *Phys. Rev. B* **1996**, *54*, 11169–11186.

(350) Blöchl, P. E. *Phys. Rev. B* **1994**, *50*, 17953–17979.

(351) Kresse, G.; Joubert, D. *Phys. Rev. B* **1999**, *59*, 1758–1775.

(352) Perdew, J. P.; Chevary, J. A.; Vosko, S. H.; Jackson, K. A.; Pederson, M. R.; Singh, D. J.; Fiolhais, C. *Phys. Rev. B* **1992**, *46*, 6671–6687.

(353) Perdew, J. P.; Chevary, J. A.; Vosko, S. H.; Jackson, K. A.; Pederson, M. R.; Singh, D. J.; Fiolhais, C. *Phys. Rev. B* **1993**, *48*, 4978–4978.

(354) Perdew, J. P. In *Electronic Structure of Solids '91*; Ziesche, P., Eschrig, H., Eds.; Akademie Verlag: Berlin, 1991; p 11.

(355) Perdew, J. P.; Burke, K.; Wang, Y. *Phys. Rev. B* **1996**, *54*, 16533–16539.

(356) Dobson, J. F.; Vignale, G.; Das, M. P.; Burke, K.; Perdew, J. P.; Wang, Y. In *Electronic Density Functional Theory: Recent Progress and New Directions*; Springer Science & Business Media, 2013.

Chapter 5: Probing the Triplet Excited State of Oligothiophenes with Transient Resonance Raman Spectroscopy

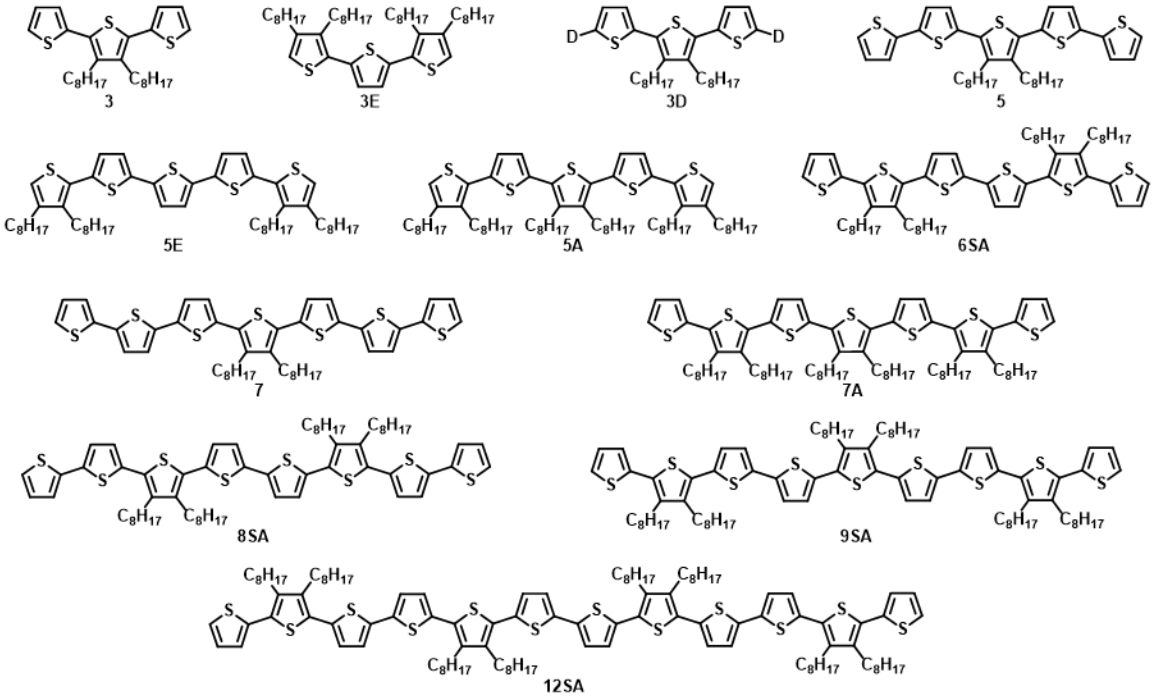

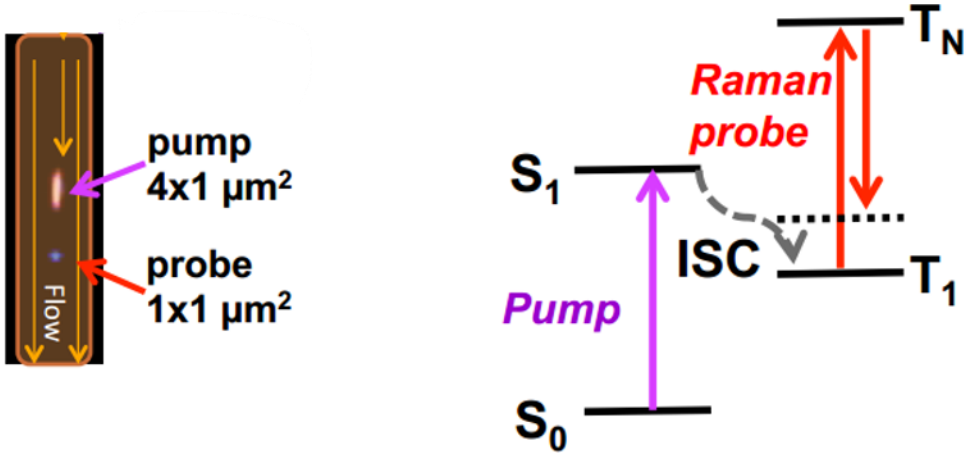

5.1. INTRODUCTION

The interesting electrochemical and photophysical properties of thiophene based materials have led to their application in a wide variety of fields.[357–359] In particular, thiophene-based chains have played a large role in the development of organic photovoltaic (OPV) devices due to their excellent charge carrier mobilities relative to most organic semiconductors.[164,165,167,168] As a result, the fundamental structure-property relationships of these materials have been well documented, including information about the excited state properties. [360–362]

One area of polythiophene-based research which remains a contentious topic is concerning the structure and delocalization of the triplet-excitons (triplet-excited state) in these oligomeric or polymeric materials.[363–369] Such a question is of interest as triplet-excitons possess many qualities which, when utilized properly, are advantageous to the field of OPVs.[148,370] For example, the collection of excitons as current requires diffusion of the exciton to an interface between the p-type and n-type materials before the exciton may be split into independent charge carriers. Singlet-excitons have diffusion lengths that are on the order of tens of nanometers which greatly limits the thickness of the absorbing active layers, limiting photon collection and complicating device fabrication. Triplet-excitons, however, have diffusion lengths on the order of tens of micrometers, and no theoretical limit is found for their diffusion length due to the Dexter energy transfer mechanism by which triplet excitons tend to operate, allowing for much thicker active layers.[156] Further interest into the structure of the triplet state has been generated in recent years with reports of singlet fission[159] in polythiophene and quinoidal bithiophene.[371] A proper understanding of the extent of delocalization of the triplet-excited state and the resulting effects on the structure of the affected thiophene rings is necessary for the development of more efficient OPV devices.

Literature reports on the structure and delocalization of the triplet excited state in oligo-and polythiophene-based materials have provided mixed results. Beljonne *et al*.[360] reported a delocalization across one to two thiophene rings for the triplet excited state with the formation of a strongly bound soliton-antisoliton pair which has been supported by alternative literature reports.[372,373] However, Bennati *et al*.[374] suggested delocalization lengths of approximately four thiophene rings while Monkman *et al*.[375] propose a delocalization up to six repeat units.

Transient Resonance Raman spectroscopy (Figure 5.1) is a powerful technique for probing the structure of these molecules in the excited state.[376] A more recent study from Michael Tabuer's research group at the University of California - San Diego probed the triplet excited states of four- and six-membered oligothiophenes, concluding that complete delocalization of the triplet excited state requires a minimum of five thiophene rings.[377] Density functional theory (DFT) results from these studies provided key insights into the effect of the excited state on the structure of these materials. To further investigate the delocalization of the triplet excited state and its structure, collaborative work with the Tauber group has been undertaken, and a series of oligothiophenes has been synthesized to elucidate new information regarding this topic.

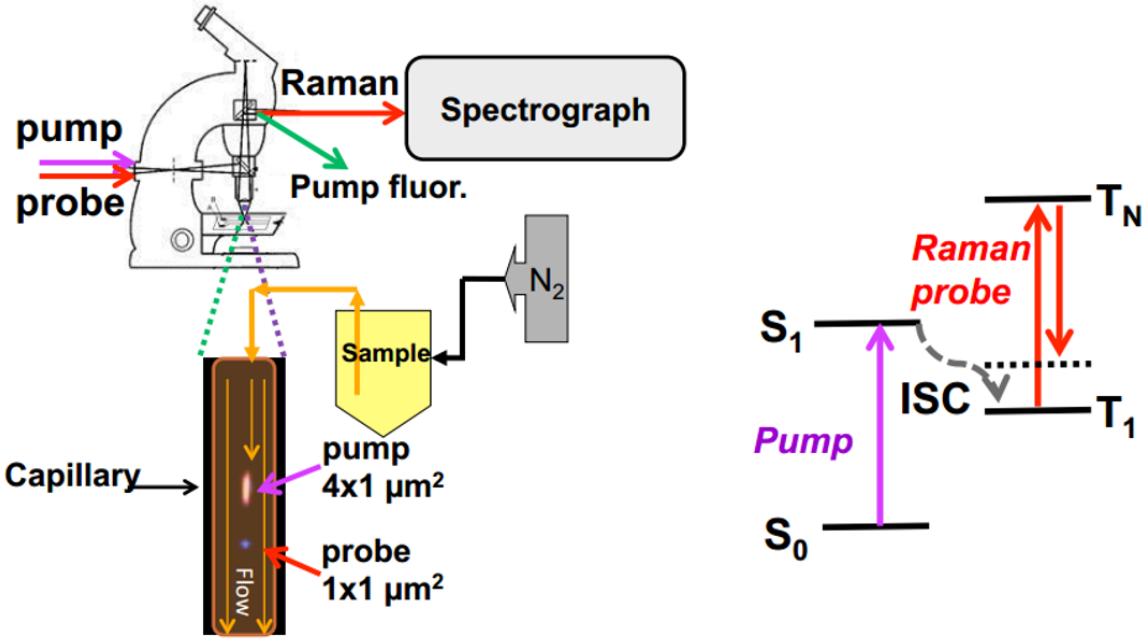

Figure 5.1. Diagram of the experimental setup for transient Raman spectroscopy. A N_2 driven flow cell pumps the sample through a capillary where the sample is excited to a higher electronic state using a pump laser and then, following a pre-determined time delay, a spatially separated probe laser is used to record the spectrum of the excited state.

5.2. Results and Discussion

5.2.1. Synthesis of Oligothiophenes

The study of polymeric materials can often be somewhat difficult due to practical concerns such as solubility, polydispersity and region-regularity. Therefore, to facilitate fundamental studies into the nature of the triplet-excited states, a series of oligothiophenes of controlled lengths and substitution have been synthesized (Scheme 5.1).

Scheme 5.1. Target oligomers.

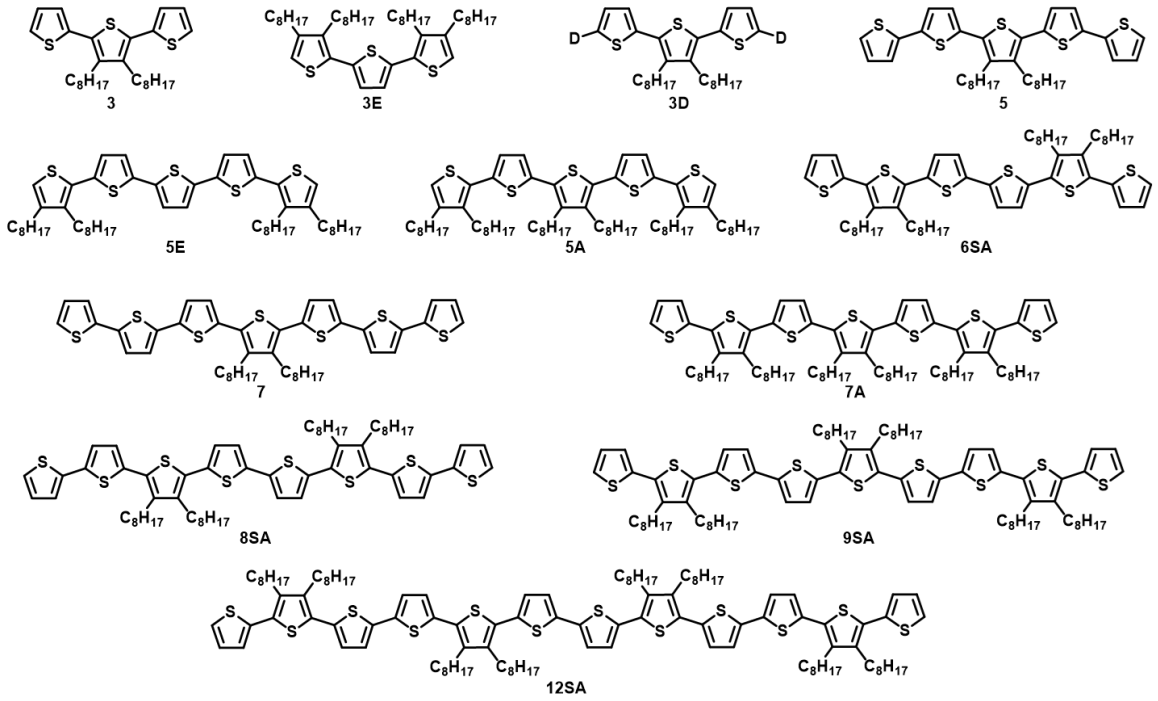

The synthesis of the proposed series began with the generation of several key building blocks consisting of a single substituted thiophene ring (Scheme 5.2).

Scheme 5.2. Synthesis of substituted thiophene rings.

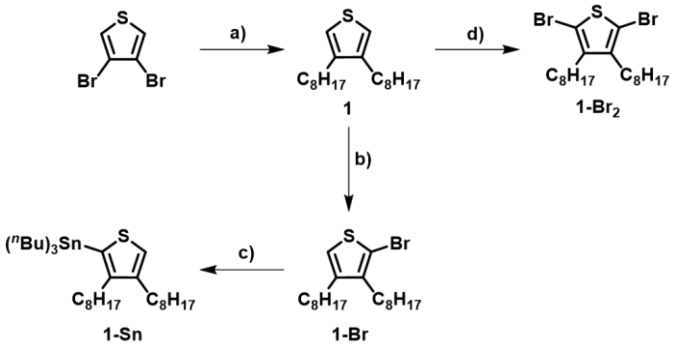

a) (i) 0.07 $Ni(dppp)Cl_2$, 2.4 $C_8H_{17}MgBr$, Et_2O, 0 °C, 2 h; (ii) Et_2O, 0 °C - reflux, overnight, 78%. b) (i) 1 NBS, DMF, 0 °C, 2 h; (ii) DMF, 0 °C - rt, overnight, 68%. c) (i) 1.2 Mg, THF, reflux, 4 h; (ii) 1 $(^nBu)_3SnCl$, THF, –78 °C - rt, overnight, 84%. d) 2 NBS, DMF, 0 °C, 2 h; (ii) DMF, 0 °C - rt, overnight, 98%.

Following literature procedures,[378] 3,4-dioctylthiophene (**1**) was synthesized via a Kumada coupling with octylmagnesium bromide using $Ni(dppp)Cl_2$ (dppp = 1,3-Bis(diphenylphosphino)propane) as the catalyst. From here, the product was split into two synthetic pathways. The addition of one equivalent of *N*-bromosuccinimide (NBS) to **1** led to the generation of 2-bromo-3,4-dioctylthiophene (**1-Br**) which was subsequently converted to tributyl(3,4-dioctylthiophen-2-yl)stannane (**1-Sn**) via *in situ* generation of the Grignard using Mg turnings and quenching with $(^nBu)_3SnCl$. The second portion of **1** was reacted with two equivalents of NBS to form 2,5-dibromo-3,4-dioctylthiophene (**1-Br2**).

Moving forward with **1-Br** and **1-Sn**, the synthesis of 3',4'-dioctyl-2,2':5',2''-terthiophene (**3**) and 3,3'',4,4''-tetraoctyl-2,2':5',2''-terthiophene (**3E**) may be achieved (Scheme 5.3).

Scheme 5.3. Synthesis of **3** and **3E**.

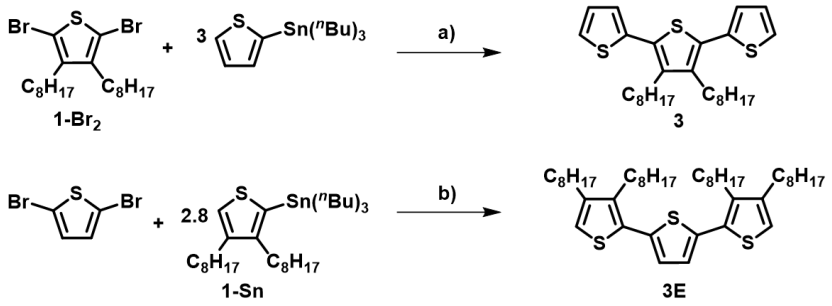

a) 5 LiCl, 0.054 $PdCl_2(PPh_3)$, DMF, 150 °C, overnight, 85%. b) 5 LiCl, 0.054 $PdCl_2(PPh_3)_2$, DMF, 150 °C, overnight, 66%.

For both oligomers **3** and **3E**, a Stille coupling using $PdCl_2(PPh)_3$ as the catalyst was used to accomplish the aryl-coupling reaction with each product being isolated as a viscous green oil. Oligomer **3** was then used for further synthetic purposes as it was either mono- or di-brominated using NBS (Scheme 5.4) to form 5-bromo-3',4'-dioctyl-2,2':5',2"-terthiophene (**3-Br**) and 5,5"-dibromo-3',4'-dioctyl-2,2':5',2"-terthiophene (**3-Br2**), respectively. A portion of **3-Br** was then converted to (3',4'-dioctyl-[2,2':5',2"-terthiophen]-5-yl)boronic acid (**3-BA**) for use in the synthesis of larger oligomers.

Scheme 5.4. Synthesis of **3-Br** and **3-Br2**.

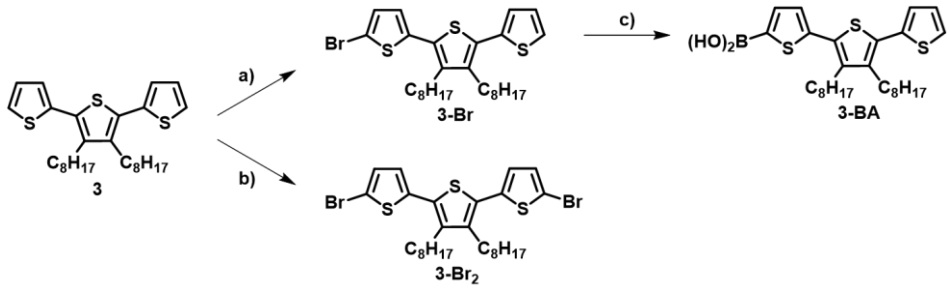

a) (i) 1 NBS, DMF, 0 °C, 2 h; (ii)DMF, 0 °C - rt, overnight, 71%. b) (i) 2 NBS, DMF, 0 °C, 2 h; (ii) DMF, 0 °C - rt, overnight, 85%. C) (i) 1.5 Mg, THF, reflux, 5 h; (ii) 2 $B(OCH_3)_3$, THF, –78 °C, 1 h; (iii) THF, –78 °C - rt, overnight; (iv) xs 10% HCl, THF, 0 °C, 1 h, 78% (crude).

The generation of **3-Br$_2$** was a useful synthetic branching point, being one step away from four target oligomers (Scheme 5.5). Di-lithiation of **3-Br$_2$** with *n*-butyllithium (*n*-BuLi) followed by quenching with D_2O generates oligomer **3D** which is to be used as a check on the peak assignments of the Raman spectroscopy.

Scheme 5.5. Synthesis of **3D**, **5A**, **7** and **9SA**.

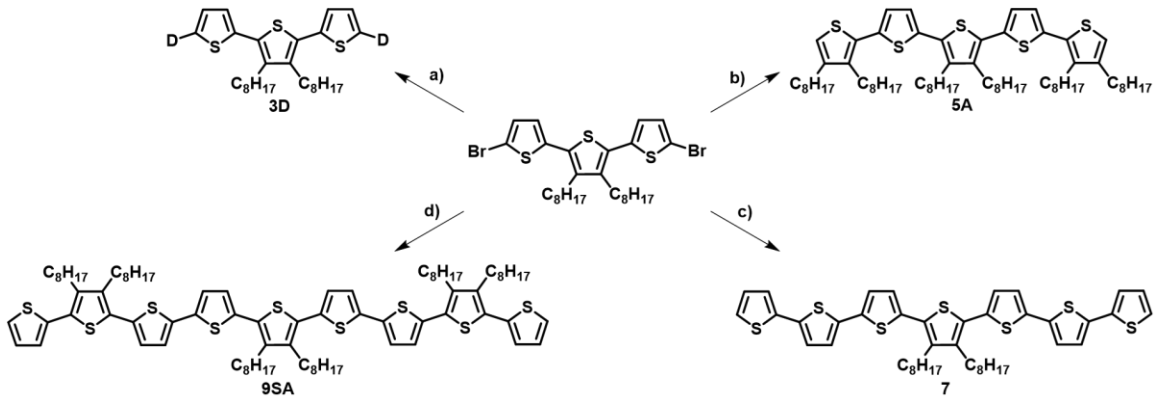

a) (i) 2.1 *n*-BuLi, THF, –78°C - rt, 30 min; (ii) 40 D_2O, THF, –78°C - rt, overnight, 62%. B) 5 LiCl, 2.8 **1-Sn**, 0.054 $PdCl_2(PPh_3)$, DMF, 150 °C, overnight, 52%. C) 5 LiCl, 2.8 [2,2'-bithiophen]-5-yltributylstannane, 0.054 $PdCl_2(PPh_3)_2$, DMF, 150 °C, overnight, 41%. d) 2.4 **3-BA**, 5 Na_2CO_3, 0.1 $Pd(PPh_3)_4$, THF/H_2O (3:1), 0 °C - 80 °C, 4 h, 60%.

Stille coupling of **3-Br$_2$** with **1-Sn** and [2,2'-bithiophen]-5-yltributylstannane generated the final products 3,3"",3"",4,4",4""-hexaoctyl-2,2':5',2":5",2"':5"',2""-quinquethiophene (**5A**) and 3"',4"'-dioctyl-2,2':5',2":5",2"':5"',2"":5"",2""':5""',2"""-sepithiophene (**7**), respectively, while 3',3"",3"""",4',4"",4""'-hexaoctyl-2,2':5',2":5",2"':5"',2"":5"",2""':5""',2"""-novithiophene (**9SA**) was synthesized via a Suzuki coupling with **3-BA**.

The series of oligothiophenes containing five thiophene rings was completed as shown in Scheme 5.6. Stille coupling of **1-Br$_2$** with [2,2'-bithiophen]-5-yltributylstannane generates **5** while **5E** was prepared by coupling **1-Sn** with 5,5''-dibromo-2,2':5',2''-terthiophene.

Scheme 5.6. Synthesis of **5** and **5E**.

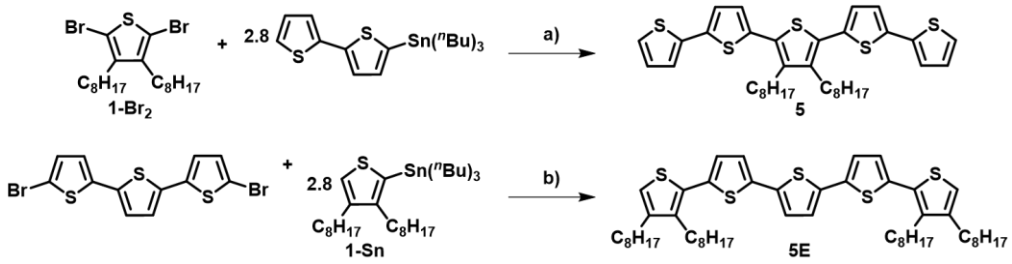

a) 5 LiCl, 0.054 $PdCl_2(PPh_3)_2$, DMF, 150 °C, overnight, 74%. b) 5 LiCl, 0.054 $PdCl_2(PPh_3)_2$, DMF, 150 °C, overnight, 54%.

The final odd-numbered oligothiophene, 3',3''',3'''',4',4''',4''''-hexaoctyl-2,2':5',2'':5'',2''': 5''',2'''':5''',2'''':5'''',2''''':-sepithiophene (**7SA**), was synthesized via the dibromination of **5A** followed by a Stille coupling with **1-Sn** (Scheme 5.7).

Scheme 5.7. Synthesis of **7A**.

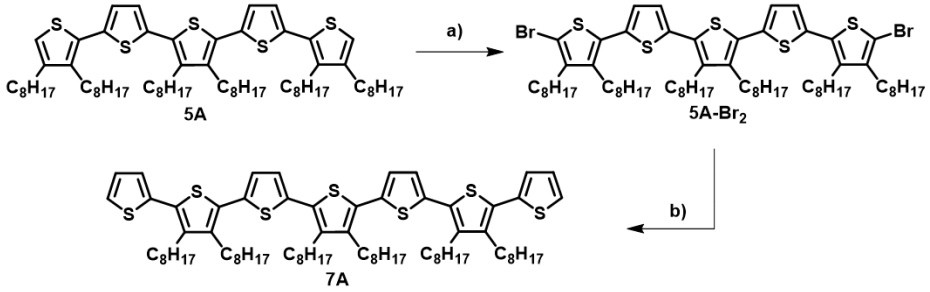

a) 2 NBS, DMF, 0 °C, 2 h; (ii) DMF, 0 °C - rt, overnight, 46%. b) 2.8 2-tributyl(thiophen-2-yl)stannane, 5 LiCl, 0.054 $PdCl_2(PPh_3)_2$, DMF, 150 °C, overnight, 43%.

Synthesis of the even-numbered oligomer chains, as shown in Scheme 5.8, began with the Suzuki coupling of **3-Br** and **3-BA** resulting in 3',3'''',4',4''''-tetraoctyl-2,2':5',2'':5'',2''':5''',2'''':5''',2''''-sexithiophene (**6SA**). Dibromination of **6SA** followed by a Stille coupling with 2-tributyl(thiophen-2-yl)stannane generated oligomer 3'',3''''',4'',4'''''-tetraoctyl-2,2':5',2'':5'',2''':5''',2'''':5''',2''''':5''''',2''''''-octithiophene (**8SA**) while a Suzuki coupling with **3-BA** produced 3',3'''',3''''''',3''''''''',4',4'''',4''''''',4''''''''-octaoctyl-

2,2':5',2":5",2"':5"',2"":5"",2""':5""',2""":5""",2"""':5"""',2""""":"""",2"""""':5"""""',2""""""':5""""""',2"""""""':5"""""""',2

"""""""""-dodecithiophene **12SA**.

Scheme 5.8. Synthesis of **6SA**, **8SA** and **12SA**

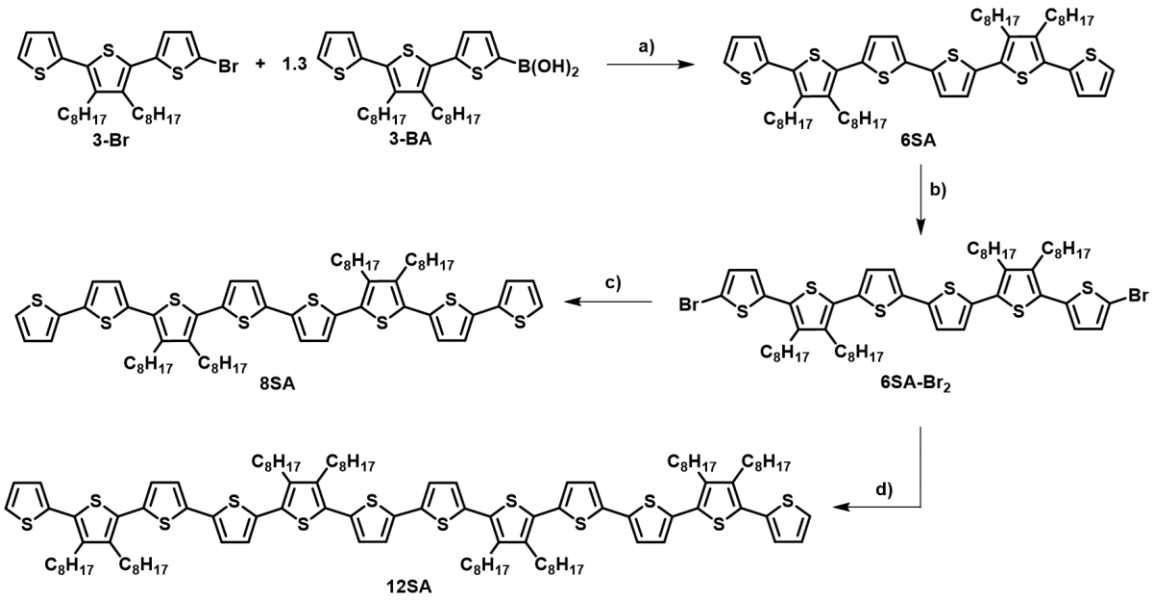

a) 5 Na_2CO_3, 0.1 $Pd(PPh_3)_4$, THF/H_2O (3:1), 0 °C - 80 °C, 6 h, 94%. b) (i) 2 NBS, DMF, 0 °C, 2 h; (ii) DMF, 0 °C - rt, overnight, 96%. c) 2.25 2-tributyl(thiophen-2-yl)stannane, 5 LiCl, 0.054 $PdCl_2(PPh_3)_2$, DMF, 150 °C, 24 h, 20%. d) 2.4 **3-BA**, 5 Na_2CO_3, 0.1 $Pd(PPh_3)_4$, THF/H_2O (3:1), 0 °C - 80 °C, 6 h, 48%.

5.2.2. Photophysical Properties

Electronic absorption spectra of the oligothiophenes display predictable tends. Increasing the chain length leads to a redshift in the absorption profiles with a concomitant increase in the full width half max of the absorption peak (Figure 5.2).

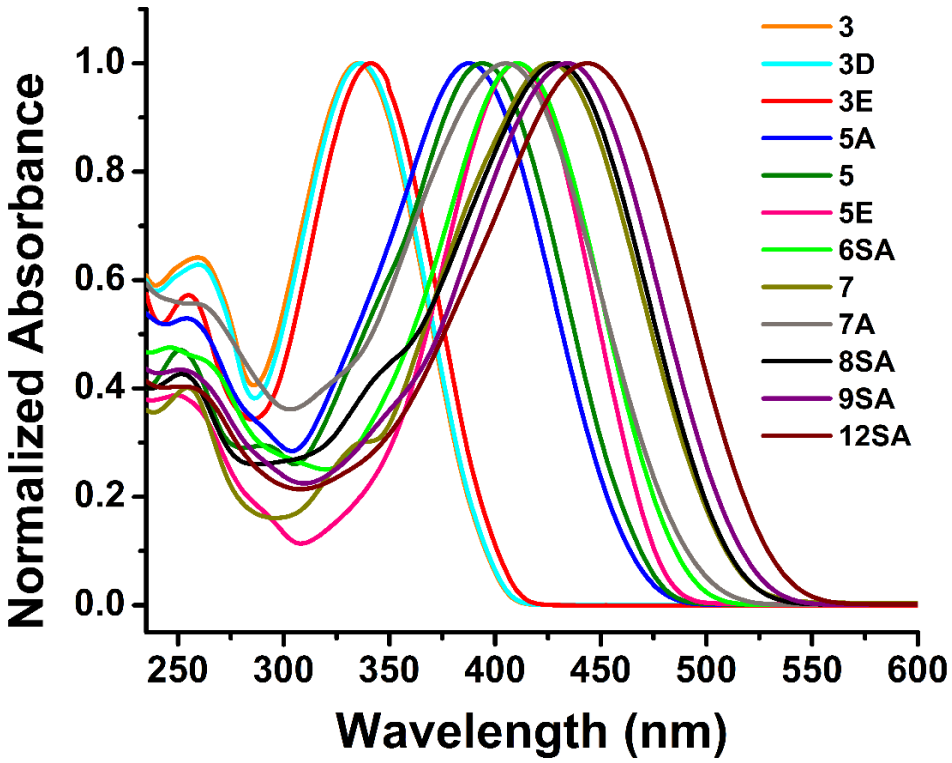

Figure 5.2. Normalized absorption profiles of the oligothiophene series taken in CH_2Cl_2.

Similar trends are observed in the fluorimetry profiles when moving to longer lengths. Increasing the chain lengths redshifts the emission profiles and broadens emission profile (Figure 5.3). It is interesting to note that the three-membered series of complexes has an increased intensity (0,1) band relative to the (0,0) band which is opposite that of the remaining series. A list of the absorbance, excitation and emission peaks may be found in table 1.

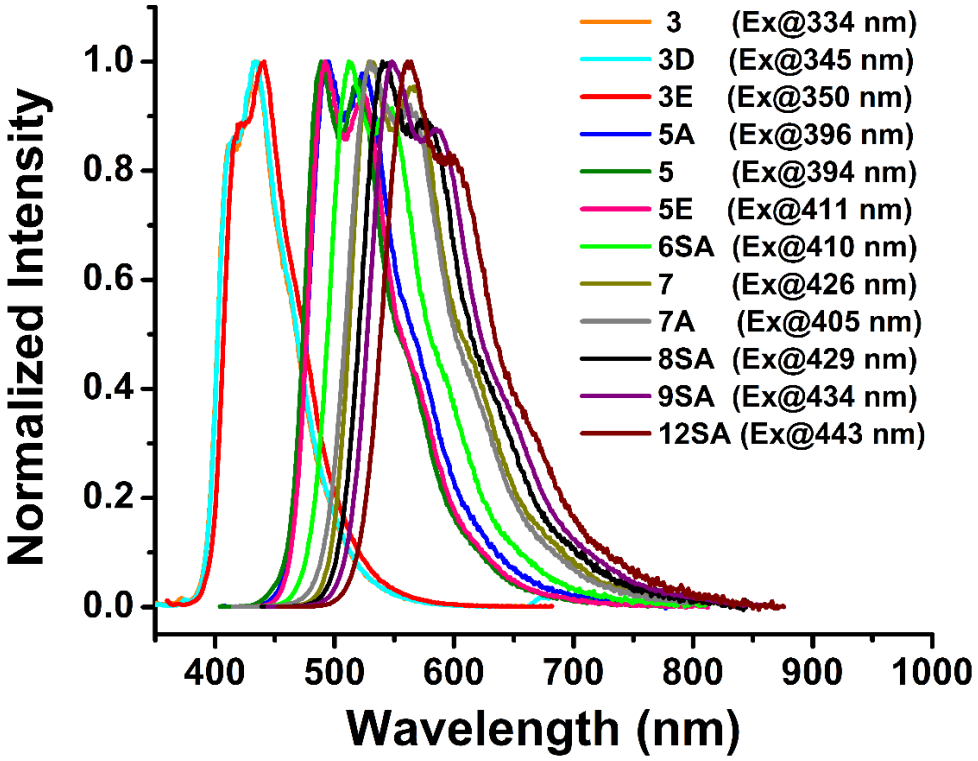

Figure 5.3. Emission profiles of the oligothiophene series taken in solution in CH_2Cl_2. Optical densities of the oligomer solutions are approximately 0.1.

Table 5.1. UV-Vis Absorption and Fluorimetry Profiles

	$\lambda_{absorbance}$ (nm)	ε_{max} (M^{-1} cm^{-1})	$\lambda_{emission}$ (nm)	$\lambda_{excitation}$ (nm)	Band Gap (eV)
3	259, **335**	15763	414, **435**	345	3.09
3D	260, **336**	15609	414, **435**	345	3.07
3E	256, **341**	17687	421, **439**	350	3.02
5A	254, 287, **387**	36541	**493**, 525	396	2.62
5	251, 290, **395**	32705	**489**, 520	394	2.59
5E	249, 291, **410**	43903	**492**, 527	411	2.58
6SA	246, 262, **410**	35026	**512**, 544	410	2.48
7	255, 335, **426**	56391	**529**, 566	426	2.39
7A	256, 335, **405**	35699	**530**, 563	405	2.43
8SA	252, 345, 4**29**	50443	**540**, 574	429	2.38
9SA	252, **434**	67940	**548**, 585	434	2.35
12SA	252, 4**44**	97553	**561**, 597	443	2.3

*The maximum absorption and emission peaks are shown in bolded text. The reported molar absoptivites correspond to the peak absorption maxima.

Comparing the peak absorbance wavelength of the lowest energy transition to the inverse of the number of thiophene rings should exhibit a linear trend according to simple molecular orbital theory arguments.[379] Such relationships have been observed in the literature.[360,375,379] Plots of the peak absorbance wavelength, as well as the wavelength of maximum emission intensity versus the inverse number of rings, may be found in Figure 5.4.

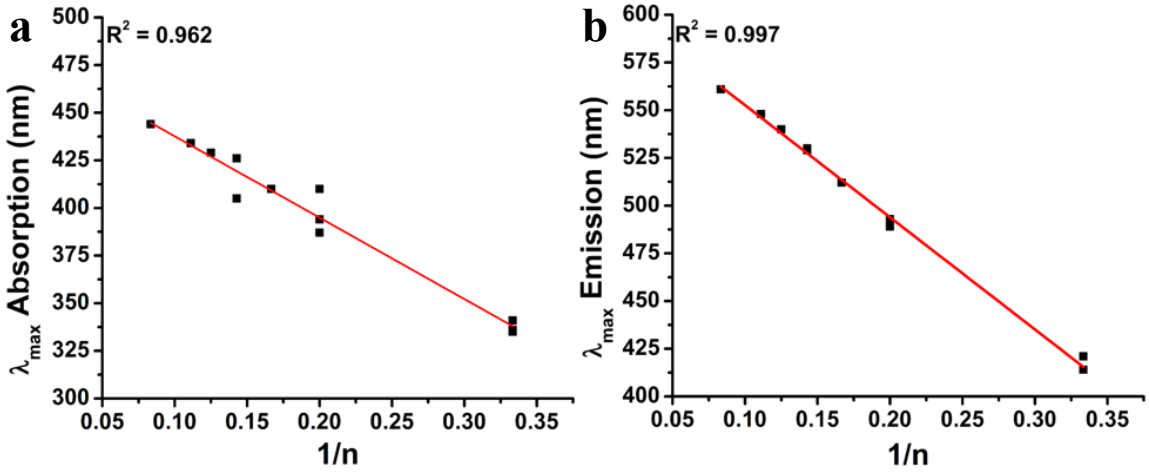

Figure 5.4. A linear trend is observed when a) the wavelength of maximum absorption and b) the wavelength of maximum emission is plotted versus the inverse of the number of thiophene rings (n).

Comparison of the trends reveals a better linear trend for the emission maxima compared to the absorption maxima, especially when comparing the values for oligomers containing the same number of thiophene rings but different numbers and substitution patterns for the octyl-chains. This indicates that the excited state properties are less affected by the alkyl-substituents than the ground state. It is expected that the driving force of stabilizing the charge-separated excited state overpowers the steric interactions of the octyl-chains. Inspection of the deviation within the linear absorption plot reveals no general trend with the number of alky substituents. However, when considering

substitution patterns, the data shows that when more unsubstituted thiophene units are connected before being interrupted by a substituted ring, the longer the wavelength of absorption; this is likely due to increased conjugation effects. Theoretically, the y-intercept of the inverse plots should correspond to a polymer of infinite length.[360] Carrying out this analysis gives an absorption maximum for a thiophene-based polymer at 480 nm with a maximum of emission at 611 nm. This compares favorably with literature reports of alkylated polythiophenes which reports a maxima of absorption near 500 nm.[166]

To more clearly visualize the effects of the octyl-chain substitution patterns on the photophysical properties, comparative graphs of the absorbance and fluorescence profiles of the series containing 3, 5 and 7 thiophene rings are shown in Figure 5.5. From these direct comparisons, it is observed that the emission spectra of the complexes change very little with respect to the degree and pattern of substitution. In the absorption spectra, which have already been shown to be more sensitive to the alkyl substituents, variations are more evident. In the three ring systems, only minimal perturbations are observed. However, in the five series, a drastic deviation in the spectra of **5E** is observed when compared to **5** and **5A**.

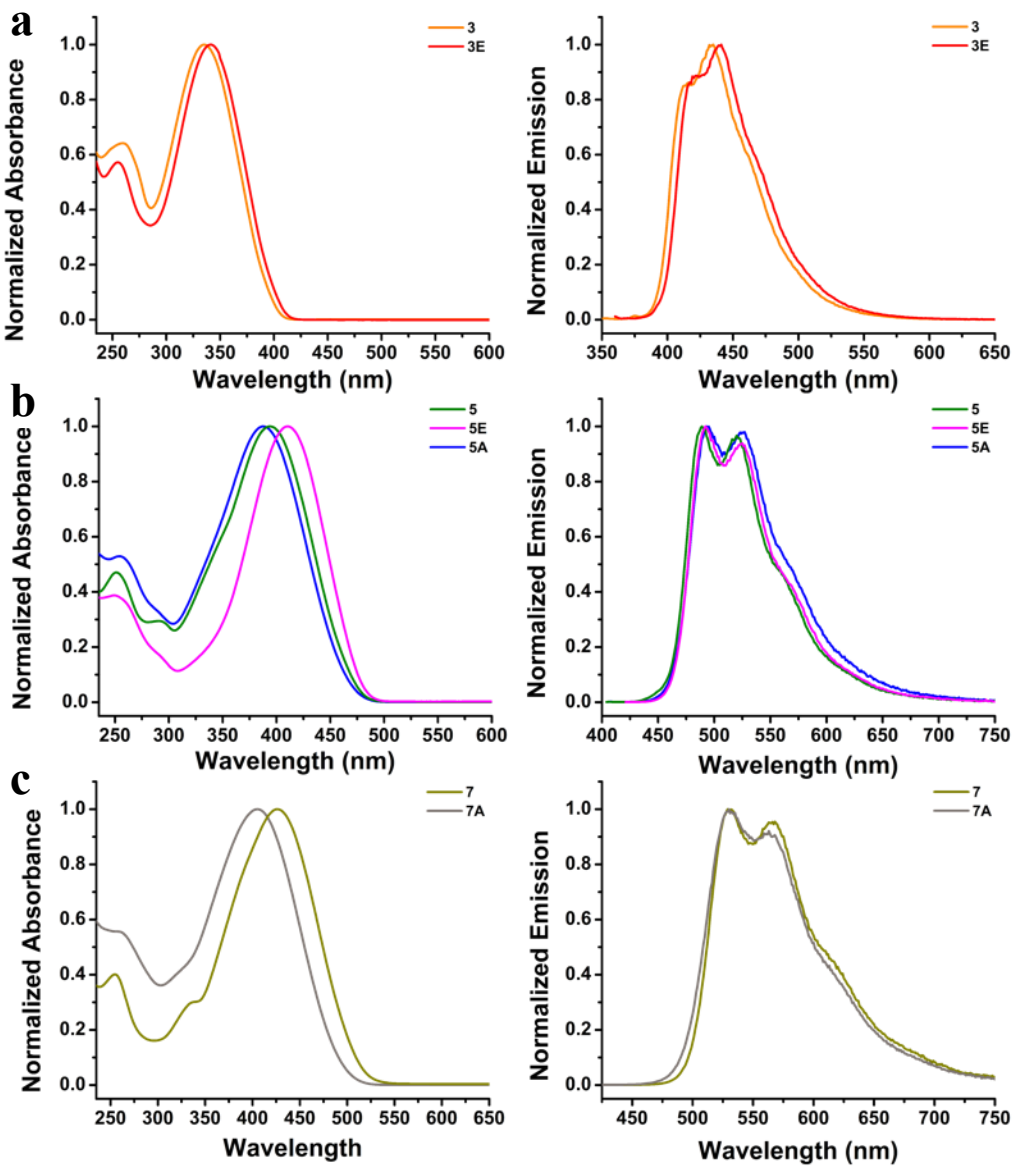

Figure 5.5. Comparison of the absorption (left column) and emission (right column) of a) the three-ring series, b) the five-ring series and c) the seven-ring series.

Most notably, the full width half max of **5E** decreased by 20 nm to a value of 80 nm, compared to approximately 100 nm for **5** and **5A.** Such a change suggests that the number of conformations available to **5E** is restricted. A possible explanation for this

phenomenon is the lack of interference in the conformation of the central three-ring core, which allows for the material to exist in a narrower conformational range. Within all of the comparative series, it was observed that disrupting the number of unsubstituted thiophenes connected to one another with substituted thiophene rings leads to a blueshift in the onset of absorbance.

5.2.3. Electrochemical Studies

The electrochemical properties of the series were investigated by cyclic voltammetry (CV) (Figure 5.6) and differential pulse voltammetry (DPV) (Figure 5.7). Oligomers **3** and **3E** display only a single oxidative event while **5**, **5E**, **5A** and **6SA** display two distinct and highly reversible oxidations. As the conjugation is extended, more oxidation events become accessible as the systems may now accommodate more charge. Oligomers **7** and **7A** display a third irreversible redox event with peak oxidative potentials (E_{pa}) of 1.12 V and 1.11 V, respectively. Four oxidation events are evident in the cyclic voltammogram of **8SA**, with the first two reversible oxidations beginning to coalesce and two irreversible oxidations occurring at 1.02 V and 1.12 V.

Similarly, **9SA** displays four oxidations as well. However, in addition to the first two reversible oxidations events, a third reversible oxidation is observed at $E_{1/2}$ = 0.69 V with a fourth irreversible peak coming at 1.02 V. The longest member of the series, **12SA**, exhibits five oxidations with the first two reversible oxidations coalesced at a cumulative $E_{1/2}$ = 0.27 V. The second two oxidations events are also reversible and have coalesced at a cumulative $E_{1/2}$ = 0.55 V.

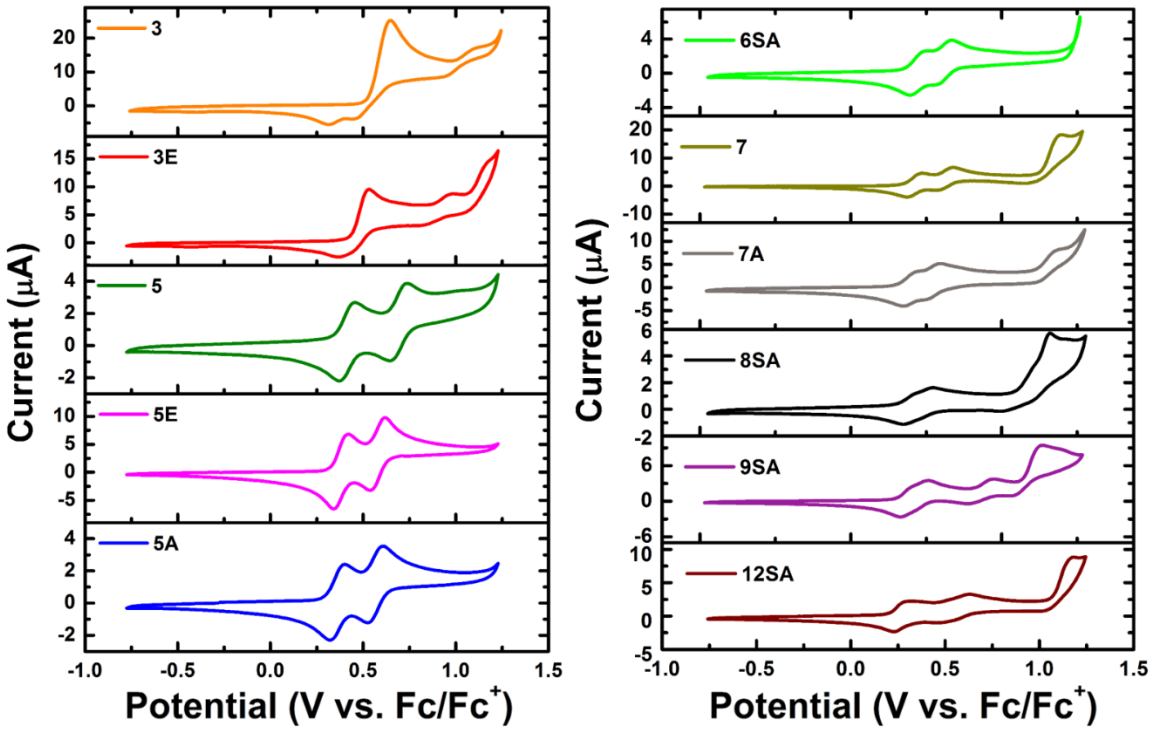

Figure 5.6. Cyclic voltammograms taken in CH_2Cl_2 containing 0.1 M $TBAPF_6$ using a 3 electrode system with a glassy carbon button (3.0 mm) working electrode, a platinum wire counter electrode and a $Ag/AgNO_3$ reference electrode. All potentials were corrected to ferrocene/ferrocenium redox couple measured as an external standard.

When inspecting the first two reversible oxidations events in the five- through twelve-membered ring series, a general decrease in the potential separation of the first and second anodic events is observed, indicating a greater stabilization of the electrochemically generated hole as the change length is increased.

The DPVs (Figure 5.7) of the oligothiophene series present a clearer picture of the electrochemistry, particularly when analyzing the voltammograms of oligomers longer than seven thiophene rings. Oligomers **3** and **3E** exhibit only one pertinent anodic peak in the DPV while the five-member ring systems show two well resolved oxidations which integrate to an approximate 1:1 ratio, indicating an equivalent number of electrons

transferred. Three oxidations are observed within the electrochemical window of CH_2Cl_2 for **6SA**, **7** and **7A** while four oxidations are observed in **8SA** and **9SA** and six are observed in **12SA**. Similar to the trends observed via cyclic voltammetry, increasing the oligothiophene chain length decreased the oxidation potential of the observed events as well as decreasing the potential separation between the first two electrochemical oxidations (Table 5.2).

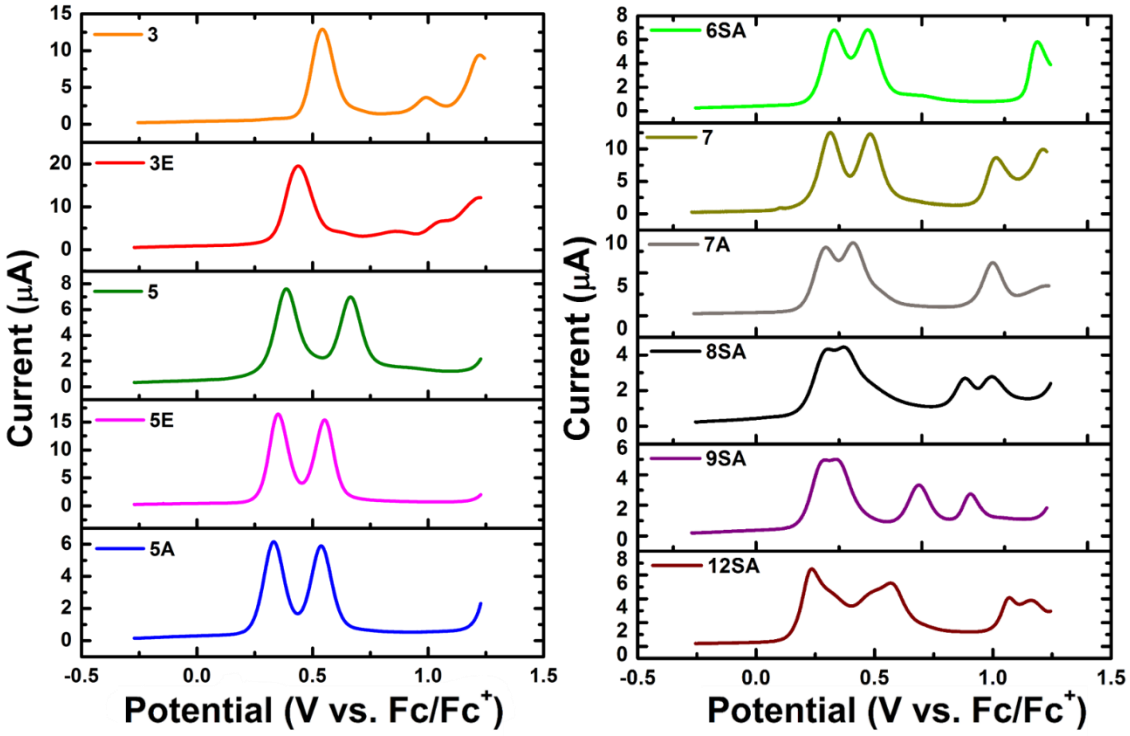

Figure 5.7. Differential pulse voltammograms taken in CH_2Cl_2 containing 0.1 M $TBAPF_6$ using a 3 electrode system as described in Figure 5.6. All potentials were corrected to ferrocene/ferrocenium redox couple measured as an external standard. A modulation amplitude of 0.050 V was employed.

Table 5.2. Electrochemical Measurements

	Cyclic Voltammetry				Differential Pulse Voltammetry		
	E_{on} (V)	$E_{1/2,1}$ (V)	$E_{1/2,2}$ (V)	$\Delta E_{1/2}$ (V)	E_{p1} (V)	E_{p2} (V)	ΔE_p (V)
3*	0.51	0.65	-	-	0.54	-	-
3E*	0.43	0.53	-	-	0.44	-	-
5A	0.29	0.36	0.56	0.20	0.33	0.54	0.21
5	0.35	0.41	0.69	0.28	0.39	0.67	0.28
5E	0.32	0.38	0.58	0.20	0.35	0.55	0.20
6SA	0.29	0.36	0.50	0.14	0.33	0.47	0.14
7	0.28	0.34	0.50	0.16	0.31	0.48	0.17
7A	0.25	0.32	0.44	0.12	0.30	0.41	0.11
8SA	0.25	0.31	0.39	0.08	0.30	0.37	0.07
9SA	0.24	0.29	0.38	0.09	0.29	0.34	0.05
12SA†	0.20	0.27	-	-	0.24	0.29	0.05

*Only an irreversible oxidation is observed. The potential of the oxidative peak current is reported. †First and second oxidation events have coalesced into a single peak in the cyclic voltammogram. The reported potential is for the cumulative $E_{1/2}$.

Direct comparison of the CVs and DPVs of the three-, five-, and seven-membered oligothiophene series allows for the elucidation of the effects of the number and substitution pattern of octyl-chains on the electrochemical properties of the materials (Figure 5.8). From these comparisons, it is observed that increasing the number of octyl-chains leads to a decrease in the oxidation potential within a series. In regards to substitution pattern, a greater peak-to-peak separation of the anodic events is realized when the only the center thiophene ring is substituted. While a decrease in the peak-to-peak separation indicates an increased propensity for charge stabilization as you increase chain length, within a series of the same length, such an observation suggests better electronic communication within the system. Following electrochemical oxidation, planarization of the ring systems is expected to occur to stabilize the electrochemically generated hole. For **5** and **7**, it is reasonable to expect that the oxidations occur on

opposite sides of the octyl-substituted ring due to coulombic repulsion of the holes generated during the electron transfer process. Therefore, the lack of octyl-chains substituted on the outer thiophene rings to hinder rotation and planarization allows the process to occur more efficiently in these systems.

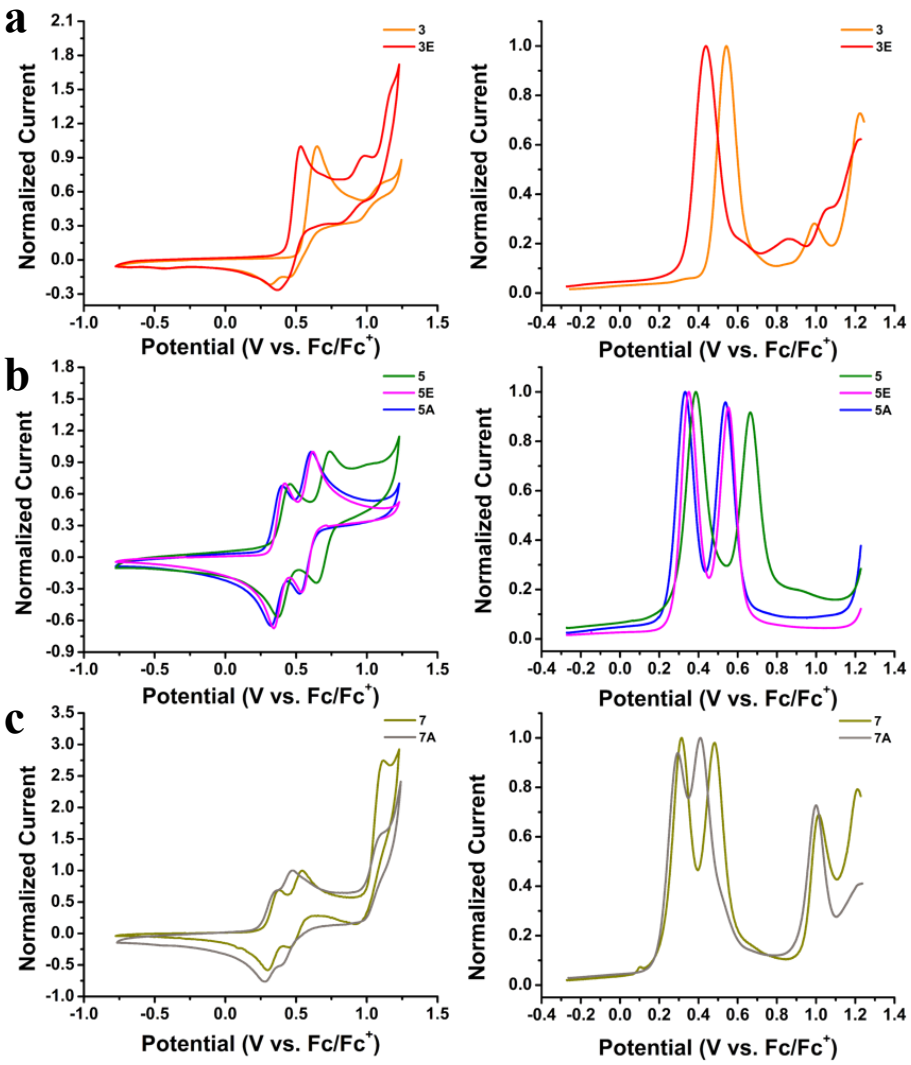

Figure 5.8. Comparison of the cyclic voltammograms (left column) and differential pulse voltammograms (right column) of a) the three-ring series, b) the five-ring series and c) the seven-ring series.

Using the red edge of absorption from the UV-Vis and the onset of electrochemical oxidation from the cyclic voltammogram, the optical band gap and frontier energy levels of the oligothiophenes may be calculated.[254] Looking specifically at the energy levels and the optical band gap, the linear trends with respect to the inverse of n still hold true (Figure 5.9). Proper matching of the highest occupied molecular orbital (HOMO) and the lowest unoccupied molecular orbitals (LUMO) of the polythiophene based materials in an OPV device with HOMO and LUMO of the adjacent active materials is an important parameter for optimizing device efficiency, charge separation and open circuit voltages.[147] Therefore, cataloging these values is of use for OPV design. As previously mentioned, the y-intercept of the linear trends should correspond to a thiophene-based polymer of infinite length. Performing this analysis predicts an optical band gap of 1.98 eV. Using the electrochemical and photophysical trends, a HOMO level of –4.88 eV and a LUMO level of –2.94 eV is predicted resulting in a band gap of 1.94 eV. Once again, these results compare favorably with literature reports for polyalkylthiophenes, which have band gaps that commonly fall in the 1.7 - 2.2 eV range.[147,380]

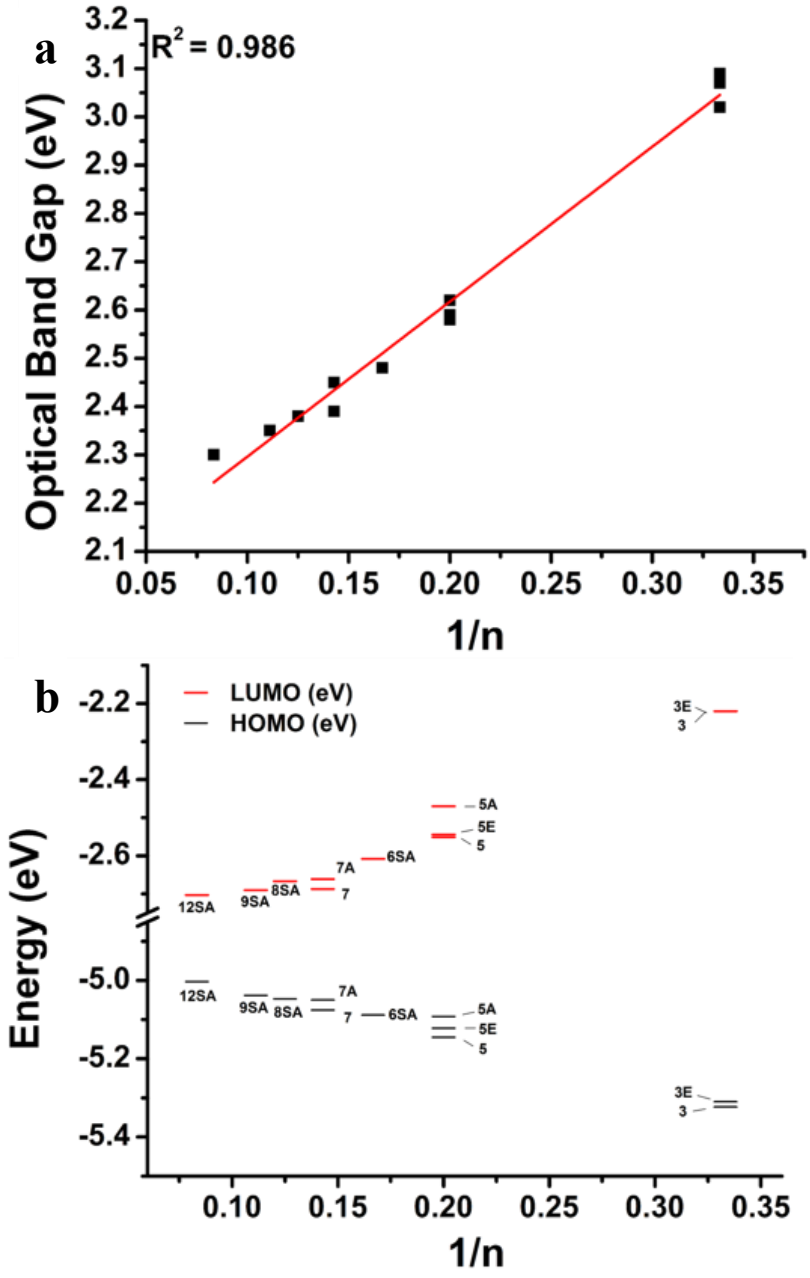

Figure 5.9. a) The optical band gaps of the synthesized series display an inverse dependence on the number of thiophene rings (n). The optical band gap is calculated from the onset of absorption of the first transition. b) Linear dependence of the HOMO and LUMO energy levels on the inverse of the number of thiophene rings. HOMO levels are calculated from the onset of electrochemical oxidation and referenced to ferrocene using previously established literature methods.[254]

5.2.4. Transient Raman Spectroscopy

The initial results for the ground state and transient triplet state Raman spectra of select oligothiophenes are shown in Figure 5.10.

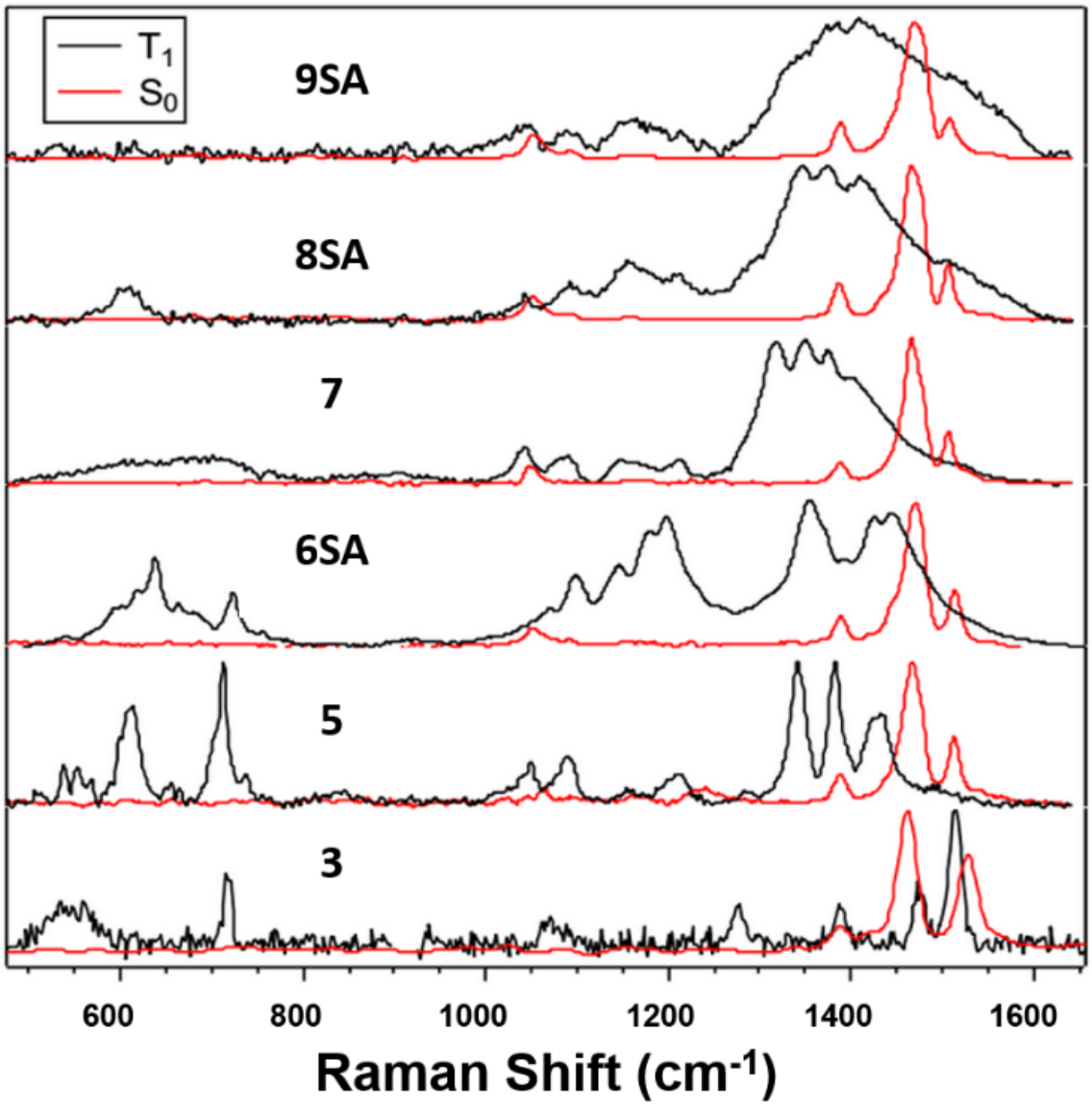

Figure 5.10. Raman spectra of the ground state (red) and transient Raman spectra for the triplet excited state (black) for select oligothiophenes.

The ground state spectra of the oligothiophenes show very little change with increasing chain length. At higher Raman shifts corresponding to carbon-carbon double-bond (C=C) stretches, three prominent stretches are observed with the peaks centered at approximately 1390 cm^{-1} and 1465 cm^{-1} exhibiting very little change. The highest energy stretch starts at 1535 cm^{-1} for **3** and redshifts 30 cm^{-1} to 1505 cm^{-1} for **9SA** with a decrease in the relative intensity to the 1465 cm^{-1} peak from 78% to 12%.

The triplet excited states show a much greater variation in the spectra. A general broadening and redshifting in the C=C stretching region is observed. Initial results suggest that the origin of the broadening is the result of numerous conformers in solution. Furthermore, the triplet spectra moving from **3** to **6SA** exhibits stretches in the 1100 - 1250 cm^{-1} range corresponding to carbon-carbon single bond (C–C) stretches and in the 500 - 800 cm^{-1} range corresponding to out-of-plane ring deformations that were not observed in the ground state spectra. The emergence of stretches in these regions is consistent with an overall decrease in the bond order of the oligothiophene chains. However, moving from **6SA** to **9SA**, the low energy bands (500 - 800 cm^{-1}) which emerged begin to decrease in intensity and are completely absent in **9SA**.

A direct comparison of the five series also exhibits interesting trends which provide information into the effects of octyl-chain substitution degree and patterns (Figure 5.11).

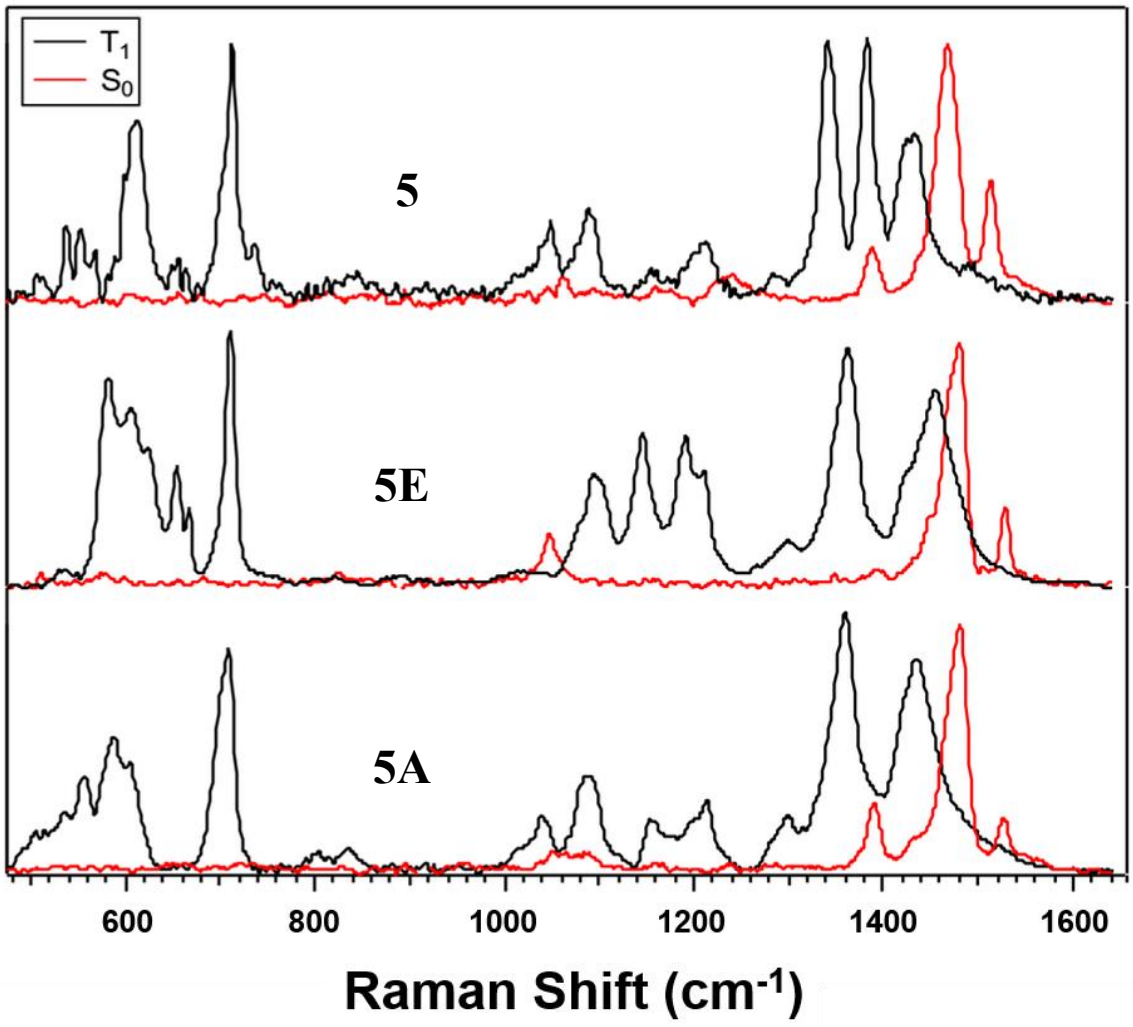

Figure 5.11. Raman spectra of the ground state (red) and transient Raman spectra for the triplet excited state (black) of **5** (top), **5E** (center), **5A** (bottom).

From the spectra, it is evident that increasing the number of octyl-substituents does not induce the broadening observed in the Raman spectra. The pattern of the substituents, however, does affect the relative intensities and resolution of the spectra. Computational studies are underway to further elucidate the effects of extending chain-lengths and altering the substituents on the triplet excited state structure.

5.3. CONCLUSIONS

Synthesis of a new library of oligothiophenes exhibiting varying chain lengths and octyl-chain substitution patterns has been realized. The ground state photophysical and electrochemical properties of these materials have been cataloged. In the electronic absorption spectra, the chain length was shown to have a significant impact on the absorption profile, as increasing the oligothiophene length resulted in a bathochromic shift which can be attributed to an increased stabilization of the excited state due to increased conjugation. Investigations into the effects of the octyl-chain substituents revealed that while the number of octyl groups had little effect on the absorption profiles, the pattern of substitution does play a significant role. Electrochemical studies revealed a significant impact of the oligothiophene length on the materials properties. Increasing conjugation length led to an increased ability to stabilize the resulting holes generated from electrochemical oxidation. In contrast to the UV-Vis absorption studies, the placement of the octyl-chains had little influence on the electrochemical properties of the materials. However, simply increasing the number of alkyl substituents led to a lowering of the oxidation potentials due to increased electron density on the oligothiophene core as well as an increased stabilization of the oxidized state.

Excited state photophysical studies were performed as well to elucidate structure-property relationships in the materials. These studies once again revealed a significant influence of chain length on the photophysical properties. Increasing the chain length induced a red shift in the emission profiles of the oligothiophenes, and no discernable influences were observed due to the number or substitution pattern of the octyl-chains. In the excited state it is likely that planarization forces to stabilize the charge separated state outcompete any influence from the alky substituents.

Plotting the electrochemical and photophysical properties against the inverse of the number of thiophene rings lead to linear trends, allowing for easy prediction and tailoring of the properties of the oligothiophenes. Furthermore, extrapolation of the linear trends to approximate the polymer properties is in excellent agreement with the observed properties of the polymer.

Initial studies into the resonance Raman spectroscopy of the oligothiophenes have been performed. The ground state spectra of the oligothiophenes exhibit minimal differences. The transient spectra, however, exhibit much richer character. An overall broadening and shift to lower energies is observed in the C=C region with increasing oligothiophene chain lengths. Furthermore, the emergence of peaks in the lower energy regions of the spectra is observed. The spectra of the five ring series indicate that the number and positioning of the octyl chains does not influence the broadening of the spectra but does have an effect on the relative intensities and resolution of the spectra.

Further studies into the structure of the triplet excited state are underway at the University of California - San Diego at the laboratories of Dr. Michael Tauber.

5.4. EXPERIMENTAL

5.4.1. Synthesis and Characterization

Air and/or moisture sensitive reactions were carried out in heat-gun dried glassware using standard Schlenk techniques under a dry nitrogen atmosphere. Dry solvents were collected in solvent bulbs from an Innovative Technology PureSolv 400 solvent purification system. All other chemicals were used as received from commercial suppliers unless otherwise specified. Thin layer chromatography (TLC) was performed using Silicycle silica gel 60 F_{254} pre-coated aluminum sheets. Column chromatography was performed using Silicycle Silica Flash® F60. NMR spectra were recorded with a Varian DirectDrive 400 MHz spectrometer at ambient temperature and were referenced internally to the residual solvent peaks. All chemical shifts are given in ppm and coupling constants are given in Hertz. Mass spectrometry was performed with a Micromass Autospec Ultima HRMS (for CI^+) or a Varian 9.4T (MALDI). [2,2'-bithiophen]-5-yltributylstannane was prepared according to literature procedures.[378] 3,4-dioctylthiophene[145] and 2,5-dibromo-3,4-dioctylthiophene[381] were prepared according to modified literature procedures. *N*-bromosuccinimide was recrystallized from boiling water and dried *in vacuo* prior to use.

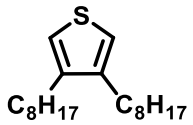

3,4-dioctylthiophene (**1**)[145]: 3,4-dibromothiophene (40.32 g, 18.43 mL, 166.7 mmol) and Ni(dppp)Cl_2 (0.650 g, 1.20 mmol) were dissolved in dry diethyl ether (400 mL) in a dry three-neck round-bottom flask equipped with a reflux condenser and addition funnel under N_2. The reaction vessel was cooled to 0 °C in an ice bath. Octylmagnesium bromide (2 M in Et_2O, 200 mL, 400.0 mmol) was transferred to the addition funnel via cannula and added dropwise to the stirring reaction solution over 2 hours. Upon complete addition of the Grignard reagent, the reaction was warmed to room temperature and then heated to reflux overnight under a N_2 atmosphere. The reaction was then cooled to 0 °C in an ice bath and concentrated HCl (10 mL) in DI H_2O (200 mL) was added dropwise to quench the reaction. Upon addition of the acidic solution, the reaction violently bubbled and changed from a dark brown, homogeneous solution to a light brown, opaque, heterogeneous solution. The solid was removed via vacuum filtration through celite and rinsed with Et_2O. The remaining solution was diluted with DI H_2O (500 mL) and extracted with CH_2Cl_2 (3 x 200 mL). The combined organic phases were dried over $MgSO_4$, vacuum filtered, and concentrated by rotary evaporation to afford a light brown oily solution. The crude material was further purified by vacuum distillation to yield a clear, light brown oil (40.163 g, 78%). ^{1}H NMR (400 MHz, $CDCl_3$): 6.89 (s, 2H), 2.51 (m, 4H), 1.62 (m, 4H), 1.34 (m, 20H), 0.89 (m, 6H). $^{13}C\{^1H\}$ NMR (100 MHz, $CDCl_3$): 142.08, 119.86, 31.91, 29.68, 29.64, 29.51, 29.31, 28.82, 22.69, 14.12. HRMS (CI^+): *m/z* calcd. for $C_{20}H_{37}S$ 309.2616 $[M+H]^+$, found 309.2618.

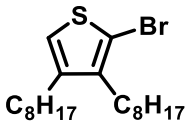

2-bromo-3,4-dioctylthiophene (**1-Br**): **1** (5.005 g, 16.24 mmol) was dissolved in DMF (100 mL) in a foil-wrapped round-bottom flask and cooled to 0 °C in an ice bath. *N*-bromosuccinimide (2.889 g, 16.24 mmol) was dissolved in DMF (40 mL) and added dropwise to the stirring solution over 2 hours via a foil-wrapped addition funnel. The reaction was warmed to room temperature overnight. Upon completion, the reaction was quenched with sodium thiosulfate, diluted with DI H_2O (200 mL), transferred to a separatory funnel, and extracted with hexanes (3 x 100 mL). The combined organic phases were washed with DI H_2O (3 x 100 mL) and brine (1 x 100 mL), and dried over $MgSO_4$. The filtered solution was rotary evaporated yielding a golden oil which was purified through a silica gel column (hexanes) to afford a clear yellow oil (4.235 g, 68%). ^{1}H NMR (400 MHz, $CDCl_3$): 6.82 (s, 1H), 2.49 (m, 4H), 1.57 (m, 2H), 1.46 (m, 2H), 1.29 (m, 20H), 0.87 (m, 6H). $^{13}C\{^1H\}$ NMR (100 MHz, $CDCl_3$): 142.04, 141.07, 119.92, 109.13, 31.89, 31.87, 29.66, 29.61, 29.49, 29.47, 29.45, 29.37, 29.33, 29.25, 28.11, 22.67, 14.10. HRMS (CI^+): *m/z* calcd. for $C_{20}H_{35}SBr$ 388.1622 $[M]^+$, found 388.1621.

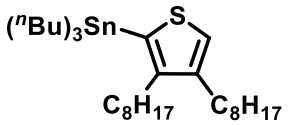

tributyl(3,4-dioctylthiophen-2-yl)stannane (**1-Sn**): **1-Br** (4.235 g, 10.97 mmol) was added to a Schlenk flask fitted with a reflux condenser and left under active vacuum overnight to remove any residual water. Then, dry THF (60 mL) was transferred to the reaction flask and freshly ground Mg turnings (0.320 g, 13.2 mmol) were added to the flask against a strong N_2 stream. The mixture was heated to reflux. After 4 hours, the reaction was allowed to cool to room temperature and then cooled to –78 °C. Tributyltin chloride (6.554 g, 10.97 mmol) was added to the reaction dropwise via syringe. Following complete addition, the reaction mixture was warmed to room temperature overnight. The reaction was quenched with DI H_2O (100 mL) and extracted into Et_2O (3 x 125 mL). The organic phases were combined, dried over $MgSO_4$, and rotary evaporated to dryness leaving a golden oil. Byproducts were removed by vacuum distillation leaving a golden residue. The residue was extracted with Et_2O and filtered through celite. Evaporation of the solvent yielded pure product as a golden oil (5.498 g, 84%). ^{1}H NMR (400 MHz, $CDCl_3$): 7.16 (s, 1H), 2.49 (m, 4H), 1.62 (m, 2H), 1.52 (m, 8H), 1.31 (m, 26H), 1.08 (m, 6H), 0.88 (m, 15H). $^{13}C\{^1H\}$ NMR (100 MHz, $CDCl_3$): 149.65, 143.38, 131.55, 125.97, 32.28, 31.90, 31.72, 30.20, 30.08, 29.78, 29.54, 29.30, 29.05, 28.93, 27.33, 22.68, 14.11, 13.63, 10.78. HRMS (CI^+): *m/z* calcd. for $C_{32}H_{62}SSn$: 598.3594 $[M]^+$, found 598.3604.

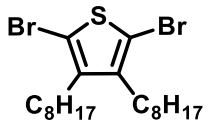

2,5-dibromo-3,4-dioctylthiophene (**1-Br$_2$**)[381]: **1** (43.364 g, 140.68 mmol) was dissolved in DMF (900 mL) in a foil-wrapped round-bottom flask and cooled to 0 °C in an ice bath. *N*-bromosuccinimide (49.421 g, 277.80 mmol) was dissolved in DMF (500 mL) and added dropwise to the stirring solution over 2 hours via a foil-wrapped addition funnel. The reaction was allowed to warm to room temperature overnight. The reaction was quenched with excess sodium thiosulfate, diluted with DI H_2O (1000 mL) and extracted with hexanes (6 x 500 mL). The combined organic phases were washed with DI H_2O (4 x 200 mL) and brine (2 x 500 mL), and dried over $MgSO_4$. The filtered solution was rotary evaporated to afford pure product as a clear yellow oil (65.6 g, 98%). ^{1}H NMR (400 MHz, $CDCl_3$): 2.51 (t, 4H, J = 8), 1.46 (m, 4H), 1.31 (m, 20H), 0.88 (m, 6H). $^{13}C\{^1H\}$ NMR (100 MHz, $CDCl_3$): 141.44, 107.80, 31.88, 29.72, 29.55, 29.32, 29.23, 28.96, 22.68, 14.12. HRMS (CI^+): *m/z* calcd. for $C_{20}H_{35}SBr_2$ 465.0826 $[M+H]^+$, found 465.0826.

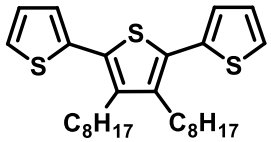

3',4'-dioctyl-2,2':5',2''-terthiophene (**3**): **1-Br$_2$** (26.526 g, 56.879 mmol), tributyl(thiophen-2-yl)stannane (58.7 g, 50.0 mL, 157 mmol), LiCl (11.911 g, 280.99 mmol), and $PdCl_2(PPh_3)_2$ (2.106 g, 3.000 mmol) were dissolved in DMF (300 mL) in a round-bottom flask equipped with a reflux condenser. The reaction solution was heated to reflux overnight, upon which the reaction became dark brown in color. Once complete, the reaction was cooled to room temperature. The reaction was then diluted with DI H_2O (500 mL), and extracted with hexanes (3 x 300 mL). The combined organic phases were washed with 1M NaOH (aq) (2 x 150 mL) and DI H_2O (1 x 200 mL), dried over $MgSO_4$, vacuum filtered, and rotary evaporated to dryness. The crude product was purified by silica gel column chromatography (hexanes) to afford the desired product as a light green oil (26.553 g, 97%). ^{1}H NMR (400 MHz, $CDCl_3$): 7.31 (dd, 2H, J = 5, 1.2), 7.14 (dd, 2H, J = 3.6 ,1.2), 7.07 (dd, 2H, J = 5.2, 3.6), 2.69 (m, 4H), 1.57 (m 4H), 1.41 (m, 4H), 1.30 (m, 16H), 0.89 (m, 6H). ^{13}C{^{1}H} NMR (100 MHz, $CDCl_3$): 140.08, 136.21, 129.79, 127.31, 125.82, 125.25, 31.88, 31.59, 30.76, 29.90, 29.26, 28.13, 22.69, 14.12. HRMS (CI^+): *m/z* calcd. for $C_{28}H_{41}S_3$ 473.2370 $[M+H]^+$, found 473.2370. Elemental analysis calcd. for $C_{28}H_{40}S_3$: C, 71.13; H, 8.53; found C, 71.15; H, 8.54.

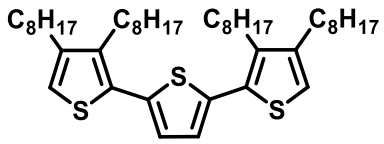

3,3'',4,4''-tetraoctyl-2,2':5',2''-terthiophene (**3E**): 2,5-dibromothiophene (0.539 g, 2.226 mmol), **1-Sn** (3.725 g, 6.233 mmol), LiCl (0.472 g, 11.130 mmol), and $PdCl_2(PPh_3)_2$ (0.084 g, 0.120 mmol) were dissolved in DMF (50 mL) in a round-bottom flask equipped with a reflux condenser. The reaction solution was sparged with N_2 and heated to reflux overnight, upon which the reaction became dark brown in color. Once complete, the reaction was cooled to room temperature. The reaction was then diluted with DI H_2O (100 mL) and extracted with Et_2O (3 x 100 mL). The combined organic phases were washed with DI H_2O (1 x 150 mL), dried over $MgSO_4$, vacuum filtered, and rotary evaporated to dryness. The crude product was purified by silica gel column chromatography (hexanes) to afford the desired product as a light green oil (1.019 g, 66%). ^{1}H NMR (400 MHz, $CDCl_3$): 7.01 (s, 2H), 6.84 (s, 2H), 2.68 (m, 4H), 2.50 (t, J = 7.3, 4H), 1.64 (q, J = 7.6, 4H) 1.52 (m, 4H), 1.29 (m, 40H), 0.86 (m, 12H). ^{13}C{^{1}H} NMR (100 MHz, $CDCl_3$): 143.61, 138.87, 136.51, 130.83, 125.77, 118.98, 31.89, 30.52, 29.89, 29.74, 29.65, 29.34, 29.29, 29.24, 27.78, 22.68, 14.11. HRMS (CI^+): *m/z* calcd. for $C_{44}H_{72}S_3$ 696.4796 $[M]^+$, found 696.4792. Elemental analysis calcd. for $C_{44}H_{72}S_3$: C, 75.80; H, 10.41; found C, 75.75; H, 10.56.

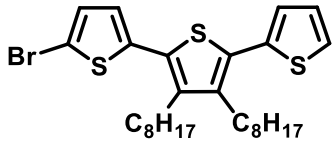

5-bromo-3',4'-dioctyl-2,2':5',2''-terthiophene (**3-Br**): **3** (11.318 g, 23.938 mmol) was dissolved in DMF (400 mL) in a round bottomed flask equipped with an addition funnel. The reaction vessel was wrapped in aluminum foil and cooled to 0 °C in ice bath while stirring. *N*-bromosuccinimide (4.272 g, 23.96 mmol) was dissolved in DMF (60 mL) and transferred to the addition funnel, which was then sealed with a rubber septum and kept under a blanket of nitrogen. The *N*-bromosuccinimide solution was added dropwise to the stirring solution over 1.5 hours. After complete addition, the reaction was warmed to room temperature overnight. The reaction was quenched with excess sodium thiosulfate and extracted with diethyl ether (2 x 500 mL). The organic phases were combined, washed with DI H_2O (3 x 500 mL) and brine (1 x 300 mL), and dried over $MgSO_4$. The solution was collected by vacuum filtration then rotary evaporated to dryness. The crude material was purified by silica gel column chromatography (hexanes) to afford a light green oil (9.012 g, 68% yield). ^{1}H NMR (400 MHz, $CDCl_3$): 7.30 (dd, 1H, J = 5.2, 1.2), 7.11 (dd, 1H, J = 3.6, 1.2), 7.05 (dd, 1H, J = 5.2, 3.6), 6.99 (d, 1H, J = 4.0), 6.86 (d, 1H, J = 4.0), 2.65 (m, 4H), 1.52 (m, 4H), 1.38 (m, 4H), 1.28 (m, 16H), 0.88 (m, 6H). ^{13}C{^{1}H} NMR (100 MHz, $CDCl_3$): 140.60, 140.10, 137.74, 135.91, 130.36, 130.15, 128.78, 127.35, 126.05, 125.99, 125.46, 111.72, 31.87, 30.78, 30.78, 30.72, 29.83, 29.23, 28.08, 22.69, 14.12. HRMS (CI$^+$): *m/z* calcd. for $C_{28}H_{39}BrS_3$ 552.1377 $[M]^+$, found 552.1364.

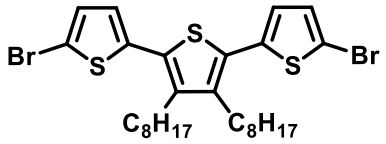

5,5″-dibromo-3′,4′-dioctyl-2,2′:5′,2″-terthiophene (**3-Br$_2$**)**: 3** (1.002 g, 2.12 mmol) was dissolved in DMF (100 mL) in a foil-wrapped round-bottom flask and cooled to 0 °C in an ice bath. *N*-bromosuccinimide (0.755 g, 4.24 mmol) was added to the reaction flask and the reaction was warmed to room temperature overnight. Upon completion, the reaction was quenched with excess sodium thiosulfate. The mixture was diluted with DI H_2O (200 mL) and extracted with hexanes (3 x 100 mL). The combined organic phases were washed with DI H_2O (3 x 100 mL) and brine (1 x 100 mL) and dried over $MgSO_4$. The filtered solution was rotary evaporated and was purified by silica gel column chromatography (hexanes). The pure material was isolated as a light green oil (1.224 g, 92% yield). ^{1}H NMR (400 MHz, $CDCl_3$): 6.99 (d, 2H, J = 3.9), 6.84 (d, 2H, J = 3.5), 2.60 (m, 4H), 1.51 (m, 4H), 1.37 (m, 4H), 1.29 (m, 16H), 0.87 (m, 6H). ^{13}C{^{1}H} NMR (100 MHz, $CDCl_3$): 140.62, 137.45, 130.17, 129.33, 126.21, 111.98, 31.86, 30.76, 29.81, 29.21, 28.05, 22.69, 14.13. HRMS (CI^+): *m/z* calcd. for $C_{28}H_{41}S_3$ $[M]^+$ 630.0482, found 630.0492.

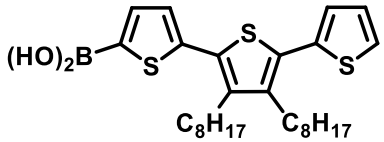

(3',4'-dioctyl-[2,2':5',2''-terthiophen]-5-yl)boronic acid (**3-BA**): In a dry, N_2 filled Schlenk flask fitted with a reflux condenser, finely-ground magnesium turnings (0.047 g, 1.93 mmol) were suspended in dry THF (5 mL). In a dry round-bottomed flask under N_2, **3-Br** (0.723 g, 1.30 mmol) was dissolved in dry THF (5 mL) and then transferred via cannula to the Schlenk flask. The reaction was heated to reflux and vigorously stirred for 3 hours, during which the reaction went from a clear, light green solution to a dark yellow-brown solution. The reaction was cooled to room temperature and then –78 °C in a dry ice/acetone bath. Meanwhile, trimethylborate (0.3 mL, 2.6 mmol) was dissolved in dry THF (5 mL) in a round-bottomed flask and then cannula-transferred in one portion to the reaction vessel. The reaction was stirred at –78 °C for 1 hour before being removed from the dry ice/acetone bath and warmed to room temperature under a N_2 atmosphere. Upon completion, the reaction mixture was cooled to 0 °C in an ice bath and 10% HCl (10 mL), DI H_2O (20 mL), and Et_2O (20 mL) were added sequentially to the reaction. After stirring for 5 minutes, the reaction was warmed room temperature and transferred to a separatory funnel. The aqueous phase was extracted with Et_2O (1 x 75 mL) and the combined organic phases were washed with DI H_2O (1 x 75 mL) and brine (1 x 75 mL) and dried over $MgSO_4$. The reaction mixture was collected via vacuum filtration, concentrated via rotary evaporation, and recrystallized twice from hexanes to yield (3',4'-dioctyl-[2,2':5',2''-terthiophen]-5-yl)boronic acid as a light green solid. ^1H NMR was consistent with a mixture of monomer and dimer. Product was carried on without further purification (0.406 g, 60%).

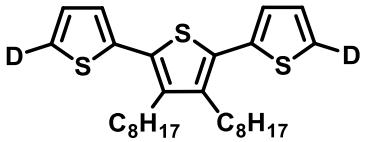

3',4'-dioctyl-2,2':5',2''-terthiophene-5,5''-d2 (**3D**): In a dry, N_2 filled Schlenk flask, **3-Br$_2$** (0.430 g, 0.682 mmol) was dissolved in 20 mL of dry THF and cooled to –78 °C over the course of 30 minutes before 0.90 mL (1.6 M in hexanes, 1.432 mmol) was added dropwise via syringe. The mixture was then removed from the cooling bath and allowed to warm for 30 minutes at room temperature before being dropped back into the –78 °C bath. After cooling for 30 minutes, D_2O (0.50 mL, 27.708 mmol) was added dropwise via syringe. The resulting mixture was then removed from the cooling bath and allowed to warm to room temperature overnight. The solvent was then removed via rotary evaporation to give a pale green oil. The crude product was purified by silica gel column chromatography (hexanes) to yield a pale green oil (0.200 g, 62%). ^{1}H NMR (400 MHz, $CDCl_3$): 7.10 (d, J = 3.5, 2H), 7.04 (d, J = 3.9, 2H), 2.67 (m, 4H), 1.54 (m, 4H), 1.38 (m, 4H), 1.26 (m, 16H), 0.87 (t, J = 6.8, 6H). ^{13}C{^{1}H} NMR (100 MHz, $CDCl_3$): 140.09, 136.11, 129.79, 127.16, 125.82, 31.88, 30.76, 29.90, 29.25, 28.13, 22.69, 14.12. HRMS (CI^+): *m/z* calcd. for $C_{28}H_{38}S_3D_2$ 474.2418 $[M]^+$, found 474.2419. Elemental analysis calcd. for $C_{28}H_{38}S_3D_2$: C, 70.83; H, 8.92; found C, 71.08; H, 8.60.

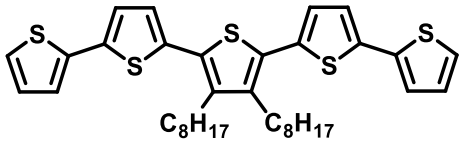

3'',4''-dioctyl-2,2':5',2'':5'',2''':5''',2'''':5'''',2''''-quinquethiophene (**5**): **1-Br$_2$** (0.500 g, 1.07 mmol), [2,2'-bithiophen]-5-yltributylstannane (1.367 g, 3.00 mmol), and lithium chloride (0.227 g, 5.36 mmol) were added to a Schlenk flask. DMF (20 mL) was sparged with N_2 and transferred to the reaction vessel via cannula. $PdCl_2(PPh_3)_2$ (0.041 g, 0.06 mmol) was added to the reaction mixture under strong N_2 back pressure. The reaction was heated to reflux at 150 °C and was stirred for 24 hours in the absence of light. The reaction was then cooled to room temperature, diluted with DI H_2O (100 mL), and extracted with hexanes (3 x 100 mL). The organic phases were combined and washed with DI H_2O (3 x 100 mL) and brine (1 x 100 mL). The organic phase was then dried over $MgSO_4$, filtered, and concentrated by rotary evaporation. The crude product was purified by silica gel column chromatography (hexanes) to yield a yellow solid (1.421 g, 74%). ^{1}H NMR (400 MHz, $CDCl_3$): 7.21 (dd, 2H, *J* = 5.0, 1.1), 7.17 (dd, 2H, *J* = 3.5, 1.2), 7.11 (d, 2H, *J* = 3.9), 7.02 (d, 2H, *J* = 3.9), 7.01 (dd, 2H, *J* = 5.0, 3.5), 2.71 (m, 4H), 1.57 (m, 4H), 1.42 (m, 4H), 1.29 (m, 20H), 0.86 (m, 6H). ^{13}C{^{1}H} NMR (100 MHz, $CDCl_3$): 140.38, 137.16, 137.08, 135.08, 129.73, 127.88, 126.36, 124.47, 123.99, 123.65, 31.91, 30.70, 29.91, 29.28, 28.23, 22.71, 14.14. HRMS (CI$^+$): *m/z* calcd. for $C_{36}H_{44}S_5$ 636.2047 $[M]^+$, found 636.2046. Elemental analysis calcd. for $C_{36}H_{44}S_5$: C, 67.87; H, 6.96.; found C, 67.98; H, 7.06.

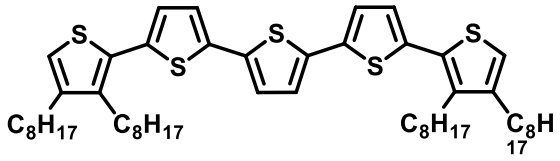

3,3'''',4,4''''-tetraoctyl-2,2':5',2'':5'',2''':5''',2''''-quinquethiophene (**5E**): 2,5-bis(5-bromothiophen-2-yl)thiophene (0.140 g, 0.345 mmol), **1-Sn** (0.558 g, 0.956 mmol), and lithium chloride (0.072 g, 1.705 mmol) were added to a Schlenk flask. DMF (20 mL) sparged with N_2 was added to the Schlenk flask via cannula. $PdCl_2(PPh_3)_2$ (0.013 g, 0.019 mmol) was added to the reaction vessel under strong N_2 back pressure. The reaction was heated to reflux at 150 °C for 24 hours in the absence of light. Following the 24 hours, the reaction was cooled to room temperature. The reaction mixture was diluted with DI H_2O (100 mL) and extracted with hexanes (3 x 100 mL). The combined organic phases were washed with DI H_2O (3 x 100 mL), dried over $MgSO_4$, filtered, and concentrated to dryness using a rotary evaporator. The product was purified by silica gel column chromatography (hexanes) to yield an orange amorphous solid (0.161 g, 54%). ^{1}H NMR (400 MHz, $CDCl_3$): 7.10 (d, 2H, J = 3.5), 7.06 (s, 2H), 6.99 (d, 2H, J = 3.9), 6.85 (s, 2H), 2.68 (m, 4H), 2.51 (m, 4H), 1.64 (m, 4H), 1.52 (m, 4H), 1.36 (m, 8H), 1.28 (m, 32H), 0.87 (m, 12H). ^{13}C{^{1}H} NMR (100 MHz, $CDCl_3$): 143.71, 139.16, 136.49, 136.09, 135.99, 130.59, 126.28, 124.12, 123.84, 119.23, 31.90, 30.42, 29.83, 29.72, 29.64, 29.50, 29.28, 27.75, 22.69, 14.13. HRMS (CI^+): *m/z* calcd. for $C_{52}H_{76}S_5$ 860.4551 $[M]^+$, found 860.4552. Elemental analysis calcd. for $C_{52}H_{76}S_5$: C, 72.50; H, 8.89; found C, 72.51; H, 9.00.

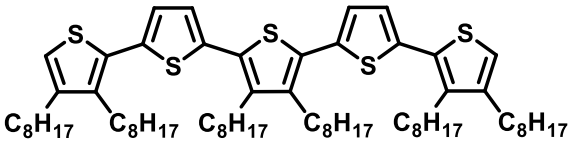

3,3'',3'''',4,4'',4''''-hexaoctyl-2,2':5',2'':5'',2''':5''',2''''-quinquethiophene (**5A**): **3-Br$_2$** (0.360 g, 0.571 mmol), **1-Sn** (0.956 g, 1.60 mmol), and lithium chloride (0.121 g, 2.85 mmol) were added to a Schlenk flask. DMF (20 mL) sparged with N_2 was transferred to the Schlenk flask via cannula. $PdCl_2(PPh_3)_2$ (0.022 g, 0.031 mmol) was added to the reaction vessel under strong N_2 back pressure and the reaction was heated to reflux at 150 °C for 24 hours in the absence of light. Following the 24 hours, the reaction was cooled to room temperature, diluted with DI water (100 mL) and extracted with hexanes (3 x 100 mL). The combined organic phases were washed with DI H_2O (3 x 100 mL), dried over $MgSO_4$, and collected via vacuum filtration. The filtrate was concentrated by rotary evaporation and the product was purified by silica gel column chromatography (hexanes) to yield a yellow solid (0.322 g, 52%). ^{1}H NMR (400 MHz, $CDCl_3$): 7.06 (d, 2H, J = 3.9), 7.03 (d, 2H, J = 3.5), 6.85 (s, 2H), 2.70 (m, 8H), 2.51 (m, 4H), 1.59 (m, 12H), 1.40 (m, 12H), 1.27 (m, 48 H), 0.86 (m, 18H). ^{13}C{^{1}H} NMR (100 MHz, $CDCl_3$): 143.66, 140.10, 138.96, 136.70, 135.75, 130.76, 129.77, 125.85, 125.82, 119.08, 31.90, 30.78, 30.51, 29.97, 29.90, 29.73, 29.65, 29.51, 29.35, 29.32, 29.29, 29.24, 28.27, 27.80, 22.69, 14.12. HRMS (CI^+): *m/z* calcd. for $C_{68}H_{108}S_5$ 1084.7055 $[M]^+$, found 1084.7048. Elemental analysis calcd. for $C_{68}H_{108}S_5$: C, 75.21; H, 10.03; found C, 75.26; H, 10.19.

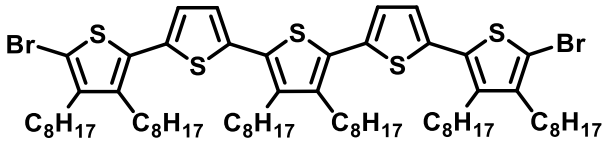

5,5''''-dibromo-3,3'',3'''',4,4'',4''''-hexaoctyl-2,2':5',2'':5'',2''':5''',2''''-quinquethiophene (**5A-Br$_2$**)**: 5A** (0.960 g, 0.884 mmol) was dissolved in DMF (100 mL) in a foil-wrapped round-bottom flask and cooled to 0 °C in an ice bath. *N*-bromosuccinimide (0.315 g, 1.768 mmol) was added to the reaction flask and the reaction was warmed to room temperature overnight. Upon completion, the reaction was quenched with excess sodium thiosulfate. The mixture was diluted with DI H_2O (200 mL) and extracted with hexanes (3 x 100 mL). The combined organic phases were washed with DI H_2O (3 x 100 mL) and brine (1 x 100 mL) and dried over $MgSO_4$. The filtered solution was rotary evaporated and was purified by silica gel column chromatography (hexanes). The pure material was isolated as a yellow solid (0.501 g, 46% yield). ^{1}H NMR (400 MHz, $CDCl_3$): 7.05 (d, J = 3.7, 2H), 6.98 (d, J = 3.7, 2H), 2.69 (m, 8H), 2.51 (m, 4H), 1.52 (m, 12H), 1.39 (m, 12H), 1.27 (m, 48H), 0.86 (m, 18H). ^{13}C{^{1}H} NMR (100 MHz, $CDCl_3$): 142.67, 140.30, 138.90, 136.19, 135.33, 130.82, 129.69, 126.24, 125.90, 108.56, 31.89, 30.77, 29.95, 29.81, 29.72, 29.63, 29.29, 28.71, 28.52, 28.25, 22.69, 14.12.

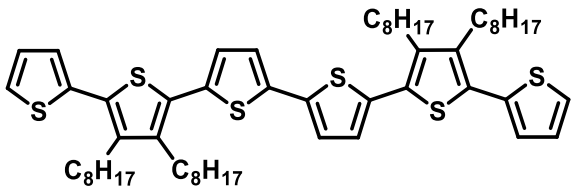

3',3'''',4',4''''-tetraoctyl-2,2':5',2'':5'',2''':5''',2'''':5'''',2''''':5''''',2'''''-sexithiophene (**6SA**): **3-Br** (0.14 g, 0.254 mmol) was dissolved in THF (20 mL) in a 100-mL Schlenk flask, sealed with a rubber septum, and sparged with N_2 for 30 minutes. Meanwhile, Na_2CO_3 (0.135 g, 1.27 mmol) was dissolved in DI H_2O (5 mL) in a 25-mL round-bottom flask, sealed with a rubber septum, and sparged with N_2 for 30 minutes. The reaction vessels were cooled to 0 °C in an ice bath, and **3-BA** (0.171 g, 0.33 mmol) and $Pd(PPh_3)_4$ (0.029 g, 0.03 mmol) were added to the Schlenk flask under a strong N_2 backpressure. The basic solution was transferred to the Schlenk flask via cannula and the reaction was sparged with N_2 for 10 minutes before warming to room temperature. The reaction vessel was equipped with a reflux condenser under N_2, and heated to reflux for 6 hours. Upon completion, the reaction was cooled to room temperature, diluted with DI H_2O (100 mL) and hexanes (100 mL), and extracted with hexanes (2 x 50 mL). The combined organic phases were washed with DI H_2O (2 x 50 mL) and brine (1 x 50 mL), and dried over $MgSO_4$. The crude product was collected via vacuum filtration, concentrated via rotary evaporation, and purified by silica gel column chromatography (5:1 (v/v) hexanes:CH_2Cl_2) to yield an orange-yellow oil that crystallized upon sitting (0.227 g, 94%). ^{1}H NMR (400 MHz, $CDCl_3$): 7.33 (dd, 2H, J = 4.8, 1.2), 7.16 (m, 4H), 7.07 (m, 4H), 2.74 (m, 8H), 1.60 (m, 8H), 1.46 (m, 8H), 1.33 (m, 32H), 0.92 (m, 12H). ^{13}C{^{1}H} NMR (100 MHz, $CDCl_3$): 140.21, 136.68, 136.11, 135.23, 129.99, 127.33, 126.29, 125.84, 125.31, 123.77, 31.91, 31.89, 30.74, 30.67, 29.91, 29.26, 28.24, 28.16, 22.71, 14.14. HRMS (CI^+): *m/z* calcd. for $C_{56}H_{78}S_6$ 942.4428 $[M]^+$, found 942.2219. Elemental analysis calcd. for $C_{56}H_{78}S_6$: C, 71.28; H, 8.33; found C, 71.28; H, 8.50.

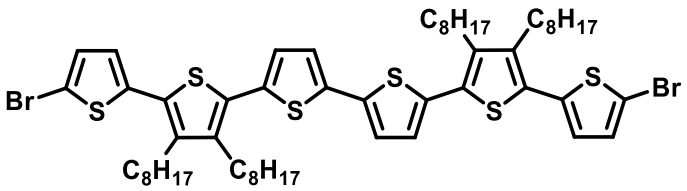

5,5''''''-dibromo-3',3'''',4',4''''-tetraoctyl-2,2':5',2'':5'',2''':5''',2'''':5'''',2''''':5''''',2''''''-sexithiophene (**6SA-Br$_2$**): **6SA** (0.050 g, 0.045 mmol) was dissolved in DMF (50 mL) in a foil-wrapped round-bottom flask and cooled to 0 °C in an ice bath. *N*-bromosuccinimide (0.016 g, 0.091 mmol) was dissolved in DMF (10 mL) and added to the stirring solution. The reaction was warmed to room temperature overnight and the reaction was quenched with aqueous sodium thiosulfate, diluted with DI H_2O (200 mL), and extracted with hexanes (3 x 100 mL). The combined organic phases were washed with DI H_2O (3 x 100 mL) and brine (1 x 100 mL), and dried over $MgSO_4$. The filtered solution was rotary evaporated to yield an orange solid (0.047 g, 96%). ^{1}H NMR (400 MHz, $CDCl_3$): 7.11 (d, 2H, J = 4.0), 7.02 (d, 2H, J = 4.0), 7.00 (d, 2H, J = 4.0), 6.86 (d, 2H, J = 4.0), 2.66 (m, 8H), 1.53 (m, 8H), 1.44 (m, 8H), 1.27 (m, 32H), 0.86 (m, 12H). ^{13}C{^{1}H} NMR (100 MHz, $CDCl_3$): 140.77, 140.28, 137.63, 136.83, 135.02, 130.19, 130.11, 128.98, 126.51, 126.11, 123.87, 111.86, 31.89, 31.87, 30.77, 30.65, 29.89, 29.83, 29.26, 29.45, 29.22, 28.20, 28.10, 22.70, 14.13. HRMS (CI$^+$): *m/z* calcd. for $C_{56}H_{76}S_6Br_2$ 1100.2618 $[M]^+$, found 1100.2596.

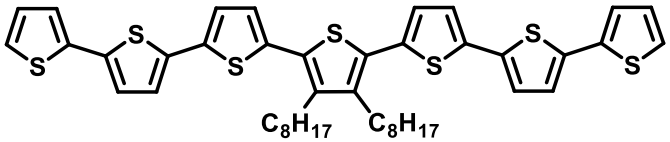

3‴,4‴-dioctyl-2,2′:5′,2″:5″,2‴:5‴,2⁗:5⁗,2⁗′:5⁗′,2⁗″:5⁗″-sepithiophene (**7**): **3-Br$_2$** (0.714 g, 1.13 mmol), [2,2'-bithiophen]-5-yltributylstannane (1.443 g, 3.17 mmol), and LiCl (0.240 g, 5.66 mmol) were added to a Schlenk flask. DMF (20 mL) was sparged with N_2 and was transferred to the reaction vessel via cannula. $PdCl_2(PPh_3)_2$ (0.054 g, 0.077 mmol) was added to the reaction mixture under strong N_2 back pressure. The reaction was heated to reflux at 150 °C for 24 hours in the absence of light. Following the 24 hours, the reaction was cooled to room temperature. The reaction mixture was diluted with DI H_2O (100 mL) and extracted with hexanes (3 x 100 mL). The combined organic phases were washed with DI H_2O (3 x 100 mL), dried over $MgSO_4$, and filtered. The filtrate was concentrated via rotary evaporation and the crude product was purified by silica gel column chromatography (10:1 (v/v) hexanes/CH_2Cl_2). The product was then collected, dissolved in a solution of 10:1 (v/v) of hexanes/CH_2Cl_2, and recrystallized by slowly cooling the solution to -20 °C. The product was collected by vacuum filtration to yield a maroon solid (0.367 g, 41%). ^{1}H NMR (400 MHz, $CDCl_3$): 7.21 (dd, 2H, J = 5.1, 1.1), 7.17 (dd, 2H, J = 3.5, 1.1), 7.10 (d, 2H, J = 3.5), 7.07 (s, 4H), 7.01 (m, 4H) 2.71 (m, 4H), 1.58 (m, 4H), 1.43 (m, 4H), 1.29 (m, 20H), 0.85 (m, 6H). $^{13}C\{^1H\}$ NMR (100 MHz, $CDCl_3$): 140.45, 137.08, 136.72, 136.29, 135.88, 135.18, 129.75, 127.90, 126.40, 124.53, 124.38, 124.17, 123.91, 123.72, 31.89, 30.64, 29.90, 29.28, 29.25, 28.23, 22.70, 14.13. HRMS (CI^+): *m/z* calcd. for $C_{44}H_{48}S_7$ 800.1801 $[M]^+$, found 800.1799. Elemental analysis cald. for $C_{44}H_{48}S_7$: C, 65.95; H, 6.04; found C, 66.05; H, 5.99.

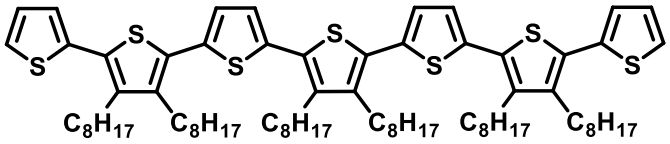

3',3''',3'''',4',4''',4''''-hexaoctyl-2,2':5',2'':5'',2''':5''',2'''':5'''',2''''':5''''',2'''''-sepithiophene (**7A**): **5A-Br$_2$** (0.501 g, 0.403 mmol), tributyl(thiophen-2-yl)stannane (0.421 g, 1.128 mmol), and LiCl (0.085 g, 2.014 mmol) were added to a Schlenk flask. DMF (80 mL) was sparged with N_2 and was transferred to the reaction vessel via cannula. $PdCl_2(PPh_3)_2$ (0.015 g, 0.022 mmol) was added to the reaction mixture under strong N_2 back pressure. The reaction was heated to reflux at 150 °C for 24 hours in the absence of light. Following the 24 hours, the reaction was cooled to room temperature. The reaction mixture was diluted with DI H_2O (100 mL) and extracted with hexanes (3 x 100 mL). The combined organic phases were washed with DI H_2O (3 x 100 mL), dried over $MgSO_4$, and filtered. The filtrate was concentrated via rotary evaporation and the crude product was purified by silica gel column chromatography using hexanes as the eluent. The product was collected as an orange solid (0.218 g, 43%). ^{1}H NMR (400 MHz, $CDCl_3$): 7.31 (dd, *J* = 5.0, 0.9, 2H), 7.17 (dd, *J* = 3.5, 0.9, 2H), 7.11 (m, 4H), 7.07 (dd, *J* = 5.0, 3.5, 2h), 2.75 (m, 12H), 1.63 (m, 12H), 1.47 (m, 12H), 1.32 (m, 48H), 0.92 (m, 18H). ^{13}C{^{1}H} NMR (100 MHz, $CDCl_3$): 140.15, 140.12, 140.00, 136.16, 135.95, 135.84, 129.89, 129.80, 129.73, 127.30, 125.85, 125.83, 125.78, 125.23, 31.93, 31.89, 30.74, 29.99, 29.90, 29.71, 29.34, 29.27, 28.29, 28.13, 22.71, 14.13. HRMS (CI^+): *m/z* calcd. for $C_{76}H_{112}S_7$ 1248.6804 $[M]^+$, found 1248.6802. Elemental analysis calcd. for $C_{76}H_{112}S_7$: C, 73.02; H, 9.03; found C, 72.62; H, 9.32.

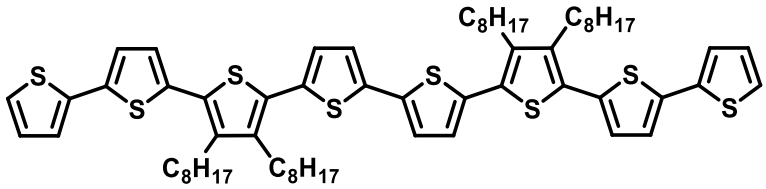

3'',3''''',4'',4'''''-tetraoctyl-2,2':5',2'':5'',2''':5''',2'''':5'''',2''''':5''''',2'''''':5'''''',2''''''-octithiophene (**8SA**): **6SA-Br$_2$** (0.309 g, 0.280 mmol), LiCl (0.060g, 1.415 mmol), $PdCl_2(PPh_3)_2$ (0.011 g, 0.016 mmol) were transferred to a N_2 filled Schlenk flask. DMF (10 mL) sparged with N_2 was transferred to the flask via cannula and 2-tributyl(thiophen-2-yl)stannane (0.235 g, 0.630 mmol) was syringed into the flask. The reaction was heated to 150 °C for 24 hours. The reaction was then cooled to room temperature, diluted with DI H_2O (100 mL), and extracted with $CHCl_3$ (3 x 100 mL). The organic layers were combined, washed with DI H_2O (2 x 150 mL) and brine (1 x 100 mL), dried over $MgSO_4$, filtered, and concentrated via rotary evaporation. The crude product was purified through silica gel chromatography (hexanes) to afford the product as a dark red solid (0.063g, 20% yield). ^{1}H NMR (400 MHz, $CDCl_3$): 7.21 (dd, 2H, J = 5.2, 1.2), 7.17 (dd, 2H, J = 3.6, 1.2), 7.12 (m, 4H), 7.03 (m, 6H), 2.71 (m, 8H), 1.58 (m, 8H), 1.43 (m, 8H), 1.28 (m, 32H), 0.87 (m, 12H). ^{13}C{^{1}H} NMR (100 MHz, $CDCl_3$): 140.72, 130.01, 128.19,126.70, 124.78, 124.30, 124.18, 123.95, 105.31, 32.22, 30.99, 30.22, 29.58, 28.54, 23.01, 14.45. HRMS (CI^+): calcd. for $C_{64}H_{82}S_8$ *m/z* 1106.418, found 1106.419. Elemental Anal. Calcd. for $C_{44}H_{48}S_7$: C, 69.39; H, 7.46; found C, 69.66; H, 7.63.

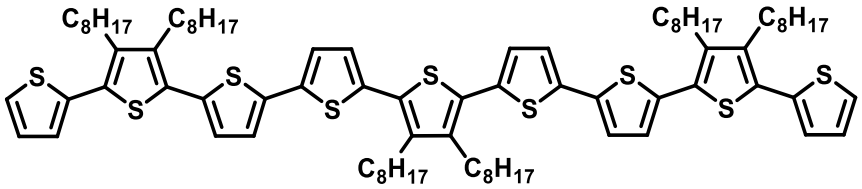

2-(5-{5-[5-(5-{5-[3,4-dioctyl-5-(thiophen-2-yl)thiophen-2-yl]thiophen-2-yl}thiophen-2-yl)-3,4-dioctylthiophen-2-yl]thiophen-2-yl}thiophen-2-yl)-3,4-dioctyl-5-(thiophen-2-yl)thiophene (**9SA**): **3-Br$_2$** (0.174 g, 0.276 mmol) was added to a Schlenk flask. Na_2CO_3 (0.146 g, 1.38 mmol) was dissolved in DI H_2O (10 mL) and sparged with N_2 for 20 minutes. The aqueous solution was transferred via cannula to the reaction vessel along with N_2 sparged THF (30 mL). **3-BA** (0.342 g, 0.662 mmol) and $Pd(PPh_3)_4$ (0.032 g, 0.028 mmol) were added to the reaction vessel under strong N_2 back pressure and the reaction was heated to reflux at 80 °C. The mixture was stirred for 24 hours in the absence of light. The reaction mixture was then diluted with DI H_2O (100 mL) and extracted with diethyl ether (3 x 100 mL). The combined organic phases were washed with DI H_2O (1 x 100 mL), dried over $MgSO_4$, filtered, and concentrated to dryness via rotary evaporation to yield the crude product as a red solid. The product was first purified by mixed solvent recrystallization using 10:1 (v/v) hexane/CH_2Cl_2. The recovered solid was purified further by silica gel column chromatography (hexanes) to yield a red solid (0.235 g, 60%). ^{1}H NMR (400 mHz, $CDCl_3$): 7.30 (dd, 2H, J = 5.1, 1.2), 7.13 (dd, 2H, J = 3.5, 1.3), 7.12 (d, 4H, J = 3.5), 7.05 (m, 6H), 2.70 (m, 12H), 1.57 (m, 12H), 1.42 (m, 12H), 1.31 (m, 48H), 0.87 (m, 18H). $^{13}C\{^1H\}$ NMR (100 MHz, $CDCl_3$): 140.43, 140.28, 136.81, 136.66, 136.11, 135.30, 135.13, 130.00, 129.78, 129.58, 127.36, 126.39, 126.34, 125.89, 125.36, 123.84, 31.90, 31.88, 30.74, 30.68, 29.91, 29.28, 29.26, 28.24, 28.13, 22.70, 22.69, 14.13. HRMS (MALDI$^+$): m/z calcd. for $C_{84}H_{116}S_9$ 1412.656 $[M]^+$, found 1412.653. Elemental analysis calcd. for $C_{84}H_{116}S_9$: C, 71.33; H, 8.27; found C, 71.49; H, 8.44.

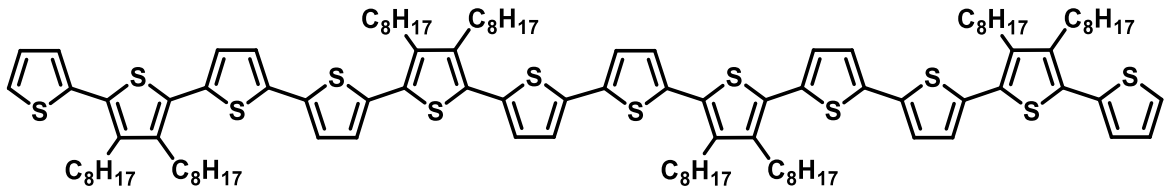

*3',3'''',3''''''',3'''''''''',4',4'''',4''''''',4''''''''''-octaoctyl-2,2':5',2'':5'',2''':5''',2'''':5'''',2''''':5''''',2''''''':5''''''',2''''''':5''''''',2''''''':5''

5.4.2. Photophysical Measurements

Absorption spectra were recorded on a Varian Cary 6000i UV-Vis-NIR spectrophotometer with Starna Quartz cells. Luminescent measurements were recorded on a Photon Technology International QM 4 spectrophotometer.

5.4.3. Electrochemical Measurements

Electrochemical measurements were recorded in a dry-box under a nitrogen atmosphere using a GPES system from Eco. Chemie B. V. All experiments were carried out in a CH_2Cl_2 solution containing 0.1 M [(*n*-Bu)$_4$N][PF_6] ($TBAPF_6$) as supporting electrolyte. The $TBAPF_6$ was purified via recrystallization three times from boiling ethanol before being dried for 3 days under active vacuum at 80 °C. A three-electrode cell consisting of a Ag/$AgNO_3$ reference electrode (Ag wire incubated in a 0.01 M $AgNO_3$ solution with 0.1M $TBAPF_6$ in CH_3CN), a glassy carbon working electrode (3.0 mm), and a Pt wire coil counter electrode was utilized. All measured potentials were corrected to the ferrocene/ferrocenium redox couple measured as an external reference.

5.4.4. Resonance Raman Spectroscopy

Experimental setup has been previously reported.[376,377]

5.5. REFERENCES

(145) Van De Wetering, K.; Brochon, C.; Ngov, C.; Hadziioannou, G. *Macromolecules* **2006**, *39*, 4289–4297.

(147) Thompson, B. C.; Fréchet, J. M. J. *Angew. Chem. Int. Ed.* **2008**, *47*, 58–77.

(148) Shao, Y.; Yang, Y. *Adv. Mater.* **2005**, *17*, 2841–2844.

(156) Yost, S. R.; Hontz, E.; Yeganeh, S.; Van Voorhis, T. *J. Phys. Chem. C* **2012**, *116*, 17369–17377.

(159) Smith, M. B.; Michl, J. *Chem. Rev.* **2010**, *110*, 6891–6936.

(164) Ewbank, P. C.; Laird, D.; McCullough, R. D. In *Organic Photovoltaics*; Brabec, C., Dyakonov, V., Scherf, U., Eds.; Wiley-VCH Verlag GmbH & Co. KGaA, 2008; pp 1–55.

(165) Hsing-Ju Wang; Chih-Ping Chen; Ru-Jong Jeng. *Mater. 1996-1944* **2014**, *7*, 2411–2439.

(166) McCullough, R. D.; Lowe, R. D.; Jayaraman, M.; Anderson, D. L. *J. Org. Chem.* **1993**, *58*, 904–912.

(167) Reid, O. G.; Pensack, R. D.; Song, Y.; Scholes, G. D.; Rumbles, G. *Chem. Mater.* **2014**, *26*, 561–575.

(168) Elschner, A.; Kirchmeyer, S. In *Organic Photovoltaics*; Brabec, C., Dyakonov, V., Scherf, U., Eds.; Wiley-VCH Verlag GmbH & Co. KGaA, 2008; pp 211–242.

(254) Al-Ibrahim, M.; Roth, H.-K.; Schroedner, M.; Konkin, A.; Zhokhavets, U.; Gobsch, G.; Scharff, P.; Sensfuss, S. *Org. Electron.* **2005**, *6*, 65–77.

(357) *Handbook of Oligo- and Polythiophenes*; Fichou, D., Ed.; Wiley-VCH: Weinheim, 1999.

(358) *Handbook of Thiophene-Based Materials*; Perepichka, I. F., Perepichka, D. F., Eds.; John Wiley & Sons, Ltd, 2009.

(359) *Handbook of Thiophene-Based Materials: Applications in Organic Electronics and Photonics*; Perepichka, I. F., Perepichka, D. F., Eds.; John Wiley & Sons Ltd.: West Sussex, U.K., 1999; Vol. I,II.

(360) Beljonne, D.; Cornil, J.; Friend, R. H.; Janssen, R. A. J.; Brédas, J. L. *J. Am. Chem. Soc.* **1996**, *118*, 6453–6461.

(361) Siegert, S.; Vogeler, F.; Marian, C. M.; Weinkauf, R. *Phys. Chem. Chem. Phys.* **2011**, *13*, 10350–10363.

(362) Becker, R. S.; Seixas de Melo, J.; Maçanita, A. L.; Elisei, F. *J. Phys. Chem.* **1996**, *100*, 18683–18695.

(363) Schaffer, H. E.; Heeger, A. J. *Solid State Commun.* **1986**, *59*, 415–421.

(364) Yamaguchi, S.; Hamaguchi, H. *Chem. Phys. Lett.* **1994**, *227*, 255–260.

(365) Sugita, A.; Shiraishi, Y.; Kobayashi, T. *Chem. Phys. Lett.* **1998**, *296*, 365–371.

(366) Weinberg-Wolf, J. R.; McNeil, L. E. *Phys. Rev. B* **2004**, *69*, 125202.

(367) Clarke, T. M.; Gordon, K. C.; Chan, W. S.; Phillips, D. L.; Wagner, P.; Officer, D. L. *ChemPhysChem* **2006**, *7*, 1276–1285.

(368) Yu, W.; Zhou, J.; Bragg, A. E. *J. Phys. Chem. Lett.* **2012**, *3*, 1321–1328.

(369) Yu, W.; Donohoo-Vallett, P. J.; Zhou, J.; Bragg, A. E. *J. Chem. Phys.* **2014**, *141*, 044201.

(370) Köhler, A.; Bässler, H. *Mater. Sci. Eng. R Rep.* **2009**, *66*, 71–109.

(371) Varnavski, O.; Abeyasinghe, N.; Aragó, J.; Serrano-Pérez, J. J.; Ortí, E.; López Navarrete, J. T.; Takimiya, K.; Casanova, D.; Casado, J.; Goodson, T. *J. Phys. Chem. Lett.* **2015**, *6*, 1375–1384.

(372) Swanson, L. S.; Lane, P. A.; Shinar, J.; Yoshino, K.; Wudl, F. *Synth. Met.* **1992**, *50*, 473–480.

(373) Shinar, J.; Swanson, L. S. *Synth. Met.* **1992**, *50*, 621–630.

(374) Bennati, M.; Németh, K.; Surján, P. R.; Mehring, M. *J. Chem. Phys.* **1996**, *105*, 4441–4447.

(375) Monkman, A. P.; Burrows, H. D.; Hamblett, I.; Navarathnam, S.; Svensson, M.; Andersson, M. R. *J. Chem. Phys.* **2001**, *115*, 9046–9049.

(376) Angelella, M.; Wang, C.; Tauber, M. J. *J. Phys. Chem. A* **2013**, *117*, 9196–9204.

(377) Wang, C.; Angelella, M.; Doyle, S. J.; Lytwak, L. A.; Rossky, P. J.; Holliday, B. J.; Tauber, M. J. *J. Phys. Chem. Lett.* **2015**, *6*, 3521–3527.

(378) Hwang, E.; de Silva, K. M. N.; Seevers, C. B.; Li, J.-R.; Garno, J. C.; Nesterov, E. E. *Langmuir* **2008**, *24*, 9700–9706.

(379) Oeter, D.; Egelhaaf, H.-J.; Ziegler, C.; Oelkrug, D.; Göpel, W. *J. Chem. Phys.* **1994**, *101*, 6344–6352.

(380) Chen, T.-A.; Rieke, R. D. *Synth. Met.* **1993**, *60*, 175–177.

(381) Krömer, J.; Bäuerle, P. *Tetrahedron* **2001**, *57*, 3785–3794.

Chapter 6: Polymeric Redox-Mediated Ionophores: A Unique Platform for the Separation of Nuclear Waste

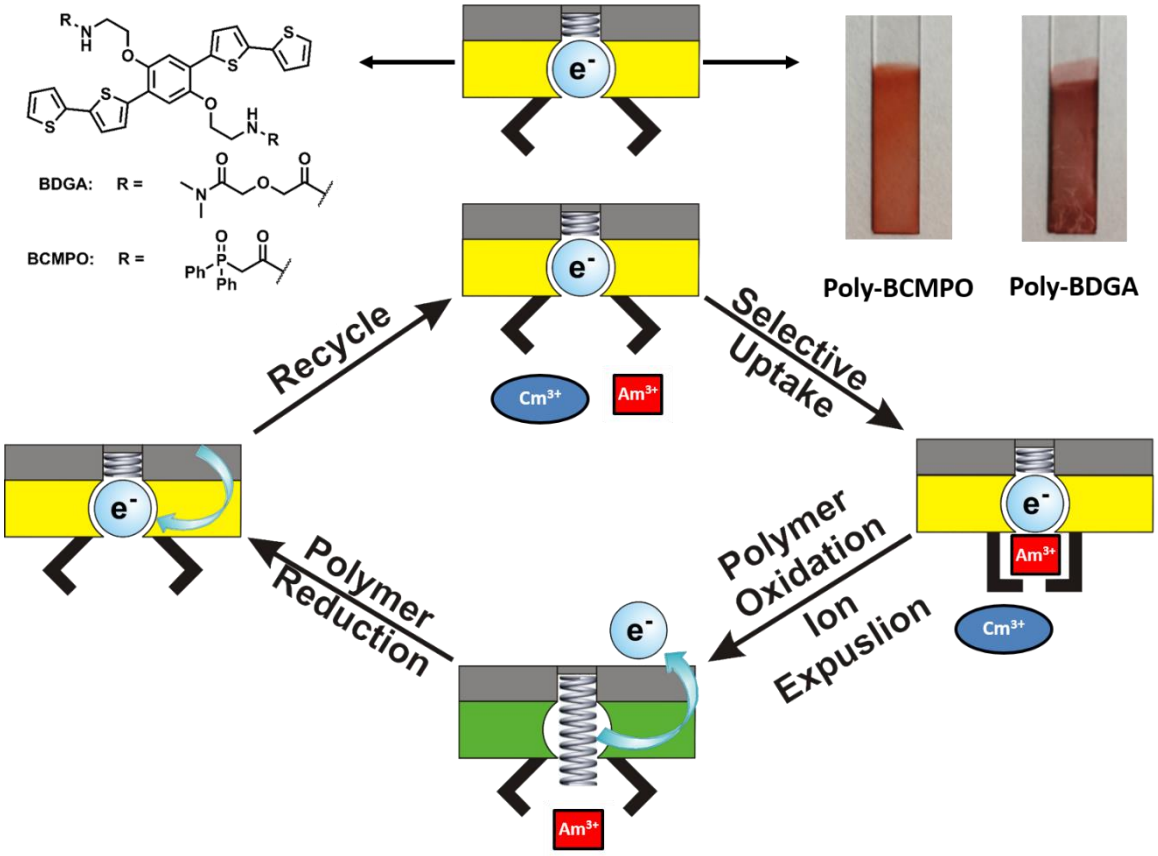

6.1. INTRODUCTION

As concerns about future energy sources persist, nuclear power is primed to be a key alternative energy source for prolonging current supplies. However, the disposal of long lived radioactive byproducts remains an important challenge to the nuclear industry. As such, the effective separation of large quantities of nuclear waste for remediation purposes remains a point of emphasis for today's researchers. Ion exchange materials and chromatographic techniques have shown excellent separation efficiencies[382–387] but are not capable of handling the high throughputs required by commercial plants. Substantial efforts have also been placed into the development of ligand-based liquid/liquid extraction systems.[388,389,143,141,142,390,391] These systems can handle high throughputs, but tend to suffer from low selectivity, generate large volumes of additional waste, and require stripping agents to recover the active separation material. Therefore, it is highly desirable to develop alternative separation systems to bypass these processing issues. To this end, modified poly(thiophene) based systems represent a new and intriguing approach to the problem of nuclear waste separation.

Poly(thiophene) based systems have been an area of interest due to the ease of synthetic manipulation and remarkable electronic properties of these materials. These polymers have found use in a wide variety of fields including organic photovoltaics, field effect transistors, nonlinear optics, catalysis, electrode modification and electrochemical sensing.[358,392,393] However, the application of poly(thiophenes) to the field of separation materials remains largely underdeveloped. In this communication, we report the synthesis of a poly(thiophene)-based material containing ionophores preorganized to perform redox-mediated separations of nuclear waste. To accomplish this selective extraction, carbamoylmethylphosphine oxide (CMPO) and diglycolamide (DGA) derivatives are utilized. CMPO- and DGA-based systems have been shown in the literature to display

both selectivity and high extraction capabilities, especially when multiple ligands are preorganized onto platform systems, such as calixarenes and tripodands, to maximize synergistic effects.[141,142,390] Furthermore, the preorganization of extractants onto heterogeneous support systems is desirable to enhance the ease of recovery of the active extractant material during processing. The usefulness of the poly(thiophene) backbone ultimately lies in its capacity to affect the binding constant of the chelated cations upon electrochemical doping. The ability to electrochemically mediate the uptake of metal ions has been demonstrated by Le Derf *et al.* for both monomeric solution based systems[394] as well as in tethered polymeric systems,[134] but has yet to be applied to nuclear waste remediation.

In this novel system, electropolymerization of the thiophene-based monomer leads to the deposition of the separation material onto the surface of an electrode. The modified electrode may then be placed into a solution of aqueous nuclear waste where the grafted ionophores selectively extract rare earth elements from the nuclear waste. Transfer of the electrode to a fresh electrolyte solution and subsequent electrochemical oxidation of the polymer membrane purges the material of any chelated cations through coulombic repulsion. Facile recovery of the separation material is then achieved via reduction of the polymer core to the neutral state in a fresh electrolyte solution. This process is illustrated in Figure 6.1.

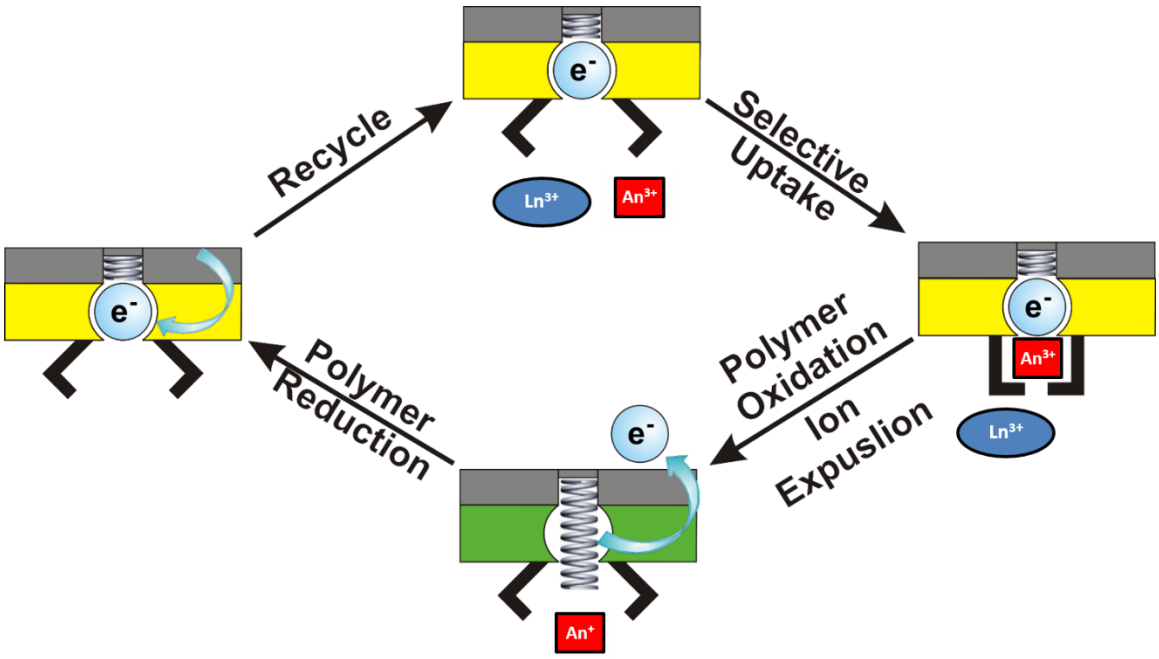

Figure 6.1. Diagram depicting the proposed operation scheme for the polymeric separation materials deposited onto an electrode. This illustrates the selective extraction and electrochemically-mediated release of metal ions from the polymer film.

6.2. Results and Discussion

6.2.1. Monomer Design and Synthesis

Preparation of the monomer core, which is shown in Scheme 6.1, began with the reaction of 2,5-dibromobenzene-1,4-diol with 1,2-dibromoethane to attach ethyl arms to the monomer core, generating 1,4-dibromo-2,5-bis(2-bromoethoxy)benzene (**2**).

Scheme 6.1. Synthesis of monomer core.

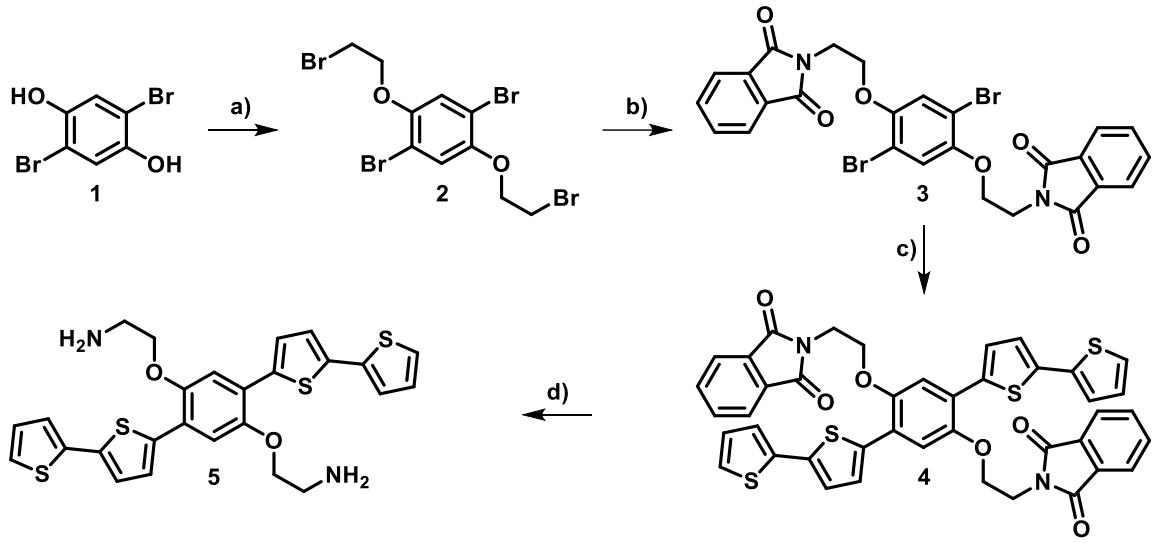

a) K_2CO_3, 18-crown-6, $BrCH_2CH_2Br$, acetone, reflux, 48 h, 69% b) potassium phthalimide, 18-crown-6, DMF, 50 °C, 14 h, 92% c) Pd_2dba_3, XPhos, 5-(tri-*n*-butyltin)-2,2'-bithiophene, DMF, 100 °C, 16 h, 84% d) $H_2NNH_2 \cdot H_2O$, $CHCl_3$\EtOH (5:3), 75 °C, 18 h, 95%.

Next, the first step in a Gabriel synthesis was undertaken by reaction of **2** with potassium phthalimide to resulting in 2,2'-(((2,5-dibromo-1,4-phenylene)bis(oxy))bis(ethane-2,1-diyl))bis(isoindoline-1,3-dione) (**3**). A Stille coupling with **3** was then utilized to attach the electropolymerizable bithiophene to synthesize 2,2'-(((2,5-bis(bithiophene)-1,4-phenylene)bis(oxy))bis(ethane-2,1-diyl))bis(isoindoline-1,3-dione) (**4**) followed by hydrazinolysis to generate 2,2'-((2,5-bis(bithiophene)-1,4-phenylene)bis(oxy))diethanamine (**5**) containing the primary ethylamine arms. A key feature of the polymer system involves placing the bithiophene units *para*- to one another to promote conductivity. Furthermore, the ethylamine arms were synthetically grafted to the monomer core via ether linkages in order to promote flexibility for coordination, while providing an attachment for the ionophoric moieties that is stable against oxidation[143] as shown in Scheme 6.2.

Scheme 6.2. Synthesis of ligand enhanced monomers

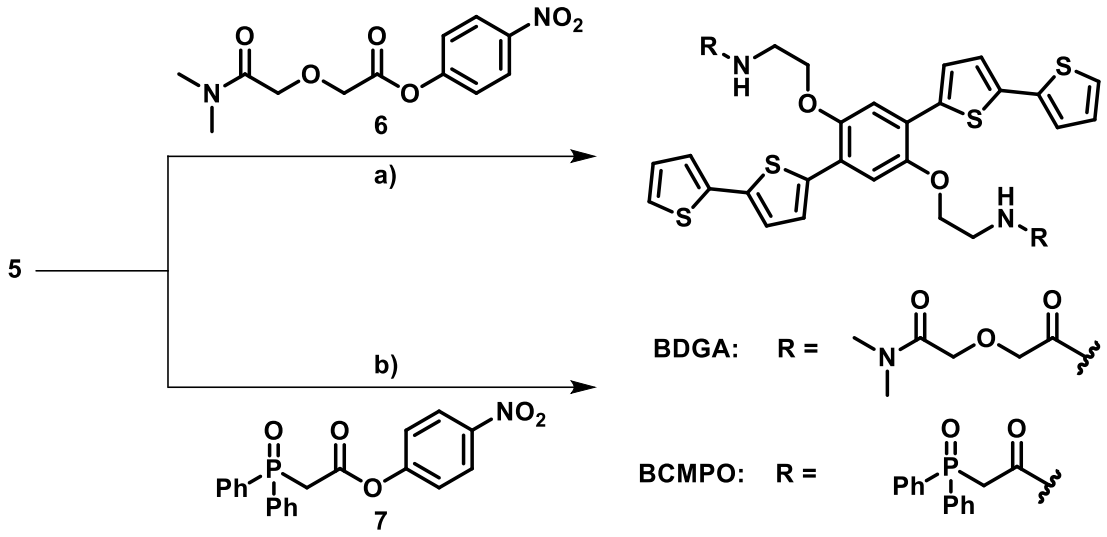

a) NEt_3, $CHCl_3$, r.t., 1 week, 61% b) NEt_3, $CHCl_3$, r.t., 1 week, 42%.

6.2.2. Monomer Coordination Studies

Monomers BCMPO and BDGA were both fully characterized by NMR, IR, UV-Vis, mass spectrometry, and elemental analysis. Chelation of the monomers to the surrogate actinide thorium, in the form of $Th(NO_3)_4$, was observed via infrared spectroscopy (IR) and matched well with previous literature values for actinide coordination.[395,396] The IR spectra for BDGA shows a single broad peak at 1646 cm^{-1} corresponding to the amide carbonyl stretching frequency which, upon introduction of Th(IV), shifts to 1633 cm^{-1}. Similarly, BCMPO shows strong peaks at 1175 cm^{-1} and 1667 cm^{-1} corresponding to the phosphine oxide and carbonyl stretching frequencies, respectively. Chelation to Th(IV) shifts the phosphine oxide peak to 1120 cm^{-1} and the carbonyl frequency to 1617 cm^{-1}. A Job's plot analysis was carried out for BCMPO by monitoring the $^{31}P\{^1H\}$ NMR, and a monomer : cation ration of 1 : 1 was observed (Figure 6.2).

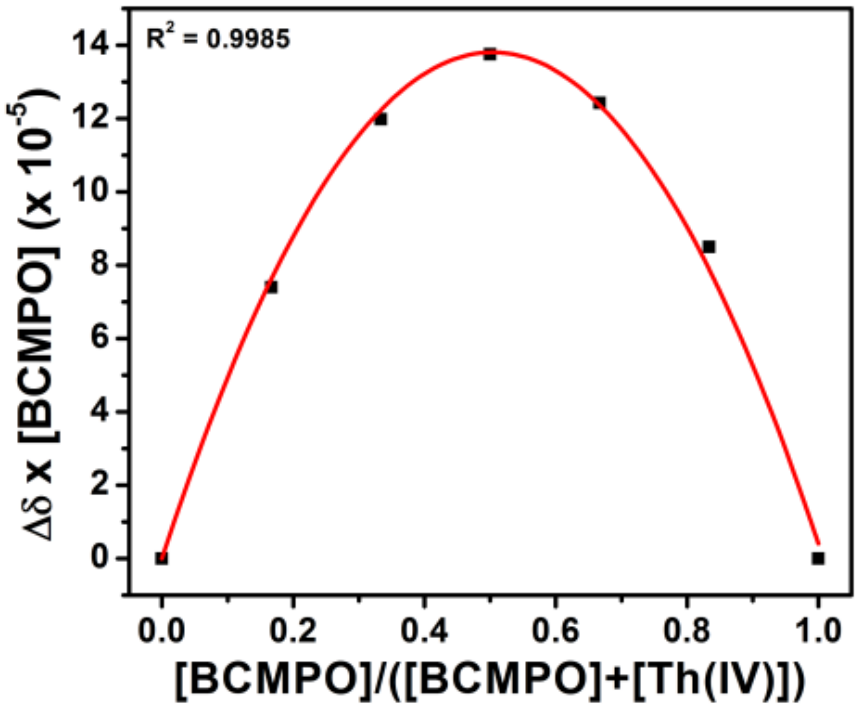

Figure 6.2. Job's plot of BCMPO. The results indicate a 1:1 binding ratio of Th(IV) to BCMPO monomer.

No suitable spectroscopic handles were observed for the BDGA monomer and, therefore, the binding ratio could not be determined. Uptake of Th(IV) into the material showed little influence on the electronic absorption spectra of the monomers implying little to no involvement of the monomer core in the coordination of Th(IV) (Figure 6.3).

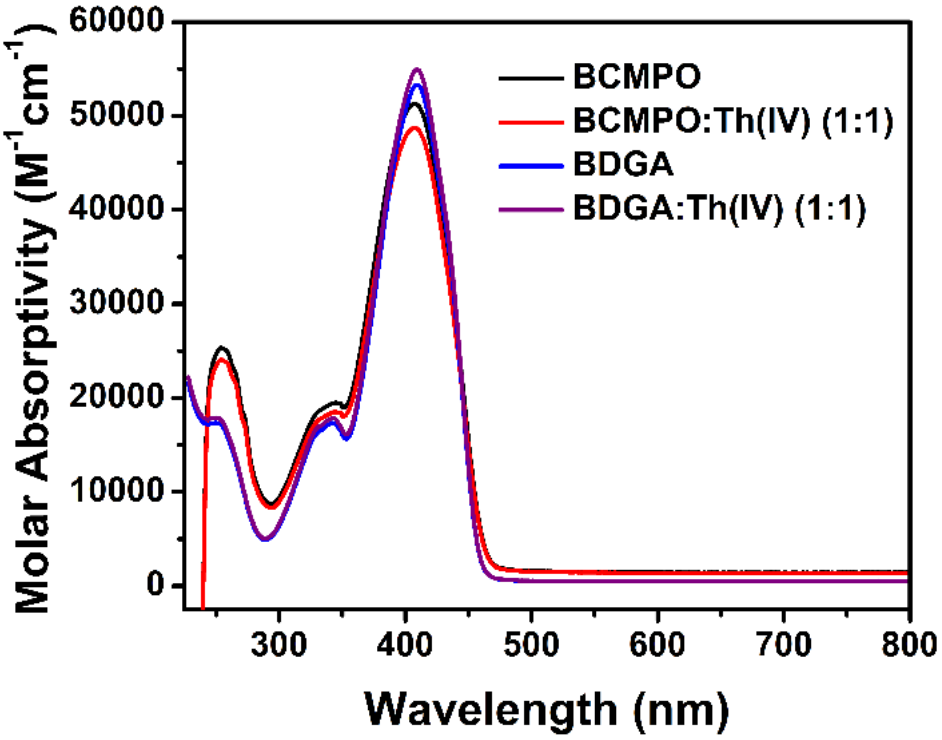

Figure 6.3. UV-Vis absorption spectra of the monomers BCMPO and BDGA in CH_3CN before and after the introduction of Th(IV) Nitrate.

6.2.3. Polymerization of BDGA and BCMPO and Polymer-Based Electrochemical Studies

The polymers may be deposited onto a variety of conducting materials (Pt, stainless steel, ITO) by electropolymerization via cyclic voltammetry (Figure 6.4a,b). Polymer growth can be observed by the increasing current, associated with polymer oxidation, with each successive scan. The observed linear increase in current (Figure 6.4a,b insets) indicates steady propagation of the polymer growth and allows for straightforward control over polymer thickness.

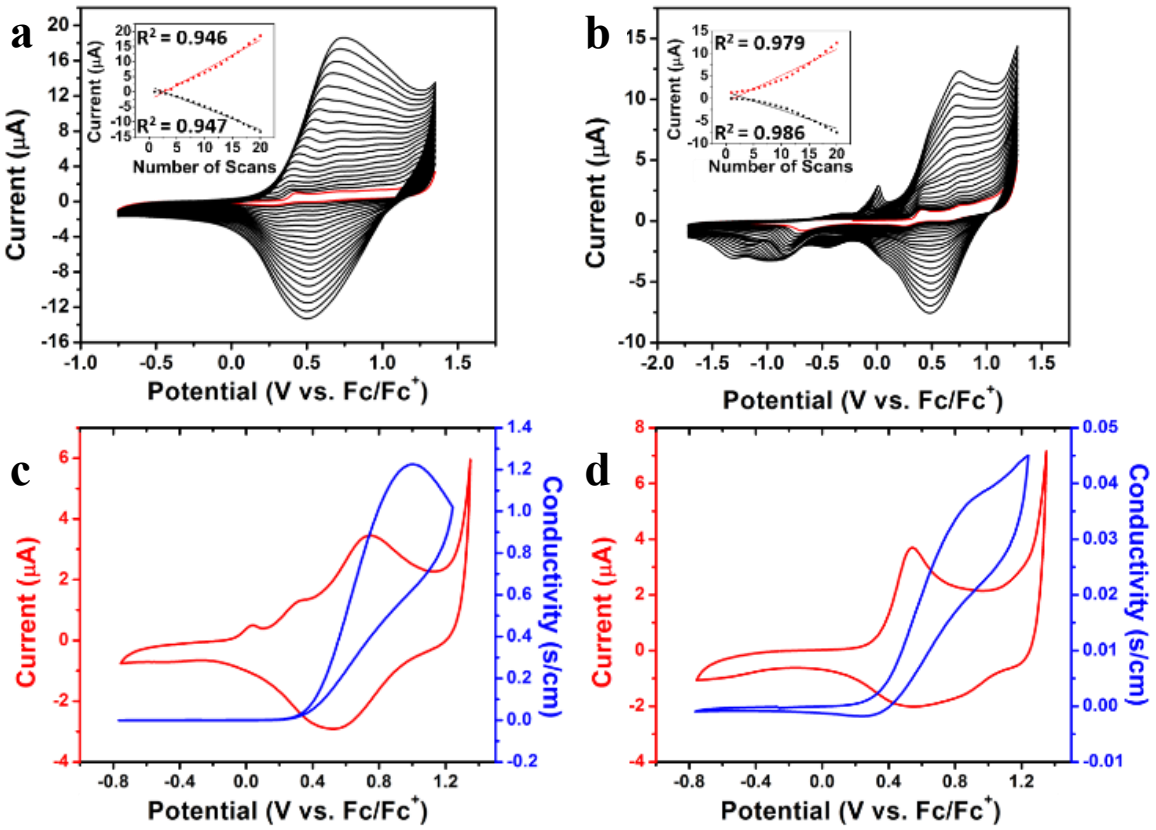

Figure 6.4. Electropolymerization of (a) poly-BDGA and (b) poly-BCMPO onto a platinum button electrode. Polymer films were deposited by cycling 20 times between the given potentials at 100 $mV \cdot s^{-1}$ in a 10^{-4} M solution of monomer. Insets show a linear increase in peak current with each successive scan suggesting linear control of polymer growth. Conductivity profiles of (c) poly-BDGA and (d) poly-BCMPO were recorded using a platinum interdigitated electrode. Conductivities were corrected to P3MT.[397]

In situ conductivity studies revealed excellent conductivity for the polymers (Figure 6.4c,d). A drastic increase in the conductivity is associated with the primary polymer peak associated with oxidation of the polymer backbone, demonstrating that the doping of the polymer films has a considerable influence on the conductivity of the material. Furthermore, scan-rate dependence studies displayed a linear trend up to 500 $mV \cdot s^{-1}$ (Figure 6.5), indicating that the polymers have excellent conductivity and high

ionic porosity which should allow for the entire polymer system to participate in the extraction and separation processes.

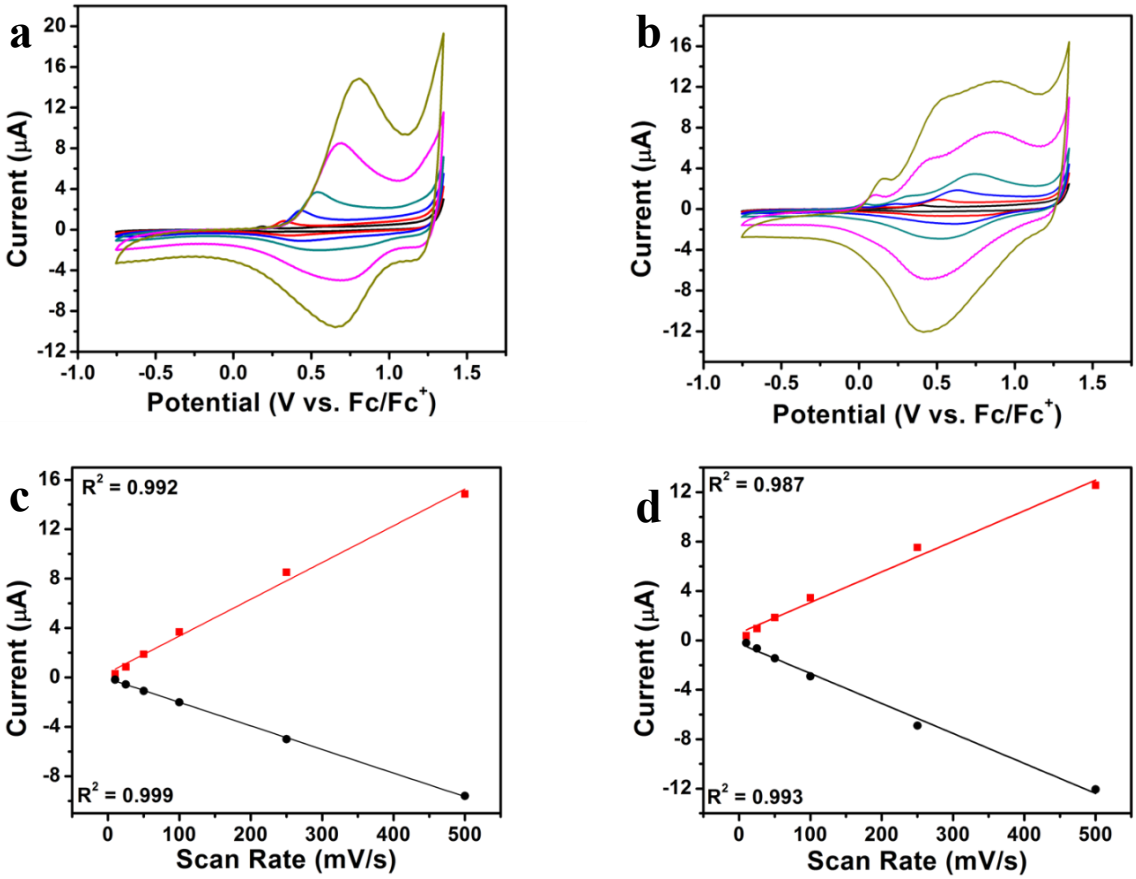

Figure 6.5. Scan rate dependence studies for (a) poly-BCMPO and (b) poly-BDGA. The plots of the peak current versus the scan rate are shown for (c) poly-BCMPO and (b) poly-BDGA. Data points are representative of the peak anodic (red) and cathodic (black) currents at the given scan rate.

The spectroelectrochemistry of the polymer films further confirmed the highly conductive nature of the film as demonstrated by the extensive delocalization of the bipolaron in the doped state evidenced by an extremely broad band in the near infrared portion of the absorption spectra (Figure 6.6).

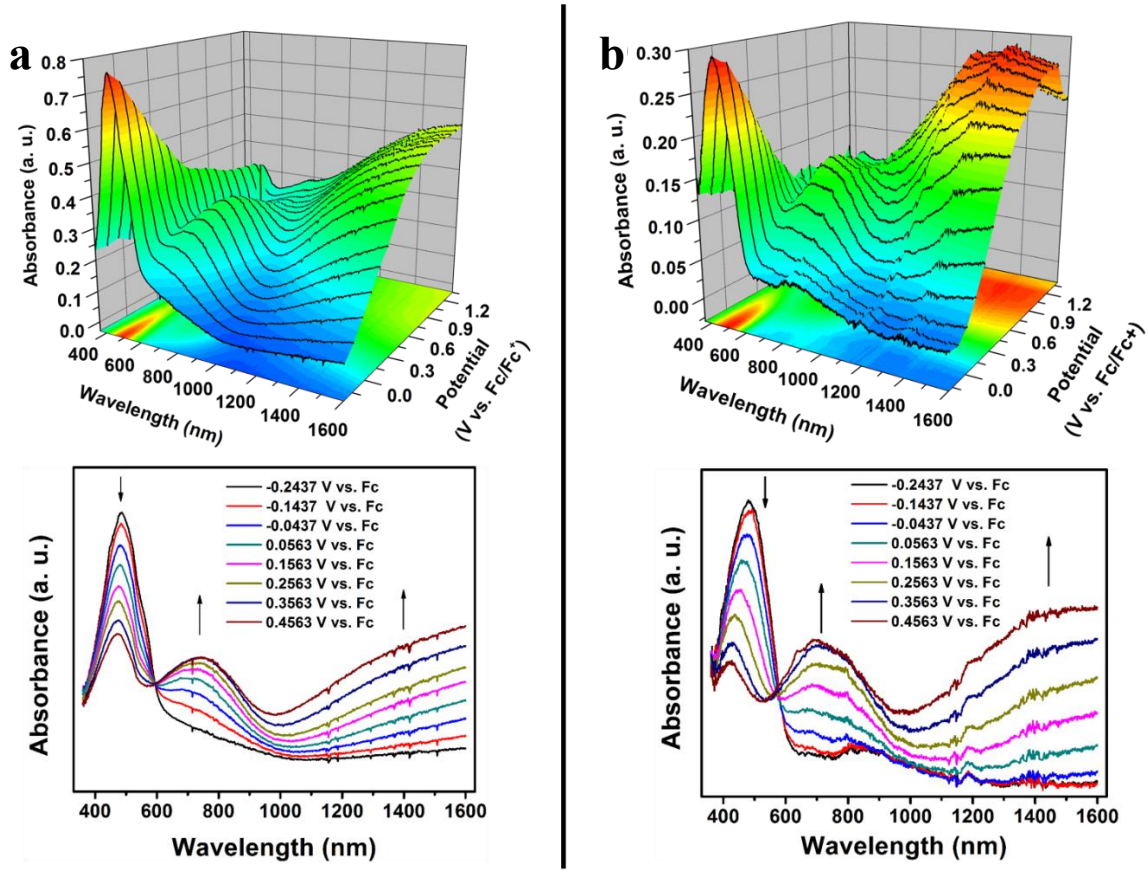

Figure 6.6. Spectroelectrochemistry of (a) poly-BDGA and (b) poly-BCMPO polymer films. As the potential is increased, the spectra show the emergence of the polaron peak at 741 nm and 700 nm, respectively. The neutral polymer peak at approximately 450 nm continuously decreases with increasing potential. Furthermore, a bipolaron peak which spans the 1000 nm to 1600 nm range was observed as well. With increasingly higher potentials the broad bipolaron peaks continues to increase with a concomitant decrease in the polaron peaks.

6.2.4. Polymer Extraction Studies

To establish cation uptake, polymer films were incubated 30 minutes in an aqueous solutions of 0.1 M $Th(NO_3)_4$, rinsed thoroughly with deionized water followed by acetonitrile, and then examined by X-ray photoelectron spectroscopy (XPS) as well as by IR. The IR spectra indicated coordination to Th(IV) with the carbonyl stretches

decreasing from 1648 cm^{-1} to 1637 cm^{-1} for poly-BDGA and from 1667 cm^{-1} to 1648 cm^{-1} for poly-BCMPO (Figure 6.7).

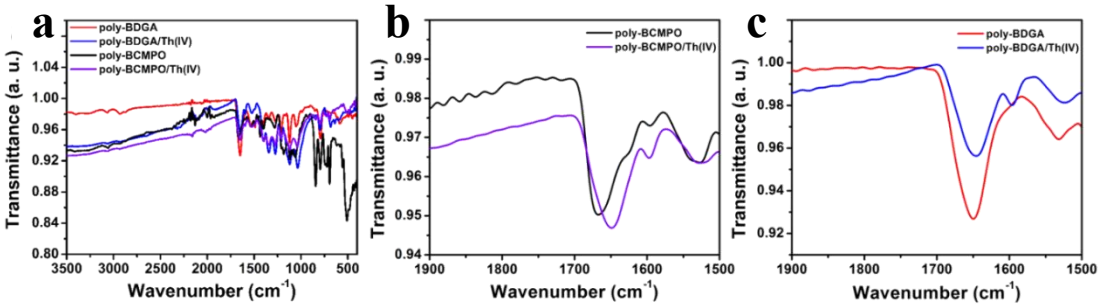

Figure 6.7. (a) Full infrared spectra of polymer films before and after Th(IV) extraction. Direct comparison of the C=O stretch before and after Th(IV) extraction for (b) poly-BCMPO and (c) poly-BDGA.

Analysis by XPS showed ion uptake into the films as evidenced by the thorium 4*f* peaks at 335 eV and 345 eV. Integration of the thorium 4*f* and sulfur 2*p* peaks allowed for the determination of the percent loading of thorium per monomer unit. The control film which lacks ionophores did not display any substantial extraction of Th(IV). A representative XPS spectra is shown in Figure 6.8a.

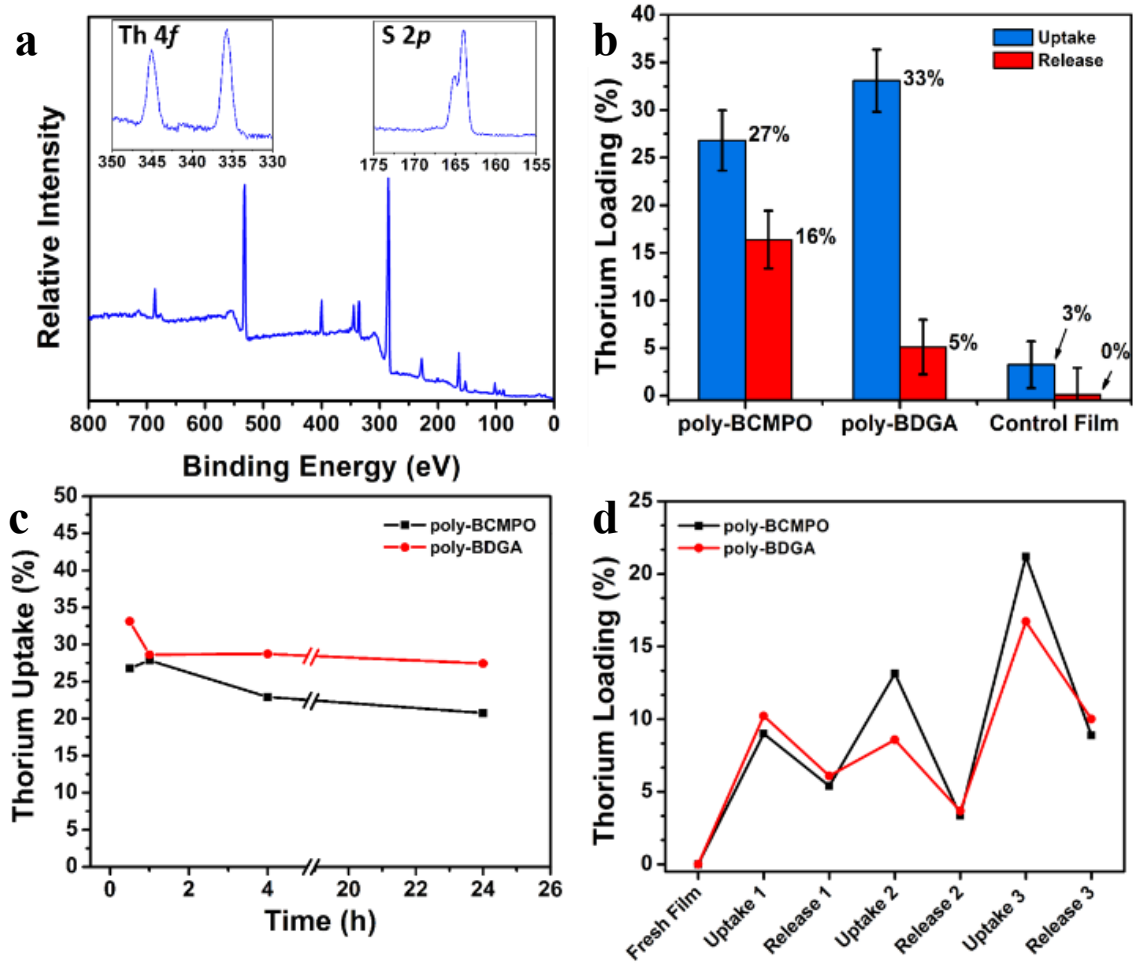

Figure 6.8. (a) Representative XPS spectra of a polymer film (poly-BDGA) after the extraction of Th(IV) from a solution containing 0.1 M Th(IV). Insets show the thorium 4*f* and sulfur 2*p* signals used for determining the percent thorium loadings in the polymer films. Control film (poly-1,4-di([2,2'-bithiophen]-5-yl)benzene) shows minimal uptake and no retention of Th(IV) (b) The XPS results show the material is capable of thorium uptake and a significant decrease in the thorium content is observed after electrochemically induced release. The variability in the results was approximately ±3%. The materials demonstrate (c) the ability to exhibit rapid uptake of thorium ions into the film and (d) undergo multiple extraction cycles.

Both poly-BCMPO and poly-BDGA showed considerable uptake of Th(IV) into the material with loadings at 27% and 33%, respectively of the maximum loading

capacity (based on a 1:1 ratio of monomer to Th(IV), Figure 6.8b). Furthermore, the extraction process is shown to be rapid, reaching peak uptake in 30 minutes for both polymers (Figure 6.8c).

As discussed above, release of the Th(IV) ions may be induced by doping the films with positive charges and allowing columbic repulsion to expel the ions from the polymer matrix. To test the ability of the films to release thorium, loaded films were transferred to an acetonitrile solution containing 0.1 M TBAH as the supporting electrolyte and were subjected to five oxidative scans from –0.25 V to 1.25 V via cyclic voltammetry to induce release. The films were once again examined by XPS and a marked decrease in thorium content was observed for both polymers with poly-BCMPO decreasing to 16% and poly-BDGA decreasing to 5%; this represents a total release of 39% and 85%, respectively (Figure 3b). Furthermore, the materials show the capability for extended uptake and release cycles as shown in Figure 3d. However, a general increase in the thorium content was observed with cycling. XPS revealed a set of Th(IV) satellite bands at 349 eV and 353 eV suggesting that some of the thorium is present in a different electronic environment from the typical position shown by uptake into the coordination pocket (Figure 6.9).

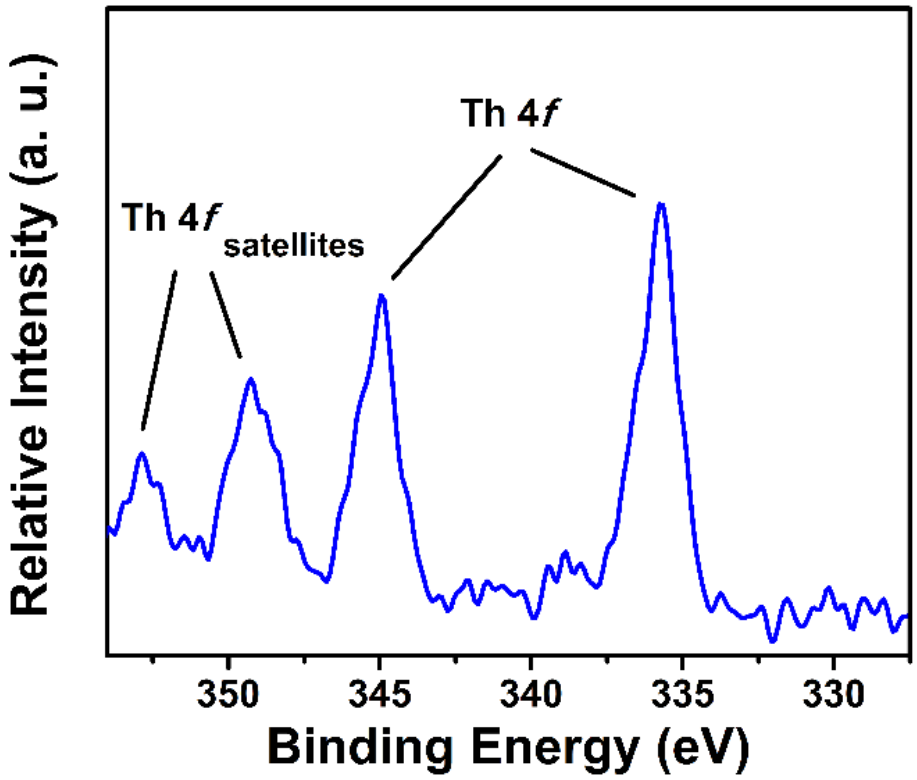

Figure 6.9. XPS signal from the thorium 4*f* region, which indicates the presence of thorium in a second electronic environment as indicated by the emergence of satellite peaks at 353 eV and 349 eV.

This is potentially caused by an irreversible deposition of thorium into the polymer films upon electrochemical cycling which would lead to the observed increase in Th(IV) uptake. Further studies into the nature of the thorium deposition are required to understand the mechanism and nature of the deposited species.

While many materials are capable of extracting various ions from solution, selectivity remains a much more elusive property. The ability of poly-BCMPO and poly-BDGA to differentiate between actinides and lanthanides was tested using an aqueous solution containing 0.1 M $Th(NO_3)_4$ and 0.1 M $Gd(NO_3)_3$. Results showed only Th(IV) uptake into the film, with no signs of Gd(III) uptake (Figure 6.10).

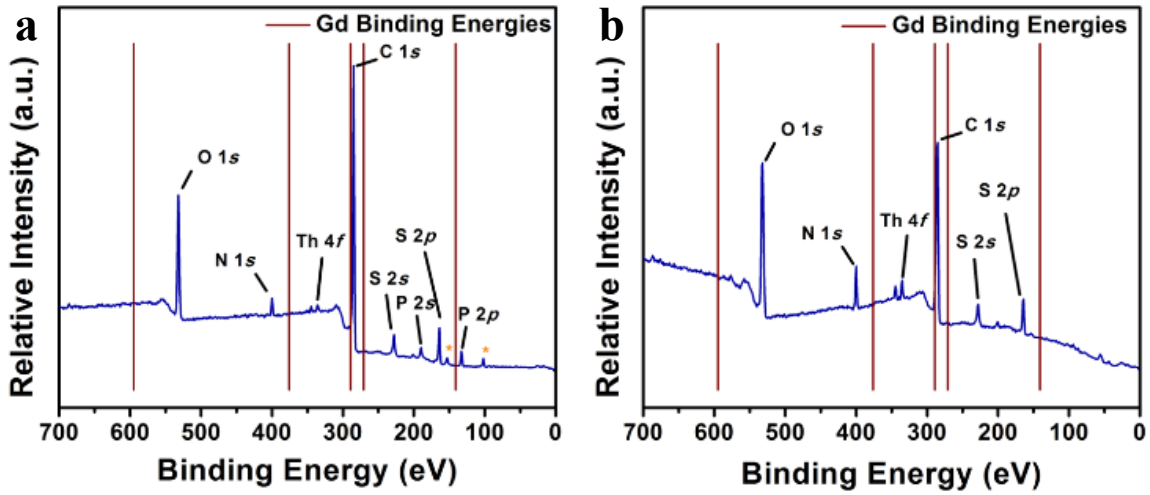

Figure 6.10. XPS survey scans of (a) poly-BCMPO and (b) poly-BDGA showing the presence of thorium but none of the characteristic peaks for gadolinium, demonstrating the ability of the films to exhibit selectivity for actinides over lanthanides.

Similar tests were performed to determine the material's ability to differentiate between two elements of the same periodic series. One of the biggest challenges of separation materials in the remediation of nuclear waste is the ability to separate americium(III) from curium(III) due to their similar ionic radii and effective nuclear charge.[387]

Americium contributes a considerable amount of radiotoxicity on both the short and long (>200,000 years) time scales due to its radioactive decay into long lived radioisotopes such as ^{237}Np ($t_{1/2}$ = 2.14 x 10^6 yr).[398] The transmutation of americium in breeder reactors before it can undergo radioactive decay can alleviate a considerable amount of the longer term radiotoxicity contributions of americium and avoid the burden placed by geologically mobile and long lived ^{237}Np.[398] It is therefore highly desirable to separate out Am(III) from Cm(III).

Therefore, to test the ability of poly-BCMPO and poly-BDGA to differentiate between Am(III) and Cm(III), the polymer films were soaked in an aqueous 1:1 solution of 0.1 M $Nd(NO_3)_3$ and 0.1 M $Sm(NO_3)_3$. Neodymium and samarium have frequently been used as surrogate atoms for the radioactive Am(III) and Cm(III) ions, respectively.[399] As seen in Figure 6.11, both systems showed selectivity for the surrogate ion Nd(III). XPS showed a Nd : Sm ratio of approximately 49 : 1 for poly-BCMPO and 4 : 1 for poly-BDGA.

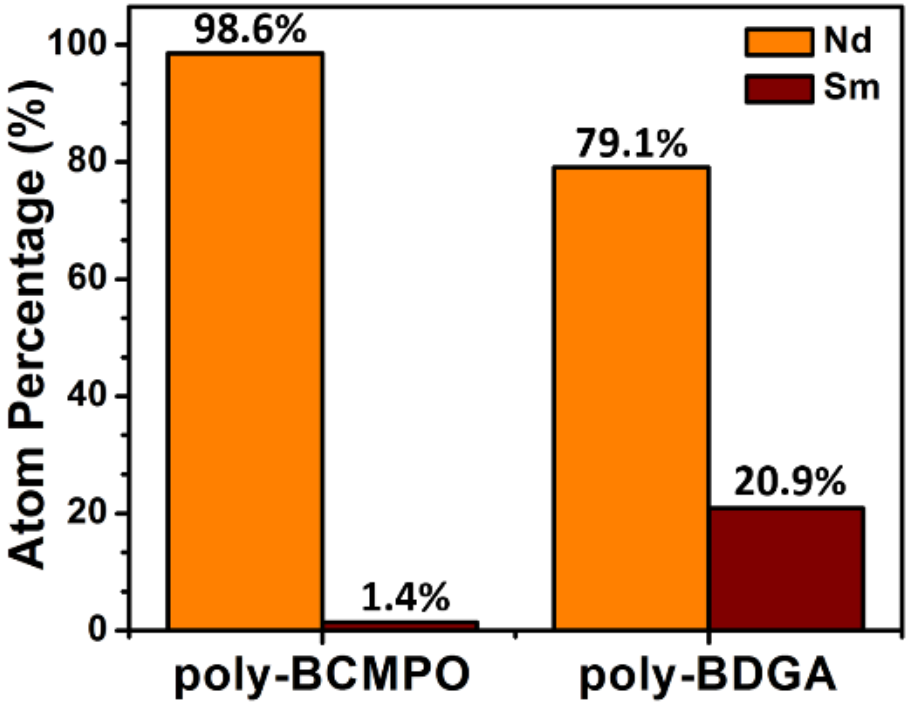

Figure 6.11. XPS results demonstrating selectivity in cation uptake from an aqueous solution containing 0.1 M Nd(III) nitrate and 0.1 M Sm(III) nitrate as surrogates for Am(III) and Cm(III), respectively.

6.3. CONCLUSION

Herein we have reported the successful synthesis of a conductive polymer system for nuclear waste remediation capable of demonstrating electrochemically controlled uptake and release of Th(IV). Infrared spectroscopy confirmed coordination of Th(IV) by the monomers and UV-Vis spectroscopy indicated little involvement of the polymer backbone in the extraction process. Job's plot analysis revealed a 1-to-1 binding ratio of the monomer to Th(IV) in solution.

Both monomer systems were shown to electropolymerize on a variety of electrode materials and exhibited excellent control over polymer growth. Furthermore, scan rate dependence, *in situ* conductivity and spectroelectrochemistry all confirm the resulting polymers are electroactive and exhibit excellent conductivity.

Coordination of Th(IV) by the conducting polymers was confirmed by infrared spectroscopy and X-ray Photoelectron Spectroscopy (XPS) and was shown to reach maximum uptake within 30 minutes. XPS comparisons of the control system with the polymer films confirmed the importance of the ionophoric arms in Th(IV) uptake. Electrochemically induced release of metal ions from the polymer matrix was observed, however, the some irreversible deposition of thorium into the polymer film also occurred. Furthermore, the system shows selectivity for actinides over lanthanides as well as displaying the ability to selectively uptake Nd(III) in the presence of Sm(III). The materials presented here show promise of being able to differentiate between Am(III) and Cm(III) as demonstrated through surrogate extractions. These systems show potential as a new class of heterogeneous separation materials for the remediation of nuclear waste.

6.4. EXPERIMENTAL

6.4.1. Synthesis and Characterization

Air and moisture sensitive reactions were carried out in heat-gun dried glassware using standard Schlenk techniques under a dry nitrogen atmosphere. Dry solvents were collected in solvent bulbs from an Innovative Technology PureSolv 400 solvent purification system, sparged with nitrogen, and stored over 3Å molecular sieves. Dry Drisolve® *N,N′*-dimethylformamide (DMF) was purchased from EMD Millipore and purged with nitrogen prior to use. 5-(tri-*n*-butyltin)-2,2'-bithiophene was prepared from literature procedures.[400] All other chemicals were used as received from commercial suppliers. Deuterated solvents were purchased from Cambridge Isotope Laboratories and used without further purification. NMR spectra were recorded with a Varian DirectDrive 400 MHz spectrometer (^{1}H 400 MHz, ^{13}C{^{1}H} 100 MHz, ^{31}P{^{1}H} 162 MHz) and referenced to residual solvent peaks except for the ^{31}P{^{1}H} spectra which was referenced to a 75% phosphoric acid sample. All NMR peak positions are reported in ppm and all coupling constants are reported in hertz (Hz).Chemical ionization (CI) mass spectra were collected on a Micromass Autospec Ultima mass spectrometer. Electrospray ionization (ESI) and atmospheric pressure chemical ionization (APCI) were collected on an Agilent Technologies 6530 Accurate Mass Q-TOF LC/MS spectrometer. Absorption spectra were recorded on a Varian Cary 6000i UV-Vis-NIR spectrophotometer. Infrared spectra were taken on a Nicolet iS50 FT-IR spectrometer. X-ray photoelectron spectroscopy (XPS) was carried out on a PHI 5700 XPS system equipped with a dual Mg X-ray source and monochromatic Al X-ray source complete with depth profile and angle-resolved capabilities. Elemental analysis services were provided by Midwest Microlab, LLC.

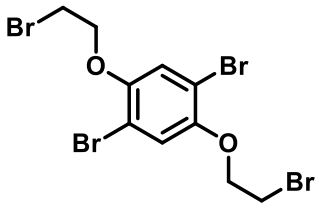

1,4-dibromo-2,5-bis(2-bromoethoxy)benzene (**2**): 2,5-dibromohydroquinone (2.03 g, 7.58 mmol), K_2CO_3 (5.86 g, 138.61 mmol), and 18-crown-6 (0.297 g, 1.10 mmol) were suspended in a sparged mixture of 1,2-dibromoethane (15 mL) and acetone (5 mL). The mixture was heated to reflux under a nitrogen blanket and stirred vigorously for 2 days. The resulting mixture was allowed to cool to room temperature. The reaction mixture was poured onto a celite® and silica pad, flushed through with CH_2Cl_2 (300 mL), and evaporated to dryness. The crude product was stirred with 10 mL of EtOH and filtered to obtain pure product as a tan solid (2.518 g, 69%). ^{1}H NMR (400 MHz, $CDCl_3$): δ 3.63 (t, 4H, J = 6.4 Hz), 4.26 (t, 4H, J = 6.4 Hz), 7.11 (s, 2H). $^{13}C\{^1H\}$ NMR (100 MHz, $CDCl_3$): δ 28.5, 70.3, 111.8, 119.7, 150.0. HRMS (CI): *m/z* calcd for $C_{10}H_{10}O_2Br_4$ $[M]^+$ 481.7368; found 481.7368.

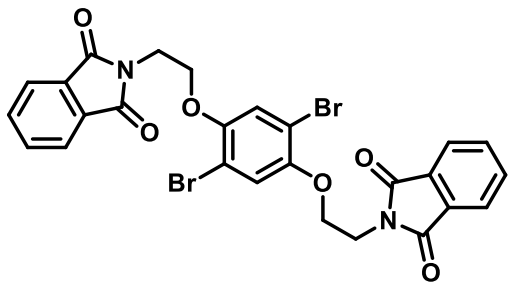

2,2'-(((2,5-dibromo-1,4-phenylene)bis(oxy))bis(ethane-2,1-diyl))bis(isoindoline-1,3-dione) (**3**): Potassium phthalimide (1.11 g, 5.99 mmol), 18-crown-6 (0.039 g, 0.163 mmol), and **2** (1.01 g, 2.10 mmol) were dissolved in 6 mL of dry, sparged DMF. The mixture was heated at 50 ˚C for 14 h. After cooling to room temperature, the reaction mixture was poured into 60 mL of H_2O and stirred for 2 h. Pure white product (1.179 g, 92%) was collected by vacuum filtration. ^{1}H NMR (400 MHz, $CDCl_3$): δ 4.11 (t, 4H, J = 4.8 Hz), 4.16 (t, 4H, J = 4.8 Hz), 7.03 (s, 2H), 7.70 (m, 4H), 7.84 (m, 4H) . ^{13}C{^{1}H} NMR (100 MHz, $CDCl_3$): δ 104.6, 123.6, 124.2, 124.4, 125.89, 127.88, 136.6, 137.1, 138.7, 140.7, 154.3.

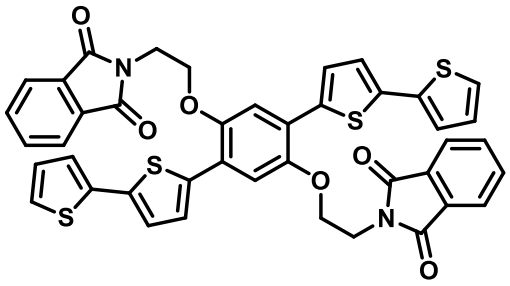

2,2'-(((2,5-bis(bithiophene)-1,4-phenylene)bis(oxy))bis(ethane-2,1-diyl))bis(isoindoline-1,3-dione) (**4**): **3** (1.00 g, 1.63 mmol) was transferred to a dry, 500 mL Schlenk flask. The reaction flask was charged with tris(dibenzylideneacetone)dipalladium(0) (0.075 g, 0.082 mmol) and XPhos (0.035 g, 0.073 mmol) in a glovebox and then placed on a Schlenk line. In a separate flask, 5-(tri-n-butyltin)-2,2′-bithiophene (2.224 g, 4.88 mmol) was dissolved in 15 mL of DMF. DMF (250 mL) was transferred via cannula into the reaction flask followed by cannula transfer of the bithiophene precursor solution. The resulting mixture was heated to 100 ºC for 16 h. Once the solution had cooled to room temperature the solvent was removed under reduced pressure. The residue was then washed with hexanes and filtered through a Celite® and silica gel pad using hexanes to flush through impurities. The desired product was then collected using CH_2Cl_2 and evaporated onto silica. The product was purified by flash chromatography using hexanes first to remove the impurity band followed by CH_2Cl_2 to collect the product. Removal of solvent *in vacuo* yielded an orange solid (1.075 g, 84%). ^{1}H NMR (400 MHz, $CDCl_3$): δ 4.18 (t, 4H, *J* = 5.9 Hz), 4.41 (t, 4H, *J* = 5.9 Hz), 7.02 (m, 4H), 7.17 (dd, 2H, *J* = 3.6, 0.6 Hz), 7.20 (dd, 2H, *J* = 5.2, 1.2 Hz), 7.21 (s, 2H), 7.36 (d, 2H, *J* = 4.0 Hz), 7.62 (m, 4H), 7.76 (m, 4H). ^{13}C{^{1}H} NMR (100 MHz, $CDCl_3$): Could not be obtained due to poor solubility. HRMS (APCI): *m*/*z* calcd for $C_{42}H_{28}N_2O_6S_4$ $[M + H]^+$ 785.09030; found 785.08951.

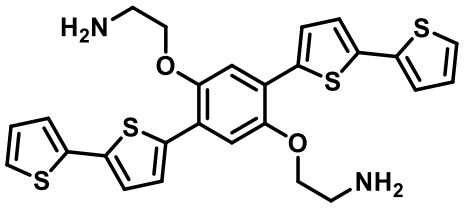

2,2'-((2,5-bis(bithiophene)-1,4-phenylene)bis(oxy))diethanamine (**5**): In air, 3.223 g (4.11 mmol) of **4** was dissolved in a minimal amount of chloroform (500 mL). Ethanol (300 mL) was then added until the solubility limit of **4** was reached. A 12 mL aliquot of an 80% hydrazine hydrate solution was added to the reaction mixtures and the reaction vessel was fitted with a condenser. The reaction mixture was refluxed at 75 ºC for 18 h. The solution was then cooled to –5 ˚C for 24 h. The solution was filtered and the yellow precipitate was discarded. The filtrate was then evaporated to dryness to yield a pure orange solid (2.038 g, 95%).^{1}H NMR (400 MHz, $CDCl_3$): δ 1.95(bs, 4H) 3.20 (t, 4H, *J* = 5.2 Hz), 4.144 (t, 4H, *J* = 5.2 Hz), 7.02 (dd, 2H, *J* = 5.2, 3.6 Hz), 7.16 (d, 2H, *J* = 4.0 Hz), 7.20 (m, 4H), 7.23 (s, 2H), 7.41 (d, 2H, *J* = 4.0 Hz). $^{13}C\{^{1}H\}$ NMR (100 MHz, $CDCl_3$): δ 41.7, 72.1, 112.1,112.9, 123.5, 124.4, 125.8, 127.9, 137.4, 137.6, 149.1, 182.9, 188.6. HRMS (APCI): *m*/*z* calcd for $C_{26}H_{24}N_2O_2S_4$ $[M + H]^+$ 525.07934; found 525.07939.

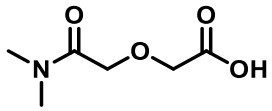

2-(2-(dimethylamino)-2-oxoethoxy)acetic acid (**6a**): In anhydrous conditions, diglycolic anhydride (5.004 g, 4.308 mmol) was dissolved in 40 mL of dry THF in a dry Schlenk flask fitted with an addition funnel, and was cooled to 0 °C. In the addition funnel, 21.54 mL of 2.0 M dimethylamine (4.308 mmol) in THF was diluted with 20 mL of dry THF and was added dropwise to the reaction mixture. The reaction was allowed to stir for 1 h at 0 °C before being quenched with 8 mL of H_2O. The solvent was removed *in vacuo*. Recrystallization from hot H_2O yields white crystals (5.295 g, 76%). ^{1}H NMR (400 MHz, $CDCl_3$): δ 2.81 (s, 3H), 2.84 (s, 3H), 4.04 (s, 2H), 4.27 (s, 2H), 12.49 (bs, 1H). $^{13}C\{^1H\}$ NMR (400 MHz, $CDCl_3$): δ 35.4, 35.5, 70.4, 71.3, 76.7, 170.7, 172.0**.** HRMS (ESI): *m*/*z* calcd for $C_6H_{11}NO_4$ $[M + Na]^+$ 184.0580; found 184.0580.

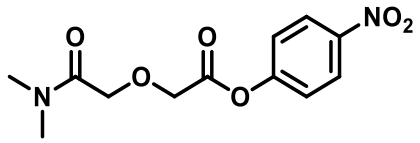

4-nitrophenyl-2-(2-(dimethylamino)-2-oxoethoxy)acetate (**6**): In a dry Schlenk flask, *p*-nitrophenol (0.863 g, 6.21 mmol)and **6a** (1.01 g, 6.27 mmol) were dissolved in 20 mL of dry chloroform. Thionyl chloride (0.74 mL, 10.19 mmol) was syringed into the reaction flask. The resulting mixture was heated for 5 h at 40 °C before cooling to room temperature, and was allowed to stir overnight. The mixture was then diluted with chloroform (10 mL) and washed with a cold 5% solution of $NaHCO_3$ (1 x 25 mL), followed by cold H_2O (3 x 30 mL). The organic layer was then dried with $MgSO_4$ and the solvent was removed. Recrystallization from chloroform with hexanes yielded a fluffy, white product (0.440 g, 25%). ^{1}H NMR (400 MHz, $CDCl_3$): δ 2.93 (s, 3H), 2.96 (s, 3H), 4.34 (s, 2H), 4.52 (s, 2H), 7.56 (d, 2H, J = 9.0 Hz), 8.23 (d, 2H, J = 9.0 Hz). ^{13}C{^{1}H} NMR (100 MHz, $CDCl_3$): δ 35.4, 36.1, 67.9, 69.3, 122.2, 125.2, 145.4, 154.7, 167.8, 168.1.

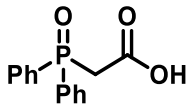

2-(diphenylphosphoryl)acetic acid (**7a**): This product was synthesized according to a modified literature procedure.[401] Chlorodiphenylphosphine (6.0 mL, 32.6 mmol), methyl bromoacetate (3.10 mL, 32.6 mmol), zinc dust (2.192 g, 33.52 mmol), and a single crystal of iodine were dissolved in 100 mL of dry benzene. The mixture was refluxed at 80 °C for 16 h. After cooling to room temperature, the reaction mixture was opened to air and 2 mL of a 30% hydrogen peroxide solution diluted with 8 mL of EtOH was added dropwise. The mixture was stirred an additional 30 minutes. The resulting mixture was poured into a brine solution slightly acidified with HCl (c.a. 0.05 M) and was extracted with CH_2Cl_2 (3 x 250 mL). The resulting organic fractions were combined, dried over $MgSO_4$, and concentrated *in vacuo* to yield a golden oil. After dissolving the oil in a minimal amount of MeOH (200 mL), an equivalent volume of 2 M NaOH was added to the reaction mixture (200 mL) and the resulting solution was heated at 70 °C for 3 days. The methanol was removed *in vacuo* and the remaining mixture was diluted with 250 ml of H_2O and washed with 350 mL of CH_2Cl_2. The aqueous fraction was then acidified with 2M HCl to yield a pH <4. The resulting suspension was extracted with CH_2Cl_2 (3 x 350 mL), dried with $MgSO_4$, and concentrated to yield a dark orange oil. Recrystallization from chloroform with hexanes yields pure **7a** as a white solid (4.775 g, 56%). ^{1}H NMR (400 MHz, $CDCl_3$): δ 3.48 (d, 2H, $J_{P\text{-}H}$ = 13.7 Hz), 7.40 - 7.45 (m, 4H), 7.49 - 7.54 (m, 2H), 7.69 - 7.75 (m, 4H) 9.90 (bs, 1H). $^{13}C\{^1H\}$ NMR (400 MHz, $CDCl_3$): δ 38.2 (d, J = 30.8 Hz), 128.7 (d, J = 12.1 Hz), 130.7 (d, J = 106.0 Hz), 131.0 (d, J = 10.0 Hz), 132.4 (J = 2.7 Hz), 166.95 (d, J = 6.0). $^{31}P\{^1H\}$ NMR (162 MHz, $CDCl_3$): δ 31.13.

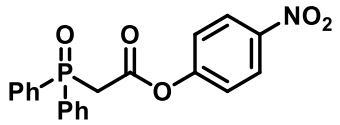

4-nitrophenyl 2-(diphenylphosphoryl)acetate (**7**): Product was synthesized according to literature procedures.[402] In a dry Schlenk flask, *p*-nitrophenol (1.37 g, 9.85 mmol) and **7a** (2.511 g, 9.65 mmol) were dissolved in 20 mL of dry chloroform. Thionyl chloride (1.2 mL, 16.52 mmol) was syringed into the reaction flask. The resulting mixture was heated for 5 h at 40 ^{0}C before cooling to room temperature, and was allowed to stir overnight. The mixture was then diluted with chloroform (10 mL) and washed with a cold 5% solution of $NaHCO_3$ (2 x 25 mL) followed by cold H_2O (3 x 30 mL). The organic layer was then dried with $MgSO_4$ and the solvent was removed. Recrystallization from ethyl acetate yielded a fluffy, white product (1.603 g, 44%). ^{1}H NMR (400 MHz, $CDCl_3$): δ 3.73 (d, 2H, $J_{P\text{-}H}$ = 14.5), 6.96 (dt, 2H, J = 9.2, 2.2 Hz), 7.49 - 7.54 (m, 4H), 7.56 - 7.61 (m, 2H), 7.80 - 7.86 (m, 4H), 8.14 (dt, 2h, J = 9.2, 2.2 Hz). ^{13}C{^{1}H} NMR (100 MHz, $CDCl_3$): δ 164.1(d, J = 6.0 Hz), 154.8, 145.5, 132.7 (d, J = 2.2 Hz), 131.1 (d, J = 104.1 Hz), 131.0 (d, J =0.6 Hz), 129.0 (d, J = 12.6 Hz), 125.1, 122.3, 39.3 (d, J = 57.3 Hz). ^{31}P{^{1}H} NMR (162 MHz, $CDCl_3$): δ 26.14.

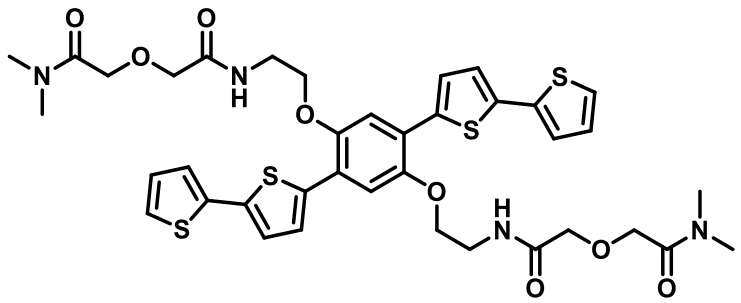

2,2'-((((((2,5-dibithiophene-1,4-phenylene)bis(oxy))bis(ethane-2,1-diyl))bis(azanediyl))bis(2-oxoethane-2,1-diyl))bis(oxy))bis(N,N-dimethylacetamide)

(**BDGA**): **5** (0.100 g, 0.191 mmol) and **6** (0.215 g, 0.762 mmol) were dissolved in 25 mL of dry chloroform. Triethylamine (0.106 mL, 0.760 mmol) was syringed into the reaction mixture and was allowed to stir for 1 week at room temperature under a nitrogen blanket. The reaction was quenched with 4 mL of 10% NaOH solution and allowed to stir for 4 h. The resulting mixture was poured into ≈ 80 mL of chloroform and washed with 1% NaOH (2 x 100 mL) and H_2O (2 x 100 mL) until the aqueous layer remained clear. The organic layer was collected, dried with $MgSO_4$, and concentrated *in vacuo*. Orange product (0.094 g, 61%) was collected by vacuum filtration after recrystallization from chloroform with hexanes. ^{1}H NMR (400 MHz, CD_2Cl_2): δ 2.68 (s, 6H), 2.74 (s, 6H), 3.84 (q, 4H, J = 5.5 Hz), 4.04 (s, 4H), 4.08 (s, 4H), 4.28 (t, 4H, J = 5.5 Hz), 7.05 (dd, 2H, J = 5.1, 3.5 Hz), 7.21 (d, 2H, J = 3.9 Hz), 7.26 (dd, 2H, J = 5.1, 1.0 Hz), 7.30 (dd, 2H, J = 3.5, 1.2 Hz), 7.33 (s, 2H), 7.53 (d, 2H, J = 3.9 Hz), 8.16 (t, 2H, J = 5.5Hz). ^{13}C{^{1}H} NMR (100 MHz, $CDCl_3$): No spectra could be obtained due to poor solubility. UV-Vis (CH_3CN) λ (ε): 250 nm (1.74 x 10^4 M^{-1} cm^{-1}), 342 nm (1.74 x 10^4 M^{-1} cm^{-1}), 408 nm (5.33 x 10^4 M^{-1} cm^{-1}). IR (cm^{-1}): ν(C=O) 1667. HRMS (CI): m/z calcd for $C_{38}H_{42}N_4O_8S_4$ $[M + H]^+$ 811.1964; found 811.1956.

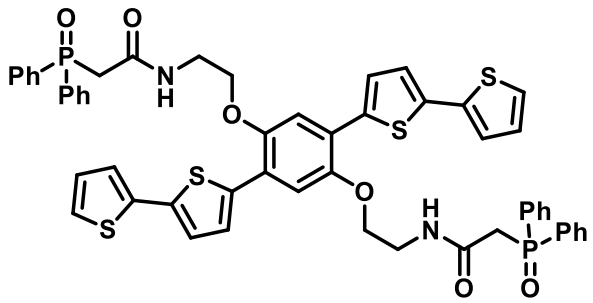

N,N'-(((2,5-dibithiophene-1,4-phenylene)bis(oxy))bis(ethane-2,1-diyl))bis(2-(diphenylphosphoryl)acetamide) (**BCMPO**): **5** (0.104 g, 0.198 mmol) and **7** (0.291 g, 0.763 mmol) were dissolved in 25 mL of dry chloroform. Triethylamine (0.106 mL, 0.760 mmol) was syringed in to the reaction mixture and was allowed to stir for 1 week at room temperature under a nitrogen blanket. The reaction was quenched with 4 mL of 10% NaOH solution and allowed to stir for 4 h. The resulting mixture was poured into ≈ 80 mL of chloroform and washed with 1% NaOH (2 x 100 mL) and H_2O (2 x 100 mL) until the aqueous layer remained clear. The organic layer was collected, dried with $MgSO_4$, and concentrated *in vacuo.* Yellow product (0.084 g, 42%) was collected by vacuum filtration after recrystallization from chloroform with hexanes. ^{1}H NMR (400 MHz, CD_2Cl_2): δ 3.34 (d, 4H, J_{P-H} = 12.8 Hz), 3.74 (q, 4H, *J* = 5.6 Hz), 4.054 (t, 4H, *J* = 2.8 Hz), 7.05 (dd, 2H, *J* = 5.2, 3.6 Hz), 7.20 (s, 2H), 7.21 (d, 2H, *J* = 3.8 Hz), 7.25 (dd, 2H, *J* = 5.0, 1.2 Hz), 7.36 (dd, 2H, *J* = 3.6, 1.2 Hz), 7.39 - 7.53 (m, 14H), 7.67 - 7.24 (m, 10H). ^{13}C{^{1}H} NMR (100 MHz, $CDCl_3$): No spectra could be obtained due to poor solubility. ^{31}P{^{1}H} NMR (162 MHz, CD_2Cl_2): δ 28.13 (s). UV-Vis (CH_3CN) λ (ε): 254 nm (2.53 x 10^4 M^{-1} cm^{-1}), 345 nm (1.95 x 10^4 M^{-1} cm^{-1}), 408 nm (5.13 x 10^4 M^{-1} cm^{-1}). IR (cm^{-1}): ν(C=O) 1667, ν(P=O) 1175. HRMS (APCI): *m/z* calcd for $C_{54}H_{46}N_2O_6P_2S_4$ $[M + H]^+$ 1009.17867; found 1009.17775.

6.4.2. Job's Plot

Stock 0.001 M solutions of BCMPO, BDGA, and $Th(NO_3)_4 \cdot 4H_2O$ were prepared in DMSO-d_6. Samples were prepared from the stock solutions by varying the mole fractions of monomer and $Th(NO_3)_4 \cdot 4H_2O$ in solution while keeping the total concentration ([monomer] + [$Th(NO_3)_4 \cdot 4H_2O$]) constant. The change in the chemical shift of the phosphorous NMR signal with respect to pure monomer was recorded. The resulting changes in the chemical shifts were multiplied by the concentration of monomer in solution and plotted versus the mole fraction of monomer. No shifts were observed upon coordination of BDGA to Th(IV).

6.4.3. Electrochemical Studies

Electrochemical studies were performed under a nitrogen atmosphere in a dry-box using a GPES system from Eco. Chemie. B. V and an Autolab Potentiostat (PGSTAT30). All of the electrochemical experiments were carried out in a three electrode cell with a $Ag/AgNO_3$ reference electrode (silver wire dipped in an CH_3CN solution containing 0.01 M silver nitrate and 0.1 M tetrabutylammonium hexafluorophosphate (TBAH)), a Pt button working electrode (1.6 mm diameter), and a Pt wire coil counter electrode unless otherwise noted. The voltammograms were recorded using a 10^{-4} M solution of monomer in a 0.1 M tetrabutylammonium hexafluorophosphate (TBAH) in CH_2Cl_2 as the supporting electrolyte. All potentials are recorded against a Ag/Ag^+ reference electrode and then corrected to the ferrocene redox couple (Fc/Fc^+). To calibrate the reference electrode, ferrocene was used as an external reference to which potentials were corrected. All electrochemical experiments were performed in dry CH_2Cl_2 solutions containing 0.1 M TBAH as the supporting electrolyte. The TBAH was recrystallized three times from hot ethanol, then dried for four days at 100 °C under vacuum.

6.4.4. Polymer Growth and Scan Rate Dependence

Data for the polymer growth of poly-BCMPO and poly-DGA were collected by electropolymerization onto a Pt button using a 10^{-4} M monomer solution. The films were polymerized by cycling 20 times at a scan rate of 100 mV/s. The films were then washed thoroughly with fresh CH_2Cl_2. Scan rate dependence studies were carried out by transferring polymers grown on the Pt electrode to a blank electrolyte solution and varying the scan rate as the potential is swept from –0.75 V to 1.25 V.

6.4.5. *In Situ* Conductivity Measurements

Conductivity was measured in a similar manner to literature methods.[397] *In situ c*onductivity measurements were performed using an interdigitated array electrode (IDA) purchased from CH Instruments (CH 012126) with 10 μm interdigit spacings, 129 gaps, and a 0.2 cm electrode length. Conductivity profiles were carried out in CH_2Cl_2/0.1 M TBAH at a scan rate of 10 mV s^{-1} with an applied potential offset of 40 mV. Film thicknesses were determined using a Dektak 3 surface profilometer. Uncorrected conductivities ($\sigma_{p,uncorr.}$) were determined using the following equation:

$$\sigma_{p,uncorr.} = \frac{i_d}{V_d} \, x \, \frac{D}{n \, T \, L} \qquad \text{(eq. 6.1)}$$

where i_d is the drain current (A), V_d is the potential offset (V), D is the spacing between the interdigitated electrodes (cm), n is the number of interdigit gaps, T is the polymer thickness (cm), and L is the length of the electrode (cm). All values were then corrected against the literature value for poly(3-methyl thiophene) (P3MT) to give the corrected conductivity (σ) using the following equation:

$$\sigma = \frac{\sigma_{p,uncorr.}}{\sigma_{P3MT}} \, x \, 60 \frac{S}{cm} \qquad \text{(eq. 6.2)}$$

where σ_{P3MT} is the measured value for P3MT and 60 S cm^{-1} is the literature value for P3MT.

6.4.6. Film Extraction Studies by X-ray Photoelectron Spectroscopy (XPS): General Procedures

Polymer films were grown onto 1 cm x 3 cm sheets of stainless steel using a second 1 cm x 3 cm sheet of stainless steel as the counter electrode. The stainless steel sheets were placed in 10^{-4} M solutions of poly-BDGA or poly-BCMPO and were electropolymerized utilizing 20 cyclic voltammetry cycles from –0.75 V to 1.25 V at scan rate of 100 mV/s. The resulting films were washed with CH_2Cl_2 and dried under a nitrogen stream prior to incubation in the extraction solutions.

The polymer films on stainless steel were incubated without stirring in an aqueous 0.1 M metal nitrate solution for 30 minutes. Once the incubation period was over, the films were thoroughly washed with deionized H_2O, followed by CH_3CN and then dried under a nitrogen stream. Samples were cut into two sections. In a glovebox, one section of the film was placed in a 0.1 M TBAH CH_3CN solution and subjected to five scans from –0.25 V to 1.25 V vs Fc/Fc^+. The film was subsequently washed with CH_3CN, then deionized H_2O and then dried under a nitrogen stream before being submitted for XPS analysis. The second half of the polymer film was soaked for two minutes in a 0.1 M TBAH CH_3CN solution. The sample was then washed with dry CH_3CN, then deionized H_2O and then dried under a nitrogen stream, and submitted for XPS analysis.

6.4.7. Calculation of Thorium Uptake for Extraction Cycles

Determination of the percentage of monomer sites occupied in the polymer was found by assuming a monomer to Th(IV) ratio of 1:1 as determined by the Job's plot analysis for BCMPO**.** The same ratio is assumed for the BDGA ligand. Integration of the

thorium 4*f* and sulfur 2*p* signals allows for the determination of the atomic ratio of sulfur to thorium. The percentage of occupied sites in the polymer was then determined using the following equation:

$$Thorium\ Uptake = \frac{Th}{\frac{1}{4}S} x100\% \qquad \text{(eq. 6.3)}$$

where Th and S are the atom percentages found by XPS for thorium and sulfur, respectively. The S content is multiplied by 1/4 to account for the fact that every monomer unit contains four sulfur atoms.

6.4.8. Time Dependent Uptake Studies

Polymer films were grown as described above (See **6.4.6.**). Incubation times in an aqueous 0.1 M $Th(NO_3)_4$ solution were varied at 0.5 h, 1 h, 4 h, and 24 h. At the end of each time period the samples were removed from the Th(IV) solution, washed with deionized H_2O and CH_3CN, dried under a nitrogen stream, and analyzed by XPS.

6.4.9. Selectivity Testing

Films were prepared as described above (see **6.4.6.**). The polymer films were incubated in an aqueous equimolar solution containing 0.1 M $Gd(NO_3)_3$ and 0.1 M $Th(NO_3)_4$ to test selectivity between lanthanides and actinides. A similar study was performed by incubation in an aqueous equimolar solution of 0.1 M $Nd(NO_3)_3$ and 0.1 M $Sm(NO_3)_3$ where Nd(III) and Sm(III) are used as surrogate ions for Am(III) and Cm(III), respectively. Selectivity was determined by direct comparison of the atomic ratios as determined by the integration of the XPS signals of the Nd 3*d* and Sm 3*d* peaks.

6.5. REFERENCES

(134) Lyskawa, J.; Le Derf, F.; Levillain, E.; Mazari, M.; Sallé, M.; Dubois, L.; Viel, P.; Bureau, C.; Palacin, S. *J. Am. Chem. Soc.* **2004**, *126*, 12194–12195.

(141) Dam, H. H.; Reinhoudt, D. N.; Verboom, W. *New J. Chem.* **2007**, *31*, 1620–1632.

(142) Dam, H. H.; Reinhoudt, D. N.; Verboom, W. *Chem. Soc. Rev.* **2007**, *36*, 367–377.

(143) Lewis, F.; Hudson, M.; Harwood, L. *Synlett* **2011**, *2011*, 2609–2632.

(358) *Handbook of Thiophene-Based Materials*; Perepichka, I. F., Perepichka, D. F., Eds.; John Wiley & Sons, Ltd, 2009.

(382) Klug, C.; Sudowe, R. *Sep. Sci. Technol.* **2013**, *48*, 2567–2575.

(383) Kimura, T.; Akatsu, J. *J. Radioanal. Nucl. Chem.* **1991**, *149*, 13–23.

(384) Kimura, T.; Akatsu, J. *J. Radioanal. Nucl. Chem.* **1991**, *149*, 25–34.

(385) Suzuki, T.; Otake, K.; Sato, M.; Ikeda, A.; Aida, M.; Fujii, Y.; Hara, M.; Mitsugashira, T.; Ozawa, M. *J. Radioanal. Nucl. Chem.* **2007**, *272*, 257–262.

(386) Burns, J. D.; Shehee, T. C.; Clearfield, A.; Hobbs, D. T. *Anal. Chem.* **2012**, *84*, 6930–6932.

(387) Burns, J. D.; Borkowski, M.; Clearfield, A.; Reed, D. T. *Radiochim. Acta* **2012**, *100*, 901–906.

(388) Panak, P. J.; Geist, A. *Chem. Rev.* **2013**, *113*, 1199–1236.

(389) Kolarik, Z. *Chem. Rev.* **2008**, *108*, 4208–4252.

(390) Ansari, S. A.; Pathak, P.; Mohapatra, P. K.; Manchanda, V. K. *Chem. Rev.* **2012**, *112*, 1751–1772.

(391) Gorden, A. E. V.; Xu, J.; Raymond, K. N.; Durbin, P. *Chem. Rev.* **2003**, *103*, 4207–4282.

(392) Roncali, J. *Chem. Rev.* **1992**, *92*, 711–738.

(393) Mishra, A.; Ma, C.-Q.; Bäuerle, P. *Chem. Rev.* **2009**, *109*, 1141–1276.

(394) Le Derf, F.; Mazari, M.; Mercier, N.; Levillain, E.; Richomme, P.; Becher, J.; Garín, J.; Orduna, J.; Gorgues, A.; Sallé, M. *Inorg. Chem.* **1999**, *38*, 6096–6100.

(395) Sharova, E. V.; Artyushin, O. I.; Turanov, A. N.; Karandashev, V. K.; Meshkova, S. B.; Topilova, Z. M.; Odinets, I. L. *Cent. Eur. J. Chem.* **2012**, *10*, 146–156.

(396) Reilly, S. D.; Gaunt, A. J.; Scott, B. L.; Modolo, G.; Iqbal, M.; Verboom, W.; Sarsfield, M. J. *Chem. Commun.* **2012**, *48*, 9732–9734.

(397) Simone, D. L.; Swager, T. M. *J. Am. Chem. Soc.* **2000**, *122*, 9300–9301.

(398) Kloosterman, J. L.; Li, J. M. In *International Conference on Evaluation of Emerging Nuclear Fuel Cycle Systems; Versailles (France)*; 1995.

(399) Seaborg, G. T. *Radiochim. Acta* **1993**, *61*, 115–122.

(400) Zhu, S. S.; Swager, T. M. *J. Am. Chem. Soc.* **1997**, *119*, 12568–12577.

(401) Kiełbasiński, P.; Mikołajczyk, M. *Synthesis* **1995**, *1995*, 144–146.

(402) Arnaud-Neu, F.; Böhmer, V.; Dozol, J.-F.; Grüttner, C.; Jakobi, R. A.; Kraft, D.; Mauprivez, O.; Rouquette, H.; Schwing-Weill, M.-J.; Simon, N.; Vogt, W. *J. Chem. Soc. Perkin Trans. 2* **1996**, 1175–1182.

Appendix A

CRYSTAL TABLES

Chapter 2 Structures

Table A.1. Crystal data and structure refinement for (4-nitrophenyl)phenyliodonium tetrafluoroborate.

Empirical formula	C_{12} H_9 B F_4 I N O_2	
Formula weight	412.91	
Temperature	100 K	
Wavelength	0.71073 Å	
Crystal system	Monoclinic	
Space group	$C\ 2/c$	
Unit cell dimensions	a = 16.725 Å	□α= 90°
	b = 10.562 Å	□β= 111.93°
	c = 16.707 Å	□γ= 90°
Volume	2737.7 $Å^3$	
Z	8	
Density (calculated)	2.004 Mg/m^3	
Absorption coefficient	2.388 mm^{-1}	
F(000)	1584	
Crystal size	0.37 x 0.12 x 0.33 mm^3	
Theta range for data collection	2.33 to 25.00°.	
Index ranges	–19<=*h*<=19, –12<=*k*<=12, –19<=*l*<=19	
Reflections collected	19955	
Independent reflections	2418 [*R*(int) = 0.0728]	
Completeness to theta = 25.00°	100.0 %	
Refinement method	Full-matrix least-squares on F^2	
Data / restraints / parameters	2418 / 0 / 190	
Goodness-of-fit on F^2	1.506	
Final *R* indices [*I*>2sigma(*I*)]	*R1* = 0.0382, *wR2* = 0.1532	
R indices (all data)	*R1* = 0.0383, *wR2* = 0.1532	
Largest diff. peak and hole	0.601 and –0.881 e·$Å^{-3}$	

Table A.2. Crystal data and structure refinement for [Cu(pycf3pz)(dppt)][PF_6].

Identification code	**1a**	
Empirical formula	C_{37} H_{28} Cu F_9 N_3 P_3 S	
Formula weight	874.13	
Temperature	100 K	
Wavelength	1.54184 Å	
Crystal system	Monoclinic	
Space group	$C\ 2/c$	
Unit cell dimensions	a = 23.9215(7) Å	α= 90°
	b = 14.5435(3) Å	β= 116.307(3)°
	c = 23.3587(6) Å	γ = 90°
Volume	7284.9(4) Å^3	
Z	8	
Density (calculated)	1.594 Mg/m^3	
Absorption coefficient	3.341 mm^{-1}	
F(000)	3536	
Crystal size	0.3721 x 0.1418 x 0.0287 mm^3	
Theta range for data collection	3.672 to 75.569°.	
Index ranges	–29<=*h*<=29, –18<=*k*<=18, –29<=*l*<=29	
Reflections collected	56482	
Independent reflections	7388 [*R*(int) = 0.0488]	
Completeness to theta = 67.684°	100.0 %	
Absorption correction	Semi-empirical from equivalents	
Max. and min. transmission	1.00000 and 0.54138	
Refinement method	Full-matrix least-squares on F^2	
Data / restraints / parameters	7388 / 265 / 611	
Goodness-of-fit on F^2	1.092	
Final *R* indices [*I*>2sigma(*I*)]	*R1* = 0.0426, *wR2* = 0.1049	
R indices (all data)	*R1* = 0.0440, *wR2* = 0.1063	
Extinction coefficient	n/a	
Largest diff. peak and hole	0.793 and –0.593 e·Å^{-3}	

Table A.3. Crystal data and structure refinement for [Cu(pypz)(dppt)][PF_6].

Identification code	**1b**	
Empirical formula	C_{36} H_{29} Cu F_6 N_3 P_3 S	
Formula weight	806.13	
Temperature	100 K	
Wavelength	0.71075 Å	
Crystal system	Monoclinic	
Space group	$C\ 2/c$	
Unit cell dimensions	a = 23.910(2) Å	α= 90°
	b = 14.4952(12) Å	β= 116.445(3)°
	c = 23.434(2) Å	γ = 90°
Volume	7271.9(11) Å^3	
Z	8	
Density (calculated)	1.473 Mg/m^3	
Absorption coefficient	0.852 mm^{-1}	
F(000)	3280	
Crystal size	0.16 x 0.21 x 0.32 mm^3	
Theta range for data collection	1.697 to 31.851°.	
Index ranges	–35<=*h*<=33, –20<=*k*<=16, –33<=*l*<=33	
Reflections collected	30409	
Independent reflections	11671 [*R*(int) = 0.0393]	
Completeness to theta = 25.242°	99.8 %	
Absorption correction	Semi-empirical from equivalents	
Max. and min. transmission	1.0000 and 0.8542	
Refinement method	Full-matrix least-squares on F^2	
Data / restraints / parameters	11671 / 453 / 591	
Goodness-of-fit on F^2	1.065	
Final *R* indices [*I*>2sigma(*I*)]	*R1* = 0.0512, *wR2* = 0.1353	
R indices (all data)	*R1* = 0.0647, *wR2* = 0.1485	
Extinction coefficient	n/a	
Largest diff. peak and hole	0.709 and –0.920 e·Å^{-3}	

Table A.4. Crystal data and structure refinement for [Cu(pympz)(dppt)][PF_6].

Identification code	**1c**	
Empirical formula	C_{37} H_{31} Cu F_6 N_3 P_3 S	
Formula weight	820.16	
Temperature	100 K	
Wavelength	1.54184 Å	
Crystal system	Monoclinic	
Space group	$C\ 2/c$	
Unit cell dimensions	a = 23.6775(5) Å	α= 90°
	b = 14.5990(2) Å	β= 116.184(3)°
	c = 23.2669(5) Å	γ= 90°
Volume	7217.3(3) Å^3	
Z	8	
Density (calculated)	1.510 Mg/m^3	
Absorption coefficient	3.207 mm^{-1}	
F(000)	3344	
Crystal size	0.3992 x 0.1699 x 0.1147 mm^3	
Theta range for data collection	3.673 to 71.511°.	
Index ranges	–29<=*h*<=28, –17<=*k*<=17, –28<=*l*<=20	
Reflections collected	20144	
Independent reflections	6928 [*R*(int) = 0.0206]	
Completeness to theta = 67.684°	100.0 %	
Absorption correction	Semi-empirical from equivalents	
Max. and min. transmission	1.00000 and 0.60799	
Refinement method	Full-matrix least-squares on F^2	
Data / restraints / parameters	6928 / 121 / 571	
Goodness-of-fit on F^2	1.014	
Final *R* indices [*I*>2sigma(*I*)]	*R1* = 0.0312, *wR2* = 0.0802	
R indices (all data)	*R1* = 0.0326, *wR2* = 0.0814	
Extinction coefficient	n/a	
Largest diff. peak and hole	0.694 and –0.380 e·Å^{-3}	

Table A.5. Crystal data and structure refinement for [Cu(pypz)(dppbz)][PF_6].

Identification code	**2b**	
Empirical formula	C_{38} H_{31} Cu F_6 N_3 P_3	
Formula weight	800.11	
Temperature	100 K	
Wavelength	1.54184 Å	
Crystal system	Monoclinic	
Space group	$I\ 2/a$	
Unit cell dimensions	a = 17.2946(2) Å	α= 90°
	b = 17.0163(2) Å	β= 92.997(1)°
	c = 26.3595(3) Å	γ= 90°
Volume	7746.73(16) Å^3	
Z	8	
Density (calculated)	1.372 Mg/m^3	
Absorption coefficient	2.484 mm^{-1}	
F(000)	3264	
Crystal size	0.2420 x 0.0710 x 0.0585 mm^3	
Theta range for data collection	3.092 to 76.083°.	
Index ranges	–21<=*h*<=21, –21<=*k*<=21, –33<=*l*<=32	
Reflections collected	41244	
Independent reflections	8032 [*R*(int) = 0.0263]	
Completeness to theta = 67.684°	100.0 %	
Absorption correction	Gaussian	
Max. and min. transmission	0.899 and 0.687	
Refinement method	Full-matrix least-squares on F^2	
Data / restraints / parameters	8032 / 279 / 634	
Goodness-of-fit on F^2	1.036	
Final *R* indices [*I*>2sigma(*I*)]	*R1* = 0.0602, *wR2* = 0.1383	
R indices (all data)	*R1* = 0.0633, *wR2* = 0.1402	
Extinction coefficient	n/a	
Largest diff. peak and hole	0.679 and –0.440 e·Å^{-3}	

Table A.6. Crystal data and structure refinement for [Cu(pympz)(dppbz)][PF_6].

Identification code	**2c**	
Empirical formula	C_{39} H_{33} Cu F_6 N_3 P_3	
Formula weight	814.13	
Temperature	100 K	
Wavelength	1.54184 Å	
Crystal system	Monoclinic	
Space group	$P\ 2_1/c$	
Unit cell dimensions	a = 10.55110(10) Å	α= 90°
	b = 31.9752(2) Å	β= 103.889(1)°
	c = 11.72890(10) Å	γ = 90°
Volume	3841.33(6) Å^3	
Z	4	
Density (calculated)	1.408 Mg/m^3	
Absorption coefficient	2.514 mm^{-1}	
F(000)	1664	
Crystal size	0.3878 x 0.2208 x 0.1515 mm^3	
Theta range for data collection	2.764 to 76.160°.	
Index ranges	–12<=*h*<=13, –24<=*k*<=40, –13<=*l*<=14	
Reflections collected	32059	
Independent reflections	7981 [*R*(int) = 0.0244]	
Completeness to theta = 67.684°	100.0 %	
Absorption correction	Semi-empirical from equivalents	
Max. and min. transmission	1.00000 and 0.78344	
Refinement method	Full-matrix least-squares on F^2	
Data / restraints / parameters	7981 / 211 / 566	
Goodness-of-fit on F^2	0.974	
Final *R* indices [*I*>2sigma(*I*)]	*R1* = 0.0595, *wR2* = 0.1578	
R indices (all data)	*R1* = 0.0603, *wR2* = 0.1583	
Extinction coefficient	n/a	
Largest diff. peak and hole	0.731 and –0.783 e·Å^{-3}	

Table A.7. Crystal data and structure refinement for $C_{34}H_{28}P_2S_2$.

Identification code	Ligand **4**	
Empirical formula	$C_{34}\ H_{28}\ P_2\ S_2$	
Formula weight	562.62	
Temperature	100 K	
Wavelength	0.71073 Å	
Crystal system	Triclinic	
Space group	$P\ \bar{1}$	
Unit cell dimensions	a = 9.745(3) Å	□α= 93.048(8)°
	b = 11.785(4) Å	□β= 92.530(8)°
	c = 12.394(4) Å	□γ= 90.761(9)°
Volume	1419.8(8) Å^3	
Z	2	
Density (calculated)	1.316 Mg/m^3	
Absorption coefficient	0.323 mm^{-1}	
F(000)	588	
Crystal size	0.2000 x 0.1400 x 0.0500 mm^3	
Theta range for data collection	3.096 to 27.483°.	
Index ranges	–12<=*h*<=12, –15<=*k*<=15, –16<=*l*<=16	
Reflections collected	15105	
Independent reflections	6468 [*R*(int) = 0.0408]	
Completeness to theta = 25.242°	99.8 %	
Absorption correction	Semi-empirical from equivalents	
Max. and min. transmission	0.0000 and 0.0000	
Refinement method	Full-matrix least-squares on F^2	
Data / restraints / parameters	6468 / 180 / 352	
Goodness-of-fit on F^2	1.029	
Final *R* indices [*I*>2sigma(*I*)]	*R1* = 0.0450, *wR2* = 0.0947	
R indices (all data)	*R1* = 0.0609, *wR2* = 0.1014	
Extinction coefficient	n/a	
Largest diff. peak and hole	0.555 and –0.265 e·Å^{-3}	

Table A.8. Crystal data and structure refinement for $[Cu(C_{34}H_{28}P_2S_2)(pycf3pz)][PF_6]$.

Identification code	**5**	
Empirical formula	$C_{90}\ H_{78}\ Cu_2\ F_{18}\ N_6\ O\ P_6\ S_4$	
Formula weight	2042.72	
Temperature	100(2) K	
Wavelength	0.71073 Å	
Crystal system	Monoclinic	
Space group	$P\ 2_1/c$	
Unit cell dimensions	a = 14.7518(6) Å	α= 90°
	b = 16.6999(6) Å	β= 94.492(2)°
	c = 36.185(1) Å	γ= 90°
Volume	8887.0(6) $Å^3$	
Z	4	
Density (calculated)	1.527 Mg/m^3	
Absorption coefficient	0.770 mm^{-1}	
F(000)	4168	
Crystal size	0.280 x 0.260 x 0.190 mm^3	
Theta range for data collection	1.129 to 27.764°.	
Index ranges	–18<=*h*<=18, –21<=*k*<=20, –42<=*l*<=45	
Reflections collected	105009	
Independent reflections	17876 [*R*(int) = 0.0517]	
Completeness to theta = 25.242°	99.0 %	
Absorption correction	Semi-empirical from equivalents	
Max. and min transmission	1.0000 and 0.8769	
Refinement method	Full-matrix least-squares on F^2	
Data / restraints / parameters	17876 / 2251 / 1270	
Goodness-of-fit on F^2	1.056	
Final *R* indices [*I*>2sigma(*I*)]	*R1* = 0.0506, *wR2* = 0.1078	
R indices (all data)	*R1* = 0.0721, *wR2* = 0.1168	
Extinction coefficient	n/a	
Largest diff. peak and hole	0.859 and –0.796 e·$Å^{-3}$	

Table A.9. Crystal data and structure refinement for $[Cu(C_{34}H_{28}P_2S_2)(pypz)][PF_6]$.

Identification code	**6**	
Empirical formula	$C_{42}\ H_{35}\ Cu\ F_6\ N_3\ P_3\ S_2$	
Formula weight	916.30	
Temperature	100 K	
Wavelength	0.71073 Å	
Crystal system	Triclinic	
Space group	$P\ \bar{1}$	
Unit cell dimensions	a = 11.2880(10) Å	α= 79.062(2)°
	b = 11.4770(10) Å	β= 79.312(2)°
	c = 17.2810(10) Å	γ= 71.593(2)°
Volume	2066.6(3) Å^3	
Z	2	
Density (calculated)	1.472 Mg/m^3	
Absorption coefficient	0.808 mm^{-1}	
F(000)	936	
Crystal size	0.472 x 0.377 x 0.193 mm^3	
Theta range for data collection	2.808 to 32.644°.	
Index ranges	–15<=*h*<=16, –17<=*k*<=16, –24<=*l*<=24	
Reflections collected	74200	
Independent reflections	13249 [*R*(int) = 0.0441]	
Completeness to theta = 25.242°	99.8 %	
Absorption correction	Semi-empirical from equivalents	
Refinement method	Full-matrix least-squares on F^2	
Data / restraints / parameters	13249 / 304 / 610	
Goodness-of-fit on F^2	1.056	
Final *R* indices [*I*>2sigma(*I*)]	*R1* = 0.0383, *wR2* = 0.0875	
R indices (all data)	*R1* = 0.0550, *wR2* = 0.0928	
Extinction coefficient	n/a	
Largest diff. peak and hole	0.658 and –0.487 e·Å^{-3}	

Table A.10. Crystal data and structure refinement for $[Cu(C_{34}H_{28}P_2S_2)(pympz)][PF_6]$.

Identification code	**7**	
Empirical formula	$C_{90}\ H_{84}\ Cu_2\ F_{12}\ N_6\ O\ P_6\ S_4$	
Formula weight	1934.77	
Temperature	100 K	
Wavelength	1.54184 Å	
Crystal system	Monoclinic	
Space group	$P\ 2_1/c$	
Unit cell dimensions	a = 14.5506(2) Å	α= 90°
	b = 16.6923(3) Å	β= 93.797(1)°
	c = 35.9687(5) Å	γ= 90°
Volume	8717.0(2) Å^3	
Z	4	
Density (calculated)	1.474 Mg/m^3	
Absorption coefficient	3.192 mm^{-1}	
F(000)	3976	
Crystal size	0.3639 x 0.1420 x 0.0767 mm^3	
Theta range for data collection	2.462 to 73.567°.	
Index ranges	–18<=*h*<=18, –18<=*k*<=20, –44<=*l*<=44	
Reflections collected	83073	
Independent reflections	17339 [*R*(int) = 0.0765]	
Completeness to theta = 67.684°	100.0 %	
Absorption correction	Semi-empirical from equivalents	
Max. and min. transmission	1.00000 and 0.65386	
Refinement method	Full-matrix least-squares on F^2	
Data / restraints / parameters	17339 / 836 / 1410	
Goodness-of-fit on F^2	1.020	
Final *R* indices [*I*>2sigma(*I*)]	*R1* = 0.0460, *wR2* = 0.1039	
R indices (all data)	*R1* = 0.0677, *wR2* = 0.1160	
Extinction coefficient	n/a	
Largest diff. peak and hole	1.472 and –0.425 e·Å^{-3}	

Chapter 4 Structures

Table A.11. Crystal data and structure refinement for [(PNP)Rh(μ^2-9,10-diisocyanoanthracene)Rh(PNP][BF_4]$_2$.

Identification code	**1**	
Empirical formula	C_{64} H_{98} B_2 Cl_4 F_8 N_4 P_4 Rh_2	
Formula weight	1568.58	
Temperature	100 K	
Wavelength	0.71073 Å	
Crystal system	Triclinic	
Space group	$P\bar{1}$	
Unit cell dimensions	a = 11.024 Å	α= 76.13°
	b = 13.286 Å	β= 68.78°
	c = 13.721 Å	γ= 81.76°
Volume	1815.2 Å^3	
Z	1	
Density (calculated)	1.435 Mg/m^3	
Absorption coefficient	0.751 mm^{-1}	
F(000)	810	
Crystal size	0.35 x 0.08 x 0.27 mm^3	
Theta range for data collection	3.16 to 27.48°.	
Index ranges	–14<=*h*<=14, –17<=*k*<=17, –17<=*l*<=17	
Reflections collected	19336	
Independent reflections	8302 [*R*(int) = 0.0816]	
Completeness to theta = 27.48°	99.6 %	
Absorption correction	Semi-empirical from equivalents	
Refinement method	Full-matrix least-squares on F^2	
Data / restraints / parameters	8302 / 0 / 409	
Goodness-of-fit on F^2	1.086	
Final *R* indices [*I*>2sigma(*I*)]	*R1* = 0.0485, *wR2* = 0.1259	
R indices (all data)	*R1* = 0.0530, *wR2* = 0.1296	
Largest diff. peak and hole	1.030 and –0.778 e·Å^{-3}	

Table A.12. Crystal data and structure refinement for 9,10-diisocyanoanthracene.

Identification code	9,10-diisocyanoanthracene	
Empirical formula	$C_8 H_4 N$	
Formula weight	114.12	
Temperature	100 K	
Wavelength	0.71073 Å	
Crystal system	Monoclinic	
Space group	$P\ 2_1/c$	
Unit cell dimensions	a = 3.801 Å	α= 90°
	b = 17.170 Å	β= 91.23°
	c = 8.546 Å	γ= 90°
Volume	557.6 $Å^3$	
Z	4	
Density (calculated)	1.359 Mg/m^3	
Absorption coefficient	0.082 mm^{-1}	
F(000)	236	
Crystal size	0.22 x 0.07 x 0.06 mm^3	
Theta range for data collection	3.36 to 27.47°.	
Index ranges	–4<=*h*<=4, –21<=*k*<=22, –11<=*l*<=11	
Reflections collected	5654	
Independent reflections	1261 [*R*(int) = 0.0944]	
Completeness to theta = 27.47°	99.8 %	
Absorption correction	Semi-empirical from equivalents	
Refinement method	Full-matrix least-squares on F^2	
Data / restraints / parameters	1261 / 0 / 82	
Goodness-of-fit on F^2	1.021	
Final *R* indices [*I*>2sigma(*I*)]	*R1* = 0.0582, *wR2* = 0.1409	
R indices (all data)	*R1* = 0.0741, *wR2* = 0.1519	
Largest diff. peak and hole	0.238 and –0.306 $e \cdot Å^{-3}$	

Table A.13. Crystal data and structure refinement for [(PNP)RhCl(CH_2Cl)][BF_4].

Identification code	**2**	
Empirical formula	C_{24} H_{45} B Cl_2 F_4 N P_2 Rh	
Formula weight	670.17	
Temperature	100 K	
Wavelength	0.71073 Å	
Crystal system	Monoclinic	
Space group	$P\ 2_1/n$	
Unit cell dimensions	a = 15.930(4) Å	α= 90°
	b = 8.4803(19) Å	β= 109.267(4)°
	c = 23.350(6) Å	γ= 90°
Volume	2977.8(12) Å^3	
Z	4	
Density (calculated)	1.495 Mg/m^3	
Absorption coefficient	0.900 mm^{-1}	
F(000)	1384	
Crystal size	0.421 x 0.227 x 0.354 mm^3	
Theta range for data collection	3.03 to 25.00°.	
Index ranges	–18<=*h*<=18, –10<=*k*<=10, –27<=*l*<=27	
Reflections collected	51910	
Independent reflections	5236 [*R*(int) = 0.0682]	
Completeness to theta = 25.00°	99.8 %	
Absorption correction	Semi-empirical from equivalents	
Refinement method	Full-matrix least-squares on F^2	
Data / restraints / parameters	5236 / 129 / 339	
Goodness-of-fit on F^2	0.941	
Final *R* indices [*I*>2sigma(*I*)]	*R1* = 0.0520, *wR2* = 0.1214	
R indices (all data)	*R1* = 0.0582, *wR2* = 0.1257	
Largest diff. peak and hole	1.554 and –0.894 e·Å^{-3}	

Table A.14. Crystal data and structure refinement for [(PCP)Rh(μ^2-9,10-diisocyanoanthracene)Rh(PCP].

Identification code	**5**	
Empirical formula	C_{64} H_{94} N_2 P_4 Rh_2	
Formula weight	1221.11	
Temperature	100 K	
Wavelength	1.54184 Å	
Crystal system	Triclinic	
Space group	$P\bar{1}$	
Unit cell dimensions	a = 10.3001(2) Å	□α= 86.176(2)°
	b = 10.9286(3) Å	□β= 88.711(2)°
	c = 28.4782(7) Å	□γ= 78.837(2)°
Volume	3137.8(1) Å^3	
Z	2	
Density (calculated)	1.292 Mg/m^3	
Absorption coefficient	5.499 mm^{-1}	
F(000)	1284	
Crystal size	0.28 x 0.14 x 0.27 mm^3	
Theta range for data collection	4.132 to 76.200°.	
Index ranges	–12<=*h*<=12, –13<=*k*<=13, –35<=*l*<=35	
Reflections collected	24001	
Independent reflections	24001 [*R*(int) = n/a]	
Completeness to theta = 67.684°	100.0 %	
Refinement method	Full-matrix least-squares on F^2	
Data / restraints / parameters	24001 / 1452 / 836	
Goodness-of-fit on F^2	1.084	
Final *R* indices [*I*>2sigma(*I*)]	*R1* = 0.0867, *wR2* = 0.2284	
R indices (all data)	*R1* = 0.0888, *wR2* = 0.2291	
Extinction coefficient	n/a	
Largest diff. peak and hole	3.185 and –1.894 e·Å^{-3}	

Table A.15. Crystal data and structure refinement for [(PCP)Rh(H)(2-isocyano-1,3-dimethylbenzene)][BF_4].

Identification code	**7**	
Empirical formula	C_{33} H_{53} B F_4 N P_2 Rh	
Formula weight	715.42	
Temperature	133(2) K	
Wavelength	0.71073 Å	
Crystal system	Triclinic	
Space group	$P\bar{1}$	
Unit cell dimensions	a = 8.778(1) Å	α= 96.628(2)°
	b = 11.391(1) Å	β= 94.877(2)°
	c = 17.456(1) Å	γ= 98.610(2)°
Volume	1704.9(3) $Å^3$	
Z	2	
Density (calculated)	1.394 Mg/m^3	
Absorption coefficient	0.640 mm^{-1}	
F(000)	748	
Crystal size	0.432 x 0.226 x 0.124 mm^3	
Theta range for data collection	2.359 to 25.000°.	
Index ranges	–9<=*h*<=10, –13<=*k*<=13, –20<=*l*<=20	
Reflections collected	31074	
Independent reflections	5991 [*R*(int) = 0.0307]	
Completeness to theta = 25.242°	96.9 %	
Absorption correction	Semi-empirical from equivalents	
Max. and min. transmission	1.000 and 0.907	
Refinement method	Full-matrix least-squares on F^2	
Data / restraints / parameters	5994 / 0 / 397	
Goodness-of-fit on F^2	1.048	
Final *R* indices [*I*>2sigma(*I*)]	*R1* = 0.0204, *wR2* = 0.0493	
R indices (all data)	*R1* = 0.0235, *wR2* = 0.0521	
Extinction coefficient	n/a	
Largest diff. peak and hole	0.595 and –0.424 e·$Å^{-3}$	

References

(1) *Nat. Mater.* **2013**, *12*, 591–591.

(2) So, F. *Organic electronics: materials, processing, devices and applications*; CRC Press: Boca Raton, FL, 2010.

(3) Zhang, X.; Rajaraman, B. R. S.; Liu, H.; Ramakrishna, S. *RSC Adv.* **2014**, *4*, 28987–29011.

(4) Novoselov, K. S.; Fal′ko, V. I.; Colombo, L.; Gellert, P. R.; Schwab, M. G.; Kim, K. *Nature* **2012**, *490*, 192–200.

(5) Yusoff, A. R. bin M. *Graphene-based Energy Devices*; John Wiley & Sons, 2015.

(6) Costa, R. D.; Ortí, E.; Bolink, H. J.; Monti, F.; Accorsi, G.; Armaroli, N. *Angew. Chem. Int. Ed.* **2012**, *51*, 8178–8211.

(7) Kitai, A. *Luminescent Materials and Applications*; John Wiley & Sons, 2008.

(8) Buckley, A. *Organic Light-Emitting Diodes (OLEDs): Materials, Devices and Applications*; Elsevier, 2013.

(9) Jou, J.-H.; Kumar, S.; Agrawal, A.; Li, T.-H.; Sahoo, S. *J. Mater. Chem. C* **2015**, *3*, 2974–3002.

(10) Li, Y. *Organic Optoelectronic Materials*; Springer, 2015.

(11) Gilbert, M.; Albinsson, B. *Chem. Soc. Rev.* **2015**, *44*, 845–862.

(12) Heckmann, A.; Lambert, C. *Angew. Chem. Int. Ed.* **2012**, *51*, 326–392.

(13) Brown, D. B. *Mixed-Valence Compounds: Theory and Applications in Chemistry, Physics, Geology, and Biology*; Springer Science & Business Media, 2012.

(14) Lu, L.; Zheng, T.; Wu, Q.; Schneider, A. M.; Zhao, D.; Yu, L. *Chem. Rev.* **2015**, *115*, 12666–12731.

(15) Brabec, C.; Scherf, U.; Dyakonov, V. *Organic Photovoltaics: Materials, Device Physics, and Manufacturing Technologies*; John Wiley & Sons, 2014.

(16) Brabec, C. J.; Dyakonov, V.; Parisi, J.; Sariciftci, N. S. *Organic Photovoltaics: Concepts and Realization*; Springer Science & Business Media, 2013.

(17) Kaur, G.; Adhikari, R.; Cass, P.; Bown, M.; Gunatillake, P. *RSC Adv.* **2015**, *5*, 37553–37567.

(18) Inzelt, G. *Conducting Polymers: A New Era in Electrochemistry*; Springer Science & Business Media, 2008.

(19) Chandrasekhar, P. *Conducting Polymers, Fundamentals and Applications: A Practical Approach*; Springer Science & Business Media, 2013.

(20) Novoselov, K. S.; Geim, A. K.; Morozov, S. V.; Jiang, D.; Zhang, Y.; Dubonos, S. V.; Grigorieva, I. V.; Firsov, A. A. *Science* **2004**, *306*, 666–669.

(21) Mayorov, A. S.; Gorbachev, R. V.; Morozov, S. V.; Britnell, L.; Jalil, R.; Ponomarenko, L. A.; Blake, P.; Novoselov, K. S.; Watanabe, K.; Taniguchi, T.; Geim, A. K. *Nano Lett.* **2011**, *11*, 2396–2399.

(22) Nair, R. R.; Blake, P.; Grigorenko, A. N.; Novoselov, K. S.; Booth, T. J.; Stauber, T.; Peres, N. M. R.; Geim, A. K. *Science* **2008**, *320*, 1308–1308.

(23) Lee, C.; Wei, X.; Kysar, J. W.; Hone, J. *Science* **2008**, *321*, 385–388.

(24) Akbar, F.; Kolahdouz, M.; Larimian, S.; Radfar, B.; Radamson, H. H. *J. Mater. Sci. Mater. Electron.* **2015**, *26*, 4347–4379.

(25) Liu, Z.; Lau, S. P.; Yan, F. *Chem. Soc. Rev.* **2015**, *44*, 5638–5679.

(26) Georgakilas, V.; Otyepka, M.; Bourlinos, A. B.; Chandra, V.; Kim, N.; Kemp, K. C.; Hobza, P.; Zboril, R.; Kim, K. S. *Chem. Rev.* **2012**, *112*, 6156–6214.

(27) Fan, X.; Zhang, G.; Zhang, F. *Chem. Soc. Rev.* **2015**, *44*, 3023–3035.

(28) Ge, S.; Lan, F.; Yu, F.; Yu, J. *New J. Chem.* **2015**, *39*, 2380–2395.

(29) Bekyarova, E.; Sarkar, S.; Niyogi, S.; Itkis, M. E.; Haddon, R. C. *J. Phys. Appl. Phys.* **2012**, *45*, 154009–154026.

(30) Kuila, T.; Bose, S.; Mishra, A. K.; Khanra, P.; Kim, N. H.; Lee, J. H. *Prog. Mater. Sci.* **2012**, *57*, 1061–1105.

(31) Sarkar, S.; Bekyarova, E.; Haddon, R. C. *Mater. Today* **2012**, *15*, 276–285.

(32) Criado, A.; Melchionna, M.; Marchesan, S.; Prato, M. *Angew. Chem. Int. Ed.* **2015**, *54*, 10734–10750.

(33) Sarkar, S.; Bekyarova, E.; Niyogi, S.; Haddon, R. C. *J. Am. Chem. Soc.* **2011**, *133*, 3324–3327.

(34) Georgakilas, V.; Bourlinos, A. B.; Zboril, R.; Steriotis, T. A.; Dallas, P.; Stubos, A. K.; Trapalis, C. *Chem. Commun.* **2010**, *46*, 1766–1768.

(35) Liu, L.-H.; Lerner, M. M.; Yan, M. *Nano Lett.* **2010**, *10*, 3754–3756.

(36) Choi, J.; Kim, K.; Kim, B.; Lee, H.; Kim, S. *J. Phys. Chem. C* **2009**, *113*, 9433–9435.

(37) Hummers, W. S.; Offeman, R. E. *J. Am. Chem. Soc.* **1958**, *80*, 1339–1339.

(38) Hansora, D. P.; Shimpi, N. G.; Mishra, S. *JOM* **2015**, 1–14.

(39) Jiang, K.; Ma, L.; Wang, J.; Chen, W. *Rev. Nanosci. Nanotechnol.* **2013**, *2*, 171–183.

(40) Nanda, S. S.; Papaefthymiou, G. C.; Yi, D. K. *Crit. Rev. Solid State Mater. Sci.* **2015**, *40*, 291–315.

(41) Yang, K.; Feng, L.; Hong, H.; Cai, W.; Liu, Z. *Nat. Protoc.* **2013**, *8*, 2392–2403.

(42) Pei, S.; Cheng, H.-M. *Carbon* **2012**, *50*, 3210–3228.

(43) Chua, C. K.; Pumera, M. *Chem. Soc. Rev.* **2013**, *43*, 291–312.

(44) Thakur, S.; Karak, N. *Carbon* **2015**, *94*, 224–242.

(45) Xu, Y.; Liu, Z.; Zhang, X.; Wang, Y.; Tian, J.; Huang, Y.; Ma, Y.; Zhang, X.; Chen, Y. *Adv. Mater.* **2009**, *21*, 1275–1279.

(46) Liu, Z.; Robinson, J. T.; Sun, X.; Dai, H. *J. Am. Chem. Soc.* **2008**, *130*, 10876–10877.

(47) Liu, H.; Ryu, S.; Chen, Z.; Steigerwald, M. L.; Nuckolls, C.; Brus, L. E. *J. Am. Chem. Soc.* **2009**, *131*, 17099–17101.

(48) Hossain, M. Z.; Walsh, M. A.; Hersam, M. C. *J. Am. Chem. Soc.* **2010**, *132*, 15399–15403.

(49) Lomeda, J. R.; Doyle, C. D.; Kosynkin, D. V.; Hwang, W.-F.; Tour, J. M. *J. Am. Chem. Soc.* **2008**, *130*, 16201–16206.

(50) Bekyarova, E.; Itkis, M. E.; Ramesh, P.; Berger, C.; Sprinkle, M.; de Heer, W. A.; Haddon, R. C. *J. Am. Chem. Soc.* **2009**, *131*, 1336–1337.

(51) Farmer, D. B.; Lin, Y.-M.; Afzali-Ardakani, A.; Avouris, P. *Appl. Phys. Lett.* **2009**, *94*, 213106.

(52) Farmer, D. B.; Golizadeh-Mojarad, R.; Perebeinos, V.; Lin, Y.-M.; Tulevski, G. S.; Tsang, J. C.; Avouris, P. *Nano Lett.* **2009**, *9*, 388–392.

(53) Fan, X.-Y.; Nouchi, R.; Yin, L.-C.; Tanigaki, K. *Nanotechnology* **2010**, *21*, 475208.

(54) Jacobsen, A.; Koehler, F. M.; Stark, W. J.; Ensslin, K. *New J. Phys.* **2010**, *12*, 125007.

(55) Koehler, F. M.; Jacobsen, A.; Ensslin, K.; Stampfer, C.; Stark, W. J. *Small* **2010**, *6*, 1125–1130.

(56) Lim, H.; Lee, J. S.; Shin, H.-J.; Shin, H. S.; Choi, H. C. *Langmuir* **2010**, *26*, 12278–12284.

(57) Niyogi, S.; Bekyarova, E.; Itkis, M. E.; Zhang, H.; Shepperd, K.; Hicks, J.; Sprinkle, M.; Berger, C.; Lau, C. N.; deHeer, W. A.; Conrad, E. H.; Haddon, R. C. *Nano Lett.* **2010**, *10*, 4061–4066.

(58) Sharma, R.; Baik, J. H.; Perera, C. J.; Strano, M. S. *Nano Lett.* **2010**, *10*, 398–405.

(59) Sinitskii, A.; Dimiev, A.; Corley, D. A.; Fursina, A. A.; Kosynkin, D. V.; Tour, J. M. *ACS Nano* **2010**, *4*, 1949–1954.

(60) Hong, J.; Niyogi, S.; Bekyarova, E.; Itkis, M. E.; Ramesh, P.; Amos, N.; Litvinov, D.; Berger, C.; de Heer, W. A.; Khizroev, S.; Haddon, R. C. *Small* **2011**, *7*, 1175–1180.

(61) Niyogi, S.; Bekyarova, E.; Hong, J.; Khizroev, S.; Berger, C.; de Heer, W.; Haddon, R. C. *J. Phys. Chem. Lett.* **2011**, *2*, 2487–2498.

(62) Gan, L.; Zhang, D.; Guo, X. *Small* **2012**, *8*, 1326–1330.

(63) Liu, J.; Wang, R.; Cui, L.; Tang, J.; Liu, Z.; Kong, Q.; Yang, W.; Gooding, J. *J. Phys. Chem. C* **2012**, *116*, 17939–17946.

(64) Liu, J.; Tang, J.; Gooding, J. J. *J. Mater. Chem.* **2012**, *22*, 12435–12452.

(65) Zhu, H.; Huang, P.; Jing, L.; Zuo, T.; Zhao, Y.; Gao, X. *J. Mater. Chem.* **2012**, *22*, 2063–2068.

(66) Paulus, G. L. C.; Wang, Q. H.; Strano, M. S. *Acc. Chem. Res.* **2013**, *46*, 160–170.

(67) Vase, K. H.; Holm, A. H.; Norrman, K.; Pedersen, S. U.; Daasbjerg, K. *Langmuir* **2007**, *23*, 3786–3793.

(68) Dirk, S. M.; Pylypenko, S.; Howell, S. W.; Fulghum, J. E.; Wheeler, D. R. *Langmuir* **2005**, *21*, 10899–10901.

(69) Matrab, T.; Combellas, C.; Kanoufi, F. *Electrochem. Commun.* **2008**, *10*, 1230–1234.

(70) Charlton, M. R.; Suhr, K. J.; Holliday, B. J.; Stevenson, K. J. *Langmuir* **2015**, *31*, 695–702.

(71) Chan, C. K.; Beechem, T. E.; Ohta, T.; Brumbach, M. T.; Wheeler, D. R.; Stevenson, K. J. *J. Phys. Chem. C* **2013**, *117*, 12038–12044.

(72) Tang, C. W.; VanSlyke, S. A. *Appl. Phys. Lett.* **1987**, *51*, 913–915.

(73) Baldo, M. A.; O'Brien, D. F.; You, Y.; Shoustikov, A.; Sibley, S.; Thompson, M. E.; Forrest, S. R. *Nature* **1998**, *395*, 151–154.

(74) O'Brien, D. F.; Baldo, M. A.; Thompson, M. E.; Forrest, S. R. *Appl. Phys. Lett.* **1999**, *74*, 442–444.

(75) *OLED Fundamentals: Materials, Devices, and Processing of Organic Light-Emitting Diodes*; Gaspar, D., Polikarpov, E., Eds.; CRC Press, 2015.

(76) Yersin, H. *Highly Efficient OLEDs with Phosphorescent Materials*; John Wiley & Sons, 2008.

(77) Baldo, M. A.; O'Brien, D. F.; Thompson, M. E.; Forrest, S. R. *Phys. Rev. B* **1999**, *60*, 14422–14428.

(78) Segal, M.; Baldo, M. A.; Holmes, R. J.; Forrest, S. R.; Soos, Z. G. *Phys. Rev. B* **2003**, *68*, 075211.

(79) Zanoni, K. P. S.; Coppo, R. L.; Amaral, R. C.; Iha, N. Y. M. *Dalton Trans.* **2015**, *44*, 14559–14573.

(80) Suzuri, Y.; Oshiyama, T.; Ito, H.; Hiyama, K.; Kita, H. *Sci. Technol. Adv. Mater.* **2014**, *15*, 054202.

(81) Liang, A.; Ying, L.; Huang, F. *J. Inorg. Organomet. Polym. Mater.* **2014**, *24*, 905–926.

(82) Choy, W. C. H.; Chan, W. K.; Yuan, Y. *Adv. Mater.* **2014**, *26*, 5368–5399.

(83) Yang, X.; Yao, C.; Zhou, G. *Platin. Met. Rev.* **2013**, *57*, 2–16.

(84) Baranoff, E.; Yum, J.-H.; Graetzel, M.; Nazeeruddin, M. K. *J. Organomet. Chem.* **2009**, *694*, 2661–2670.

(85) Flamigni, L.; Barbieri, A.; Sabatini, C.; Ventura, B.; Barigelletti, F. In *Photochemistry and Photophysics of Coordination Compounds II*; Balzani, V., Campagna, S., Eds.; Springer Berlin Heidelberg, 2007; pp 143–203.

(86) Tanaka, D.; Sasabe, H.; Li, Y.-J.; Su, S.-J.; Takeda, T.; Kido, J. *Jpn. J. Appl. Phys.* **2007**, *46*, L10.

(87) Costa, R. D.; Tordera, D.; Ortí, E.; Bolink, H. J.; Schönle, J.; Graber, S.; Housecroft, C. E.; Constable, E. C.; Zampese, J. A. *J. Mater. Chem.* **2011**, *21*, 16108–16118.

(88) Tao, Y.; Yuan, K.; Chen, T.; Xu, P.; Li, H.; Chen, R.; Zheng, C.; Zhang, L.; Huang, W. *Adv. Mater.* **2014**, *26*, 7931–7958.

(89) Armaroli, N.; Accorsi, G.; Cardinali, F.; Listorti, A. In *Photochemistry and Photophysics of Coordination Compounds I*; Balzani, V., Campagna, S., Eds.; Springer Berlin Heidelberg, 2007; pp 69–115.

(90) Tsuge, K.; Chishina, Y.; Hashiguchi, H.; Sasaki, Y.; Kato, M.; Ishizaka, S.; Kitamura, N. *Coord. Chem. Rev.* **2016**, *306, Part 2*, 636–651.

(91) Lavie-Cambot, A.; Cantuel, M.; Leydet, Y.; Jonusauskas, G.; Bassani, D. M.; McClenaghan, N. D. *Coord. Chem. Rev.* **2008**, *252*, 2572–2584.

(92) Ford, P. C.; Cariati, E.; Bourassa, J. *Chem. Rev.* **1999**, *99*, 3625–3648.

(93) Dumur, F. *Org. Electron.* **2015**, *21*, 27–39.

(94) Volz, D.; Wallesch, M.; Fléchon, C.; Danz, M.; Verma, A.; Navarro, J. M.; Zink, D. M.; Bräse, S.; Baumann, T. *Green Chem.* **2015**, *17*, 1988–2011.

(95) Hashimoto, M.; Igawa, S.; Yashima, M.; Kawata, I.; Hoshino, M.; Osawa, M. *J. Am. Chem. Soc.* **2011**, *133*, 10348–10351.

(96) Barbara, P. F.; Meyer, T. J.; Ratner, M. A. *J. Phys. Chem.* **1996**, *100*, 13148–13168.

(97) Brunschwig, B. S.; Sutin, N. *Coord. Chem. Rev.* **1999**, *187*, 233–254.

(98) Meyer, T. J. *Acc. Chem. Res.* **1978**, *11*, 94–100.

(99) Nelsen, S. F.; Ismagilov, R. F.; Trieber, D. A. *Science* **1997**, *278*, 846–849.

(100) Robin, M. B.; Day, P. In *Advances in Inorganic Chemistry and Radiochemistry*; Sharpe, H. J. E. and A. G., Ed.; Academic Press, 1967; Vol. 10, pp 247–422.

(101) Day, P.; Hush, N. S.; Clark, R. J. H. *Philos. Trans. R. Soc. Lond. Math. Phys. Eng. Sci.* **2008**, *366*, 5–14.

(102) Demadis, K. D.; Hartshorn, C. M.; Meyer, T. J. *Chem. Rev.* **2001**, *101*, 2655–2686.

(103) Brunschwig, B. S.; Creutz, C.; Sutin, N. *Chem. Soc. Rev.* **2002**, *31*, 168–184.

(104) Marcus, R. A. *J. Chem. Phys.* **1956**, *24*, 966–978.

(105) Hush, N. S. *Trans. Faraday Soc.* **1961**, *57*, 557–580.

(106) Hush, N. S. In *Progress in Inorganic Chemistry*; Cotton, F. A., Ed.; John Wiley & Sons, Inc., 1967; pp 391–444.

(107) Hush, N. S. *Electrochimica Acta* **1968**, *13*, 1005–1023.

(108) Cotton, F. A.; Wilkinson, G.; Murillo, C. A.; Bochmann, M. *Advanced Inorganic Chemistry*, 6th ed.; John Wiley & Sons, 1999.

(109) Tejel, C.; Ciriano, M. A.; del Río, M. P.; van den Bruele, F. J.; Hetterscheid, D. G. H.; Tsichlis i Spithas, N.; de Bruin, B. *J. Am. Chem. Soc.* **2008**, *130*, 5844–5845.

(110) Tommasino, J. B.; De Montauzon, D.; He, X.; Maisonnat, A.; Poilblanc, R.; Verpeaux, J. N.; Amatore, C. *Organometallics* **1992**, *11*, 4150–4156.

(111) Carano, M.; Careri, M.; Cicogna, F.; D'Ambra, I.; Houben, J. L.; Ingrosso, G.; Marcaccio, M.; Paolucci, F.; Pinzino, C.; Roffia, S. *Organometallics* **2001**, *20*, 3478–3490.

(112) Nafady, A.; Chin, T. T.; Geiger, W. E. *Organometallics* **2006**, *25*, 1654–1663.

(113) He, F.; Ruhlmann, L.; Gisselbrecht, J.-P.; Choua, S.; Orio, M.; Wesolek, M.; Danopoulos, A. A.; Braunstein, P. *Dalton Trans.* **2015**, *44*, 17030–17044.

(114) Shibata, Y.; Zhu, B.; Kume, S.; Nishihara, H. *Dalton Trans.* **2009**, 1939–1943.

(115) Sakamoto, R.; Kambe, T.; Tsukada, S.; Takada, K.; Hoshiko, K.; Kitagawa, Y.; Okumura, M.; Nishihara, H. *Inorg. Chem.* **2013**, *52*, 7411–7416.

(116) Festus Agbo, S. F. *Int. J. Chem.* **2011**, *3*, 9698–1916.

(117) Evans, P. A. *Modern Rhodium-Catalyzed Organic Reactions*; John Wiley & Sons, 2005.

(118) Press Release: The 2000 Nobel Prize in Chemistry http://www.nobelprize.org/nobel_prizes/chemistry/laureates/2000/press.html (accessed Feb 18, 2016).

(119) Balint, R.; Cassidy, N. J.; Cartmell, S. H. *Acta Biomater.* **2014**, *10*, 2341–2353.

(120) Bredas, J. L.; Street, G. B. *Acc. Chem. Res.* **1985**, *18*, 309–315.

(121) Li, X.; Wang, Y.; Yang, X.; Chen, J.; Fu, H.; Cheng, T.; Wang, Y. *TrAC Trends Anal. Chem.* **2012**, *39*, 163–179.

(122) Sairam, M.; Nataraj, S. K.; Aminabhavi, T. M.; Roy, S.; Madhusoodana, C. D. *Sep. Purif. Rev.* **2006**, *35*, 249–283.

(123) Pellegrino, J. *Ann. N. Y. Acad. Sci.* **2003**, *984*, 289–305.

(124) Sarrazin, J.; Persin, M.; Cretin, M. *Macromol. Symp.* **2002**, *188*, 1–12.

(125) Fabre, B.; Simonet, J. *Coord. Chem. Rev.* **1998**, *178–180*, 1211–1250.

(126) Simonet, J. *Pure Appl. Chem.* **1998**, *70*, 1253–1257.

(127) Bagheri, H.; Ayazi, Z.; Naderi, M. *Anal. Chim. Acta* **2013**, *767*, 1–13.

(128) Tian, Y.; Wang, J.; Wang, Z.; Wang, S. *Sens. Actuators B Chem.* **2005**, *104*, 23–28.

(129) Liljegren, G.; Forsgard, N.; Zettersten, C.; Pettersson, J.; Svedberg, M.; Herranen, M.; Nyholm, L. *Analyst* **2005**, *130*, 1358–1368.

(130) Qiu, B.; Xu, C.; Sun, D.; Wang, Q.; Gu, H.; Zhang, X.; Weeks, B. L.; Hopper, J.; Ho, T. C.; Guo, Z.; Wei, S. *Appl. Surf. Sci.* **2015**, *334*, 7–14.

(131) Li, X.; Li, C.; Chen, J.; Li, C.; Sun, C. *J. Chromatogr. A* **2008**, *1198–1199*, 7–13.

(132) Caris, J. A.; Chaves, A. R.; Queiroz, M. E. C. *J. Braz. Chem. Soc.* **2012**, *23*, 57–64.

(133) Yates, B. J.; Temsamani, K. R.; Ceylan, Ö.; Öztemiz, S.; Gbatu, T. P.; LaRue, R. A.; Tamer, U.; Mark Jr, H. B. *Talanta* **2002**, *58*, 739–745.

(134) Lyskawa, J.; Le Derf, F.; Levillain, E.; Mazari, M.; Sallé, M.; Dubois, L.; Viel, P.; Bureau, C.; Palacin, S. *J. Am. Chem. Soc.* **2004**, *126*, 12194–12195.

(135) Weinberger, D. A.; Higgins, T. B.; Mirkin, C. A.; Stern, C. L.; Liable-Sands, L. M.; Rheingold, A. L. *J. Am. Chem. Soc.* **2001**, *123*, 2503–2516.

(136) Mokhtari, B.; Pourabdollah, K.; Dallali, N. *J. Radioanal. Nucl. Chem.* **2010**, *287*, 921–934.

(137) Boerrigter, H.; Verboom, W.; Reinhoudt, D. N. *J. Org. Chem.* **1997**, *62*, 7148–7155.

(138) Boerrigter, H.; Tomasberger, T.; Verboom, W.; Reinhoudt, D. N. *Eur. J. Org. Chem.* **1999**, *1999*, 665–674.

(139) Peters, M. W.; Werner, E. J.; Scott, M. J. *Inorg. Chem.* **2002**, *41*, 1707–1716.

(140) Matloka, K.; Gelis, A.; Regalbuto, M.; Vandegrift, G.; Scott, M. J. *Dalton Trans.* **2005**, 3719–3721.

(141) Dam, H. H.; Reinhoudt, D. N.; Verboom, W. *New J. Chem.* **2007**, *31*, 1620–1632.

(142) Dam, H. H.; Reinhoudt, D. N.; Verboom, W. *Chem. Soc. Rev.* **2007**, *36*, 367–377.

(143) Lewis, F.; Hudson, M.; Harwood, L. *Synlett* **2011**, 2609–2632.

(144) Halls, J. J. M.; Walsh, C. A.; Greenham, N. C.; Marseglia, E. A.; Friend, R. H.; Moratti, S. C.; Holmes, A. B. *Nature* **1995**, *376*, 498–500.

(145) Van De Wetering, K.; Brochon, C.; Ngov, C.; Hadziioannou, G. *Macromolecules* **2006**, *39*, 4289–4297.

(146) Yu, G.; Heeger, A. J. *J. Appl. Phys.* **1995**, *78*, 4510–4515.

(147) Thompson, B. C.; Fréchet, J. M. J. *Angew. Chem. Int. Ed.* **2008**, *47*, 58–77.

(148) Shao, Y.; Yang, Y. *Adv. Mater.* **2005**, *17*, 2841–2844.

(149) Castrucci, J. S.; Josey, D. S.; Thibau, E.; Lu, Z.-H.; Bender, T. P. *J. Phys. Chem. Lett.* **2015**, *6*, 3121–3125.

(150) Zhen, H.; Hou, Q.; Li, K.; Ma, Z.; Fabiano, S.; Gao, F.; Zhang, F. *J. Mater. Chem. A* **2014**, *2*, 12390–12396.

(151) Tritsch, J. R.; Chan, W.-L.; Wu, X.; Monahan, N. R.; Zhu, X.-Y. *Nat. Commun.* **2013**, *4*, 2679.

(152) Lee, J.; Jadhav, P.; Reusswig, P. D.; Yost, S. R.; Thompson, N. J.; Congreve, D. N.; Hontz, E.; Van Voorhis, T.; Baldo, M. A. *Acc. Chem. Res.* **2013**, *46*, 1300–1311.

(153) Winroth, G.; Podobinski, D.; Cacialli, F. *J. Appl. Phys.* **2011**, *110*, 124504.

(154) Arif, M.; Yang, K.; Li, L.; Yu, P.; Guha, S.; Gangopadhyay, S.; Förster, M.; Scherf, U. *Appl. Phys. Lett.* **2009**, *94*, 063307.

(155) Bardeen, C. J. *Nat. Mater.* **2014**, *13*, 1001–1003.

(156) Yost, S. R.; Hontz, E.; Yeganeh, S.; Van Voorhis, T. *J. Phys. Chem. C* **2012**, *116*, 17369–17377.

(157) Musser, A. J.; Al-Hashimi, M.; Maiuri, M.; Brida, D.; Heeney, M.; Cerullo, G.; Friend, R. H.; Clark, J. *J. Am. Chem. Soc.* **2013**, *135*, 12747–12754.

(158) Monahan, N.; Zhu, X.-Y. *Annu. Rev. Phys. Chem.* **2015**, *66*, 601–618.

(159) Smith, M. B.; Michl, J. *Chem. Rev.* **2010**, *110*, 6891–6936.

(160) Singh-Rachford, T. N.; Castellano, F. N. *Coord. Chem. Rev.* **2010**, *254*, 2560–2573.

(161) Ceroni, P. *Chem. – Eur. J.* **2011**, *17*, 9560–9564.

(162) Tayebjee, M. J. Y.; McCamey, D. R.; Schmidt, T. W. *J. Phys. Chem. Lett.* **2015**, *6*, 2367–2378.

(163) Shang, Y.; Hao, S.; Yang, C.; Chen, G. *Nanomaterials* **2015**, *5*, 1782–1809.

(164) Ewbank, P. C.; Laird, D.; McCullough, R. D. In *Organic Photovoltaics*; Brabec, C., Dyakonov, V., Scherf, U., Eds.; Wiley-VCH Verlag GmbH & Co. KGaA, 2008; pp 1–55.

(165) Hsing-Ju Wang; Chih-Ping Chen; Ru-Jong Jeng. *Mater. 1996-1944* **2014**, *7*, 2411–2439.

(166) McCullough, R. D.; Lowe, R. D.; Jayaraman, M.; Anderson, D. L. *J. Org. Chem.* **1993**, *58*, 904–912.

(167) Reid, O. G.; Pensack, R. D.; Song, Y.; Scholes, G. D.; Rumbles, G. *Chem. Mater.* **2014**, *26*, 561–575.

(168) Elschner, A.; Kirchmeyer, S. In *Organic Photovoltaics*; Brabec, C., Dyakonov, V., Scherf, U., Eds.; Wiley-VCH Verlag GmbH & Co. KGaA, 2008; pp 211–242.

(169) Weissmann, M.; Baranton, S.; Coutanceau, C. *Langmuir* **2010**, *26*, 15002–15009.

(170) Fontanesi, C.; Bortolotti, C. A.; Vanossi, D.; Marcaccio, M. *J. Phys. Chem. A* **2011**, *115*, 11715–11722.

(171) Florini, N.; Michelazzi, M.; Parenti, F.; Mucci, A.; Sola, M.; Baratti, C.; Renzi, V. D.; Daasbjerg, K.; Pedersen, S. U.; Fontanesi, C. *J. Electroanal. Chem.* **2013**, *710*, 41–47.

(172) Vase, K. H.; Holm, A. H.; Pedersen, S. U.; Daasbjerg, K. *Langmuir* **2005**, *21*, 8085–8089.

(173) Saby, C.; Ortiz, B.; Champagne, G. Y.; Bélanger, D. *Langmuir* **1997**, *13*, 6805–6813.

(174) Bielawski, M.; Aili, D.; Olofsson, B. *J. Org. Chem.* **2008**, *73*, 4602–4607.

(175) Gui, A. L.; Liu, G.; Chockalingam, M.; Le Saux, G.; Luais, E.; Harper, J. B.; Gooding, J. J. *Electroanalysis* **2010**, *22*, 1824–1830.

(176) Maldonado, S.; Smith, T. J.; Williams, R. D.; Morin, S.; Barton, E.; Stevenson, K. J. *Langmuir* **2006**, *22*, 2884–2891.

(177) Allongue, P.; Delamar, M.; Desbat, B.; Fagebaume, O.; Hitmi, R.; Pinson, J.; Savéant, J.-M. *J. Am. Chem. Soc.* **1997**, *119*, 201–207.

(178) Tsierkezos, N. G. *J. Solut. Chem.* **2007**, *36*, 289–302.

(179) Bruno, I. J.; Cole, J. C.; Edgington, P. R.; Kessler, M.; Macrae, C. F.; McCabe, P.; Pearson, J.; Taylor, R. *Acta Crystallogr. B* **2002**, *58*, 389–397.

(180) Bailly, F.; Barthen, P.; Frohn, H.-J.; Köckerling, M. *Z. Für Anorg. Allg. Chem.* **2000**, *626*, 2419–2427.

(181) Frohn, H.-J.; Hirschberg, M. E.; Boese, R.; Bläser, D.; Flörke, U. *Z. Für Anorg. Allg. Chem.* **2008**, *634*, 2539–2550.

(182) Hubbard, C. R.; Himes, V. L.; Mighell, A. D.; Page, S. W. *Acta Crystallogr. B* **1980**, *36*, 2819–2821.

(183) Schäfer, S.; Wirth, T. *Angew. Chem. Int. Ed.* **2010**, *49*, 2786–2789.

(184) Li, Y.; Chopra, N. *JOM* **2014**, *67*, 34–43.

(185) Li, Y.; Chopra, N. *JOM* **2014**, *67*, 44–52.

(186) Whitener Jr., K. E.; Sheehan, P. E. *Diam. Relat. Mater.* **2014**, *46*, 25–34.

(187) Riedl, C.; Coletti, C.; Iwasaki, T.; Zakharov, A. A.; Starke, U. *Phys. Rev. Lett.* **2009**, *103*, 246804.

(188) Brar, V. W.; Zhang, Y.; Yayon, Y.; Ohta, T.; McChesney, J. L.; Bostwick, A.; Rotenberg, E.; Horn, K.; Crommie, M. F. *Appl. Phys. Lett.* **2007**, *91*, 122102.

(189) Deretzis, I.; La Magna, A. *Phys. Rev. B* **2011**, *84*, 235426.

(190) Goler, S.; Coletti, C.; Piazza, V.; Pingue, P.; Colangelo, F.; Pellegrini, V.; Emtsev, K. V.; Forti, S.; Starke, U.; Beltram, F.; Heun, S. *Carbon* **2013**, *51*, 249–254.

(191) Hiura, H. *J. Mater. Res.* **2001**, *16*, 1287–1292.

(192) Ohta, T.; Bartelt, N. C.; Nie, S.; Thürmer, K.; Kellogg, G. L. *Phys. Rev. B* **2010**, *81*, 121411.

(193) Cançado, L. G.; Jorio, A.; Ferreira, E. H. M.; Stavale, F.; Achete, C. A.; Capaz, R. B.; Moutinho, M. V. O.; Lombardo, A.; Kulmala, T. S.; Ferrari, A. C. *Nano Lett.* **2011**, *11*, 3190–3196.

(194) Ferrari, A. C.; Meyer, J. C.; Scardaci, V.; Casiraghi, C.; Lazzeri, M.; Mauri, F.; Piscanec, S.; Jiang, D.; Novoselov, K. S.; Roth, S.; Geim, A. K. *Phys. Rev. Lett.* **2006**, *97*, 187401.

(195) Malard, L. M.; Pimenta, M. A.; Dresselhaus, G.; Dresselhaus, M. S. *Phys. Rep.* **2009**, *473*, 51–87.

(196) Ugeda, M. M.; Brihuega, I.; Guinea, F.; Gómez-Rodríguez, J. M. *Phys. Rev. Lett.* **2010**, *104*, 096804.

(197) Chen, J.-H.; Cullen, W. G.; Jang, C.; Fuhrer, M. S.; Williams, E. D. *Phys. Rev. Lett.* **2009**, *102*, 236805.

(198) Stevenson, K. J.; Veneman, P. A.; Gearba, R. I.; Mueller, K. M.; Holliday, B. J.; Ohta, T.; Chan, C. K. *Faraday Discuss.* **2014**, *172*, 273–291.

(199) Gearba, R. I.; Mueller, K. M.; Veneman, P. A.; Holliday, B. J.; Chan, C. K.; Stevenson, K. J. *J. Electroanal. Chem.* **2015**, *753*, 9–15.

(200) Bekyarova, E.; Itkis, M. E.; Ramesh, P.; Haddon, R. C. *Phys. Status Solidi RRL - Rapid Res. Lett.* **2009**, *3*, 184–186.

(201) Ferrari, A. C.; Basko, D. M. *Nat. Nanotechnol.* **2013**, *8*, 235–246.

(202) Mizes, H. A.; Foster, J. S. *Science* **1989**, *244*, 559–562.

(203) Kelly, K. F.; Mickelson, E. T.; Hauge, R. H.; Margrave, J. L.; Halas, N. J. *Proc. Natl. Acad. Sci.* **2000**, *97*, 10318–10321.

(204) Kelly, K. F.; Halas, N. J. *Surf. Sci.* **1998**, *416*, L1085–L1089.

(205) Ceperley, D. M.; Alder, B. J. *Phys. Rev. Lett.* **1980**, *45*, 566–569.

(206) Yazyev, O. V.; Helm, L. *Phys. Rev. B* **2007**, *75*, 125408.

(207) Boukhvalov, D. W.; Katsnelson, M. I.; Lichtenstein, A. I. *Phys. Rev. B* **2008**, *77*, 035427.

(208) Jiang, D.; Sumpter, B. G.; Dai, S. *J. Phys. Chem. B* **2006**, *110*, 23628–23632.

(209) Yazyev, O. V. *Rep. Prog. Phys.* **2010**, *73*, 056501.

(210) Kim, S.; Jo, I.; Dillen, D. C.; Ferrer, D. A.; Fallahazad, B.; Yao, Z.; Banerjee, S. K.; Tutuc, E. *Phys. Rev. Lett.* **2012**, *108*, 116404.

(211) Kim, S.; Nah, J.; Jo, I.; Shahrjerdi, D.; Colombo, L.; Yao, Z.; Tutuc, E.; Banerjee, S. K. *Appl. Phys. Lett.* **2009**, *94*, 062107.

(212) *Crystal Clear, 1.40*; Rigaku Americas Corporation: The Woodlands, Texas, 2008.

(213) Altomare, A.; Burla, M. C.; Camalli, M.; Cascarano, G. L.; Giacovazzo, C.; Guagliardi, A.; Moliterni, A. G. G.; Polidori, G.; Spagna, R. *J. Appl. Crystallogr.* **1999**, *32*, 115–119.

(214) Sheldrick, G. M. *Acta Cryst.* **2008**, *A64*, 112–122.

(215) Spek, A. L. *PLATON, A Multipurpose Crystallographic Tool.*; Utrecht University: Utrecht University, The Netherlands, 1998.

(216) Farrugia, L. J. *J. Appl. Crystallogr.* **1999**, *32*, 837–838.

(217) Farrugia, L. J. *WinGX an Integrated System of Windows Programs for the Solution, Refinement and Analysis of Single Crystal X-Ray Diffraction Data*; University of Glasgow: Glasgow, U.K., 1999.

(218) In *International Tables for X-Ray Crystallography*; Wilson, A. J. C., Ed.; Kluwer Academic Press: Boston, 1992; Vol. C, p Tables 4.2.6.8 and 6.1.1.4.

(219) Chelikowsky, J. R.; Troullier, N.; Saad, Y. *Phys. Rev. Lett.* **1994**, *72*, 1240–1243.

(220) Kronik, L.; Makmal, A.; Tiago, M. L.; Alemany, M. M. G.; Jain, M.; Huang, X.; Saad, Y.; Chelikowsky, J. R. *Phys. Status Solidi B* **2006**, *243*, 1063–1079.

(221) Yersin, H. In *Transition Metal and Rare Earth Compounds*; Topics in Current Chemistry; Springer Berlin Heidelberg, 2004; pp 1–26.

(222) Yersin, H.; Rausch, A. F.; Czerwieniec, R.; Hofbeck, T.; Fischer, T. *Coord. Chem. Rev.* **2011**, *255*, 2622–2652.

(223) Turro, N. J. *Modern Molecular Photochemistry*; Benjamin/Cummings Pub. Co.: Menlo Park, Calif., 1978.

(224) Raithby, P. R.; Shields, G. P.; Allen, F. H.; Motherwell, W. D. S. *Acta Crystallogr. Sect. B* **2000**, *56*, 444–454.

(225) Cuttell, D. G.; Kuang, S.-M.; Fanwick, P. E.; McMillin, D. R.; Walton, R. A. *J. Am. Chem. Soc.* **2002**, *124*, 6–7.

(226) Kuang, S.-M.; Cuttell, D. G.; McMillin, D. R.; Fanwick, P. E.; Walton, R. A. *Inorg. Chem.* **2002**, *41*, 3313–3322.

(227) Zhang, Q.; Zhou, Q.; Cheng, Y.; Wang, L.; Ma, D.; Jing, X.; Wang, F. *Adv. Mater.* **2004**, *16*, 432–436.

(228) Armaroli, N.; Accorsi, G.; Holler, M.; Moudam, O.; Nierengarten, J.-F.; Zhou, Z.; Wegh, R. T.; Welter, R. *Adv. Mater.* **2006**, *18*, 1313–1316.

(229) McCormick, T.; Jia, W.-L.; Wang, S. *Inorg. Chem.* **2006**, *45*, 147–155.

(230) Zhang, Q.; Zhou, Q.; Cheng, Y.; Wang, L.; Ma, D.; Jing, X.; Wang, F. *Adv. Funct. Mater.* **2006**, *16*, 1203–1208.

(231) Czerwieniec, R.; Yu, J.; Yersin, H. *Inorg. Chem.* **2011**, *50*, 8293–8301.

(232) Hsu, C.-W.; Lin, C.-C.; Chung, M.-W.; Chi, Y.; Lee, G.-H.; Chou, P.-T.; Chang, C.-H.; Chen, P.-Y. *J. Am. Chem. Soc.* **2011**, *133*, 12085–12099.

(233) Bergmann, L.; Friedrichs, J.; Mydlak, M.; Baumann, T.; Nieger, M.; Bräse, S. *Chem. Commun.* **2013**, *49*, 6501–6503.

(234) Chen, X.-L.; Yu, R.; Zhang, Q.-K.; Zhou, L.-J.; Wu, X.-Y.; Zhang, Q.; Lu, C.-Z. *Chem. Mater.* **2013**, *25*, 3910–3920.

(235) Chen, X.-L.; Lin, C.-S.; Wu, X.-Y.; Yu, R.; Teng, T.; Zhang, Q.-K.; Zhang, Q.; Yang, W.-B.; Lu, C.-Z. *J. Mater. Chem. C* **2015**, *3*, 1187–1195.

(236) Keller, S.; Constable, E. C.; Housecroft, C. E.; Neuburger, M.; Prescimone, A.; Longo, G.; Pertegás, A.; Sessolo, M.; Bolink, H. J. *Dalton Trans.* **2014**, *43*, 16593–16596.

(237) Linfoot, C. L.; Leitl, M. J.; Richardson, P.; Rausch, A. F.; Chepelin, O.; White, F. J.; Yersin, H.; Robertson, N. *Inorg. Chem.* **2014**, *53*, 10854–10861.

(238) Czerwieniec, R.; Yersin, H. *Inorg. Chem.* **2015**, *54*, 4322–4327.

(239) Igawa, S.; Hashimoto, M.; Kawata, I.; Yashima, M.; Hoshino, M.; Osawa, M. *J. Mater. Chem. C* **2013**, *1*, 542–551.

(240) Li, X.-L.; Ai, Y.-B.; Yang, B.; Chen, J.; Tan, M.; Xin, X.-L.; Shi, Y.-H. *Polyhedron* **2012**, *35*, 47–54.

(241) Blasse, G.; McMillin, D. R. *Chem. Phys. Lett.* **1980**, *70*, 1–3.

(242) Breddels, P. A.; Berdowski, P. A. M.; Blasse, G.; McMillin, D. R. *J. Chem. Soc. Faraday Trans. 2 Mol. Chem. Phys.* **1982**, *78*, 595–601.

(243) Saito, K.; Arai, T.; Takahashi, N.; Tsukuda, T.; Tsubomura, T. *Dalton Trans.* **2006**, 4444–4448.

(244) Saito, K.; Tsukuda, T.; Tsubomura, T. *Bull. Chem. Soc. Jpn.* **2006**, *79*, 437–441.

(245) Barbieri, A.; Accorsi, G.; Armaroli, N. *Chem. Commun.* **2008**, 2185–2193.

(246) Czerwieniec, R.; Kowalski, K.; Yersin, H. *Dalton Trans.* **2013**, *42*, 9826–9830.

(247) Li, Q.; Xu, S.-X.; Wang, J.-L.; Xia, H.-Y.; Zhao, F.; Wang, Y.-B. *Int. J. Quantum Chem.* **2014**, *114*, 1685–1691.

(248) Nishikawa, M.; Sawamura, S.; Haraguchi, A.; Morikubo, J.; Takao, K.; Tsubomura, T. *Dalton Trans.* **2015**, *44*, 411–418.

(249) Ohara, H.; Kobayashi, A.; Kato, M. *Dalton Trans.* **2014**, *43*, 17317–17323.

(250) Moudam, O.; Kaeser, A.; Delavaux-Nicot, B.; Duhayon, C.; Holler, M.; Accorsi, G.; Armaroli, N.; Séguy, I.; Navarro, J.; Destruel, P.; Nierengarten, J.-F. *Chem. Commun.* **2007**, 3077–3079.

(251) Tsuboyama, A.; Kuge, K.; Furugori, M.; Okada, S.; Hoshino, M.; Ueno, K. *Inorg. Chem.* **2007**, *46*, 1992–2001.

(252) Osawa, M. *Chem. Commun.* **2014**, *50*, 1801–1803.

(253) Osawa, M.; Hoshino, M.; Hashimoto, M.; Kawata, I.; Igawa, S.; Yashima, M. *Dalton Trans.* **2015**, *44*, 8369–8378.

(254) Al-Ibrahim, M.; Roth, H.-K.; Schroedner, M.; Konkin, A.; Zhokhavets, U.; Gobsch, G.; Scharff, P.; Sensfuss, S. *Org. Electron.* **2005**, *6*, 65–77.

(255) Pownall, H. J.; Schaffer, A. M.; Becker, R. S.; Mantulin, W. W. *Photochem. Photobiol.* **1978**, *27*, 625–628.

(256) Lancelot, G. *Mol. Phys.* **1976**, *31*, 241–254.

(257) Saadeh, H.; Goodson, T.; Yu, L. *Macromolecules* **1997**, *30*, 4608–4612.

(258) Kubas, G. J. *Inorg. Synth.* **1979**, 90–92.

(259) *CrysAlisPro, 1.171.37.31*; Agilent Technologies UK Ltd.: Oxford, UK, 2013.

(260) Palatinus, L.; Chapuis, G. *J. Appl. Crystallogr.* **2007**, *40*, 786–790.

(261) Sheldrick, G. M. *Acta Crystallogr. Sect. C Struct. Chem.* **2015**, *71*, 3–8.

(262) Sheldrick, G. M. *SHELXTL/PC*; Siemens Analytical X-ray Instruments, Inc.: Madison, Wisconsin, USA, 1994.

(263) Frisch, M. J.; Trucks, G. W.; Schlegel, H. B.; Scuseria, G. E.; Robb, M. A.; Cheeseman, J. R.; Scalmani, G.; Barone, V.; Mennucci, B.; Petersson, G. A.; Nakatsuji, H.; Caricato, M.; Li, X.; Hratchian, H. P.; Izmaylov, A. F.; Bloino, J.; Zheng, G.; Sonnenberg, J. L.; Hada, M.; Ehara, M.; Toyota, K.; Fukuda, R.; Hasegawa, J.; Ishida, M.; Nakajima, T.; Honda, Y.; Kitao, O.; Nakai, H.; Vreven, T.; Montgomery, J. A., Jr.; Peralta, J. E.; Ogliaro, F.; Bearpark, M.; Heyd, J. J.; Brothers, E.; Kudin, K. N.; Staroverov, V. N.; Kobayashi, R.; Normand, J.; Raghavachari, K.; Rendell, A.; Burant, J. C.; Iyengar, S. S.; Tomasi, J.; Cossi, M.; Rega, N.; Millam, N. J.; Klene, M.; Knox, J. E.; Cross, J. B.; Bakken, V.; Adamo, C.; Jaramillo, J.; Gomperts, R.; Stratmann, R. E.; Yazyev, O.; Austin, A. J.; Cammi, R.; Pomelli, C.; Ochterski, J. W.; Martin, R. L.; Morokuma, K.; Zakrzewski, V. G.; Voth, G. A.; Salvador, P.; Dannenberg, J. J.; Dapprich, S.; Daniels, A. D.; Farkas, O.; Foresman, J. B.; Ortiz, J. V.; Cioslowski, J.; Fox, D. J. *Gaussian 09, Revision B.01*; Gaussian, Inc.: Wallingford, CT, 2009.

(264) Bauernschmitt, R.; Ahlrichs, R. *Chem. Phys. Lett.* **1996**, *256*, 454–464.

(265) Casida, M. E.; Jamorski, C.; Casida, K. C.; Salahub, D. R. *J. Chem. Phys.* **1998**, *108*, 4439–4449.

(266) Stratmann, R. E.; Scuseria, G. E.; Frisch, M. J. *J. Chem. Phys.* **1998**, *109*, 8218–8224.

(267) Becke, A. D. *J. Chem. Phys.* **1993**, *98*, 5648–5652.

(268) Lee, C.; Yang, W.; Parr, R. G. *Phys. Rev. B* **1988**, *37*, 785–789.

(269) Miehlich, B.; Savin, A.; Stoll, H.; Preuss, H. *Chem. Phys. Lett.* **1989**, *157*, 200–206.

(270) Stephens, P. J.; Devlin, F. J.; Chabalowski, C. F.; Frisch, M. J. *J. Phys. Chem.* **1994**, *98*, 11623–11627.

(271) Dunning Jr., T. H.; Hay, P. J. In *Modern Theoretical Chemistry*; Schaefer, H. F., Ed.; Plenum: New York, 1977; Vol. 3, pp 1–28.

(272) Hay, P. J.; Wadt, W. R. *J. Chem. Phys.* **1985**, *82*, 270–283.

(273) Wadt, W. R.; Hay, P. J. *J. Chem. Phys.* **1985**, *82*, 284–298.

(274) Hay, P. J.; Wadt, W. R. *J. Chem. Phys.* **1985**, *82*, 299–310.

(275) Ditchfield, R.; Hehre, W. J.; Pople, J. A. *J. Chem. Phys.* **1971**, *54*, 724–728.

(276) Hehre, W. J.; Ditchfield, R.; Pople, J. A. *J. Chem. Phys.* **1972**, *56*, 2257–2261.

(277) Hariharan, P. C.; Pople, J. A. *Theor. Chim. Acta* **1973**, *28*, 213–222.

(278) Hariharan, P. C.; Pople, J. A. *Mol. Phys.* **1974**, *27*, 209–214.

(279) Gordon, M. S. *Chem. Phys. Lett.* **1980**, *76*, 163–168.

(280) Francl, M. M.; Pietro, W. J.; Hehre, W. J.; Binkley, J. S.; Gordon, M. S.; DeFrees, D. J.; Pople, J. A. *J. Chem. Phys.* **1982**, *77*, 3654–3665.

(281) Rassolov, V. A.; Pople, J. A.; Ratner, M. A.; Windus, T. L. *J. Chem. Phys.* **1998**, *109*, 1223–1229.

(282) Rassolov, V. A.; Ratner, M. A.; Pople, J. A.; Redfern, P. C.; Curtiss, L. A. *J. Comput. Chem.* **2001**, *22*, 976–984.

(283) Martin, R. L. *J. Chem. Phys.* **2003**, *118*, 4775–4777.

(284) Forrest, S. R. *Org. Electron.* **2003**, *4*, 45–48.

(285) Meier, S. B.; Tordera, D.; Pertegás, A.; Roldán-Carmona, C.; Ortí, E.; Bolink, H. J. *Mater. Today* **2014**, *17*, 217–223.

(286) Minaev, B.; Baryshnikov, G.; Agren, H. *Phys. Chem. Chem. Phys.* **2014**, *16*, 1719–1758.

(287) Cariati, E.; Lucenti, E.; Botta, C.; Giovanella, U.; Marinotto, D.; Righetto, S. *Coord. Chem. Rev.* **2016**, *306,* 566–614.

(288) Harvey, P. D.; Knorr, M. *Macromol. Rapid Commun.* **2010**, *31*, 808–826.

(289) Liu, Z.; Djurovich, P. I.; Whited, M. T.; Thompson, M. E. *Inorg. Chem.* **2012**, *51*, 230–236.

(290) Deaton, J. C.; Switalski, S. C.; Kondakov, D. Y.; Young, R. H.; Pawlik, T. D.; Giesen, D. J.; Harkins, S. B.; Miller, A. J. M.; Mickenberg, S. F.; Peters, J. C. *J. Am. Chem. Soc.* **2010**, *132*, 9499–9508.

(291) Zink, D. M.; Bächle, M.; Baumann, T.; Nieger, M.; Kühn, M.; Wang, C.; Klopper, W.; Monkowius, U.; Hofbeck, T.; Yersin, H.; Bräse, S. *Inorg. Chem.* **2013**, *52*, 2292–2305.

(292) Leitl, M. J.; Küchle, F.-R.; Mayer, H. A.; Wesemann, L.; Yersin, H. *J. Phys. Chem. A* **2013**, *117*, 11823–11836.

(293) Lotito, K. J.; Peters, J. C. *Chem. Commun.* **2010**, *46*, 3690–3692.

(294) Holliday, B. J.; Swager, T. M. *Chem. Commun.* **2005**, 23–36.

(295) Bonnafoux, L.; Gramage-Doria, R.; Colobert, F.; Leroux, F. R. *Chem. – Eur. J.* **2011**, *17*, 11008–11016.

(296) Kyle, K. R.; Ryu, C. K.; Ford, P. C.; DiBenedetto, J. A. *J. Am. Chem. Soc.* **1991**, *113*, 2954–2965.

(297) Maini, L.; Braga, D.; Mazzeo, P. P.; Ventura, B. *Dalton Trans.* **2011**, *41*, 531–539.

(298) Kubas, G. J.; Monzyk, B.; Crumblis, A. L. In *Inorganic Syntheses*; Angelici, R. J., Ed.; John Wiley & Sons, Inc.: Hoboken, NJ, USA, 1990; Vol. 28, pp 68–70.

(299) Imin, P.; Imit, M.; Adronov, A. *Macromolecules* **2011**, *44*, 9138–9145.

(300) Otwinowski, Z.; Minor, W. In *Methods in Enzymology, Macrocolecular Cyrstallography, Part A*; Carter Jr., C. W., Sweet, R. M., Eds.; 1997; Vol. 276, pp 307–326.

(301) Creutz, C.; Taube, H. *J. Am. Chem. Soc.* **1969**, *91*, 3988–3989.

(302) Creutz, C.; Taube, H. *J. Am. Chem. Soc.* **1973**, *95*, 1086–1094.

(303) Marcus, R. A. *Discuss. Faraday Soc.* **1960**, *29*, 21–31.

(304) Marcus, R. A. *J. Chem. Phys.* **1965**, *43*, 679–701.

(305) Marcus, R. A. *Rev. Mod. Phys.* **1993**, *65*, 599–610.

(306) Wenger, O. S. *Chem. Soc. Rev.* **2012**, *41*, 3772–3779.

(307) Kaim, W. *Coord. Chem. Rev.* **2011**, *255*, 2503–2513.

(308) Kaim, W.; Bruns, W.; Poppe, J.; Kasack, V. *J. Mol. Struct.* **1993**, *292*, 221–228.

(309) Garner, C. D. *J. Chem. Soc. Dalton Trans.* **1997**, No. 21, 3903–3908.

(310) Ward, M. D. *Chem. Soc. Rev.* **1995**, *24*, 121–134.

(311) *Mixed Valency Systems: Applications in Chemistry, Physics and Biology*; Prassides, K., Ed.; Springer Netherlands: Dordrecht, 1991.

(312) Lorkovic, I. M.; Duff, R. R.; Wrighton, M. S. *J. Am. Chem. Soc.* **1995**, *117*, 3617–3618.

(313) Slone, C. S.; Mirkin, C. A.; Yap, G. P. A.; Guzei, I. A.; Rheingold, A. L. *J. Am. Chem. Soc.* **1997**, *119*, 10743–10753.

(314) Gregson, C. K. A.; Gibson, V. C.; Long, N. J.; Marshall, E. L.; Oxford, P. J.; White, A. J. P. *J. Am. Chem. Soc.* **2006**, *128*, 7410–7411.

(315) Broderick, E. M.; Guo, N.; Vogel, C. S.; Xu, C.; Sutter, J.; Miller, J. T.; Meyer, K.; Mehrkhodavandi, P.; Diaconescu, P. L. *J. Am. Chem. Soc.* **2011**, *133*, 9278–9281.

(316) Arumugam, K.; Varnado, C. D.; Sproules, S.; Lynch, V. M.; Bielawski, C. W. *Chem. – Eur. J.* **2013**, *19*, 10866–10875.

(317) Pandey, K. K. *Coord. Chem. Rev.* **1992**, *121*, 1–42.

(318) DeWit, D. G. *Coord. Chem. Rev.* **1996**, *147*, 209–246.

(319) Smith, D. A.; Herbert, D. E.; Walensky, J. R.; Ozerov, O. V. *Organometallics* **2013**, *32*, 2050–2058.

(320) Salem, H.; Shimon, L. J. W.; Leitus, G.; Weiner, L.; Milstein, D. *Organometallics* **2008**, *27*, 2293–2299.

(321) Feller, M.; Ben-Ari, E.; Gupta, T.; Shimon, L. J. W.; Leitus, G.; Diskin-Posner, Y.; Weiner, L.; Milstein, D. *Inorg. Chem.* **2007**, *46*, 10479–10490.

(322) Doux, M.; Mézailles, N.; Ricard, L.; Le Floch, P.; Adkine, P.; Berclaz, T.; Geoffroy, M. *Inorg. Chem.* **2005**, *44*, 1147–1152.

(323) Gerisch, M.; Krumper, J. R.; Bergman, R. G.; Tilley, T. D. *Organometallics* **2003**, *22*, 47–58.

(324) Balzani, V.; Juris, A.; Venturi, M.; Campagna, S.; Serroni, S. *Chem. Rev.* **1996**, *96*, 759–834.

(325) Jaffe, I. *Rev. Inorg. Chem.* **1993**, *13*, 1.

(326) Carson, C. G.; Gerhardt, R. A.; Tannenbaum, R. *J. Phys. Chem. B* **2007**, *111*, 14114–14120.

(327) Chaplin, A. B.; Weller, A. S. *Organometallics* **2011**, *30*, 4466–4469.

(328) Hanson, S. K.; Heinekey, D. M.; Goldberg, K. I. *Organometallics* **2008**, *27*, 1454–1463.

(329) Feller, M.; Iron, M. A.; Shimon, L. J. W.; Diskin-Posner, Y.; Leitus, G.; Milstein, D. *J. Am. Chem. Soc.* **2008**, *130*, 14374–14375.

(330) Adams, G. M.; Chadwick, F. M.; Pike, S. D.; Weller, A. S. *Dalton Trans.* **2015**, *44*, 6340–6342.

(331) Huang, K.-W.; Grills, D. C.; Han, J. H.; Szalda, D. J.; Fujita, E. *Inorganica Chim. Acta* **2008**, *361*, 3327–3331.

(332) Mark D. Doherty, S. J. K. *J. Organomet. Chem.* **2014**, *762*, 94–97.

(333) Denuault, G.; Mirkin, M. V.; Bard, A. J. *J. Electroanal. Chem. Interfacial Electrochem.* **1991**, *308*, 27–38.

(334) Bard, A. J.; Faulkner, L. R. *Electrochemical Methods: Fundamentals and Applications*; Wiley, 2000.

(335) Dixon, F. M.; Masar, M. S.; Doan, P. E.; Farrell, J. R.; Arnold, F. P.; Mirkin, C. A.; Incarvito, C. D.; Zakharov, L. N.; Rheingold, A. L. *Inorg. Chem.* **2003**, *42*, 3245–3255.

(336) Hetterscheid, D. G. H.; de Bruin, B.; Smits, J. M. M.; Gal, A. W. *Organometallics* **2003**, *22*, 3022–3024.

(337) Montag, M.; Schwartsburd, L.; Cohen, R.; Leitus, G.; Ben-David, Y.; Martin, J. M. L.; Milstein, D. *Angew. Chem. Int. Ed.* **2007**, *46*, 1901–1904.

(338) Vigalok, A.; Uzan, O.; Shimon, L. J. W.; Ben-David, Y.; Martin, J. M. L.; Milstein, D. *J. Am. Chem. Soc.* **1998**, *120*, 12539–12544.

(339) Montag, M.; Efremenko, I.; Cohen, R.; Shimon, L. J. W.; Leitus, G.; Diskin-Posner, Y.; Ben-David, Y.; Salem, H.; Martin, J. M. L.; Milstein, D. *Chem. – Eur. J.* **2010**, *16*, 328–353.

(340) Frank, H. A.; Bautista, J. A.; Josue, J.; Pendon, Z.; Hiller, R. G.; Sharples, F. P.; Gosztola, D.; Wasielewski, M. R. *J. Phys. Chem. B* **2000**, *104*, 4569–4577.

(341) Laguitton-Pasquier, H.; Pansu, R.; Chauvet, J.-P.; Collet, A.; Faure, J.; Lapouyade, R. *Chem. Phys.* **1996**, *212*, 437–455.

(342) Holliday, B. J.; Farrell, J. R.; Mirkin, C. A.; Lam, K.-C.; Rheingold, A. L. *J. Am. Chem. Soc.* **1999**, *121*, 6316–6317.

(343) Kaska, W. C.; Nemeh, S.; Shirazi, A.; Potuznik, S. *Organometallics* **1988**, *7*, 13–15.

(344) Moulton, C. J.; Shaw, B. L. *J. Chem. Soc. Dalton Trans.* **1976**, No. 11, 1020–1024.

(345) Doherty, M. D.; Grills, D. C.; Huang, K.-W.; Muckerman, J. T.; Polyansky, D. E.; van Eldik, R.; Fujita, E. *Inorg. Chem.* **2013**, *52*, 4160–4172.

(346) Kresse, G.; Hafner, J. *Phys. Rev. B* **1993**, *47*, 558–561.

(347) Kresse, G.; Hafner, J. *Phys. Rev. B* **1994**, *49*, 14251–14269.

(348) Kresse, G.; Furthmüller, J. *Comput. Mater. Sci.* **1996**, *6*, 15–50.

(349) Kresse, G.; Furthmüller, J. *Phys. Rev. B* **1996**, *54*, 11169–11186.

(350) Blöchl, P. E. *Phys. Rev. B* **1994**, *50*, 17953–17979.

(351) Kresse, G.; Joubert, D. *Phys. Rev. B* **1999**, *59*, 1758–1775.

(352) Perdew, J. P.; Chevary, J. A.; Vosko, S. H.; Jackson, K. A.; Pederson, M. R.; Singh, D. J.; Fiolhais, C. *Phys. Rev. B* **1992**, *46*, 6671–6687.

(353) Perdew, J. P.; Chevary, J. A.; Vosko, S. H.; Jackson, K. A.; Pederson, M. R.; Singh, D. J.; Fiolhais, C. *Phys. Rev. B* **1993**, *48*, 4978–4978.

(354) Perdew, J. P. In *Electronic Structure of Solids '91*; Ziesche, P., Eschrig, H., Eds.; Akademie Verlag: Berlin, 1991; p 11.

(355) Perdew, J. P.; Burke, K.; Wang, Y. *Phys. Rev. B* **1996**, *54*, 16533–16539.

(356) Dobson, J. F.; Vignale, G.; Das, M. P.; Burke, K.; Perdew, J. P.; Wang, Y. In *Electronic Density Functional Theory: Recent Progress and New Directions*; Springer Science & Business Media, 2013.

(357) *Handbook of Oligo- and Polythiophenes*; Fichou, D., Ed.; Wiley-VCH: Weinheim, 1999.

(358) *Handbook of Thiophene-Based Materials*; Perepichka, I. F., Perepichka, D. F., Eds.; John Wiley & Sons, Ltd, 2009.

(359) *Handbook of Thiophene-Based Materials: Applications in Organic Electronics and Photonics*; Perepichka, I. F., Perepichka, D. F., Eds.; John Wiley & Sons Ltd.: West Sussex, U.K., 1999; Vol. I,II.

(360) Beljonne, D.; Cornil, J.; Friend, R. H.; Janssen, R. A. J.; Brédas, J. L. *J. Am. Chem. Soc.* **1996**, *118*, 6453–6461.

(361) Siegert, S.; Vogeler, F.; Marian, C. M.; Weinkauf, R. *Phys. Chem. Chem. Phys.* **2011**, *13*, 10350–10363.

(362) Becker, R. S.; Seixas de Melo, J.; Maçanita, A. L.; Elisei, F. *J. Phys. Chem.* **1996**, *100*, 18683–18695.

(363) Schaffer, H. E.; Heeger, A. J. *Solid State Commun.* **1986**, *59*, 415–421.

(364) Yamaguchi, S.; Hamaguchi, H. *Chem. Phys. Lett.* **1994**, *227*, 255–260.

(365) Sugita, A.; Shiraishi, Y.; Kobayashi, T. *Chem. Phys. Lett.* **1998**, *296*, 365–371.

(366) Weinberg-Wolf, J. R.; McNeil, L. E. *Phys. Rev. B* **2004**, *69*, 125202.

(367) Clarke, T. M.; Gordon, K. C.; Chan, W. S.; Phillips, D. L.; Wagner, P.; Officer, D. L. *ChemPhysChem* **2006**, *7*, 1276–1285.

(368) Yu, W.; Zhou, J.; Bragg, A. E. *J. Phys. Chem. Lett.* **2012**, *3*, 1321–1328.

(369) Yu, W.; Donohoo-Vallett, P. J.; Zhou, J.; Bragg, A. E. *J. Chem. Phys.* **2014**, *141*, 044201.

(370) Köhler, A.; Bässler, H. *Mater. Sci. Eng. R Rep.* **2009**, *66*, 71–109.

(371) Varnavski, O.; Abeyasinghe, N.; Aragó, J.; Serrano-Pérez, J. J.; Ortí, E.; López Navarrete, J. T.; Takimiya, K.; Casanova, D.; Casado, J.; Goodson, T. *J. Phys. Chem. Lett.* **2015**, *6*, 1375–1384.

(372) Swanson, L. S.; Lane, P. A.; Shinar, J.; Yoshino, K.; Wudl, F. *Synth. Met.* **1992**, *50*, 473–480.

(373) Shinar, J.; Swanson, L. S. *Synth. Met.* **1992**, *50*, 621–630.

(374) Bennati, M.; Németh, K.; Surján, P. R.; Mehring, M. *J. Chem. Phys.* **1996**, *105*, 4441–4447.

(375) Monkman, A. P.; Burrows, H. D.; Hamblett, I.; Navarathnam, S.; Svensson, M.; Andersson, M. R. *J. Chem. Phys.* **2001**, *115*, 9046–9049.

(376) Angelella, M.; Wang, C.; Tauber, M. J. *J. Phys. Chem. A* **2013**, *117*, 9196–9204.

(377) Wang, C.; Angelella, M.; Doyle, S. J.; Lytwak, L. A.; Rossky, P. J.; Holliday, B. J.; Tauber, M. J. *J. Phys. Chem. Lett.* **2015**, *6*, 3521–3527.

(378) Hwang, E.; de Silva, K. M. N.; Seevers, C. B.; Li, J.-R.; Garno, J. C.; Nesterov, E. E. *Langmuir* **2008**, *24*, 9700–9706.

(379) Oeter, D.; Egelhaaf, H.-J.; Ziegler, C.; Oelkrug, D.; Göpel, W. *J. Chem. Phys.* **1994**, *101*, 6344–6352.

(380) Chen, T.-A.; Rieke, R. D. *Synth. Met.* **1993**, *60*, 175–177.

(381) Krömer, J.; Bäuerle, P. *Tetrahedron* **2001**, *57*, 3785–3794.

(382) Klug, C.; Sudowe, R. *Sep. Sci. Technol.* **2013**, *48*, 2567–2575.

(383) Kimura, T.; Akatsu, J. *J. Radioanal. Nucl. Chem.* **1991**, *149*, 13–23.

(384) Kimura, T.; Akatsu, J. *J. Radioanal. Nucl. Chem.* **1991**, *149*, 25–34.

(385) Suzuki, T.; Otake, K.; Sato, M.; Ikeda, A.; Aida, M.; Fujii, Y.; Hara, M.; Mitsugashira, T.; Ozawa, M. *J. Radioanal. Nucl. Chem.* **2007**, *272*, 257–262.

(386) Burns, J. D.; Shehee, T. C.; Clearfield, A.; Hobbs, D. T. *Anal. Chem.* **2012**, *84*, 6930–6932.

(387) Burns, J. D.; Borkowski, M.; Clearfield, A.; Reed, D. T. *Radiochim. Acta* **2012**, *100*, 901–906.

(388) Panak, P. J.; Geist, A. *Chem. Rev.* **2013**, *113*, 1199–1236.

(389) Kolarik, Z. *Chem. Rev.* **2008**, *108*, 4208–4252.

(390) Ansari, S. A.; Pathak, P.; Mohapatra, P. K.; Manchanda, V. K. *Chem. Rev.* **2012**, *112*, 1751–1772.

(391) Gorden, A. E. V.; Xu, J.; Raymond, K. N.; Durbin, P. *Chem. Rev.* **2003**, *103*, 4207–4282.

(392) Roncali, J. *Chem. Rev.* **1992**, *92*, 711–738.

(393) Mishra, A.; Ma, C.-Q.; Bäuerle, P. *Chem. Rev.* **2009**, *109*, 1141–1276.

(394) Le Derf, F.; Mazari, M.; Mercier, N.; Levillain, E.; Richomme, P.; Becher, J.; Garín, J.; Orduna, J.; Gorgues, A.; Sallé, M. *Inorg. Chem.* **1999**, *38*, 6096–6100.

(395) Sharova, E. V.; Artyushin, O. I.; Turanov, A. N.; Karandashev, V. K.; Meshkova, S. B.; Topilova, Z. M.; Odinets, I. L. *Cent. Eur. J. Chem.* **2012**, *10*, 146–156.

(396) Reilly, S. D.; Gaunt, A. J.; Scott, B. L.; Modolo, G.; Iqbal, M.; Verboom, W.; Sarsfield, M. J. *Chem. Commun.* **2012**, *48*, 9732–9734.

(397) Simone, D. L.; Swager, T. M. *J. Am. Chem. Soc.* **2000**, *122*, 9300–9301.

(398) Kloosterman, J. L.; Li, J. M. In *International Conference on Evaluation of Emerging Nuclear Fuel Cycle Systems; Versailles (France)*; 1995.

(399) Seaborg, G. T. *Radiochim. Acta* **1993**, *61*, 115–122.

(400) Zhu, S. S.; Swager, T. M. *J. Am. Chem. Soc.* **1997**, *119*, 12568–12577.

(401) Kiełbasiński, P.; Mikołajczyk, M. *Synthesis* **1995**, *1995*, 144–146.

(402) Arnaud-Neu, F.; Böhmer, V.; Dozol, J.-F.; Grüttner, C.; Jakobi, R. A.; Kraft, D.; Mauprivez, O.; Rouquette, H.; Schwing-Weill, M.-J.; Simon, N.; Vogt, W. *J. Chem. Soc. Perkin Trans. 2* **1996**, 1175–1182.